Single electron transfer oxidation of bis-catecholato silicates for the formation of alkyl and aryl radicals. Computational study of palmitic acid interactions with various types of cyclodextrins

Hengrui Zhang

Sorbonne Université

Ecole doctorale de Chimie Moléculaire de Paris-Centre – ED406

Institut Parisien de Chimie Moléculaire / Equipe Méthodes et Applications en Chimie Organique

Single electron transfer oxidation of bis-catecholato silicates for the formation of alkyl and aryl radicals. Computational study of palmitic acid interactions with various types of cyclodextrins.

Par Hengrui ZHANG

Thèse de doctorat de Chimie Moléculaire

Dirigée par Dr Cyril OLLIVIER,
Pr Louis FENSTERBANK et Dr Etienne DERAT

Présentée et soutenue publiquement le 19/11/2021

Devant un jury composé de :

Dr Henri DOUCET, *Directeur de Recherche CNRS à l'Université de Rennes 1*	Rapporteur
Pr Vincent GANDON, *Professeur à l'Université Paris-Saclay*	Rapporteur
Dr Kawthar BOUCHEMAL, *Maître de Conférences à l'Université Paris-Saclay*	Examinatrice
Dr Yongming ZHANG, *Directeur de Recherche CNRS à Sorbonne Université*	Examinateur
Dr Etienne DERAT, *Maître de conférences à Sorbonne Université*	Examinateur
Dr Cyril OLLIVIER, *Directeur de Recherche CNRS à Sorbonne Université*	Examinateur

Don't regret about your past as it's useless, but prevent the same mistakes in the future.

Acknowledgments

This work was carried out in the laboratory “Méthodes et Applications en Chimie Organique (MACO)” at Institut Parisien de Chimie Moléculaire (IPCM), Sorbonne Université, from October 2017 to October 2021, under the supervision of Dr. Cyril Ollivier, Prof. Louis Fensterbank, and Dr. Etienne Derat.

First and foremost, I would like to express my gratitude to the members of the jury for agreeing to serve as reviewers for this thesis: Dr Henri Doucet from Université de Rennes 1, Prof Vincent Gandon from Université de Paris-Saclay, and Dr Yongming Zhang from Sorbonne Université.

I am truly grateful to my gratitude to my supervisor, Dr. Cyril Ollivier. He has a broad understanding of radical chemistry and photocatalysis, and he offers me valuable informations and guidance. I enjoy discussing mechanisms with him since he always gives me expert advice on my concerns. Also, his gentleness and enthusiasm usually make me feel calm and energized. I would like to say thanks for his patience in teaching experimental procedures and correcting my thesis.

I would like to thank Prof. Louis Fensterbank, my co-advisor, for offering me a chance to pursue my Ph.D. in the MACO group and for his kindhearted attention and outstanding supervision throughout the previous four years of my study and research. On our road to pursue science, he reminds me to think about a problem more comprehensively and deeply. He has a broad knowledge base and works efficiently and diligently. His open conversation, appropriate criticism, frequent support, and surprising humor accompanied this four-year study life.

I want to say thanks to Dr. Etienne Derat, my co-advisor, and the computational chemist, for his guidance and supports in my calculations. I would like to thank him for his patience in teaching me how to calculate. I indeed appreciate his patience and ability to cheer me up, even when my calculation is less than ideal; his support drives me to reach my goal. I would like to say thanks for correcting my thesis

I would like to thanks Dr. Olivier Jackowski, Dr. Tahar Ayad, and Dr. Yongmin Zhang, members of my "comité de suivi," for their advice to my study.

I would like to say merci to the MACO team. Dr. Corinne Aubert, Dr. Gilles Lemière, Dr. Marc Petit, Dr. Marion Barbazanges and Dr. Clément Chauvier for their kindness.

I also would like to express my sincere gratitude to all of my present and past MACO colleagues. Etienne, the friendly guy, inspires me with his hard work and optimism. Thanks to Christophe, the nice and responsible guy, I still remember how he taught me to synthesize the Iridium photocatalyst and copper catalysts, and I followed his process and suggestions, and it worked. Thanks to Valérie (Vava) for her warmth and generosity and for her ability to communicate in a variety of languages, including French, English, Spanish, Chinese, Japanese, and maybe more... Thanks for her assistance when I have questions about French. Thanks to Alexandre P. for his kindness and great sense of humor. Thanks also to Mehdi, Thomas, Maud, Cassandre, Khaoula, and Alexandre.P...

Also, I would like to express my gratitude to my Chinese colleagues, Fen, Xueyan, Yufeng, Ye, and Zhonghua, who bring me pleasure and companionship. It is precious!

Last but not least, I am deeply grateful to my parents for their love, understanding, and support in all of my endeavors. I am very grateful to my girlfriend, Jie Huang, for always encouraging me and making sacrifices for me. Her love and support have always been a source of immense strength for me. Without them, I would not have been able to accomplish my Ph.D. This thesis is dedicated to them.

Hengrui ZHANG

September 27, 2021

Table of Contents

Abbreviations

°C	degree Celsius
Ac	acetyl
Ar	aryl
aq.	aqueous
Bz	benzoyl
Bn	benzyl
Cy	cyclohexyl
CD	cyclodextrin
cat.	catalyst
DFT	density functional theory
eq./equiv.	equivalent
ESI	electrospray ionization
Et	ethyl
HOMO	highest occupied molecular orbital
HRMS	high-resolution mass spectrometry
i-Pr	iso-propyl
IR	infrared
Ir	iridium
J	coupling constant
L	ligand
LUMO	lowest occupied molecular orbital
m	*meta*
M	molar (mol/L)
m.p.	melting point
Me	methyl
MHz	mega hertz
mw	molecular weight
NMR	nuclear magnetic resonance
Nu	nucleophile
o	*ortho*

p	*para*
Ph	phenyl
rt	room temperature
SET	single electron transfer

Résumé en français

La lumière visible pourrait être considérée comme une sorte d'énergie verte. En 1912, le chimiste italien Ciamician, pionnier de la photochimie organique, a imaginé le développement futur de l'énergie solaire pour la synthèse.[1]

Bien que les gens reconnaissent généralement les avantages économiques et écologiques potentiels de la photochimie, la photochimie dans l'industrie est encore très limitée. L'une des raisons est que la plupart des molécules organiques ne peuvent pas absorber la lumière visible. La plupart des synthèses photochimiques nécessitent une lumière ultraviolette. De plus, dans la composition de la lumière solaire, les ultraviolets représentent moins de 3%. Si la lumière visible est utilisée directement, l'efficacité de la réaction sera considérablement réduite. En outre, certaines réactions photochimiques organiques sont généralement réalisées dans de petits réacteurs spécialement conçus pour produire de la lumière ultraviolette à haute énergie. Le coût de conception et d'installation de grands photoréacteurs dédiés à la synthèse industrielle est très élevé. Dès les années 1950 et 1960, David M. Hercules[2] et D. M. Klassen ont[3] remarqué que l'utilisation de complexes de métaux de transition tris(2,2'-bipyridine) ruthénium (II) représentés par $Ru(bpy)_3^{2+}$ pouvait être excitée sous irradiation de lumière visible, et qu'une réaction de transfert monoélectronique pouvait se produire. Au cours des trente années suivantes, les études ont principalement porté sur les propriétés photophysiques, photochimiques et électrochimiques du $Ru(bpy)_3^{2+}$. Cependant, son implication dans les transformations organiques a été rarement rapportée, et son développement a été lent.

En général, les catalyseurs photoredox qui ont été utilisés en synthèse organique peuvent être divisés en deux catégories principales. La première est celle des catalyseurs photoredox à base de métaux de transition, comme Ru(Ⅱ), Ir(Ⅲ) ou d'autres complexes centrés sur les métaux de transition. L'autre est le photocatalyseur organique non métallique tel que les colorants fluorescents organiques. Les exemples les plus représentatifs sont l'éosine Y, le bleu de méthylène et la fluorescéine.

[1] G. Ciamician, *Science*. **1912**, *36*, 385–394.

[2] F. E. Lytle, D. M. Hercules, *J. Am. Chem. Soc.* **1969**, *91*, 253–257.

[3] D. M. Klassen, G. A. Crosby, *J. Chem. Phys.* **1968**, *48*, 1853–1858..

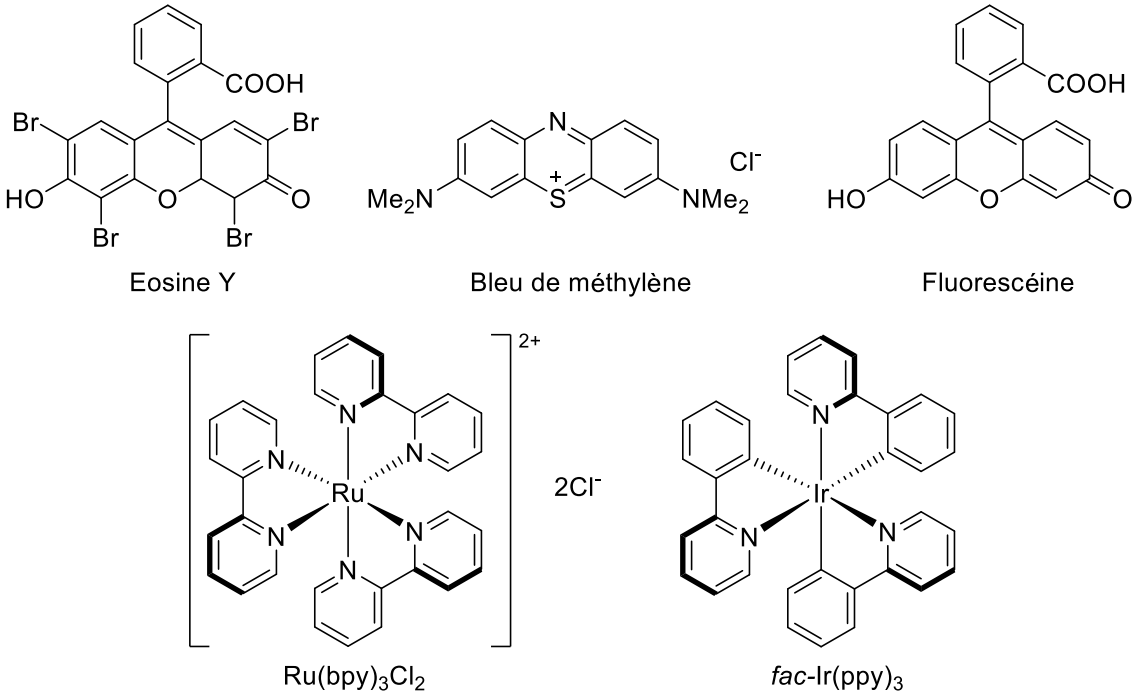

Schéma R-1. Exemples représentatifs de photocatalyseurs organiques non métalliques et de photocatalyseurs à base de complexes de métaux de transition

Comme indiqué précédemment, le catalyseur photoexcité (PC*) peut transférer un électron aux substrats, générant ainsi des radicaux capables de participer à des réactions radicalaires. Pour catalyser l'ensemble du processus, le catalyseur photoredox ($PC^{+/-}$) doit effectuer une autre SET avec un intermédiaire ou un additif. Lorsque le catalyseur photoredox réduit le substrat, le processus est appelé photoréduction ; lorsque le substrat est oxydé, le processus est appelé photooxydation.

Plus précisément, après avoir absorbé le photon, le catalyseur photoredox excité (PC*) interagit ensuite avec un "quencher réducteur" ou agent d'extinction réducteur pour former le photocatalyseur réduit PC^-. Le catalyseur photoredox modifié transfère ensuite ses électrons supplémentaires à l'accepteur d'électrons A. Ce processus permet de régénérer le catalyseur photoredox initial et de conclure le "cycle d'extinction réductif". Le terme "cycle d'extinction oxydatif" fait référence à la réaction entre le PC* et un accepteur d'électrons A qui sert de « quencheur oxydatif » ou ou agent d'extinction oxydatif. Le catalyseur photoredox oxydé PC^+ est ensuite régénéré en réagissant avec un donneur D.

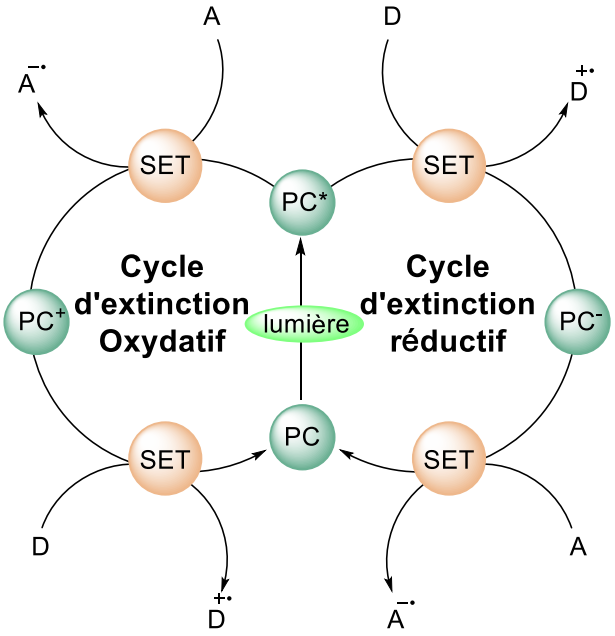

Schéma R-2. Cycles d'extinction oxydatif et réducteur dans la catalyse photoredox

La photoréduction ou la photooxydation peuvent être utilisées pour produire les radicaux qui ont été utilisés dans diverses méthodes de synthèse. Dans le cas de la photoréduction, le catalyseur photoexcité réduit directement un accepteur dans cet exemple si les potentiels redox sont compatibles. Cependant, il arrive que le potentiel redox du catalyseur photoréduit soit insuffisant pour réduire l'accepteur d'électrons. Un donneur d'électrons approprié, comme les amines organiques et les esters de Hantzsch, réagirait d'abord avec le photocatalyseur excité PC* pour produire le photocatalyseur réduit PC^- et donner un réducteur plus efficace capable de réduire le substrat. La photooxydation est une réaction dans laquelle un catalyseur photoexcité oxyde immédiatement un donneur de radicaux. Comme indiqué précédemment, comme dans le cas de la photoréduction, si le PC* n'est pas suffisamment oxydant, l'accepteur d'électrons supplémentaire tel que le dioxygène, le méthylviologène et le persulfate peut être considéré comme un choix alternatif pour réagir avec le PC* et obtenir ainsi le photocatalyseur oxydé PC+ qui a une capacité d'oxydation beaucoup plus grande.

Les bis-catécholatosilicates d'alkyle ont récemment suscité un vif intérêt dans le domaine de la catalyse photooxydante en tant que précieux précurseurs de radicaux alkyle dans les réactions d'addition radicalaire, les réactions radical-polaire ainsi que les couplages croisés photoredox-nickel. En revanche, les silicates d'aryle ont été beaucoup moins utilisés. Leur principale utilisation a été developpée par DeShong dans des réactions de couplage croisé catalysées par le palladium avec des halogénures d'aryle (schéma 1, éq. 1) et par Hashmi pour

des réactions de couplage croisé avec des sels d'aryldiazonium par catalyse à l'or(I) (schéma 1, éq. 2).

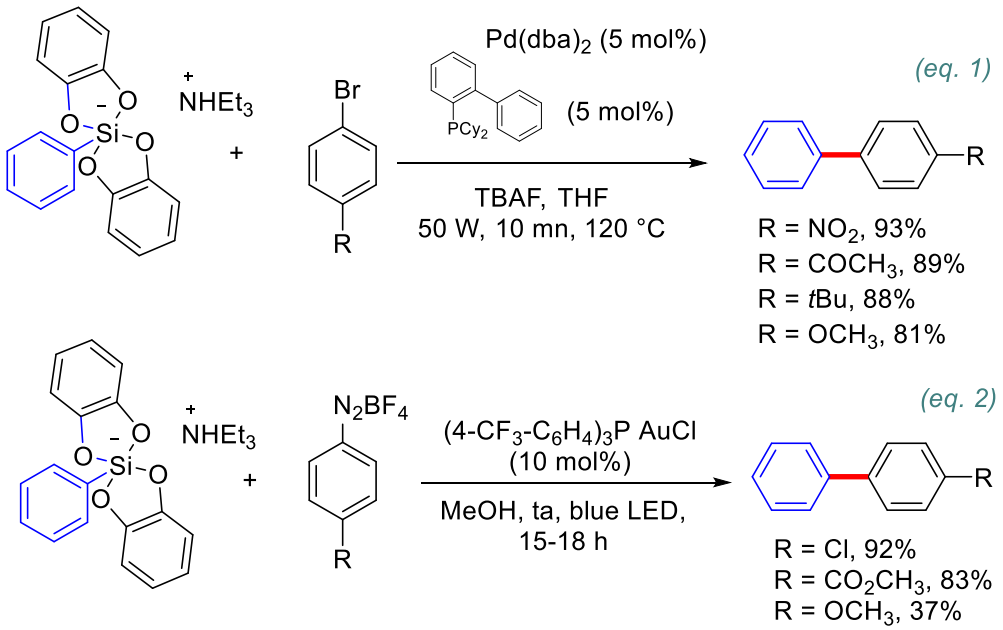

Scheme R-3. Utilisation de silicates d'aryle pour des réactions de couplage croisé sp^2-sp^2

La photooxydation des arylsilicates serait intéressante pour deux raisons. Premièrement, la génération de radicaux aryles par catalyse photoredox est bien documentée dans des conditions photoréductives à partir d'une variété de précurseurs tels que les aryldiazoniums, les iodoniums, les sulfoniums, les arylhalogénures et également les hypohalites de benzoyle (Schéma 2). En revanche, et à notre connaissance, une seule étude complète a été publiée récemment par le groupe Yoshimi dans des conditions photooxydantes avec des carboxylates d'aryle. Jusqu'à 150 % molaire de biphényle (BP)/1,4-dicyanonaphtalène (DCN) comme mélange photocatalytique a dû être utilisé sous irradiation UV pour obtenir des rendements modérés (~50%) de produits d'addition de radicaux aryles. A noter également, à l'occasion d'une étude très récente de Morofuji et Kano consacrée à la photooxydation d'alkylsilicates portant le ligand dianion de l'alcool hexafluorocumyle (ligand de Martin), un seul exemple d'oxydation du phénylsillicate correspondant a donné 10% d'adduit de type Giese à partir du radical phényle. Ceci souligne le fait que la génération de radicaux aryles dans des conditions photooxydantes est très difficile.

Deuxièmement, une nouvelle classe de dérivés de silicates de phényle pourrait ouvrir de nouvelles perspectives en termes de réactivité, soit dans les réactions d'addition radicalaire, soit en catalyse duale.

Cette étude visait à déterminer l'influence de la substitution des ligands catéchol dans leur capacité à favoriser la génération de radicaux aryles. Nous avons donc entrepris la synthèse de différents silicates de phényle et étudié leurs caractéristiques structurales et leur réactivité.

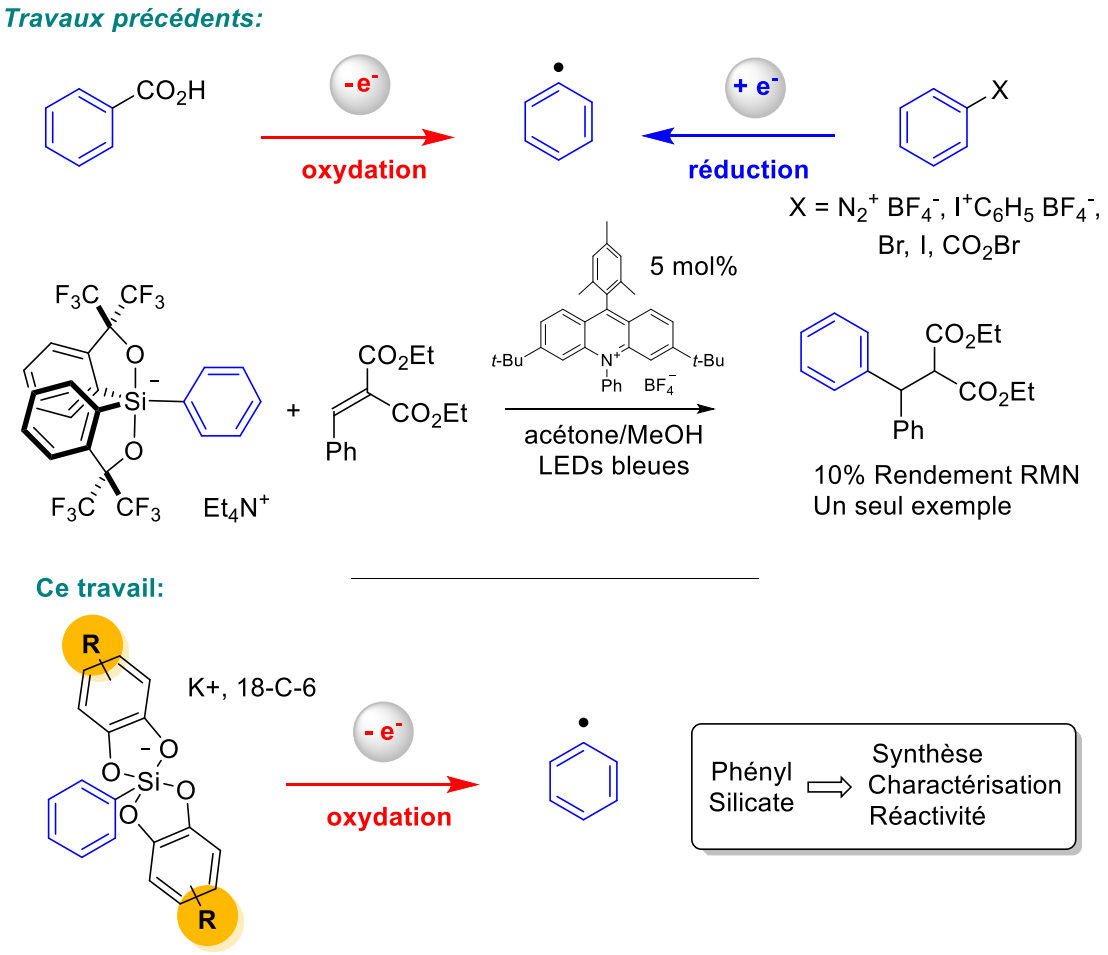

Scheme R-4. Génération de radicaux aryles dans des conditions photocatalytiques

Nous nous sommes tout d'abord intéressés à la réactivité du terme le plus simple, le phényl bis-catécholatosilicate **1a**. Il a été synthétisé sur la base d'un protocole précédemment rapporté en utilisant du catéchol (2 équiv), du 18-C-6 (1 équiv), du MeOK (1 équiv) et du phényltriméthoxysilane (1 équiv). Le silicate **1a** a été obtenu avec un rendement satisfaisant de 87% (temps de réaction : 2 h à température ambiante, solvant de cristallisation : acétone/Et_2O). Son potentiel d'oxydation de demi-vague dans le DMF a été mesuré par voltamétrie cyclique et la valeur observée ($E_{1/2}^{ox}$ = + 0,89 V vs SCE) a été comparée au potentiel de réduction du photocatalyseur [Ir(dF(CF_3)ppy)$_2$(bpy)]PF_6 (**3**) dans son état excité (E^{red}(Ir(III)*/Ir(II) = + 1,32 V vs SCE). Ces données suggèrent que le silicate **1a** pourrait être oxydé par ce photocatalyseur sous irradiation. Néanmoins, toutes les tentatives de générer un

radical phényle avec le photocatalyseur **3** et de le piéger avec l'allylsulfone **2** ont rencontré un succès limité. Le produit d'allylation **4** a été observé avec un rendement de seulement 5 %. Ce résultat a semblé surprenant car une extinction efficace de la phosphorescence de **3** avec **1a** a été observée. En effet, la constante de vitesse d'extinction (kq) a été déterminée par une analyse de Stern-Volmer et s'est avérée être kq = 5,7 x 10^8 mol^{-1} L s^{-1} (en comparaison avec kq = 7,9 x 10^9 mol^{-1} L s^{-1} pour le silicate de benzyle). Afin de vérifier si ce faible rendement était dû à l'instabilité de **1a**, des expériences de RMN ^{29}Si ont été réalisées avant et après réaction avec l'accepteur **2**. Après 24 heures d'irradiation par une LED bleue (λ_{max} = 450 nm) dans du DMF-d7, seul le **1a** sous forme de dérivé de silicium a pu être détecté dans le mélange et aucune dégradation évidente n'a également été mise en évidence par RMN ^{1}H (Figure 1).

De plus, lorsqu'un mélange équimolaire de **1a** et **3** a été irradié sous une LED bleue dans du THF deutéré comme solvant, la formation de C_6H_5D **5** a pu être observée par RMN ^{1}H (^{1}H 7,29 ppm dans THF-d8) et quantifiée par RMN ^{2}H (^{2}H 7,35 ppm dans THF-d8) pour un rendement RMN de 21 % (voir le schéma 3).

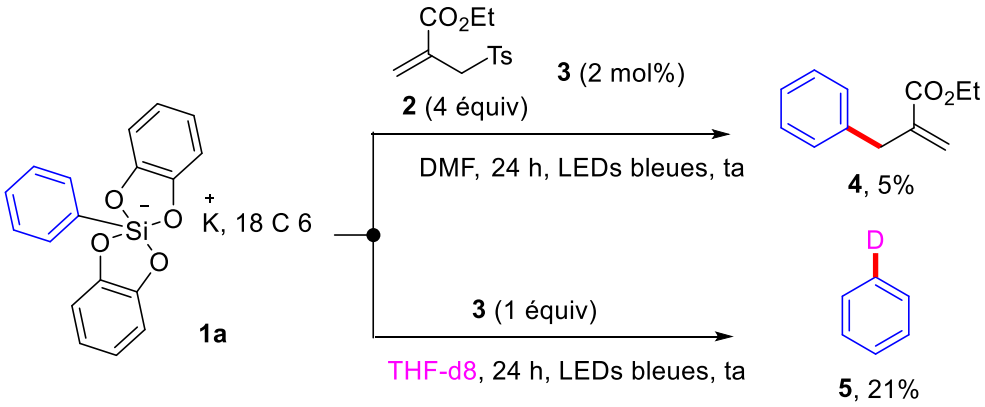

Schéma R-5. Photooxydation du silicate de phényle **1a** et piégeage du radical phényle

L'ensemble de ces résultats suggère un processus d'oxydation inefficace du 1a. Compte tenu des potentiels redox favorables et de l'extinction efficace de la luminescence (voir ci-dessus), cette faible réactivité de **1a** a éveillé notre curiosité et nous a conduit à étudier le rôle des substituants sur la partie catéchol et leur effet potentiel sur la réactivité des silicates de phényle correspondants.

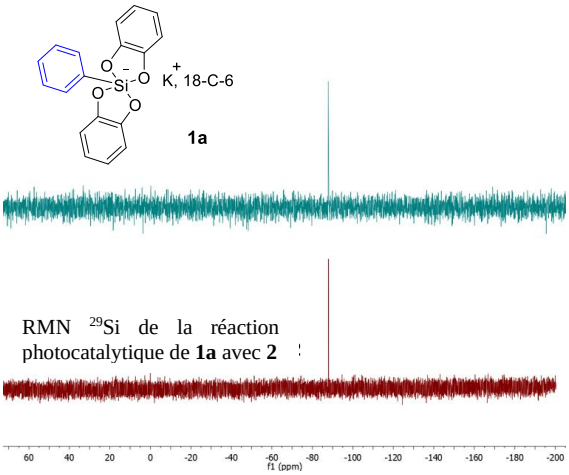

Figure R-1. Suivi par RMN ^{29}Si de la réaction photocatalytique de **1a** avec **2** dans du DMF-d7.

Dans un premier temps, nous avons d'abord testé l'effet de substitution exercé par les catéchols sur le substrat très réactif cyclohexyl bis-catecholatosilicate. Nous avons notamment voulu vérifier que la formation du radical cyclohexyle était toujours possible. Sur la base de la procédure précédemment décrite, en utilisant le cyclohexyl-triméthoxysilane, le MeOK, le 18-C-6 et des catéchols avec divers schémas de substitution (groupes donneurs ou attracteurs d'électrons), les cyclohexylsilicates **6a-6d** ont été obtenus après cristallisation dans l'acétone/Et_2O (**Schéma R-6**).

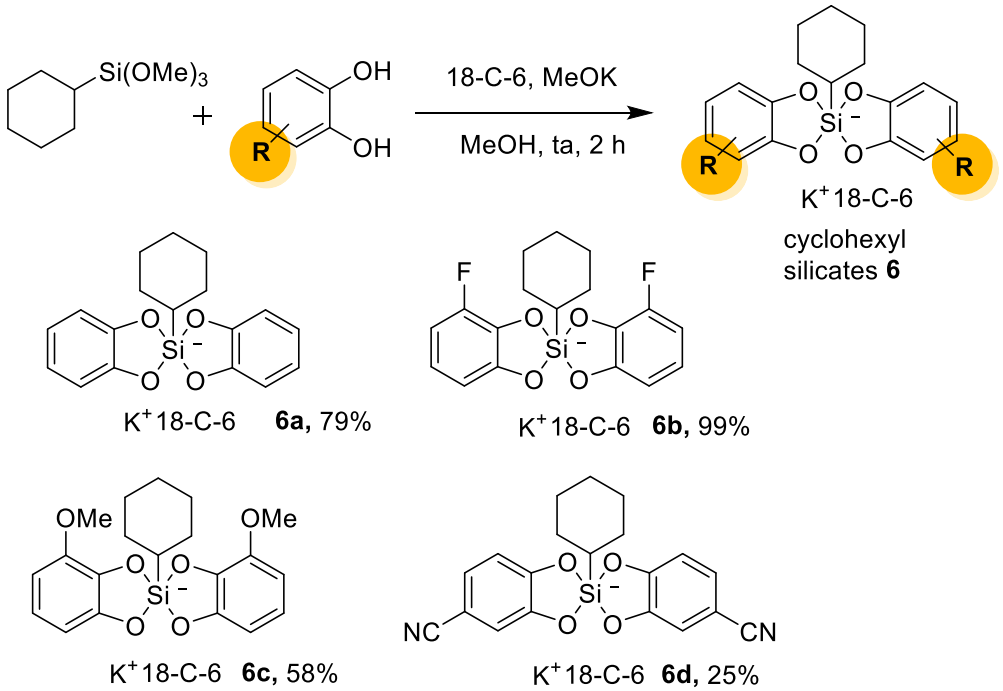

Schéma R-6. Synthèse de silicates de cyclohexyle **6** portant des catéchols différemment

substitués

Après traitement avec le photocatalyseur **3** et l'allylsulfone **2** sous irradiation par des LEDs bleues, les silicates **6b** ($E_{1/2}^{ox}$ = + 0,91 V *vs* SCE (Tous les potentiels donnés sont référencés par rapport à SCE) et **6d** ($E_{1/2}^{ox}$ = + 1,01 V), portant des groupes attracteurs d'électrons, ont donné le produit d'allylation radicalaire correspondant **7**, mais avec des rendements légèrement inférieurs (77% et 60% respectivement) à ceux du silicate ordinaire **6a** ($E_{1/2}^{ox}$ = + 0,69 V, 88% de **7**) (**Tableau 1**). Il est intéressant de noter qu'un groupe donneur d'électrons tel qu'un méthoxy sur les catéchols (**6c**) a considérablement diminué le rendement de cette réaction et que la plupart du produit de départ a été récupéré. Compte tenu du potentiel d'oxydation plus faible de **6c** ($E_{ox}^{1/2}$ = + 0,63 V), ce résultat semble contradictoire mais a été corroboré par les calculs DFT (*vide infra*).

Tableau R-1. Génération du radical cyclohexyle à partir des silicates de cyclohexyle **6** piégés par réaction d'allylation

Silicate de cyclohexyle **6**	Rendement de **7** (en %)[a]
6a	88
6b	77
6c	14
6d	60

a Rendement RMN ^{1}H de **7** en utilisant le 1,3,5 triméthoxybenzène comme étalon interne

Encouragés par ces résultats montrant que la substitution par un catéchol peut moduler la réactivité des silicates correspondants mais n'empêche pas le processus de photooxydation, nous avons préparé une bibliothèque de silicates de phényle avec des catéchols mono- et polysubstitués.

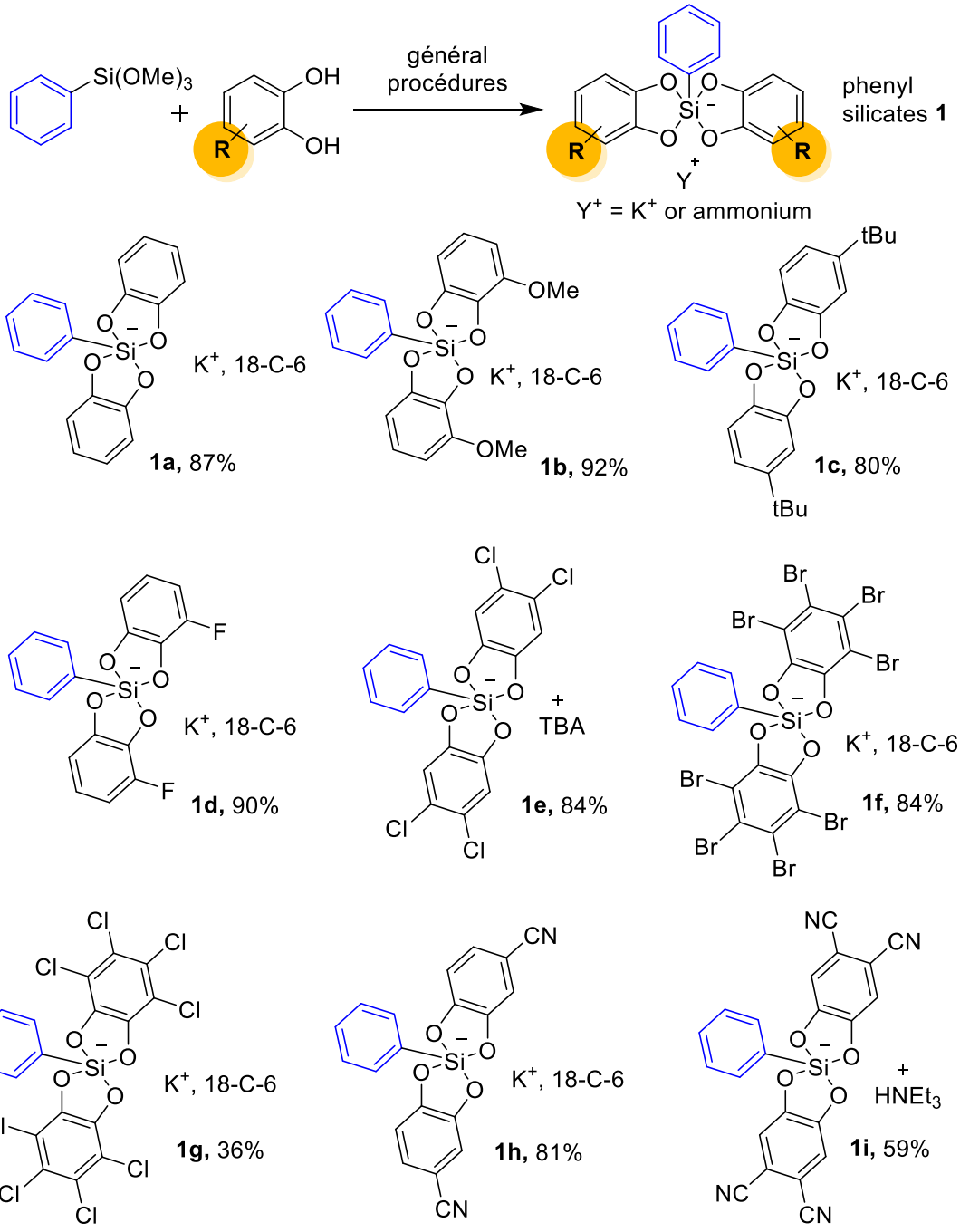

Schéma R-7. Préparation de silicates de phényle **1** portant des catéchols substitués

En utilisant la même procédure que ci-dessus avec le catéchol approprié, la plupart des silicates **1** ont été préparés efficacement (rendement > 80 %) sous forme cristalline adaptée à l'analyse par diffraction des rayons X (**Figure R-2**). Ainsi, les silicates **1**b, **1**d et **1**h portant des groupes donneurs d'électrons (MeO) et attracteurs d'électrons (F, CN) respectivement ont été

analysés par XRD (**Figure R−2**). [4]

Ces trois structures cristallines présentent des silicates dans lesquels le centre du siliciumadopte une géométrie pyramidale carré, assez similaire à celle de **1a**. En effet, les caractéristiques électroniques du catéchol ne semblent pas avoir beaucoup d'impact sur l'environnement de l'atome de silicium. **1b** et **1h** montrent une interaction marquée entre le silicate et le potassium avec des distances K-O allant de 2,7 à 3,0 Å, similaires aux structures de silicates hypervalents de potassium publiées précédemment. [29a] Seule la structure **1d** présente des interactions plus faibles. Alors que les unités asymétriques de **1b** et **1h** ne contiennent qu'un seul silicate discret, le silicate **1d** présente un désordre statistique des atomes de fluor qui suggère la présence d'isomères *cis* et *trans* mais dans des proportions indéterminées (voir SI pour plus de détails).

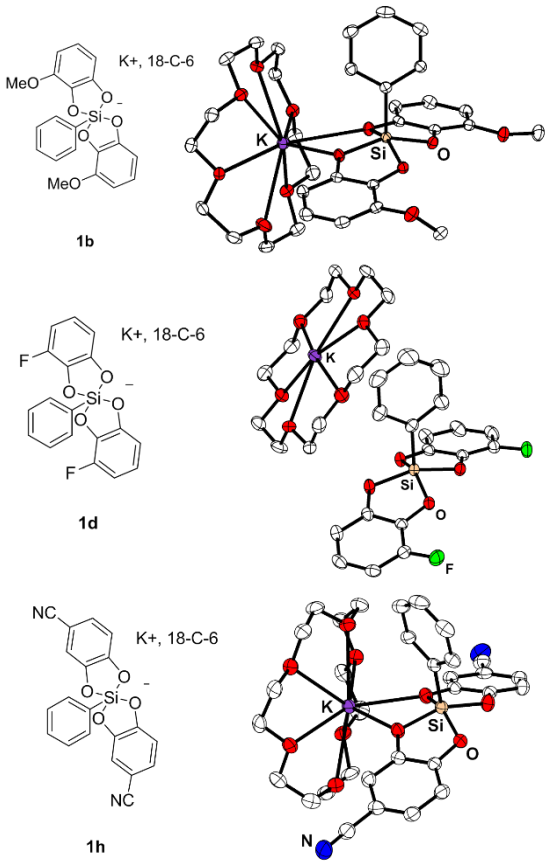

Figure R-2. Analyses XRD des silicates **1b**, **1d** et **1h**. Seul l'isomère *cis* de **1d** est représenté et les hydrogènes sont omis pour plus de clarté. Ce travail a été réalisé par le Dr. Etienne Levernier.

[4] Les numéros de dépôt 2009048 (pour **1b**), 2009049 (pour **1h**) et 2009050 (pour **1d**) contiennent les données cristallographiques supplémentaires pour cet article. Ces données sont fournies gratuitement par le service conjoint du Cambridge Crystallographic Data Centre et du Fachinformationszentrum Karlsruhe Access Structures www.ccdc.cam.ac.uk/structures.

La présence de deux isomères a également été confirmée par RMN ^{13}C. Toutes les résonances des groupements catéchol non symétriques en RMN ^{13}C ont été doublées avec une intégration identique pour les deux espèces dans le cas de **1d**, mais aussi pour les autres phénylsilicates non symétriques **1b**, **1c**, **1h**. Il faut mentionner que ce type de mélange 1:1 de deux isomères a également été observé dans la série cyclohexyle (silicates **6b-6d**).

Intrigués par ce résultat, nous nous sommes demandés si un équilibre existe entre les isomères *cis* et *trans* en solution. Pour répondre à cette question, la RMN ^{13}C de **1h** à différentes températures a été réalisée (dans l'acétone-d6 à basse température (en dessous de 273 K) et dans le DMSO-d6 à plus haute température (à partir de 303 K), **Figure R-3**).

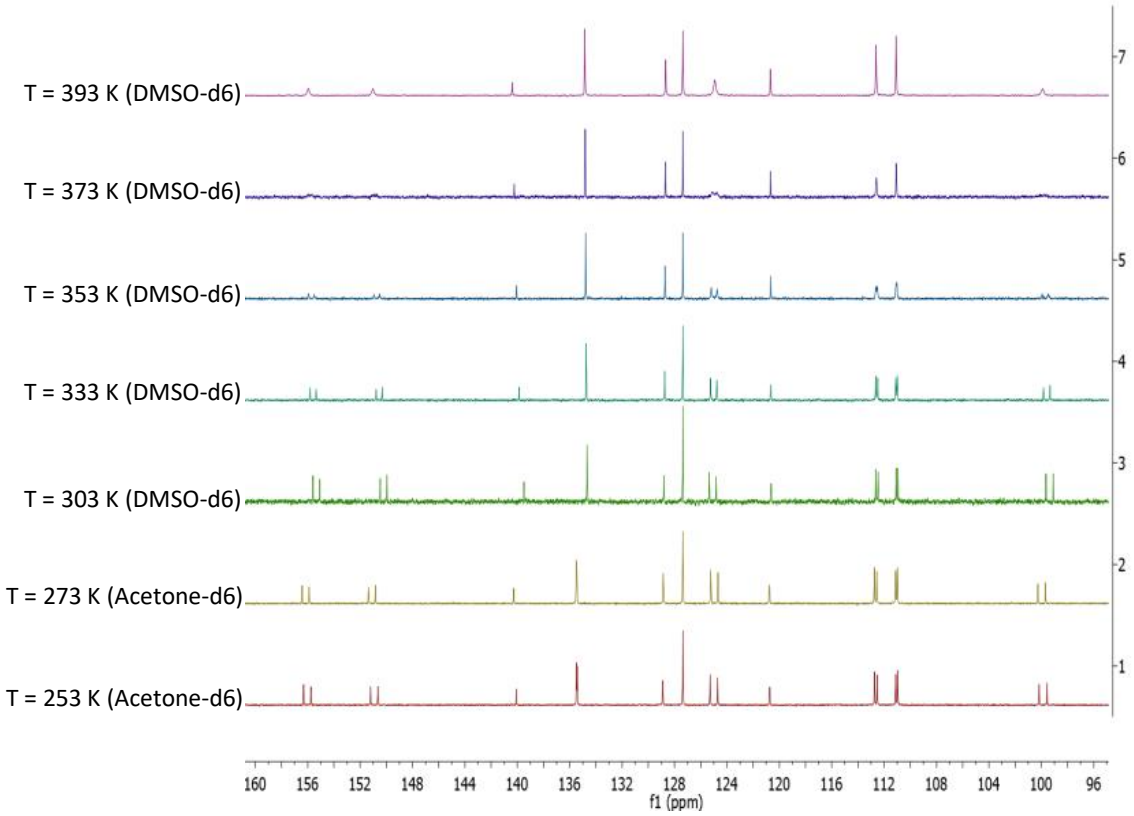

Figure R-3. RMN ^{13C} du silicate **1h** à différentes températures

Une coalescence des pics a été observée au-dessus de 333 K, probablement due à la pseudo-rotation de Berry[5], suggérant qu'un équilibre existe entre les deux isomères. Les calculs DFT ont également indiqué que l'écart énergétique entre les formes *cis* et *trans* pour **1b** est de 3,3

[5] a) A. R. Bassindale, M. Sohail, P. G. Taylor, A. A. Korlyukov, D. E. Arkhipov, *Chem. Commun.* **2010**, *46*, 3274-3276, b) D. Kost, I. Kalikhman, *Acc. Chem. Res.* **2009**, *42*, 303-314.

kcal/mol en faveur de la forme *cis*. Pour **1h**, la forme *trans* est légèrement favorisée de 0,6 kcal/mol.

Après avoir étudié les caractéristiques structurelles de ces nouveaux dérivés du silicium, nous avons examiné d'autres propriétés clés. Tout d'abord, des spectres d'absorption UV-vis ont été enregistrés. Tous les silicates **1** présentaient une bande d'absorption unique s'étendant de 276 nm pour le **1d** à 303 nm pour le **1g**. Il est important de noter que, quel que soit le schéma de substitution, aucune absorption notable n'a été observée dans la gamme de longueurs d'onde de la LED bleue, précédemment utilisée pour la photooxydation des silicates d'alkyle (de 400 à 520 nm) (voir la **Figure R-4** et les informations complémentaires pour plus de détails et de données UV).

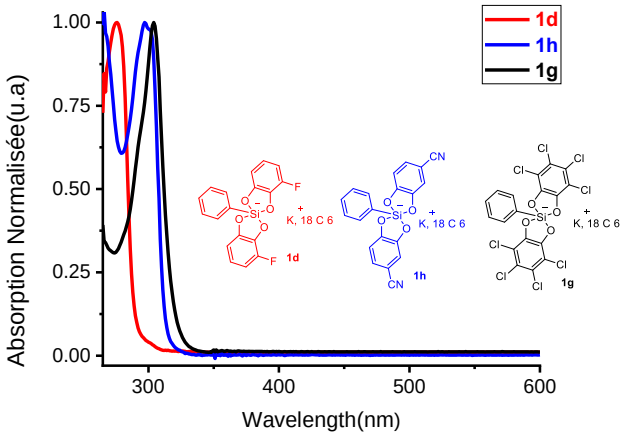

Figure R-4. Spectres d'absorption des silicates **1d**, **1h** et **1g.** Ce travail a été réalisé par le Dr. Etienne Levernier.

Ensuite, les potentiels d'oxydation des silicates **1a-i** ont été mesurés dans le DMF comme indiqué dans le tableau 2.

Tableau R-2. Potentiels d'oxydation en demi-onde des silicates 1a-i

Silicate 1	$E_{ox}^{1/2}$ (vs SCE ds DMF)	Silicate 1	$E_{ox}^{1/2}$ (vs SCE ds DMF)
1a	+ 0.89 V	**1f**	+ 1.46 V
1b	+ 0.81 V	**1g**	+ 1.37 V
1c	+ 1.09 V	**1h**	+ 1.33 V
1d	+ 1.05 V	**1i**	+1.62 V
1e	+ 1.13 V		

Il est intéressant de noter que les modifications du catéchol ont entraîné des variations importantes des potentiels d'oxydation, de $E_{1/2}^{ox}$ = + 0,81 V pour 1b à $E_{1/2}^{ox}$ = + 1,62 V pour 1i avec $E_{1/2}^{ox}$ = + 0,89 V pour le phénylsilicate non substitué 1a. Ainsi, un groupe donneur sur les catéchols comme pour 1b s'est avéré diminuer logiquement le potentiel d'oxydation tandis que les groupes attracteurs d'électrons ont augmenté significativement les valeurs au-dessus de + 1,0 V ($E_{1/2}^{ox}$= + 1,05 V pour 1d). Des potentiels d'oxydation plus élevés ont même pu être atteints en utilisant le per-bromocatéchol ou en ajoutant deux groupes cyano ($E_{1/2}^{ox}$ (1f) = + 1,46 V et $E_{1/2}^{ox}$ (1f) = + 1,62 V). Même si l'oxydation de 1f et 1i par le photoactivé 3 [Ir(dF(CF3)ppy)2-(bpy)]PF6 (E^{red}(Ir(III)*/Ir(II) = + 1.32 V) semblait difficile, tous les autres silicates 1 pouvaient potentiellement conduire à la génération du radical phényle. Ainsi, nous avons poursuivi cette étude avec la réaction d'allylation photocatalytique des silicates 1a-i avec l'allylsulfone 2 en présence de 2 mol% de 3. Les résultats sont résumés dans le tableau 3. Bien qu'un rendement < 10% ait été obtenu à partir des silicates 1a-e et 1i, le silicate 1h portant un groupe cyano sur le catéchol a donné 4 avec un rendement de 35%. Les catéchols 1f et 1g per-bromés et per-chlorés ont également fourni le produit souhaité 4 avec des rendements légèrement meilleurs que le silicate 1a (15% et 23% respectivement). Néanmoins, ces rendements sont toujours inférieurs à celui obtenu avec le silicate 1h. Les potentiels d'oxydation plus élevés de 1f et 1g par rapport à 1h pourraient expliquer ce résultat. De plus, comme nous l'avons déjà observé dans le tableau 1 avec les silicates de cyclohexyle, la substitution méthoxy s'est avérée néfaste, entraînant une diminution du rendement. Ainsi, la modification de la partie catéchol s'est avérée moduler la réactivité des silicates de phényle 1 dans la réaction de type allylation photocatalytique.

Tableau R-3. Réaction d'allylation photocatalytique des phénylsilicates1. Ce travail a été réalisé par le Dr. Etienne Levernier.

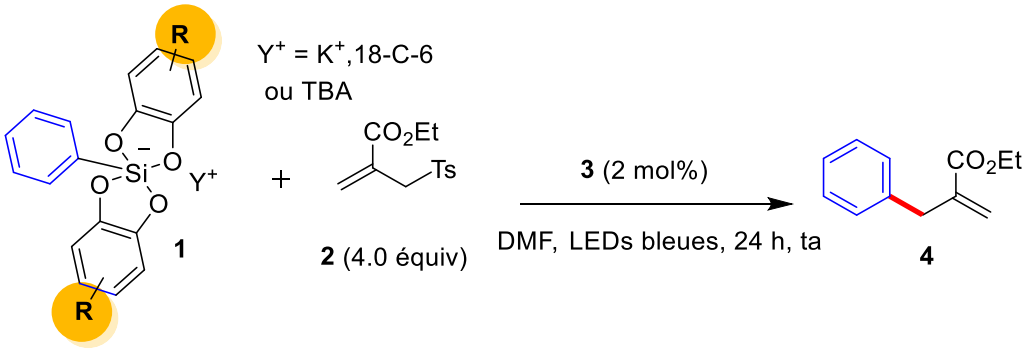

Silicate 1	Rendt 4 (%)[1]	Silicate 1	Rendt 4 (%)[1]
1a	5%	**1f**	15%
1b	9%	**1g**	23%
1c	8%	**1h**	35%
1d	6%	**1i**	7%
1e	6%		

[1] Rendement RMN ^{1}H de **4** en utilisant le 1,3,5 triméthoxybenzène comme standard RMN

Encouragés par ces résultats, nous avons optimisé la réaction du silicate 1h le plus prometteur avec l'accepteur 2 (Tableau 4). L'influence de différents contre-ions (ammoniums et potassium avec et sans 18-C-6, entrées 6, 11 et 12) a été étudiée mais aucune amélioration significative n'a été observée. La température (température ambiante ou 100°C, entrées 5 et 6) n'a pas affecté l'efficacité de la réaction. Le passage à certains photocatalyseurs organiques a entraîné une diminution du rendement (entrées 1, 2 et 3). Même l'acridinium de Fukuzumi, très oxydant (Ered(PC*/PC--) = + 2,06 V vs SCE), n'a pas permis d'obtenir un meilleur rendement pour le composé 4. Ces résultats sont cohérents avec ce qui a été observé précédemment avec les alkylsilicates. Différents solvants (DMF, DMSO, MeCN, EtOH), temps de réaction et concentrations ont également été examinés mais, malgré tous nos efforts, le rendement est resté modeste. Notamment, des temps de réaction prolongés n'ont pas donné lieu à des améliorations significatives (entrée 6 vs entrées 9 et 10). Par conséquent, les meilleures conditions ont été trouvées dans le DMSO avec 3 à température ambiante pendant 24 h (40%, entrée 4). Quelques expériences de contrôle ont également été réalisées. La réaction dans l'obscurité ou dans des conditions sans photocatalyseur n'a donné aucun produit (entrées 7 et 8). Par conséquent, la présence d'un photocatalyseur sous irradiation est obligatoire pour générer le radical phényle.

Tableau R-4. Optimization de la réaction d'allylation. Ce travail a été réalisé par le Dr. Etienne Levernier.

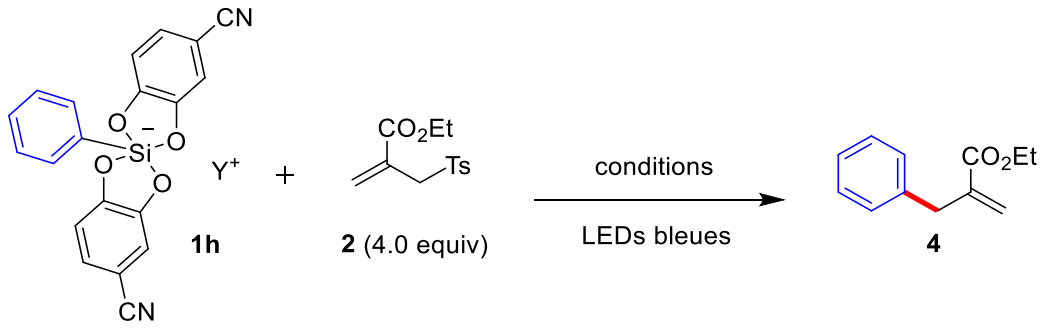

Entrée	Solvant	Température	Photocatalyseur	Temps	Y^+	Rendt 4 (%)[1]
1	DMF	rt	Fukuzumi's acridinium	24 h	K^+/18-C-6	6%
2	DMF	rt	Pyrylium salt[2]	24 h	K^+/18-C-6	7%
3	DMF	rt	4CzIPN	24 h	K^+/18-C-6	7%
4	DMSO	rt	3	24 h	K^+/18-C-6	40%
5	DMF	100°C	3	24 h	K^+/18-C-6	38%
6	DMF	rt	3	24 h	K^+/18-C-6	35%
7	DMF	rt	-	24 h	K^+/18-C-6	0%
8	DMF	rt	3	24 h	K^+/18-C-6	0%[3]
9	DMF	rt	3	68 h	K^+/18-C-6	35%
10	DMF	rt	3	68 h	K^+/18-C-6	41%[4]
11	DMF	rt	3	24 h	K^+/18-C-6	30%
12	DMF	rt	3	24 h	Et_3NH^+	35%
13	CH_3CN	rt	3	24 h	TBA^+	0%
14	EtOH	rt	3	24 h	TBA^+	20%
15	DMSO	rt	3	24 h	TBA^+	35%
16	DMF	rt	3[5]	24 h	K^+/18-C-6	40%

[1] [Silicate] = 0,1 mol.L-1, 3 (2 % en moles), rendement RMN 1H de 4 en utilisant le 1,3,5 triméthoxybenzène comme étalon RMN ; 2 sel tétrafluoroborate de 2,4,6-tri(p-tolyl)pyrylium ; 3 réaction dans l'obscurité ; 4 [Silicate] = 0,2 mol.L-1 ; 5 3 (10 % en moles).

Inspiré par les travaux pionniers de Nishigaichi montrant que les silicates portant des ligands catéchol ou 2,3-hydroxynaphtalène peuvent être photoactivés par irradiation directe, la réaction de photoallylation du silicate 1h a également été testée à 300 nm avec et sans 3 mais le succès a été limité puisque seulement 10% et 6% du produit 4 ont été isolés respectivement. Ainsi, même si ce silicate absorbe la lumière UV-B, l'utilisation de 3 comme photocatalyseur sous irradiation par LED bleue reste plus efficace. Ceci a été corroboré par le fait que

l'extinction de la phosphorescence de 3 avec le silicate 1h a également été observée et grâce à un tracé de Stern-Volmer, une constante d'extinction de 1,31 x 108 mol-1 L s-1 a été obtenue (comparée à 5,7 x 108 mol-1 L s-1 pour le silicate 1a). Ainsi, le silicate 1h n'éteint pas le photocatalyseur d'iridium plus efficacement que le silicate 1a (Figure 5).

L'abstraction de D à partir de THF-d8 deutéré a également été étudiée et a conduit à la formation de C6H5D avec un rendement de 51% (quantifié par RMN 2H) à partir de 1h, par rapport au rendement de 21% obtenu avec le silicate 1a non substitué (voir ci-dessus), ce qui confirme l'effet de la substitution par un catécholate.

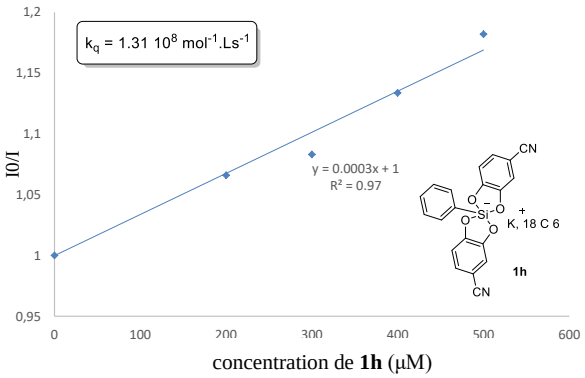

Figure R-5. Tracé de Stern-Volmer - extinction du silicate **1h** et **3**. Ce travail a été réalisé par le Dr. Etienne Levernier.

Dans une seconde partie, nous avons envisagé de développer l'oxydation catalytique de bis-catécholato silicates d'alkyle par des complexes de cuivre avec des ligands non-innocents. Des complexes de cuivre $[Cu(L_{BQ})_2(OTf)_2]$ **44** coordonnés par des ligands non innocents o-benzoquinone seront préparés par oxydation à partir de complexes $[Cu(L_{SQ})_2]$ (voir **Schema R-8**). Concernant les propriétés redox de $Cu(L_{SQ})_2$, la voltammétrie cyclique sera utilisée pour déterminer le potentiel redox et la capacité de ces complexes à être réduits et à oxyder les silicates.

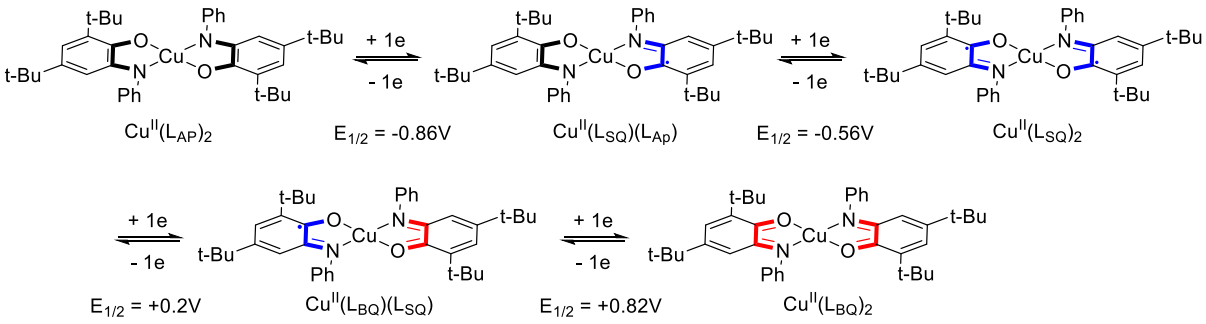

Schéma R-8. Propriétés redox de $Cu(L_{SQ})_2$

La réaction de [Cu(L_{SQ})$_2$] **41** avec du dibrome (Br_2) comme agent oxydant suivie de la métathèse avec du trifluorométhanesulfonate d'argent (AgOTf) conduit à la formation du [Cu(L_{BQ})$_2$(OTf)$_2$] correspondant (**Schéma R-9**). Après filtration, le [Cu(L_{BQ})$_2$(OTf)$_2$] **44** a pu être isolé avec un rendement modéré.

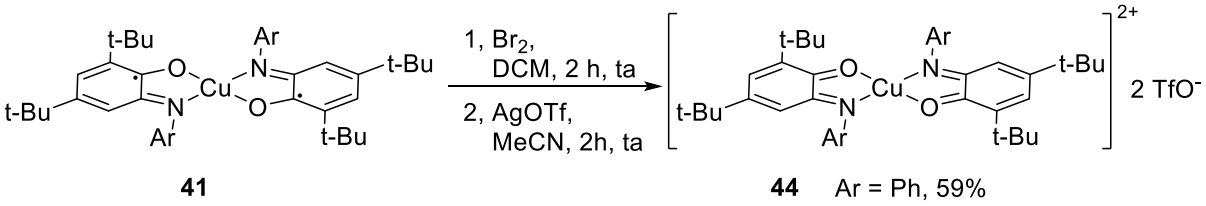

41 **44** Ar = Ph, 59%

Schéma R-9. Préparation du complexe [Cu(L_{BQ})$_2$(OTf)$_2$] **44**

Application à l'oxydation du silicate d'anilinométhyle et optimisation du procédé

Comme le silicate d'anilinométhyle **45** a un faible potentiel d'oxydation ($E_{1/2}^{ox}$ = +0,34 V *vs* SCE dans le DMF), le substrat est facilement oxydé pour produire le radical aminométhyle approprié. En se basant sur le potentiel d'oxydation du complexe de cuivre Cu(L_{BQ})$_2$(OTf)$_2$ **44** ($E_{1/2}^{ox}$ = +0.82 V *vs* SCE dans DCM), nous avons anticipé que le complexe de cuivre oxyderait le silicate, produisant ainsi le radical approprié qui peut être piégé par un accepteur de radical approprié.

Nous avons commencé par étudier la réaction d'allylation modèle entre le silicate d'anilinométhyle **45** et l'allylsulfone **2** comme piège à radicaux dans différents solvants. L'utilisation d'une quantité catalytique de Cu(L_{BQ})$_2$(OTf)$_2$ **44** (10 % mol) dans le NMP comme solvant fournit un faible rendement (9 %) (Tableau R-5, entrée 1). Cependant, en changeant la nature du solvant pour de l'acétonitrile, un rendement de 15 % du produit souhaité a été obtenu (entrée 2). Le rendement de **46** a été amélioré à 18 % en effectuant le processus dans le THF ou le DCM (entrée 3 ou entrée 4). Comparé aux autres solvants halogénés, le $CHCl_3$ s'est avéré favorable à la réaction, conduisant à un rendement de 19 % (entrée 5) mais à seulement 11 % dans le DCE (entrée 6). Nous avons ensuite choisi le DCM comme solvant optimisé. En augmentant la quantité de **2** à 6 équivalents，un rendement isolé de 25% de **46** (entrée 5). Le catalyseur a également été soumis à une expérience de contrôle. Le catalyseur au cuivre Cu(L_{BQ})$_2$(OTf)$_2$ **44** est nécessaire pour que la réaction se déroule, aucun produit ne peut être obtenu en l'absence de Cu(L_{BQ})$_2$(OTf)$_2$ **44** (entrée 8)**.** Le catalyseur au cuivre en quantité

stœchiométrique (1 équiv.) s'est avéré être nuisible ; aucun produit n'a été observé (entrée 9). L'excès de catalyseur de cuivre pourrait permettre la génération rapide des radicaux correspondants, et une série de réactions secondaires médiées par les radicaux a provoqué ce phénomène.

Tableau R-5. Optimisation de l'oxydation de l'anilinométhylsilicate par le complexe de cuivre $Cu(L_{BQ})_2(OTf)_2$

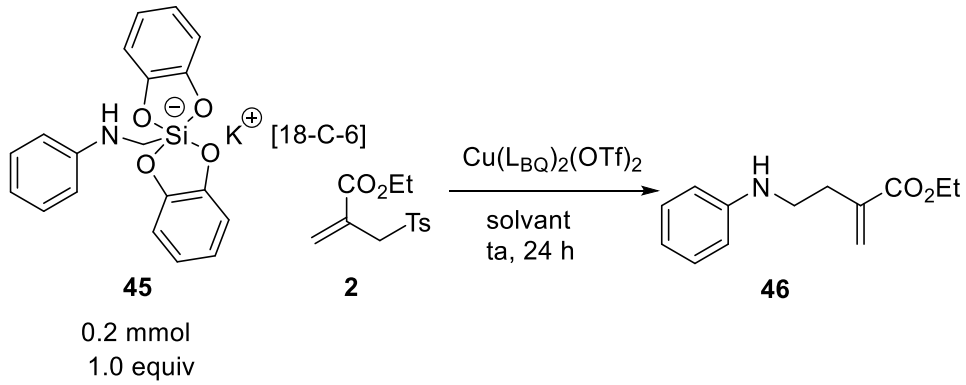

Entrée 1	Tosylate	Solvant	Catalyseur	Rendement
1	4 eq	NMP	$Cu(L_{BQ})_2(OTf)_2$	9%
2	4 eq	MeCN	$Cu(L_{BQ})_2(OTf)_2$	14%
3	4 eq	DCM	$Cu(L_{BQ})_2(OTf)_2$	18%
4	4 eq	THF	$Cu(L_{BQ})_2(OTf)_2$	18%
5	4 eq	CHCl3	$Cu(L_{BQ})_2(OTf)_2$	19 %
6	4 eq	DCE	$Cu(L_{BQ})_2(OTf)_2$	11%
7	6 eq	DCM	$Cu(L_{BQ})_2(OTf)_2$	25%[2]
8[3]	4 eq	DCM	$Cu(L_{BQ})_2(OTf)_2$	Aucun produit
9[4]	4 eq	DCM	$Cu(L_{BQ})_2(OTf)_2$	Aucun produit

1. Conditions de réaction : **45** (0,2 mmol), **2** (0,8 mmol) et catalyseur au cuivre $Cu(L_{BQ})_2(OTf)_2$ (10 % molaire) dans un solvant (2 mL) à température ambiante sous atmosphère d'argon en agitant pendant 24 h. 2. Rendement isolé par chromatographie. 3. Aucun catalyseur au cuivre $Cu(L_{BQ})_2(OTf)_2$ **44** (1 équiv.) n'a été utilisé. 4. Un catalyseur au cuivre $Cu(L_{BQ})_2(OTf)_2$ **44** (1 équiv.) a été utilisé.

L'optimisation du complexe de cuivre

Une approche viable pour améliorer la réactivité du système serait une modification synthétique du catalyseur pour obtenir un potentiel redox approprié. En raison du potentiel électrochimique favorable des complexes de bis-iminosemiquinonate de cuivre $Cu(L_{SQ})_2$ avec des parties *t-butyle* ou CF_3 modifiées ($E_{1/2}^{ox}$ [$Cu(L_{SQ})_2$ (3,5-di-t-Bu-substitué)] = +0.97 V vs SCE et $E_{1/2}^{ox}$ [$Cu(L_{SQ})_2$ (4-CF3-substitué)] = + 0.84 V vs SCE respectivement)[6], nous avons préparé différents dérivés de $Cu(L_{BQ})_2(OTf)_2$ **44** en insérant des substituants attracteurs d'électrons ou donneurs d'électrons dans le groupe phényle latéral de $Cu(L_{BQ})_2(OTf)_2$ **44**.

La préparation des dérivés de $Cu(_{LSQ})_2$ peut être divisée en deux étapes. La première étape est la synthèse du ligand aminophénol par réaction du 3,5-di-tert-butylcatechol avec l'aniline substituée en présence de triméthylamine (Et_3N). Après précipitation, le ligand aminophénol est isolé par filtration. La deuxième étape est la réaction de complexation du chlorure de cuivre (I) avec les ligands aminophénol à l'air. Les ligands aminophénol sont oxydés en iminosemiquinonate et le cuivre (I) en cuivre (II), ce qui conduit au complexe $Cu(L_{SQ})_2$. Selon la procédure générale de préparation de $Cu(L_{BQ})_2(OTf)_2$ **44** par le dibrome (Br_2), nous pouvons préparer les dérivés de $Cu(L_{BQ})_2(OTf)_2$ **44a** et **44b**. (**Schéma R-10**)

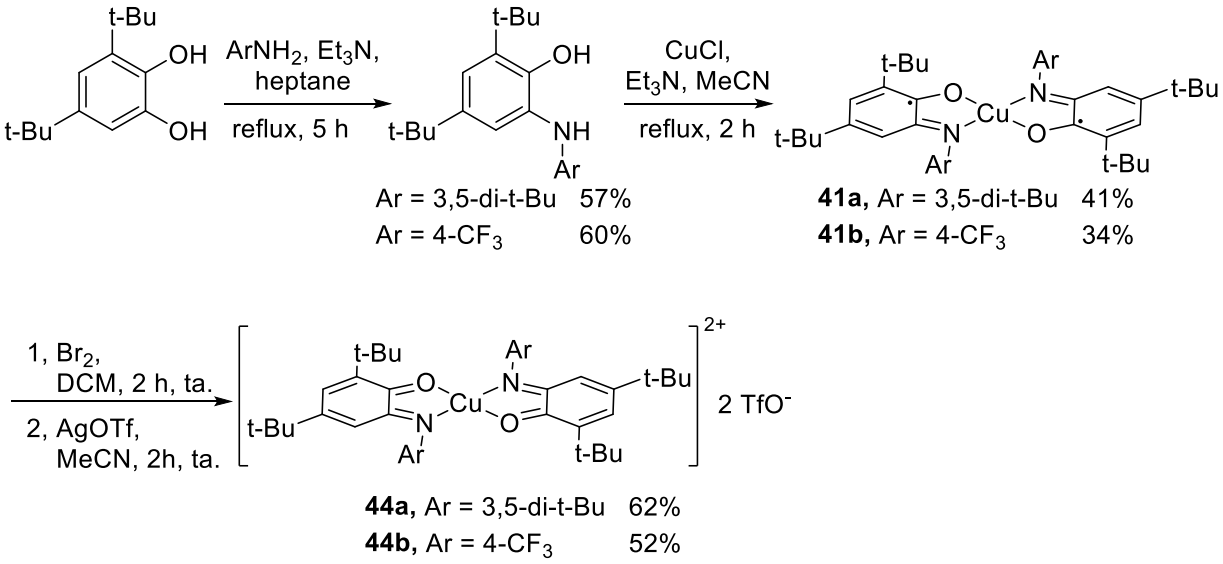

Schéma R-10. Préparation des dérivés complexes de $Cu(L_{SQ})_2$ **44a** et **44b**

[6] C. Mukherjee, U. Pieper, E. Bothe, V. Bachler, E. Bill, T. Weyhermüller, P. Chaudhuri, *Inorg. Chem.* **2008**, *47*, 8943–8956.

Nous avons ensuite mesuré les potentiels électrochimiques des catalyseurs de cuivre(II) **44a** substitué par 4-CF_3 et **44b** substitué par 3,5-di-t-Bu qui sont listés dans le tableau 8. Le potentiel d'oxydation des complexes analogues **44a** et **44b** ($E_{1/2}^{ox}$ = +0,69 V *vs* SCE, dans DCM) est légèrement inférieur à celui de $Cu(L_{BQ})_2(OTf)_2$ **44** ($E_{1/2}^{ox}$ = +0,82 V *vs* SCE, DCM) (**Tableau R-6**).

Tableau R-6. Potentiels électrochimiques du complexe de cuivre $Cu(L_{BQ})_2(OTf)_2$ **44** et de ses dérivés **44a** et **44b** dans le DCM.

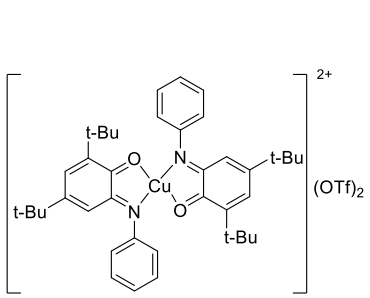

$Cu(L_{BQ})_2(OTf)_2$ **44**
(non substitué)

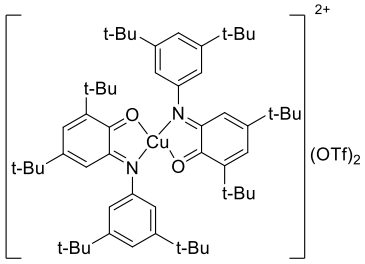

$Cu(L_{BQ})_2(OTf)_2$ **44 a**
(R = 3,5-di-t-Bu)

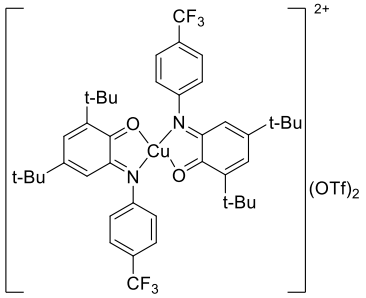

$Cu(L_{BQ})_2(OTf)_2$ **44 b**
(R = 4-CF_3)

Complexe (substituant)	$E_{1/2}^{(ox2)}$	$E_{1/2}^{(ox1)}$	$E_{1/2}^{(rouge1)}$	$E_{1/2}^{(rouge2)}$
44 (non substitué)	+0.82	+0.17	-0.55	-0.84
44a (3,5-di-t-Bu)	+0.69	+0.07	-0.7	-1.02
44b (4-CF_3)	+0.69	+0.31	-0.45	-0.69

Le catalyseur $Cu(L_{BQ})_2(OTf)_2$ substitué **44a** avec 3,5-di-t-Bu a significativement diminué le rendement (14 %) de la réaction (Tableau R-7, entrée 2), et le pire cas a été observé avec l'analogue du complexe de cuivre **44b** avec un groupe CF_3 en position 4 (7 %) (entrée 3). En considérant la génération oxydative d'un radical alkyle en utilisant le silicate d'anilinométhyle **45** comme substrat, le potentiel d'oxydation plus faible des catalyseurs de cuivre (II) **44a** et **44b** ($E_{1/2}^{ox}$ = + 0,69 V vs SCE, DCM) explique pourquoi ces deux nouveaux catalyseurs de cuivre (II) pourraient donner des rendements de réaction plus faibles même si le potentiel du silicate d'anilinométhyle **45 (**$E_{1/2}^{ox}$ = +0,34 V *vs* SCE dans DMF) est suffisament faible pour réaliser l'oxydation.

Tableau R-7. Optimisation des catalyseurs au cuivre $Cu(L_{BQ})_2(OTf)_2$

Entrée	Tosylate	Solvant	Catalyseur	Rendement
1	4 eq	DCM	**44**	18%
2	4 eq	DCM	**44a**	14%
3	4 eq	DCM	**44b**	7%

1. Conditions de réaction : **45** (0,2 mmol), **2** (0,8 mmol) et catalyseur au cuivre **44** (10 % molaire) dans DCM (2 mL) à température ambiante sous atmosphère d'argon en agitant pendant 24 h

Selon le mécanisme de la réaction, le silicate ($E_{1/2}^{ox}$ = +0,34 V *vs* SCE dans le DMF) a été oxydé par le catalyseur au cuivre $Cu(L_{BQ})_2(OTf)_2$ ($E_{1/2}^{ox}$ $[Cu(L_{BQ})_2/Cu(L_{BQ})(L_{SQ}))]$ = +0,82 V *vs* SCE dans le DCM), donnant le radical anilinométhyle et le complexe de Cu ($Cu(L_{BQ})(L_{SQ})$). Ensuite, le radical nouvellement formé a été piégé par l'allylsulfone. Le produit a été obtenu par addition et fragmentation de la liaison C-S libérant un radical tosyle ($E_{1/2}^{ox}$ ($PhSO_2$-/$PhSO_2Na$) = + 0.50V). Celui-ci peut oxyder le complexe et ainsi régénérer le catalyseur en formant un anion sulfonate (**Schéma R-11**).

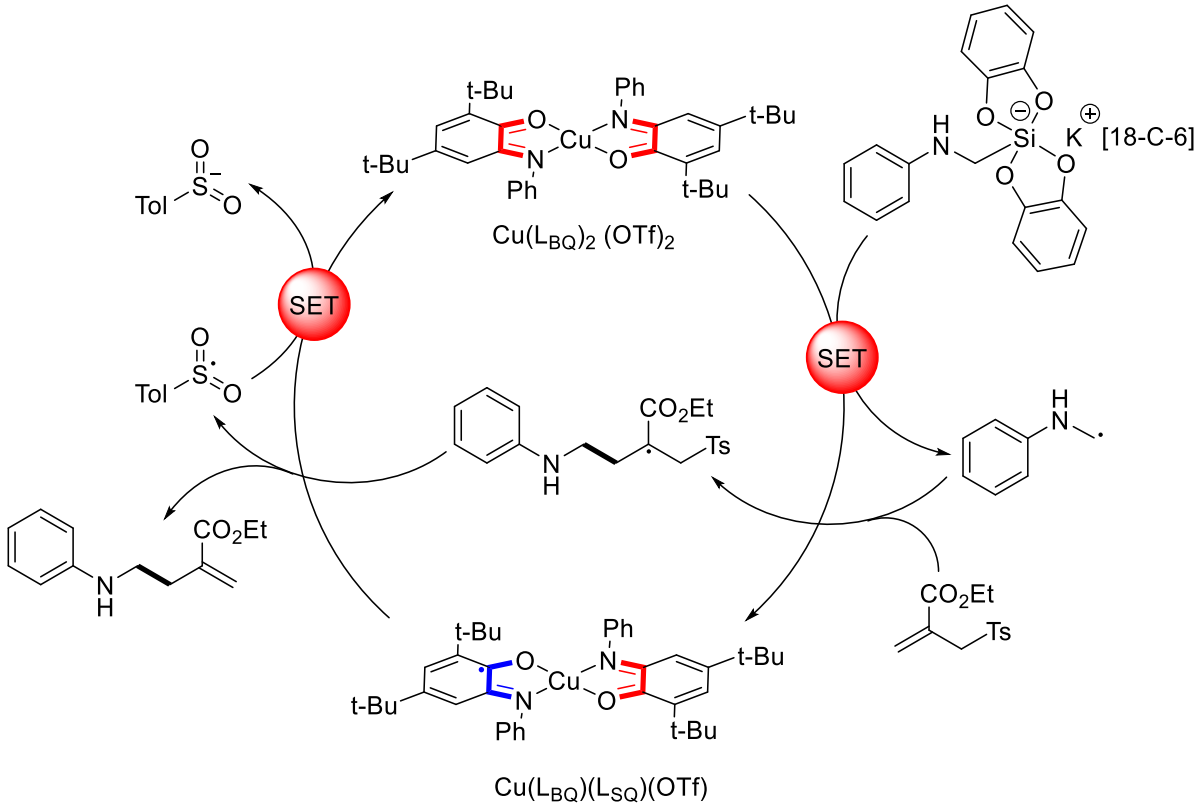

Schéma R-11. Mécanisme envisagé pour l'oxydation des silicates médiée par le cuivre

Pour générer l'intermédiaire radicalaire, le catalyseur $Cu(LBQ)_2(OTf)_2$ **44** pourrait oxyder l'acide aminé N-protégé pour produire un radical α-aminé après décarboxylation. En remplaçant le substrat silicaté par du N-tosyl-L-prolinate de sodium, dans les conditions de réaction optimisées, le produit d'allylation attendu n'a pas été observé. (**Schéma R-12**)

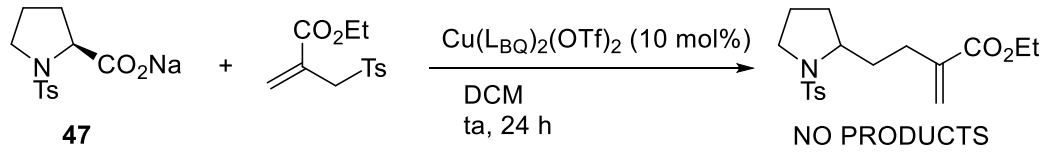

47

Schéma 126. La réaction du tosyl-L-prolinate de sodium **47** avec l'allylsulfone **2** catalysée par le catalyseur $Cu(LBQ)_2(OTf)_2$ **44**

Nous avons utilisé le 2-phénylacétate de sodium **48** comme substrat. Cependant, le carboxylate de sodium n'a pas pu subir la réaction séquentielle d'oxydation/décarboxylation pour réagir avec le substrat allylsulfone sous la catalyse de $Cu(LBQ)_2(OTf)_2$ **44**. Le produit attendu n'a pas été obtenu. (**Schéma R-13**)

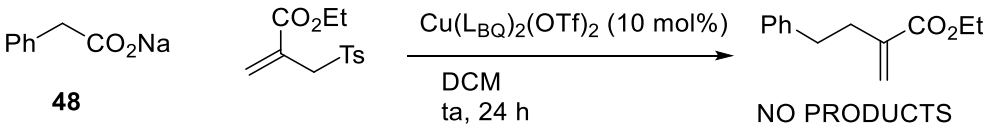

48

Schéma R-13. La réaction du 2-phénylacétate **48** avec l'allylsulfone **2** catalysée par le catalyseur $Cu(LBQ)_2(OTf)_2$ **44**

Comme prévu, nous avons utilisé la N,N-diméthylaniline comme substrat, mais la diméthylaniline **49** n'a pas réagi avec le substrat allylsulfone en présence du catalyseur au cuivre, même après avoir changé le solvant de DCM à NMP. (**Schéma R-14**)

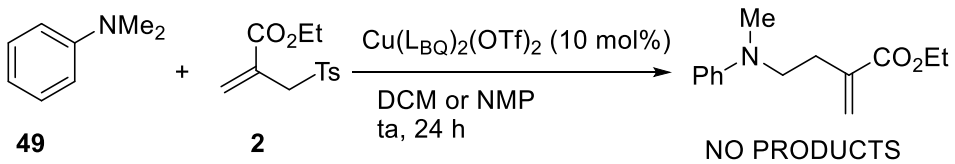

49 **2**

Schéma R-14. La réaction de la N,N-diméthylaniline **49** avec l'allylsulfone **2** catalysée par le catalyseur $Cu(L_{BQ})_2(OTf)_2$ **44**

Une autre option consiste à utiliser des accepteurs alternatifs tels que les bromures d'allyle qui génèrent un radical oxydant intermédiaire plus fort, un radical brome. Le bromure d'allyle **50** a été choisi comme substrat. Le bromure d'allyle **50** n'a pas réagi avec l'aminométhylsilicate en présence du complexe oxydant de cuivre **44**. La raison possible pourrait être attribuée au faible potentiel réducteur du **50**. Il a conduit le bromure plus favorable que le silicate à être réduit par le catalyseur Cu, et à provoquer d'autres réactions secondaires. (**Schéma R-15**)

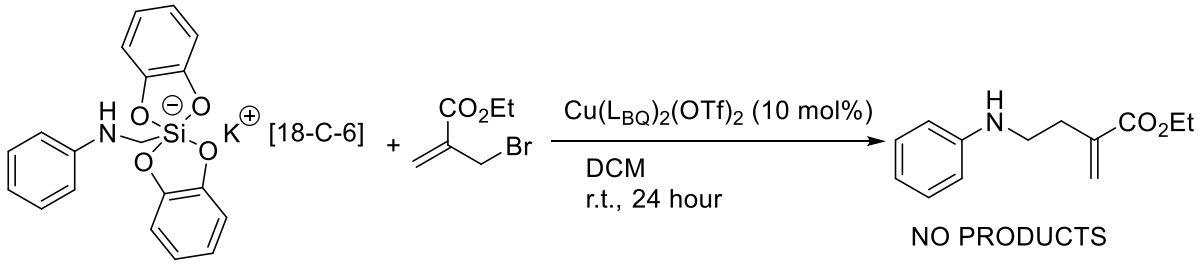

45 **50**

Schéma R-15. La réaction du silicate d'anilinométhyle **45** avec l'organobromure **50** catalysée par le catalyseur $Cu(L_{BQ})_2(OTf)_2$ **44**

La troisième partie est consacrée à étude computationnelle des interactions de l'acide palmitique avec divers types de cyclodextrine.

Sur la base de leurs résultats précédents, le groupe de Bouchemal a caractérisé la morphologie et la cristallinité de ces particules comprennaid des acides gras et des complexes d'inclusion α-CD.[7] Les formes hexagonales des plaquettes de chitosane observées à partir des images TEM, cryo-TEM, AFM, CLSM et SEM suggèrent la formation de structures cristallines. Différents types de chaînes alkyle (acide oléique, acide palmitique et acide stéarique) greffées sur le chitosane ont donné lieu à des formes de plaquettes presque identiques, ce qui indique fortement que l'interaction des acides gras avec l'α-CD est le facteur moteur de la formation de plaquettes hexagonales.

Le complexe hexasaccharide-6CDs contient trois unités répétées de disaccharide. Les unités de base qui forme le disaccharide sont la N-acétylglucosamine et l'acide glucuronique.

[7] Z. Ahmed, S. Malli, R. Diaz-Salmeron, P. L. Destruel, A. Da Costa, J. M. Guigner, F. Porcher, B. Baptiste, G. Ponchel, K. Bouchemal, *Int. J. Pharm.* **2018**, *548*, 23–33.

L'acide palmitique peut effectuer une estérification avec le groupe hydroxyle de l'acide glucuronique. Les groupes alkyle des résidus de l'acide palmitique sont entourés pour les molécules de cyclodextrine.

Ce projet de recherche doctorale vise à étudier le processus d'élimination des cyclodextrines du complexe hexasaccharide-6CDs. En appliquant des méthodologies computationnelles, nous obtenons un nouvel aperçu du mécanisme réactionnel qui sous-tend ce processus.

L'extraction requise présentée lors de l'élimination des molécule de cyclodextrine une par une du complexe acide palmitique-2CDs peut être obtenue par optimisation de la géométrie. Après avoir obtenu la valeur de l'énergie d'extraction et de l'énergie d'insertion, nous pouvons potentiellement identifier les propriétés pour comprendre le comportement du complexe hexasaccharide-6CDs.

À ce stade, nous prévoyons d'appliquer le processus d'extraction et d'insertion à un ensemble de complexes d'inclusion monomères et dimères de l'acide palmitique afin de fournir l'énergie d'insertion et l'énergie d'extraction correspondantes.

Enfin, nous souhaitons étendre la portée de l'analyse au complexe hexasaccharide-6CDs.

À ce stade, après avoir comparé la valeur de l'énergie d'extraction de différents complexes hexasaccharide-CD, nous pouvons sélectionner le type approprié de dimère de cyclodextrine dans le complexe hexasaccharide-6CDs. Nous prévoyons d'effectuer des scans du complexe hexasaccharide-6CDs pour éliminer les CD une par une afin d'obtenir les énergies d'extraction correspondantes, et d'obtenir la structure. Ensuite, après avoir comparé la valeur de l'énergie ainsi extraite, nous pouvons effectuer un autre scan en utilisant la structure précédente. Grâce à les processus itératif, nous pouvons déterminer un mécanisme raisonnable pour l'élimination des cyclodextrines (voir **Figure R-6)**.

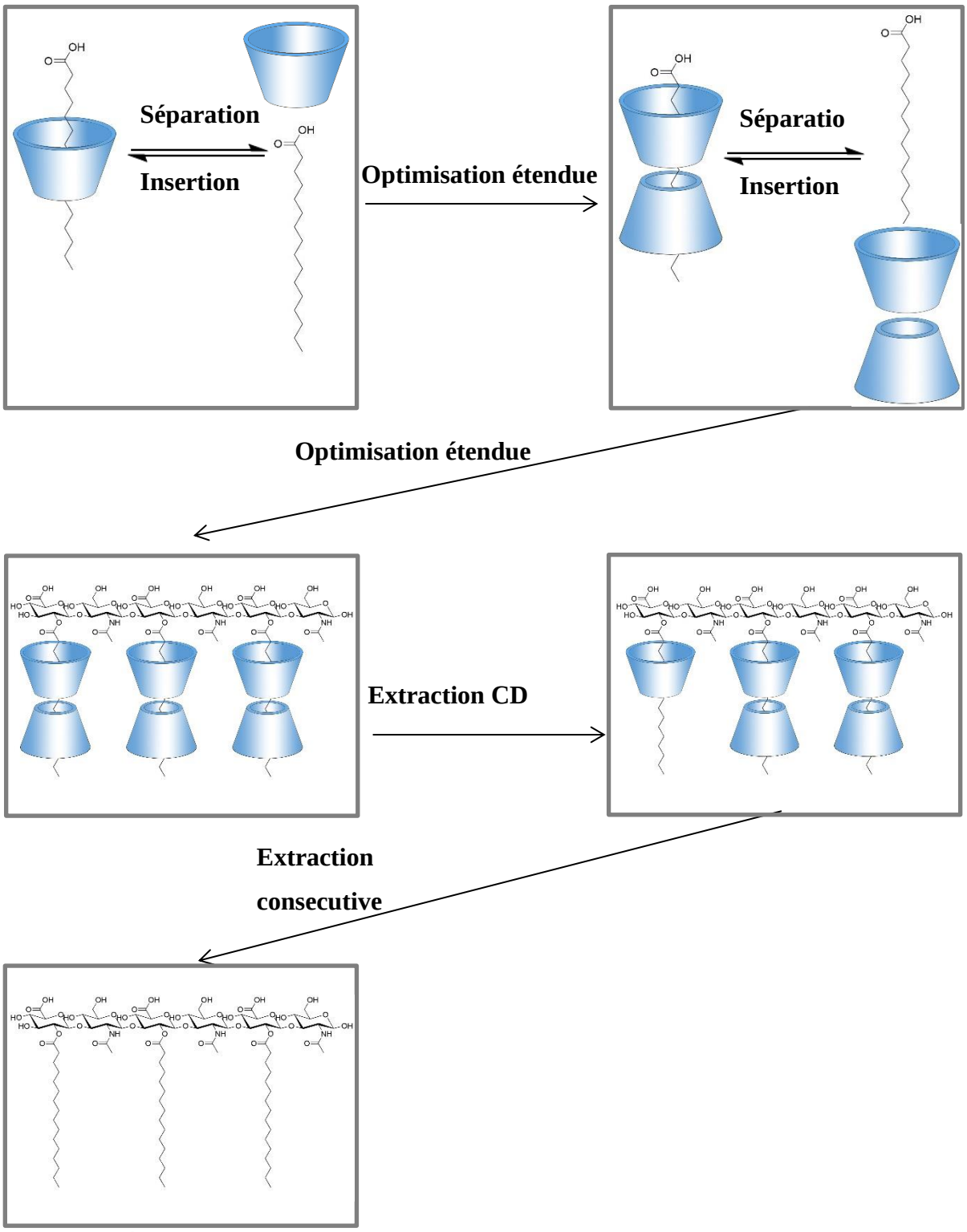

Figure R-6. Étapes de réalisation de l'optimisation du complexe hexasaccharide-6CDs à partir du modèle de l'acide palmitique-cyclodextrine.

Les énergies obtenues par les scans seront discutées dans cette section pour le balayage du complexe hexasaccharide cyclodextrine.

Dans un premier temps, nous aimerions trouver la relation entre le complexe d'inclusion monomère et dimère de l'acide palmitique. La structure de l'α-cyclodextrine est généralement décrite comme un cylindre effilé (**Figure R-7)**. Les groupes hydroxyles primaires sont sur le côté étroit, et les groupes hydroxyles secondaires sont sur le côté large.

Figure R-7. La structure de l'α-cyclodextrine

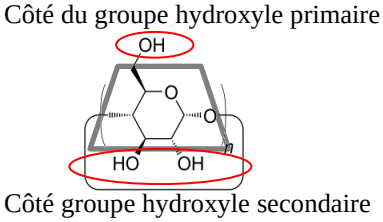

Le complexe d'inclusion monomère de l'acide palmitique peut être classé en deux types différents d'inclusion monomère (inclusion a et inclusion b). Dans l'inclusion a, le groupe carboxyle de l'acide palmitique se trouve à côté du côté du groupe hydroxyle primaire de la cyclodextrine. Dans l'inclusion b, le groupe carboxyle de l'acide palmitique se trouve du côté du groupe hydroxyle secondaire de la cyclodextrine. (**Figure R-8**)

Sur la base de l'interaction entre les côtés du groupe hydroxyle des cyclodextrines du dimère, les complexes d'inclusion du dimère peuvent être classés en quatre types différents : 1, l'interaction se fait entre le côté du groupe hydroxyle primaire de la cyclodextrine et le côté du groupe hydroxyle primaire de l'autre cyclodextrine du même complexe d'inclusion, et le groupe carboxyle de l'acide palmitique est proche du côté du groupe hydroxyle secondaire de la cyclodextrine (pri-pri) ; 2, l'interaction est entre le côté du groupe hydroxyle primaire de la cyclodextrine et le côté du groupe hydroxyle secondaire de l'autre cyclodextrine du même complexe d'inclusion, et le groupe carboxyle de l'acide palmitique est proche du côté du groupe hydroxyle secondaire de la cyclodextrine (pri-sec) ; 3, l'interaction entre le côté du groupe hydroxyle secondaire de la cyclodextrine et le côté du groupe hydroxyle primaire de l'autre cyclodextrine du même complexe d'inclusion, et le groupe carboxyle de l'acide palmitique est proche du côté du groupe hydroxyle primaire de la cyclodextrine (sec-pri) ; 4, l'interaction est entre le côté du groupe hydroxyle secondaire de la cyclodextrine et le côté du groupe hydroxyle secondaire de l'autre cyclodextrine du même complexe d'inclusion, et le groupe carboxyle de l'acide palmitique est proche du côté du groupe hydroxyle primaire de la cyclodextrine (sec-sec). (voir **Figure R-8.**)

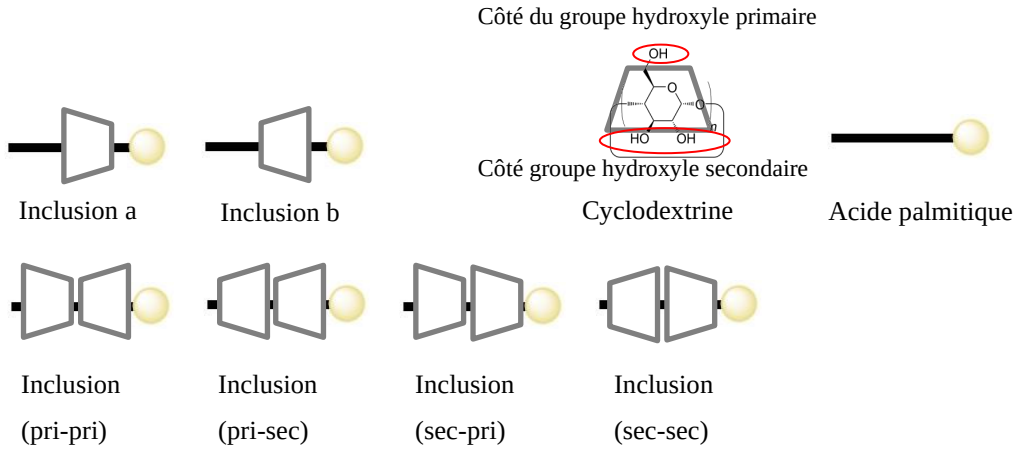

Figure R-8. La classification du complexe d'inclusion monomère et dimère de l'acide palmitique

Afin de comparer les différents phénomènes entre l'élimination de la cyclodextrine du monomère et du complexe d'inclusion dimère de l'acide palmitique, les courbes distance-énergie moyennes du monomère correspondant et du complexe d'inclusion dimère ont été assemblées (**Figure R-9**). Les conformations correspondantes des différents états indexés dans la **Figure R-9** a également été répertoriée dans la **Figure R-10**.

A est la conformation de la structure initiale de l'inclusion a, B est la conformation de la structure initiale de l'inclusion b, C est la conformation de la structure initiale de l'inclusion pri-pri, D est la conformation de la structure initiale de l'inclusion pri-sec, E est la conformation de la structure initiale de l'inclusion sec-pri, et F est la conformation de la structure initiale de l'inclusion sec-sec. Lorsque l'énergie du système est devenue stable, G est l'état de configuration final de l'inclusion a avec l'acide palmitique n'interagissant pas avec la cyclodextrine, H est l'état de configuration final de l'inclusion b avec l'acide palmitique n'interagissant pas avec la cyclodextrine, I est l'état de configuration final de l'inclusion pri-pri avec l'acide palmitique n'interagissant pas avec le dimère de cyclodextrine, J est l'état de configuration final de l'inclusion pri-sec avec l'acide palmitique n'interagissant pas avec le dimère de cyclodextrine, K est l'état final de configuration de l'inclusion sec-pri avec l'acide palmitique n'interagissant pas avec le dimère de cyclodextrine, et L est l'état final de configuration de l'inclusion sec-sec avec l'acide palmitique n'interagissant pas avec le dimère de cyclodextrine. M est le point minimum de la courbe énergie-distance de l'inclusion b. A la fin de chaque scan, la molécule de cyclodextrine correspondante a été complètement é liminatoire.

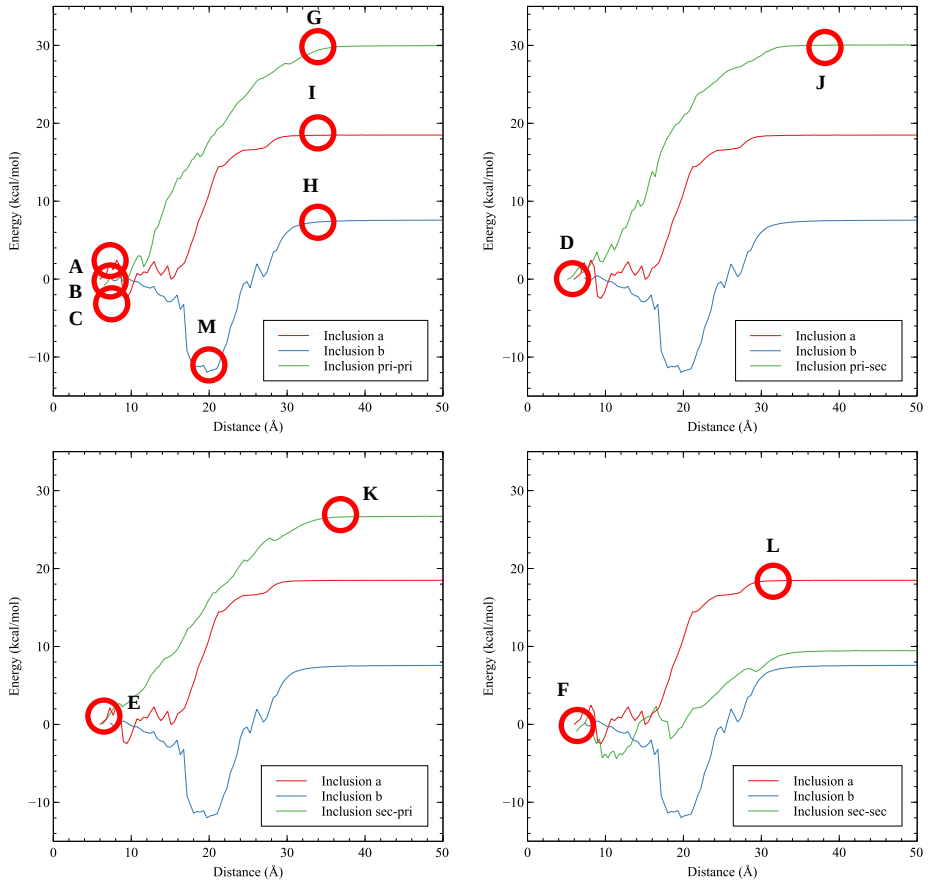

Figure R-9. Courbe énergie-distance moyenne de l'inclusion de monomères et de dimères.

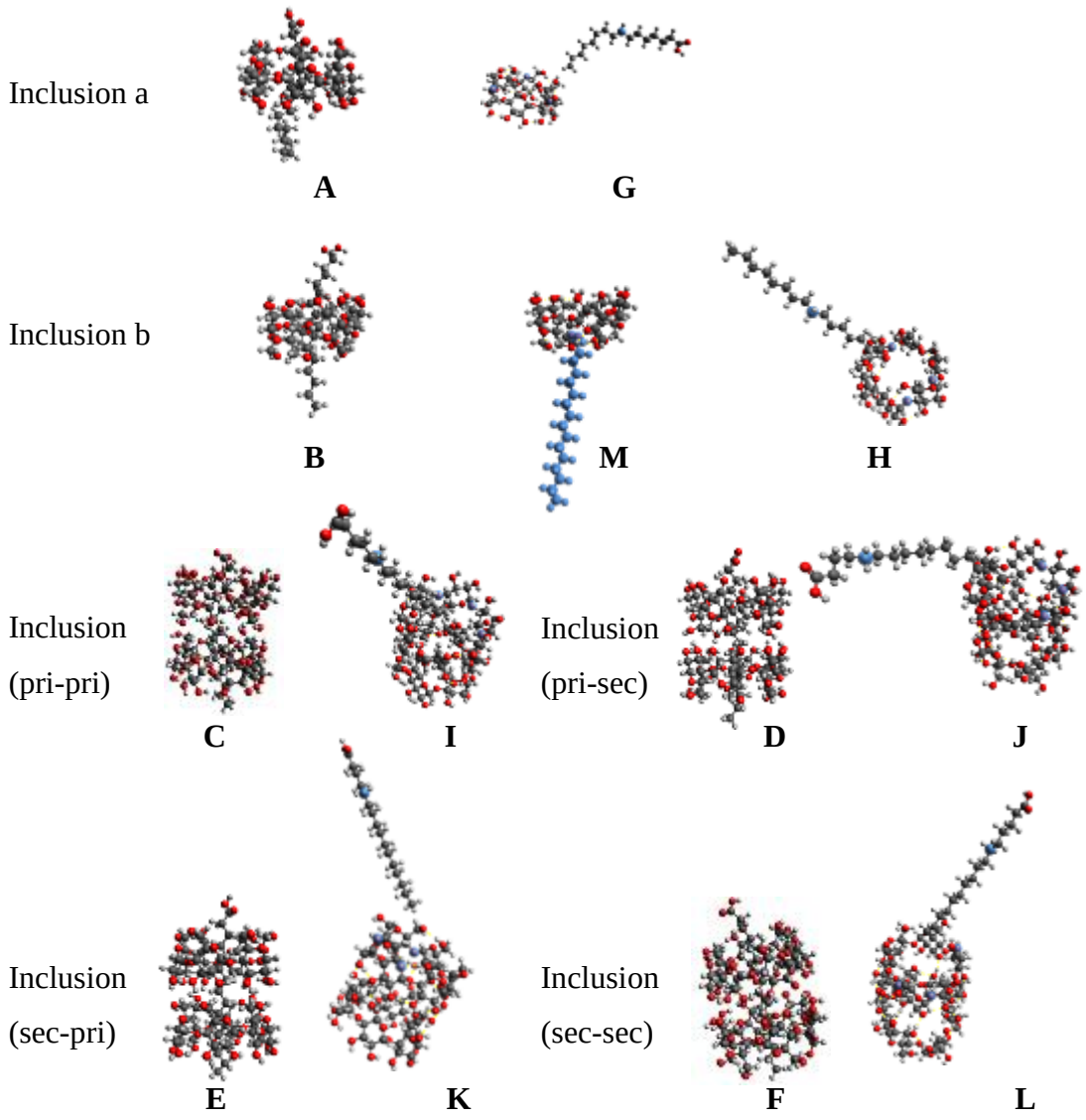

Figure R-10. La conformation des états de configuration marqués (Le point A-M représenté sur la **Figure R-9**)

À la conformation de la structure de départ A et B, l'acide palmitique (dans l'inclusion a ou l'inclusion b) était entièrement placé dans la cavité de la cyclodextrine ; à la conformation de la structure de départ C, D, E et F, l'acide palmitique dans chaque conformation de la structure de départ était entièrement placé dans la cavité du dimère de cyclodextrines. L'acide palmitique n'a pas interagi avec la molécule de cyclodextrine dans les états de configuration G, H, I, J, K et L. Dans les états de configuration M, le groupe carboxyle de l'acide palmitique interagit avec le groupe hydroxyle de la molécule de cyclodextrine.

Il existe un ensemble de différences entre les énergies d'extraction que l'on peut obtenir à partir du complexe d'inclusion monomère et dimère. En comparant l'énergie d'extraction du monomère et du complexe d'inclusion dimère de l'acide palmitique, pour le complexe

d'inclusion monomère de l'acide palmitique, l'énergie d'extraction de l'inclusion a est de 18,46 kcal/mol, et l'énergie d'extraction de l'inclusion b est de 20,49 kcal/mol séparément. En revanche, pour le complexe d'inclusion dimère de l'acide palmitique, l'énergie d'extraction de l'inclusion pri-pri est de 30,71 kcal/mol, l'énergie d'extraction de l'inclusion pri-sec est de 30,03 kcal/mol, l'énergie d'extraction de l'inclusion sec-pri est de 26,60 kcal/mol, et l'énergie d'extraction de l'inclusion sec-sec est de 10,12 kcal/mol. Dans la plupart des situations (comme l'inclusion pri-pri, l'inclusion pri-sec et l'inclusion sec-pri), l'énergie d'extraction du complexe d'inclusion dimère de l'acide palmitique est supérieure à celle du complexe d'inclusion monomère de l'acide palmitique. En revanche, l'énergie d'extraction de l'inclusion sec-sec est inférieure à celle des autres complexes d'inclusion.

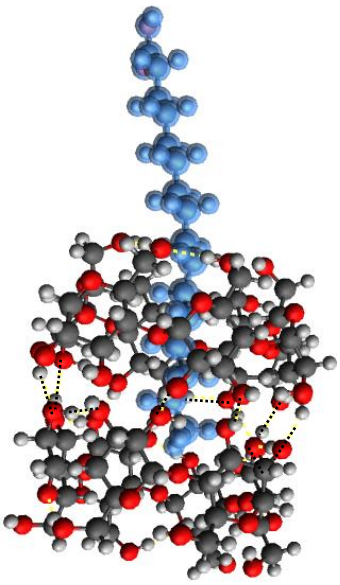

Figure R-11. Liaisons hydrogène entre les deux cyclodextrines d'inclusion sec-sec (la ligne noire en tirets indique la liaison hydrogène).

Dans l'inclusion sec-sec, les liaisons hydrogène supplémentaires entre les cyclodextrines du dimère peuvent former un dimère plus stable, et la stabilité supplémentaire du dimère peut diminuer l'énergie du système. L'énergie d'extraction de l'inclusion sec-sec est donc inférieure à celle des autres inclusions (10,12 kcal/mol). (voir **Figure R-11**)

Au cours du processus de scan tel que prévu, nous pouvons retirer la molécule de cyclodextrine une par une du complexe hexasaccharide-cyclodextrine. Comme trois branches d'acide palmitique sont attachées à la molécule de hexasaccharide, lorsque nous avons effectué des scans de la même structure de départ, il y a trois molécules de cyclodextrine possibles qui peuvent être retirées lors des scans. Trois énergies d'extraction différentes de la même molécule de cyclodextrine hexasaccharide peuvent être obtenues via trois voies

distinctes de scan. Après avoir comparé la valeur obtenue de l'énergie d'extraction, nous pouvons choisir la voie la plus raisonnable pour obtenir la structure cible utilisée dans le balayage suivant. En répétant ce processus, nous pouvons trouver une voie de mécanisme appropriée pour enlever la molécule de cyclodextrine qui suit le principe d'énergie minimale. De plus, nous pouvons éliminer toutes les cyclodextrines en employant cette méthode.

Nous pouvons effectuer le scan et obtenir l'énergie d'extraction correspondante. Sur la base de la valeur donnée de l'énergie d'extraction, l'ordre d'élimination des molécules de cyclodextrine du complexe cyclodextrine-hexasaccharide est représenté sur la **Figure R-12**. Le cheminement des balayages et ces énergies d'extraction ont été systématiquement répertoriés dans les **Figure R-12** (sous la molécule CD correspondante retirée par scan).

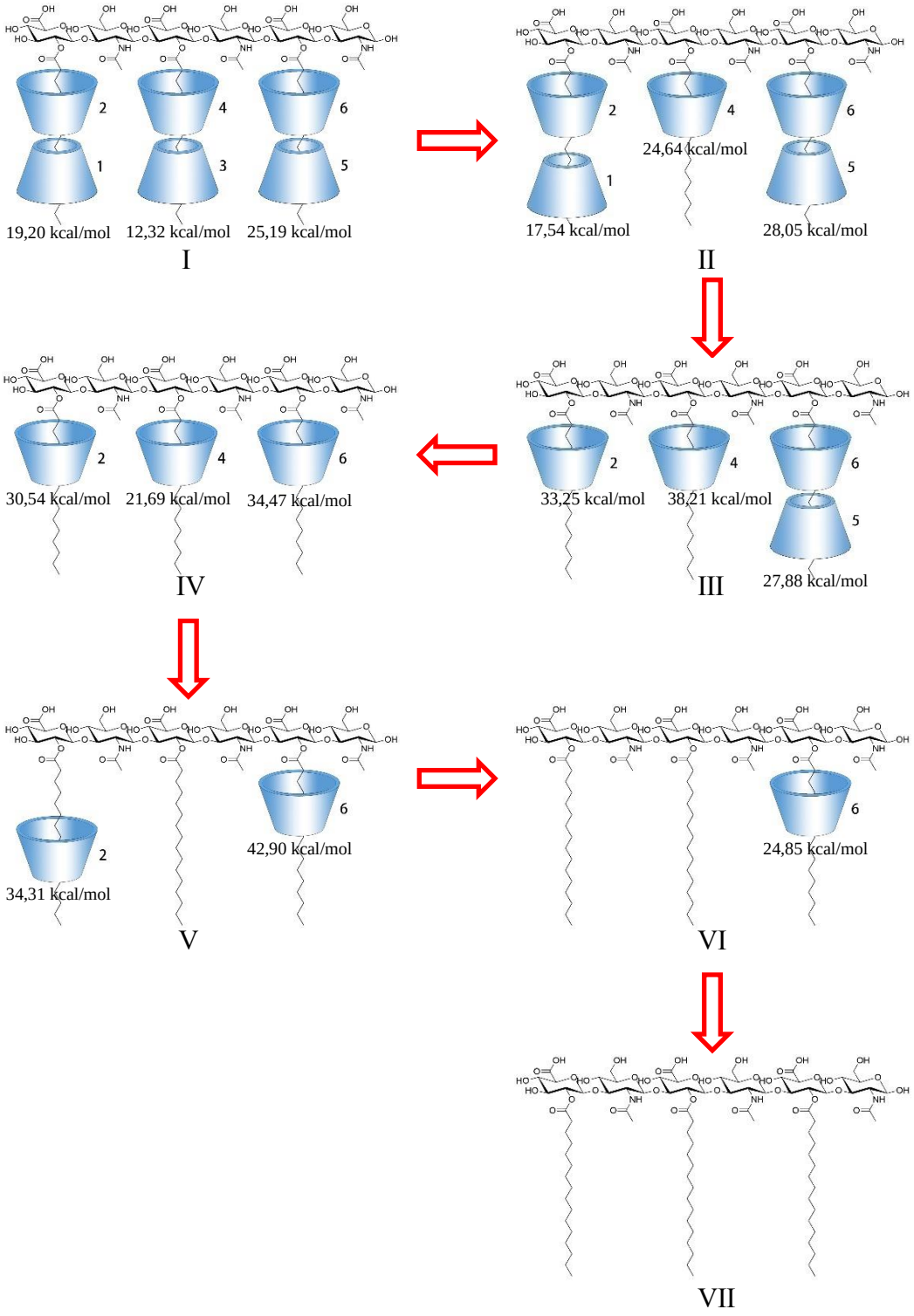

Figure R-12. Proposition d'une voie raisonnable pour éliminer les molécules de cyclodextrine.

Après avoir effectué le scan du complexe hexasaccharide-cyclodextrine I, lorsque nous avons retiré la cyclodextrine #3, nous pouvons obtenir la structure de plus basse énergie des

balayages du complexe hexasaccharide-cyclodextrine I. La valeur minimale de l'énergie d'extraction est de 12,32 kcal/mol.

Au point minimum des scans de la structure de départ I (voir **Figure R-13**), les groupes hydroxyles secondaires de la cyclodextrine #5 et de la cyclodextrine #3 peuvent former des liaisons hydrogène. La cyclodextrine #5 et la cyclodextrine #4 sont encore à l'extrémité de la chaîne lipidique. La cyclodextrine #3 est complètement séparée de la chaîne lipidique. De plus, le groupe carboxyle de l'acide palmitique est toujours près de la cyclodextrine #4.

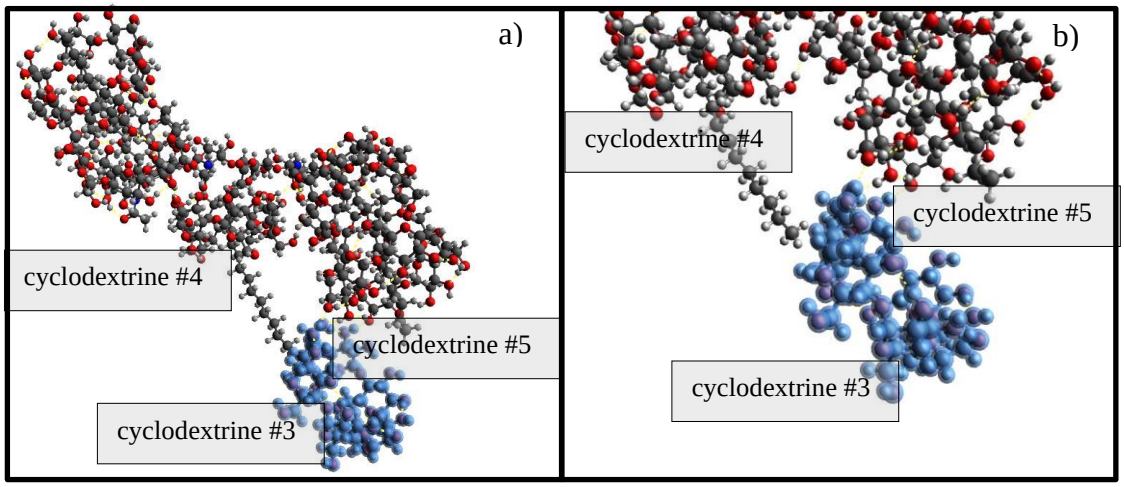

Figure R-13. a) La structure du point minimal du complexe hexasaccharide-cyclodextrine I. b) La position de la cyclodextrine #5 et de la cyclodextrine #4 par rapport à la cyclodextrine #3 retirée. (La cyclodextrine retirée #3 est colorée en bleu pour plus de clarté, et la ligne noire en tirets indique la liaison hydrogène entre la cyclodextrine #3 et la cyclodextrine #5).

Le résultat approprié de ces balayages de la structure de départ I était le complexe hexasaccharide-cyclodextrine II. Il peut être employé comme structure de départ des prochains scans. La valeur minimale correspondante de l'énergie d'extraction est de 17,54 kcal/mol (lorsque nous avons retiré la cyclodextrine #1 de la structure de départ II).

Aux points minimaux des balayages de la structure II (voir **Figure R-14**), les groupes hydroxyles secondaires de la cyclodextrine #2 et de la cyclodextrine #1 peuvent former des liaisons hydrogène. En considérant l'interaction entre la cyclodextrine #2 et la cyclodextrine #1, le mouvement de la cyclodextrine #1 a fait bouger la cyclodextrine #2 de manière significative, mais la cyclodextrine #2 est toujours autour de la chaîne alkyle. Enfin, la cyclodextrine #1 a été complètement retirée de la chaîne lipidique lorsque la distance entre la cyclodextrine #1 et le résidu d'acide palmitique a augmenté.

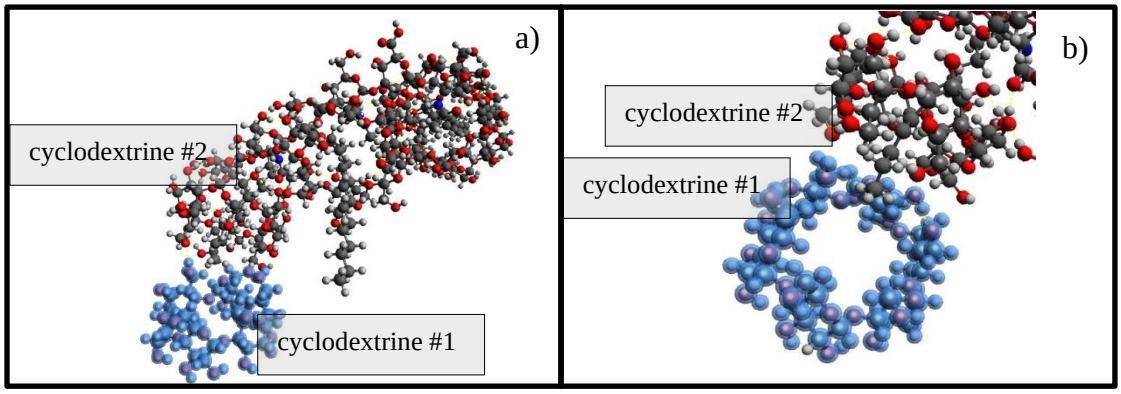

Figure R-14. a) La structure des points minimaux du complexe hexasaccharide-cyclodextrine II. b) La position du résidu chitosan par rapport à la cyclodextrine #1 retirée. (La cyclodextrine #1 retirée est colorée en bleu pour plus de clarté, et la ligne noire en tirets indique la liaison hydrogène entre la cyclodextrine #1 et la cyclodextrine #2).

Après avoir effectué les scans du complexe hexasaccharide-cyclodextrine, lorsque nous avons retiré la cyclodextrine #5, nous pouvons obtenir la structure du complexe hexasaccharide-cyclodextrine de plus basse énergie IV. La valeur minimale de l'énergie d'extraction est de 27,88 kcal/mol.

Au point minimum des scans de la structure III (**Figure R-15**), lorsque la cyclodextrine #5 a été retirée du complexe hexasaccharide-cyclodextrine III, en raison de l'interaction entre les groupes hydroxyles de la cyclodextrine #5 et de la cyclodextrine #6, la cyclodextrine #6 s'est légèrement déplacée et se trouvait toujours autour de la chaîne lipidique. Finalement, la cyclodextrine #5 a été complètement retirée du système.

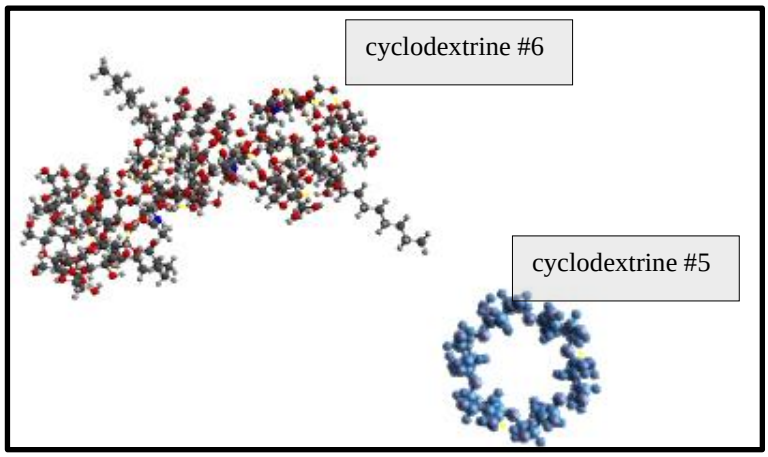

Figure R-15. La structure des points minimaux du complexe hexasaccharide cyclodextrine III.

Les scans suivants du complexe hexasaccharide-cyclodextrine IV permettent d'obtenir le complexe hexasaccharide-cyclodextrine V comme structure de plus basse énergie des balayages du complexe hexasaccharide-cyclodextrine IV. Lorsque nous avons retiré la cyclodextrine #4 de la structure de départ IV, la valeur minimale correspondante de l'énergie d'extraction est de 21,69 kcal/mol.

Au point minimum des scans de la structure IV (voir **Figure 126**), les groupes hydroxyle de la cyclodextrine #4 et de la cyclodextrine #6 peuvent former des liaisons hydrogène. Cependant, la distance du groupe hydroxyle de la cyclodextrine #2 et de la cyclodextrine #4 était si longue qu'ils ne peuvent pas former la liaison hydrogène. Au point minimum, la cyclodextrine #4 a été complètement retirée de l'extrémité de la chaîne lipidique.

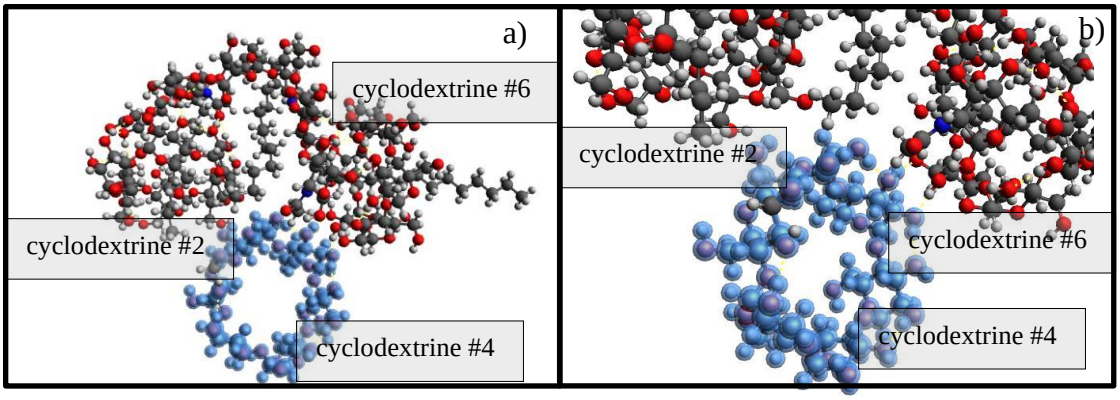

Figure R-16. a) Structure du point minimal du complexe hexasaccharide-cyclodextrine (la cyclodextrine #4 retirée est colorée en bleu pour plus de clarté). b) Position de la cyclodextrine #2 et de la cyclodextrine #6 par rapport à la cyclodextrine #4 retirée (la cyclodextrine #4 retirée est colorée en bleu pour plus de clarté et le trait noir indique la liaison hydrogène entre la cyclodextrine #4 et la cyclodextrine #6).

Les balayages suivants du complexe hexasaccharide-cyclodextrine V peuvent obtenir le complexe hexasaccharide-cyclodextrine VI comme structure de plus basse énergie des balayages du complexe hexasaccharide-cyclodextrine V. Lorsque nous avons retiré la cyclodextrine #2 de la structure de départ V, la valeur minimale correspondante de l'énergie d'extraction est de 34,31 kcal/mol.

Au point minimum des scans de la structure de départ V, la cyclodextrine #2 a été séparée complètement de la chaîne lipidique et s'est rapprochée de la cyclodextrine #6 et du résidu de chitosan. Les groupes hydroxyle de la cyclodextrine #2 peuvent former des liaisons hydrogène avec la cyclodextrine #6 et le résidu de chitosan séparément. A ce moment, le

mouvement de la cyclodextrine #2 a provoqué le mouvement de la cyclodextrine #6, et la

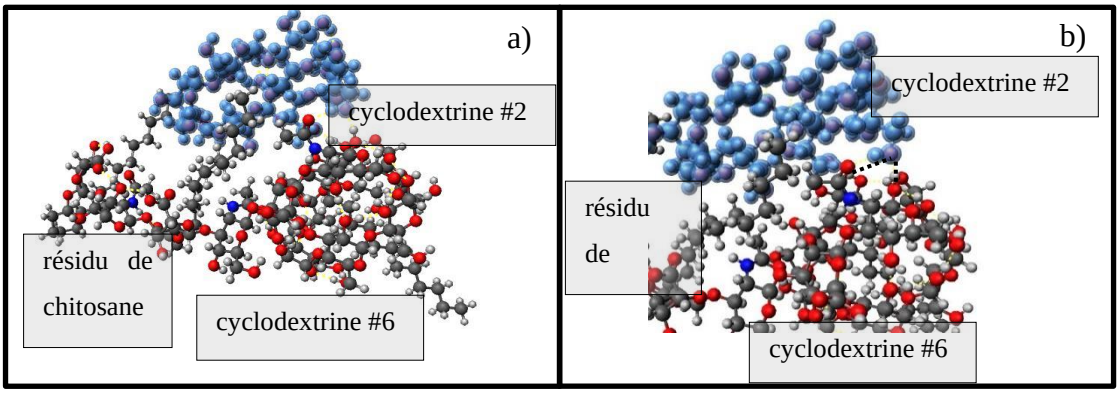

cyclodextrine #6 était toujours près du groupe carboxyle de la chaîne lipidique. La conformation des chaînes alkyle sans cyclodextrine est devenue pliée. (**Figure R-17**)

Figure R-17. a) La structure du point minimum du complexe hexasaccharide-cyclodextrine. b) La position du cyclodextrine #4 et du résidu de chitosan par rapport au cyclodextrine #2 retiré. (La cyclodextrine retirée cyclodextrine #2 est colorée en bleu pour plus de clarté, et la ligne pointillée noire indique la liaison hydrogène entre cyclodextrine #4 et cyclodextrine #2).

Les balayages suivants du complexe hexasaccharide-cyclodextrine VI peuvent obtenir le composé hexasaccharide VII comme structure finale des balayages du complexe hexasaccharide-cyclodextrine VI. Lorsque nous avons retiré la cyclodextrine #2 de la structure de départ V, la valeur minimale correspondante de l'énergie d'extraction est de 24,85 kcal/mol.

Au point minimum des balayages de la structure de départ VI, les groupes hydroxyles de la cyclodextrine #6 peuvent former plusieurs liaisons hydrogène avec le résidu chitosan par l'intermédiaire de son groupe hydroxyle. La cyclodextrine #6 est encore vers l'extrémité de la chaîne lipidique à ce stade. Avec une augmentation de la distance entre la cyclodextrine #6 et le résidu d'acide palmitique, la cyclodextrine #6 est devenue entièrement isolée de la chaîne lipidique. (voir **Figure R-18).**

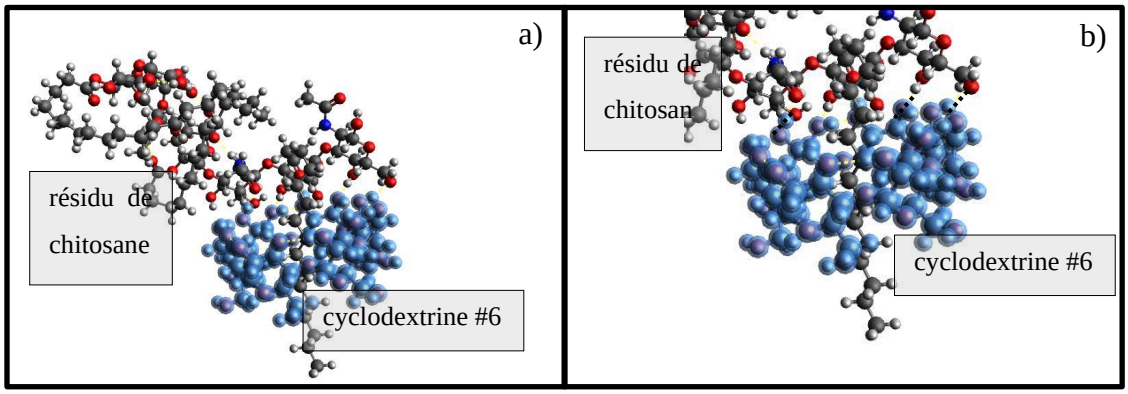

Figure R-18. a) La structure du point minimum du complexe hexasaccharide-cyclodextrine. b) La position du résidu chitosan par rapport à la cyclodextrine retirée #6. (La cyclodextrine retirée #6 est colorée en bleu pour plus de clarté, et la ligne en tirets noirs indique la liaison hydrogène entre la cyclodextrine #6 et le résidu chitosan).

Cette méthode d'analyse permet de trouver la voie appropriée pour éliminer toutes les molécules de cyclodextrine du complexe hexasaccharide-cyclodextrine.

Sur la base de l'énergie d'extraction obtenue, il existe un mécanisme plausible qui nous permet d'éliminer les molécules de cyclodextrine une par une pour obtenir le saccharide ramifié sans molécules de cyclodextrine. Cela nous aide à mieux comprendre le mécanisme de réaction de la formation du complexe hexasaccharide-cyclodextrine.

D'autre part, la coopérativité des liaisons hydrogène est non seulement capable d'avoir un effet sur les énergies d'extraction du complexe hexasaccharide-cyclodextrine mais est également capable d'expliquer la stabilité de ces conformations d'intermédiaires. Nous espérons que cette coopérativité de la liaison hydrogène sera utile pour fournir des informations sur le mécanisme d'extraction de la cyclodextrine du complexe hexasaccharide-cyclodextrine et du complexe d'inclusion. Par exemple, une raison partielle de la transformation de la conformation du complexe hexasaccharide-cyclodextrine, provoquée par le mouvement coopératif de deux molécules de cyclodextrine (voir **Figure R-17**), peut résider dans l'interaction des liaisons hydrogène intermoléculaires entre les molécules de cyclodextrine. Nous pensons que les résultats de cette étude seront utiles pour de telles recherches détaillées dans les études futures.

General Introduction

The radical-mediated reaction can be considered as a powerful and efficient tool to construct the C-C bonds in organic chemistry. With the development of chemistry, physics, medicine, and pharmaceutical industry, the application of radical-mediated reactions in various fields has gained a considerable attention from both academy and industry. Traditionally, the practical approaches for the generation of radical intermediate include the use of organometallic reagents in stoichiometric amounts for single-electron transfer processes or mixtures of a radical initiator, like azobisisobutyronitrile (AIBN), dibenzoyl peroxide (BPO), and tert-butyl hydroperoxide (TBHP) under heat treatment or irradiation of ultraviolet light, and a radical mediator such as tributyltin hydride (Bu_3SnH) for radical chain mechanisms. Due to the pollution of the traditional radical source, it is desirable to find an environment-friendly method to generate radical intermediate. Developing novel catalysis methods is a feasible strategy. Numerous novel catalysis methods such as electrocatalysis, photoelectron catalysis, and photoredox catalysis are developed for the generation of radical intermediates. Photoredox catalysis can avoid the utilization of expensive equipment and extra strong oxidants or reductants. Additionally, a photoredox catalyst can catalyze reactions under mild reaction conditions (usually at ambient temperature). A wide scope of organic compounds can generate corresponding radical intermediate under photoredox catalysis. In contrast to traditional radical chemistry, photoredox catalysis offers a green, low energy-consumption alternative to prepare various organic compounds.

As a promising radical precursor, bis-catecholato silicates gain a lot of attention from chemists. Considering alkyl bis-catecholato silicates are easily photooxidized, the corresponding phenyl silicates also can be considered as a potential source of phenyl radical via an oxidative pathway. In general, phenyl radicals can be generated via reductive photoredox catalysis. Diazonium salts, iodonium salts, sulfonium salts, pyridinium salts, and aryl halides can generate aryl radicals via a photoreduction process. In contrast, only aryl carboxylates can generate aryl radicals via a photooxidation process. The investigation of phenyl bis-catecholato silicates can provide a novel feasible method to generate radical intermediates. It still has been a challenge to obtain the phenyl radical utilizing phenyl bis-catecholato silicates as substrate under oxidative reaction conditions[8] (Figure GI-a).

[8] I. Ghosh, L. Marzo, A. Das, R. Shaikh, B. König, *Acc. Chem. Res*. **2016**, *49*, 1566-1577

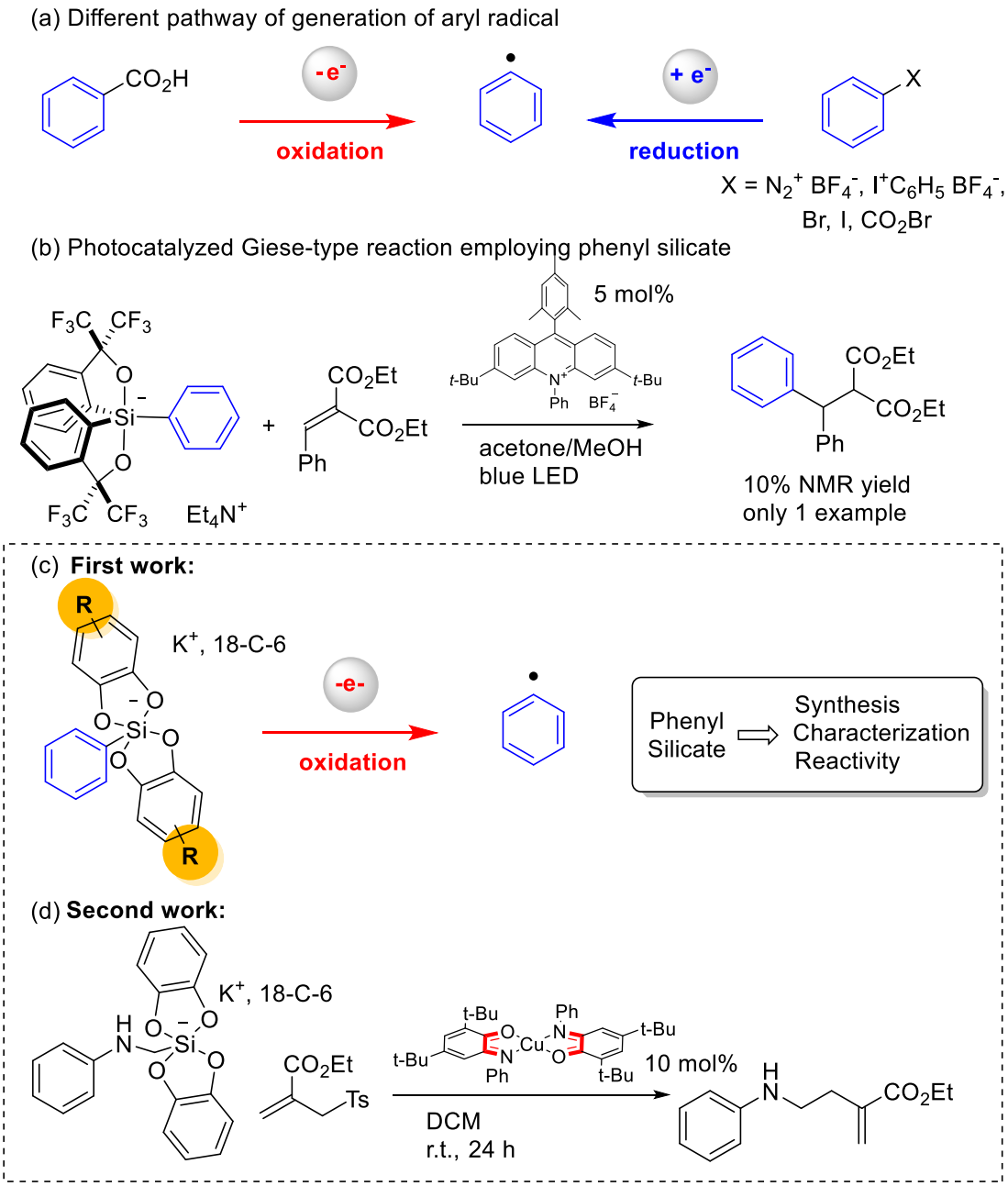

Figure GI Oxidation of bis-catecholato silicates for the formation of alkyl and aryl radicals

Recently, Morofuji and Kano[9] reported a photocatalyzed Giese-type reaction employing phenyl silicate bearing Martin's ligand as substrate. In this reaction, phenyl silicate generates aryl radicals under visible light irradiation. However, the lower yield indicated that the generation of aryl radicals through the photooxidation process is highly challenging (Figure GI-b).

Inspired by the previous finding, utilizing the phenyl bis-catecholato silicates as a novel

[9] T. Morofuji, Y. Matsui, M. Ohno, G. Ikarashi, N. Kano, *Chem. – A Eur. J.* **2021**, *27*, 6713–6718.

resource of phenyl radical via the photooxidation process is a promising pathway. The redox potential of bis-catecholato silicates can be altered by modifying the catecholato moiety. It can be a feasible strategy to find an appropriate substrate that can be photooxidized by a photoredox catalyst.

Metal complexes bearing non-innocent ligands can catalyze radical-mediated reactions under mild conditions. It can be considered as a powerful and reliable tool for the formation of C-C bond. Based on the previous work about non-innocent ligand of our group,[10] bis-iminobenzoquinone copper(II) complex have the potential to carry out the oxidation of alkyl bis-catecholate silicates to generate radical intermediates (Figure GI-d). We could extend the application of silicates to other catalytic systems and develop a novel organic reaction method.

Considering the properties of the inclusion complex formed by these modified hexasaccharides and cyclodextrin are similar to those of a drug delivery system excipient, the inclusion complex shows potential applications in the pharmaceutical industry. In 2016, K. Bouchemal and co-workers prepared various inclusion complexes of grafted hexasaccharides with α-CD dissolved at room temperature in aqueous solutions.

The extraction and insertion process of the inclusion monomer and dimer inclusion complex of palmitic acid and cyclodextrin can provide us a chance to get insight into the energy changement during the process. The further investigation of extraction energy has the potential to explore how the cyclodextrin molecule is removed from the hexasaccharide-6cyclodextrins. It helps us to explore the mechanism of the decomposition or formation of the hexasaccharide-cyclodextrins complex.

[10] J. Jacquet, P. Chaumont, G. Gontard, M. Orio, H. Vezin, S. Blanchard, M. Desage-El Murr, L. Fensterbank, *Angew. Chemie Int. Ed.* **2016**, *55*, 10712–10716.

Chapter 1. Photooxidation of Phenyl Silicates with Substituted Catecholate Ligand: Synthesis, Structural Studies, and Reactivity

1. Project Aims and Introduction

This chapter focuses on photoredox catalysis and particularly on the photooxidation of phenyl pentacoordinate silicon complex. This section will start with the basic principle of photoredox catalysis and general information on silicon derivatives. Some examples of photoredox catalyzed reactions employing the pentacoordinate silicon complex for the generation of alkyl radicals will also be presented. The second part of this chapter mainly focuses on the photocatalyzed generation of the aryl radical under photooxidizing conditions using bis-catecholate silicates as the substrate. In addition, the published work has explored the mechanism of this reaction by calculations and experiments.

2. Background on the photoredox catalysis and bis-catecholato silicates

2.1 General informations on photoredox catalysis in organic chemistry

2.1.1. Visible light and photoredox catalysis: pioneer works

Visible light could be considered as a kind of green energy. In 1991, the Italian chemist Ciamician, a pioneer in organic photochemistry, conceived the future development of solar energy for synthesis.[11]

Although people generally recognize the possible economic and environmental benefits of photochemistry, photochemistry in the industry is still very limited. One reason is that most organic molecules cannot be irradiated by visible light. Most photochemical syntheses require

[11]G. Duret, R. Quinlan, P. Bisseret, N. Blanchard, *Chem. Sci.* **2015**, *6*, 5366–5382.

ultraviolet light. Moreover, in the composition of sunlight, ultraviolet light represents less than 3%. If visible light is used directly, the reaction efficiency will be significantly reduced. In addition, some organic photochemical reactions are usually carried out in specially designed small reactors that can produce high-energy ultraviolet light. The cost of designing and installing large photoreactors dedicated to industrial synthesis is very high. As early as the 1950s and 1960s, David M. Hercules[12] and D. M. Klassen[13] noticed that the use of tris(2,2'-bipyridine) ruthenium (II) transition metal complexes represented by ($Ru(bpy)_3^{2+}$) could be irradiated by visible light, and a single electron transfer (SET) process can occur. In the following thirty years, studies mainly concerned the photophysical, photochemical, and electrochemical properties of $Ru(bpy)_3^{2+}$. However, its involvement in organic transformations has been rarely reported, and its development has been slow.

In 1978, Kellogg and colleagues published the first example of photocatalytic reaction.[14] The ruthenium photocatalyst $Ru(bpy)_3Cl_2$ in combination with a stoichiometric 1,4-dihydropyridine (which were considered to be NADH mimics) may be used to reduce phenacyl sulfonium salts to their corresponding acetophenone through the intermediate ketyl radical (**Scheme 1).**

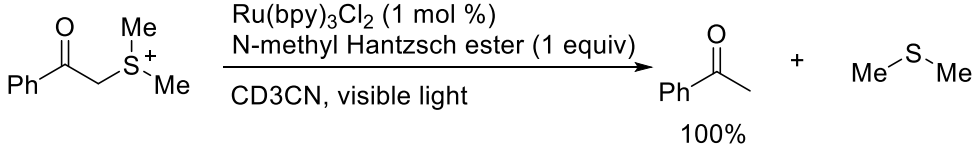

Scheme 1. Photocatalyzed reduction of phenacyl sulfonium salts by Kellogg

In 1981, Pac and co-workers[15] described the reduction of alkenes bearing electron-withdrawing group catalyzed by $Ru(bpy)_3^{2+}$. The stoichiometric reductant 1-benzyl-1,4-dihydro-nicotinamide (BNAH) (analog of the biomimetic reductant 1,4-dihydro-nicotinamide adenine dinucleotide (NADH)) was employed in the reaction. In the presence of the photocatalyst $Ru(bpy)_3^{2+}$, the electron-deficient olefins like dimethyl maleate could be reduced to the corresponding dihydrogenated product dimethyl succinate. Additionally, this

[12] F. E. Lytle, D. M. Hercules, *J. Am. Chem. Soc.* **1969**, *91*, 253–257.

[13] D. M. Klassen, G. A. Crosby, *J. Chem. Phys.* **1968**, *48*, 1853–1858.

[14] (a) D. M. Hedstrand, W. H. Kruizinga, R. M. Kellogg, *Tetrahedron Lett.* **1978**, *19*, 1255–1258. (b) T. J. Van Bergen, D. M. Hedstrand, W. H. Kruizinga, R. M. Kellogg, *J. Org. Chem.* **1979**, *44*, 4953–4962.

[15] C. Pac, M. Ihama, M. Yasuda, Y. Miyauchi, H. Sakurai, *J. Am. Chem. Soc.* **1981**, *103*, 6495–6497.

photocatalyzed reduction was shown to be capable with the olefins substituted with electron-deficient groups, including esters, ketones, arenes, and nitriles (**Scheme 2).**

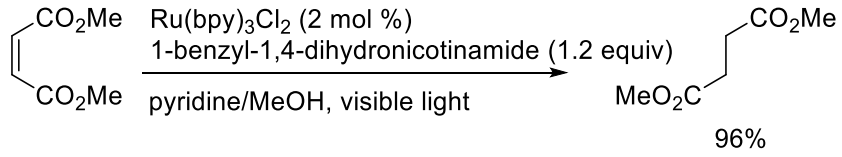

Scheme 2. Photocatalyzed reduction of electron-deficient olefins by Pac

In 1984, Willner and colleagues[16] reported the reductive dehalogenation of *meso*-1,2-dibromostilbene to stilbene using a biphasic dual catalytic system consisting of the photoredox catalyst $Ru(bpy)_3^{2+}$ and the viologen catalyst N,N'-dioctyl-4,4'-bipyridinium, Inspired by earlier work, Willner and co-workers[17] reported that photoredox reductive dehalogenation of *meso*-1,2-dibromostilbene produces the reduction product stilbene in the presence of the stoichiometric reductant 1,4- dihydro-nicotinamide adenine dinucleotide (NADH) (**Scheme 3).**

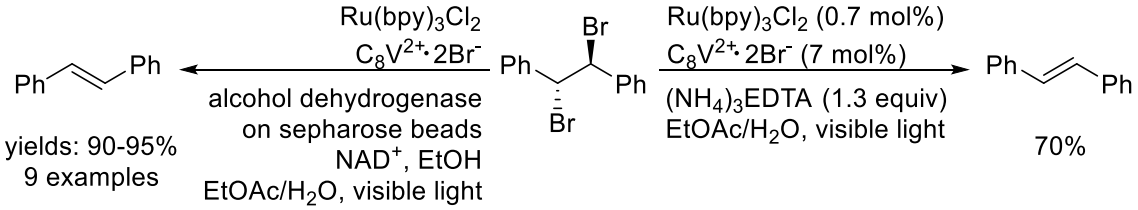

Scheme 3. The photocatalyzed dehalogenation of *meso*-1,2-dibromostilbene by Willner

In an early contribution, Derozier and Cano-Yelo reported[18] the first reaction of photocatalytic oxidation of benzylic alcohols. In the presence of ruthenium photocatalyst and a large amount of aryldiazonium salt as a sacrificial oxidant, the benzylic alcohol could be oxidized to corresponding aldehydes (**Scheme 4).**

[16] (a) Z. Goren, I. Willner, *J. Am. Chem. Soc.*, **1983**, *105*, 7764–7765. (b) R. Maidan, Z. Goren, J. Y. Becker, I. Willner, *J. Am. Chem. Soc.*, **1984**, *106*, 6217–6222. (c) I. Willner, Z. Goren, D. Mandler, R. Maidan, Y. Degani, *J. Photochem.*, **1985**, *28*, 215–228.

[17] R. Maidan, I. Willner, *J. Am. Chem. Soc.* **1986**, *108*, 1080–1082.

[18] H. Cano-Yelo, A. Deronzier, *Tetrahedron Lett.* **1984**, *25*, 5517–5520.

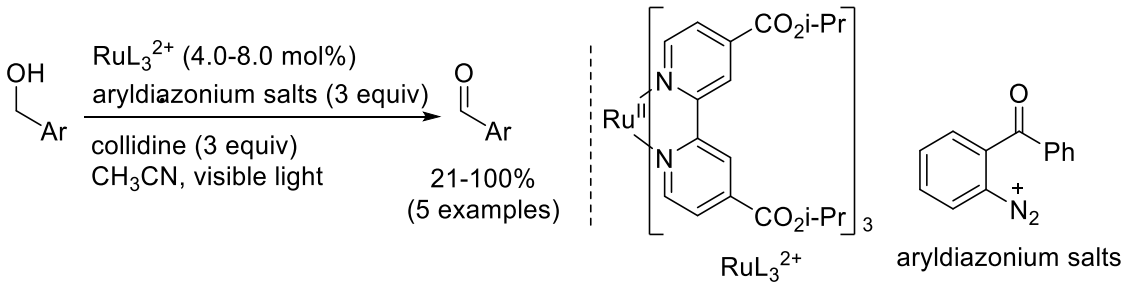

Scheme 4. Photocatalytic oxidation of benzylic alcohols by Cano-Yelo and Deronzier

In 1984, Tanaka and colleagues[19] used $Ru(bpy)_3^{2+}$ as a photoredox catalyst that was used to reduce benzyl bromide. Rather than converting benzyl bromide to toluene, the main product detected is 1,2-diphenyl-ethane (**Scheme 5).** Tanaka proposed that the coupling product can be generated by the reductive homocoupling of benzyl radical or by a successive single-electron reduction of benzyl radical to the benzyl carbanion, which can combine with benzyl bromide through a nucleophilic S_N2 process to yield 1,2-diphenyl-ethane. (**Scheme 5**)

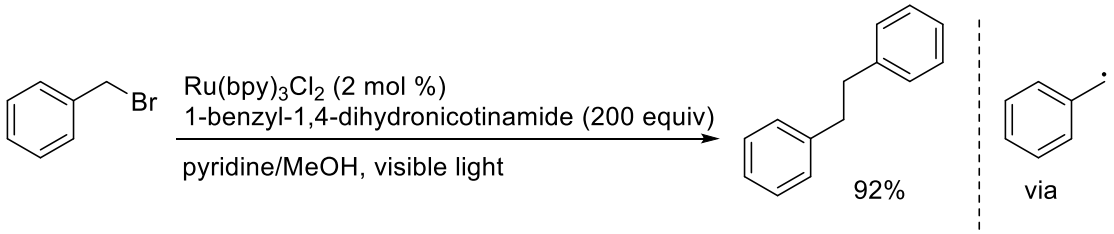

Scheme 5. Photocatalyzed reductive dimerization of benzyl bromide by Tanaka

In 1991, Okada and co-workers[20] described that N-(acyloxy)phthalimides could be utilized as potential precursors to generate alkyl radicals. In the presence of the benzyl-1,4-dihydro-nicotinamide (BNAH), using the ruthenium complex $Ru(bpy)_3^{2+}$ as the photoredox catalyst, N-(acyloxy)phthalimides could generate alkyl radical after decarboxylation, which could carry out a set of reactions to give the corresponding alkylated product (**Scheme 6**).

[19] K. Hironaka, S. Fukuzumi, T. Tanaka, *J. Chem. Soc. Perkin Trans. 2* **1984**, 1705–1709.

[20] (a) K. Okada, K. Okamoto, N. Morita, K. Okubo, M. Oda, *J. Am. Chem. Soc.*, **1991**, *113*, 9401–9402. (b) K. Okada, K. Okubo, N. Morita, M. Oda, *Chem. Lett.*, **1993**, *22*, 2021–2024. (c) K. Okada, K. Okubo, N. Morita and M. Oda, *Tetrahedron Lett.*, **1992**, *33*, 7377–7380.

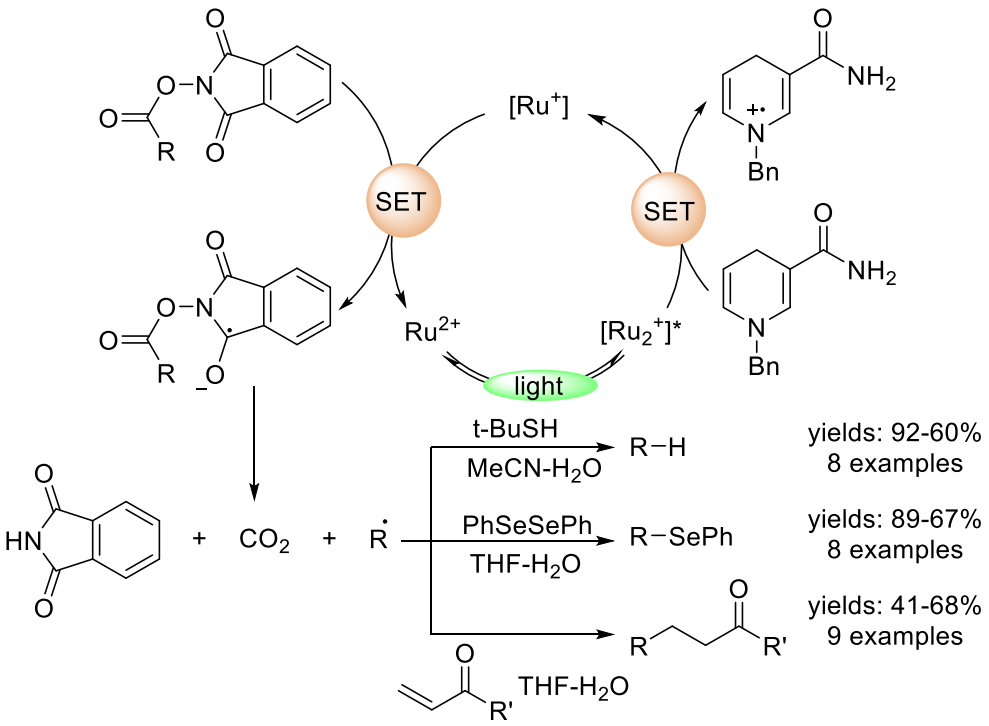

Scheme 6. Photocatalyzed oxidation of N-(acyloxy)phthalimides and its subsequent reactions by Okada

In 1990, Fukuzumi and co-workers [21] provided an early example of reductive dehalogenation of α-bromocarbonyl compounds using $Ru(bpy)_3Cl_2$ as a photocatalyst. The reaction conditions employed (1 mol % of $Ru(bpy)_3Cl_2$ and 3.0 equivalents of 9,10-dihydro-10-methyl-acridine in pyridine/MeOH) can provide transformation of α-bromocarbonyl compounds to desired reduction product. (**Scheme 7).**

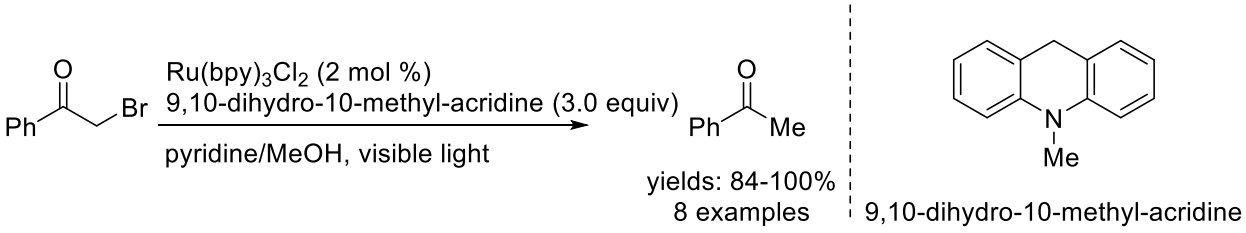

Scheme 7. Photocatalyzed reductive dehalogenation of α-bromocarbonyl compounds by Fukuzumi

In 1994, Barton and co-workers[22] demonstrated that $Ru(bpy)_3^{2+}$ catalyzed the radical-mediated addition of Se-phenyl *p*-tolueneselenosulfonate to a variety of vinyl ethers,

[21] S. Fukuzumi, S. Mochizuki, T. Tanaka, *J. Phys. Chem.* **1990**, *94*, 722–726.

[22] D. H. R. Barton, M. A. Csiba, J. C. Jaszberenyi, *Tetrahedron Lett.* **1994**, *35*, 2869–2872.

providing the phenylselenosulfones in good yields (**Scheme 8).**

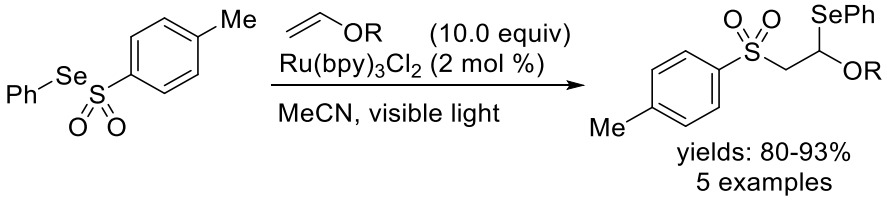

Scheme 8. $Ru(bpy)_3^{2+}$ catalyzed the radical-mediated addition of Se-phenyl *p*-tolueneselenosulfonate by Barton

The scope of photoredox catalysis has been expanded to include protein-protein complex crosslinking. In the biological area, Kodadek [23] has performed the visible-light-induced photoredox catalyzed dimerization of electron-rich arenes in order to investigate the interactions between different proteins. In these reported methods, the phenol of a tyrosine residue can be oxidized by a photocatalyst to generate radical cation. If the second tyrosine residue (or another nucleophilic residue) also can be oxidized, the construction of C-C bonds occurs similarly to the dimerization of naphthol (**Scheme 9).** Because this process occurred exclusively between adjacent amino acids, it can be used to crosslink two proteins at the interface of proteins (**Scheme 9).**

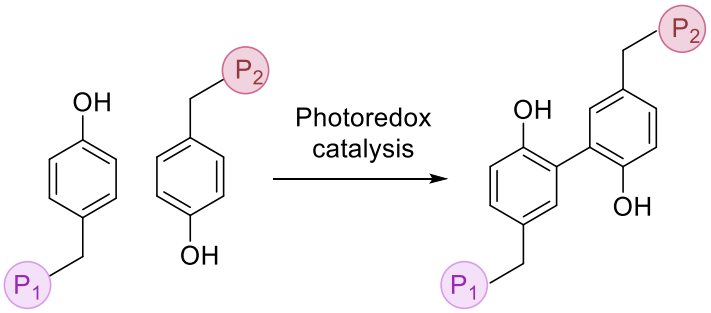

Scheme 9. Photoredox catalyzed protein-protein complex crosslinking by Kodadek

In 2008, The MacMillan group [24] firstly reported the enantioselective α-alkylation of aldehydes employing the dual catalytic system merging the photoredox catalysis and

[23] (a) T. Kodadek, I. Duroux-Richard, J.-C. Bonnafous, *Trends Pharmacol. Sci.* **2005**, *26*, 210–217. (b) F. Amini, C. Denison, H.-J. Lin, L. Kuo, T. Kodadek, *Chem. Biol.* **2003**, *10*, 1115–1127.. (c) D. A. Fancy, C. Denison, K. Kim, Y. Xie, T. Holdeman, F. Amini, T. Kodadek, *Chem. Biol.* **2000**, *7*, 697–708. (d) K. Kim, D. A. Fancy, D. Carney, T. Kodadek, *J. Am. Chem. Soc.* **1999**, *121*, 11896–11897.. (e) D. A. Fancy, T. Kodadek, *Proc. Natl. Acad. Sci.* **1999**, *96*, 6020–6024.

[24] D. A. Nicewicz, D. W. C. MacMillan, Science. **2008**, *322*, 77–80.

organocatalysis, causing a sensation in the scientific research community. Since then, the field of visible light catalysis has entered a period of rapid development(**Scheme 10**).

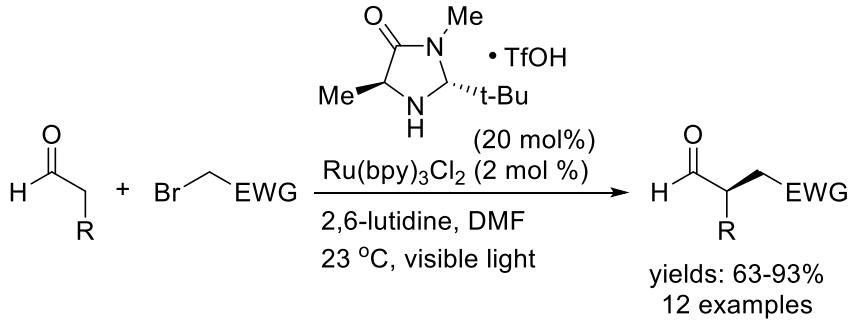

Scheme 10. Photoredox-organocatalyzed enantioselective α-alkylation of aldehydes by MacMillan

2.1.2 The photoredox catalyst

In general, photoredox catalysts that were utilized in organic reactions can be classified into two different categories. One is transition metal photoredox catalysts based on Ru(II), Ir(III), or other transition metal-centered complexes. The other is non-metallic organic photocatalyst such as organic fluorescent dyes. The representative examples are Eosin Y, Methylene Blue, and fluorescein. (**Scheme 11**)

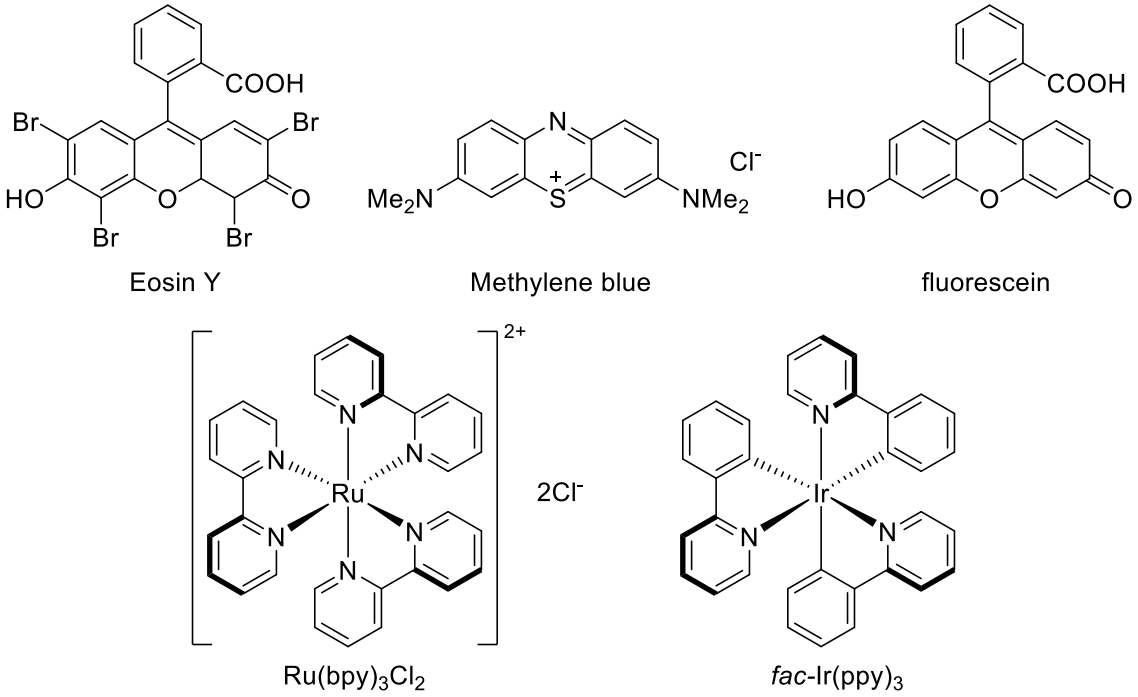

Scheme 11. Representative examples of non-metallic organic photocatalysts and transition metal complex photocatalysts

In photocatalysis, the transition metal photoredox catalyst can be polypyridine transition metal complexes such as $Ru(bpy)_3Cl_2$ and *fac*-$Ir(ppy)_3$. After absorbing the photon, the MLCT (Metal-to-Ligand Charge-Transfer) transition leads to a singlet excited state ($MLCT^1$) of the photoredox catalyst. The Inter-System Crossing (ISC) that was observed in the heavy transition metal complex allowed the electronic transition from the singlet ($MLCT^1$) excited state to the triplet ($MLCT^3$) excited state. Due to there was a heavy transition metal atom in the complex, the corresponding excited state had a long lifetime (usually around 1000 ns). The longer luminescence lifetime led to the possibility that the transition metal photoredox catalyst could be applied in the organic synthesis, and the loading amount of the catalyst is low. (**Scheme 12**)

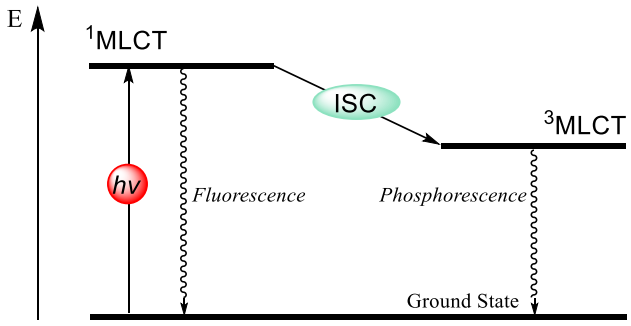

Scheme 12. Energy diagram of absorbing and emission processes

Generally speaking, by changing the types of aromatic ring ligands or ligand substituents, the electrochemical potential of the transition metal photoredox catalyst can be adjusted. The introduction of the electron-rich group on the ligand will enhance the reductive character of the photocatalyst, while the introduction of electron-deficient electron-withdrawing groups will enhance the oxidation property of the photocatalyst.

Comparing to the transition metal photoredox catalyst, the inefficient Inter-System Crossing (IRC) of the organic photoredox catalyst led to the short time of the S1 singlet excited state (the time of the organic photoredox catalyst usually less than 50 ns). The narrow singlet-triplet energy gap and the high photoluminescence quantum yield of the 4CzIPN make it attract much attention from organic chemists. The potential of the 4CzIPN has been reported by many chemists. (**Scheme 13**)

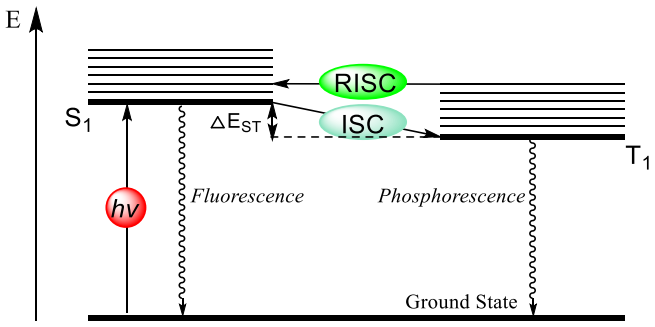

Scheme 13. Energy diagram for organic day photocatalyst.

Similar to the transition metal photoredox catalyst, the type of the organic compounds and the substituents of the organic dye molecule can modify the electrochemical potential of the organic photoredox catalyst. The structure-effect relationship of the organic photoredox catalyst has been summarized by organic chemists.

In 2018, Kirsten Zeitler and colleagues[25] chose 4CzIPN as the template molecule for systematically investigating the structure-reactivity correlations. They introduced electron-withdrawing or electron-donor substituents into the arene core of the 4CzIPN molecule to prepare various derivatives of 4CzIPN. On the one hand, electron-donor substituents would result in an increase in reductive ability. On the other hand, electron-acceptor substituents were necessary to increase the oxidation potential. Additionally, they extensively evaluated all the modified organic photoredox catalysts in various oxidation or reduction reactions in comparison to current best performance catalysts. (**Scheme 14**)

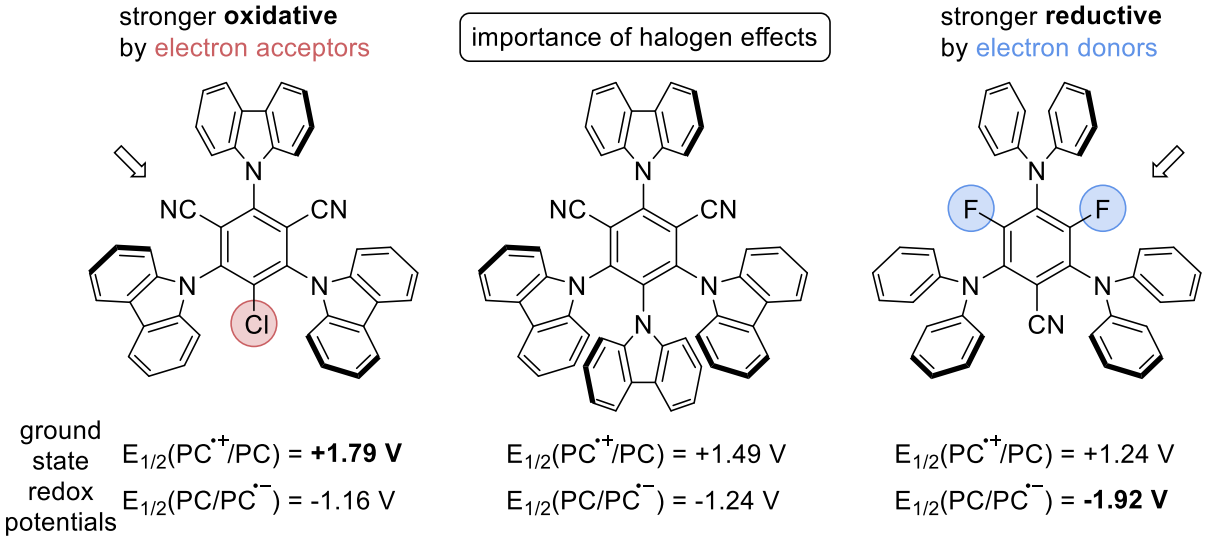

Scheme 14. Structure-reactivity correlations of 4CzIPN and its analogs.

[25] E. Speckmeier, T. G. Fischer, K. Zeitler, *J. Am. Chem. Soc.*, **2018**, *140*, 15353–15365.

2.1.3 Two Modes of catalysis: oxidative and reductive quenching cycles

The reaction can be classified into two modes: oxidation quenching cycle or reduction quenching cycle.

As previously stated, a photoexcited catalyst (PC^*) could transfer one electron to the starting substrates, thus generating radicals capable of participating in radical reactions. To catalyze the whole process, the photoredox catalyst ($PC^{+/-}$) must perform another single-electron-transfer (SET) process with an intermediate species or an extra reagent. When the photoredox catalyst reduces the substrate, the process is called Photoreduction; when the substrate is oxidized, the process is called Photooxidation.

More specifically, after absorbing the photon, the excited photoredox catalyst (PC^*) subsequently interacts with a commonly named "reductive quencher" to form the reduced photocatalyst PC^-. The modified photoredox catalyst then transfers its extra electron to electron acceptor A. This process could regenerate the initial photoredox catalyst and bringing the "reductive quenching cycle" to a conclusion. The term "oxidative quenching cycle" refers to the transformation between PC* and an electron acceptor A that serves as an oxidative quencher. The oxidized photoredox catalyst (PC^+) is then regenerated by reacting with an electron donor D. (**Scheme 15**)

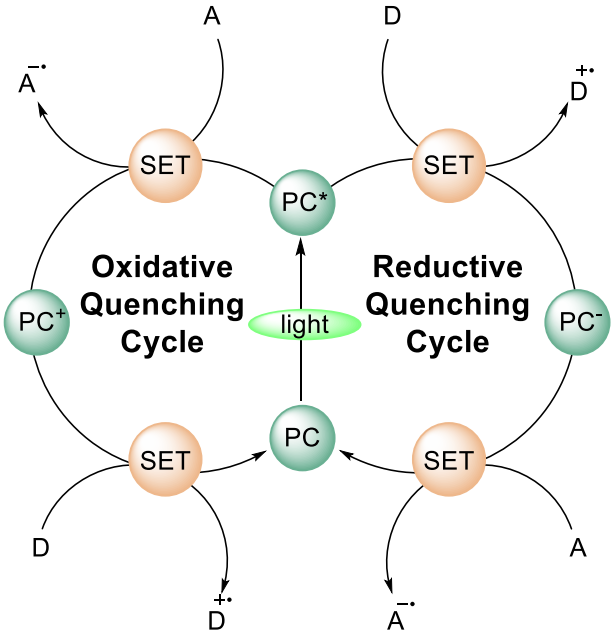

Scheme 15. Oxidative and reductive quenching cycles in photoredox catalysis

Photoreduction or photooxidation can be used to produce the radicals that have been

used in various synthetic methods. In the case of photoreduction, the photoexcited catalyst would directly reduce an acceptor in this example if the redox potentials were compatible. However, sometimes the redox potential of the photoreduced catalyst is insufficient to react with the electron acceptor. A suitable electron donor, such as (triethyl)amine and Hantzsch esters, can react with the PC^* firstly to produce PC^- and give a more efficient reducing agent feasible of reducing the substrate. On the other hand, photooxidation is a reaction in which a photoexcited catalyst immediately oxidizes a radical donor. As mentioned earlier, as with photoreduction, if PC^* is not sufficiently oxidizing, the additional electron acceptor such as oxygen, methylviologen, and persulfate agent can be considered as an alternative choice to react with PC^*, yielding PC^+ which have a much greater oxidizing capacity.

2.1.4 Selected photoreductive and photooxidative transformations in organic synthesis

Photoreductive transformations

Photoreduction of organohalide

In general, due to their high reductive potential, both alkyl halide and aryl halide can be used in the photoreductive processes. Considering the effect of the substituted group and halogen type, the reduction potential of bromide derivative decreases in the following order: 4-bromotoluene ($E_{1/2}^{red}$ = -1.79 V *vs* SCE)[26] > 1-bromohexane ($E_{1/2}^{red}$ = -2.09 V *vs* SCE). In contrast, depending the nature of the halogen, the reduction potential of decreases in the following order: 4-iodotoluene ($E_{1/2}^{red}$ = -1.2 V *vs* SCE) > 4-bromotoluene ($E_{1/2}^{red}$ = -1.79 V *vs* SCE) > 4-chlorotoluene ($E_{1/2}^{red}$ = -2.1 V *vs* SCE). Additionally, similar phenomena could also be observed for the alkyl halogen derivatives.[27]

In 2016, H. Fu and his colleagues[28] realized a photoredox-catalyzed cross-coupling reaction utilizing aryl iodides or aryl bromides as the substrates for the preparation of the desired aryl borate products. In the reported protocol, results from a preliminary study revealed that aryl halide can be borylated with bis(pinacolato)diboron in the presence of iridium polypyridyl complex *fac*-$Ir(ppy)_3$ and n-Bu_3N under the irridation of visible light. Furthermore, they managed to synthesis the substituted phenols from the intermediate borylated products in moderate to good yields (**Scheme 16**).

[26] S. Rondinini, P. R. Mussini, P. Muttini, G. Sello, *Electrochim. Acta* **2001**, *46*, 3245–3258.

[27] A. A. Isse, C. Y. Lin, M. L. Coote, A. Gennaro, *J. Phys. Chem. B* **2011**, *115*, 678–684.

[28] M. Jiang, H. Yang, H. Fu, *Org. Lett.* **2016**, *18*, 5248–5251.

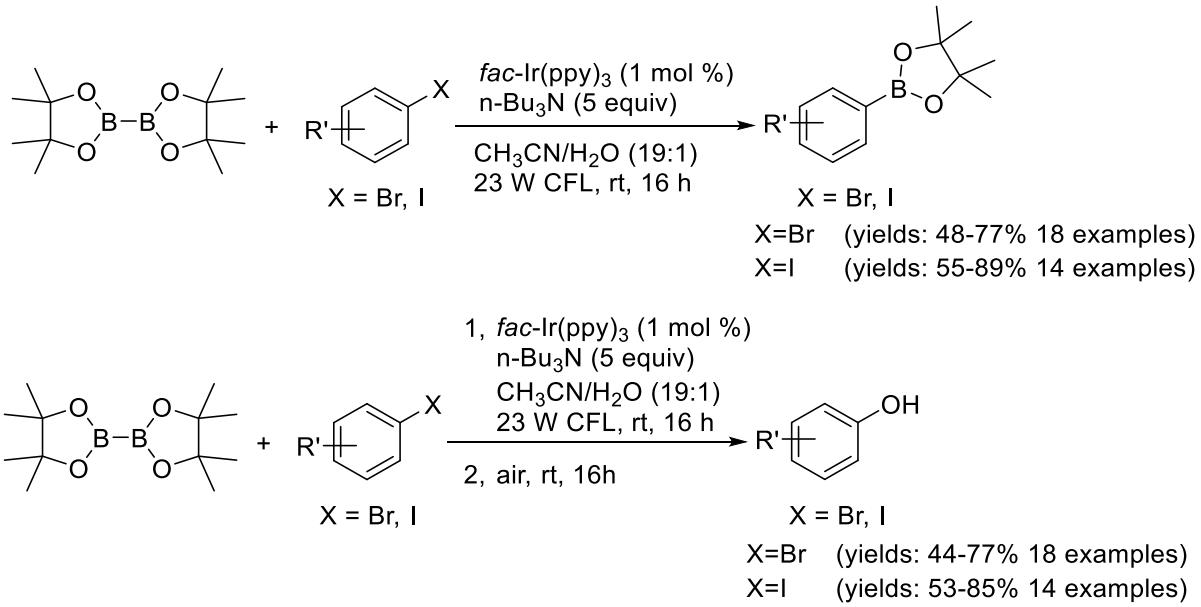

Scheme 16. Photoredox-catalyzed cross-coupling reaction utilizing aryl iodides or aryl bromides for the formation of aryl pinacol borates and substituted phenols.

ESR spin trapping experiments indicated that the free radical intermediate species are involved in the proposed mechanism. According to the authors, the catalysis cycle is initiated *via* the irridation of the iridium complex [Ir^{III}] (*fac*-Ir(ppy)$_3$) to its excited state [Ir]*. The reduced state of iridium complex [Ir^{II}] was generated via single-electron reduction of [Ir]* with nBu_3N. The aryl radical anion intermediate could form via the single electron transfer (SET) of [Ir^{II}] to aryl halide, affording the regenerated iridium catalyst [Ir^{III}]. Then, the decomposition of the aryl radical anion led to the formation of aryl radical. Then, trapping with the hydroxylated borate and following the single electron transfer (SET) process provided the target cross-coupling product. (**Scheme 17**)

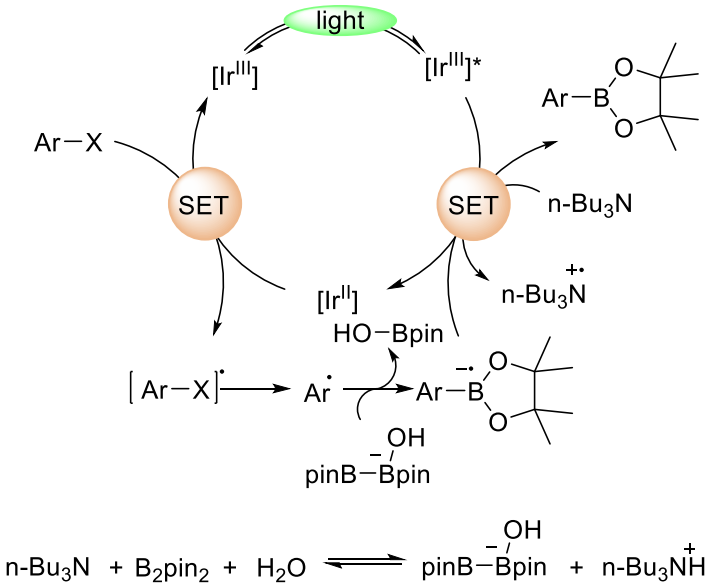

Scheme 17 Proposed mechanism of photoredox-catalyzed cross-coupling reaction

In 2017, Burkhard König[29] and coworkers reported reductive activation of carbon-halogen bonds employing derivatives of N-methylpyrrole as radical traps and aryl halides as substrates. In their case, they established a photoredox catalyst system using the transition metal complex $Ru(bpy)_3Cl_2$ and polycyclic aromatic hydrocarbons (PAHs) such as pyrene, naphthalene, and triphenylene. The organic amine N,N-diisopropylethylamine (DIPEA) was employed as an electron donor. Following Ru-catalyzed photoreduction, the generated aryl radical was bonded with different radical trapping reagents. The aryl halides could be cross-coupled with various radical trapping reagents to give high yields of the target products. (**Scheme 18**).

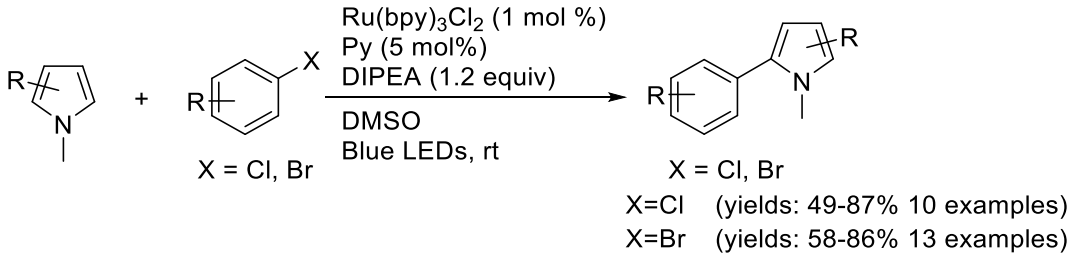

Scheme 18 PAHs co-catalyzed photoredox-catalyzed cross-coupling reaction

The catalytic cycle described in **Scheme 19** is supported by spectroscopic studies and the

[29] I. Ghosh, R. S. Shaikh, B. König, *Angew. Chemie Int. Ed.* **2017**, *56*, 8544–8549.

previous literature reports. Upon visible-light-induced photoexcitation, the energy transfer processes between the excited state of Ru catalyst $Ru(bpy)_3^{2+}$ and Pyrene yield the excited form $[Pyrene]^*$. The excited $[Pyrene]^*$ can be reductively quenched by DIPEA to generate anion radical species $[Pyrene]^{\bullet-}$ and the radical cation of DIPEA ($DIPEA^{\bullet+}$). The one-electron reductive addition of aryl halides catalyzed by $[Pyrene]^{\bullet-}$ occurs, forming the aryl radical anion $ArX^{\bullet-}$ and regenerating the ground state of Pyrene to complete the catalytic cycle. The cleavage of the carbon-halogen bond of the $Ar\text{-}X^{\bullet-}$ provided the aryl radical, which was trapped by (hetero)arenes, alkenes, or electrophiles ($(EtO)_3P$) to give the target coupling products.

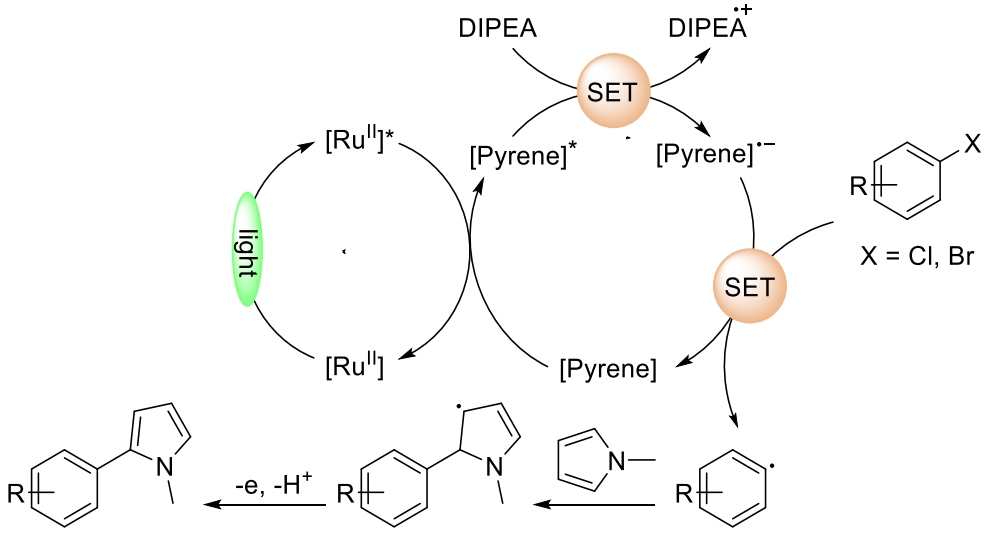

Scheme 19 Proposed mechanism of PAHs co-catalyzed photoredox cross-coupling reactions with aryl halides and methyl pyrrole

In the same year, Leonori and co-workers[30] reported a cross-coupling reaction of vinyl-BF_3K reagents and alkyl bromides. In their case, Eosin Y was used as a photoredox catalyst, and aryl halides were used as a radical precursor. After the photoreduction catalyzed by Eosin Y, alkyl radicals were coupled with various vinyl-BF_3K reagents to provide the desired product with good yields (**Scheme 20**).

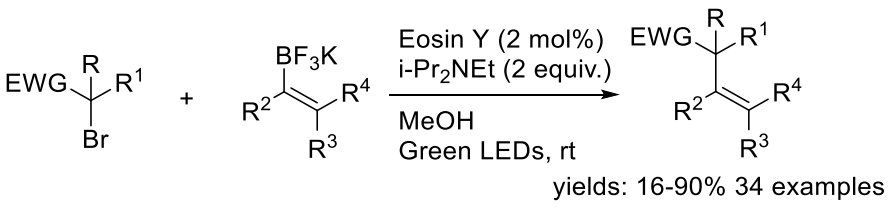

Scheme 20. Cross-coupling reaction of aryl halides and vinyl-BF_3K reagents

[30] D. Fernandez Reina, A. Ruffoni, Y. S. S. Al-Faiyz, J. J. Douglas, N. S. Sheikh, D. Leonori, *ACS Catal.* **2017**, *7*, 4126–4130.

By SET reduction and fragmentation, the alkyl bromides can be quenched oxidatively by Eosin Y, allowing obtain the desired carbon radicals. The carbon-centered radical would be produced by radical addition to the vinyl-BF_3K reagent in a regioselective manner. The following SET oxidation could provide the desired cross-coupling product. (**Scheme 21**)

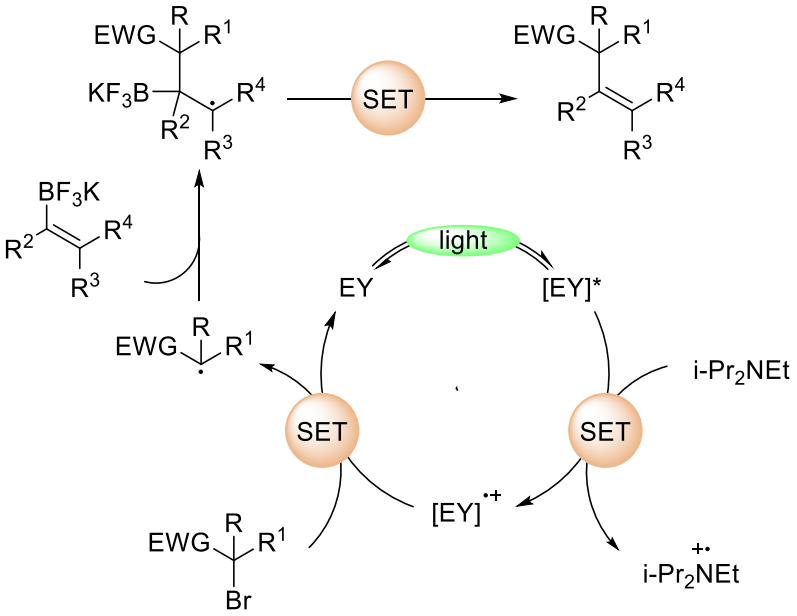

Scheme 21. The proposed mechanism for the cross-coupling reaction of vinyl-BF_3K reagents and alkyl bromides

In 2021, S. Yu and his colleagues[31] demonstrated a glycosyl cross-coupling reaction between the glycosyl bromides and heteroarenes, yielding the desired C-heteroaryl glycosides. In their reported method, they utilized an Ir-based polypyridyl complex $[Ir(ppy)_2(dtbbpy)]PF_6$ as a photoredox catalyst and the triethylamine (Et_3N) as both the electron donor and a proton scavenger. As a result of the evaluation of the substrate scope, this glycosyl cross-coupling protocol was shown to be tolerant with both coupling partners: heteroarenes and glycosyl bromides. The glycosyl bromides and their various analogs could react with the coupling partner heteroarenes to give a high yield of the target products (**Scheme 22**).

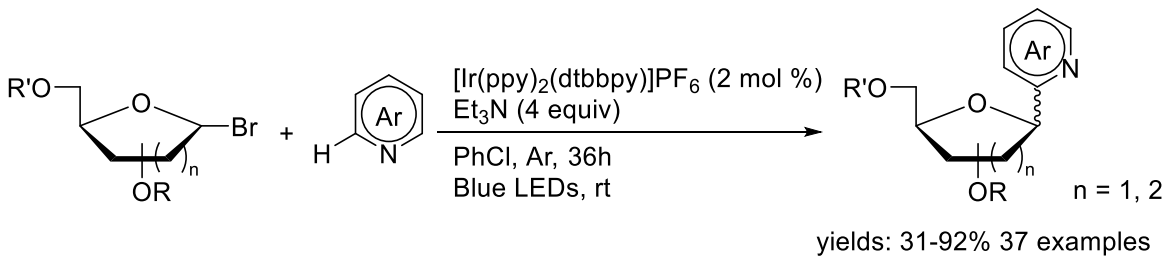

Scheme 22. Photoredox catalyzed cross-coupling reaction between glycosyl bromides and heteroarenes

[31] L. Xia, W. Fan, X.-A. Yuan, S. Yu, *ACS Catal.* **2021**, *11*, 9397–9406.

This proposed catalysis cycle included a series of events involving the radical-mediated bond formation and the single-electron-transfer process. In the proposed catalysis cycle, galactose-derived bromide and purine as the model to illustrate the mechanism. Considerable attention has been given to the subsequent sequence of events: (1) photoexcitation of the appropriate photocatalyst [Ir^{III}] to its excited state [Ir]* by visible light; (2) reductive quenching of the excited form [Ir]* with the electron donor Et_3N; (3) homolytic fragmentation of glycosyl bromides followed by coupling with heteroarenes resulting radical intermediate A; (4) single-electron oxidation of A by $Et_3N^{+\bullet}$ to form the cation intermediate B; (5) the following deprotonation of the cation by Et_3N lead to the target product. It is worth mentioning that the radical intermediate's regioselective addition is dependent on the electron density of the heteroarene substrate. The Fukui indices (f+)[32] show that the C6 (0.160) location has a higher electron density than the C2 (0.067) position. As a result, the nucleophilic addition of galactosyl radical A at the C6 position is preferred.

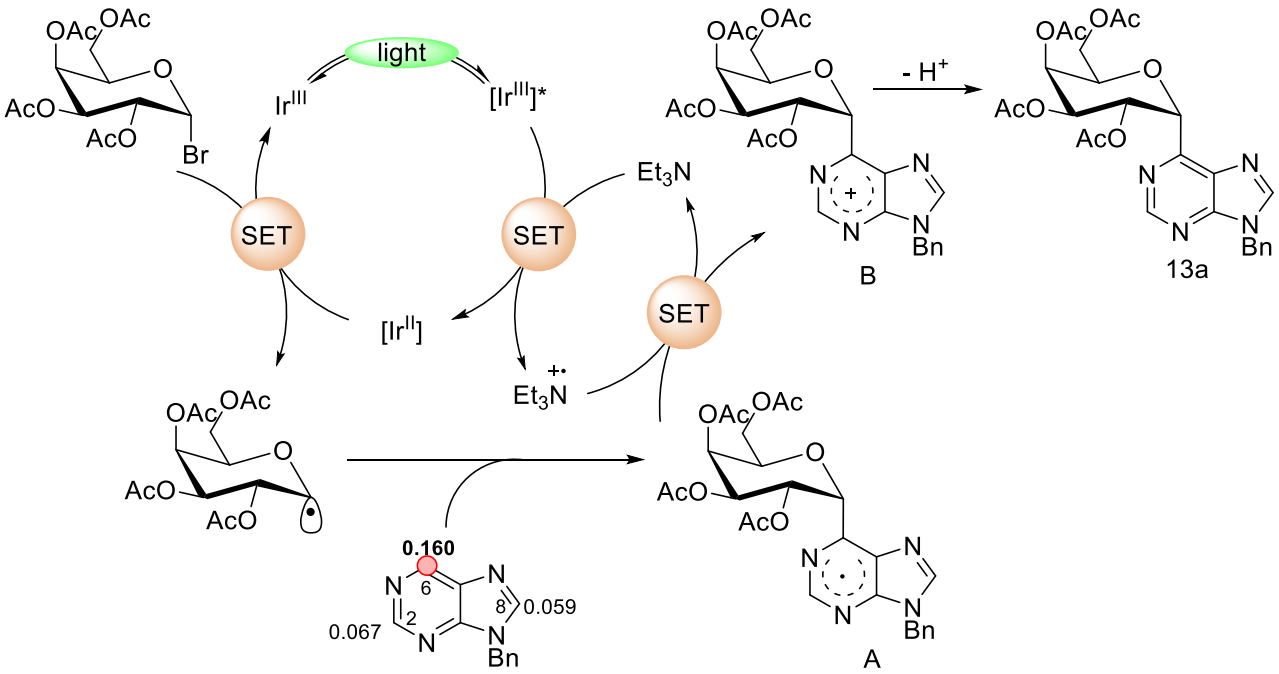

Scheme 23. the proposed catalysis cycle of the cross-coupling reaction between glycosyl bromides and heteroaromatic compound

Photoreduction of pyridinium salts

[32] H. Chen, W. Fan, X.-A. Yuan, S. Yu, *Nat. Commun.* **2019**, *10*, 1–9.

Due to the suitable reductive potential of pyridinium salt and its analogs ($E_{1/2}^{red}$ = -1.32 ~ -0.50 V *vs* SCE)[33], the pyridinium salts employed as radical precursors are rather facile to oxidize to generate the radical intermediate through photoreduction by an appropriate photoredox catalyst.

N-Functionalized pyridinium compounds could result in the generation of radicals, which are then produced via the dissociative electron transfer (DET) process.[34] It is possible for dissociative electron transfer to proceed through two distinct pathways to generate various radical fragments. The pathways of the cleavage of the N-X bond of the pyridinium salt could be divided into the homolytic cleavage and the heterolytic cleavage. On the one hand, in most situations, homolytic cleavage of the N-X bond occurs to yield applicable X free radical (X•) accompanied by simultaneous generation of the pyridine equivalent. On the other hand, heterolytic cleavage of the N-X bond of the electron-deficient pyridinium compounds could provide the X anion(X^-) concurrently formed radical cation of pyridine. (**Scheme 24**)

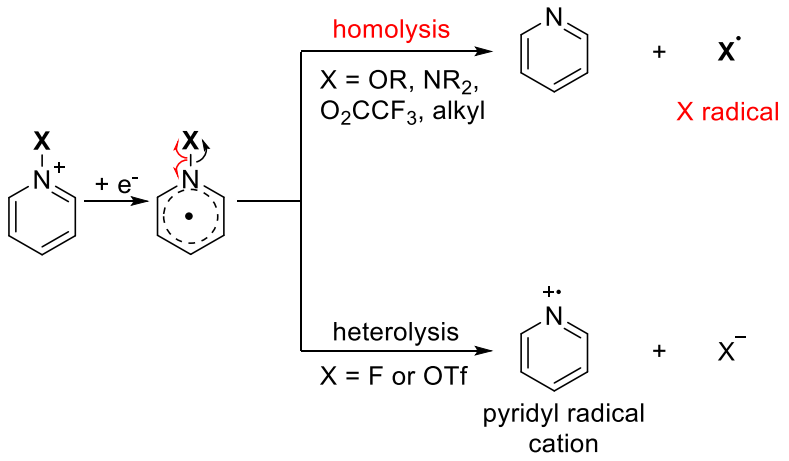

Scheme 24. Reduction of N-Functionalized pyridinium compounds: Two distinct routes of dissociative electron transfer (DET) process

Due to the commercial availability and accessible preparation of the N-alkyl pyridinium compounds, the pyridinium salts have gained significant interest as the latent radical precursors for the formation of various radicals. The pyridinium salts have therefore evolved as a powerful tool for numerous reactions. In the late 1970s, Katritzky and his coworkers[35] realized the first reaction via the intermediate N-alkyl pyridinium salt. The corresponding

[33] (a) C. W. Kazakoff, R. T. B. Rye, O. S. Tee, *Can. J. Chem.* **1989**, *67*, 183–186. (b) I. R. Gould, D. Shukla, D. Giesen, S. Farid, *Helv. Chim. Acta* **2001**, *84*, 2796–2812.

[34] E. D. Lorance, W. H. Kramer, I. R. Gould, *J. Am. Chem. Soc.* **2002**, *124*, 15225–15238.

[35] A. R. Katritzky, *Tetrahedron*, **1980**, *36*, 679–699.

primary amines could covert to the desired nucleophilic substitution product *via* the corresponding pyridinium salt. (**Scheme 25**)

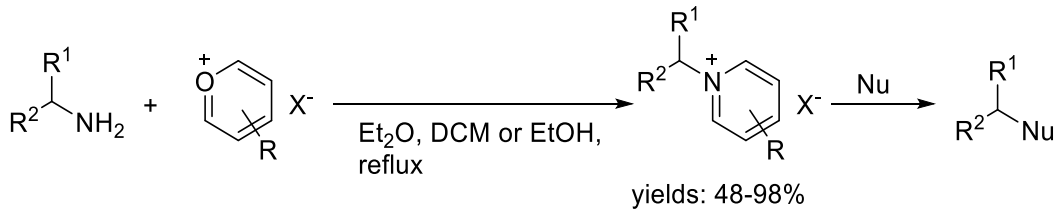

Scheme 25. Synthesis of N-alkyl pyridinium salt and the following nucleophilic substitution reaction

Understanding the redox properties of the photocatalytic substrates is necessary for a thorough comprehension of the catalysis process. These findings establish the thermodynamic plausibility of a process. Numerous research groups have shown interest in the method taken by this visible-light photoredox catalysis, which uses N-alkyl pyridinium salts as a substrate. Additionally, the extensive usage of pyridinium salts in organic synthesis is due to the numerous kinds of radicals that are capable of undergoing the radical-mediated reaction and yielding the required product under photoredox catalysis. The success of these methods for producing substituted pyridinium compounds prompted other research groups to investigate new reactions and broaden the application area. $C(sp^3)$-$C(sp^3)$ Bond formation[36], $C(sp^3)$-$C(sp^2)$ bond formation[37], $C(sp^3)$-C(sp) bond formation[26], Giese reaction[38], and other various reactions[39] continue to be reported at a rapid pace. (**Scheme 26**)

[36] M. Ociepa, J. Turkowska, D. Gryko, *ACS Catal.* **2018**, *8*, 11362–11367.

[37] M.-M. Zhang, F. Liu, *Org. Chem. Front.* **2018**, *5*, 3443–3446.

[38] J. Wu, P. S. Grant, X. Li, A. Noble, V. K. Aggarwal, *Angew. Chemie Int. Ed.* **2019**, *58*, 5697–5701.

[39] (a) T. W. Greulich, C. G. Daniliuc, A. Studer, *Org. Lett.* **2015**, *17*, 254–257. (b) W.-D. Liu, G.-Q. Xu, X.-Q. Hu, P.-F. Xu, *Org. Lett.* **2017**, *19*, 6288–6291. (c) W.-L. Yu, J.-Q. Chen, Y.-L. Wei, Z.-Y. Wang, P.-F. Xu, *Chem. Commun.* **2018**, *54*, 1948–1951. (d) K. Miyazawa, T. Koike, M. Akita, *Chem. – A Eur. J.* **2015**, *21*, 11677–11680.

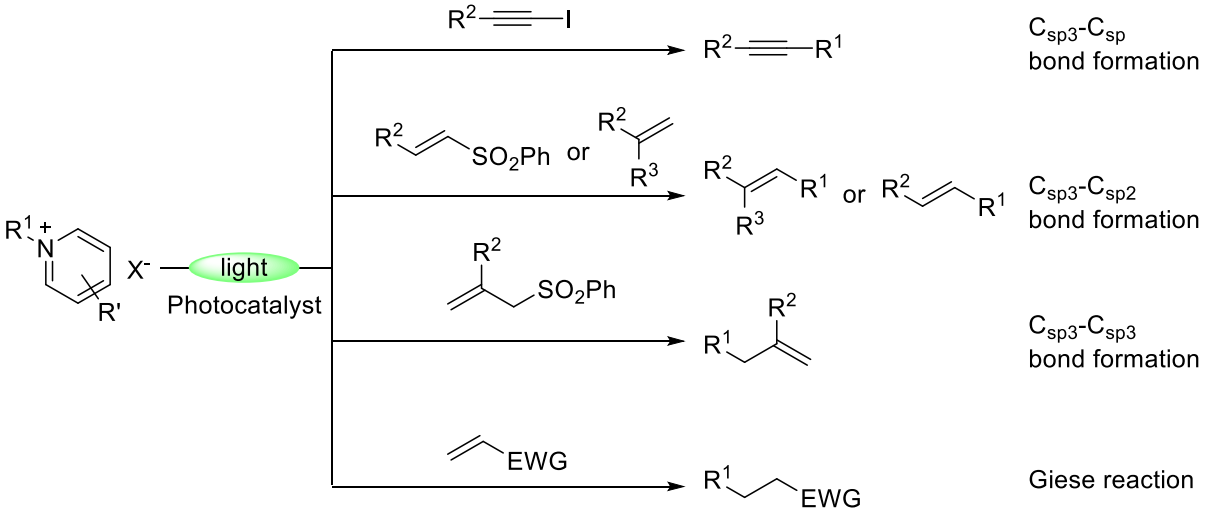

Scheme 26. Expansion of substituted pyridinium salts to a variety of bond formation processes

In 2017, inspired by the pioneering work of Katritzky[25], Frank Glorius [40] and his colleagues performed the efficient visible-light-induced deaminative cross-coupling reaction of various N-alkyl pyridinium salts derivated from corresponding aliphatic primary amines with heteroarene via photoreduction process(**Scheme 27**). The realized deaminative cross-coupling reaction could undergo in the presence of 2.5 mol% iridium-based photocatalyst $[Ir(ppy)_2(dtbbpy)]PF_6$ in DMA to obtain the alkylated cross-coupling product efficiently. The extension of diamination pyridinium salts to the corresponding pyridinium salts of various amino acid methyl esters and substituted primary amines and the scope of the coupling partner heteroarene to the N-contained heteroaromatic compound like pyridine, isoquinolines, quinolines, and indoles.

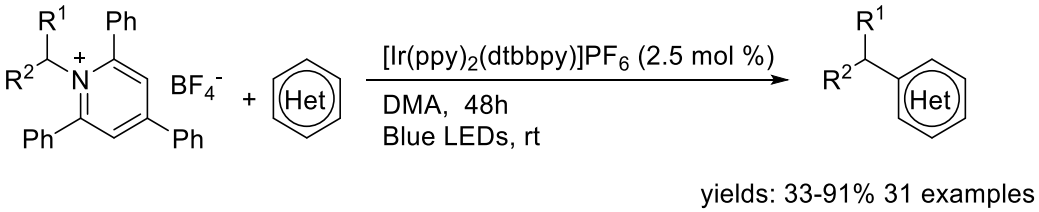

Scheme 27. Visible light-induced deaminative cross-coupling reaction of various N-alkyl pyridinium salts

The addition of TEMPO ((2,2,6,6-tetramethylpiperidin-1-yl)oxyl) totally inhibited the

[40] F. J. R. Klauck, M. J. James, F. Glorius, *Angew. Chemie Int. Ed.* **2017**, *56*, 12336–12339.

deaminative cross-coupling reaction under the optimized reaction. ESI-MS analysis also identified a TEMPO-alkyl radical adduct. All the results of the mechanism experiment strongly indicated that an alkyl radical intermediate is generated in this process.

In 2019, inspired by the previous work, Zhu's group[41] demonstrated a chemo- and regio-selective three-component 1,2-aminoisothiocyanation reactions of 1,3-dienes under photoredox catalysis (**Scheme 28**). Employing Ir-based polypyridyl complex $[Ir(dF(CF_3)ppy)_2(dtbbpy)]PF_6$ as the photoredox catalyst and trimethylsilyl isothiocyanate (TMSNCS) as the source of NCS^-, the photoreduction of the N-aminopyridinium salt can result in the nitrogen-centered radicals capable of undergoing the three-component aminoisothiocyanation reactions with the various substituted 1,3-dienes 17 and TMSNCS to give the desired 1,2-difunctionalization products in good yields with chemo- and regio-selectivity. Additionally, the scope of pyridinium salts could be expanded to include N-aminopyridinium salts that could generate the amidyl radicals (like $(RSO_2\text{-}N^{\bullet}\text{-}CR^1$, $RCO\text{-}N^{\bullet}\text{-}CR^1$ and $Boc\text{-}N^{\cdot}\text{-}R^1$). (**Scheme 28**)

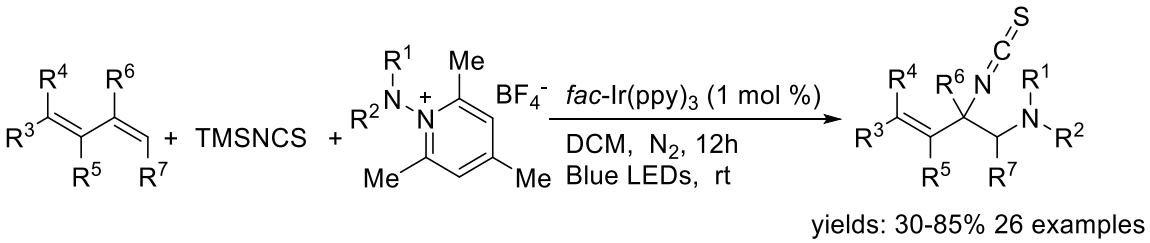

Scheme 28. Photocatalyzed three-component 1,2-aminoisothiocyanation reactions

The Stern–Volmer quenching experiment indicated that the reductive quenching process employing the pyridinium salt as the reductive quencher proposed to be involved in the catalysis cycle. This catalysis cycle is initiated by the irridation of the iridium complex $[Ir^{III}]$ (fac-$Ir(ppy)_3$) to its excited state $[Ir^*]$. The reduce quenching process of excited state $[Ir^*]$ with nBu_3N could provide the reductive iridium complex $[Ir^{II}]$, N-centered radical, and the by-product 2,4,6-collidine via a single electron transfer (SET) process. The regioselective addition of the resulting radical to a 1,3-diene to produce the allylic radical. Subsequently, the carbocation specie could be produced through single-electron oxidation of $[Ir^{IV}]$ to allylic radical, resulting in the regeneration of the iridium catalyst $[Ir^{III}]$ simultaneously. Finally, the nucleophilic trapping of allylic carbocation with TMSNCS could afford the desired 1,2-substituted product in a highly regioselective manner. (**Scheme 29**)

[41] W. Guo, Q. Wang, J. Zhu, *Angew. Chemie Int. Ed.* **2021**, *60*, 4085–4089.

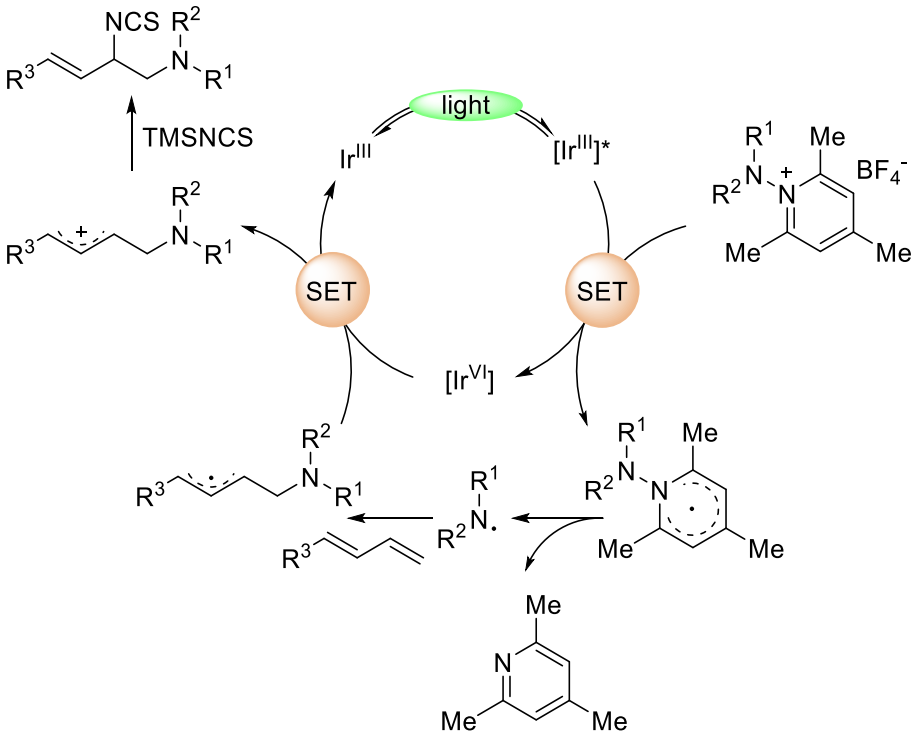

Scheme 29. The proposed mechanism of the regioselective aminoisothiocyanation reaction

In 2018, based on previous work, Alexander D. Dilman's group[42] realized the solvent-involving trifluoromethylation reaction of alkenes with the catalysis of Cu(I) photocatalyst (**Scheme 30**). Using bis(1,10-phenanthroline) Cu(I) salts ($Cu(dap)_2PF_6$) as the photoredox catalyst, the trifluoromethyl borate N-oxypyridinium salts could be utilized to undergo the solvent-involved trifluoromethylation reaction. This trifluoromethylation reagent could rapidly react with the various substituted alkenes to give the desired difunctionalization products in a regioselective manner.

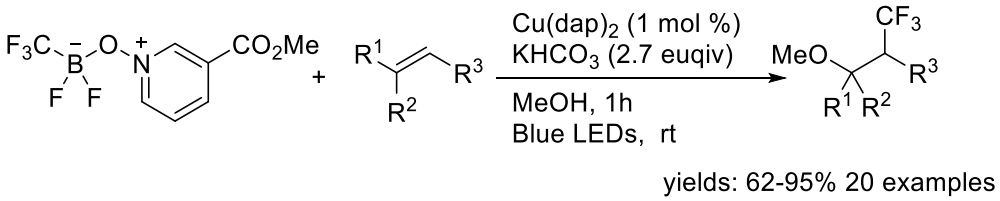

Scheme 30. Photoreduction of the trifluoromethyl borate salts resulting in trifluoromethylation reaction

This hypothesized mechanism involved a sequence of radical-mediated bond-forming processes. Especially, the steps of the mechanism were given due consideration: : (1) visible-

[42] V. O. Smirnov, A. S. Maslov, V. A. Kokorekin, A. A. Korlyukov, A. D. Dilman, *Chem. Commun*. **2018**, *54*, 2236–2239.

light-induced photoactivation of the appropriate photosensitizer [Cu^{I}] to its excited state [Cu^{*}]; (2) reductive quenching of the radical precursor N-oxypyridinium salts via SET reduction affording the trifluoromethyl radicals (CF_3•); (3) the regioselective addition of the resulting trifluoromethyl radicals to an olefin to generate the intermediate A; (4) single-electron oxidation of A by the [Cu^{II}] to form the alkyl cation species adduct B and concurrent regenerate the photosensitizer [Cu^{I}] to finish the catalytic cycle; (5) trapping of the carbocation by MeOH could yield the target 1,2-difunctionalized product. (**Scheme 31**)

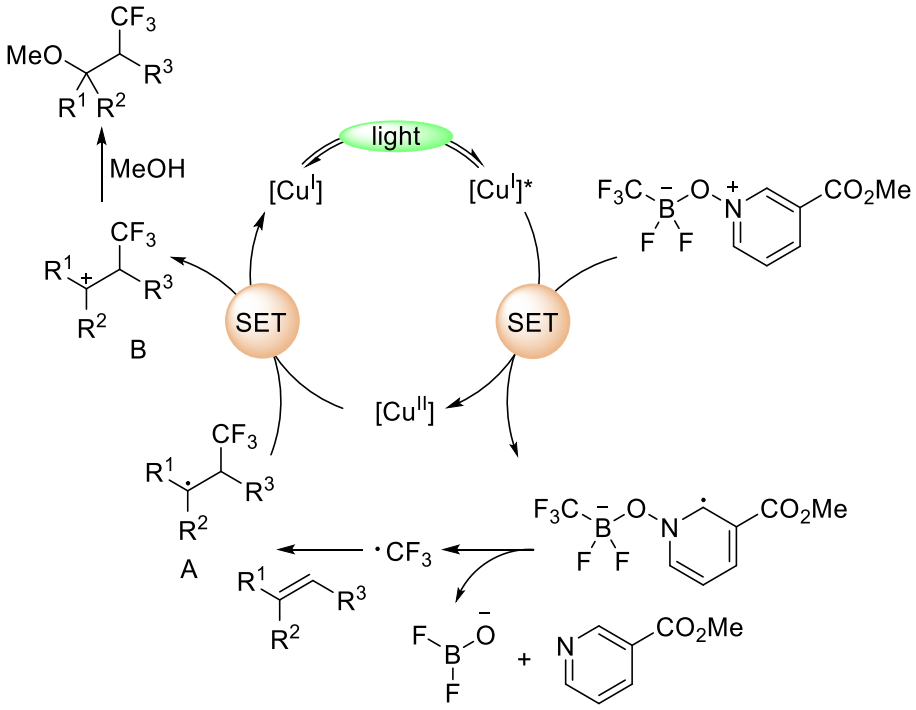

Scheme 31. The suggested mechanism of the photocatalyzed solvent-involving trifluoromethylation reaction

In some cases of photocatalyzed reaction, visible-light-induced excitation of an interaction complex consisted of two molecules, which was termed electron-donor-acceptor (EDA) complex, which can efficiently transfer electrons without an extra photoredox catalyst. Katritzky[43], Kochi[44], and Olah[45]'s pioneering work have demonstrated the potential of pyridinium salts to generate EDA complexes. In general, the electron-deficient molecule like N-alkyl pyridinium salt could be coupled with the appropriate electron-rich molecule that has suitable oxidation potential, affording the corresponding EDA complex. Depending on the electrochemical properties of the EDA complex (like the electrochemical potentials of the

[43] A. R. Katritzky, G. Z. de Ville, R. C. Patel, *Tetrahedron Lett.* **1980**, *21*, 1723–1726.

[44] (a) K. Y. Lee, J. K. Kochi, *J. Chem. Soc., Perkin Trans. 2* **1994**, 237–245. (b) K. Y. Lee, J. K. Kochi, *J. Chem. Soc., Perkin Trans. 2* **1992**, 1011–1017.

[45] G. A. Olah, S. C. Narang, J. A. Olah, R. L. Pearson, C. A. Cupas, *J. Am. Chem. Soc.* **1980**, *102*, 3507–3510.

components of the EDA complex), a photoinduced electron transfer (PET) process could provide an appealing option to inducing reductive fragmentation of an N-substituted pyridinium salt.

The Aggarwal group[46] demonstrated the deaminative borylation of N-alkyl pyridinium salts prepared from aliphatic amines using bis(catecholato)diboron (B_2cat_2) as a source of boryl species. Bis(catecholato)diboron (B_2cat_2) was discovered as a suitable electron-rich component for the formation of 1:1 EDA complexes with the electron-deficient pyridinium salt. The photoinduced electron transfer (PET) process is capable of providing the radical ion pair intermediate. The following fragmentation of the radical ion pair species can produce the desired alkyl radical. And then, the alkyl radical was trapped by bis(catecholato)diboron (B_2cat_2) to obtain the borylated product. The UV/Vis absorption spectroscopy indicated the formation of an EDA complex composed of N-substituted pyridinium salts and B_2cat_2. The further mechanism experiment[47] supported the stoichiometric ratio of the EDA complex as 1:1. (**Scheme 32**)

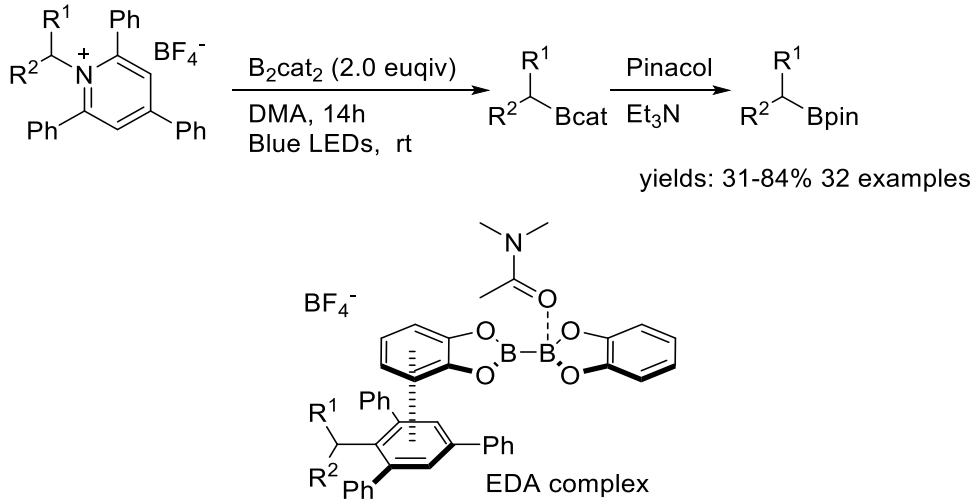

Scheme 32. The photo-induced deaminative borylation via EDA complex

The PET process could theoretically be utilized in a wide scope of appropriate substrates that generate EDA complexes with pyridinium salts. Recent studies of the EDA complex mediated arylation [48] or alkylation [49] employing N-substituted pyridinium salts without photocatalyst demonstrate the potential use of the EDA complex in photocatalysis.

[46] J. Wu, L. He, A. Noble, V. K. Aggarwal, *J. Am. Chem. Soc.* **2018**, *140*, 10700–10704.

[47] P. MacCarthy, *Anal. Chem.*, **1978**, *50*, 2165.

[48] A. de A. Bartolomeu, R. C. Silva, T. J. Brocksom, T. Noël, K. T. de Oliveira, *J. Org. Chem.* **2019**, *84*, 10459–10471.

[49] (a) A. de A. Bartolomeu, R. C. Silva, T. J. Brocksom, T. Noël, K. T. de Oliveira, *J. Org. Chem.* **2019**, *84*, 10459–10471. (b) J. Hu, B. Cheng, X. Yang, T.-P. Loh, *Adv. Synth. Catal.* **2019**, *361*, 4902–4908.

Photoreduction of onium salts (diazoniums, sulfoniums, iodoniums)

Based on the electrochemical properties of the the onium salts ($E_{1/2}^{red}$(aryl diazonium)[50] = -0.11 to -0.23 V *vs* SCE, $E_{1/2}^{red}$(aryl sulfonium)[51] = -1.05 to -1.37 V *vs* SCE and $E_{1/2}^{red}$(aryl iodonium)[52] = +0.65 V *vs* SCE) , , the onium salts, like diazoniums, sulfoniums and iodoniums, can be used as substrates of photoredox reactions. They are easily reduced to generate the radical intermediate in the presence of a suitable photoredox catalyst.

In 2020, Pedro Almendros and his colleagues[53] realized a novel photoredox catalyzed sulfonylation-rearrangement cascade of allenol with arene diazonium salts, employing $Ru(bpy)_3(PF_6)_2$ as a reducing photocatalyst and DABSO [$DABCO{\cdot}(SO_2)_2$], as the source of sulfur dioxide. (**Scheme 33**)

First, the 1,4-diazabicyclo-[2.2.2]octanyl (DABCO) ion radical and the aryl sulfonyl radical **A** was generated. Allylic radicals **B** reacted with the allenol and produced allylic cations **C** via oxidation. Photoredox catalyst ruthenium complex catalyzed this oxidation process, which involves a single electron transfer (SET) process. As a result of 1,2-aryl migration, homoallylic alcohols **D** can generate the protonated aldehydes **E**. The spontaneous deprotonation of intermediate **E** led to the final products 2,2-disubstituted-3-(arylsulfonyl)but-3-enals

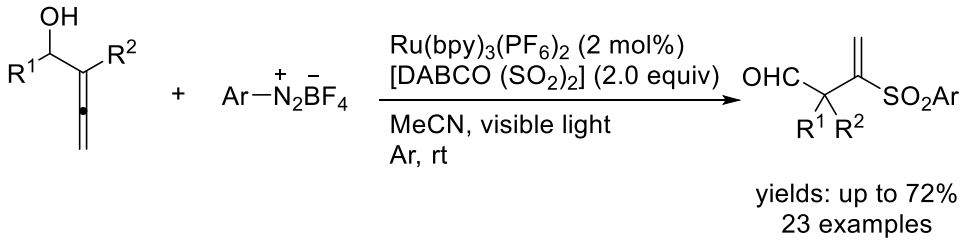

[50] J. K. Kochi, *J. Am. Chem. Soc.*, **1955**, *77*, 3208–3211.

[51] L. Liang, H.-Y. Niu, R.-L. Li, Y.-F. Wang, J.-K. Yan, C.-G. Li, H.-M. Guo, *Org. Lett.* **2020**, *22*, 6842–6846.

[52] (a) L. Koefoed, K. H. Vase, J. H. Stenlid, T. Brinck, Y. Yoshimura, H. Lund, S. U. Pedersen, K. Daasbjerg, *ChemElectroChem* **2017**, *4*, 3212–3221. (b) P. P. Romańczyk, S. S. Kurek, *Electrochim. Acta*, **2017**, *255*, 482–485.

[53] F. Herrera, A. Luna, P. Almendros, *Org. Lett.* **2020**, *22*, 9490–9494.

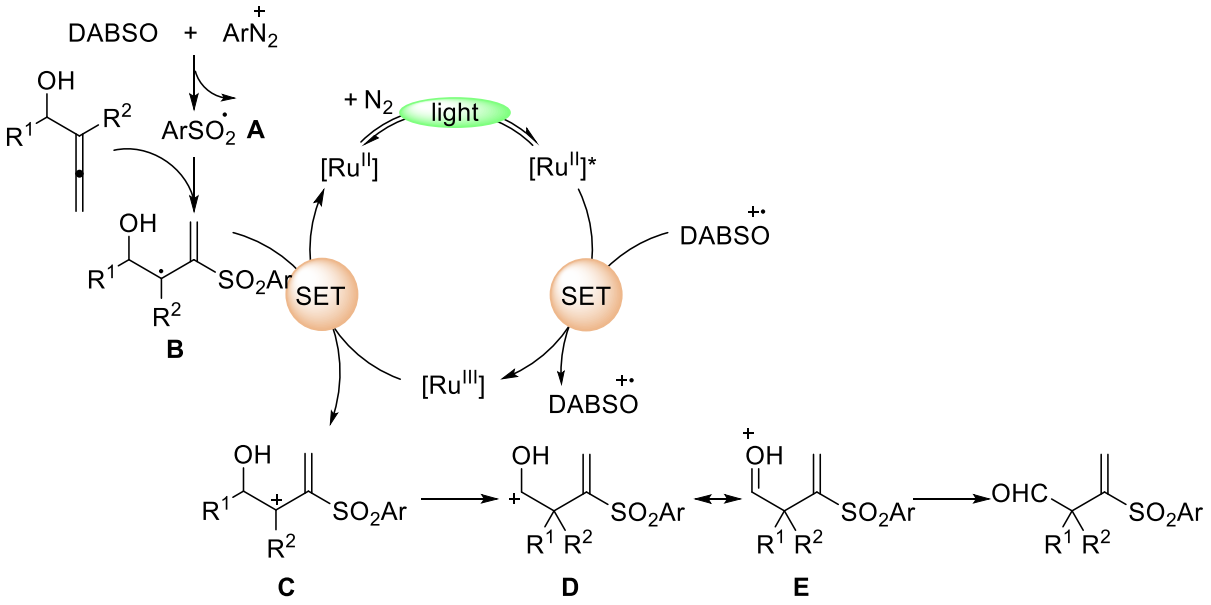

Scheme 33. The photoredox catalyzed sulfonylation-rearrangement cascade of allenol and the proposed mechanism.

In 2020, David J. Procter and his colleagues[54] developed an aryl cross-coupling reaction between the aryl sulfonium salts and heteroarenes, yielding the desired heterobiaryl products (**Scheme 34**). In their reported method, they utilized the organic dye 10-phenylphenothiazine as a photoredox catalyst. As a result of the evaluation of the substrate scope, this photocatalyzed metal-free cross-coupling protocol was shown to be compatible with a wide range of substituents on both coupling partners: heteroarenes and aryl sulfonium salts. The aryl sulfonium salts could react with the coupling partner heteroarenes to give high yields of the target products.

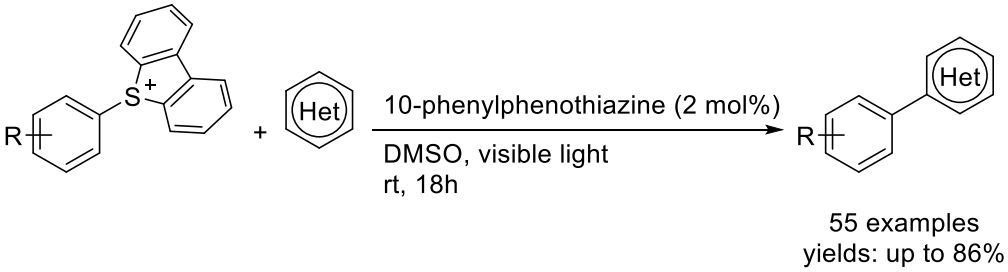

Scheme 34. The photocatalyzed cross-coupling reaction of the aryl sulfonium salts

In 2016, Denton's group[55] established a protocol for the phosphonation of aryl iodonium salts with phosphine upon the visible-light-induced photocatalysis (**Scheme 35**). Using the polypyridyl ruthenium complex $Ru(bpy)_3Cl_2$ as a photoredox catalyst, aryl iodonium salts

[54] M. H. Aukland, M. Šiaučiulis, A. West, G. J. P. Perry, D. J. Procter, *Nat. Catal.* **2020**, *3*, 163–169.

[55] A. F. Fearnley, J. An, M. Jackson, P. Lindovska, R. M. Denton, *Chem. Commun.* **2016**, *52*, 4987–4990.

could provide aryl radicals that can undergo phosphonation reactions with a set of substituted phosphines to produce the desired quaternary aryl phosphonium salts.

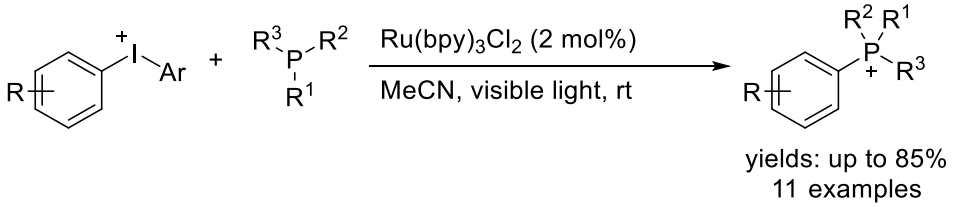

Scheme 35. The photocatalyzed phosphonation of aryl iodonium salts

Photooxidative transformations

Photooxidation of organoborates

Due to their high oxidative potential of substituted trifluoroborates ($E_{1/2}^{ox}$ = +2.32 to +0.36 V *vs* SCE)[56], trifluoroborates are difficult to generate unstabilized radicals. The photooxidation step is the constraint of the process.

In 2014, Chen's group[57] demonstrated that the photooxidation of alkyltrifluoroborate can be carried out, affording a corresponding alkyl radical as a product of the elimination of BF_3. The yield radicals could be cross-coupled with substituted alkynyl benziodoxoles (BI−alkyne) to give a set of desired deboronative alkynylation products in high yield. The reported method employed Ru-polypyridyl complex $Ru(bpy)_3(PF_6)_2$ as an oxidizing photocatalyst, Na_2CO_3 as the base, and the mixture of CH_2Cl_2/H_2O (1/1 vol ratio) as solvent. (**Scheme 36**)

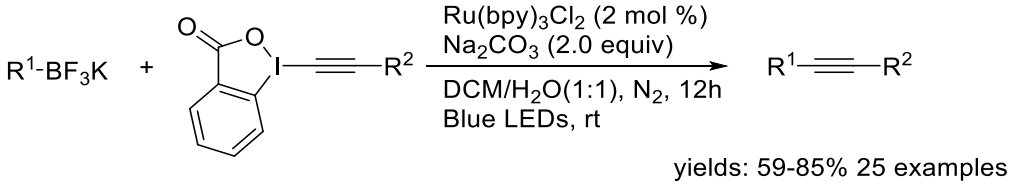

Scheme 36. The photooxidative cross-coupling of alkyltrifluoroborate

A mechanism involving the formation of the alkyl radical intermediate via the SET process was proposed, as shown in **Scheme 37**. Firstly, the catalytic cycle was initiated by the photoreduction of the excited state of ruthenium complex $[Ru^{II}]^*$ with the benziodoxole radical. The alkyltrifluoroborate underwent the single-electron oxidization by the oxidized Ru species $[Ru^{III}]$, yielding the alkyl radical and the regenerated ruthenium catalyst. The regioselective addition of the newly formed alkyl radical to alkynyl benziodoxole led to the

[56] D. Zhu, W. Zheng, Y. Zheng, H. Chang, H. Xie, *New J. Chem.* **2019**, *43*, 8590–8605.

[57] H. Huang, G. Zhang, L. Gong , S. Zhang, Y. Chen , *J. Am. Chem. Soc.*, **2014**, *136* , 2280 —2283

generation of intermediate A. Finally, elimination of intermediate A assisted by base can produce the intended product and benziodoxole radical. (**Scheme 37**)

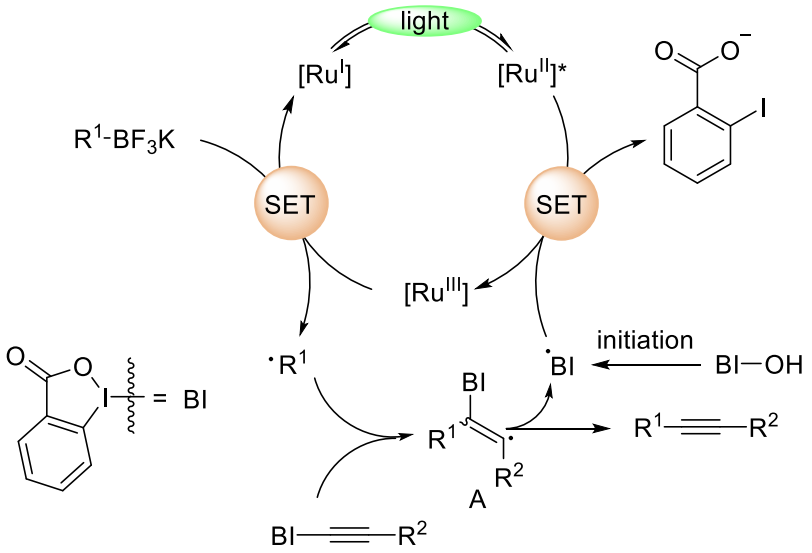

Scheme 37. The proposed mechanism of photooxidative cross-coupling of alkyltrifluoroborate

In 2015, Akita and his colleagues[58] realized a novel transition-metal-free photoredox catalyzed Giese-type reaction employing alkyltrifluoroborate or alkyl carboxylic acid as the radical precursor (**Scheme 38**). The proposed method utilized Fukuzumi's acridinium ([Acr^+–Mes]ClO_4) as an oxidizing photocatalyst and the mixture of Acetone/MeOH (1/1 vol ratio) as solvent. The photooxidation of alkyltrifluoroborate and alkyl carboxylic acid with [Acr^+–Mes]ClO_4 ($E_{1/2}^{red}$ = +2.06 V *vs* SCE)[59] can proceed under mild conditions. The provided alkyl radical was engaged in Giese-type reactions with electron-deficient alkenes. The desired products were separated in moderate to good yields. The mechanism experiment indicated that the H-abstraction from the solvent MeOH was involved in the proposed mechanism.

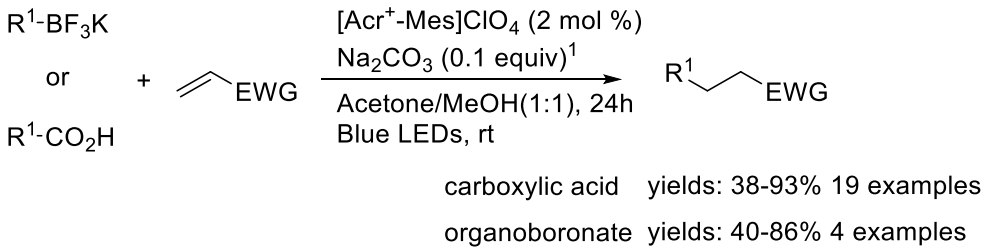

[58] T. Chinzei, K. Miyazawa, Y. Yasu, T. Koike, M. Akita, *RSC Adv.* **2015**, *5*, 21297–21300.

[59] A. C. Benniston, A. Harriman, P. Li, J. P. Rostron, H. J. van Ramesdonk, M. M. Groeneveld, H. Zhang, J. W. Verhoeven, *J. Am. Chem. Soc.* **2005**, *127*, 16054–16064.

Scheme 38. The photooxidative transition-metal-free photooxidative Giese-type reaction with alkyltrifluoroborates or alkyl carboxylic acids.

As illustrated in **Scheme 39**, based on the available literature[60] and the result of the mechanism experiment, a mechanism involving the generation of the intermediate alkyl radical through the SET process was hypothesized. The first step is the single-electron oxidation of the alkyltrifluoroborate or the deprotonated carboxylic acid by the excited photocatalyst* [Acr^+–Mes]*, thus affording the alkyl radical via elimination of CO_2 or BF_3. The following Giese addition of the newly formed alkyl radical to alkenes bearing electron-withdrawing group (EWG) could give the alkyl radical intermediate A. Finally, the photoredox catalytic cycle was completed by the single-electron-transfer (SET) to the radical intermediate A, yielding the alkyl carbanion and regenerated Fukuzumi's acridinium catalyst [Acr^+–Mes], and the protonation of the alkyl carbanion by the solvent MeOH provided the desired product. (**Scheme 39**)

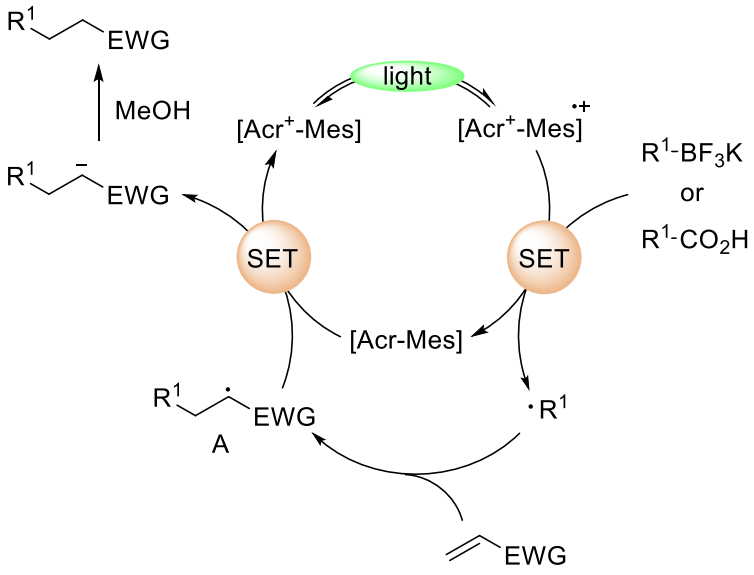

Scheme 39. The suggested mechanism of photooxidative Giese-type reaction alkyltrifluoroborates or alkyl carboxylic acids

In 2017, Molander and co-workers[61] reported a photoredox catalyzed radical/polar crossover reaction with trifluoromethyl alkenes and alkyl organotrifluoroborates that was utilized in the preparation of *gem*-difluoroalkenes. Using the 4CzIPN or [Ru (bpy)$_3$](PF$_6$)$_2$ as

[60] (a) Y. Yasu, T. Koike, M. Akita, *Adv. Synth. Catal.* **2012**, *354*, 3414–3420. (b) M. Hoshino, H. Uekusa, A. Tomita, S. Koshihara, T. Sato, S. Nozawa, S. Adachi, K. Ohkubo, H. Kotani, S. Fukuzumi, *J. Am. Chem. Soc.* **2012**, *134*, 4569–4572. (c) D. S. Hamilton, D. A. Nicewicz, *J. Am. Chem. Soc.*, **2012**, *134*, 18577–18580.

[61] S. B. Lang, R. J. Wiles, C. B. Kelly, G. A. Molander, *Angew. Chemie - Int. Ed.* **2017**, *56*, 15073–15077.

the photocatalyst, they can prepare the desired *gem*-difluoroalkenes in excellent yields (**Scheme 40**).

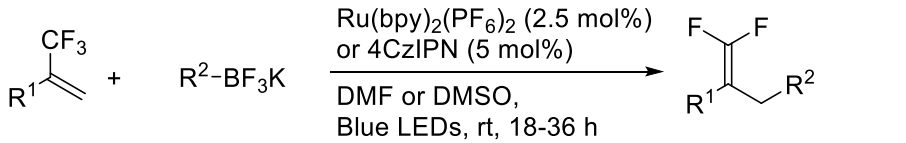

Scheme 40. Synthesis of *gem*-difluoroalkenes using trifluoromethyl alkenes and alkyl organotrifluoroborates

The authors proposed that the reaction is initiated by photoredox catalyzed single electron transfer (SET) to the organotrifluoroborate, generating an alkyl radical intermediate. Then, the addition of alkyl radical to trifluoromethyl alkenes provides the radical intermediate bearing CF_3 group. Then, the single-electron reduction assisted by the reduced state of photocatalyst $[4CzIPN]^-$ gave the corresponding carbanion. In the next step, based on the previous theoretical studies accomplished by Alunni[62], the E1cB-type fluoride elimination of carbanions provided the desired gem-difluoroalkene via a radical/polar crossover process. (**Scheme 41**)

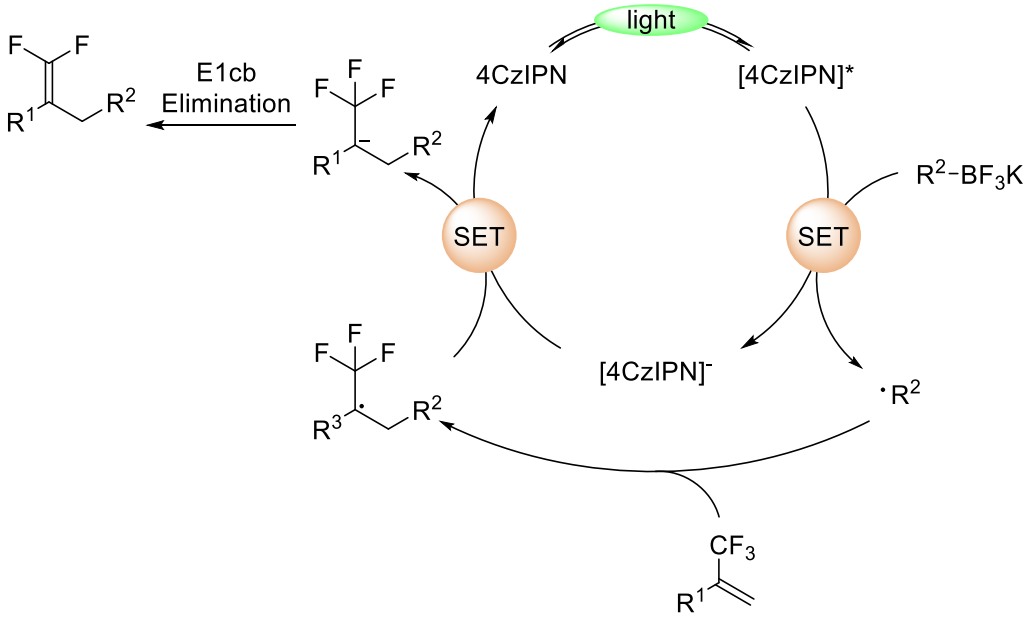

Scheme 41. The proposed mechanism for the synthesis of *gem*-difluoroalkenes

In 2019, the Molander group[63] reported a novel multicomponent Petasis-type reaction involving alkyltrifluoroborates, aryl aldehydes, and anilines (**Scheme 42**). The proposed

[62] S. Alunni, F. De Angelis, L. Ottavi, M. Papavasileiou, F. Tarantelli, *J. Am. Chem. Soc.* **2005**, *127*, 15151–15160.

[63] J. Yi, S. O. Badir, R. Alam, G. A. Molander, *Org. Lett.*, **2019**, *21*, 4853–4858.

method utilized [Ir(dF(CF_3)ppy)$_2$(dtbbpy)](PF_6) as an oxidizing photocatalyst. We employed sodium bisulfate as an additive, and the reaction could proceed in 1,4-dioxane to provide the desired product in excellent yield under the irritation of blue LED. In the presence of the radical scavenger TEMPO [(2,2,6,6-tetramethylpiper-idin-1-yl)oxyl], the desired product was not detected, and the reaction was fully inhibited. A TEMPO-alkyl adduct, as well as the imine, were isolated.

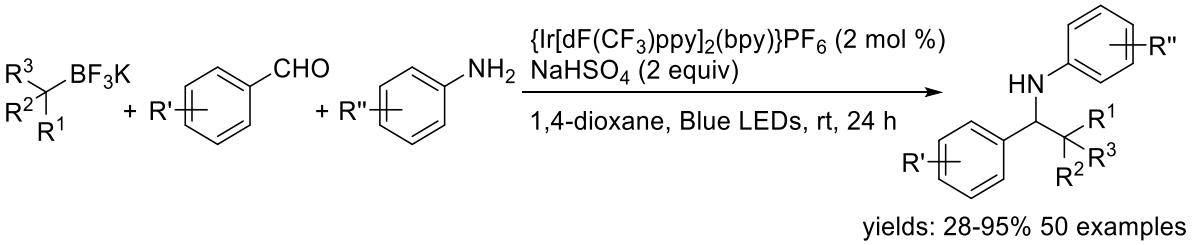

Scheme 42. The photoredox catalyzed multicomponent Petasis-type reaction

Molander and co-worker hypothesized that an appropriately excited iridium photocatalyst ([Ir]*) would start the reaction via oxidation of organotrifluoroborate to the required radical species (Scheme 40), thus producing BF_3. The radical may then react with the imine generated in situ to produce the amine radical cation. The photocatalytic cycle is terminated when the radical cation is reduced by the reduced state of iridium complex state ([Ir^{IV}]). The utilization of trifluoroborates as radical precursors was deemed important in performing the protocol correctly as it was anticipated that the BF_3 Lewis acid produced via the SET process would be feasible of combining the aldehyde and the amine and would also activate the resulting imine for the following radical addition. (**Scheme 43**)

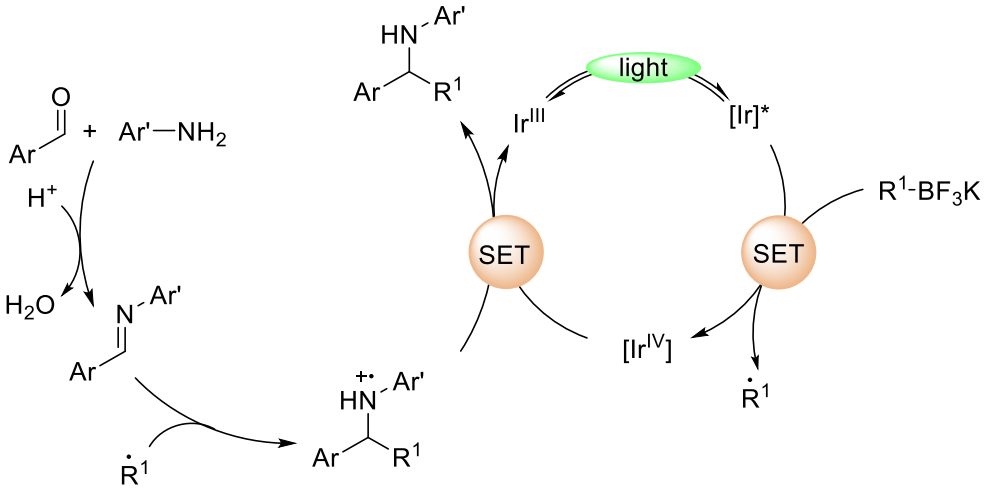

Scheme 43. Proposed mechanism of photoredox catalyzed multicomponent Petasis-type reaction

Photooxidation of carboxylic acid and its derivatives

Given the high oxidative potential of substituted carboxylates ($E_{1/2}^{ox}$(R-CO_2^-/R-CO2•) = +0.95 to +1.47 V *vs* SCE)[64], the photocatalyst-catalyzed oxidation of the carboxylates that were employed as radical precursors was difficult to provide the radical species. The constraint of the decarboxylative method of the substituted carboxylate salts is the photooxidation process. Due to the strong oxidative potential of these compounds and the intrinsically unfavorable kinetic process,[65] the decarboxylative process involving the radicals generated from carboxylate salts was a challengeable task.

In 2015, MacMillan's group [66] realized a photoredox catalyzed decarboxylative fluorination of alkyl carboxylic acid employing Selectfluor as fluorination reagent (**Scheme 44**). In the presence of the 1 mol% of the iridium photoredox catalyst [Ir(dF(CF_3)ppy)$_2$(dtbbpy)]PF_6, A set of alkyl carboxylic acids could be employed to produce alkyl radicals capable of performing the decarboxylative fluorination reaction with Selectfluor, yielding the desired fluorinated products.

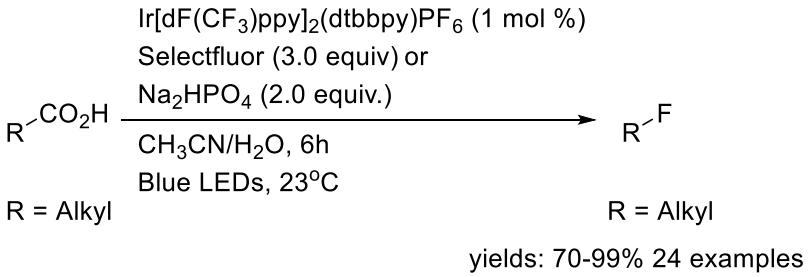

Scheme 44. The photoredox catalyzed decarboxylative fluorination reaction

Y. Yoshimi and his colleagues [67] have previously demonstrated photoredox catalyzed decarboxylative reactions of alkyl carboxylic acids, which were generated via decarboxylation of the alkyl carboxyl radicals. Under UV light irradiation, the organic photoredox catalyst system that was composed of phenanthrene and 1,4-dicyanobenzene can undergo the photoinduced electron transfer (PET) process to produce the alkyl carboxyl radicals. (**Scheme 45**)

---

[64] (a) M. Galicia, F. J. J. Gonzalez, *J. Electrochem. Soc.*, **2002**, *149*, D46-D50. (b) 1 H. G. Roth, N. A. Romero, D. A. Nicewicz, Synlett, **2016**, *27*, 714–723. (c) Z. Zuo, D. W. C. MacMillan, *J. Am. Chem. Soc*., **2014**, *136*, 5257–5260.

[65] J. Chateauneuf, J. Lusztyk, K. U. Ingold, *J. Am. Chem. Soc.*, **1988**, *110*, 2886–2893.

[66] S. Ventre, F. R. Petronijevic, D. W. C. MacMillan, *J. Am. Chem. Soc.*, **2015**, *137*, 5654–5657.

[67] (a) Y. Yoshimi, T. Itou, M. Hatanaka, *Chem. Commun.* **2007**, *48*, 5244–5246. (b) Y. Yoshimi, M. Masuda, T. Mizunashi, K. Nishikawa, K. Maeda, N. Koshida, T. Itou, T. Morita, M. Hatanaka, *Org. Lett.*, **2009**, *11*, 4652–4655.

Inspired by their previous work, they attempted the decarboxylation of benzoic acids[68] under the catalysis of biphenyl (BP) and 1,4-dicyanonaphthalene (DCN). Under the photoredox catalysis of the metal-free catalysts BP and DCN, using the NaOH as the base, the visible-light-induced photooxidation and decarboxylation of benzoic acids could occur directly. The aryl radical generated via the photo-electron-transfer (PET) process employing the catalytic amount of BP and DCN could react with the olefins bearing electron withdraw group to provide the desired product. In addition, the intermediate aryl radical species also could react with bis(pinacolato)diboron to obtain the aryl boronate product.

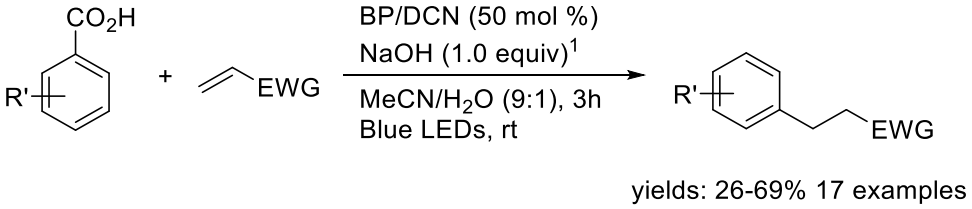

Scheme 45. The decarboxylative radical reactions of aromatic carboxylic acids *via* PET process.

Based on the deuteration experiments and the fluorescence quenching experiment in the mechanistic studies, the proposed mechanism was depicted as **Scheme 46.** In a transition-metal-free decarboxylation mechanism, base and solvent-induced aryl radical formation via the sequence consisted of the successive photo-electron transfer process (SET) and back electron transfer (BET) process, followed by radical addition to electron-deficient s and single electron transfer (SET) oxidation, afford the corresponding adducts of electron-deficient alkenes upon protonation of the anion intermediate. The TEMPO scavenger experiment also suggested that radical intermediates are involved in the process. (**Scheme 46**)

[68] S. Kubosaki, H. Takeuchi, Y. Iwata, Y. Tanaka, K. Osaka, M. Yamawaki, T. Morita, Y. Yoshimi, *J. Org. Chem.*, **2020**, *85*, 5362–5369.

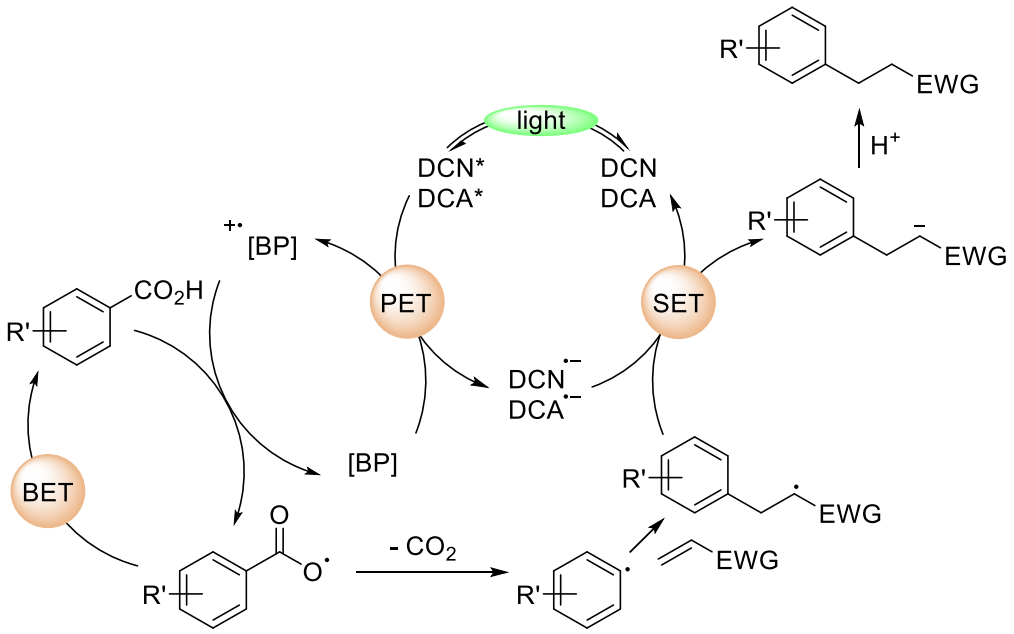

Scheme 46. The proposed mechanism of the photooxidative decarboxylation of benzoic acids via the PET process.

In 2021, based on previous work, Ritter and his colleagues [69] performed a decarboxylative polyfluoroarylation of unactive aliphatic carboxylic acid upon the visible-light-induced photocatalysis (**Scheme 47**). Using the inorganic alkali salts Li_2CO_3 or CsF as the base and polypyridyl iridium complex $Ir(dFFppy)_2(dtbpy)PF_6$ as photoredox catalyst, alkyl carboxylic acids could provide alkyl radicals that can undergo cross-coupling reactions with numerous substituted polyfluoroarenes to produce the desired polyfluoroarylation products efficiently. A set of polyfluoroarene derivatives could undergo the polyfluoroarylation reaction with N-Boc-protected glycine to generate a set of polyfluoroarylated derivatives of α-amino acid, Ritter, and co-workers could readily extend their work.

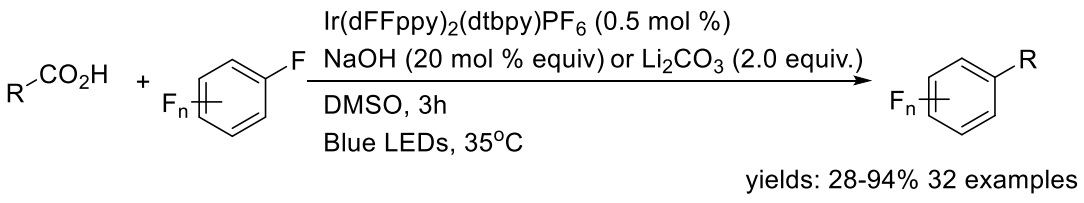

Scheme 47. The photocatalyzed decarboxylative polyfluoroarylation reaction of carboxylic acids

[69] X. Sun, T. Ritter, *Angew. Chemie Int. Ed.*, **2021**, *60*, 10557–10562.

As illustrated in **Scheme 48**, based on the available literature[70] and the result of the fluorescence quenching experiment, a mechanism involving the generation of the intermediate alkyl radical through the SET process was hypothesized. The first step is the single-electron oxidation of the deprotonated carboxylic acid by the excited iridium complex $[Ir^{III}]^*$, thus yielding the alkyl radical via extrusion of CO_2. The following addition of the newly generated alkyl radical to the perfluoroarene could provide the perfluoroaromatic radical. Finally, the catalytic cycle is finished by the single-electron-transfer (SET) process to the perfluoroaromatic radical, yielding the perfluoroaromatic anion and regenerated iridium catalyst $[Ir^{III}]$. The protonation of the perfluoroaromatic anion provided the desired product. (**Scheme 48**)

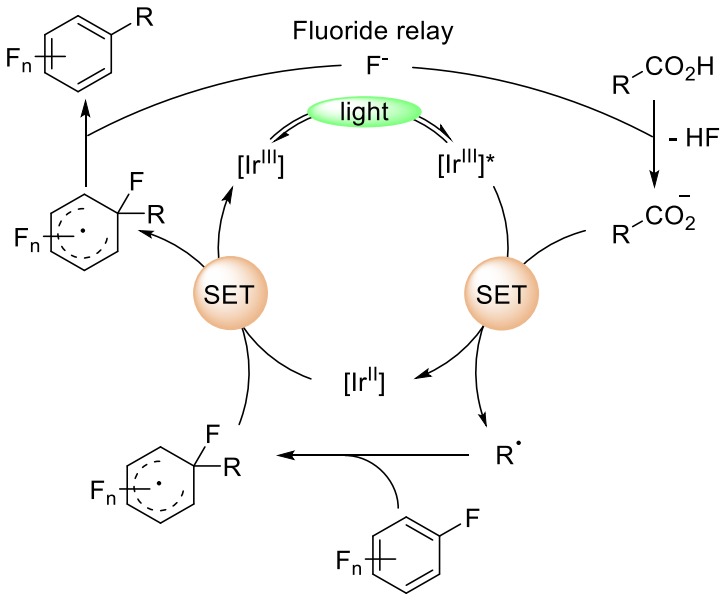

Scheme 48. The suggested mechanism of photocatalyzed decarboxylative polyfluoroarylation reaction

In the same year, Markus D. Kärkäs and his colleagues[71] developed a feasible method for the stereoselective synthesis of a set of novel α-amino acids, using abundant carboxylic acids as potential radical precursors (**Scheme 49**). Under the catalysis of the organic photocatalyst, this protocol enables the preparation of highly functionalized s that are difficult to elaborate through conventional two-electron reaction manifolds.

[70] (a) J. Xie, M. Rudolph, F. Rominger, A. S. K. Hashmi, *Angew. Chemie Int. Ed.* **2017**, *56*, 7266–7270. (b) Z. Zuo, D. W. C. MacMillan, *J. Am. Chem. Soc*. **2014**, *136*, 5257 – 5260

[71] A. Shatskiy, A. Axelsson, E. V Stepanova, J.-Q. Liu, A. Z. Temerdashev, B. P. Kore, B. Blomkvist, J. M. Gardner, P. Dinér, M. D. Kärkäs, *Chem. Sci*. **2021**, *12*, 5430–5437.

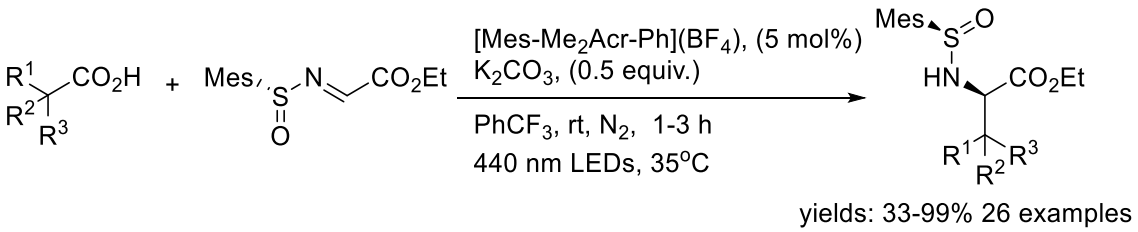

Scheme 49. Stereoselective synthesis of α-amino acids employing carboxylic acids as the radical precursors

Based on the precedents in the literature and evidence from fluorescence quenching experiments and computational studies, a mechanism involving the formation of the intermediate carboxyl radical through the SET process has been proposed in **Scheme 46.** The first step is the abstraction of the electron from the deprotonated carboxylic acid with the excited photocatalyst Acr^{+*} to provide the carboxylate radical. The subsequent process of extrusion of CO_2 from the carboxylate radical causes the formation of alkyl radical intermediate species. The following addition between the newly formed alkyl radical and various N-sulfonylimines can allow α-alkylation to provide the desired N-centered radical. Finally, the photoredox catalytic cycle was closed by the reduction of the N-centered radical and the acridinium radical Acrc•, and thus the protonation of the N-centered anion offered the desired product. (**Scheme 50**)

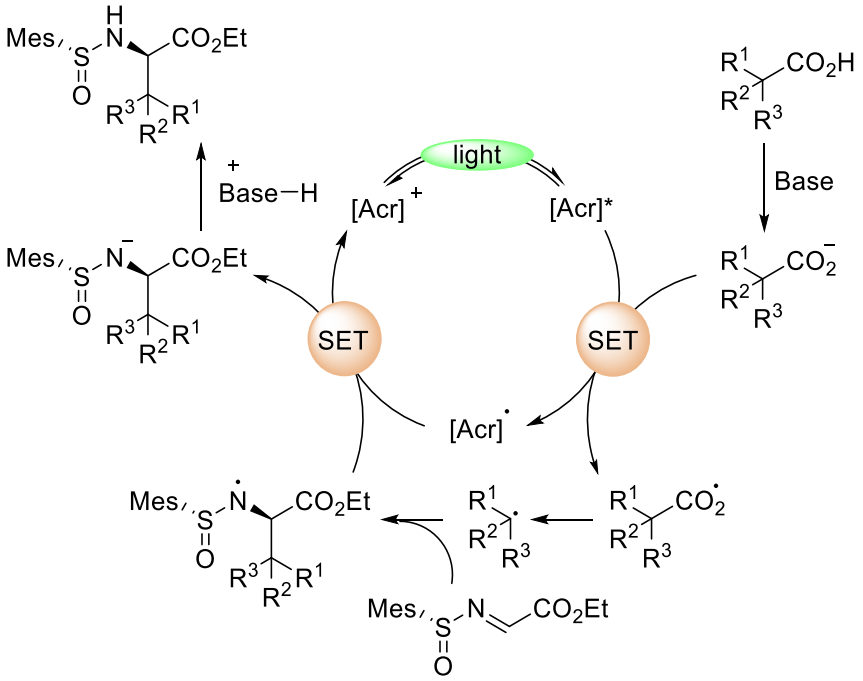

Scheme 50. The proposed mechanism for the stereoselective synthesis of α-amino acids.

Photooxidation of sulfinate salts

Due to the appropriate oxidative potential of the sodium benzenesulfinate ($E_{1/2}$($PhSO_2$•/$PhSO_2Na$) = +0.50V *vs* SCE)[72] and its analogs ($E_{1/2}$(*p*-$MePhSO_2$•/*p*-$MePhSO_2Na$) = +0.56 V *vs* SCE)[73], the carboxylates used as radical precursors were relatively facile to oxidize to produce the radical intermediate via the photooxidation of a suitable photoredox catalyst.

In 2016, inspired by their previous research of the preparation of the vinyl sulfones employing sulfinate salts and olefin as substrate[74], Burkhard König and colleagues[75] reported a photoredox-catalyzed sulfonylation reaction of the alkenes with the substituted sulfinate salts to further explore the reaction in detail (**Scheme 51**). The process employed the organic dye compound Eosin Y (EY) as a reducing photocatalyst. The nitrobenzene was utilized as an extra oxidant, and the reaction could proceed in the DMF/H_2O (3/1 vol ratio) mixture solvent under the irritation of green LED (535 nm) to yield the final product. The scope of substrates was significantly expanded to include a range of substituted sulfinates and alkenes.

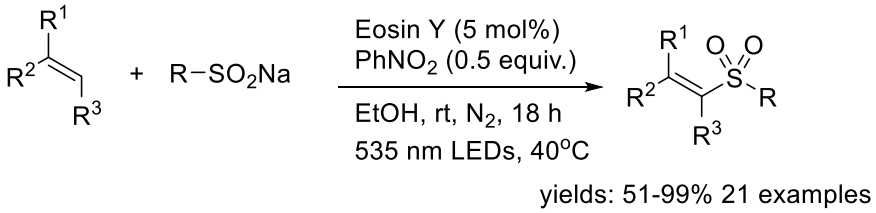

Scheme 51. The organic dye catalyzed the sulfonylation reaction of the alkenes

The reaction was completely inhibited by the addition of the radical scavenger TEMPO [(2,2,6,6-tetramethylpiper-idin-1-yl)oxyl], and the intended product was not found. The detection of a sulfinated TEMPO-trapped adduct strongly implied the formation of the radical intermediate during the reaction process. The mechanistic study employing triethanolamine (TEOA) indicated that the reaction could proceed entirely through an oxidative quenching pathway. (**Scheme 52**)

[72] (a) B. Persson, *Acta Chem. Scand*., **1977**, *31B*, 88-89. (b) Z. Tian, Q. Gong, T. Huang, L. Liu and T. Chen, *J. Org. Chem.*, , DOI:10.1021/acs.joc.1c00260.

[73] J. M. Parry, R. Parsons, *J. Electrochem. Soc.*, **1966**, *113*, 992.

[74] A. U. Meyer, S. Jäger, D. Prasad Hari, B. König, *Adv. Synth. Catal.* **2015**, *357*, 2050–2054.

[75] A. U. Meyer, K. Straková, T. Slanina, B. König, *Chem. – A Eur. J.* **2016**, *22*, 8694–8699.

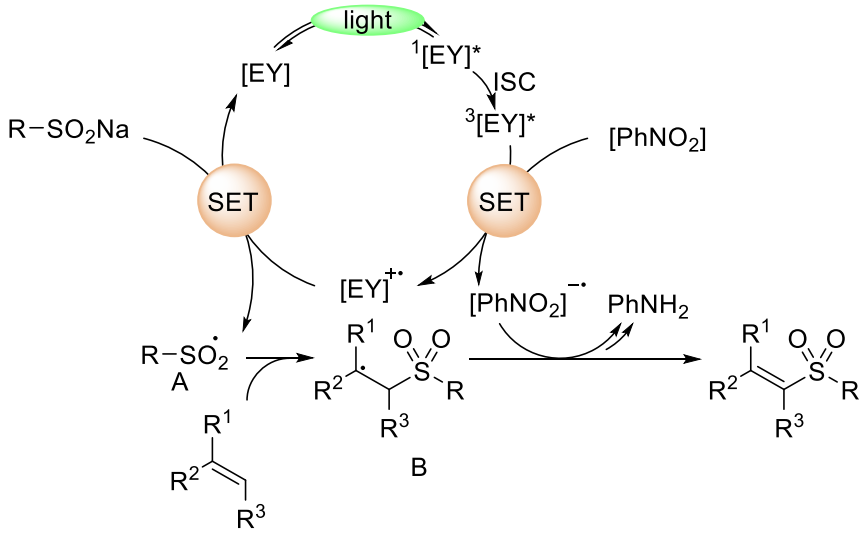

Scheme 52. The suggested photocatalytic sulfonylation mechanism via an oxidative quenching pathway

The suggested photocatalytic sulfonylation process employing eosin Y is shown in **Scheme 52**. The catalytic cycle is initiated by the excitation of the photoredox catalyst. The ISC process from a singlet excited state can convert to a triplet excited state. Thus, oxidative quenching of the triplet excited state by nitrobenzene can yield a radical cation of the Eosin Y catalyst and a radical anion of nitrobenzene. Photooxidation of sulfinate by radical cation species gave S-centered sulfinate radical **A** and the regenerated photoredox catalyst Eosin Y. The addition of the sulfinate radical **A** to the alkene can afford the radical intermediate **B**. H-abstraction of the radical by the radical anion of nitrobenzene generated the desired sulfonylated product.

In 2019, Zhu's group[76] described a new regioselective pyridylation reaction of substituted olefins with 4-cyanopyridine derivatives (**Scheme 53**). The presented protocol employed Ir-based polypyridyl complex *fac*-Ir(ppy)$_3$ as a suitable oxidizing photocatalyst. The sodium methanesulfinate was employed as a co-catalyst or promoter, and 1,8-diazabicyclo[5.4.0]undec-7-ene (DBU) was employed as an organic base. Under the irradiation of blue LED (455 nm), the reaction can carry out in the MeCN/EtOH (1/1 vol ratio) mixture solvent to produce the desired product in good yields. In the absence of the organic base (DBU), the β-sulfonyl pyridine intermediate product was detected and separated in 65% yield. Additionally, a control experiment with DBU could obtain the expected pyridylated product in excellent yield.

[76] S. Zhu, J. Qin, F. Wang, H. Li, L. Chu, *Nat. Commun.* **2019**, *10*, 1–7.

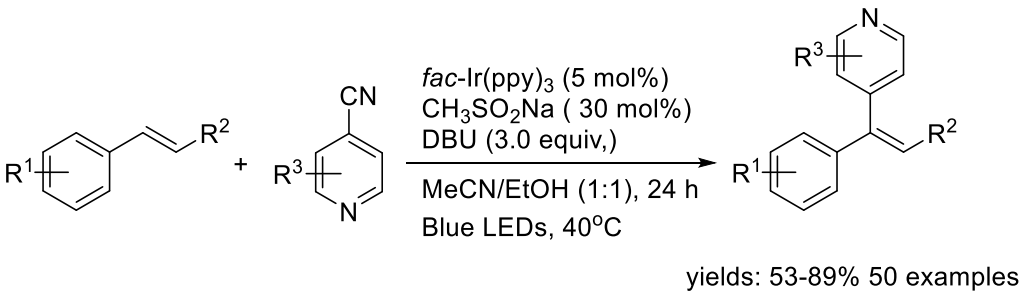

Scheme 53. The photooxidative regioselective pyridylation reaction of alkenes

The mechanism study indicated that it was observed to quench the excited state of $Ir(ppy)_3$ $[Ir^{III}]^*$ exclusively in the Stern–Volmer fluorescence quenching experiments, providing evidence for the hypothesized oxidative quenching mechanism. The following series of the process was considered in detail : (1) the visible-light-induced irridation of the suitable photocatalyst $[Ir^{III}]$ to its excited state $[Ir]^*$; (2) reductive quenching of the cyanopyridine by SET reduction affording the iridium species $[Ir^{IV}]$ and the radical anion; (3) SET oxidation of sodium methanesulfinate by oxidizing iridium species $[Ir^{IV}]$ followed by regioselective addition of the newly formed sulfinate radical to an alkene to produce the intermediate A; (4) radical–radical cross-coupling of newly generated an intermediate **A** with the open-shell pyridyl species-the radical anion followed by the decyanation, to yield the intermediate **B**; (5) elimination by organic base (DBU) yielding the desired pyridyl product and regenerated co-catalyst, sodium methanesulfinate. (**Scheme 54**)

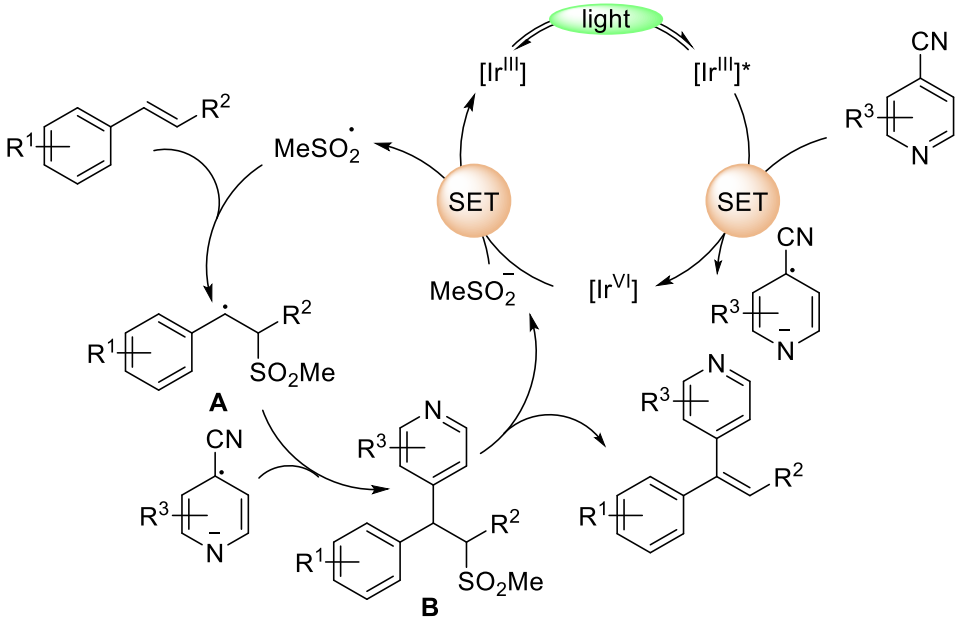

Scheme 54. The suggested mechanism of photooxidative pyridylation involving the co-catalysis of sulfinate.

In 2021, the same group[77] realized a transition-metal-free three-component sulfonylative pyridylation of alkenes with photoredox catalyst of polycyclic aromatic hydrocarbons (PAHs) (**Scheme 55**). Using acidic ammonium salt NH_4Cl as an additive and 9,10-diphenylanthracene (DPA) as the organic photoredox catalyst, numerous sulfinate salts can generate S-center radicals capable of undergoing the intermolecular sulfonyl-pyridylation reaction with a set of substituted alkenes and 4-cyanopyridine derivatives to afford the desired difunctionalization products in good yields.

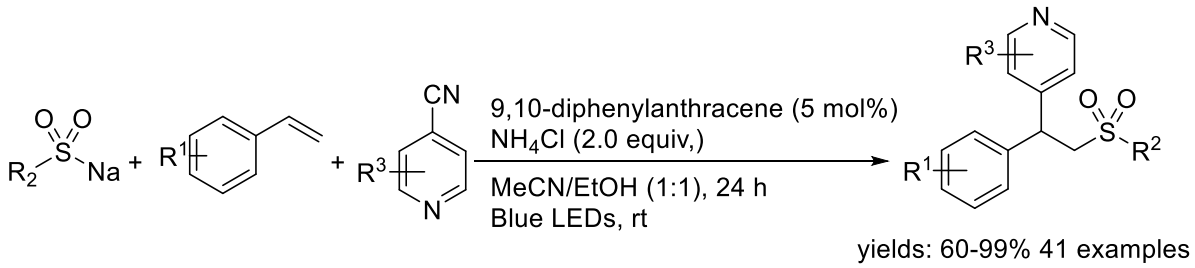

Scheme 55. The organic dye catalyzed photoredox sulfonylative pyridylation of alkenes

Given the suitable electrochemical characteristics and commercial availability of sulfinate salts, they can also be considered as a suitable substrate for dual transition metal/photoredox. In 2018, the Molander group[78] reported the $C(sp^2)–SO_2R$ bond formation *via* cross-coupling reactions employing sulfonate salts and aryl halides as substrates under dual Ni/photoredox catalysis. Employing a Ni/photoredox catalytic system composed of the Ru-based photoredox catalyst $Ru(bpy)_3(PF_6)_2$ and the pre-functionalized nickel catalyst $[Ni(phen)\cdot(H_2O)_4]Cl_2$, aryl sulfinate salts can generate sulfonyl radicals that can carry out the cross-coupling process with the various substituted aryl halides to give the desired diaryl sulfone products. In general, this strategy suggested by Molander and colleagues resulted in further diversification of the cross-coupling products. (**Scheme 56**)

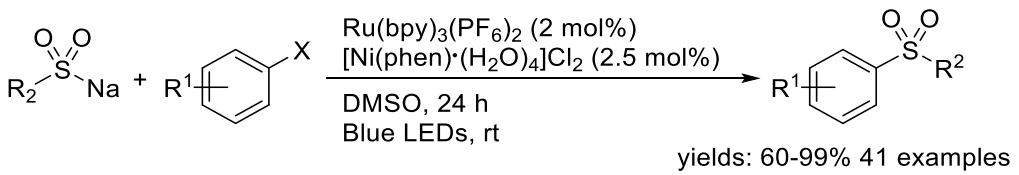

Scheme 56. The Ni/photoredox catalyzed cross-coupling reactions employing sulfonate salts

[77] F. Wang, J. Qin, S. Zhu, L. Chu, *RSC Adv.* **2021**, *11*, 142–146.

[78] M. J. Cabrera-Afonso, Z.-P. Lu, C. B. Kelly, S. B. Lang, R. Dykstra, O. Gutierrez, G. A. Molander, *Chem. Sci.* **2018**, *9*, 3186–3191.

2.1.5 Examples of cross-coupling reactions merging of photoredox/organometallic catalysis

Nickel mediated reaction

In general, nickel is a fourth-period transition metal capable of undergoing the SET process. A nickel has analogous reactivity with its adjacent element palladium and can realize the same basic processes in transition catalyzed cross-coupling reaction, including transmetallation, oxidative addition, C-H activation, and reductive elimination. Furthermore, considering the many oxidation numbers that can be obtained in cross-coupling reactions, nickel has been demonstrated to be an effective catalyst in a variety of transformations. Additionally, diverse oxidation numbers from +1 to +4 have been observed in the nickel catalyzed reaction. Nickel has the potential to reactivate a range of methods and establish radical pathways. In this way, various oxidation states can be observed in a radical-mediated catalytic cycle. In light of these features of nickel, a new method combined with photoredox catalysis for C-C and C-X bond construction has been considered, and research is ongoing.

To initiate the reaction catalyzed by Ni/photoredox co-catalysis, the alkyltrifluoroborate must be photooxidized to produce a radical. However, it is possible to facilitate single electron transfer (SET) processes by using redox agents that can be anticipated by measuring electrochemical potentials.

In 2017, inspired by the previous works, the group of Molander[79] reported a new dual catalytic method for cross-coupling reactions between alkyltrifluoroborates and aryl halides (**Scheme 57**). The reported dual catalytic system was composed of [Ir(dF(CF_3)ppy)$_2$(dtbbpy)](PF_6) Iridium complex, $NiCl_2$.dme nickel catalyst and (4,4′-di-tert-butyl-2,2′-dipyridyl) dtbbpy ligand. Photooxidation of trifluoroborates can provide corresponding alkyl radicals, which can react with aryl halides (**Scheme 57**). The organotrifluoroborates bearing a free hydroxyl group also can undergo the cross-coupling reaction.

[79] R. Alam, G. A. Molander, *J. Org. Chem.* **2017**, *82*, 13728–13734

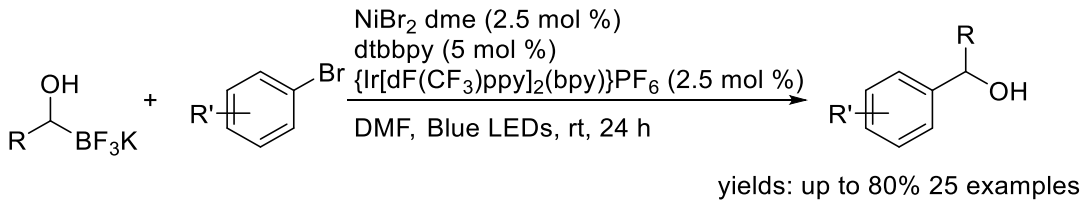

Scheme 57. Cross-coupling reactions between alkyltrifluoroborate bearing free alcohol and alkyl bromides.

A proposed mechanism was designed (**Scheme 58**) on the basis of their previous research. The excited state of a suitable photocatalyst, $[Ir(dF(CF_3)ppy)_2(dtbbpy)](PF_6)$, has an oxidative potential high enough to cause single-electron oxidation of the trifluoroborate (The feasibility of this oxidation was established by cyclic voltammetric measurement of alkyltrifluoroborate (E_{ox} =+1.22 V vs SCE), yielding the hydroxyalkyl radical via cleavage of C-B bond. Following the capture of the newly formed alkyl radical with Ni(0) species, Ni(I) species are formed, which may then oxidatively add to aryl halides to form the high-valent Ni(III) species. Reductive elimination of the diorgano Ni(III) intermediate gives the desired cross-coupling product and Ni(I) species. Finally, reduction of photocatalyst can regenerate both the Nickel catalyst and Ir-based photoredox catalyst, completing the whole catalytic cycle. (**Scheme 58**)

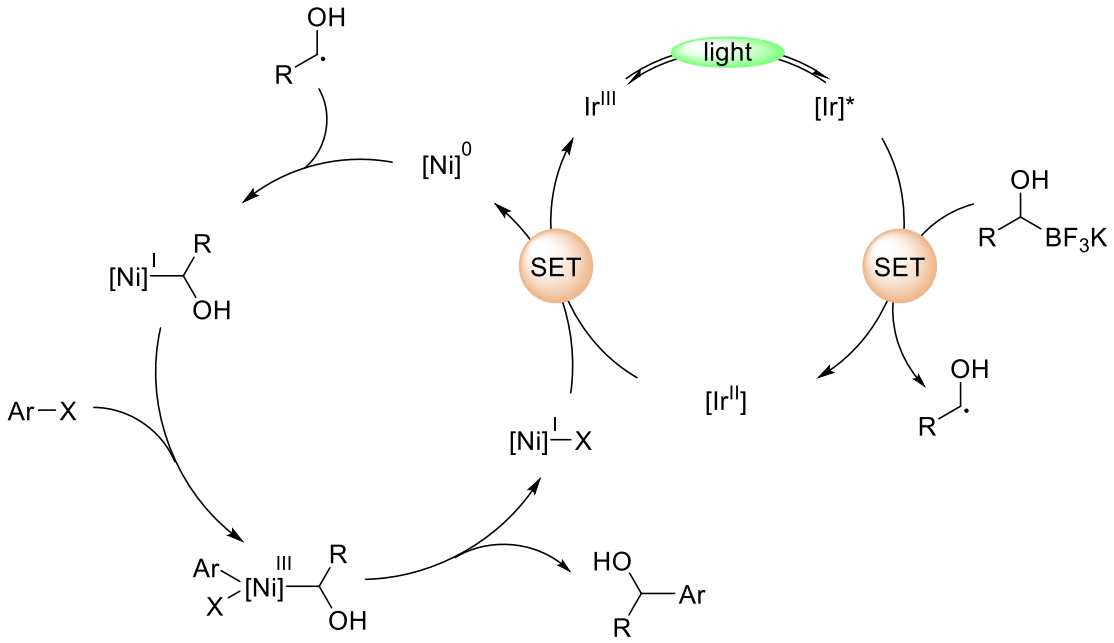

Scheme 58. Proposed mechanism for cross-coupling reactions between hydroxyalkyl trifluoroborates and alkyl bromides

In 2019, the Molander group[80] performed the dicarbofunctionalization of olefins with dual Ni/photoredox catalysis(**Scheme 59**). In the presence of K_2HPO_4 as the base, using a catalyst system consisting of the photoredox catalyst $[Ir(dF(CF_3)ppy)_2(dtbbpy)]PF_6$ and the nickel catalyst $Ni(bpy)Br_2$, alkyl trifluoroborates can generate alkyl radicals that can undergo Giese-type addition with the various substituted alkenes bearing a boronate ester group and aryl halides to give the desired difunctionalization products. Molander and coworkers can be easily diversified by using a set of vicinal difunctionalization reactions to establish various 1,2-substituted alkanes.

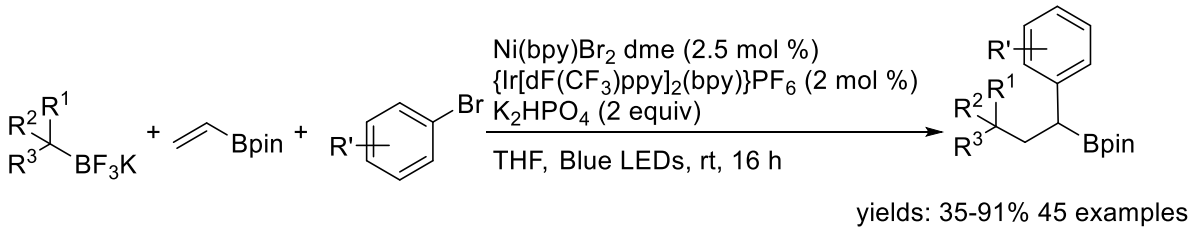

Scheme 59. Ni/photoredox dual catalyzed dicarbofunctionalization of olefins with aryl halides and alkyl radicals from alkyltrifluoroborates

This strategy is a sequence of bond-forming activities mediated by radicals. Specifically, the following sequence of events was considered : (1) visible-light-induced irradiation of the suitable photoredox catalyst [Ir^{III}] to its excited state [Ir]* by visible light; (2) reductive quenching of the radical precursor by SET oxidation; (3) homolytic cleavage of the C-B bond followed by Giese-type addition of the new formed radical to an alkene to generate the intermediate **A**; (4) single-electron metalation of **A** to form the alkyl-nickel(I) adduct **B**; notably, the mechanism depends on selective addition of the radical to the olefin rather than direct cross-coupling to Ni0 species by single-electron metalation.

[80] M. W. Campbell, J. S. Compton, C. B. Kelly, G. A. Molander, *J. Am. Chem. Soc.* **2019**, *141*, 20069–20078.

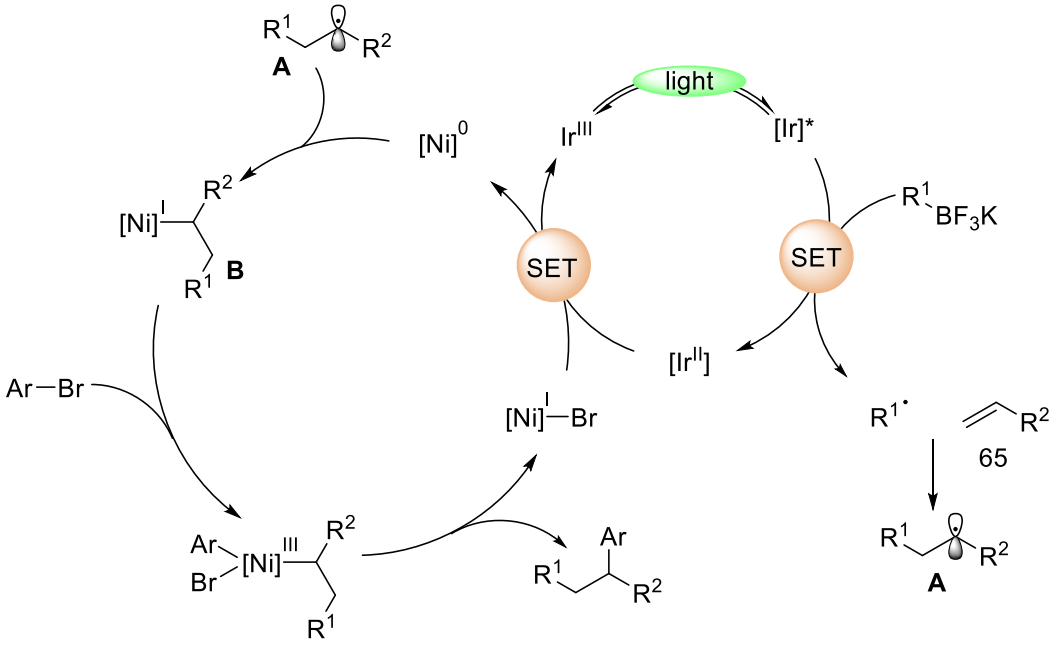

Scheme 60. The proposed mechanism for the dicarbofunctionalization of olefins

In 2020, based on previous work, Osvaldo Gutierrez's group[81] performed an asymmetric three-component difunctionalization of olefins with dual Ni/photoredox catalysis (**Scheme 61**). Using chiral bioxazoline (BiOx) (S,S)-sec-Bu-BiOx as a chiral ligand and a dual catalytic system consisting of the photoredox catalyst $[Ir(dF(CF_3)ppy)_2(dtbbpy)]PF_6$ and the nickel catalyst $NiCl_2(Py)_4$, alkyl trifluoroborates can generate alkyl radicals capable of undergoing the three-component asymmetric alkylarylation reaction with the various substituted alkenes and aryl halides to give the desired asymmetric difunctionalization products in good yields.

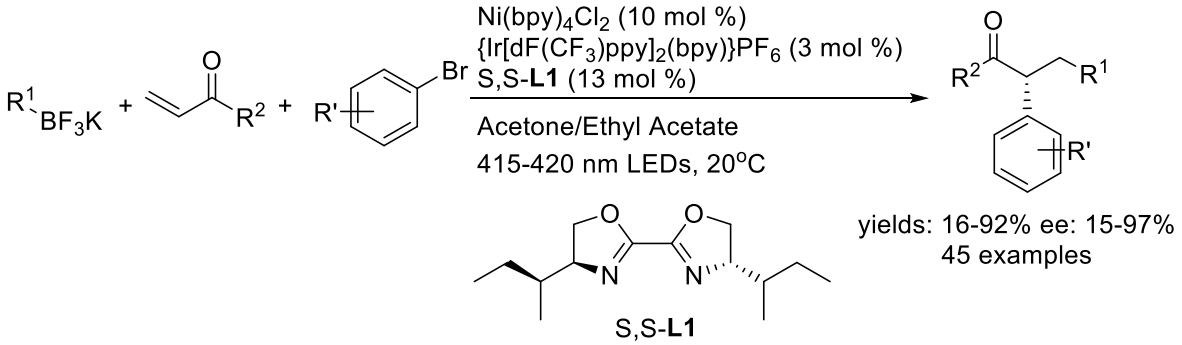

Scheme 61. Three-component enantioselective carboarylation of alkenes with dual Ni/photoredox catalysis

[81] L. Guo, M. Yuan, Y. Zhang, F. Wang, S. Zhu, O. Gutierrez, L. Chu, *J. Am. Chem. Soc.* **2020**, *142*, 20390–20399.

Copper mediated reaction

Regarding the potential benefits of using dual nickel and photoredox catalysis, there are distinct disadvantages to using nickel catalysts, including toxicological issues. Therefore, the development of less toxic alternatives would be advantageous. The use of inexpensive copper salts that can be used with photoredox catalysts could be considered a reasonable choice. Without the need for ligands, these copper salts also catalyze processes and are less hazardous than nickel compounds. The dual catalytic system, combining the copper catalyst and the photoredox catalyst, has not been sufficiently studied compared to the Ni/photoredox catalytic system.

In 2017, the Liu group [82] realized a novel reaction protocol for asymmetric decarboxylative cyanation involving N-hydroxy-phthalimide (NHP) esters and TMSCN (**Scheme 62**). The decarboxylative cyanation of N-hydroxy-phthalimide (NHP) esters was carried out over a dual-catalyst system combining a photoredox catalyst *fac*-Ir(ppy)$_3$ and a Cu (I) catalyst CuBr. The C 2-symmetric bisoxazoline was employed as the chiral ligand to generate the key reactive intermediate of the asymmetric radical transformations. The stereoselective decarboxylative cyanation of various derivatives of the substituted N-hydroxy-phthalimide (NHP) esters 72 could yield the desired asymmetric cyanation products 73 in good to excellent yield and satisfied enantioselectivities (ee).

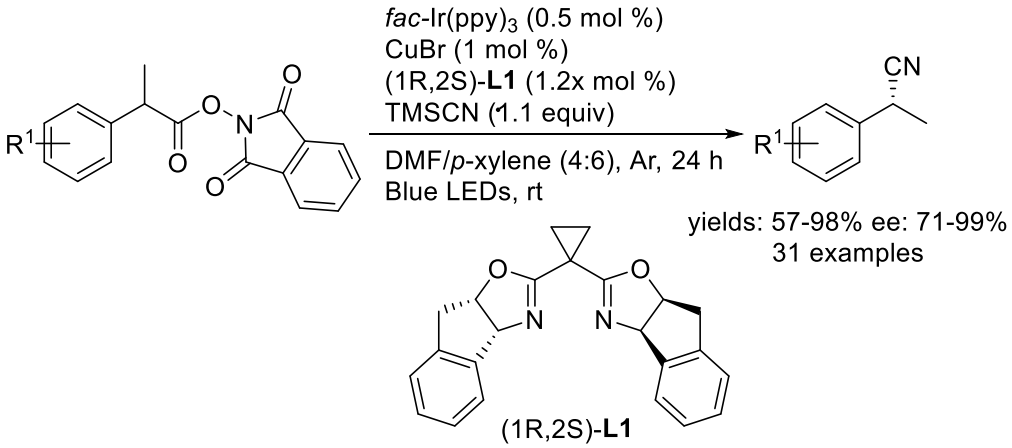

Scheme 62. Cu/photoredox dual catalyzed asymmetric decarboxylative cyanation of (NHP) esters

More recently, The MacMillan group[83] has performed the trifluoromethylation reaction

[82] D. Wang, N. Zhu, P. Chen, Z. Lin, G. Liu, **2017**, *2*, 15632–15635.

[83] (a) C. Le, T. Q. Chen, T. Liang, P. Zhang, D. W. C. Macmillan, **2018**, *1014*, 1010–1014. (b) D. J. P. Kornfilt, D. W. C. MacMillan, *J. Am. Chem. Soc.*, **2019**, *141*, 6853–6858.

of various alkyl and aryl bromides (**Scheme 63**). The reported protocol involves the use of $[Ir(dF(CF_3)ppy)_2(dtbbpy)]PF_6$ as photoredox photocatalyst, The Cu(II) halide salts ($CuBr_2$ or $CuCl_2$) as a copper catalyst, and silanol reagent as a novel silyl radical source. Dimesityl(trifluoromethyl)sulfonium trifluoromethanesulfonate ($dMesSCF_3$) could produce CF_3 radicals capable of undergoing the trifluoromethylation reaction with the various substituted alkyl and aryl halides to provide the desired cross-coupling products in good to excellent yields.

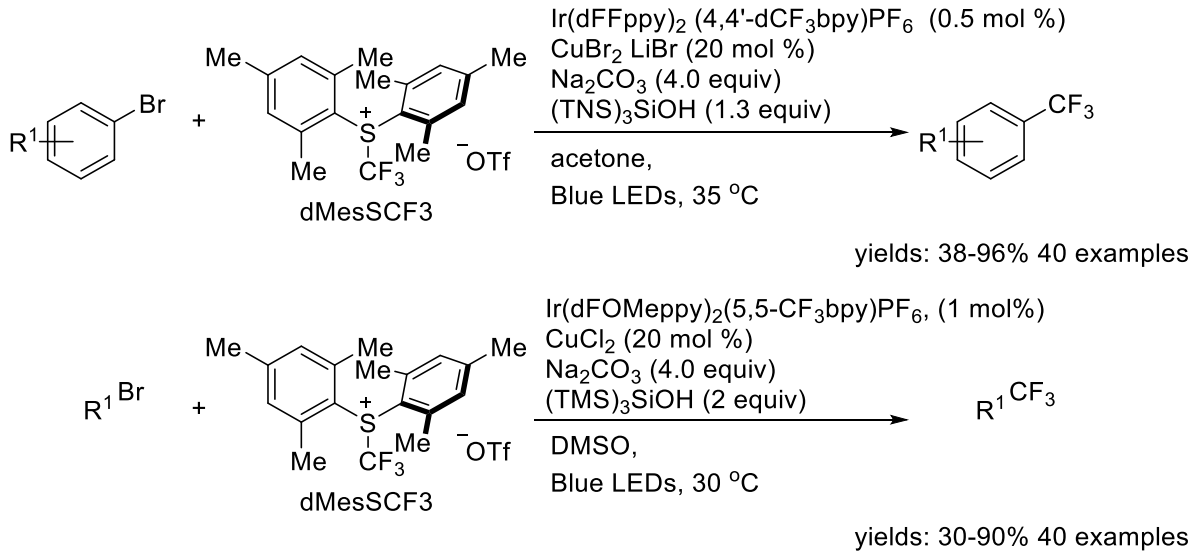

Scheme 63. Cu/photoredox catalyzed trifluoromethylation reaction of alkyl and aryl bromides.

This proposed photoredox/Cu catalysis cycle is accomplished through a sequence of radical-mediated electron transfer processes. The following step of the catalysis cycle was considered in detail: (1) visible-light-induced irradiation of the suitable photoredox catalyst $[Ir^{III}]$ to its excited state $[Ir]^*$; (2) The single-electron oxidation of the silanol reagent tris-(trimethylsilyl) silanol affording the silyl radical; (3) The photocatalyzed SET reduction of electrophilic trifluoromethylation reagent ($dMesSCF_3$) providing the CF_3• radicals capable of the generation of $LCu(II)X(CF_3)$ complex **B**; (4) the silyl radical-mediated halogen abstraction of the organohalide followed by radical trapping of the reactive $LCu(II)X(CF_3)$ complex **B** to generate the critical intermediate aryl–Cu(III)–CF_3 or alkyl–Cu(III)–CF_3 adduct **C**; and (5) Reductive elimination of the hypervalent Cu(III) complex (aryl–Cu(III)–CF_3 or alkyl–Cu(III)–CF_3) **C** to form the cross-coupling product and regenerate the novel Cu(II) catalyst. (**Scheme 64**)

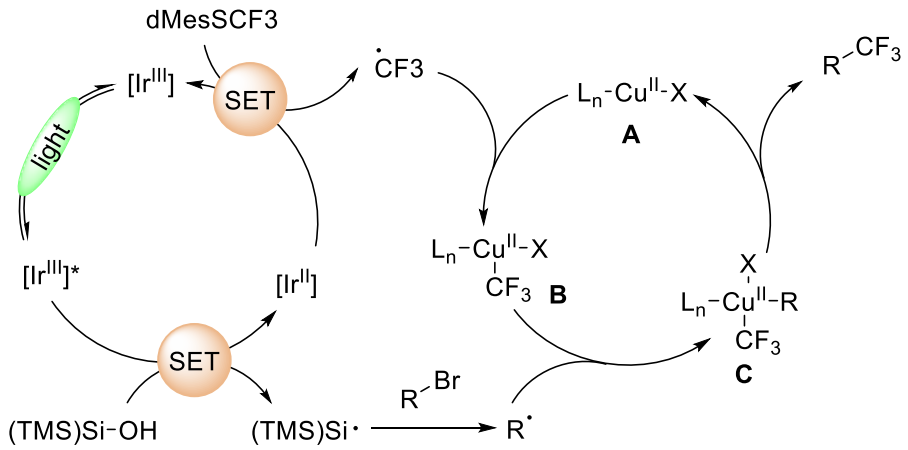

Scheme 64. The proposed mechanism of Cu/photoredox catalyzed trifluoromethylation reaction

In 2021, based on previous work, Jin's group[84] realized a Cu/photoredox catalyzed cycloisomerization of 2-alkynyl-cyclohexenones employing alkyl bis(catecholato)silicates as the radical precursor (**Scheme 65**). In the presence of the 2 mol% of the iridium photoredox catalyst [Ir(dF(CF$_3$)ppy)$_2$(dtbbpy)]PF$_6$ and 20 mol% of Cu(OTf)$_2$, A series of alkyl bis(catecholato)silicates or 4-alkyldihydropyridines could be utilized to produce alkyl radicals capable of performing the tandem addition-cyclization reaction with a variety of 2-(1-alkynyl)-2-alken-1-ones, yielding the desired cycloisomerized products.

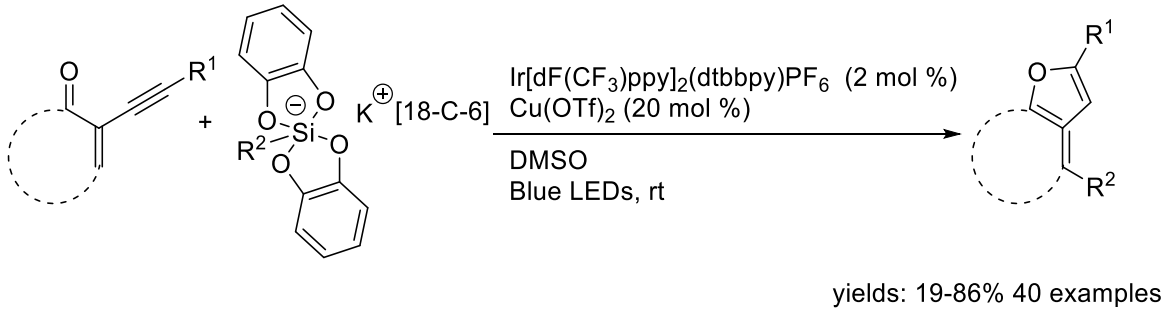

Scheme 65. Cu/photoredox catalyzed cycloisomerization of 2-alkynyl-cyclohexenones

Gold mediated reaction

In general，a considerably higher electrochemical potential of a couple Au(I) to Au(III) ($E_{1/2}^{ox}$ = 1.41 V)[85] could be regarded as the intrinsic electron property of Au(I) species. For this reason, most oxidative transformations from Au(I) to Au(III) cannot routinely proceed

[84] Y. Liu, W. Luo, T. Xia, Y. Fang, C. Du, X. Jin, Y. Li, L. Zhang, W. Lei, H. Wu, *Org. Chem. Front.*, **2021**, *8*, 1732–1738.

[85] S. Bratsch, *J. Phys. Chem. Ref. Data*, **1989**, *18*, 1–21.

and require the application of an extremely strong external oxidant. The protocol of the gold-catalyzed reaction, such as the gold-catalyzed nucleophilic addition reaction and the gold-catalyzed oxidative cross-coupling reactions using hypervalent iodine species or Selectfluor as the oxidant, has been established.[86]

An Au(I) catalyst is transformed to an organogold(III) intermediate, which is the main obstacle in these reactions. An alternate mechanistic sequence containing two single-electron oxidation processes could be found using the single electron transfer (SET) process identified in photoredox catalysis instead of the two-electron transfer process in one step. Single-electron oxidation of Au(I) would be the preliminary step would include the addition of a radical species produced by photoredox catalysis and which could then perform second single-electron oxidation to produce the corresponding organogold(III) intermediate. This devised process could be observed in the Au/photocatalyzed reaction. (**Scheme 66**)

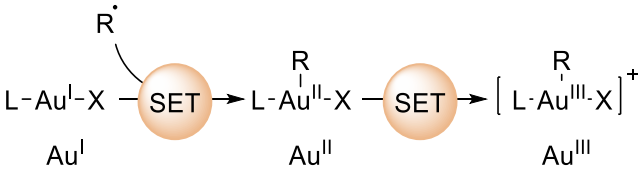

Scheme 66. The devised mechanistic paradigm for the transformation from Au(I) to Au(III)

In 2017, the Xu group[87] reported a novel reaction protocol for trifluoromethylthio-sulfonylation reactions involving styrene and $PhSO_2SCF_3$ (**Scheme 67**). The proposed synthesis method employed ruthenium complex $Ru(bpy)_3Cl_2$ as a photoredox catalyst, IPrAuCl as a gold catalyst, and $AgSbF_6$ as an additive. Difunctionalization reaction of the alkenes bearing electron-deficient and electron-deficient alkenes could provide the desired trifluoromethylthio-sulfonylation products in moderate to excellent yields.

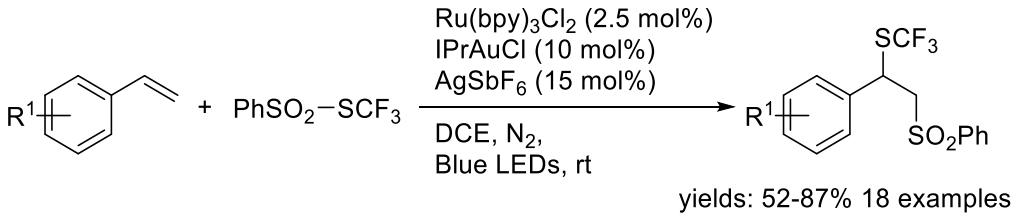

Scheme 67. Au/photoredox catalyzed trifluoromethylthio-sulfonylation reactions of olefins

[86] (a) A. Simonneau, P. Garcia, J.-P. Goddard, V. Mouriès-Mansuy, M. Malacria, L. Fensterbank, *Beilstein J. Org. Chem.* **2011**, *7*, 1379–1386. (b) S. Banerjee, V. W. Bhoyare. N. T. Patil, *Chem. Commun.*, **2020**, *56*, 2677–2690.

[87] H. Li, C. Shan, C.-H. Tung, Z. Xu, *Chem. Sci.*, **2017**, *8*, 2610–2615.

In 2018, Nitin T. Patil and his colleagues[88] described that aryl diazonium salts could be utilized as a precursor for the aryl radical (**Scheme 68**). Substituted aryl diazonium salts could undergo the cross-coupling reaction with organosilanes to provide the corresponding product. The cross-coupling reaction occurs employing dual catalysis with a combination of a ruthenium photoredox catalyst and an Au (I) catalyst in excellent yields.

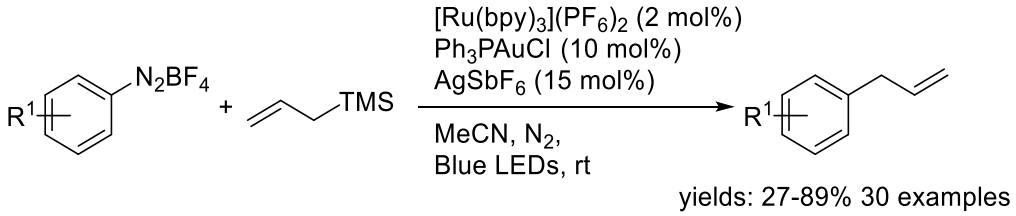

Scheme 68. Au/photoredox catalyzed cross-coupling reaction of aryl diazonium salts

In 2019, our group[89] expanded synthetic uses of the dual catalysis system, merging iridium photoredox catalysis and gold catalysis. At room temperature, under the dual catalysis of the photoredox catalyst $Ir[dF(CF_3)ppy]_2(dtbbpy)PF_6$ and the gold catalyst $(p\text{-}CF_3Ph)_3PAuCl$, we could prepare alkynylbenzofuran derivatives from o-alkynylphenols and iodoalkynes by using the K_2CO_3 and the 1,10-phenanthroline ligand. The electron-deficient aryl iodoethynyl and even various substituted alkyl alkynes were all capable partners in this reaction, yielding the cyclization products in moderate to high yields (**Scheme 69**).

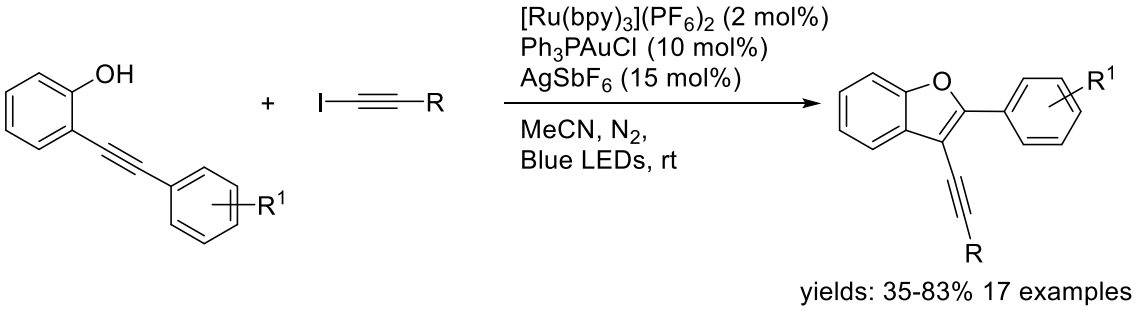

Scheme 69. Au/photoredox catalyzed tandem cyclization of o-alkynylphenols with iodoalkynes

Based on the previous discovery about the Ni/photoredox catalyzed reaction by the MacMillan group and the evidence from the DFT calculation and mechanism experiment, we suggested a catalysis cycle including triplet excited state of the vinyl gold intermediate. In

[88] M. O. Akram, P. S. Mali, N. T. Patil, *Org. Lett.*, **2017**, *19*, 3075–3078.

[89] Z. Xia, V. Corcé, F. Zhao, C. Przybylski, A. Espagne, L. Jullien, T. Le Saux, Y. Gimbert, H. Dossmann, V. Mouriès-Mansuy, C. Ollivier, L. Fensterbank, *Nat. Chem.*, **2019**, *11*, 797–805.

general, we discovered a novel kind of dual catalysis process combining electrophilic gold catalysis and iridium photosensitization that enables a C_{sp2}-C_{sp} cross-coupling reaction beneficial for alkynylation of benzofurans. The catalytic cycle is initiated by the photoexcitation of the suitable photocatalyst [Ir^{III}] to its excited state [Ir]*. Indeed, the excited form of the iridium catalyst [Ir]* transferred its energy to gold (I) cyclized intermediate derived from o-alkynylphenol. The following step is the oxidative addition at the triplet excited state of the Au (I) intermediate. As a result of this process, the carbon-carbon bond was constructed, followed by reductive elimination, yielding the desired benzofuran product. (**Scheme 70**)

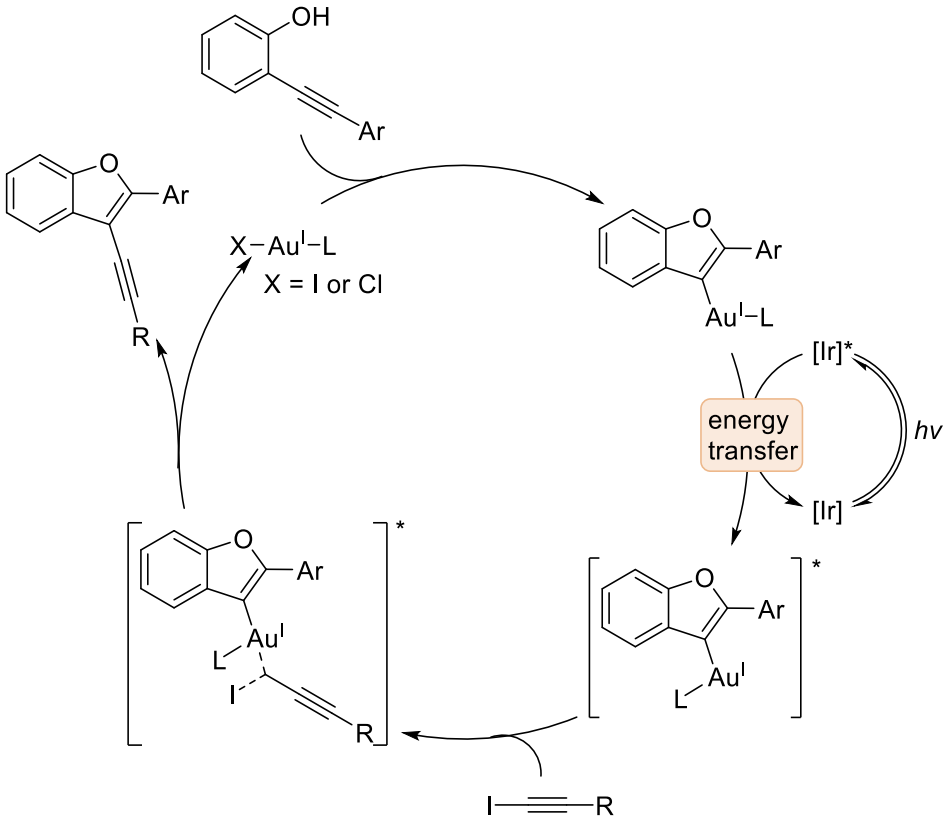

Scheme 70. The proposed mechanism of Au/photoredox catalyzed tandem cyclization/alkynylation

2.2 General informations on silicon-based compounds

2.2.1 Silicon

Etymologically, as we all know, the word silicon could date back to the Latin *silex*. The atomic number of the silicon element is 14, and the silicon electron conformation is $1s^2 2s^2 2p^6 3s^2 3p^2$. The pure form of the silicon is a rock-like and brittle crystalline solid with a blue-grey metallic lustre. Silicon has accompanied humanity from ancient times. Because of

the physical property of the corresponding oxide of silicon, humans utilize silicon as the construction material of early human habitations.

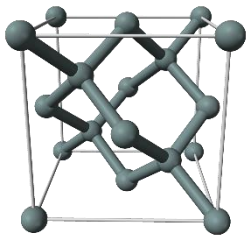

Figure 1 The crystal structure of silicon

The synthesis of the pure form of the silicon element could be regarded as an odyssey of the development of chemistry[90]. The bond energy of C-Si is high enough that there is no way to reduce the silicon oxide and isolate the pure form of silicon. After an effort to prepare the pure form of silicon in 1808, the silicon element was named "silicium" by Sir Humphry Davy[91]. Gay-Lussac and Thénard[92] prepared amorphous silicon, but they did not perform the purification and characterization of the newly formed product or identify it as a new element. In 1823, Jöns Jacob Berzelius[93] prepared amorphous silicon. After washing the crude product several times, the product was purified to a brown powder. As a consequence, he is often credited with discovering the element. Silicon is classified as a main group element according to its position in the periodic table. It belongs to the same family as carbon. One of the most unusual properties of silicon is its ability to exceed the tetracoordinate limit, which is impossible for carbon and thus exhibits hypercoordination.[94] Chemists are very interested in this feature because of the potential applications in organic and inorganic chemistry, such as the discovery of new reactivities or intriguing structures.

2.2.2 Hypervalent versus hypercoordinated Silicon species

Based on the general chemistry, similar to the carbon element, the silicon element

[90] M. E. Weeks, *J. Chem. Educ.*, **1932**, *9*, 1386.

[91] a) J. Z. Fullmer, *Sir Humphry Davy's Published Works*, Harvard University Press, 2013.; b) H. Davy, *The Collected Works of Sir Humphry Davy: Agricultural lectures, pt. 2, and other lectures*, Johnson Reprint Corporation, 1840, vol. 8.

[92] J. L. Gay-Lussac and L. J. baron Thénard, *Recherches physico-chimiques: faites sur la pile, sur la préparation chimique et les propriétés du Potassium et du Sodium; sur la décomposition de l'acide boracique; sur les acides fluorique, muriatique oxigéné; sur l'action chimique de la lumière; sur l'analyse végétale et animale, etc... Tome second*, Deterville, 1811, vol. 2.

[93] a) J. J. Berzelius, *Undersökning af flusspatssyran och dess märkvärdigaste föreningar*, PA Norstedt & Söner, 1825.; b)M. Berzelius, *Philos. Mag.*, **1825**, *65*, 254–267.

[94] C. Chuit, R. J. P. Corriu, C. Reye, J. C. Young, *Chem. Rev.* **1993**, *93*, 1371–1448.

tended to form four covalent bonds to provide a complete octet in some silicon compounds, different from the typical example of the silicon complex, such as the $SiCl_4$, SiH_4, and SiO_2. In some situations, the silicon element will be extended its number of coordinates to exhibit the hypercoordination of the silicon element.

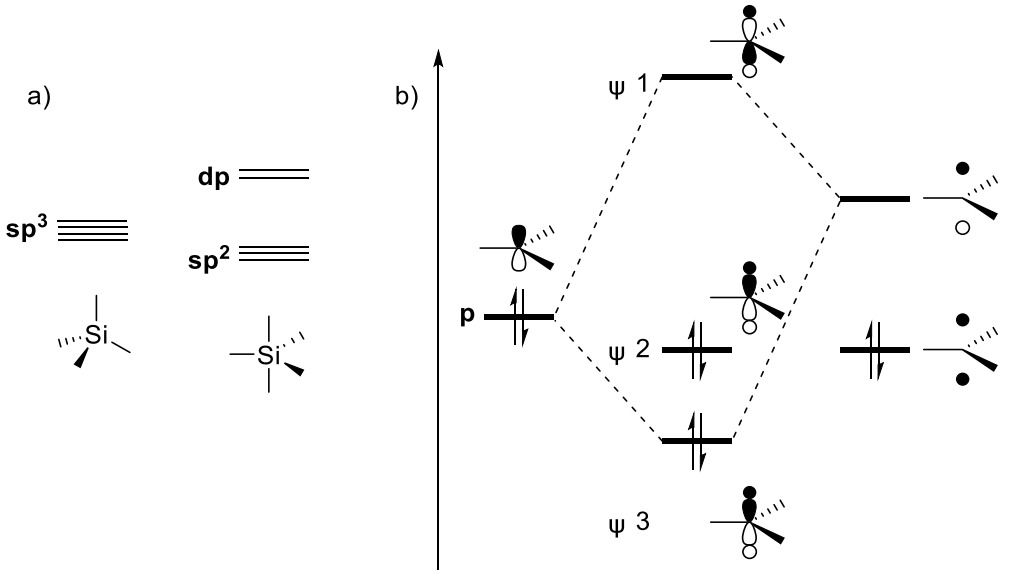

Figure 2 a) Diagram of hybridized silicon orbitals. b) Molecular orbital diagram of 3c/4e bonding

According to the Hybrid Orbital theory, when the silicon is sp3 hybridized, the tetravalent silicon could be seen in the molecule. The d, s, and p orbital of the silicon could be employed in hybridization, and the silicon is sp2dp hybridization. The geometry of the pentacoordinate silicon is trigonal bipyramid, as shown in **Figure 2 a**.

On the basis of MO Theory, the three-center four-electron concept has been established by Rundle and Pimentel[95]. Musher's pioneering work[96] demonstrated the possibility of extending the application scope of concept to other systems, such as the pentacoordinate silicon. Two s orbitals from the ligand and a p orbital from the central atom could be reorganized via a linear combination of atomic orbitals (LCAO). Based on the molecular orbital (MO) theory, the nonbonding atomic orbital of the system could be considered as the hypercoordinate bond. The other two combining atomic orbitals of the system are a bonding (ψ 1) orbital and a nonbonding (ψ 2) orbital (**Figure 2 b**). The compounds containing the hypervalent silicon atom could be regarded as a result of MO theory.

Since the early nineteenth century, silicon compounds having a coordination number

[95] R. E. Rundle, *J. Am. Chem. Soc.* **1963**, *85*, 112–113.

[96] J. I. Musher, *Angew. Chemie Int. Ed. English* **1969**, *8*, 54–68.

greater than four have been known[97]. Over the last three decades, a great deal of attention has been devoted to the unique reactivity of hypervalent silicon compounds.[98]

In 1982, Kumada and his colleagues[99] first discovered that using the hexachloroplatinic acid could be used as a catalyst in the presence of an excess of potassium fluoride, and a terminal alkyne could react with the tricholorosilane to yield the hypervalent intermediate organopentafluorosiliconate in moderate yield. Thus, the palladium acetate catalyzed cross-coupling between the hexacoordinated organopentafluorosiliconates and allyl chloride could provide the corresponding product 1,4-diene. (**Scheme 71**)

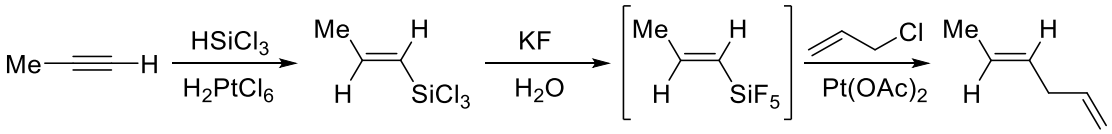

Scheme 71. The first cross-coupling reaction using organopentafluorosiliconates

Inspired by the previous work, chemists found that a bidentate ligand may be used to create pentacoordinate silicon species, resulting in either an anionic or cationic pentacoordinate complex, depending on the type of the bidentate ligand. Complexes containing oxygen directly coordinated to silicon through a cyclic bidentate ligand are easily produced and have been known for a long period of time. The pioneering work by Cecil L. Frye[100] provided the pentacoordinated bis-catecholato silicate. Following that, Boer and co-workers [101] established the structure of the tetramethylammonium salt, confirming the presence of a pentacoordinate silicon anion.

[97] a) J. L. Gay-Lussac and L. J. baron Thénard, *Mémoires de Physique et de Chimie de la Société d'Arcueil* **1809**, *2*, 317.; b) J. Davy, *Philos. Trans. R. Soc. London*, **1812**, 352–369.

[98] a) R. Mueller, *Chem. Rev*, **1966**, *1*, 359–377.; b) R. Müller, *Zeitschrift für Chemie*, **1984**, *24*, 41–51.

[99] J. Yoshida, K. Tamao, M. Takahashi, M. Kumada, *Tetrahedron Lett.* **1978**, *19*, 2161–2164.

[100] C. L. Fryb, *J. Am. Chem. Soc.*, **1964**, *86*, 3170–3171.

[101] F. P. Boer, J. J. Flynn, J. W. Turley, *J. Am. Chem. Soc.*, **1968**, *90*, 6973–6977.

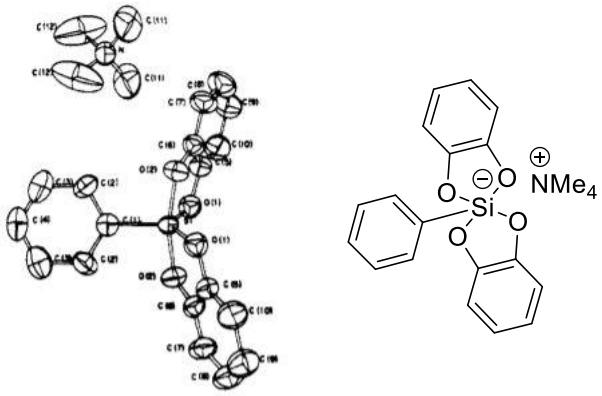

Figure 3. XRD analyses of the tetramethylammonium bis (o-phenylenedioxy) phenylsiliconate

2.3 Preparation of bis-catecholato silicates

In 1964, Cecil L. Frye[32] reported the first synthesis of bis-catecholato silicate compounds. In this article, using a simple tertiary amine as the base, trialkoxysilanes bearing various alkyl groups could react with catechol to provide the corresponding bis-catecholato silicates. The survey of the solvent indicated that methanol is the best choice of solvent. Moreover, the optimization of the base indicated that a weak base such as pyridine could obtain the middle yield. This study lays the groundwork for future research into the preparation of the bis-catecholato silicate compounds.

In the latter half of the 1980s, after Frye published his findings, Corriu[102] realized the preparation of the alkali salts of alkyl bis-catecholato silicates. On the contrary, he preferred to utilize methoxide salts as the base rather than amines. The reaction was carried out in the methanol solution of corresponding methoxide salts (like MeOK or MeONa) to produce the target sodium or potassium salts of silicates. (**Scheme 72**)

[102] (a) G. Cerveau, C. Chuit, R. J. P. Corriu, L. Gerbier, C. Reye, J. L. Aubagnac, B. El Amrani, *Int. J. Mass Spectrom. Ion Process.*, **1988**, *82*, 259–271. (b) A. Boudin, G. Cerveau, C. Chuit, R. J. P. Corriu, C. Reye, *Bull. Chem. Soc. Jpn.*, **1988**, *61*, 101–106.

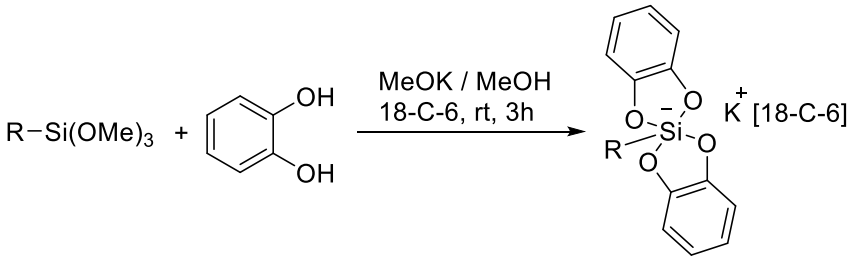

Scheme 72. The preparation of bis-catecholato silicates

Due to the degradation of the bis-catecholato silicates, the use of [18-C-6] crown ether could strengthen the hypervalent bond and stabilize the silicate by charge separation. The desired product could be obtained according to this method and stored at room temperature without decomposition. As for the group tolerance, the bis-catecholato silicates bearing various alkyl or aryl groups (including the primary alkyl group, secondary alkyl group, and the aryl group) could be prepared via this synthesis route.

Inspired by the pioneering work of R. R. Holmes[103] and H. Sakurai[104], using tertiary amine as the base, the trichlorosilane could react with catechol to provide the desired product in moderate to excellent yield. In the presence of tetraethylammonium bromide (NEt_4Br), the metathesis in MeCN could obtain the corresponding tetraethylammonium bis-catecholato silicates. (**Scheme 73**)

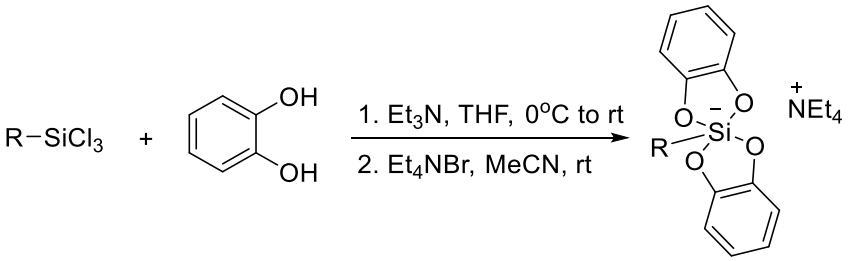

Scheme 73. The preparation of bis-catecholato silicates

In 2016, inspired by the pioneering work of Frye's, Molander's group[105] developed a novel method to prepare the ammonium silicates without using any metathesis techniques. The triethylamine or diisopropylamine can be used as the base, and the various alkoxysilanes could react with catechol in a suitable solvent(THF or dioxane) to provide the desired product in excellent yield. (**Scheme 74**)

[103] R. R. Holmes, R. O. Day, J. J. Harland, A. C. Sau, J. M. Holmes, *Organometallics*, **1984**, *3*, 341–347.

[104] (a) M. Kira, K. Sato, H. Sakurai, *J. Org. Chem.*, **1987**, *52*, 948–949. (b) M. Kira, K. Sato, H. Sakurai, *J. Am. Chem. Soc.*, **1988**, *110*, 4599–4602.

[105] M Jouffroy, D N. Primer, G A. Molander, *J. Am. Chem. Soc.*, **2016**, *138*, 475-478.

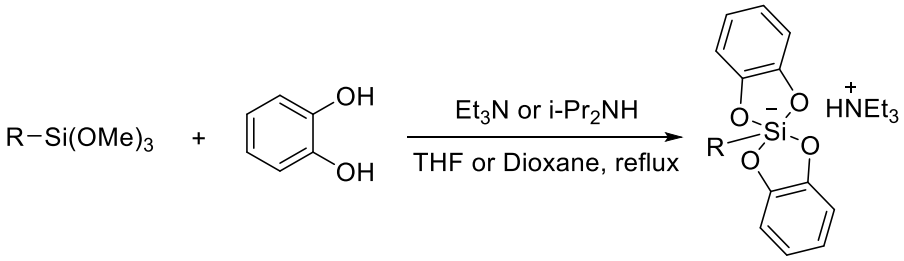

Scheme 74. Molander's Ammonium silicates synthesis

2.4. The oxidative potential of bis-catecholato silicates

It is critical to understand the electrochemical properties of the bis-catecholato silicates substrates in photoredox catalysis. These values of electrochemical potential, in fact, notify us about the thermodynamic favorability of a reaction.

In 2014, after preparing the various silicate bearing different alkyl groups, our group evaluated the redox potential of the bis-catecholato silicates bearing various groups. After performing the measurement via cyclic voltammetric analysis, we obtained the oxidation potential of the silicate bearing various group. Based on the experiment result, the oxidation potential of bis-catecholato silicates increases in the following order: activated silicates ($E_{1/2}^{ox}$ from + 0.34 V *vs* SCE to + 0.72 V *vs* SCE) < secondary silicates ($E_{1/2}^{ox}$ from + 0.69 V *vs* SCE to + 0.76 V *vs* SCE) < primary silicates($E_{1/2}^{ox}$ from + 0.74 V *vs* SCE to + 0.90 V *vs* SCE) < aryl silicates($E_{1/2}^{ox}$ > +0,88 V *vs* SCE). The hypothesis that the homolytic fragmentation of the C-Si bond in silicates could generate the carbon-centered radical indicated that there is a relationship between the oxidation potential of the bis-catecholato silicates and the stability of the radical intermediate.

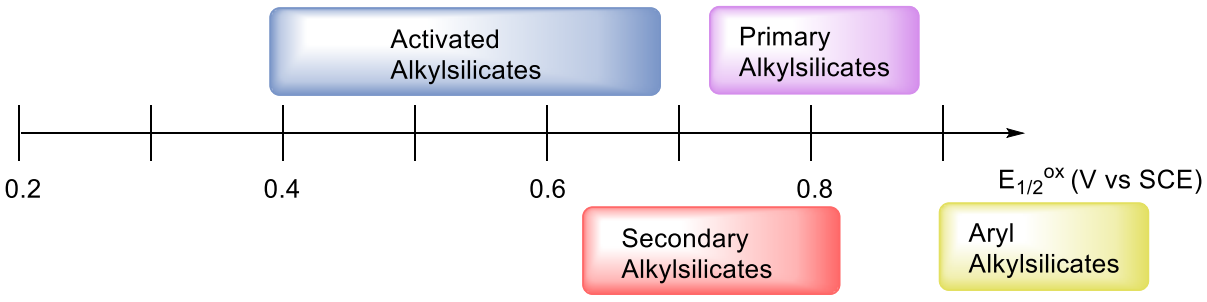

Figure 4. The relative order of the oxidation potential of the silicates

2.5. Photoredox catalysis with alkyl bis-catecholato silicates

Over the last years, bis-catecholato silicate has emerged as a promise latent radical

precursor for the formation of carbon-carbon bonds, functionalization of alkenes, alkynes, and other compounds.

In 2005, Nishigaishi[106] first demonstrated the photoallylation of 1,2-diphenylethane 1,2-dione (benzil) using the hypercoodinated silicon reagents such as tetramethylammonium bis-catecholato allylsilicate derivatives (**Scheme 75**). The allylation product, the homoallylic alcohols, could be synthesized in reasonable to excellent yields. The mechanism hypothesis postulated a photoinduced electron transfer between bis-catecholato allyl silicates and benzil.

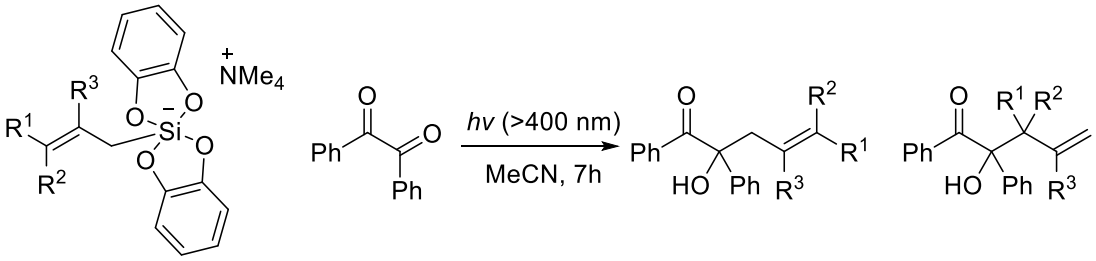

Scheme 75. Photoallylation of benzyl with allyl bis-catecholato silicate

Nishigaishi suggested that after the absorption of the light, the diketone was in the excited state and then oxidized the silicate, forming a ketyl radical and a radical allyl cation. After cleavage of C-Si bond, the bis-catecholato silicate could generate the allyl radical, and radical coupling with the diketone forms the homoallylic alcohol. (**Scheme 76**)

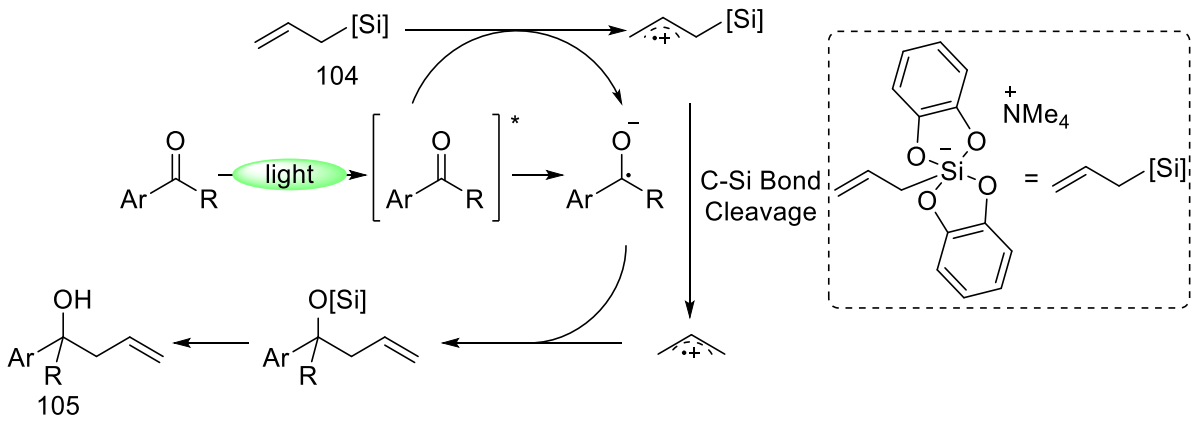

Scheme 76. The suggested mechanism of photoinduced allylation of bis allyl catecholato silicate through the PET process

In 2014, Nishigaichi[107] reported the UV light-induced anthracene catalyzed substitution of dicyanoarenes with allyl bis-catecholato silicates. Since hypervalent allylsilicon reactants have a lower oxidation potential than tetracoordinate reactants, the photoinduced electron

[106] Y. Nishigaichi, A. Suzuki, T. Saito, A. Takuwa, *T*etrahedron Lett., **2005**, *46*, 5149–5151

[107] D. Matsuoka, Y. Nishigaichi, *Chem. Lett.*, **2014**, *43*, 559–561

transfer process is more efficient. The photoexcited anthracene can reduce 1,4-dicyanobenzene through the PET process, liberating the intermediate aryl radical anion. The cationic anthracene can oxidize the bis-catecholato silicate, providing the formation of the allyl radical. Finally, the intermediate is converted into the desired allyl-substituted product (**Scheme 77**).

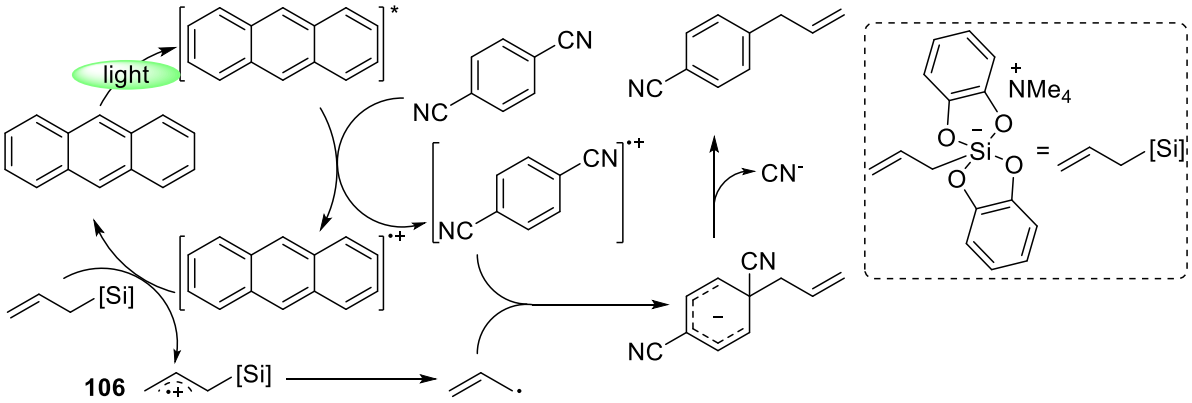

Scheme 77. Proposed mechanism of photo-induced allylation of dicyanoarenes

More recently, our group[108] realized a methodology for efficient carbon-carbon bond formation employing alkyl bis-catecholato silicates as the radical precursors (**Scheme 78**). The proposed method utilized iridium complex ($Ir[(dF(CF_3)ppy)_2(bpy)](PF_6)$) as an oxidizing photocatalyst and DMF as solvent. The radical trapping experiment of the bis-catecholato silicates with the radical scavenger TEMPO can afford the corresponding TEMPO-alkyl adduct in excellent yield. Additionally, the result of the radical scavenger strongly implied that the relative reaction utilizing the bis-catecholato silicates as substrate proceeds via the radical-mediated pathway. Subsequently, employing bis-catecholato silicates and numerous radical acceptors as substrate, a set of photoredox catalyzed radical-mediate reactions like allylation, alkynylation, vinylation, and Giese-type reactions could proceed efficiently and adequately. Additionally, most reaction products are formed with high yields.

[108] V. Corcé, L.-M. Chamoreau, E. Derat, J.-P. Goddard, C. Ollivier, L. Fensterbank, *Angew. Chemie Int. Ed.* **2015**, *54*, 11414–11418.

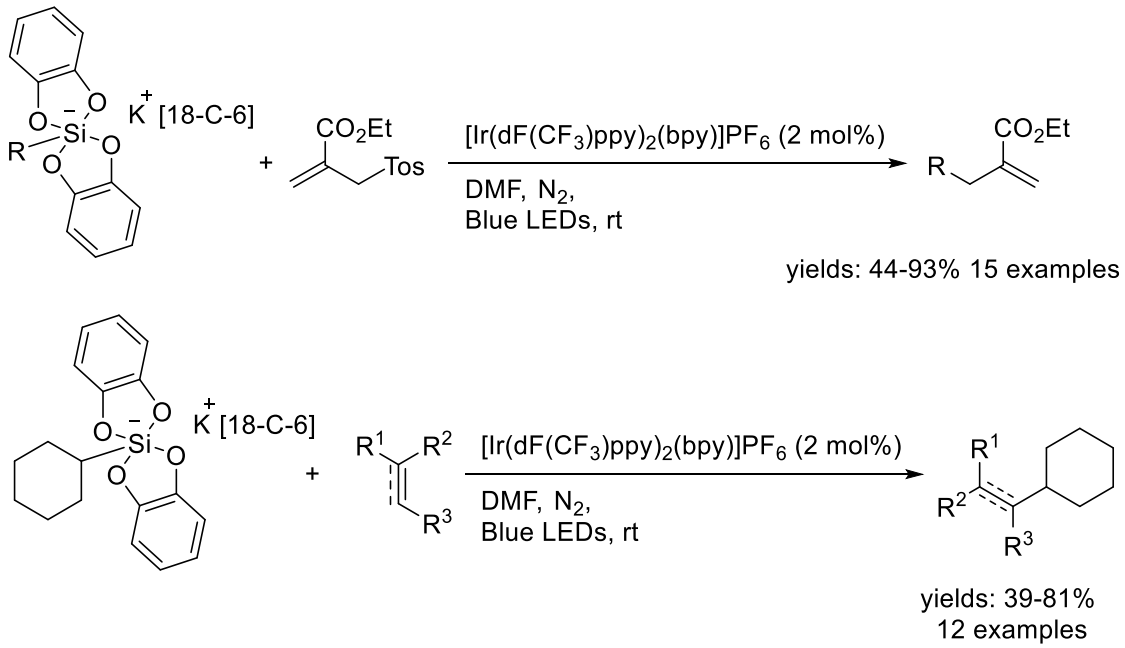

Scheme 79. Numerous photoredox catalyzed reactions employing alkyl bis-catecholato silicates as the radical precursors.

The overall mechanism shown in **Scheme 79** was established by our group. The photocatalyst is first excited upon irradiation of visible light. Single-electron oxidation of the alkyl bis(catecholato)silica by the oxidizing species $[Ir^{III}]^*$ resulted in the iridium species $[Ir^{II}]$ and the formation of the alkyl radical via the homolytic fragmentation of the alkyl silicates. The following radical addition of alkyl radical with acceptor alkenes could afford the adduct radical. The homolytic cleavage of C-Si bond of the radical adduct intermediate could yield the desired product and the sulfonyl radical. The reduction of sulfonyl radical with reducing species $[Ir^{II}]$ could provide sulfinate anion and return the photoredox catalyst to its ground state, completing the photoredox catalytic cycle and establishing its propagation. In the same mechanism that the TEMPO-trapping catalytic cycle works, the TEMPO•, as a radical scavenger, could react with the newly generated alkyl radical. In contrast, the excess TEMPO • also could oxidize the reducing species $[Ir^{II}]$ to finish the catalytic cycle.

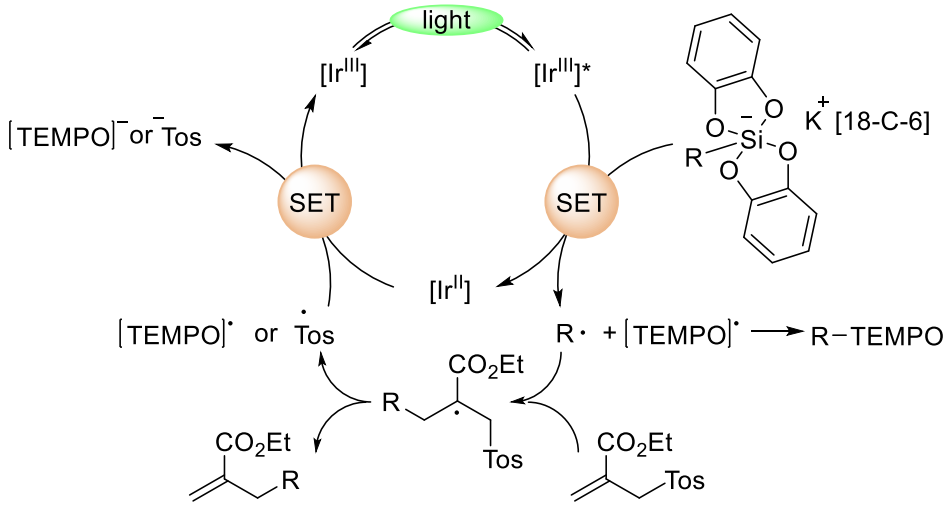

Scheme 79. The proposed mechanism of photooxidative C-C formation employing silicate as substrate

Furthermore, our group also demonstrated the C(sp^2)–C(sp^3) bond formation via cross-coupling reactions employing alkyl bis-catecholato silicates and 4-bromobenzonitrile as substrate with dual Ni/photoredox catalysis (**Scheme 80**). Utilizing 4,4'-di-tert-butyl-2,2'-bipyridine (dtbpy) as ligand and a Ni/photoredox catalytic system composed of the Ir-based photocatalyst Ir[(dF(CF_3)ppy)$_2$(bpy)](PF_6) and the nickel catalyst Ni(COD)$_2$, alkyl bis-catecholato silicates aryl sulfonate salts can generate alkyl radicals that can carry out the cross-coupling process with the 4-bromobenzonitrile to give the desired cross-coupling products.

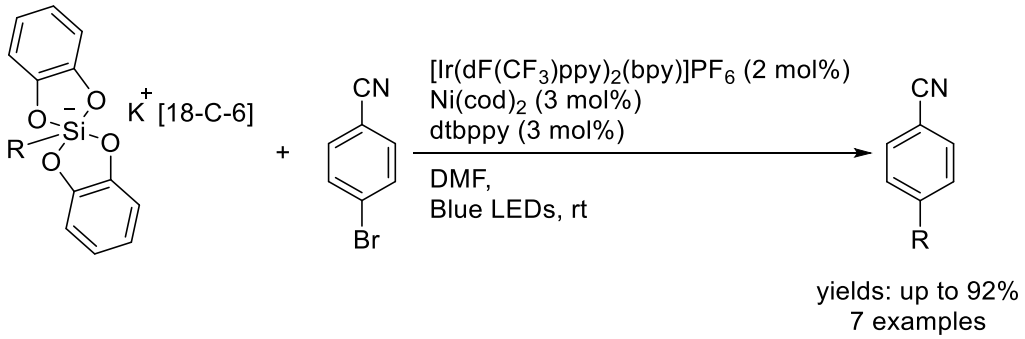

Scheme 80. Ni/photoredox catalyzed cross-coupling reaction of alkyl bis-catecholato silicates

Inspired by the pioneering work of Zhang,[109] considering the intrinsic electrochemical properties ($E_{1/2}^{red}$ ([4CzIPN]*/[4CzIPN]$^-$) = +0.83V *vs* SCE) and ($E_{1/2}^{Ox}$ ([Si(catechol)]*/[Si(catechol)]$^-$) = +0.3 V *vs*. SCE to +0.9 V *vs*. SCE) and commercial

[109] J. Luo, J. Zhang, *ACS Catal.*, **2016**, *6*, 873–877.

availability, our group [110] proposed the application in carbon-carbon bond formation employing alkyl bis-catecholato silicates as substrate under the organic dye photoredox catalyst 4CzIPN (**Scheme 81**). Utilizing 4CzIPN, the spin trapping experiment of bis-catecholato silicates with the radical scavenger TEMPO results in a high yield of the corresponding TEMPO-alkyl adduct. Furthermore, the results of the radical scavenger experiment clearly suggested that the relative reaction using 4CzIPN as a photoredox catalyst occurs through a radical-mediated mechanism. As a result, a wide range of 4CzIPN catalyzed radical-mediate reactions involving bis-catecholato silicates and a variety of radical acceptors as substrate, such as allylation, alkynylation, vinylation, and Giese-type reactions can proceed efficiently, with the majority of reaction products forming in high yields.

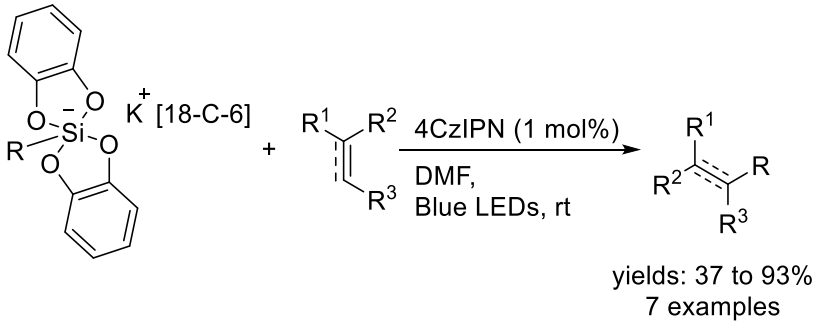

Scheme 81. Transition-metal-free photoredox photoredox catalyzed reaction employing alkyl bis-catecholato silicates

Based on the results of the mechanism experiment and previous literature[90], the following catalytic cycle was hypothesized. The alkyl silicate derivative would be oxidized by photoexcited $[4CzIPN]^*$ through a SET process, yielding the $[4CzIPN]^-$ anion species and a hypercoordinated silicon radical. The following homolytic fragmentation of the C-Si bond leads to the formation of the alkyl radical. The addition of allyl sulfone could result in α,β-sulfonyl radical. Finally, the cleavage of C-Si bond liberated the allylation adduct and a tosyl radical. The single-electron reduction of tosyl radical could provide the regenerated photocatalyst and a sulfinate anion. (**Scheme 82**)

[110] C. Lévêque, L. Chenneberg, V. Corcé, C. Ollivier, L. Fensterbank, *Chem. Commun*. **2016**, *52*, 9877–9880.

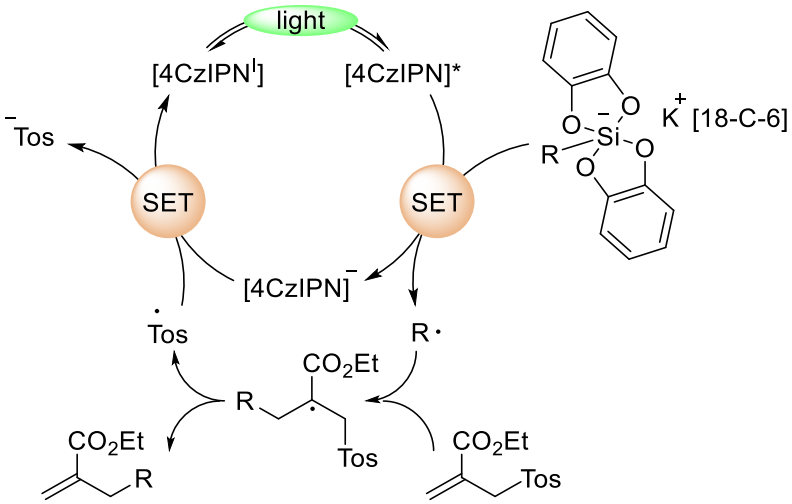

Scheme 82. Proposed mechanism of the organic dye 4CzIPN catalyzed photoredox reaction of alkyl silicate

Additionally, our research realized the construction of the C(sp2)–C(sp3) bond via cross-coupling reactions employing alkyl bis-catecholato silicates and diverse aryl bromides or alkenyl halides as substrates and utilizing dual Ni/photoredox catalysis (**Scheme 83**). The reported method was composed of the 4,4'-di-tert-butyl-2,2'-bipyridine (dtbpy) as ligand, and a Ni/photoredox catalytic system consisted of organic dye 4CzIPN and the nickel catalyst $NiCl_2$·dme. Following photooxidation with 4CzIPN, the alkyl radical produced by alkyl bis-catecholato silicates could be coupled with the aryl halide via nickel catalysis to provide the required cross-coupling products.

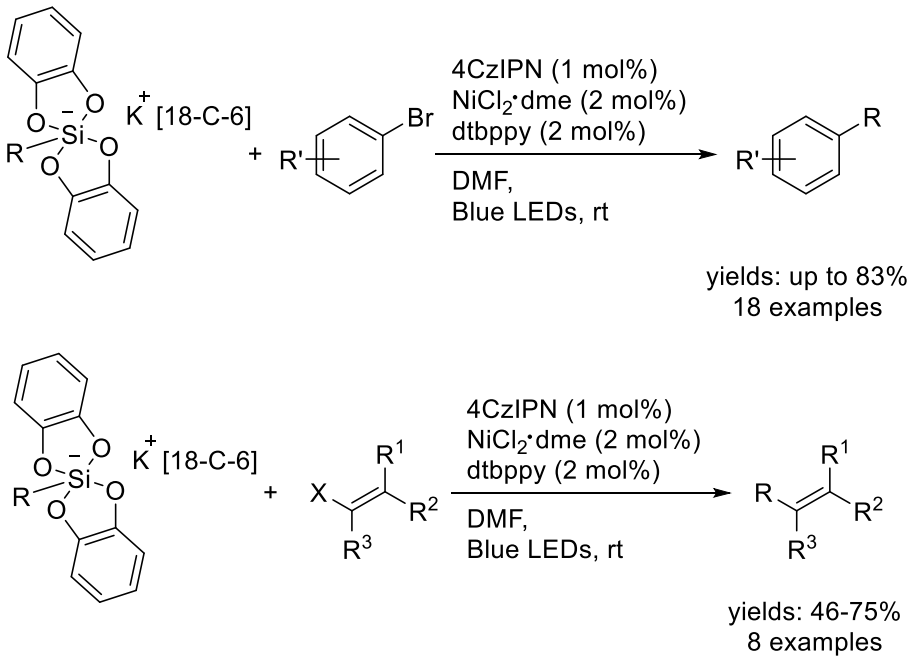

Scheme 83. Ni/photoredox catalyzed cross-coupling reaction of alkyl bis-catecholato silicates

using 4CzIPN as photoredox catalyst

In 2017, the Molander group [111] extended the application scope of bis-catecholato silicates. The generated alkyl radical was engaged in addition reactions with imines (**Scheme 84**). Radical addition products were obtained in moderate to excellent yields. Alkylation of primary alkyl biscatecholato silicate could be performed by the action of the ruthenium catalyst $Ru(bpy)_3(PF_6)_2$ and N-sulfonyl aldimines as radical acceptor, gave the good yields. N-sulfonyl, N-Methyl-, phenyl-, *p*-toluenesulfonyl, and even N, N-dimethyl- sulfamidyl aldimines were all suitable substrates in this transformation, providing the addition products in good yields. This approach also makes it easier to introduce a variety of alkyl groups, including those with protic functional groups and those derived from non-stabilized radicals.

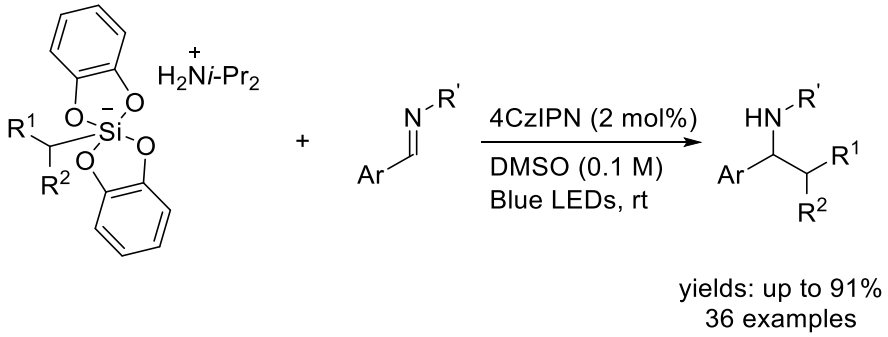

Scheme 84. Photoredox catalyzed alkylation of imines

Single-electron oxidation of the alkyl bis(catecholato)silicate by the excited $[4CzIPN]^*$, followed by radical addition to imine and single-electron transfer (SET) reduction, afford the corresponding alkylated product upon H-abstraction of the N-centered radical intermediate. (**Scheme 85**)

[111] N. R. Patel, C. B. Kelly, A. P. Siegenfeld, G. A. Molander, *ACS Catal.*, **2017**, *7*, 1766–1770.

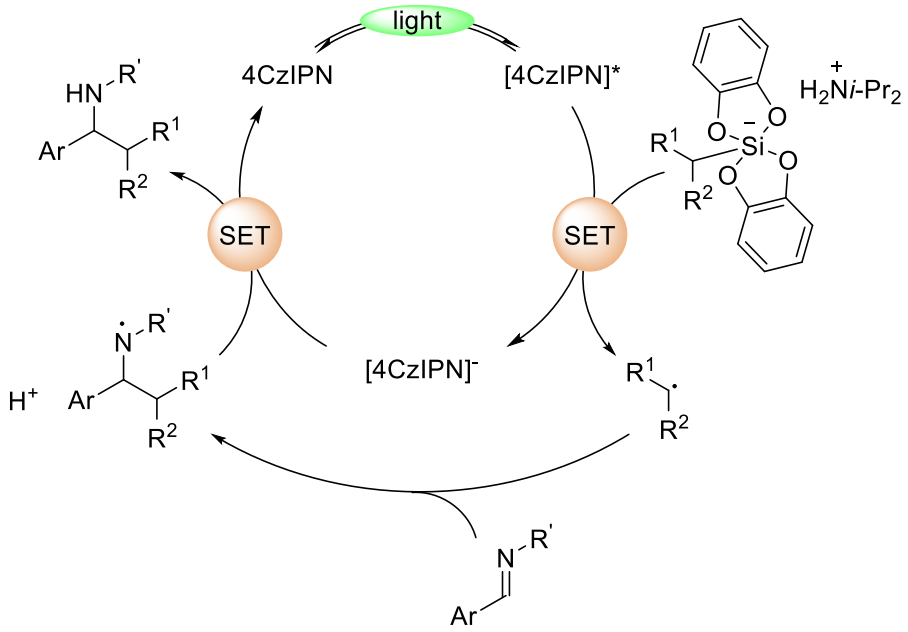

Scheme 85. The proposed mechanism for the alkylation of imines

In 2018, the Molander group[112] developed a methodology for the cyclopropanation of the substituted alkene with iodomethylsilicate to provide desired cyclopropane ketones (**Scheme 86**). Comparing to other α-halomethyl bis-(catecholato)silicates such as the α-chloro-, α-bromo-, α-iodomethylsilicate could undergo the cyclopropanation of trifluoromethyl-substituted alkenes regiospecificaly. The corresponding alkenes bearing electron-deficient groups or electron-rich groups can provide the desired products in good yields. α,β-Unsaturated esters, amides, and ketones were also valuable substrates of cyclopropanation.

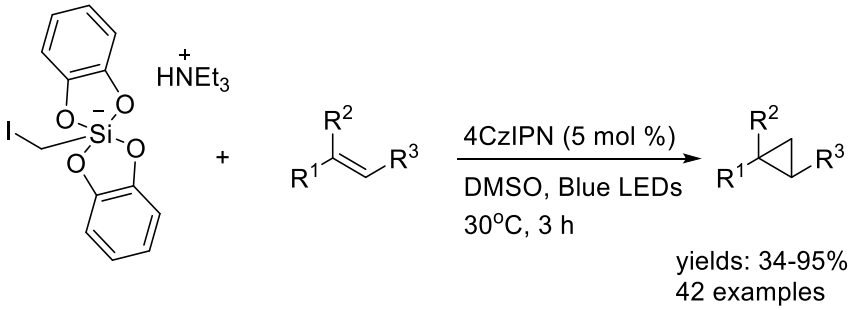

Scheme 86. Photoredox cyclopropanation of substituted alkenes with iodomethylsilicates

The proposed mechanism for this homocoupling reaction is outlined in **Scheme 87**. Firstly, based on the experiment results of Stern−Volmer quenching experiments and on the values of oxidation potentials of silicates ($E_{1/2}^{ox}$= + 0.4 V vs SCE to + 0.7 V vs SCE), visible-

[112] J. P. Phelan, S. B. Lang, J. S. Compton, C. B. Kelly, R. Dykstra, O. Gutierrez, G. A. Molander, *J. Am. Chem. Soc.*, **2018**, *140*, 8037–8047.

light-induced irradiation of 4CzIPN to its excited state underwent the single-electron reduction with the halomethyl silicate to obtain the halomethyl radical intermediate. The Giese-type addition of disubstituted olefin by the iodomethyl radical generates the addition product. In the next step, single-electron reduction of the addition product by the photoreducing $[4CzIPN]^-$ gives anions and regenerate 4CzIPN to its ground state. The anionic cyclization (3-exo-tet ring closure) of the anion intermediates afforded cyclopropanes. In examples where the alkene is 1,2-disubstituted or trisub- stituted, stereoconvergence is observed.

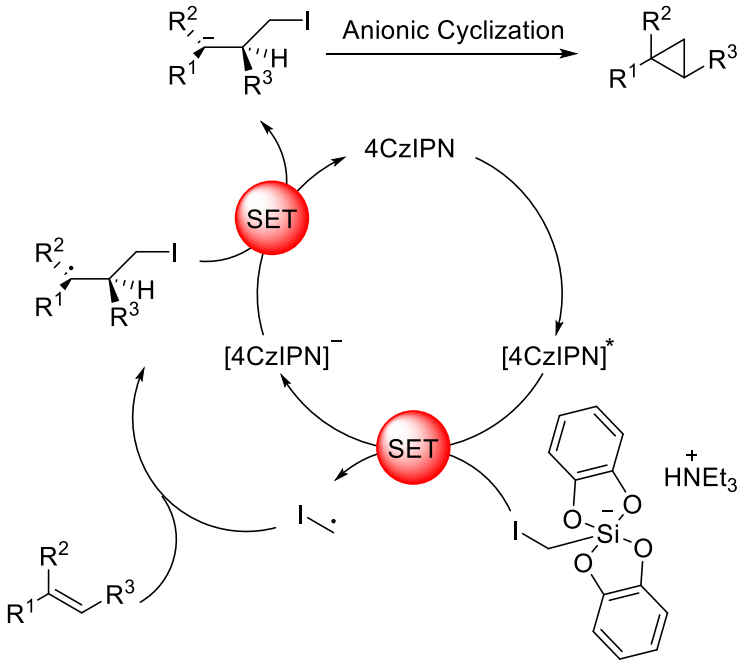

Scheme 87. The proposed mechanism for the cyclopropanation of substituted alkenes with iodomethylsilicates

On the same line, inspired by the previous result, Molander and co-workers [113] demonstrated another methodology involving ammonium alkyl bis-catecholato silicates and tosylated alkenes (**Scheme 88**). Fragmentation of alkyl bis-catecholato silicates gave primary, non-stabilized alkyl radicals, which could be coupled with tosylated alkenes bearing electron-rich or electron-deficient groups efficiently.

[113] J. A. Milligan, J. P. Phelan, V. C. Polites, C. B. Kelly, G. A. Molander, *Org. Lett.*, **2018**, *20*, 6840–6844.

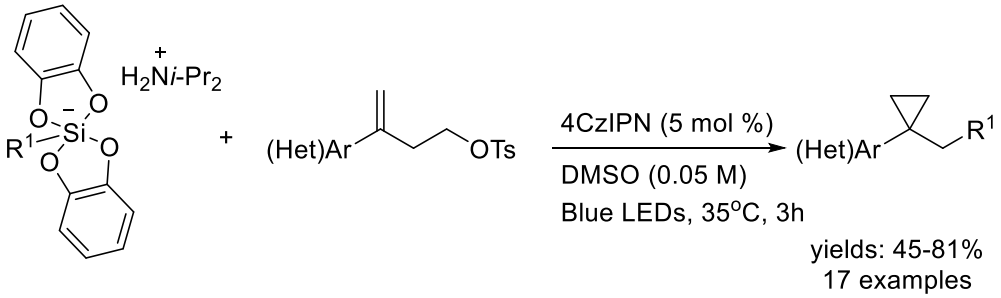

Scheme 88. The cyclopropanation of tosylated alkenes with alkyl bis-catecholato silicates

Recently, our group[114] reported a multi-component cross-coupling reaction between bis catecholato silicate, CO, and the olefin bearing the electron withdraw group. We photooxidized biscatecholato silicate with 4CzIPN at room temperature. The generated alkyl radical was engaged in a carbonylation reaction followed by the addition of the generated acyl radical to the olefin bearing the electron withdraw group as the radical acceptor. Radical adducts were isolated in moderate to excellent yields (**Scheme 89**). A series of electron-deficient olefins bearing ester group, phenyl group, *p*-toluene-sulfonyl group, or carbonyl group were all competent partners in this reaction, providing the cross-coupling products in good yields. This method also facilitates the installation of various alkyl groups.

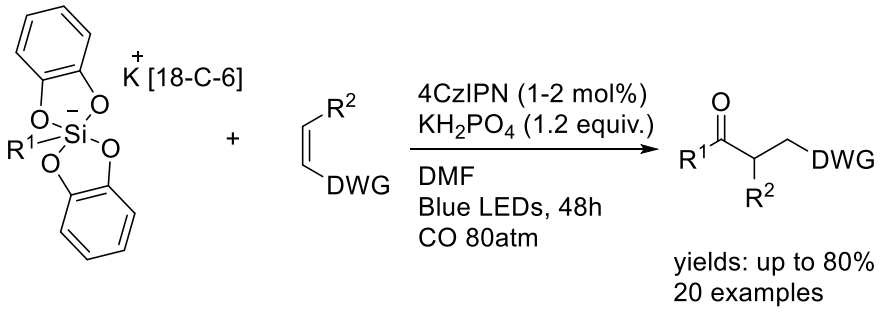

Scheme 89. Photoredox catalyzed multi-component cross-coupling reaction between bis catecholato silicate, CO, and the olefin

We proposed the mechanism illustrated in **Scheme 90.** Under visible-light irradiation, the photocatalyst is initially stimulated. Homolytic fragmentation of the bis catecholato silicate radical, single-electron oxidation of the alkyl bis(catecholato)silicate by the excited state of the photocatalyst *4CzIPN resulted in the reduced form of photocatalyst [4CzIPN] and the

[114] A. Cartier, E. Levernier, V. Corcé, T. Fukuyama, A. L. Dhimane, C. Ollivier, I. Ryu, L. Fensterbank, *Angew. Chemie - Int. Ed.* **2019**, *58*, 1789–1793.

newly formed alkyl radical. The alkyl radical interacts with CO to produce the acyl radical, which then reacts with the radical acceptor olefin to produce the adduct radical. [4CzIPN] can reduce the new formed radical to get the corresponding carbanion and renew the photocatalyst to its ground state, therefore completing the catalytic cycle and assuring its propagation. The final product is obtained after protonation with KH_2PO_4.

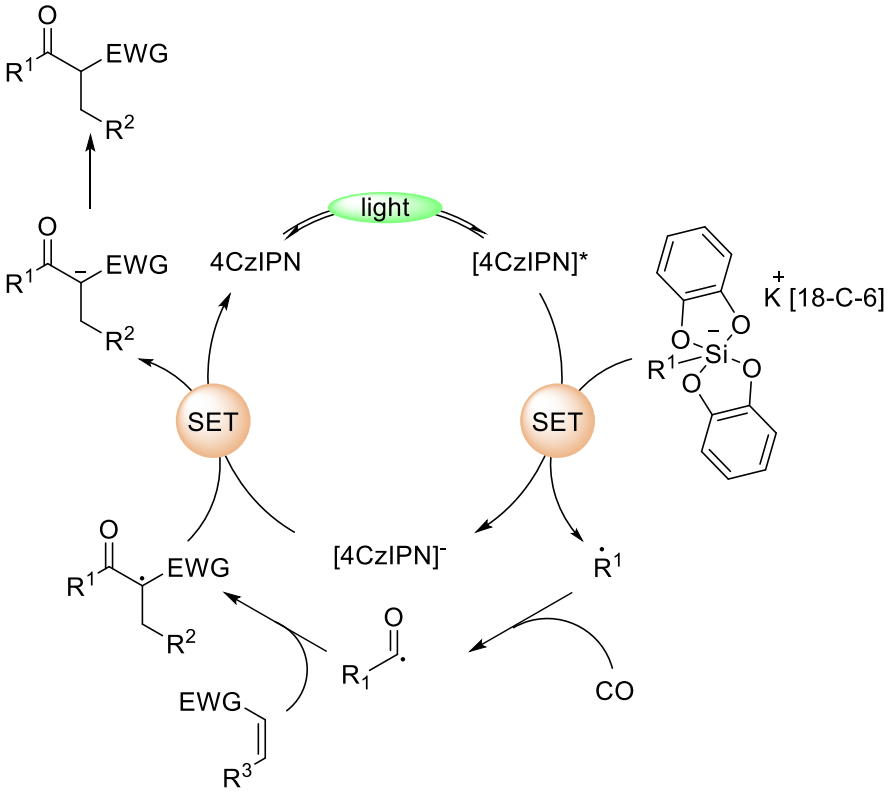

Scheme 90. The proposed mechanism for the three-component coupling reaction between bis(catecholato)cyclohexylsilicate, CO, and the alkene

Fensterbank, Ollivier and Goddard[115] , and later Molander[116] reported a cross-coupling reaction of alkyl bis(catecholato)silicate and aryl halides (**Scheme 91**). In their case, a $NiCl_2$.dme was used as precatalyst with 4,4'-di-tert-butyl- 2,2'-bipyridine as ligand, and bis(catecholato) silicate was used as radical precursor. After the photooxidation catalyzed by $Ru(bpy)_3(PF_6)_2$, the alkyl radical was coupled with the aryl halide through nickel catalysis. Ligand optimization indicated that changes in the substitution pattern of the phenanthryl could affect the conversion and selectivity. Efficiently, both primary and secondary alkyl radicals were engaged with aryl bromides with satisfactory chemoselectivity.

[115] C. Lévêque, L. Chennenberg, V. Corcé, J.-P. Goddard, C. Ollivier, L. Fensterbank, *Org. Chem. Front.* **2016**, *3*, 462-465

[116] K. Lin, R. J. Wiles, C. B. Kelly, G. H. M. Davies, G. A. Molander, *ACS Catal.* **2017**, *7*, 5129–5133.

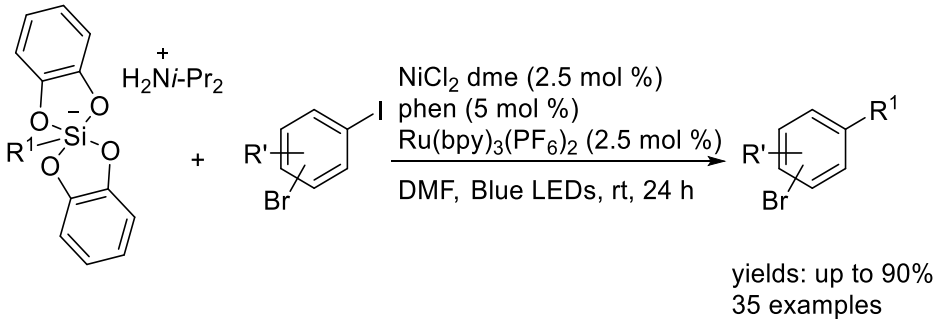

Scheme 91. Cross-coupling reaction of alkyl bis(catecholato)silicate and aryl halide

The authors proposed that the reaction is initiated by photoredox catalyzed single electron transfer (SET) from the bis(catecholato)silicate, generating an alkyl radical intermediate. Then, the addition of alkyl radical to phen·Ni(0) provides an alkyl–Ni(I) species. The resulting active complex alkyl–Ni(I) would react with the aryl halide to generate the intermediate ArX-[Ni(II)]-Alky. Then, reductive elimination provides the alkylated cross-coupling product. In the next step, assisted by the photocatalyst, the nickel(I) species could regenerate phen·Ni(0) via single electron transfer (SET). (**Scheme 92**)

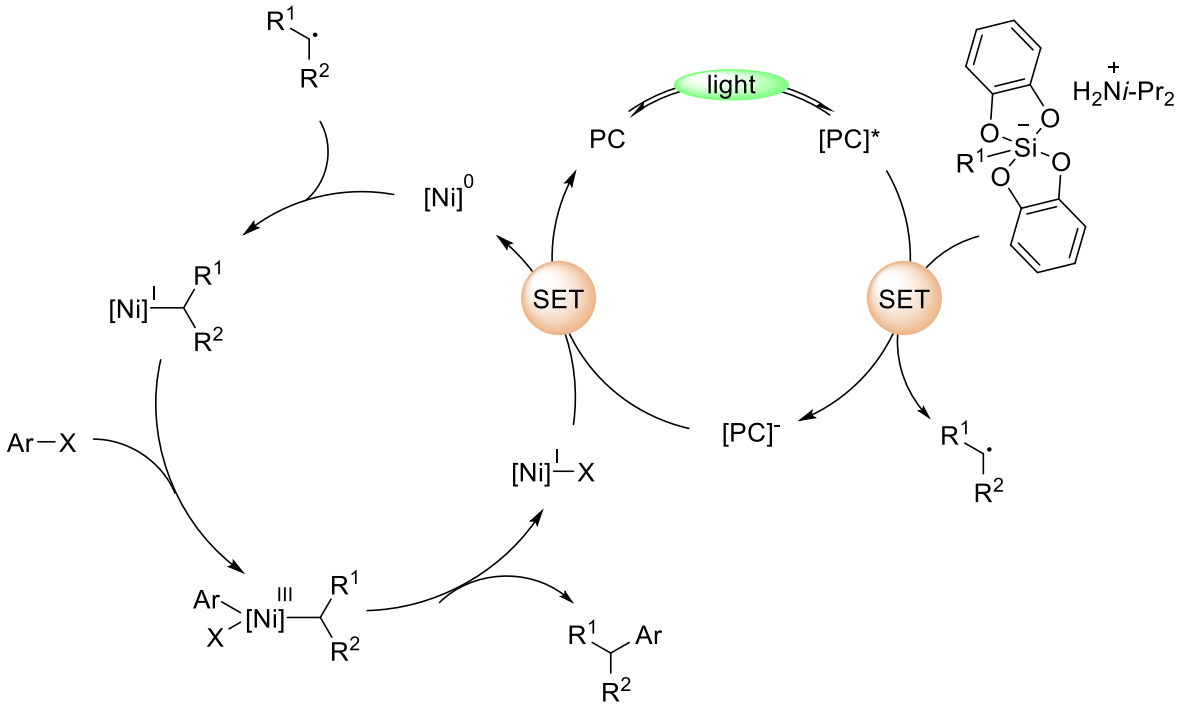

Scheme 92. The proposed mechanism of cross-coupling reaction of alkyl bis(catecholato)silicate and aryl halide

3. Photooxidation of Phenyl Silicates with Substituted Catecholate Ligand: Synthesis, Structural Studies and Reactivity

Published in *Chem. Eur. J* , **2021**, *27*, 8782-8790

My contribution to these studies consisted in the preparation of the phenyl silicates and the cyclohexyl silicate. The analytical and spectroscopic techniques of phenyl silicates with substituted catecholate ligand in this project were realized in collaboration with my colleague Dr. Etienne Levernier. Khaoula Jaouadi performed UV-vis and DFT studies. All that remains was accomplished by Dr. Etienne Levernier

3.1 Abstract

While the generation of aryl radicals by photoredox catalysis is well-documented under reductive conditions, it has remained challenging under an oxidative pathway. Because of the easy photooxidation of alkyl bis-catecholato silicates, a general study on phenyl silicates bearing substituted catecholate ligands has been achieved. The newly synthesized phenyl silicates have been fully characterized and their reactivity has been explored. It was found that thanks to the substitution of the catecholate moiety and notably with the 4-cyanocatecholato ligand, the phenyl radical could be generated and trapped. Computational studies provided a rationale for these findings.

3.2. Introduction

Alkyl bis-catecholatosilicates have recently elicited intense interest in photooxidative catalysis as valuable alkyl radical precursors in radical addition reactions,[117] radical-polar

[117] a) V. Corcé, L.-M. Chamoreau, E. Derat, J.-P. Goddard, C. Ollivier and L. Fensterbank, *Angew. Chemie Int. Ed.*, 2015, **54**, 11414–11418.; *Angew. Chem.* **2015**, *127*, 11576-11580; b) A. Cartier, E. Levernier, V. Corcé, T. Fukuyama, A.-L. Dhimane, C. Ollivier, I. Ryu and L. Fensterbank, *Angew. Chemie Int. Ed.*, 2019, **58**, 1789–1793.; *Angew. Chem. Int. Ed.* **2019**, *131*, 1803-1807; c) A. Cartier, E. Levernier, A.-L. Dhimane, T. Fukuyama, C. Ollivier, I. Ryu, L. Fensterbank, *Adv. Synth. Catal.* **2020**, *362*, 2254-2259; d) N. R. Patel, C. B. Kelly, A. P. Siegenfeld, G. A. Molander, *ACS Catal.* **2017**, *7*, 1766-1770; e) S. T. J. Cullen, G. F. Friestad, *Org. Lett.* **2019**, *21*, 8290-8294.

crossover reactions[118]as well as dual photoredox-nickel cross-couplings.[119] In contrast, aryl silicates counterparts have been much less utilized. Their main use has been disclosed by DeShong in palladium catalyzed cross-coupling reactions with arylhalides[120] (**Scheme 93**, *eq. 1*) and by Hashmi for cross-coupling reactions with aryldiazonium salts by gold(I) catalysis[121](**Scheme 93**, *eq. 2*).

The photooxidation of arylsilicates would be of interest for two reasons. First, the generation of aryl radicals by photoredox catalysis is well-documented under photoreductive conditions from a variety of precursors such as aryl diazoniums, [122] iodoniums, [123 , 124] sulfoniums,[125] arylhalides,[126] and also benzoyl hypohalites[127] (**Scheme 94).** In contrast and to

---

[118] a) S. B. Lang, R. J. Wiles, C. B. Kelly, G. A. Molander, *Angew.Chem.Int. Ed.* **2017**, *56*, 15073–15077; *Angew. Chem.* **2017**,*129*,15269–15273; b) J. P. Phelan, S. B. Lang, J. S. Compton, C. B. Kelly, R. Dykstra, O. Gutierrez, G. A. Molander, *J. Am. Chem. Soc.* **2018**, *140*, 8037-8047; c) T. Guo, L. Zhang, X. Liu, Y. Fang, X. Jin, Y. Yang, Y. Li, B. Chen, M. Ouyang, *Adv. Synth. Catal.* **2018**, *360*, 4459-4463; d) L. R. E. Pantaine, J. A. Milligan, J. K. Matsui, C. B. Kelly, G. A. Molander, *Org. Lett.* **2019**, *21*, 2317–2321

[119] a) C. Lévêque, L. Chennenberg, V. Corcé, J.-P. Goddard, C. Ollivier, L. Fensterbank, *Org. Chem. Front.* **2016**, *3*, 462-465; b) E. Levernier, V. Corcé, L.-M. Rakotoarison, A. Smith, M. Zhang, S. Ognier, M. Tatoulian, C. Ollivier, L. Fensterbank, *Org. Chem. Front.* **2019**, *6*, 1378-1382; c) M. Jouffroy, D. N. Primer, G. A. Molander, *J. Am. Chem. Soc.* **2016**, *138*, 475-478; d) N. R. Patel, C. B. Kelly, M. Jouffroy and G. A. Molander, *Org. Lett.* **2016**, *18*, 764-767; e) M. Jouffroy, C. B. Kelly, G. A. Molander, *Org. Lett.* **2016**, *18*, 876-879; f) J. P. Phelan, S. B. Lang, J. Sim, S. Berritt, A. K. Peat, K. Billings, L. Fan, G. A. Molander, *J. Am. Chem. Soc.* **2019**, *141*, 3723-3732; g) J. K. Matsui, S. B. Lang, D. R. Heitz, G. A . Molander, *ACS Catal.* **2017**, *7*, 2563-2575; h) K. Lin, R. J. Wiles, C. B. Kelly, G. H. M. Davies, G. A. Molander, *ACS. Catal.* **2017**, *7*, 5129-5133; i) B. A. Vara, X. Li, S. Berritt. C. R. Walters, E. J. Petersson, G. A. Molander, *Chem. Sci.* **2018**, *9*, 336-344; j) S. O. Badir, J. Sim, K. Billings, A. Csakai, X. Zhang, W. Dong, G. A. Molander, *Org. Lett.* **2020**, *22*, 1046-1051; k) K. D. Raynor, G. D. May, U. K. Bandarage, M. J. Boyd, *J. Org. Chem*. **2018**, *83*, 1551-1557.

[120] a) W. M. Seganish, P. DeShong, *J. Org. Chem.* **2004**, *69*, 1137-1143; b) W. M. Seganish, P. DeShong, *Org. Lett.* **2004**, *5*, 4379-4381.

[121] S. Witzel, K. Sekine, M. Rudolf, S. K. Hashmi, *Chem. Commun.* **2018**, *54*, 13802-13804.

[122] For a general revue on radical precursor in reduction see: I. Ghosh, L. Marzo, A. Das, R. Shaikh, B. König, *Acc. Chem. Res*. **2016**, *49*, 1566-1577; For a revue on diazoniums see: F. Mo, G. Dong, Y. Zhang, J. Wang, *Org. Biomol. Chem.* **2013**, *11*, 1582-1593; a) T. Hering, D. P. Hari, B. König, *J. Org. Chem.* **2012**, *77*, 10347-10352; b) Z. Xia, O. Khaled, V. Mouriès-Mansuy, C. Ollivier, L. Fensterbank, *J. Org. Chem*, **2016**, *81*, 7182-7190; b) D. P. Hari, T. Hering, B. König, *Org. Lett.* **2012**,*14*, 5334−5337; d) P. Maity, D. Kundu,B. C. Ranu, *Eur. J. Org. Chem.* **2015**, *2015*, 1727−1734; e) J. Zhang, J. Chen, X. Zhang, X. Lei, *J. Org. Chem.* **2014**, *79*, 10682−10688.

[123] L. Fensterbank, J.-P. Goddard, M. Malacria, C. Ollivier, *Chimia* **2012**, *66*, 425-432.

[124] a) E. A. Merritt, B. Olofsson, *Angew. Chem. Int. Ed*, **2009**, *48*, 9052-9070; b) A. Baralle, L. Fensterbank, J. P. Goddard, C. Ollivier, *Chem. Eur. J.* **2013**, *19*, 10809-10813.

[125] a) J. Li, J. Chen, R. Sang, W.-S. Ham, M. B. Plutschack, F. Berger, S. Chabbra, A. Schnegg, C. Genicot, T. Ritter, *Nat.* Chem. **2020**, *12*, 56-62; b)M. H. Aukland, M.Šiaučiulis, A. West, G. J. P. Perry, D. J. *Procter*, *Nat. Catal **2020**, 3, 163*-169; c) S. Donck, A. Baroudi, L. Fensterbank, J.-P. Goddard, C. Ollivier, *Adv. Synth. Catal.* **2013**, *355*, 1477–1482. For recent a review: d) Á. Péter, G. J. P. Perry, D. J. Procter, ***Adv.*** *Synth. Catal.* **2020**, *362*, 2135-2142.

[126] a) J. D. Nguyen, E. M. D'amato, M. R. Narayanam, C. R. J. Stephenson, *Nature Chem.* **2012**, *4*, 854-859; b) H. Kim, C.

the best of our knowledge, only one full study was published recently by the Yoshimi group under photooxidative conditions with aryl carboxylates.[128] Up to 150 mol % of biphenyl (BP)/1,4-dicyanonaphthalene (DCN) as photocatalytic mixture had to be used under UV irradiation to provide moderate yields (~50%) of aryl radical adducts. Of note also, at the occasion of a very recent study by Morofuji and Kano[129] dedicated to the photooxidation of alkylsilicates bearing the hexafluorocumyl alcohol dianion ligand (Martin's ligand), a single example of oxidation of the corresponding phenylsillicate gave 10% of Giese-type adduct from the phenyl radical. This underlines that the generation of aryl radicals under photooxidative conditions is highly challenging.

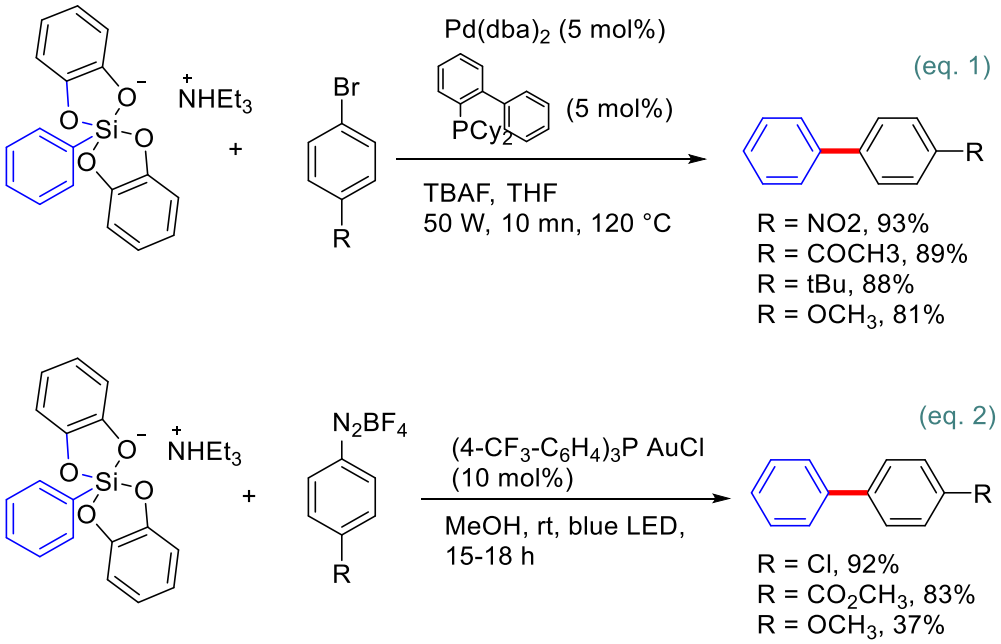

Scheme 93. Use of aryl silicates for sp^2-sp^2 cross-coupling reactions

Second, a new class of phenyl silicate derivatives could open new perspectives in terms of reactivity either in radical addition reactions or in dual catalysis. This study aimed at determining the influence of the substitution of the catechol ligands in their ability to promote the generation of aryl radicals. We therefore undertook the synthesis of various phenyl

---

Lee, *Angew. Chem. Int. Ed*. **51**, 12303–12306; c) E. H. Discekici, N. J. Treat, S. O. Poelma, K. M. Mattson, Z. M. Hudson, Y. D. Luo, C. J. Hawker, J. R. de Alaniz, *Chem. Commun.* **2015**, *51*, 11705−11708, d) I. Ghosh, B. König, *Angew. Chem. Int. Ed.* **2016**, *55*, 7676−7679; *Angew. Chem.* **2016**, *128*, 7806−7810; e) M. Majek, U. Faltermeier, B. Dick, R. Perez-Ruiz, Jacobi von Wangelin, A. *Chem. Eur. Joc.* **2015**, *21*, 15496−15501.

[127] L. Candish, M. Freitag, T. Gensch, F. Glorius, *Chem. Sci.* **2017**, *8*, 3618-3622.

[128] S. Kubosaki, H. Takeuchi, Y. Iwata, Y. Tanaka, K. Osaka, M. Yamawaki, T. Morita, Y. Yoshimi, *J. Org. Chem.* **2020**, *85*, 5362-5369.

[129] T. Morofuji, Y. Matsui, M. Ohno, G. Ikarashi and N. Kano, *Chem. – A Eur. J.*, 2021, **27**, 6713–6718.

silicates and studied their structural features and reactivity.

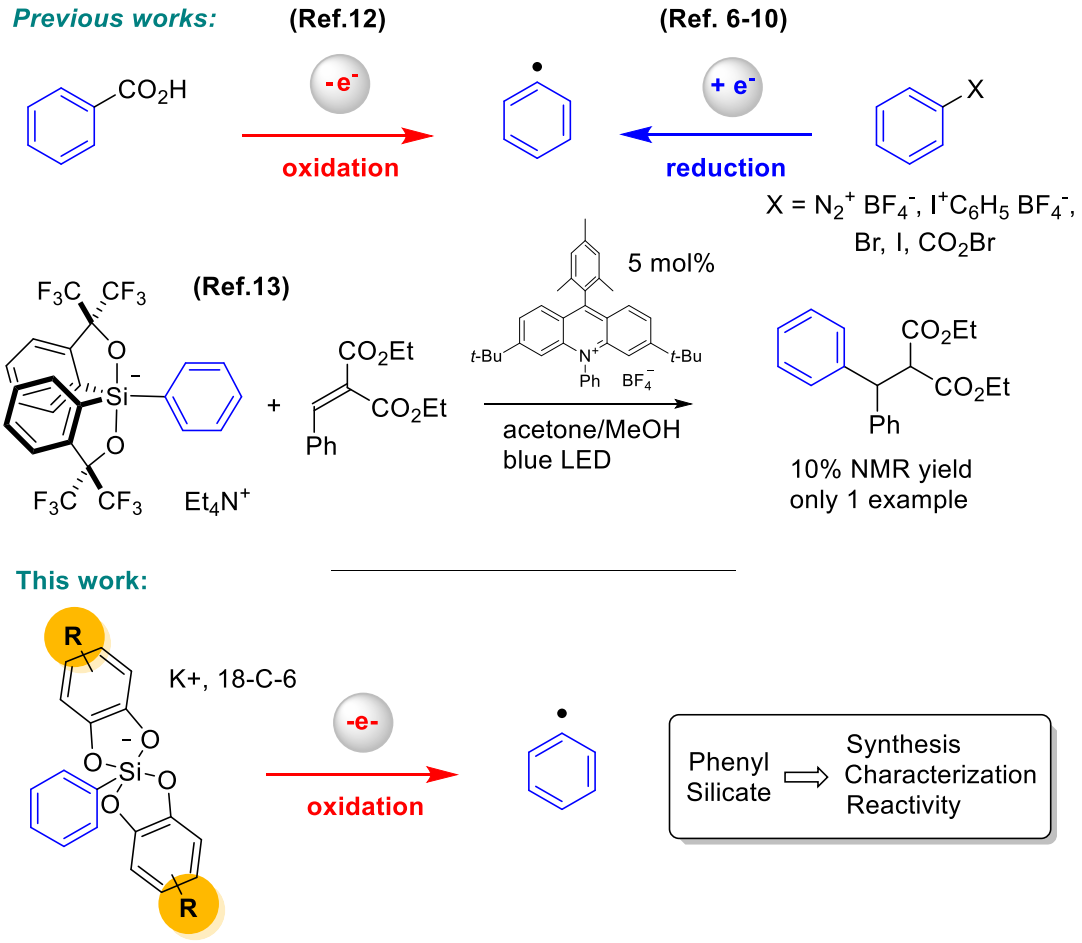

Scheme 94. Generation of aryl radicals through photocatalytic conditions

3.3. Results and Discussion

We first focused on the reactivity of the simplest term, the phenyl bis-catecholatosilicate **1a**. It was synthesized based on a previously reported protocol[130] using catechol (2 equiv), 18-C-6 (1 equiv), MeOK (1 equiv) and phenyltrimethoxysilane (1 equiv). Silicate **1a** was obtained in a satisfying 87% yield (reaction time: 2 h at room temperature, solvent of crystallization: acetone/Et_2O). Its half-wave oxidation potential in DMF was measured by cyclic voltammetry and the observed value ($E_{1/2}^{ox}$ = + 0.89 V vs. SCE[29a]) was compared with the reduction

[130] a) C. L. Frye, *J. Am. Chem. Soc.* **1964**, *86*, 3170-3171; b) G. Cerveau, C. Chuit, R. J. P. Corriu, L. Gerbier, C. Reye, J. L. Aubagnac, B. El Amrani, *Int. J. Mass. Spectron Ion Phys.* **1988**, *82*, 259-271; c) V. Corcé, C. Lévêque, C. Ollivier, L. Fensterbank, *Science of Synthesis: Photocatalysis in Organic Synthesis*, **2019**, 427.

potential of the photocatalyst $[Ir(dF(CF_3)ppy)_2(bpy)]PF_6$ (**3**) in its excited state (E^{red}(Ir(III)*/Ir(II) = + 1.32 V vs SCE[131]). These data suggested that silicate **1a** could be oxidized by this photocatalyst under irradiation. Nevertheless, all attempts to generate a phenyl radical with photocatalyst **3** and to trap it with allylsulfone **2** met limited success. Allylation product **4** was observed in only 5 % yield. This finding appeared puzzling since efficient phosphorescence quenching of **3** with **1a** was observed. Indeed, the quenching rate (*kq*) constant was determined by Stern-Volmer analysis and found to be *kq* = 5.7 x 10^8 mol^{-1} L s^{-1} (in comparison to *kq* = 7.9 x 10^9 mol^{-1} L s^{-1} for benzyl silicate[29a]). In order to check whether this low yield was due to the instability of **1a**, ^{29}Si NMR experiments were carried out before and after reaction with acceptor **2**. After 24 hours of blue LED irradiation (λ_{max} = 450 nm) in DMF-d7, only **1a** as silicon derivative could be detected in the mixture and no obvious degradation was also evidenced by ^{1}H NMR (**Figure 5**).

Additionally, when an equimolar mixture of **1a** and **3** was irradiated under blue LED in deuterated THF as solvent, the formation of C_6H_5D **5** could be observed by ^{1}H NMR (δ ^{1}H 7.29 ppm in THF-d8) and quantified by ^{2}H NMR (δ ^{2}H 7.35 ppm in THF-d8) to 21% NMR yield (see **Scheme 95** and the supporting information for more details).

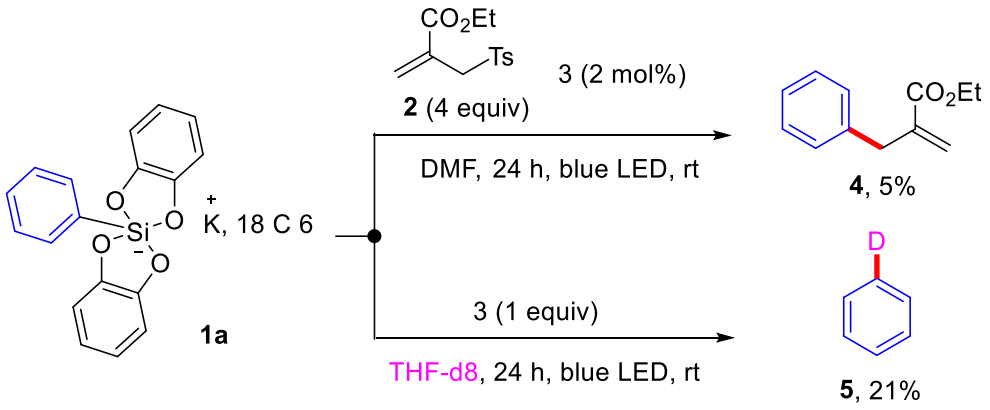

Scheme 95. Photooxidation of phenyl silicate **1a** and phenyl radical trapping

All together, these findings suggest an inefficient oxidation process of **1a**. Considering the favorable redox potentials and the efficient luminescence quenching (see above), this low reactivity of **1a** aroused our curiosity and led us to study the role of substituents on the catechol moiety and their potential effect on the reactivity of the corresponding phenyl silicates.

[131] D. Hanss, J. C. Freys, G. Bernardinelli, O. S. Wenger, *Eur. J. Inorg. Chem.* **2009**, *2009*, 4850-4859.

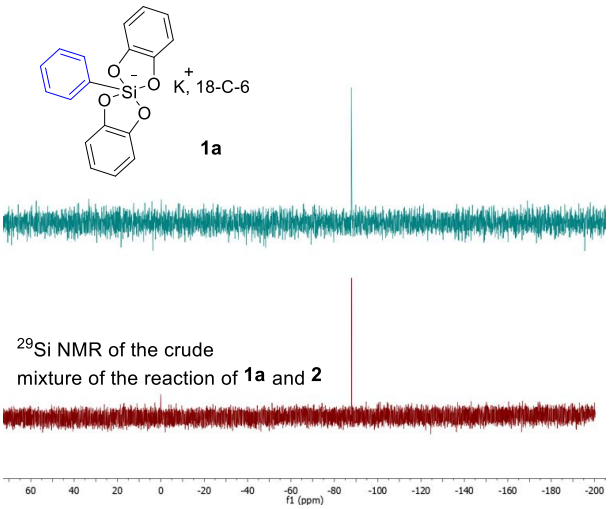

Figure 5. ^{29}Si NMR monitoring of the photocatalytic reaction of **1a** with **2** in DMF-d7.

1.10.3 The preparation of silicate

We first tested the putative substitution effect exerted by the catechols on the highly reactive cyclohexyl bis-catecholatosilicate substrate. Notably, we wished to check that the formation of the cyclohexyl radical was still possible. Based on the previously described procedure using cyclohexyl-trimethoxysilane, MeOK, 18-C-6 and catechols with diverse substitution patterns (electron donating or withdrawing groups), cyclohexylsilicates **6a-6d** were obtained after crystallization in acetone/Et_2O (**Scheme 96).**[29a, 132]

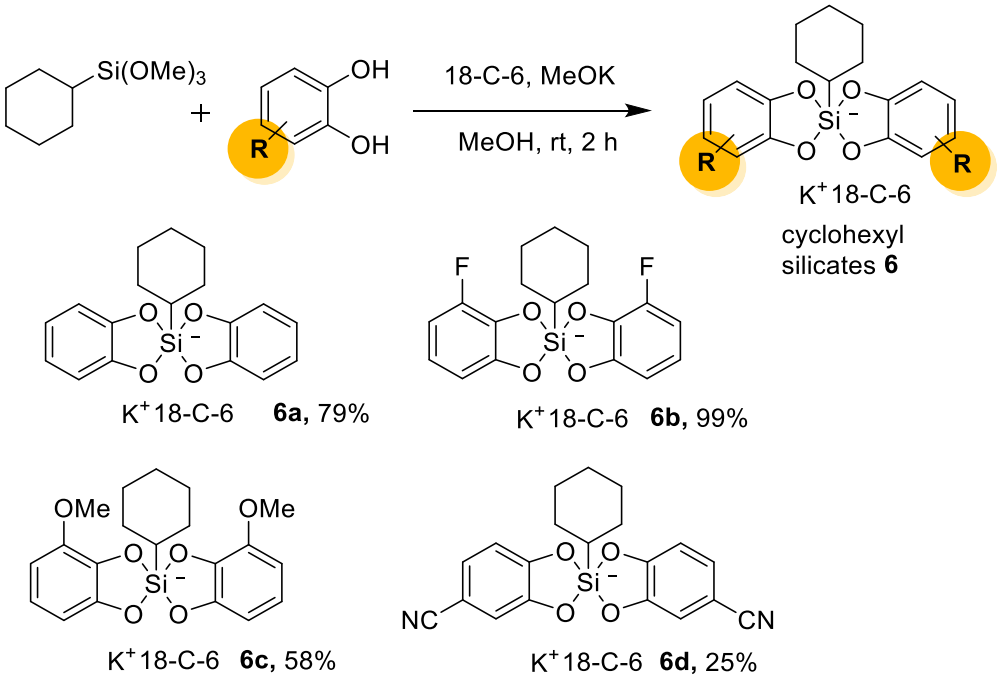

[132] a) C. L. Frye, *J. Am. Chem. Soc.* **1964**, *86*, 3170-3171; b) K. Lin, C. B. Kelly, M. Jouffroy, G. A. Molander, *Org. Synth.* **2017**, *94*, 16-33.

Scheme 96. Synthesis of cyclohexyl silicates **6** bearing differently substituted catechol moieties

Upon treatment with photocatalyst **3** and allylsulfone **2** under blue LED irradiation, silicates **6b** ($E_{1/2}^{ox}$ = + 0.91 V *vs* SCE (All given potentials are referenced to SCE.)) and **6d** ($E_{1/2}^{ox}$ = + 1.01 V), bearing electron withdrawing groups, afforded the corresponding radical allylation product **7**, but in slightly lower yields (77% and 60% yields respectively) than plain silicate **6a** ($E_{1/2}^{ox}$ = + 0.69 V, 88% of **7**) (**Table 1**). Interestingly, an electron donating group such as a methoxy on the catechols (**6c**) drastically decreased the yield of this reaction and most of the starting material was recovered. In view of the lower oxidation potential of **6c** ($E_{1/2}^{ox}$ = + 0.63 V) this result appears contradictory but was corroborated by DFT calculations (*vide infra*).

Table 1. Generation of cyclohexyl radical from cyclohexyl silicates **6** probed by allylation reaction

Cyclohexyl silicate **6**	Yield of **7** (in %)[a]
6a	88
6b	77
6c	14
6d	60

[a] ^{1}H NMR yield of 7 using 1,3,5 trimethoxybenzene as NMR standard

Encouraged by these results showing that the catechol substitution can modulate the reactivity of the corresponding silicates but does not prevent the photooxidation process, we prepared a library of phenyl silicates with mono- and polysubstituted catechols.

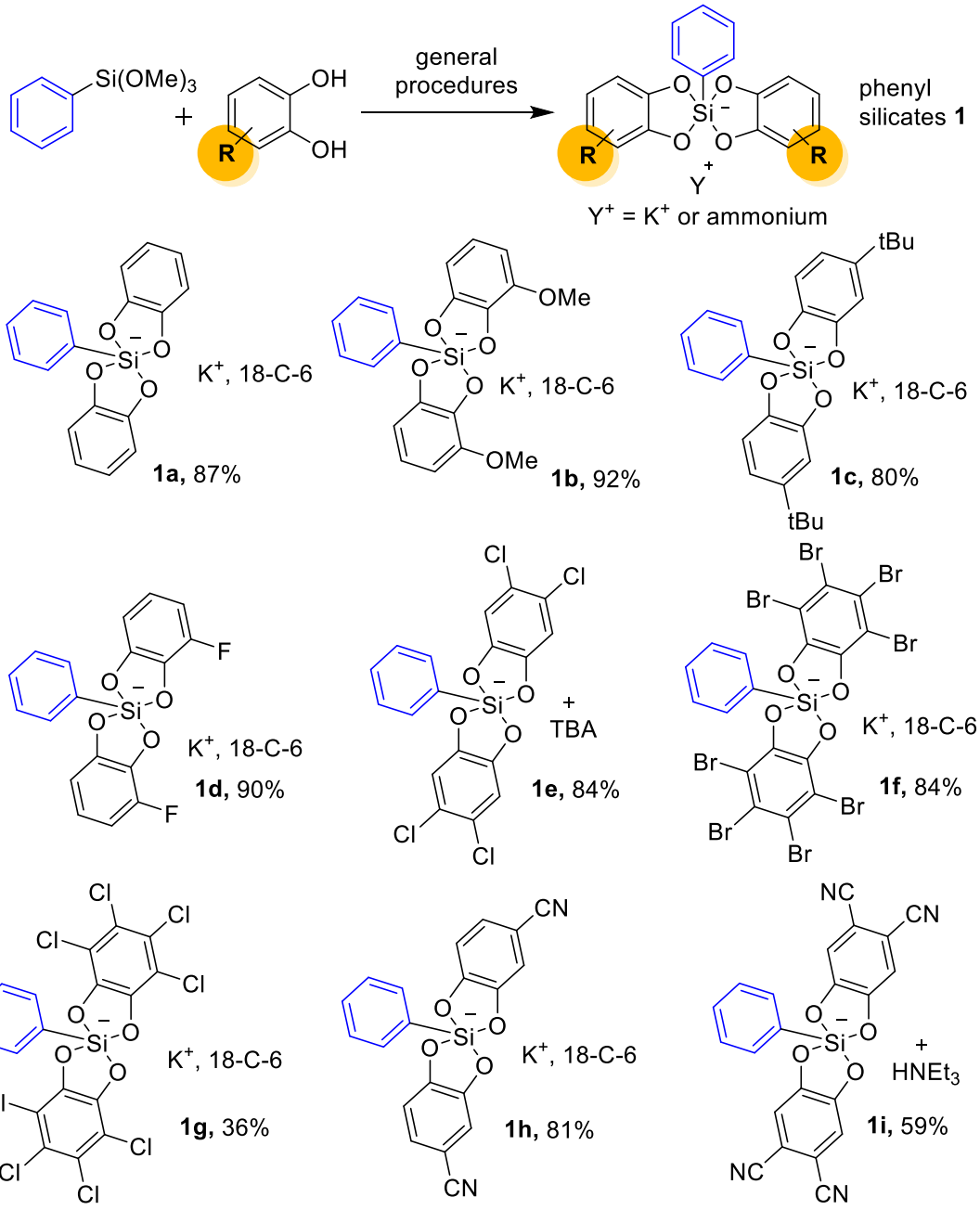

Scheme 97. Preparation of phenyl silicates **1** bearing substituted catechols

Using the same procedure as above with the appropriate catechol, most of the silicates **1** were efficiently prepared (yield > 80%) in crystalline form suitable for X-ray diffraction analysis (**Scheme 96**). Thus, silicates silicates **1b**, **1d** and **1h** bearing electron donating (MeO) and electron withdrawing (F, CN) groups respectively were analyzed by XRD (**Figure 6**).[133]

All three crystal structures exhibit silicates in which the silicon center adopts a square pyramidal geometry, quite similar to that of **1a**. Indeed, the electronic features of the catechol

[133] Deposition Numbers 2009048 (for **1b**), 2009049 (for **150**), and 2009050 (for **146**) contain the supplementary crystallographic data for this paper. These data are provided free of charge by the joint Cambridge Crystallographic Data Centre and Fachinformationszentrum Karlsruhe Access Structures service www.ccdc.cam.ac.uk/structures.

do not seem to have much impact on the environment of the silicon atom. **1b** and **1h** show a marked interaction between silicate and potassium with K-O distances ranging from 2.7 to 3.0 Å, similar to previously published structures of potassium hypervalent silicates.[29a] Only **1d** features weaker interactions. While the asymmetric units of **1b** and **1h** contain only one discrete silicate, silicate **1d** shows a statistical disorder of the fluorine atoms that suggests the presence of *cis* and *trans* isomers but in undetermined proportions (see SI for more details).

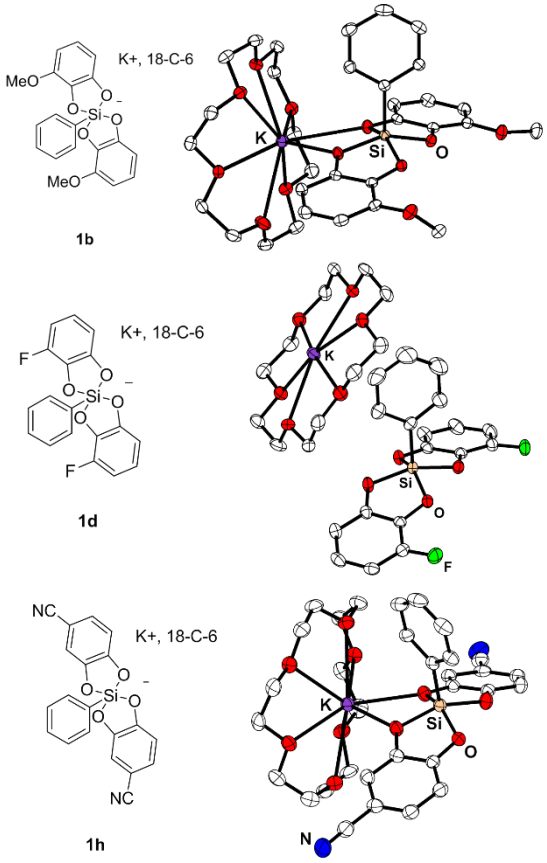

Figure 6. XRD analyses of silicates **1b**, **1d** and **1h**. Only *cis* isomer of **1d** depicted and hydrogens omitted for clarity. This work was done by Dr. Etienne Levernier.

The presence of two isomers was also confirmed by ^{13}C NMR. All resonances of the non-symmetrical catechol moieties in ^{13}C NMR were doubled with identical integration for both species in the case of **1d**, but also for the other non-symmetrical phenylsilicates **1b**, **1c**, **1h**. It has to be mentioned that this type of 1:1 mixture of two isomers was also observed in the cyclohexyl series (silicates **6b-d**).

Intrigued by this finding, we wondered if an equilibrium exists between both *cis* and *trans* isomers in solution. To answer this question, ^{13}C NMR of **1h** at various temperatures was conducted (in acetone-d6 at low temperature (below 273 K) and DMSO-d6 at higher

temperature (from 303 K), **Figure 7**).[134]

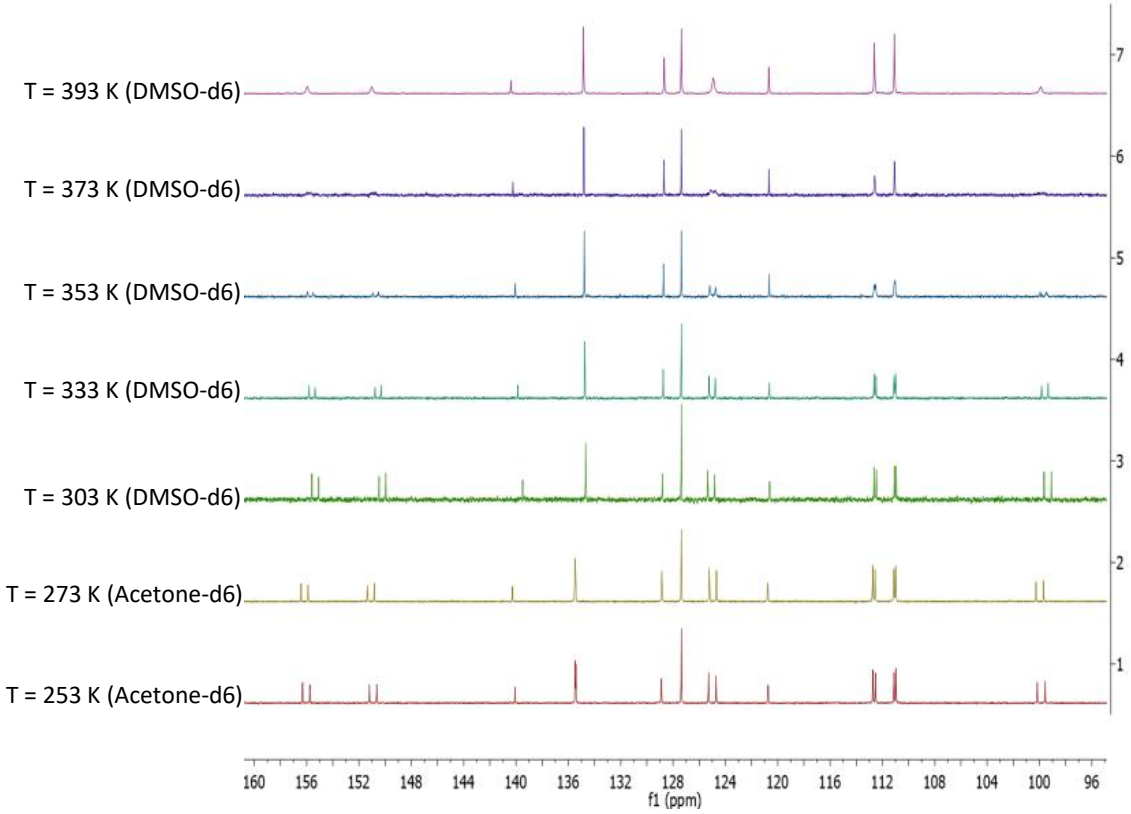

Figure 7. ^{13}C NMR of silicate **1h** at various temperatures

A coalescence of the peaks was observed above 333 K probably due to Berry pseudo-rotation [135]suggesting that an equilibrium exists between the two isomers. DFT calculations also indicated that the energetic gap between the *cis* and *trans* form for **1b** is 3.3 kcal/mol in favor of the *cis* form. For **1h**, the *trans* form is slightly favored by 0.6 kcal/mol.

After studying the structural features of these new silicon derivatives, we examined other key properties. First, UV-vis absorption spectra were recorded. All silicates **1** exhibited a unique absorption band spanning from 276 nm for **1d** to 303 nm for **1g**. Importantly, whatever the substitution pattern, no noticeable absorption was observed in the wavelength range of blue LED, previously used for the photooxidation of alkyl silicates (from 400 to 520 nm) (see **Figure 8** and the supporting information for more details and UV data).

[134] R. J. Abraham, D. S. Ribeiro, *J. Chem. Soc. Perkin. Trans.* **2001**, *2*, 302-307.

[135] a) A. R. Bassindale, M. Sohail, P. G. Taylor, A. A. Korlyukov, D. E. Arkhipov, *Chem. Commun.* **2010**, *46*, 3274-3276, b) D. Kost, I. Kalikhman, *Acc. Chem. Res.* **2009**, *42*, 303-314.

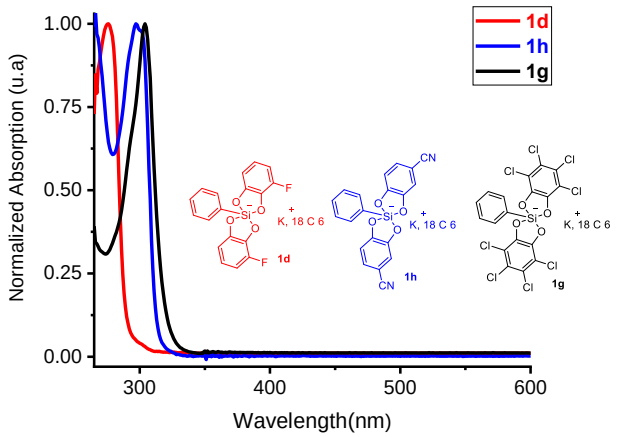

Figure 8. Absorption spectra of silicates **1d**, **1h** and **1g.** This work was done by Dr. Etienne Levernier.

Second, the oxidation potentials of silicates **1a-i** were measured in DMF as displayed in **Table 2.**

Table 2. Half-wave oxidation potentials of silicates **1a-i**

Silicate 1	$E_{ox}^{1/2}$ (vs SCE in DMF)	Silicate 1	$E_{ox}^{1/2}$ (vs SCE in DMF)
1a	+ 0.89 V	**1f**	+ 1.46 V
1b	+ 0.81 V	**1g**	+ 1.37 V
1c	+ 1.09 V	**1h**	+ 1.33 V
1d	+ 1.05 V	**1i**	+1.62 V
1e	+ 1.13 V		

Interestingly, catechol modifications resulted in important variations of the oxidation potentials, from $E_{1/2}^{ox}$ = + 0.81 V for **1b** to $E_{1/2}^{ox}$ = + 1.62 V for **1i** with $E_{1/2}^{ox}$ = + 0.89 V for the unsubstituted phenylsilicate **1a**. Thus, a donating group on the catechols as for **1b** was found to logically decrease the oxidation potential while electron withdrawing groups significantly increased the values above + 1.0 V ($E_{1/2}^{ox}$ = + 1.05 V for **1d**).[136] Higher oxidation potentials could even be reached by using the *per*-bromocatechol or by adding two cyano groups ($E_{1/2}^{ox}$ (**1f**) = + 1.46 V and $E_{1/2}^{ox}$ (**1i**) = + 1.62 V). Even if the oxidation of **1f** and **1i** by the photoactivated **3** [Ir(dF(CF$_3$)ppy)$_2$-(bpy)]PF$_6$ (E^{red}(Ir(III)*/Ir(II) = + 1.32 V) appeared difficult, all the other silicates **1** could potentially lead to the generation of the phenyl radical. Thus, we proceeded this study with the photocatalytic allylation reaction from silicates **1a-i** with allylsulfone **2** in the presence of 2 mol% of **3**. Results are summarized in **Table 3**.

Although a yield < 10% was obtained from silicates **1a-e** and **1i**, silicate **1h** bearing a cyano

[136] A. G. Larsen, A. H. Holm, M. Roberson, K. Daasbjerg, *J. Am. Chem. Soc.* **2001**, *123*, 1723-1729.

group on the catechol afforded **4** in 35% yield. *Per*-brominated and *per*-chlorinated catechols **1f** and **1g** also provided the desired product **4** in slightly better yields than silicate **1a** (15% and 23% respectively). Nevertheless, these yields are still lower than the one obtained with silicate **1h**. The higher oxidation potentials of **1f** and **1g** in comparison to **1h** might explain this result. Also, as previously observed in **Table 1** with cyclohexyl silicates, the methoxy substitution was found to be detrimental resulting in a decreased yield. Thus, the modification of the catechol moiety proved to modulate the reactivity of the phenyl silicates **1** in the photocatalytic allylation type reaction.

Table 3. Photocatalytic allylation reaction of phenylsilicates**1.** This work was done by Dr. Etienne Levernier.

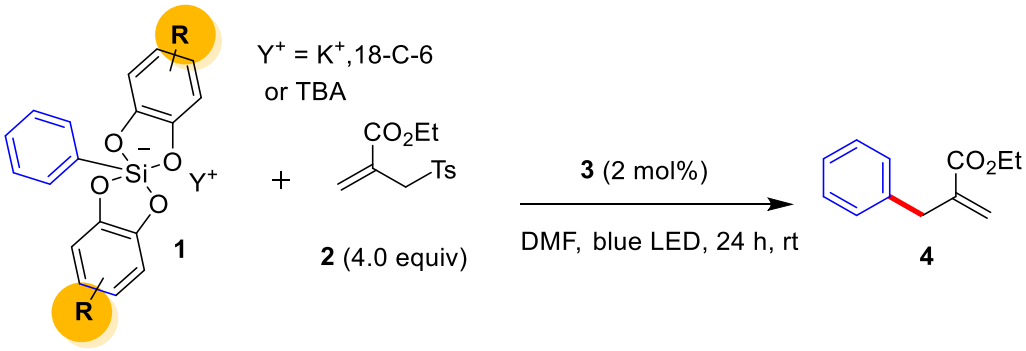

Silicate 1	Yield of 4 (in %)[1]	Silicate 1	Yield of 4 (in %)[1]
1a	5%	**1f**	15%
1b	9%	**1g**	23%
1c	8%	**1h**	35%
1d	6%	**1i**	7%
1e	6%		

[1] ^{1}H NMR yield of **4** using 1,3,5 trimethoxybenzene as NMR standard

Encouraged by these results, we optimized the reaction of the most promising silicate **150** with acceptor **2** (**Table 4**). The influence of different counterions (ammoniums and potassium with and without 18-C-6, entries **6**, **11** and **12**) was studied but no significant improvement was observed. The temperature (room temperature or 100°C, entries **5** and **6**) did not affect the reaction efficiency. Switching to some organic photocatalysts resulted in a decreased yield (entries **1**, **2** and **3**).[137, 138] Even the very oxidizing Fukuzumi's acridinium ($E_{red}(PC^*/PC^{\bullet-})$ = +

[137] C. Lévêque, L. Chenneberg, V. Corcé, C. Ollivier, L. Fensterbank, *Chem. Commun.* **2016**, *52*, 9877-9880.

2.06 V vs SCE[139]) did not afford **4** in a better yield. These results are consistent with what was previously observed with alkylsilicates.[140] Different solvents (DMF, DMSO, MeCN, EtOH), reaction times and concentrations were also screened but, despite all our efforts, the yield remained modest. Notably, prolonged reaction times did not result in significant improvements (entry **6** *vs* entries **9** and **10**). Hence, the best conditions were found to be in DMSO with **3** at room temperature for 24 h (40%, entry **4**). Some control experiments were also carried out. The reaction in the dark or photocatalyst free conditions did not afford any product (entries **7** and **8**). Therefore, the presence of a photocatalyst under irradiation is mandatory to generate the phenyl radical.

Table 4. Optimization of the allylation reaction. This work was done by Dr. Etienne Levernier.

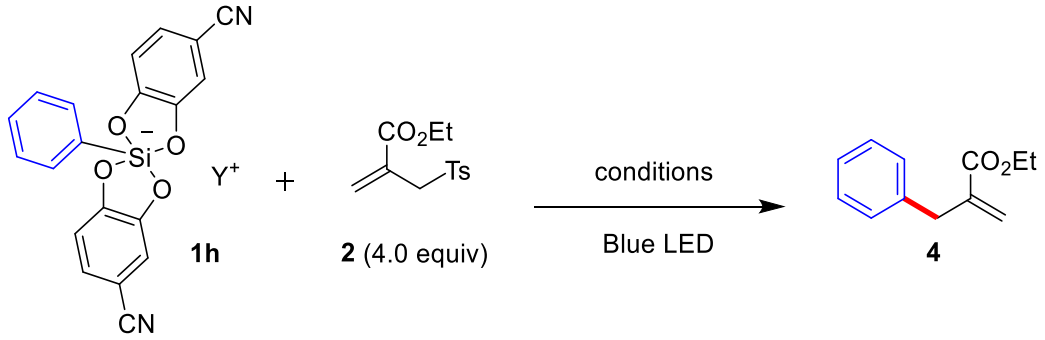

Entry	Solvent	Temperature	Photocatalyst	Time	Y^+	Yield of 4[1]
1	DMF	rt	Fukuzumi's acridinium	24 h	K^+/18-C-6	6%
2	DMF	rt	Pyrylium salt[2]	24 h	K^+/18-C-6	7%
3	DMF	rt	4CzIPN	24 h	K^+/18-C-6	7%
4	DMSO	rt	3	24 h	K^+/18-C-6	40%
5	DMF	100°C	3	24 h	K^+/18-C-6	38%
6	DMF	rt	3	24 h	K^+/18-C-6	35%
7	DMF	rt	-	24 h	K^+/18-C-6	0%
8	DMF	rt	3	24 h	K^+/18-C-6	0%[3]
9	DMF	rt	3	68 h	K^+/18-C-6	35%
10	DMF	rt	3	68 h	K^+/18-C-6	41%[4]
11	DMF	rt	3	24 h	K^+/18-C-6	30%

[138] J. Zhou, P.S. Mariano, *Photochem. Photobiol. Sci.* **2008**, *7*, 3936404.

[139] K. Ohkubo, K. Mizushima, R. Iwata, K. Souma, N. Suzuki, S. Fukuzumi, *Chem. Commun.* **2010**, *46*, 601-603.

[140] L. Chenneberg, C. Lévêque, V. Corcé, A. Baralle, J. P. Goddard, C. Ollivier, L. Fensterbank, *Synlett* **2016**, *27*, 731-735.

12	DMF	rt	3	24 h	Et_3NH^+	35%
13	CH_3CN	rt	3	24 h	TBA^+	0%
14	EtOH	rt	3	24 h	TBA^+	20%
15	DMSO	rt	3	24 h	TBA^+	35%
16	DMF	rt	3[5]	24 h	K^+/18-C-6	40%

[1] [Silicate] = 0.1 mol.L^{-1}, **3** (2 mol%), ^{1}H NMR yield of **4** using 1,3,5 trimethoxybenzene as NMR standard; [2] 2,4,6-tri(p-tolyl)pyrylium tetrafluoroborate salt; 3 reaction in the dark; 4 [Silicate] = 0.2 mol.L-1; 5 3 (10 mol%).

Inspired by the pioneering work of Nishigaichi showing that silicates bearing catechol or 2,3-hydroxynaphthalene ligands can be photoactivated by direct irradiation,[141] the photo allylation reaction of silicate **1h** was also tested at 300 nm with and without **3** but limited success was met since only 10% and 6% of product **2** were isolated respectively. So, even if this silicate absorbs UV-B light, the use of **3** as photocatalyst under blue LED irradiation remains more efficient. This was further corroborated by the fact that the phosphorescence quenching of **3** with silicate **1h** was also observed and thanks to a Stern-Volmer plot, a quenching constant of 1.31 x 10^8 mol^{-1} L s^{-1} was obtained (compared to 5.7 x 10^8 mol^{-1} L s^{-1} for silicate **1a**). Thus, silicate **1h** does not quench the iridium photocatalyst more efficiently than silicate **1a** (**Figure 5**).

D-abstraction from deuterated THF-d8 was also probed and led to the formation of C_6H_5D in 51% yield (as quantified by ^{2}H NMR) from **1h**, in comparison to 21% yield obtained with unsubstituted silicate **1a** (see above) confirming the effect of the catecholate substitution.[142]

[141] a) D. Matsuoka, Y. Nishigaichi, *Chem. Lett.* **2015**, *44*, 163-165; b) Y. Nishigaichi, A. Suzuki, T. Saito, A. Takuwa, *Tetrahedron Lett.* **2005**, *46*, 5149-5151; c) Y. Nishigaichi, A. Suzuki, A. Takuwa, *Tetrahedron Lett.* **2007**, *48*, 211-214.

[142] T. A. Halgren, J. L. Firkins, T. A. Fujimoto, H. H. Suzukawa, J. D. Roberts, *Proc. Natl. Acad. SCI. USA.* **1971**, *68*, 3216-3218.

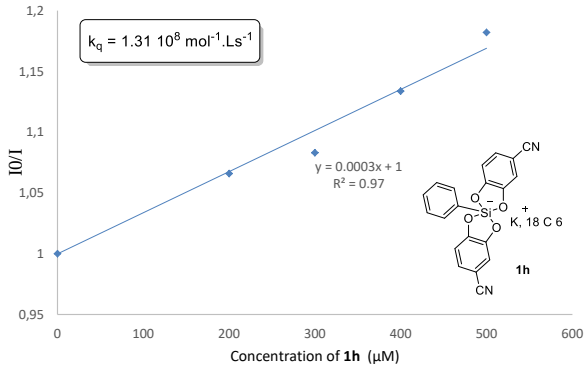

Figure 9. Stern-Volmer plot - quench of silicate **150** and **3.** This work was done by Dr. Etienne Levernier.

To better understand the difference of reactivity between alkylsilicates and phenyl silicates, we resorted to computational studies. The fragmentation of the intermediate hypercoordinated radical resulting from the oxidation by the photocatalyst was assessed for both types of silicates. Energy barriers for the cleavage of the silicon-carbon bond and the free energy of the reaction are summarized in **Table 5**, in the presence or absence of DMF as coordinating ligand on the silicon center. In all cases, it was found that the presence of DMF reduces the barrier of radical expulsion. With DMF, the generation of a primary alkyl radical is rather easy with an energy barrier of 17.45 kcal/mol, which explains why various transformations have been observed with this type of substrates.[29, 31] For cyclohexyl silicates, we observe a consistent and slightly lower barrier of 13.23 kcal/mol to expel the cyclohexyl radical from **I•Cy**. Adding cyano groups helps to reduce this barrier (**I•Cy•CN➔II•Cy•CN**) to 10.51 kcal/mol. Interestingly, methoxy groups on **I•Cy•OMe** resulted in a much higher calculated barrier (37.73 kcal/mol) that is corroborated by the poor reactivity of **6c** in an allylation reaction (see Table 1). Calculations also featured a distinct scenario for this silicate. While in the other cases, upon departure of the radical, the DMF strongly interacts with the silicon center of the generated bis-catecholato spirosilane to give a square pyramid hypercoordinated silicon species, **II•Cy•OMe** fragments differently and the resulting methoxy substituted bis-catecholato spirosilane adopts a tetrahedral shape with no coordination of the DMF. The electron donation of the methoxy groups presumably disfavors the formation of the hypercoordinated species.

Table 5. Barrier and Gibbs free energy of the reaction (in kcal/mol) corresponding to radical formation for various oxidized silicates, as calculated at the wB97M-D3BJ/def2-SV(P) level. Values in parentheses correspond to calculations done without DMF. This work was done by

Dr. Khaoula Jaouadi.

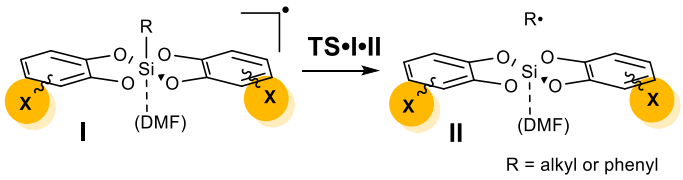

Silicate	Barrier (kcal/mol)	Free energy of reaction (kcal/mol)
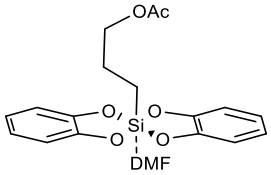	17.45 (28.88)	1.86 (13.78)
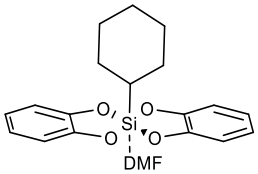 **I•Cy**	13.23	7.77
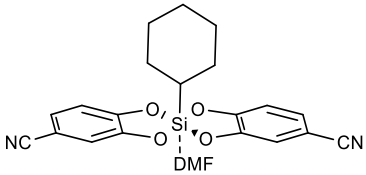 **I•Cy•CN**	10.51	2.03
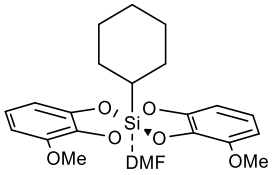 **I•Cy•OMe**	37.73	17.45
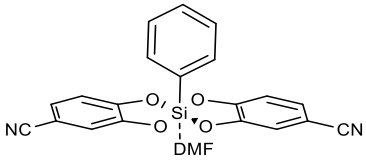 **I•Ph•CN**	18.99 (34.89)	19.05 (25.57)
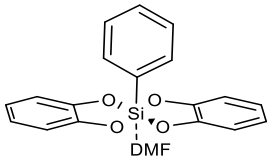 **I•Ph**	27.46 (36.49)	22.61 (25.98)

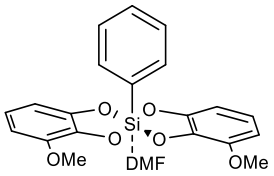

I•Ph•OMe

32.53	29.16
(43.00)	(28.03)

Importantly, the calculations also supported that phenylsilicates **1** are less prone to expel a radical upon oxidation. Without any substituent on the catechol moiety, the energy barrier was calculated to be 27.46 kcal/mol, which is 10 kcal/mol more than for the extrusion of a primary radical and 14 kcal/mol more than for the cyclohexyl one, and the generated intermediate radical is rather unstable (with a Gibbs free energy of 22 kcal/mol).[143] When the C-Si bond starts to elongate to reach **II•Ph**, the silicon species maintains a square-planar pyramid geometry around the silicon center through an interaction with one molecule of solvent (DMF) and with the phenyl radical being π-stacked on top of one of the catechol moieties, which brings stablization. Thus, for **II•Ph** and analogs the expelled phenyl radical interacts through π-π interactions with one of the catechol moieties and interaction distances between centroids are respectively 3.21 Å, 3.23 Å and 3.12 Å for **II•Ph**, **II•Ph•CN** and **II•Ph•OMe** (Figures 6 and 7). This marks a sharp contrast with the expelled alkyl radicals that do not interact at all with the catechol ligands and are less bound to the silicon entity. Finally, the situation proved to be different with the experimentally more reactive silicate **1h** since the energy barrier to generate the radical was about 19 kcal/mol (**I•Ph•CN**), thus far more accessible. Nevertheless, the radical is still rather unstable with a highly endergonic process of 19 kcal/mol (**I•Ph•CN➔II•Ph•CN**). Finally, the high barrier for **I•Ph•OMe** (>40 kcal/mol) is consistent with what was found for **I•Cy•OMe**. These results prompted us to investigate the electronic structure of these radicals more in detail.

[143] These high barrier values are reminiscent of the values found in ref. 41.

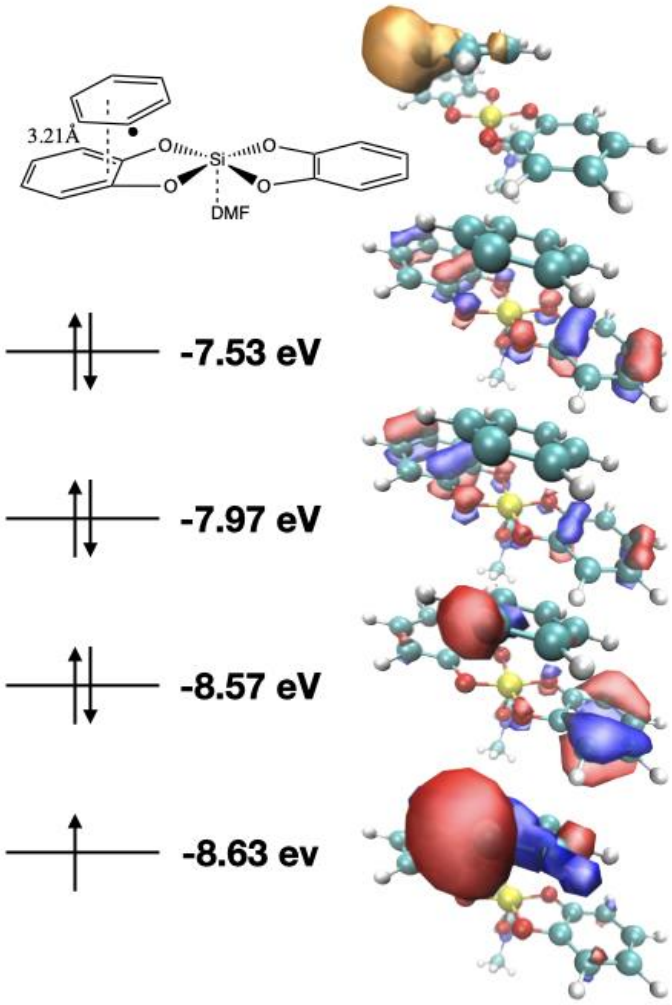

Figure 10. Spin density and frontier orbitals diagram for the oxidized aryl silicate **II•Ph.** This work was done by Dr. Khaoula Jaouadi.

To our surprise, these radicals are not classical and do not follow the Aufbau principle. Indeed, for most of the radicals, the orbital encompassing the unpaired electron corresponds to the highest occupied molecular orbital (HOMO). Here, the orbital better suited to describe the calculated spin density is not the HOMO but a lower lying molecular orbital. This phenomenon is known as SOMO-HOMO inversion and has been previously described for various systems. Their common feature is to combine a stable radical moiety with a donor unit, presenting numerous π-conjugated orbitals.[144] Our system constitutes an original example since it is originating from a hypercoordinated species.

[144]In metalloporphyrins, a) B. L. Westcott; N. E. Gruhn; L. J. Michelsen, D. L. Lichtenberger *J. Am. Chem. Soc.* **2000**, *122*, 8083-8084; In metalladithiolenes, b) T. Kusamoto, S. Kume, H. Nishihara, *J. Am. Chem. Soc.* **2008**, *130*, 13844–13845; In distonic radical anions, c) G. Gryn'ova, D. L. Marshall, S. J. Blanksby, M. L. Coote, *Nature Chem.* **2013**, *5*, 474–481, d) G. Gryn'ova, M. L. Coote, *J. Am. Chem. Soc.* **2013**, *135*, 15392–15403; in DNA base pairs, e) A. Kumar, M. D. Sevilla, *J. Phys. Chem. B* **2017**, *122*, 98–105.

The frontier orbitals, as well as the spin density, are depicted in **Figures 6** and **7** for radicals **II•Ph** and **II•Ph•CN** originating from **1a** and **1h**. It can be observed that, in the case of the radical species **II•Ph•CN**, the SOMO is lower in energy (-9.10 eV) than for the non-substituted catechol radical species (-8.63 eV). Overall, these findings could rationalize why the CN substituted silicate **1h** behaves differently from the unsubstituted species **1a**. First, the barrier for radical extrusion is weaker (27.46 kcal/mol for **I•Ph** *vs* 19 kcal/mol for **I•Ph•CN**) allowing an easier generation of the phenyl radical. In the case of **II•Ph•CN,** the extra stability of the radical (-9.10 eV vs. -8.63 eV) would result in an optimized radical reactivity with presumably less side reactions.

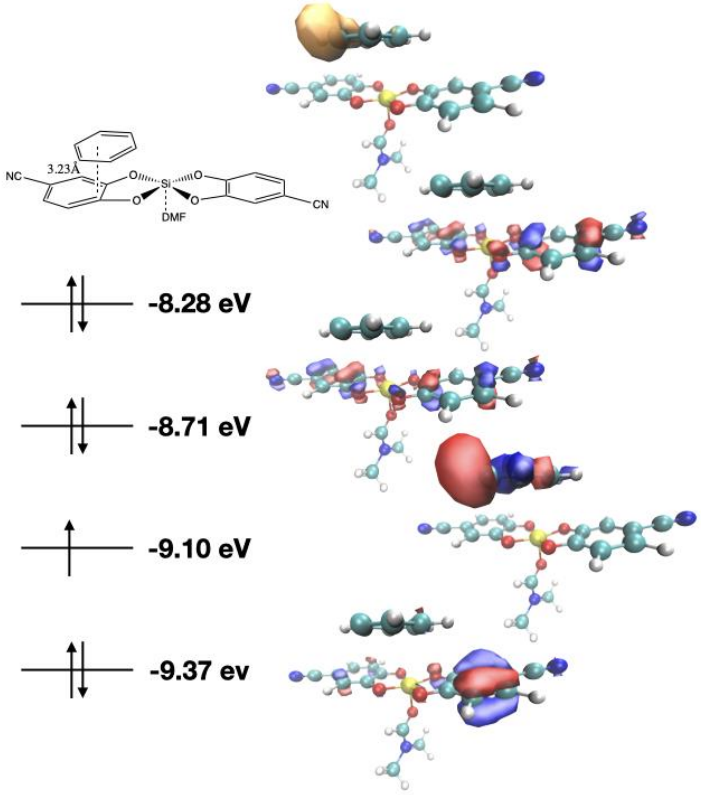

Figure 11. Spin density and frontier orbitals diagram for the oxidized phenylsilicate **II•Ph•CN.** This work was done by Dr. Khaoula Jaouadi.

3.4. Conclusions

In this study, we have synthesized and fully characterized by NMR, UV-vis absorption, X-ray diffraction and cyclic voltammetry a series of phenyl bis-catecholatosilicate derivatives 1 featuring electronic modulation on the catechol ligand. While they share a lot of common features with their alkylsilicate congeners, a notable difference with these compounds resides

in their higher oxidation potentials that generally lay above 1.0 V vs SCE, except for the unsubstituted phenylsilicate **1a** or the methoxy substituted one **1b**, and bode for a less favorable oxidation. The study of their photooxidation gave average results from a synthetic point of view but revealed for the first time an important effect of the catechol substitution. Counter-intuitively, phenyl silicates with the most donor substituents on catechol, and therefore with the lowest oxidation potentials, did not give the best results. It is the 4-cyanocatecholato ligand (silicate **1h**) that provided the best results and led to about 40% of allylation of the phenyl radical. Although modest, these yields should be understood in a context where the generation of aryl radicals by oxidative photoredox catalysis is hardly described. DFT calculations have allowed to rationalize the different observations and have highlighted an intriguing SOMO-HOMO inversion that has never been described for hypervalent species. These results also emphasize that silicates should be considered as first-rate precursors to challenging radicals

3.5. Supporting information

I. General informations

Unless otherwise noted, reactions were carried out under an argon atmosphere in oven-dried glassware. Methanol was distillated over CaH_2 and DMF was dried on molecular sieves with a *PureSolv solvent* purification system from Innovative Technology. Catechol was purchased from commercial source and purified by crystallization from chloroform. Reagents and chemicals were purchased from commercial sources and used as received. Infrared (IR) spectra were recorded on a Bruker Tensor 27 (ATR diamond) spectrophotometer. Melting points were determined on a melting point apparatus SMP3 (Stuart scientific). Electrochemical measurements were carried out an Origaflex (Origalys) electrochemical workstation. Absorption spectra of molecules were recorded at 25°C on a Cary 300 UV/Vis spectrophotometer (Agilent Technologies, Santa Clara, CA), equipped with a Peltier thermostated cell holder (t2x2 Sport/Cary300, Quantum Northwest, Liberty Lake, WA). The samples were placed in 2 mL quartz cuvettes (1 cm × 1 cm light path; Hellma Optics, Jena, Germany). Emission intensities were recorded on a Jasco FP-6200 spectrofluorometer. ^{1}H, ^{13}C and ^{19}F NMR spectra were recorded at room temperature at 400, 100 and 376 MHz respectively, on **400 MHz** Bruker AVANCE I spectrometer and at 300, 75 and 282 MHz respectively, on **300 MHz** Bruker AVANCE II spectrometer. ^{29}Si NMR spectra were recorded at room temperature at **79 MHz** on **400 MHz** Bruker AVANCE I spectrometer. Chemical shifts (δ) are reported in ppm and coupling constants (J) are given in Hertz (Hz). ^{2}H spectra were recorded at 27 °C at 600 and 92,1 MHz, respectively, on a Bruker Avance III 600 MHz spectrometer equipped with a 5 mm inverse probe head (^{1}H / ^{19}F, ^{31}P, ^{13}C). The ^{1}H NMR spectra were recorded using a pulse sequence of proton (zg30) with a spectral width of 9615 Hz, an acquisition time of 3,4 s and a number of scans of 8. The ^{2}H NMR spectra were recorded using a pulse sequence zg2h with a spectral width of 1660 Hz, an acquisition time of 4,9 s and a number of scans between 8 and 16. The spectra were analyzed with MestreNova. Abbreviations used for peak multiplicity are: s (singlet); bs (broad singlet); d (doublet); t (triplet); q (quartet); quint (quintet); sept (septet); m (multiplet) etc. Thin layer chromatographies (TLC) were performed on Merck silica gel 60 F 254 and revealed with a UV lamp (λ = 254 nm) and $KMnO_4$ staining. Flash Column Chromatographies were conducted on *Silica gel 60 M, 0.04–0.063* mm, from Macherey Nagel. High resolution mass spectrometries were performed on a microTOF (ESI). All the solvents used in flash

chromatography (toluene, petroleum ether, pentane and Et_2O) were distillated.

II. General procedures

a) Synthesis of the silicates

a1. General procedure A1 for silicates synthesis

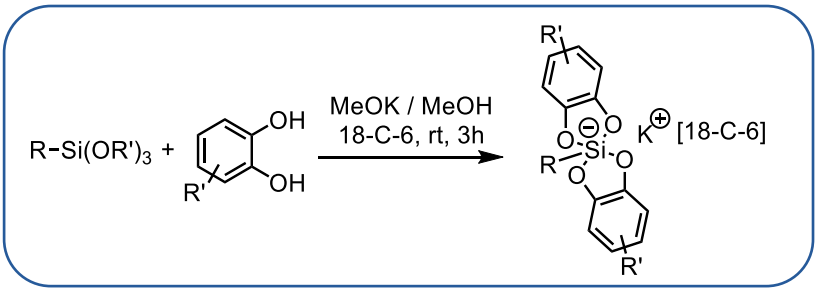

To a stirred solution of appropriate catechol (2 equiv) in dry methanol (0.1 or 0.13 M) was added 18-crown-6 [18-C-6] (1 equiv). After dissolution of the crown ether, the trialkoxyorganosilane (1 equiv) was added, followed by a solution of potassium methoxide in methanol (1 equiv). The reaction mixture was stirred for 3 hours and the solvent was removed under reduced pressure. The residue was dissolved in a minimum volume of acetone and diethyl ether was added until a cloudy solution was obtained (scrapping on the edge of the flask could be done to induce crystallization). The flask was placed at –20°C overnight. The crystals were collected by filtration, washed with diethyl ether and dried under vacuum to afford [18-C-6] silicate.

a2. General procedure A2 for silicates synthesis

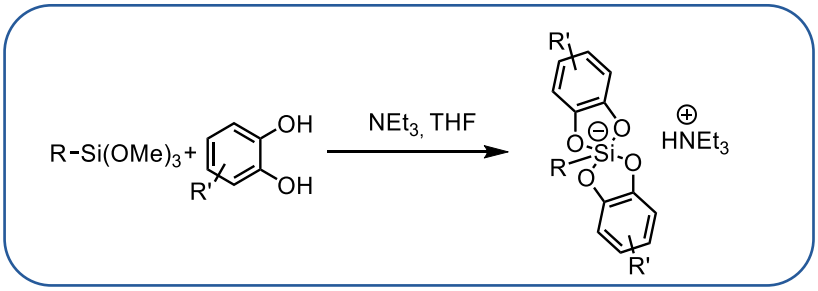

To a stirred solution of appropriate catechol (2 equiv) in dry THF (0.1 M) was added triethylamine (4.7 equiv). Then the corresponding trimethoxysilane (1 equiv) was added dropwise. The reaction mixture was stirred for 20 hours under reflux and the solvent was removed under reduced pressure. The residue was dissolved in a minimum volume of acetone

and diethyl ether was added until a cloudy solution was obtained (scrapping on the edge of the flask could be done to induce crystallization). The flask was placed at −20°C overnight. The crystals were collected by filtration, washed with diethyl ether and dried under vacuum to afford triethylammonium silicate.

b) Photocatalytic reaction

b1. General procedure for conjugate addition

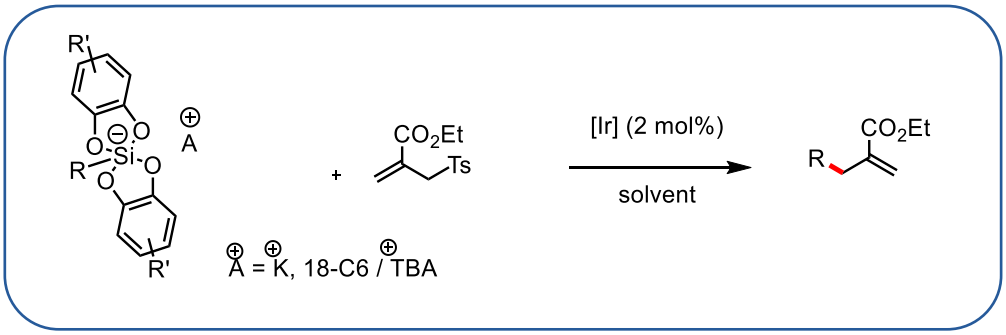

To a dried Schlenk flask was added the appropriate silicate (1.0 equiv), $[Ir(dF(CF_3)ppy)_2(bpy)]PF_6$ (2 mol %), and the allyl sulfone (4 equiv). The Schlenk flask was sealed with a rubber septum and evacuated / purged with vacuum / argon three times. Then degassed solvent (0.1 M) was introduced and the reaction mixture was irradiated with blue LED (477 nm) at room temperature for 24 hours under an argon atmosphere. The reaction mixture was diluted with diethyl ether, washed with water (2 times), dried over $MgSO_4$ and evaporated under reduced pressure. The crude residue was analyzed by ^1H NMR (with 1 equiv of 1,3,5 trimethoxybenzene as NMR standard).

b2. General procedure for D abstraction

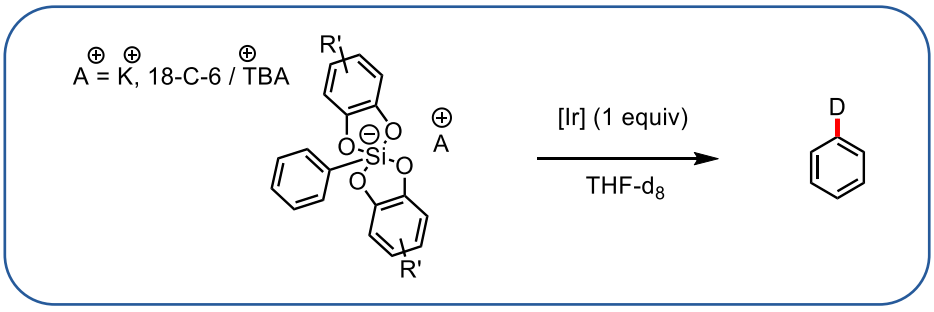

To a dried round bottom flask was added the appropriate silicate (1.0 equiv) and $[Ir(dF(CF_3)ppy)_2(bpy)]PF_6$ (1 equiv). Then deuterated THF (THF-D8) (0.034 M) was introduced and the reaction mixture was irradiated with blue LED (477 nm) at room temperature for 24 hours under an argon atmosphere. The mixture was analyzed by ^1H NMR (with 1 equiv of 1,3,5 trimethoxybenzene as NMR standard). The formation of C_6H_5D **5** could be observed (δ ^1H 7.29 ppm and δ ^2D 7.35 ppm in THF-D) in 20% NMR yield (**1a**) and 50% NMR yield (**150**).

NMR references: benzene (THF-D) δ 7.31 ppm,*145* [18-C-6] (THF-D8) δ 3.57 ppm,[1] TMOP (THF-D8) δ 6.04, 3.70 ppm, Toluene-D_8 (THF-D8) δ 7.10, 2.33 ppm.

III. Compound characterizations

a) Cyclohexyl series

Potassium [18-Crown-6] bis(catecholato)-cyclohexylsilicate (6a)

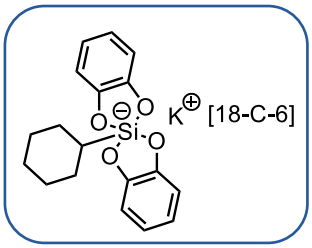

Silicate **6a** was synthesized following the general procedure **a1**, with cyclohexyltrimethoxysilane (5 mmol, 1.022 mL), catechol (10 mmol, 1.1 g), 18-Crown-6 (5 mmol, 1.32 g) and potassium methoxide (5 mmol, 1.4 mL of a 3.56 M solution in methanol) in 20 mL of dry methanol. The crude product was purified according the general procedure to afford **6a** (2.5 g, 79%) as a white solid. Data are in agreement with those reported in the literature.[146]

Potassium [18-Crown-6] bis(3-fluorocatecholato)-cyclohexylsilicate (6b)

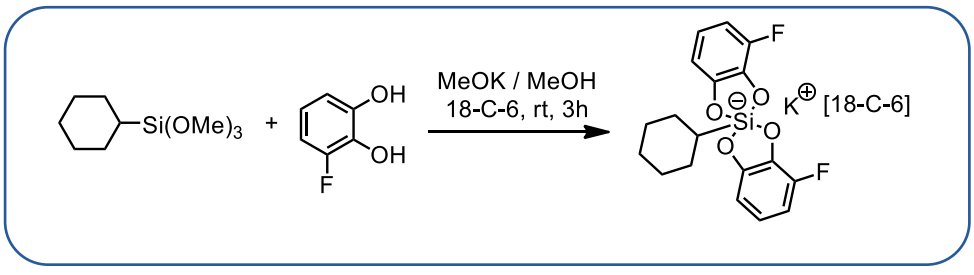

[145] V. Corcé, L.-M. Chamoreau, E. Derat, J.-P. Goddard, C. Ollivier, L. Fensterbank, *Angew. Chemie Int. Ed.* **2015**, *54*, 11414–11418.

To a stirred solution of 3-fluorocatechol (5 mmol, 641 mg) in 25 mL of dry methanol was added 18-C-6 (2.5 mmol, 660 mg). After dissolution of the crown ether, cyclohexytrimethoxysilane (2.5 mmol, 510 µL) was added, followed by a solution of potassium methoxide in methanol (2.5 mmol, 700 µL of a 3.56 M solution in methanol). The reaction mixture was stirred for 3 hours and the solvent was removed under reduced pressure. The residue was dissolved in a minimum volume of acetone and diethyl ether was added until a cloudy solution was obtained (scrapping on the edge of the flask could be done to induce crystallization). The flask was placed at -20°C overnight. The crystals were collected by filtration, washed with diethyl ether and dried under vacuum to afford potassium [18-Crown-6] bis(3-fluorocatecholato)-cyclohexylsilicate (**6b**) (1.65 g, 99%) as a white solid and a mixture of two isomers (50/50 ratio) at rt.

^{1}H NMR (400 MHz, Methanol-d4): δ 6.54-6.47 (m, 4H), 6.45-6.39 (m, 2H), 3.54 (s, 24H), 1.66-1.57 (m, 5H), 1.29-1.10 (m, 5H), 0.86 (tt, J = 12.0 Hz and 4.0 Hz, 1H). **^{13}C NMR** (75 MHz, Methanol-d4): δ 153.9 (d, J = 10.9 Hz, 2C), 153.8 (d, J = 10.9 Hz, 2C), 149.9 (d, J = 238.5 Hz, 2C), 149.8 (d, J = 238.1 Hz, 2C), 138.4 (d, J = 11.1 Hz, 2C), 138.2(d, J = 11.1 Hz, 2C), 118.0 (d, J = 11.5 Hz, 2C), 117.8 (d, J = 11.5 Hz, 2C), 107.4 (d, J = 4.7 Hz, 2C), 107.3 (d, J = 4.6 Hz, 2C), 107.2 (d, J = 9 Hz, 2C), 107.0 (d, J = 8.9 Hz, 2C), 69.9 (24C), 29.9, 29.8, 28.1 (4C), 27.9 (4C), 26.9 (2C). **^{29}Si NMR** (79 MHz, Methanol-d4): δ -74.9. **^{19}F NMR** (376 MHz, Methanol-d4): δ -141.9, -142.1. **HRMS**: calc. for $[C_{18}H_{17}F_2O_4Si]^-$: 363.0870; found: 363.0869. **IR (neat)**: 2889, 2847, 1615, 1495, 1270, 1231, 1046, 1034, 964, 754, 723 cm^{-1}. **mp** 186°C.

Potassium [18-Crown-6] bis(3-methoxycatecholato)-cyclohexylsilicate (6c)

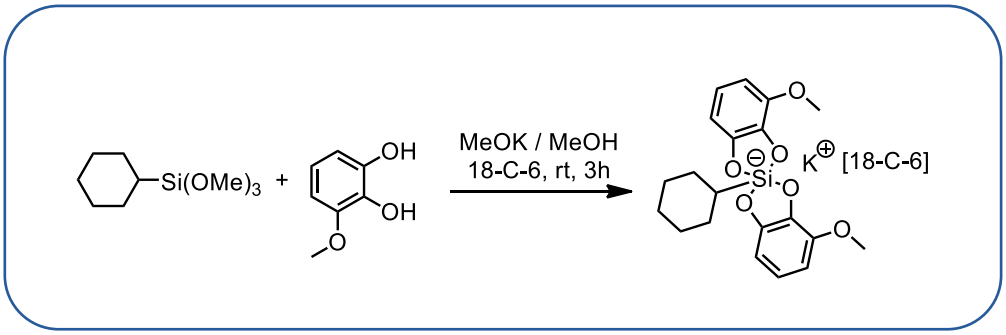

To a stirred solution of 3-methoxycatechol (4.0 mmol, 408 mg) in 15 mL of dry methanol was added 18-C-6 (2.0 mmol, 500 mg). After dissolution of the crown ether, cyclohexytrimethoxysilane (2.0 mmol, 410 µL) was added, followed by a solution of

potassium methoxide in methanol (2.0 mmol, 560 µL of a 3.56 M solution in methanol). The reaction mixture was stirred for 3 hours and the solvent was removed under reduced pressure. The residue was dissolved in a minimum volume of acetone and diethyl ether was added until a cloudy solution was obtained (scrapping on the edge of the flask could be done to induce crystallization). The flask was placed at -20°C overnight. The crystals were collected by filtration, washed with diethyl ether and dried under vacuum to afford potassium [18-Crown-6] bis(3-methoxycatecholato)-cyclohexylsilicate (**6c**) (800 mg, 58%) as a white solid and a mixture of two isomers (50/50 ratio) at rt.

^{1}H NMR (400 MHz, Methanol-d4): δ 6.54-6.50 (m, 2H), 6.46 -6.43 (m, 2H), 6.38-6.35 (m, 2H), 3.87 (m, 6H), 3.57 (s, 24H), 1.70-1.49 (m, 5H), 1.31-1.01 (m, 5H), 0.88 (tt, J = 12.0 Hz and 2.8 Hz, 1H). **^{13}C NMR** (100 MHz, Methanol-d4): δ 152.7 (2C), 152.6 (2C), 146.2 (4C), 140.4 (2C), 140.3 (2C), 118.0 (2C), 117.9 (2C), 106.0 (2C), 105.9 (4C), 105.83 (2C), 71.1 (24C), 57.2 (2C), 57.1 (2C), 31.5, 31.4, 29.5 (4C), 29.3 (4C), 28.2 (2C). **^{29}Si NMR** (79 MHz, Methanol-d4): δ -76.1, -76.2. **HRMS**: calc. for $[C_{20}H_{23}O_6Si]^-$: 387.1269; found: 387.1267. **IR (neat)**: 2911, 1706, 1604, 1495, 1468, 1350, 1296, 1275, 1101, 964, 845, 768, 583 cm^{-1}. **mp** 152.6°C.

Potassium [18-Crown-6] bis(4-cyanocatecholato)-cyclohexylsilicate (6d)

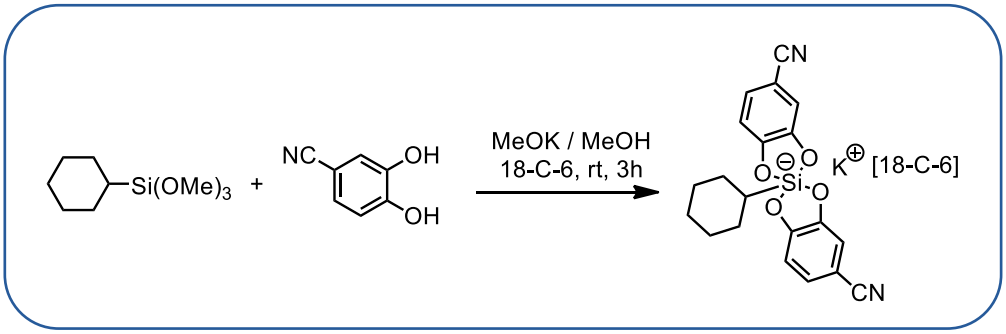

To a stirred solution of 4-cyanocatechol (10 mmol, 1.35 g) in 40 mL of dry methanol was added 18-C-6 (5 mmol, 1.32 g). After dissolution of the crown ether, cyclohexytrimethoxysilane (5.0 mmol, 1.0 mL) was added, followed by a solution of potassium methoxide in methanol (5 mmol, 1.40 mL of a 3.56 M solution in methanol). The reaction mixture was stirred for 3 hours and the solvent was removed under reduced pressure. The residue was dissolved in a minimum volume of acetone and diethyl ether was added until a cloudy solution was obtained (scrapping on the edge of the flask could be done to induce crystallization). The flask was placed at -20°C overnight. The crystals were collected by filtration, washed with diethyl ether and dried under vacuum to afford [18-Crown-6] bis(4-

cyanocatecholato)-cyclohexylsilicate (**6d**) (850 mg, 25%) as a white solid and a mixture of two isomers (50/50 ratio) at rt.

^{1}H NMR (400 MHz, Methanol-d4): δ 7.06-6.92 (m, 4H), 6.79-6.71 (m, 2H), 3.61 (s, 24H), 1.66-1.56 (m, 5H), 1.35-1.10 (m, 5H), 0.88 (tt, J = 12.0 Hz and 4.0 Hz, 1H). **^{13}C NMR** (100 MHz, Acetone-d6): δ 157.7 (2C), 157.1 (2C), 152.5 (2C), 151.9 (2C), 125.3 (2C), 124.6 (2C), 121.4 (2C), 121.3 (2C), 112.5 (2C), 112.3 (2C), 110.9 (2C), 110.8 (2C), 100.2 (2C), 99.4 (2C), 70.7 (24C), 31.2, 31.1, 29.2, 29.1, 29.0, 28.8, 28.7, 28.6, 27.7 (4C). **^{29}Si NMR** (79 MHz, Acetone-d6): δ -75.0, -75.1. **HRMS**: calc. for $[C_{20}H_{17}N_2O_4Si]^-$: 377.0963; found: 377.0960. **IR (neat)**: 2215, 2160, 1493, 1350, 1266, 959, 831, 572cm^{-1}. **mp** 147°C.

b) Phenyl series

Potassium [18-Crown-6] bis(catecholato)-phenylsilicate (1a)

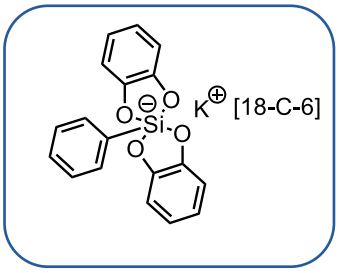

Silicate **1a** was synthesized following the general procedure **a1**, with phenyltrimethoxysilane (2.5 mmol, 466 µL), catechol (5 mmol, 550.6 mg), 18-Crown-6 (2.5 mmol, 660 mg) and potassium methoxide (2.5 mmol, 700 µL of a 3.56 M solution in methanol) in 10 mL of dry methanol. The crude product was purified according the general procedure to afford **1a** (1.36 g, 87%) as a white solid. Data are in agreement with those reported in the literature.[3]

Potassium [18-Crown-6] bis(3-methoxycatecholato)-phenylsilicate (1b)

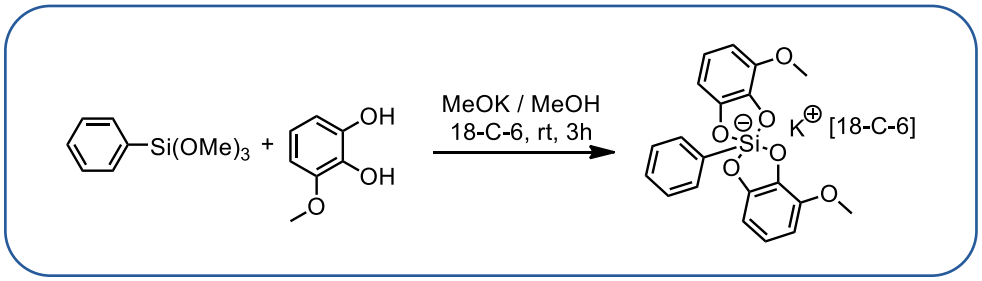

To a stirred solution of 3-methoxycatechol (5.0 mmol, 701 mg) in 25 mL of dry methanol was added 18-C-6 (2.5 mmol, 660 mg). After dissolution of the crown ether, phenyltrimethoxysilane (2.5 mmol, 466 µL) was added, followed by a solution of potassium

methoxide 3.56 M in methanol (2.5 mmol, 700 µL). The reaction mixture was stirred for 3 hours and the solvent was removed under reduced pressure. The residue was dissolved in a minimum volume of acetone and diethyl ether was added until a cloudy solution was obtained (scrapping on the edge of the flask could be done to induce crystallization). The flask was placed at -20°C overnight. The crystals were collected by filtration, washed with diethyl ether and dried under vacuum to afford potassium [18-Crown-6] bis(3-methoxycatecholato)-phenylsilicate (**1b**) (1.43 g, 92%) as a white solid and a mixture of two isomers (50/50 ratio) at rt.

^{1}H NMR (400 MHz, Methanol-d4): δ 7.69-7.66 (m, 2H), 7.19-7.17 (m, 3H), 6.58-6.52 (m, 4H), 6.44-6.41 (m, 2H), 3.85 (s, 6H), 3.53 (s, 24H). **^{13}C NMR** (100 MHz, Methanol-d4): δ 152.1 (4C), 146.6 (4C), 141.9, 141.8, 139.9, 139.8, 135.8 (4C), 129.1 (4C), 127.9 (4C), 118.5 (4C), 106.2 (4C), 106.1 (4C), 71.1 (24C), 57.1 (2C), 57.0 (2C). **^{29}Si NMR** (79 MHz, Methanol-d4): δ -86.2, -86.3. **HRMS**: calc. for $[C_{20}H_{17}O_6Si]^-$: 381.0800; found: 381.0798. **IR (neat)**: 2898, 1706, 1604, 1498, 1247, 1067, 964, 846, 770, 583 cm^{-1}. **mp** 165°C.

Potassium [18-Crown-6] bis(3-tert-butylcatecholato)-phenylsilicate (1c)

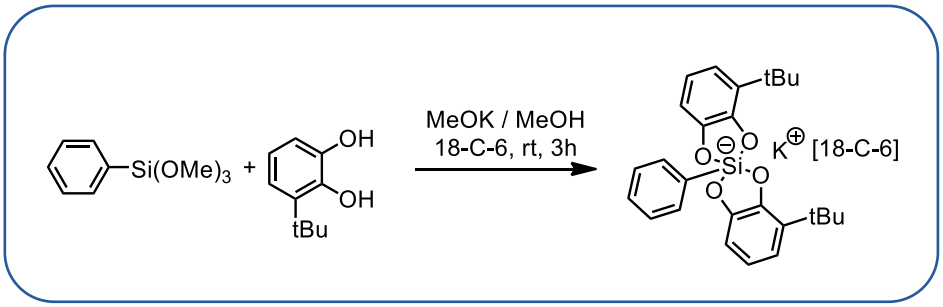

To a stirred solution of 3-tertbutyl catechol (5.0 mmol, 831 mg) in 25 mL of dry methanol was added 18-C-6 (2.5 mmol, 660 mg). After dissolution of the crown ether, phenyltrimethoxysilane (2.5 mmol, 466 µL) was added, followed by a solution of potassium methoxide 3.56 M in methanol (2.5 mmol, 700 µL). The reaction mixture was stirred for 3 hours and the solvent was removed under reduced pressure. The residue was dissolved in a minimum volume of acetone and diethyl ether was added until a cloudy solution was obtained (scrapping on the edge of the flask could be done to induce crystallization). The flask was placed at -20°C overnight. The crystals were collected by filtration, washed with diethyl ether and dried under vacuum to afford potassium [18-Crown-6] bis(3-tert-butylcatecholato)-phenylsilicate (**1c**) (1.47 g, 80%) as a white solid and a mixture of two isomers (50/50 ratio) at rt.

^{1}H NMR (400 MHz, DMSO-d6): δ 7.56-7.51 (m, 2H), 7.16-7.07 (m, 3H), 6.67-6.61 (m, 2H), 6.51-6.41 (m, 4H), 3.53(s, 24H), 1.21 (s, 18H). **^{13}C NMR** (100 MHz, DMSO-d6): δ 150.7

(2C), 150.6 (2C), 148.6 (2C), 148.5 (2C), 142.6 (2C), 142.5 (2C), 141.9 (2C), 135.5 (4C), 129.1 (2C), 127.9 (4C), 115.6 (2C), 115.5 (2C), 110.5 (4C), 109.3 (4C), 71.3 (24C), 35.1 (4C), 21.3 (12C). **^{29}Si NMR** (79 MHz, DMSO-d6): δ -87.1. **HRMS**: calc. for $[C_{26}H_{29}O_4Si]^-$: 433.1835; found: 433.1837. **IR (neat)**: 2857, 1428, 1350, 1248, 1108, 820, 804, 652 cm^{-1}. **mp** 290°C.

Potassium [18-Crown-6] bis(3-fluorocatecholato)-phenylsilicate (1d)

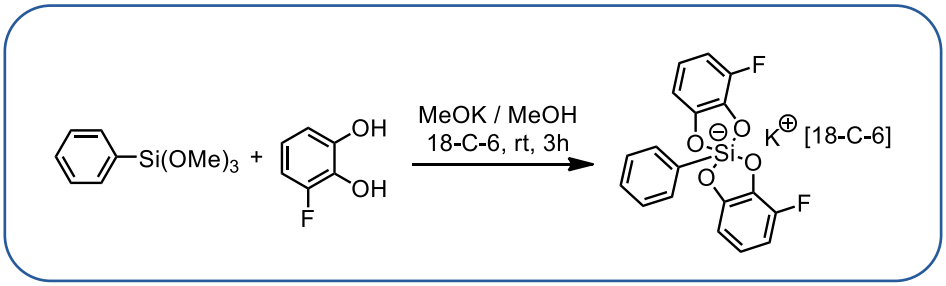

To a stirred solution of 3-fluorocatechol (5.0 mmol, 641 mg) in 25 mL of dry methanol was added 18-C-6 (2.5 mmol, 660 mg). After dissolution of the crown ether, phenyltrimethoxysilane (2.5 mmol, 466 µL) was added, followed by a solution of potassium methoxide 3.56 M in methanol (2.5 mmol, 700 µL). The reaction mixture was stirred for 3 hours and the solvent was removed under reduced pressure. The residue was dissolved in a minimum volume of acetone and diethyl ether was added until a cloudy solution was obtained (scrapping on the edge of the flask could be done to induce crystallization). The flask was placed at -20°C overnight. The crystals were collected by filtration, washed with diethyl ether and dried under vacuum to afford potassium [18-Crown-6] bis(3-fluorocatecholato)-phenylsilicate (**1d**) (1.48 g, 90%) as a white solid and a mixture of two isomers (50/50 ratio) at rt.

^{1}H NMR (400 MHz, Methanol-d4): δ 7.70-7.67 (m, 2H), 7.24-7.22 (m, 3H), 6.67-6.65 (m, 2H), 6.63-6.57 (m, 2H), 6.55-6.49 (m, 2H), 3.52 (s, 24H). **^{13}C NMR** (100 MHz, Methanol-d4): δ 153.4 (d, J = 11.2 Hz, 2C), 153.3 (d, J = 11.6 Hz, 2C), 150.0 (d, J = 239 Hz, 2C), 149.9 (d, J = 239 Hz, 2C), 140.6 (d, J = 1.7 Hz, 2C), 137.8 (d, J = 20.8 Hz, 2C), 137.7 (d, J = 1.6 Hz, 2C), 135.8 (4C), 129.5 (2C), 128.1 (4C), 118.4 (d, J = 12.6 Hz, 2C), 118.3 (d, J = 12.6 Hz, 2C), 107.8 (d, J = 5.1 Hz, 2C), 107.7 (d, J = 5.1 Hz, 2C), 107.6 (d, J = 18.2 Hz, 2C), 107.4 (d, J = 18.1 Hz, 2C), 71. 3 (24C). **^{29}Si NMR** (79 MHz, Methanol-d4): δ -85.1. **^{19}F NMR** (376 MHz, Methanol-d4): δ -141.9, -142.1. **HRMS**: calc. for $[C_{18}H_{11}F_2O_4Si]^-$: 357.0395; found: 357.0391.

IR (neat): 2892, 1713, 1618, 1515, 1496, 1471, 1352, 1273, 1231, 965, 868,726, 703 cm^{-1}. **mp** 170ºC.

Tetrabutylammonium bis(4,5-dichlorocatecholato)-phenylsilicate (1e)

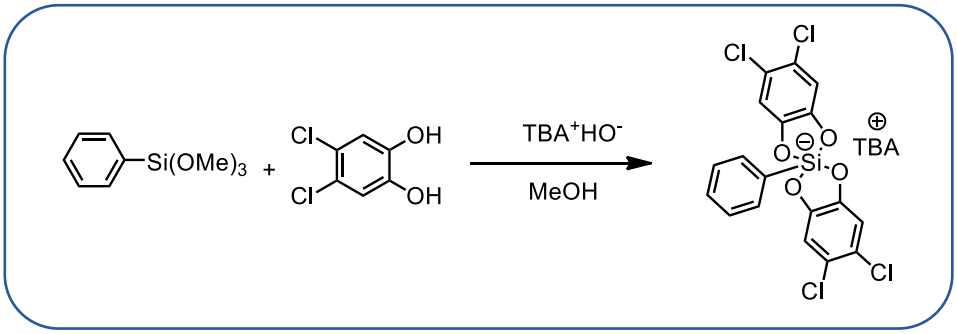

To a stirred solution 4,5 dichlorocatechol (2 mmol, 358 mg) in 25 mL of dry methanol was added tetrabutylammonium hydroxide (1 mmol, 1 mL) (salt 1M in MeOH) and phenyltrimethoxysilane (1 mmol, 188 µL). The reaction mixture was stirred for 1 hour. After that, Et_2O was added and a white solid appeared. This solid was filtered and washed with Et_2O to afford tetrabutylammonium bis(4,5-dichlorocatecholato)-phenylsilicate (**1e**) (590 mg, 84%) as a white solid.

^{1}H NMR (400 MHz, Acetone-d6): δ 7.71-7.55 (m, 2H), 7.24-7.29 (m, 3H), 6.78 (s, 4H), 3.38 (t, J = 11.2 Hz, 8H), 1.84-1.65 (m, 8H), 1.47-1.31 (m, 8H), 0.94 (t, J = 9.6 Hz, 12H). **^{13}C NMR** (100 MHz, Acetone-d6): δ 152.0 (4C), 141.3, 136.0 (4C), 129.2, 127.8 (2C), 120.0 (2C), 112.0 (4C), 59.4 (4C), 24.5 (4C), 20.4 (4C), 13.9 (4C). **^{29}Si NMR** (79 MHz, Methanol-d4): δ -84.4 ppm. **HRMS**: calc. for $[C_{18}H_9Cl_4O_4Si]^-$: 456.9030; found: 456.9031. **IR (neat)**: 2961, 2873, 1482, 1427, 1377, 1239, 1093, 872, 695 cm^{-1}. **mp** 160.2°C.

Potassium [18-Crown-6] bis(tetrabromocatecholato)-phenylsilicate (1f)

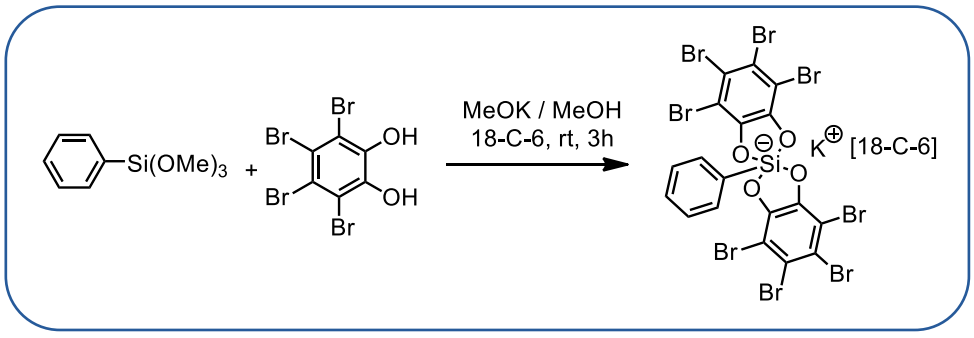

To a stirred solution of tetrabromocatechol (2.0 mmol, 852 mg) in 10 mL of dry methanol was added 18-C-6 (1.0 mmol, 264 mg). After dissolution of the crown ether, phenyltrimethoxysilane (1.0 mmol, 187 µL) was added, followed by a solution of potassium methoxide 3.36 M in methanol (1.0 mmol, 294 µL). The reaction mixture was stirred for 3 hours and the solvent was removed under reduced pressure. The residue was dissolved in a minimum volume of acetone and diethyl ether was added until a cloudy solution was obtained (scrapping on the edge of the flask could be done to induce crystallization). The flask was placed at -20°C overnight. The crystals were collected by filtration, washed with diethyl ether and dried under vacuum to afford potassium [18-Crown-6] bis(tetrabromocatecholato)-phenylsilicate (**1f**) (1.064 mg, 84%) as a white solid.

^{1}H NMR (400 MHz, Acetone-d6): δ 7.74-7.71 (m, 2H), 7.24-7.21 (m, 3H), 3.62 (s, 24H). **^{13}C NMR** (100 MHz, Acetone-d6): δ 149.8 (4C), 138.6, 136.5 (4C), 130.0, 128.1 (4C), 115.2 (2C), 106.9 (2C), 70.8 (12C). **^{29}Si NMR** (79 MHz, Acetone-d6): δ -85.8. **HRMS**: calc. for $[C_{18}H_5Br_8O_4Si]^-$: 952.3352; found: 952.3358. **IR (neat)**: 2882, 1536, 1445, 1347, 1218, 1100, 944, 702, 678, 599 cm^{-1}. **mp** 266ºC.

Potassium [18-Crown-6] bis(tetrachlorocatecholato)-phenylsilicate (1g)

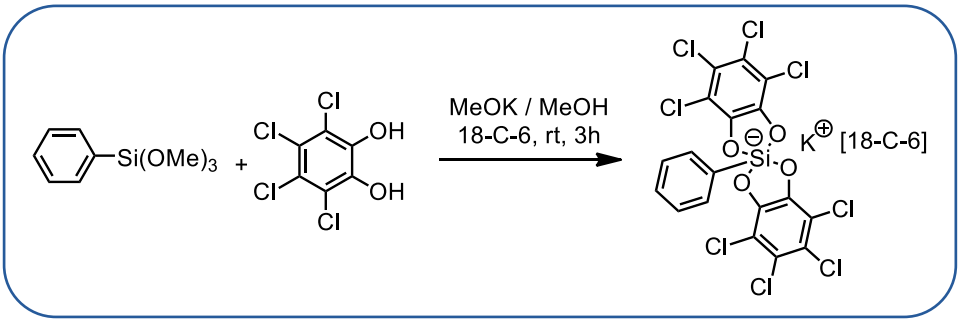

To a stirred solution of tetrachlorocatechol (5.0 mmol, 1.239 g) in 25 mL of dry methanol was added 18-C-6 (2.5 mmol, 660 mg). After dissolution of the crown ether, phenyltrimethoxysilane (2.5 mmol, 466 µL) was added, followed by a solution of potassium methoxide 3.56 M in methanol (2.5 mmol, 700 µL). The reaction mixture was stirred for 3 hours and the solvent was removed under reduced pressure. The residue was dissolved in a minimum volume of acetone and diethyl ether was added until a cloudy solution was obtained

(scrapping on the edge of the flask could be done to induce crystallization). The flask was placed at -20°C overnight. The crystals were collected by filtration, washed with diethyl ether and dried under vacuum to afford potassium [18-Crown-6] bis(tetrachlorocatecholato)-phenylsilicate (**1g**) (810 mg, 36%) as a white solid.

^{1}H NMR (400 MHz, Methanol-d4): δ 7.51-7.49 (m, 2H), 7.29-7.24 (m, 3H), 3.51 (s, 24H). **^{13}C NMR** (100 MHz, DMSO-d6): δ 146.4 (4C), 136.8, 134.5 (4C), 129.4, 127.6 (4C), 119.5 (2C), 113.3 (2C), 69.3 (12C). **^{29}Si NMR** (79 MHz, DMSO-d6): δ -84.0. **HRMS**: calc. for $[C_{18}H_5Cl_8O_4Si]^-$: 594.7441; found: 594.7428. **IR (neat)**: 2894, 1597, 1497, 1327, 1105, 1067, 963, 823, 733, 701 cm^{-1}. **mp** 246°C.

Potassium [18-Crown-6] bis(4-cyanocatecholato)-phenylsilicate (1h)

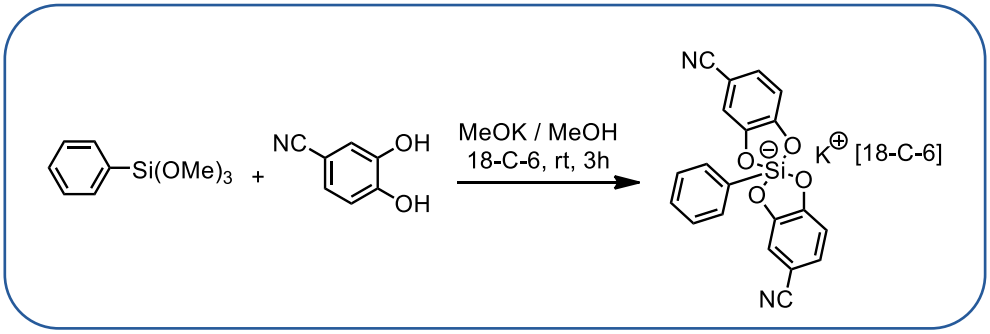

To a stirred solution of appropriate 4-cyanocatechol (5.0 mmol, 676 mg) in 25 mL of dry methanol was added 18-C-6 (2.5 mmol, 660 mg). After dissolution of the crown ether, phenyltrimethoxysilane (2.5 mmol, 466 µL) was added, followed by a solution of potassium methoxide 3.56 M in methanol (2.5 mmol, 700 µL). The reaction mixture was stirred for 3 hours and the solvent was removed under reduced pressure. The residue was dissolved in a minimum volume of acetone and diethyl ether was added until a cloudy solution was obtained (scrapping on the edge of the flask could be done to induce crystallization). The flask was placed at -20°C overnight. The crystals were collected by filtration, washed with diethyl ether and dried under vacuum to afford potassium [18-Crown-6] bis(4-cyanocatecholato)-phenylsilicate (**1h**) (1.37 g, 81%) as a white solid and a mixture of two isomers (50/50 ratio) at rt.

^{1}H NMR (400 MHz, Methanol-d4): δ 7.58-7.55 (m, 2H), 7.25-7.19 (m, 3H), 7.13-7.09 (m, 2H), 7.03 (m, 2H), 6.89-6.86 (m, 2H), 3.65 (s, 24H). **^{13}C NMR** (100 MHz, Methanol-d4): δ 155.4 (2C), 154.9 (2C), 150.2 (2C), 149.7 (2C), 139.2 (2C), 134.6 (2C), 135.5 (2C), 128.6

(2C), 127.1 (4C), 125.1 (2C), 124.6 (2C), 120.4 (4C), 112.4 (2C), 112.2 (2C), 110.8 (2C), 110.7 (2C), 99.4 (2C), 98.9 (2C), 69.3 (24C). **^{29}Si NMR** (79 MHz, Methanol-d4): δ -85.3. **HRMS**: calc. for $[C_{20}H_{11}N_2O_4Si]^-$: 371.0488; found: 371.0495. **mp** 147°C.

Triethylammonium bis(4,5-dihydroxyphthalonitrile catecholato)-phenylsilicate (1i)

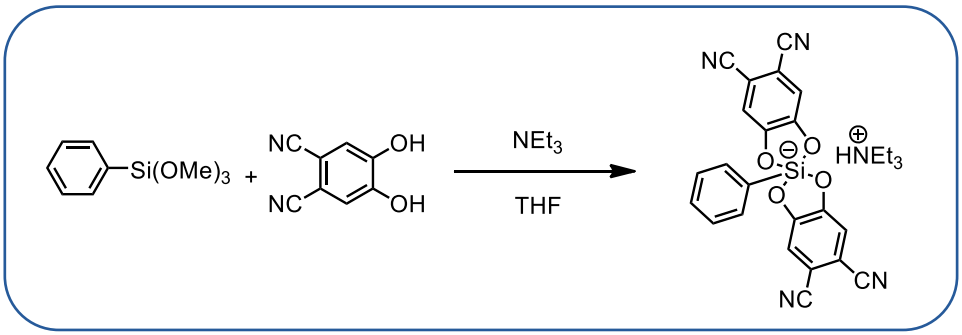

To a stirred solution of 4,5-dihydroxyphthalonitrile (0.9 mmol, 145 mg) in 4.5 mL of dry THF added phenyltrimethoxysilane (0.45 mmol, 84 µL) and NEt_3 (2.1 mmol, 300 µL). The reaction mixture was stirred for 20 hours at reflux and the solvent was removed under reduced pressure. The residue was dissolved in a minimum volume of acetone and diethyl ether (+ pentane) was added until a cloudy solution was obtained (scrapping on the edge of the flask could be done to induce crystallization). The flask was placed at -20°C overnight. The crystals were collected by filtration, washed with diethyl ether and dried under vacuum to afford triethylammonium bis(4,5-dihydroxyphthalonitrile catecholato)-phenylsilicate (**1i**) (140 mg, 59%) as a white solid.

^{1}H NMR (400 MHz, DMSO-d6): δ 7.46-7.43 (m, 2H), 7.38 (s, 4H), 7.28-7.21 (m, 3H), 3.09 (bs, 6H), 1.17 (bs, 9H). **^{13}C NMR** (100 MHz, DMSO-d6): δ 154.1 (4C), 137.3, 134.2 (2C), 129.2, 127.5 (2C), 117.0 (4C), 114.6 (4C), 105.4 (4C), 45.8 (3C), 8.6 (3C). **^{29}Si NMR** (79 MHz, DMSO-d6): δ -83.5. **HRMS**: calc. for $[C_{22}H_9N_4O_4Si]^-$: 421.0399; found: 421.0396. **IR (neat)**: 3107, 2225, 1589, 1493, 1373, 1290, 1092, 876, 856, 737, 682, 596 cm^{-1}. **mp** 241°C.

IV. Stern-Volmer experiments

Emission intensities were recorded on a Jasco FP-6200 spectrofluorometer. Dry DMF was degassed by freeze-pump-thaw cycles before use. The photocatalyst $[Ir(dF(CF_3)ppy)_2(bpy)]PF_6$ was excited at 436 nm and the emission spectra were recorded between 470 and 700 nm. In a typical experiment, 10 µM solutions of [Ir] in DMF were prepared with the appropriate concentration of quencher **1a** and **1h** a 1.0 cm quartz cuvette and covered. After degassing with a stream of argon for 10 minutes, the emission spectrum of the sample was recorded. The Stern-Volmer plot was done according the following equation: $\frac{I_f^0}{I_f} = 1 + k_q t_0 \cdot [Q]$. A quenching constant of 5.7 10^8 $mol^{-1}.L.s^{-1}$ for **1a** and of 1.31 10^8 $mol^{-1}.L.s^{-1}$ for **1h**.

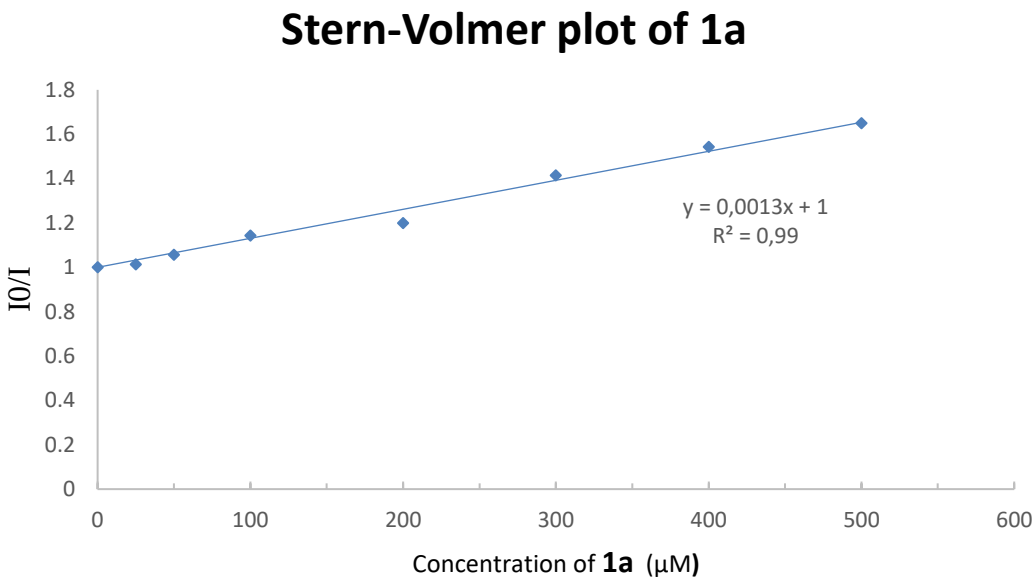

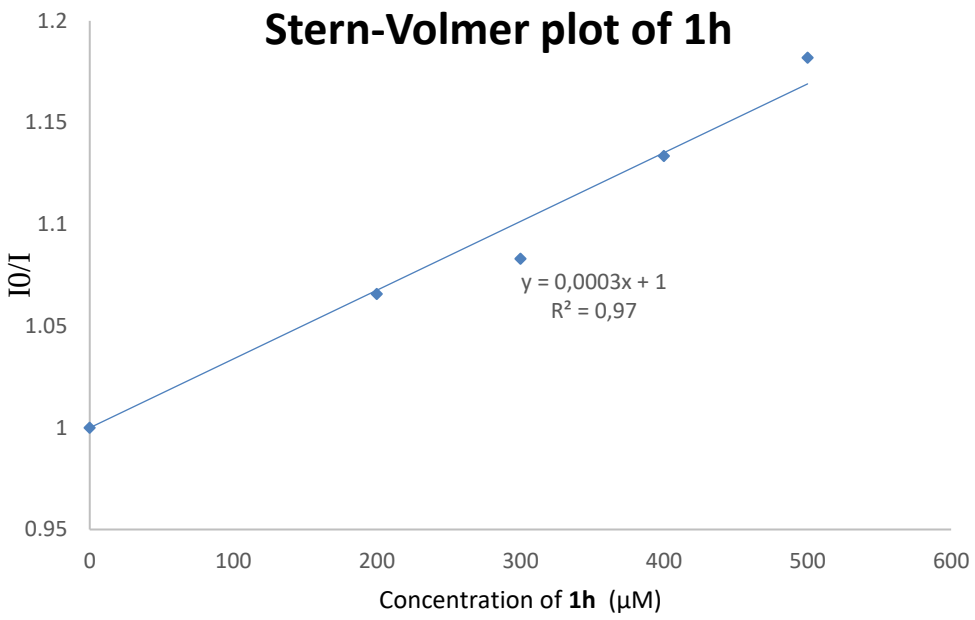

V. Electrochemical measurements

The voltammetric measurement was recorded in a three-electrodes cell in degassed DMF with Bu_4NPF_6 (0.1 M) as support electrolyte at 22°C. Measurements were monitored with an AutoLab PSTAT10 electrochemical workstation. Cyclic voltammetry (CV) was used to estimate the half-wave oxidation potentials. The CVs were obtained at a scan rate of 0.1 V s^{-1}. Glassy carbon, platinum plate, and saturated calomel were used as working, counter, and reference electrodes, respectively.

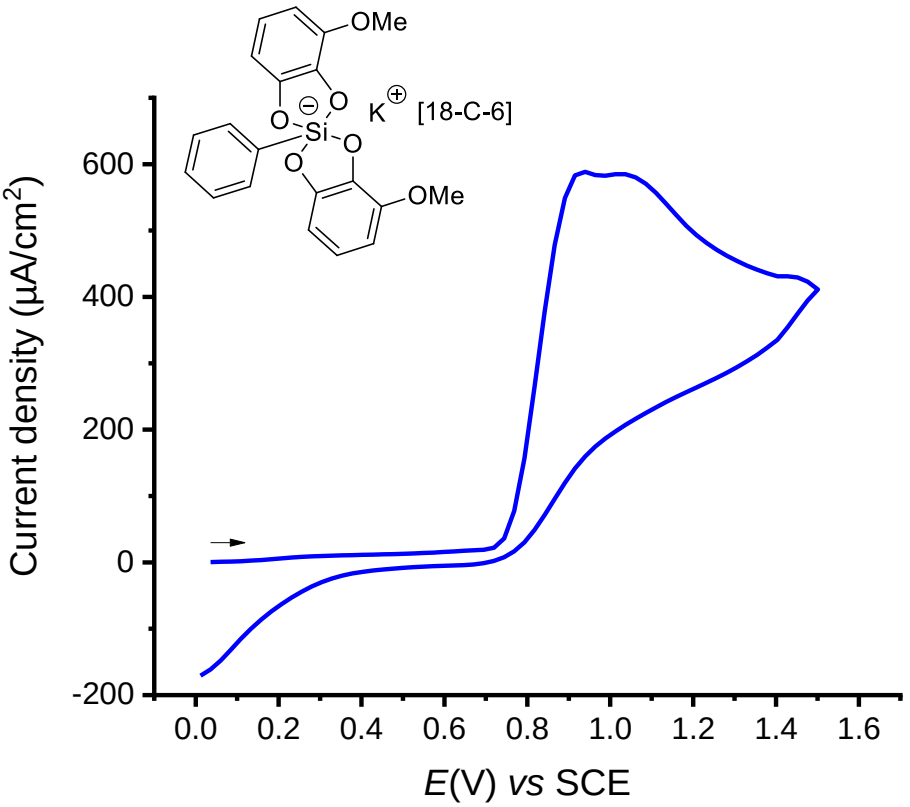

CV performed towards oxidative potentials of DMF solution containing 0.3 M of n-Bu_4NBF_4 at room temperature, at a scan rate of 0.1 $V.s^{-1}$ using steady glassy carbon disk electrode (d = 3 mm) as working electrode, a SCE as reference and Pt wire as counter-electrode. CV with **1b** (2mM).

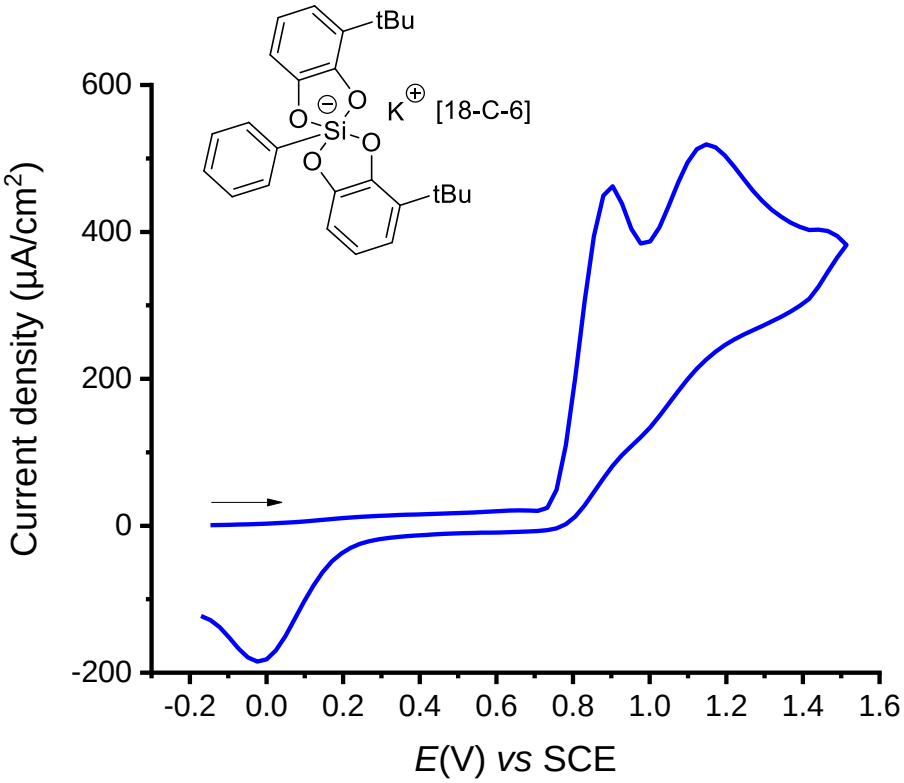

CV performed towards oxidative potentials of DMF solution containing 0.3 M of n-Bu_4NBF_4 at room temperature, at a scan rate of 0.1 $V.s^{-1}$ using steady glassy carbon disk electrode (d = 3 mm) as working electrode, a SCE as reference and Pt wire as counter-electrode. CV with **1c** (2mM).

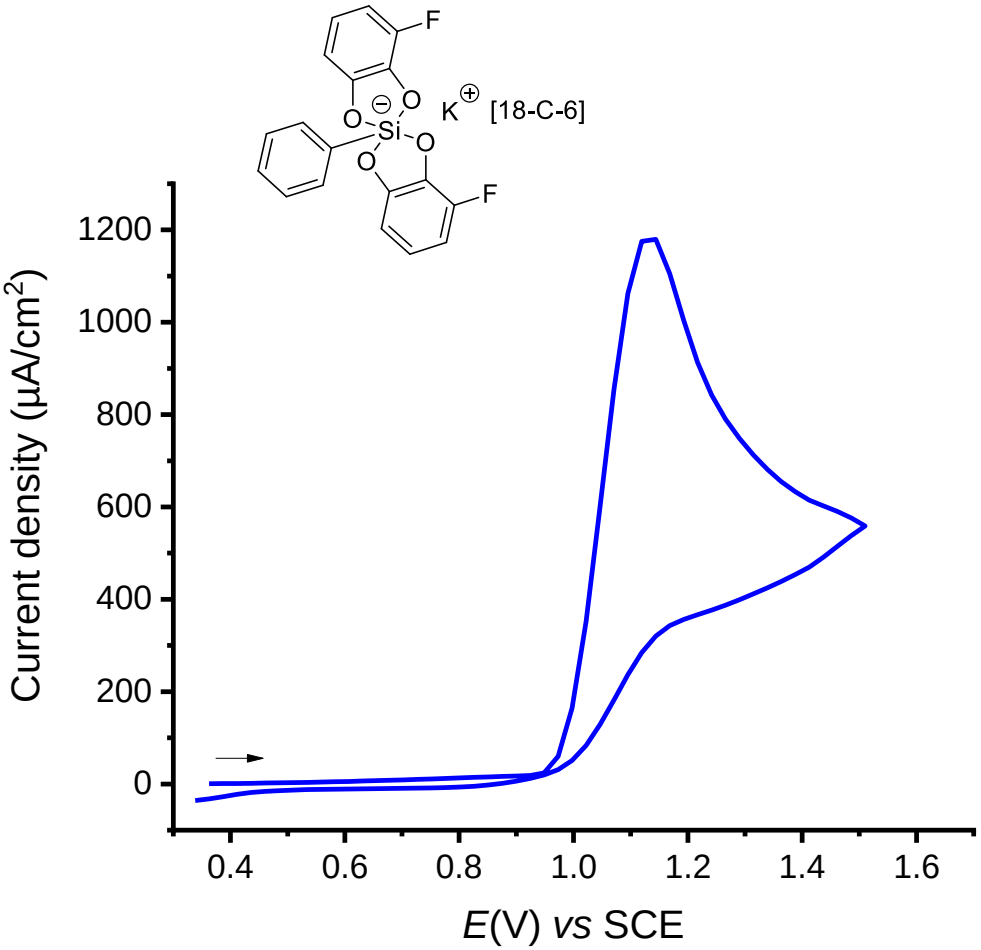

CV performed towards oxidative potentials of DMF solution containing 0.3 M of n-Bu_4NBF_4 at room temperature, at a scan rate of 0.1 $V.s^{-1}$ using steady glassy carbon disk electrode (d = 3 mm) as working electrode, a SCE as reference and Pt wire as counter-electrode. CV with **1d** (2mM).

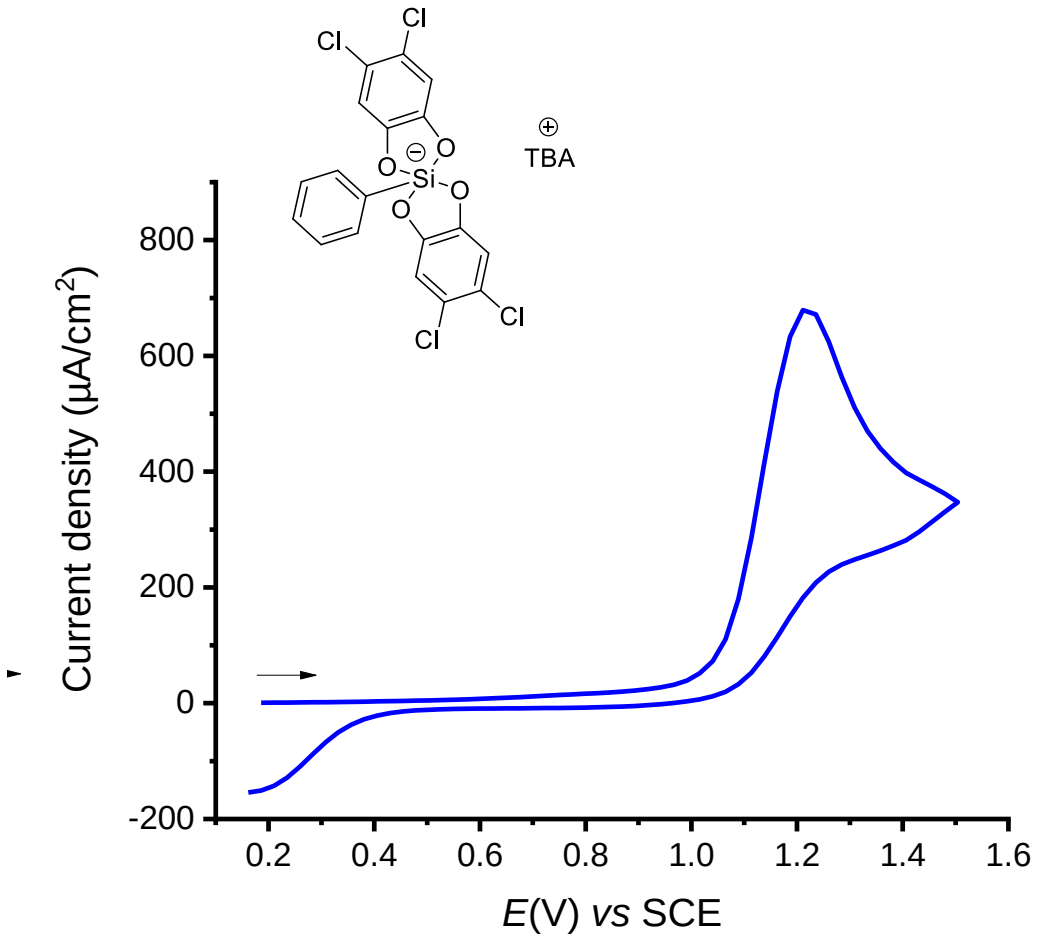

CV performed towards oxidative potentials of DMF solution containing 0.3 M of n-Bu_4NBF_4 at room temperature, at a scan rate of 0.1 $V.s^{-1}$ using steady glassy carbon disk electrode (d = 3 mm) as working electrode, a SCE as reference and Pt wire as counter-electrode. CV with **1e** (2mM).

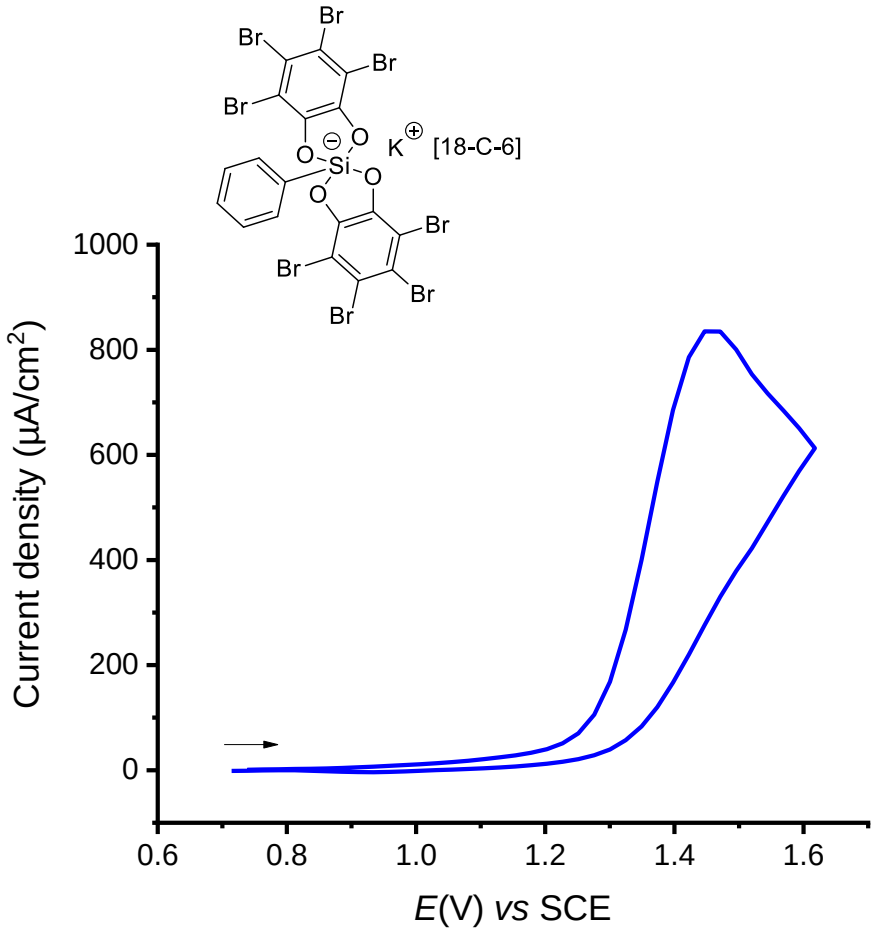

CV performed towards oxidative potentials of DMF solution containing 0.3 M of n-Bu_4NBF_4 at room temperature, at a scan rate of 0.1 $V.s^{-1}$ using steady glassy carbon disk electrode (d = 3 mm) as working electrode, a SCE as reference and Pt wire as counter-electrode. CV with **1f** (2mM).

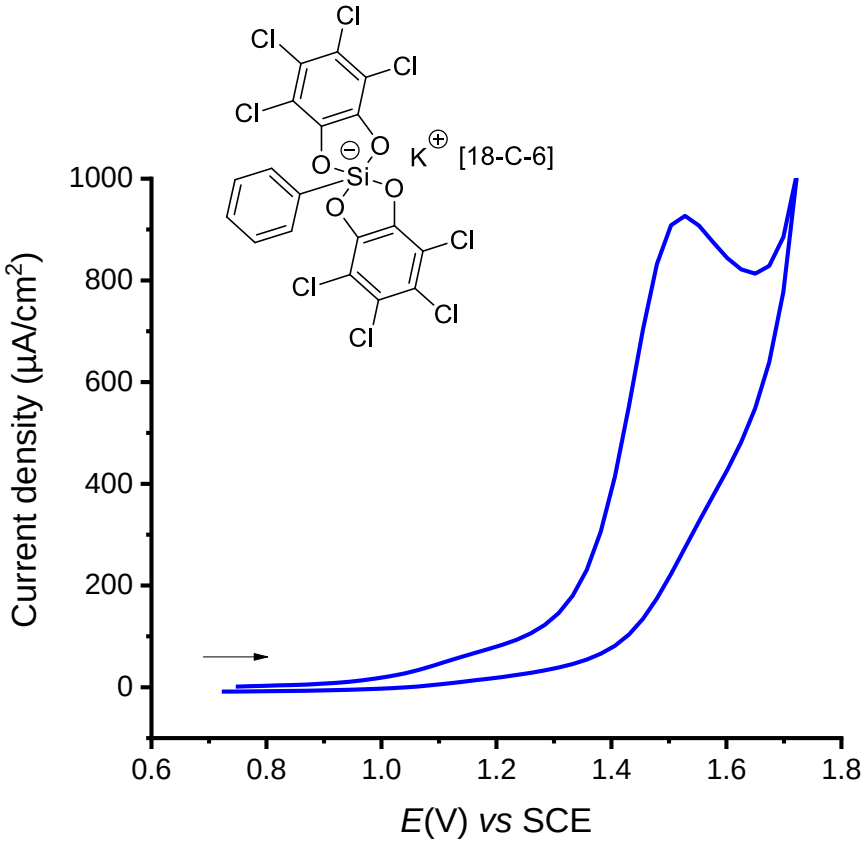

CV performed towards oxidative potentials of DMF solution containing 0.3 M of n-Bu_4NBF_4 at room temperature, at a scan rate of 0.1 $V.s^{-1}$ using steady glassy carbon disk electrode (d = 3 mm) as working electrode, a SCE as reference and Pt wire as counter-electrode. CV with **1g** (2mM).

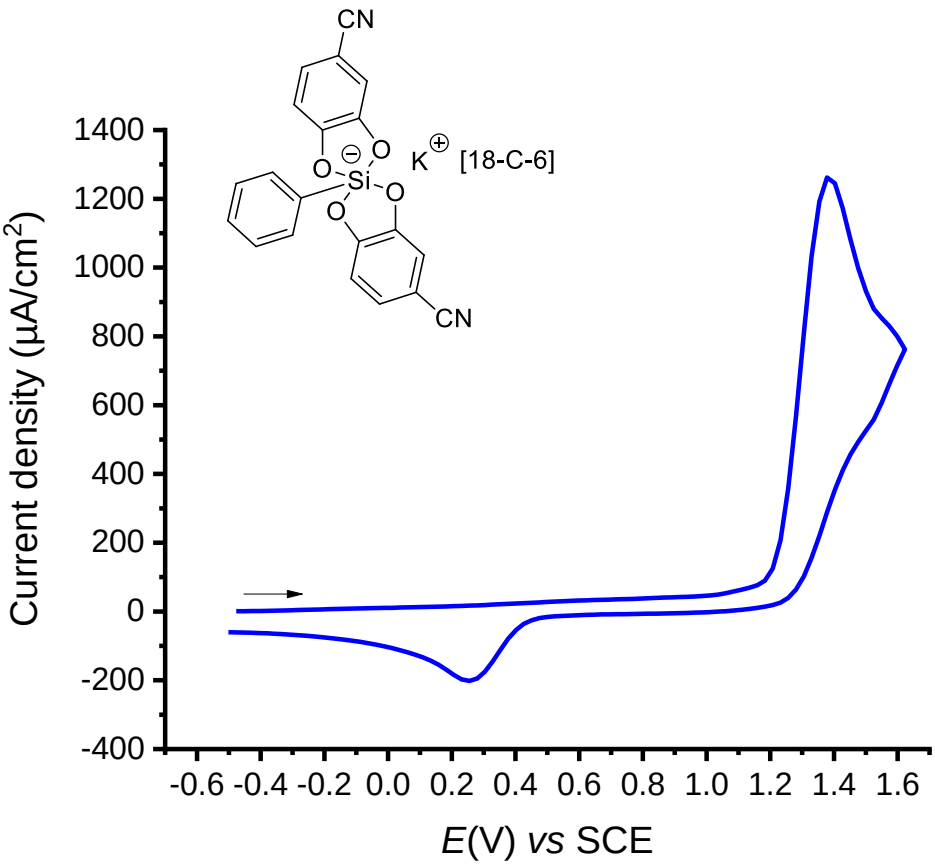

CV performed towards oxidative potentials of DMF solution containing 0.3 M of n-Bu_4NBF_4 at room temperature, at a scan rate of 0.1 $V.s^{-1}$ using steady glassy carbon disk electrode (d = 3 mm) as working electrode, a SCE as reference and Pt wire as counter-electrode. CV with **1h** (2mM).

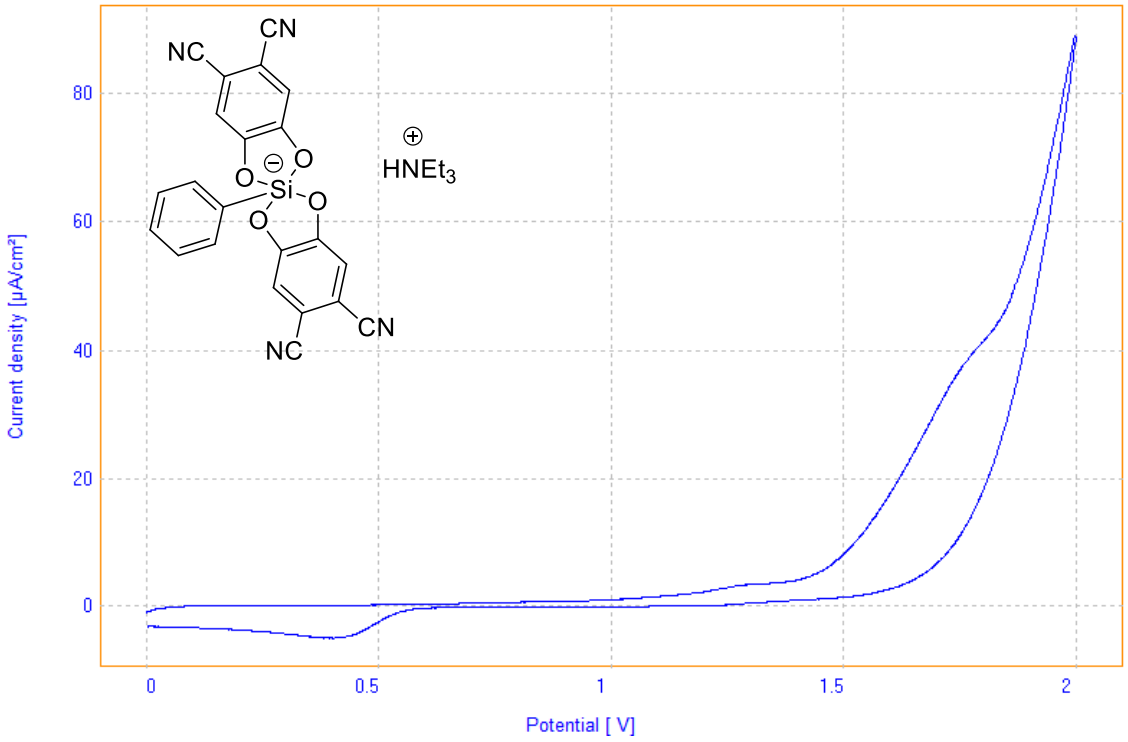

CV performed towards oxidative potentials of DMF solution containing 0.1 M of n-Bu_4NBF_4 at room temperature, at a scan rate of 0.1 $V.s^{-1}$ using steady glassy carbon disk electrode (d = 2 mm) as working electrode, a SCE as reference and Pt wire as counter-electrode. CV with **1i** (10 mM).

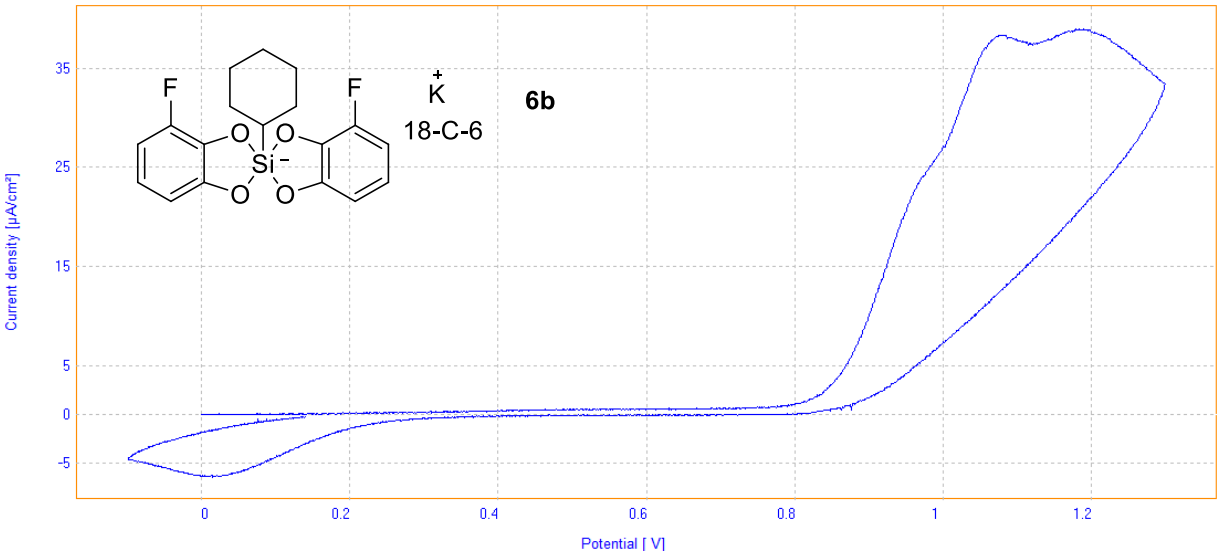

CV performed towards oxidative potentials of DMF solution containing 0.1 M of n-Bu_4NBF_4 at room temperature, at a scan rate of 0.1 $V.s^{-1}$ using steady glassy carbon disk electrode (d = 2 mm) as working electrode, a SCE as reference and Pt wire as counter-electrode. CV with **6b** (10 mM).

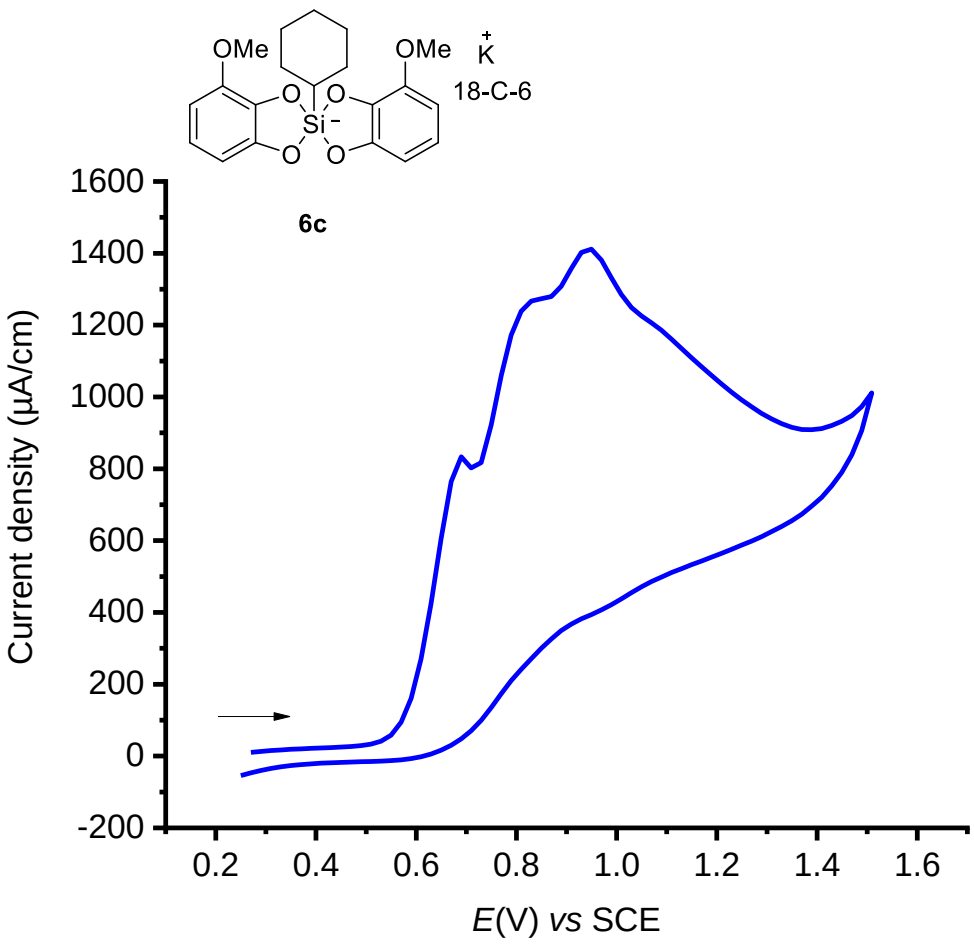

CV performed towards oxidative potentials of DMF solution containing 0.3 M of n-Bu_4NBF_4 at room temperature, at a scan rate of 0.2 $V.s^{-1}$ using steady glassy carbon disk electrode (d = 3 mm) as working electrode, a SCE as reference and Pt wire as counter-electrode. CV with **6c** (2mM).

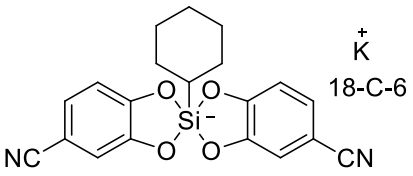

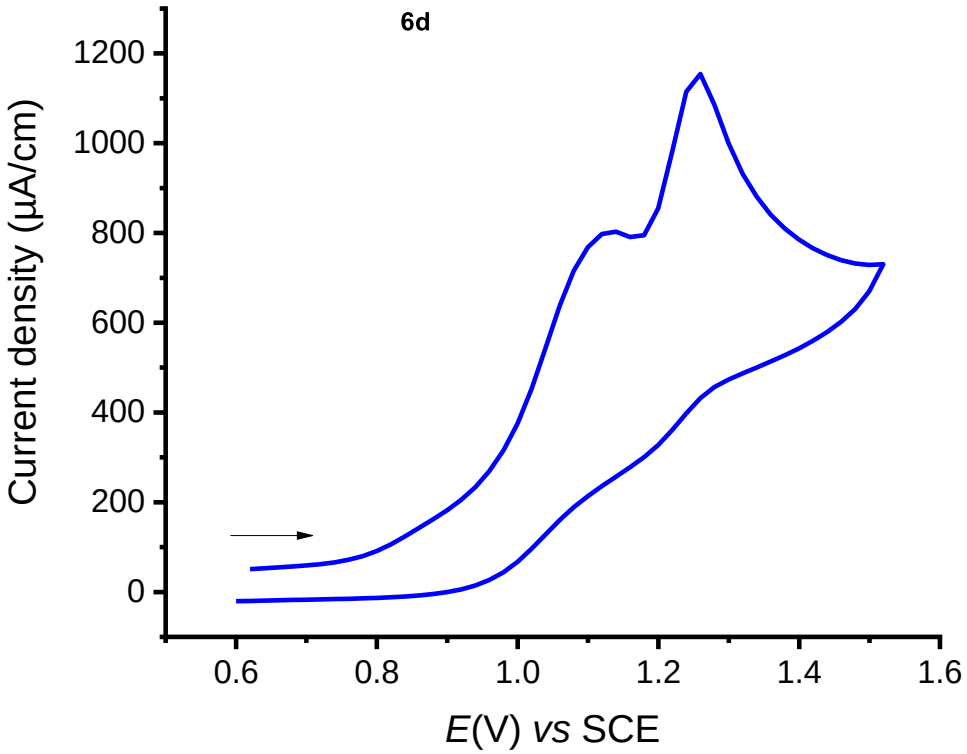

CV performed towards oxidative potentials of DMF solution containing 0.3 M of n-Bu_4NBF_4 at room temperature, at a scan rate of 0.2 $V.s^{-1}$ using steady glassy carbon disk electrode (d = 3 mm) as working electrode, a SCE as reference and Pt wire as counter electrode. CV with **6d** (2mM).

Silicate	***$E_{ox}^{1/2}$ (vs SCE in DMF)***
1a	+ 0.89 V
1b	+ 0.81 V
1c	+ 1.09 V
1d	+ 1.05 V
1e	+ 1.13 V
1f	+ 1.46 V
1g	+ 1.37 V
1h	+ 1.33 V
1i	+ 1.62 V
6a	+ 0.69 V
6b	+ 0.91 V
6c	+ 0.63 V
6d	+ 1.01 V

VI. Spectroscopic analyses

Absorption spectra of molecules were recorded at 25°C on a Cary 300 UV/Vis spectrophotometer (Agilent Technologies, Santa Clara, CA), equipped with a Peltier thermostated cell holder (t2x2 Sport/Cary300, Quantum Northwest, Liberty Lake, WA). The samples were placed in 2 mL quartz cuvettes (1 cm × 1 cm light path; Hellma Optics, Jena, Germany). The UV spectrums were investigated in DMF (C = 1.6 10^{-4} mol.L^{-1}).

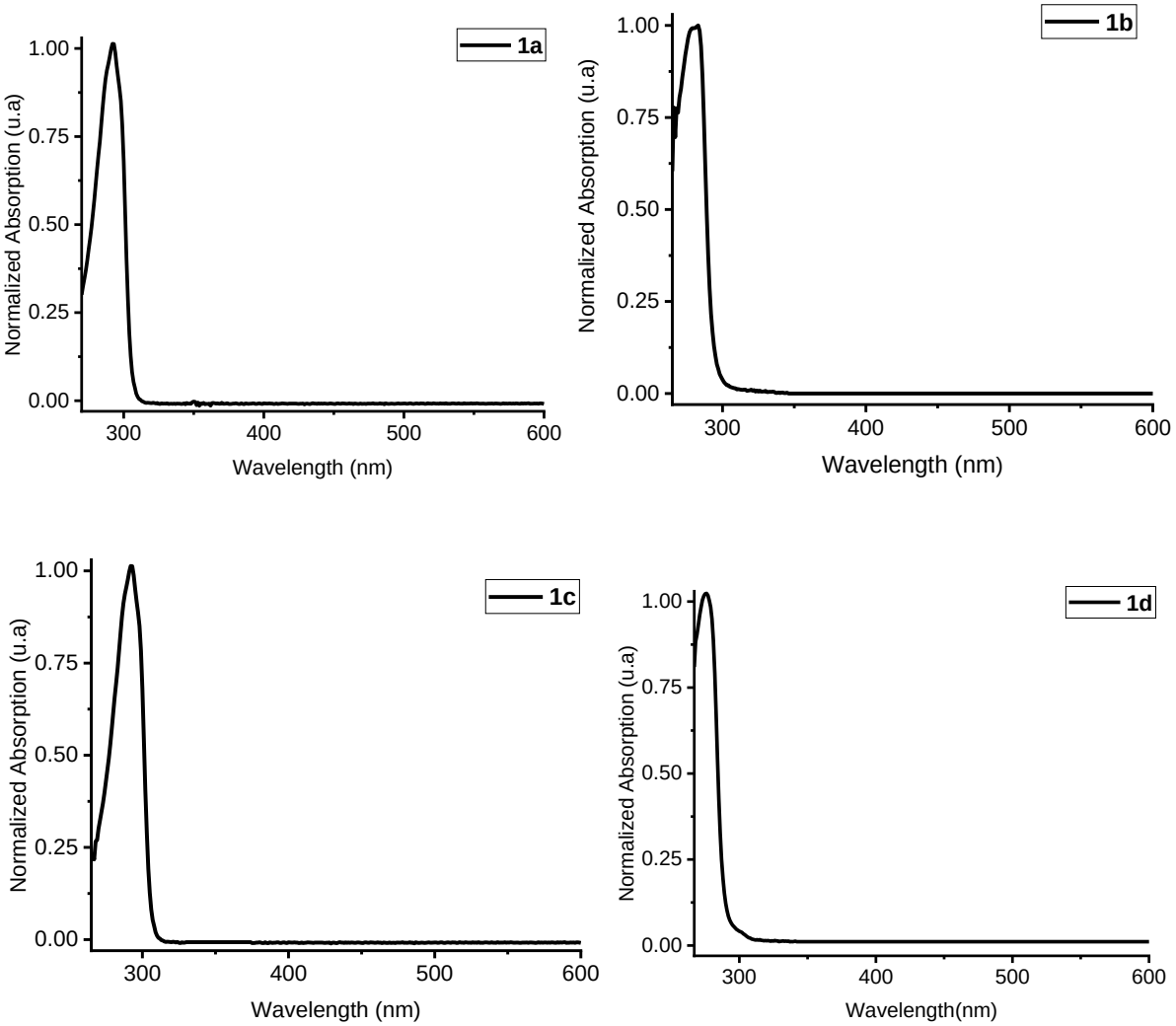

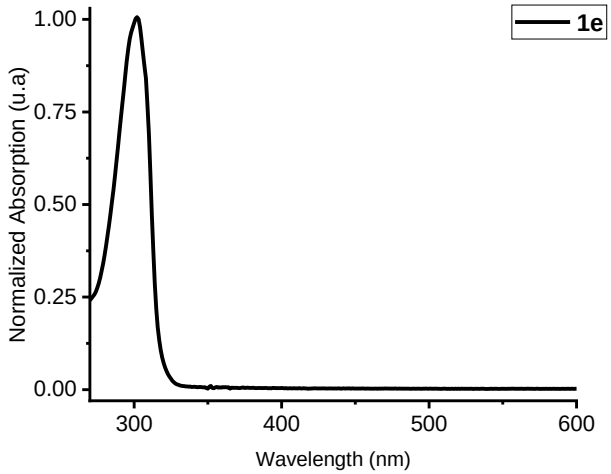
1e
Normalized Absorption (u.a)
1.00
0.75
0.50
0.25
0.00
300
400
500
600
Wavelength (nm)

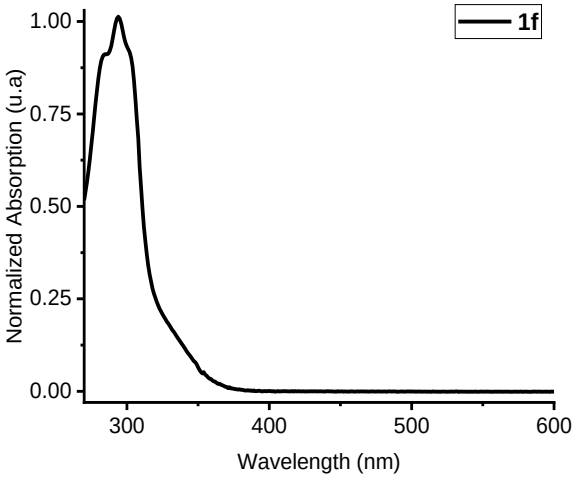
1f
Normalized Absorption (u.a)
1.00
0.75
0.50
0.25
0.00
300
400
500
600
Wavelength (nm)

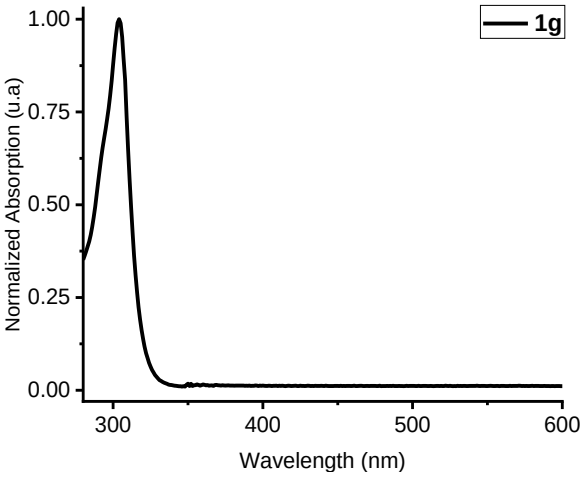
1g
Normalized Absorption (u.a)
1.00
0.75
0.50
0.25
0.00
300
400
500
600
Wavelength (nm)

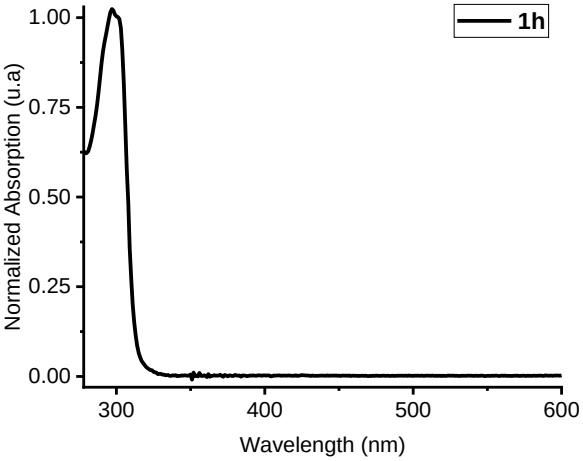
1h
Normalized Absorption (u.a)
1.00
0.75
0.50
0.25
0.00
300
400
500
600
Wavelength (nm)

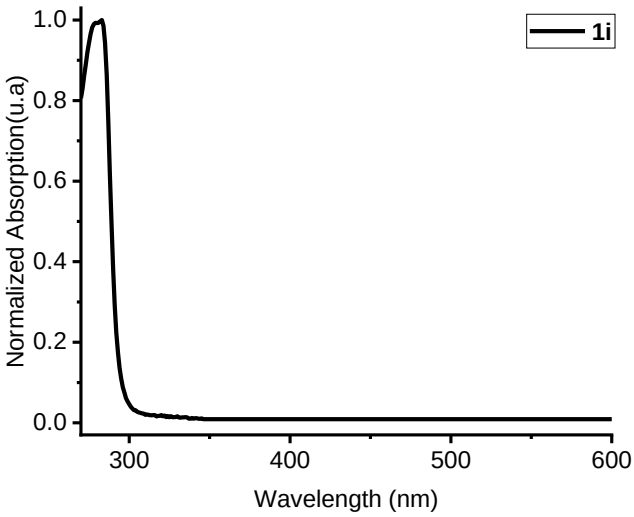
1i
Normalized Absorption(u.a)
1.0
0.8
0.6
0.4
0.2
0.0
300
400
500
600
Wavelength (nm)

Silicate	λ_{max} *(nm)*
1a	**292**
1b	**284**
1c	**291**
1d	**276**
1e	**301**
1f	**293**
1g	**303**
1h	**298**
1i	**280**

Chapter 2. Copper catalysis with non-innocent ligands for oxidation of alkyl silicates

1. Project Aims and Introduction

This chapter focuses on metal complexes with non-innocent ligands, with emphasis on their characterization and corresponding reactions. Various synthetic uses of non-innocent ligands will be discussed in the context of organic chemistry. In addition, the second part of this chapter will attempt to undergo the oxidation of silicates, carboxylates, and methyl aniline with bis-aminophenolate copper complexes.

2. Concept of non-innocent ligands

The concept of “innocent ligand' and “non-innocent ligand' was first introduced in organometallic chemistry in 1966. As suggested by Jørgensen[147], " Ligands are innocent when they allow oxidation states of the central atoms to be defined."

Jørgensen introduced the concept "non-innocent ligand" by citing the nitrosyl ligand NO as an example. In contrast to charge-defined ligands such as H_2O, NH_3, or Cl, the electron configuration of the non-innocent ligand NO in pentacyanonitrosyl complexes such as $[Fe(CN)_5(NO)]_2$, $[Co(CN)_5(NO)]_3$, and other related octahedral complexes $[M(CN)_5(NO)]_2$ may be regarded as NO, NO-, or NO+. In general, for the metal-centered complex bearing the NO ligand $[M(L_1)_m(NO)_n]^q$, the electron configuration of the NO ligand is determined by the type of the central metal atom M and the complex's total charge q.

The second example of a non-innocent ligand is the stilbene dithiolate which can be involved in nickel bisdithiolene complexes. In the 1960s, G. N. Schrauzer and his colleagues reported the synthesis of dithiolene (enedithiol) molecules.[148] The structure of dithiolene

[147] C. K. Jørgensen, *Coord. Chem. Rev.* **1966**, *1*, 164–178.

[148] a） G. N. Schrauzer, V. Mayweg, *J. Am. Chem. Soc.* **1962**, *84*, 3221. b） A. Davison, N. Edelstein, R. H. Holm, A. H.

compounds has been found to be a square planar configuration of a nickel atom surrounded by two dithiobenzil molecules. However, many questions have been raised about the precise state of oxidation of the metal and ligand in these planar-square complexes. As shown in **Scheme 98**, the complex may be described by three distinct types of resonance, referred to as valence tautomers. Two electrons in this combination must be placed into the complex's LUMO, depending on the molecule's magnetic properties.

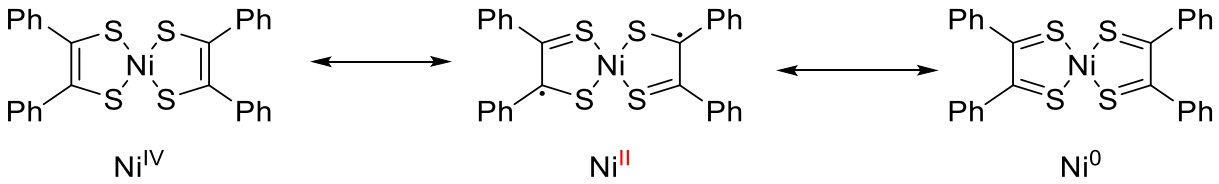

Scheme 98. Valence tautomers of a nickel dithiolene complex

2.1 Important non-innocent Ligands

Although there are no clear criteria to predict the non-innocent behavior of a ligand in a specific complex, it turns out that currently known non-innocent ligands have certain characteristics, such as their conjugated structure, which allows for the stability of an unpaired electron, or a radical. We will focus on some of these structures in this section

2.1.1 Non-innocence of catecholate and its derivatives

Due to the fact that dithiolenes[149], o-phenylenediamines[150], o-aminophenols[151], and other similar compounds[152] may undergo reversible single-electron oxidation or reduction, in the

---

Maki, *Inorg. Chem.* **1963**, *2*, 1227–1232. c) S. I. Shupack, E. Billig, R. J. H. Clark, R. Williams, H. B. Gray, *J. Am. Chem. Soc.* **1964**, *86*, 4594–4602.

[149] a) R. Eisenberg, *Coord. Chem. Rev.* **2011**, *255*, 825–836. b) F. J. Hine, A. J. Taylor, C. D. Garner, *Coord. Chem. Rev.* **2010**, *254*, 1570–1579.

[150] a) Y. Shimazaki, T. D. P. Stack, T. Storr, *Inorg. Chem.* **2009**, *48*, 8383–8392. b) T. J. Dunn, L. Chiang, C. F. Ramogida, M. I. Webb, D. Savard, M. Sakaguchi, T. Ogura, Y. Shimazaki, T. Storr, *Dalt. Trans.* **2012**, *41*, 7905–7914.

[151] a) M. Curcio, J. R. Pankhurst, S. Sproules, D. Mignard, J. B. Love, *Angew. Chemie Int. Ed.* **2017**, *56*, 7939–7943.. b) C. Römelt, J. Song, M. Tarrago, J. A. Rees, M. van Gastel, T. Weyhermüller, S. DeBeer, E. Bill, F. Neese, S. Ye, *Inorg. Chem.* **2017**, *56*, 4745–4750.

[152] E. Safaei, H. Bahrami, A. Pevec, B. Kozlevčar, Z. Jagličić, *J. Mol. Struct.*, **2017**, *1133*, 526–533.

1960s, Holm and co-workers [153] proposed that these ligands might be considered as the prototype of non-innocent ligands.

It was shown that in the complexes, o-catecholate existed as single or doubly charged closed-shell aromatic anions (**A**), neutral 11-electron o-quinones (**C**), or open-shell (S=1/2) o-benzosemiquinonate radicals (**B**). Similarly, their nitrogen or sulfur counterparts show a similar situation. With increasing oxidation state, these ligands can exist in three redox states: catecholate (Lcat), *o*-semiquinonate (L_{SQ}), and *o*-benzoquinone (L_{BQ}) (**Scheme 99**).

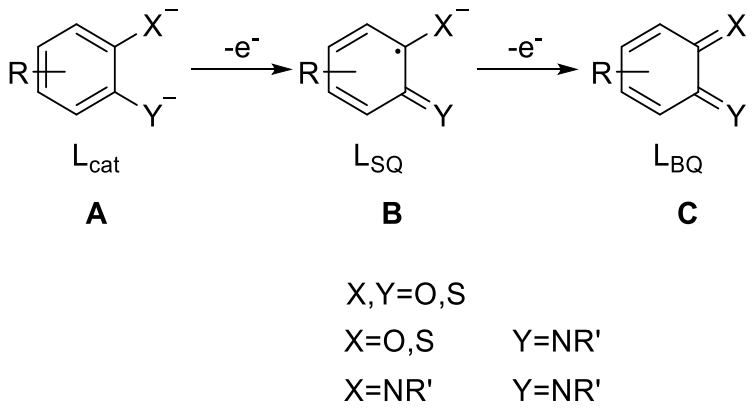

Scheme 99. Redox states of the catecholate ligand and its derivatives

In 2013, a series of copper (II) complexes coordinated to an aminophenol non-innocent ligand involving tridentate benzoxazole group was described by Safael[154] and his colleagues, which can facilitate appropriate oxidation of substituted alcohol to corresponding aldehydes or ketones (Scheme **100**). In particular, copper(II) complex **7** demonstrates distortion in its tetragonal structure, whereas copper(II) complex **7** has a square pyramidal geometry. Improved catalytic efficiency can be seen in the copper (II) complex **7**. The solubility of copper (II) complex **7** in toluene can be enhanced by the assistance of the acetate ligand, which can be engaged in the catalysis process.

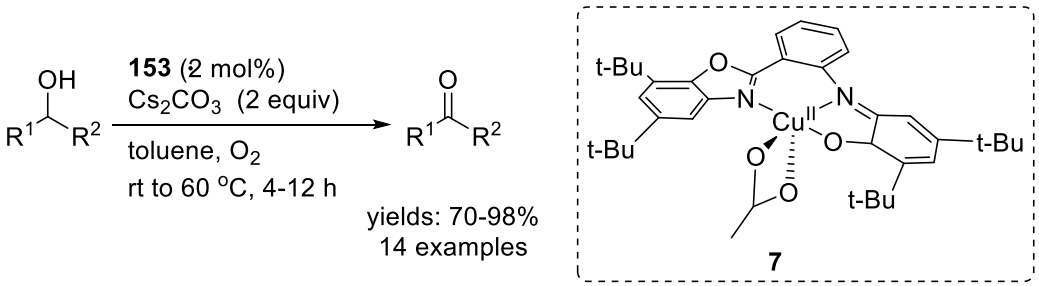

Scheme 100. The copper(II) complex **7** coordinated to an aminophenol type

[153] A. L. Balch, F. Röhrscheid, R. H. Holm, *J. Am. Chem. Soc.* **1965**, *87*, 2301–2302.

[154] S. E. Balaghi, E. Safaei, L. Chiang, E. W. Y. Wong, D. Savard, R. M. Clarke, T. Storr, *Dalt. Trans.*, **2013**, *42*, 6829–6839.

benzoxazole ligand for oxidation of alcohol

In 2020, the same group [155] developed a Mo (II) complexes **8** coordinated to an aminophenol non-innocent ligand involving the tridentate benzoxazole structure. Mo (II) can enable the effective oxidation of a variety of substituted sulfides to corresponding sulfones by using an H_2O_2 25% aqueous solution as the environmentally friendly oxidant. Additionally, the Mo (II) complexes could be utilized to catalyze the conversion from hexanedioic acid via numerous oxygen intermediate species (like cyclohexene oxide, 1,2-cyclohexanediol, and adipic anhydride). In particular, Mo (II) complex demonstrates distortion in its optimized trigonal bipyramid structure. (Scheme **101**)

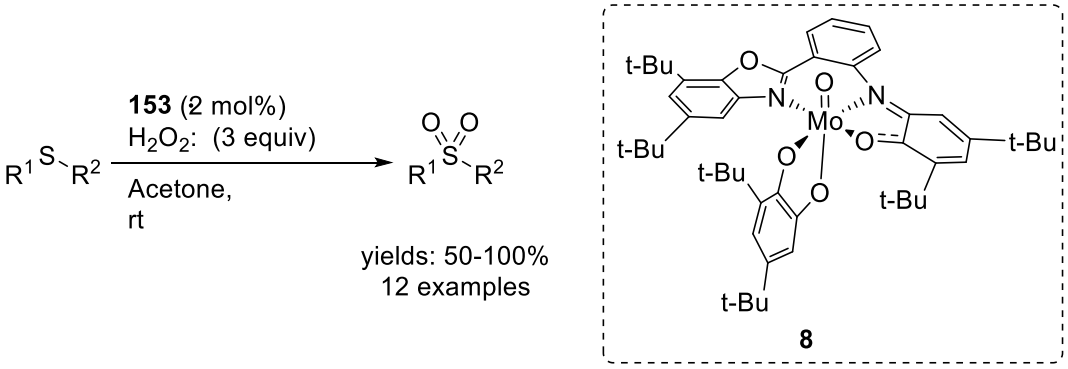

Scheme 101. Complexes **153** oxidation of a variety of substituted sulfides to corresponding sulfone

2.1.2 Non-innocence of bisiminopyridines

Catecholates and their derivatives are not the only substances that exhibit non-innocent behavior. Bisiminopyridines are trident ligands with three distinct redox states: the neutral bisiminopyridine ligand (L0), the anion radical (L), and the diradical-anion (L2). (Scheme **102**).

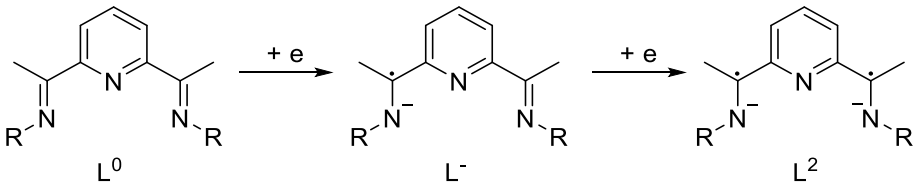

Scheme 102. The redox states of bisiminopyridine ligand redox states

[155] M. Nasibipour, E. Safaei, A. Wojtczak, Z. Jagličić, A. Galindo, M. S. Masoumpour, *RSC Adv.*, **2020**, *10*, 40853–40866.

In 2019, the Neidig group[156] demonstrated the ability of the Fe(III) complex **9** that coordinated to non-innocent bisiminopyridine ligand to catalyze the hydromagnesiation of substituted styrenes with excess Grignard reagent, yielding various benzylic Grignard reagents efficiently (Scheme **103**). The Grignard reagents were able to undergo hydrofunctionalization to yield various target hydrofunctionalized products. In this study, a crystal structure of intermediate of the Fe(III) species ([Fe(η_2-styrene)$_3$(κ1-CH(CH$_3$)Ph)][MgX-(THF)$_5$]) that was captured at temperatures as low as -80 °C determined by X-ray crystallography reveals that three molecules of styrene coupled to an iron-aryl species had replaced the i-Pr-substituted bisiminopyridine as the ligand. The styrene hydrometalation is estimated to be associated with the substitution.

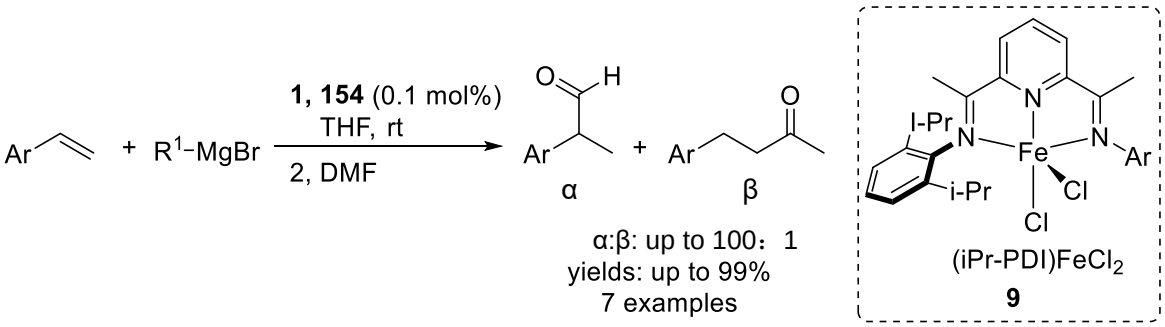

Scheme 103. A Fe(III) complex **9** catalyzed hydromagnesiation of substituted styrenes

In the same year, Y. Deng[157] and his colleagues realized novel carbene transfer reactions. The reported method employed the Fe(III) complex **10** that coordinated to non-innocent chiral bisiminopyridine ligand as the iron (III) catalyst and the methyl phenyldiazoacetate as the source of the carbene group (**Scheme 104**). The carbene transfer reactions could undergo employing olefin derivatives as substrates to provide a set of substituted cyclopropanes in high yield.

[156] P. G. N. Neate, M. D. Greenhalgh, W. W. Brennessel, S. P. Thomas, M. L. Neidig, *J. Am. Chem. Soc.*, **2019**, *141*, 10099–10108.

[157] 1 B. Wang, I. G. Howard, J. W. Pope, E. D. Conte, Y. Deng, *Chem. Sci*., **2019**, *10*, 7958–7963.

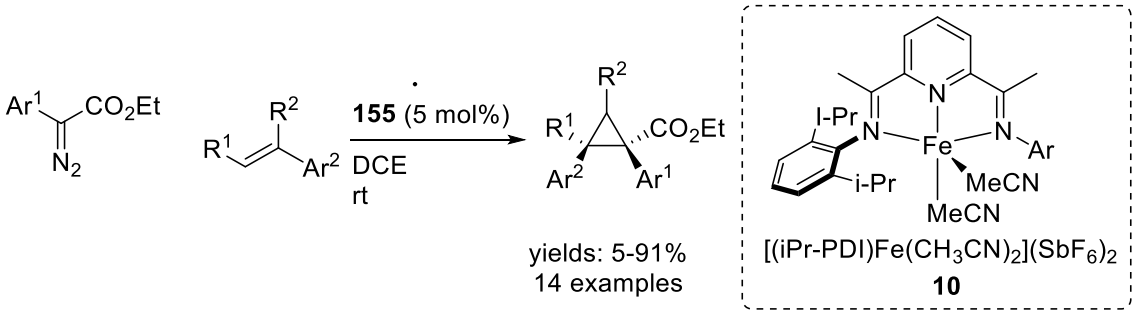

Scheme 104. A novel Fe(III) complex **10** catalyzed carbene transfer reactions

2.2. Characterization of non-innocent ligands

Numerous techniques are available to the chemist for characterizing a metal complex that is coordinated by a non-innocent ligand(s) and exhibits several redox states. The structure determined by X-ray diffraction allows the identification of the bond lengths (single, double, or "intermediate") and, therefore, the assignment of the ligand's redox state. The electrical properties of substituents, on the other hand, may cloud this attribution.

Electronic Paramagnetic Resonance (EPR) is based on the energy transition of a single electron's spin induced by electromagnetic wave absorption in a magnetic field. Additionally, modulation is used to determine the absorption signal's first derivative. Thus, this technique provides a number of types of information, including the spin density distribution. The spin density distribution, or more simply, the location of the unpaired electron, is related to the tensor g values for a species with spin S = 1/2. When the unpaired electron is centered on the metal, the tensor g values vary considerably from the free-electron g_o = 2.0023 value. This is owing to the high spin-orbit coupling constants of transition metals. When empirically measured values of the tensor g are less than 1.95 or higher than 2.10, this is referred to as strong anisotropy. When the electron is restricted to the lighter atoms of the ligand, the lower spin-orbit coupling constants provide a moderate anisotropy in the tensor g, resulting in experimental values comparable to those of the free electron. Measurements of hyperfine coupling between unpaired electrons and atomic nuclei may provide structural information, especially when coupled with DFT calculations.

UV-visible spectroscopy, which is sensitive to electronic transitions, gives a spectral fingerprint for the complex's and ligand's redox state.

Cyclic voltammetry allows the study of the complex's redox properties, giving

information on the reversibility of redox reactions and the values of redox potentials, but does not provide a correct redox state assignment for the ligand.

2.3. The classification of model of reaction induced by non-innocent ligand

The redox state of the non-innocent ligand in a complex was determined by both the center metal atom and the degree of oxidation. According to the previous research, non-innocent ligands affected the stability and reactivity of metal complexes coordinated to the non-innocent ligands due to their unique chemical properties. This strategy has the potential to develop novel catalytic methods. In this section, we will discuss the various catalysis modes of the non-innocent ligand complex. These are critical for comprehending and justifying the reactivity of complexes with non-innocent ligands and newly developed catalytic systems. Bas de Bruin summarized the non-innocent ligand reaction and divided it into four distinct catalyst models.[158] As previously mentioned, the non-innocent ligands could enhance the reactivity of metal-centered complex in four distinct ways. In this section, we selected sample cases to demonstrate each situation. (**Figure 12**)

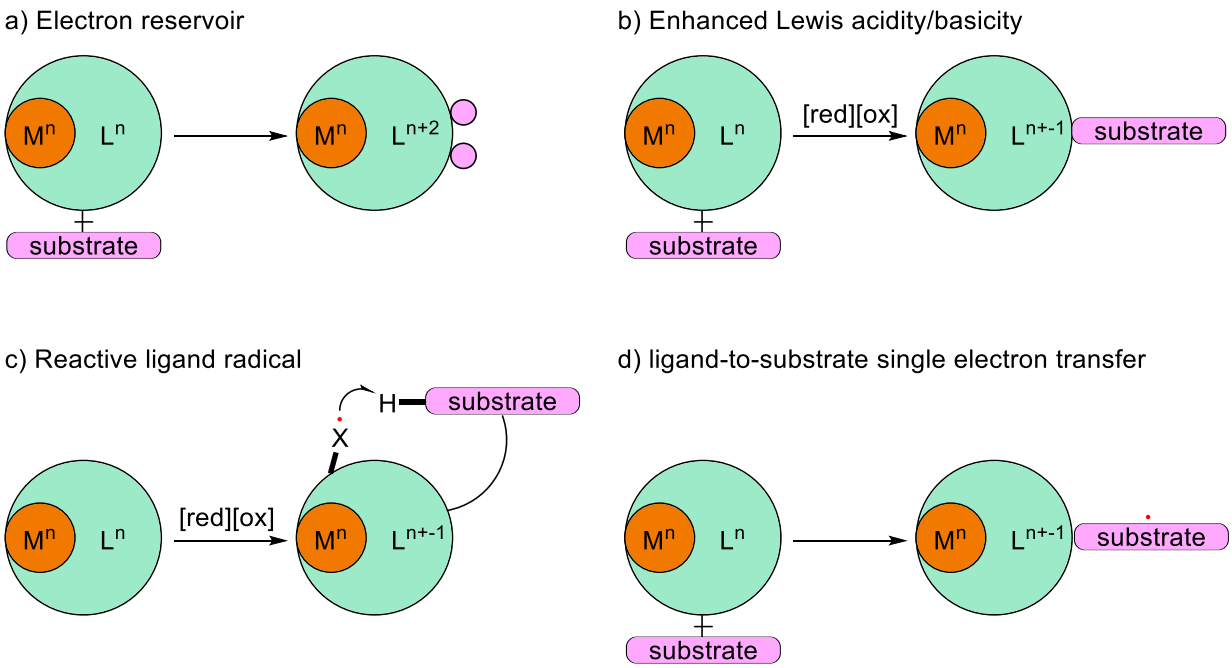

Figure 12. General depiction of four "established" modes (a–d) of redox-active ligand

[158] V. Lyaskovskyy, B. de Bruin, *ACS Catal.* **2012**, *2*, 270–279

reactivity (Scheme adapted from reference)

(a) The ligand can serve as an electron reservoir during the reaction process. Furthermore, the role of the redox ligand allows the complex to store or provide electrons, thus maintaining the most stable oxidation state of the central metal atom or avoiding abnormal oxidation states. Connecting the metal atom with a non-innocent ligand allows to bridge an electronic defect or excess while maintaining the "favorable" oxidation states. It is a frequently used method in the field of non-innocent ligands. So far, this ability of ligands has allowed the discovery of new reactivities.

(b) Alteration of the Lewis acidity or basicity of the center atom of the complex, which can occur via reduction or oxidation of the non-innocent ligand, has a significant effect on the affinity of the metal atom with the substrate.

(c) The reactive non-innocent ligand-radical intermediate can be involved in the formation and dissolution of chemical bonds during the catalysis process. The cooperative substrate can be engaged by the non-innocent redox ligand, and the metal-central complex allows the progression of reactions to obtain the final products

(d) The metal complex serves as a non-innocent redox ligand, activating the substrate into a substrate-radical. This activation can occur as a result of an electron transfer from the ligand to the substrate in certain situations.

2.2.1 The non-innocent ligand serving as a reservoir for electrons

A typical approach in reactions employing non-innocent ligands is to consider the non-innocent ligand as an electron repository. The cooperative effect between the central transition metal atom and the coordinated non-innocent ligands can facilitate the electron exchange between the reaction system and the ‘electron repository’ to retain the favored oxidation degree of the central transition metal atom.

In 2018, Chandan Mukherjee [159] reported that cobalt-(III) complexes **11**-catalyzed isocyanate to corresponding urea conversion under sunlight. In the presence of cobalt-(III)complexes (2.5 mol%) and in dry CH_2Cl_2 under sunlight stimulus, the isocyanate could convert to the corresponding urea derivatives. (**Scheme 105**)

[159] G. C. Paul, S. Ghorai, C. Mukherjee, *Chem. Commun.* **2017**, *53*, 8022–8025.

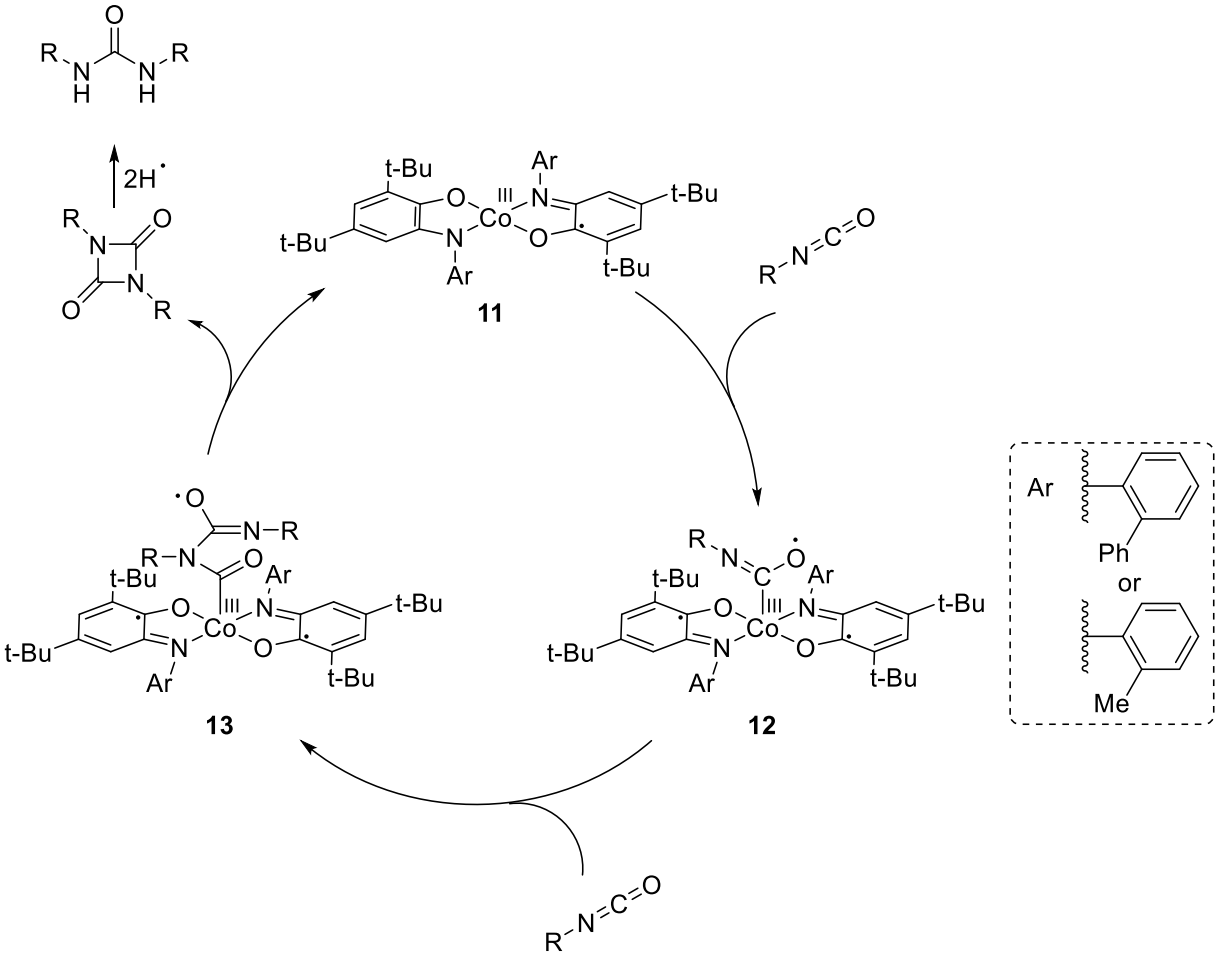

Scheme 105. Formation of an urea derivative from an isocyanate compound and proposed mechanism

Mechanistic investigations suggest that the substrate-bound five-coordinate intermediate **12** and **13** are formed during catalysis (**Scheme 105**). The resultant five-coordinate intermediate **13** can undergo the cleavage of the cobalt-substrate bond to regenerate the cobalt(III) catalyst **11** via the photo-stimulus process. Evidence suggests that the dimerization product of the isocyanate could abstract a hydrogen atom from the solvent molecule and then obtain the urea derivatives.

In 2020, Elham Safaei [160] reported that nickel-(II) complexes catalyzed C–C homocoupling of phenyl acetylene. In the presence of nickel-(II)complexes **14** (3 mol%) and base KOH (2 equiv), phenyl acetylene underwent homocoupling and delivered the desired biphenyl compounds (**Scheme 106**).

[160] M. Nasibipour, E. Safaei, G. Wrzeszcz, A. Wojtczak, *New J. Chem.* **2020**, *44*, 4426–4439.

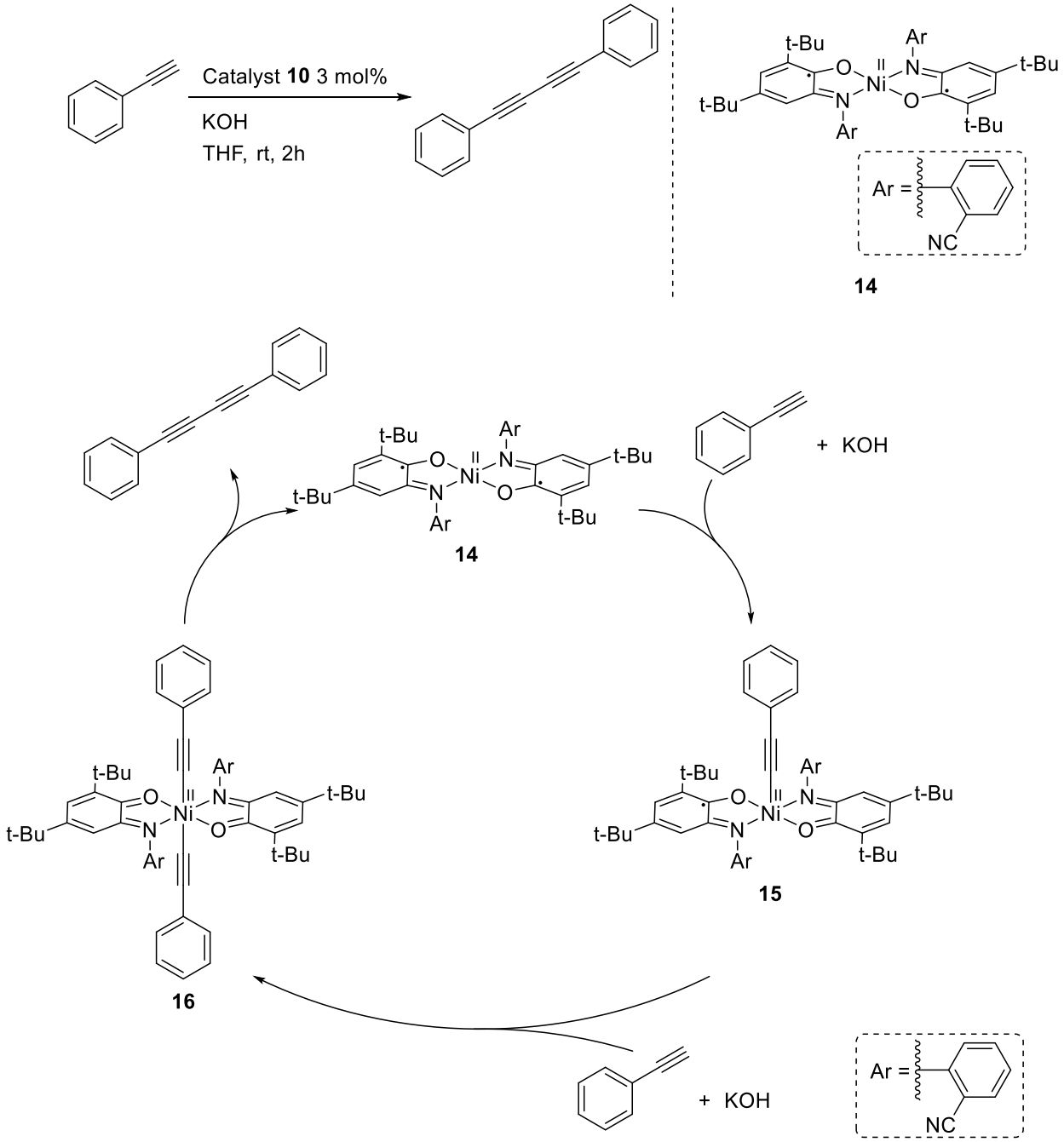

Scheme 106. Nickel-(II) Complexes-catalyzed homocoupling of phenyl acetylene and plausible reaction mechanism.

The proposed mechanism for this homocoupling reaction is outlined in Scheme **106**. Firstly, deprotonation of the phenyl acetylene to the phenyl acetylide generates the five-coordinate intermediate **15**. In the rest step, the deprotonation of phenyl acetylene by KOH yields phenyl acetylide. Then the newly formed acetylide will be coordinated to Ni(II) center,

and one of the iminosemiquinone ligands alters its oxidation state so that the corresponding iminosemiquinonate/iminoquinonate complex **15** could keep the total oxidation state of the complex unchanged. Then the resulted complex **16** is coordinated with the second phenyl acetylide species and forms four coordinate nickel complex **14**.

In 2021, Elham Safaei reported a three-component coupling of aldehyde, alkyne, and amine.[161] In the presence of nickel(II) complexes **17** (3 mol%), aldehydes, alkynes, and amines underwent three-component coupling and delivered the desired biphenyl compounds (**Scheme 107**).

The proposed mechanism for this three-component coupling reaction is outlined in **Scheme 107**. Firstly, the coordination of the alkyne to the nickel(II) complexes **17** generates the five-coordinate intermediate **18**. The oxidation state of non-innocent iminosemiquinone ligands was changed so that the total oxidation state of the whole iminosemiquinonate/iminoquinonate complex **18** was constant. Then the resulted complex **18** transfer alkyne to the imine intermediate that generated from aldehyde and amine could provide the final product and regenerate the catalyst **17**. (**Scheme 107**)

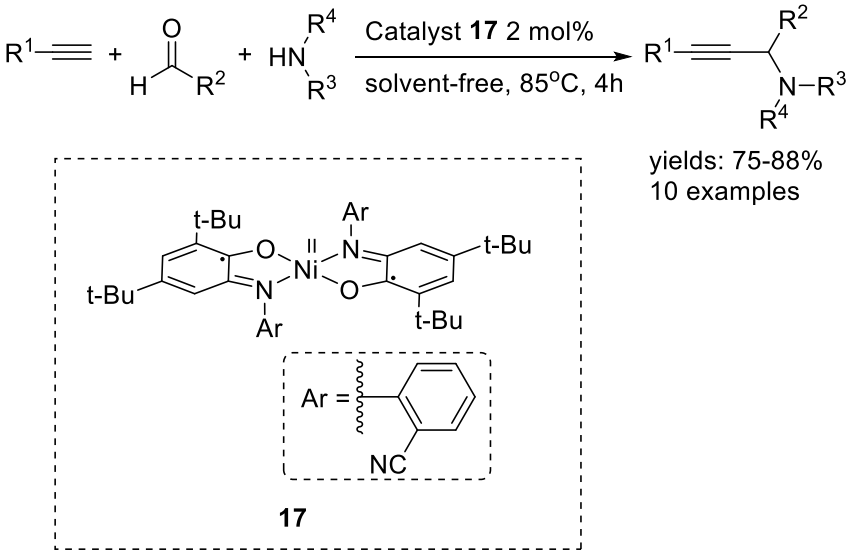

[161] M. Nasibipour, E. Safaei, A. Moaddeli, M. S. Masoumpour, A. Wojtczak, *RSC Adv.* **2021**, *11*, 12845–12859.

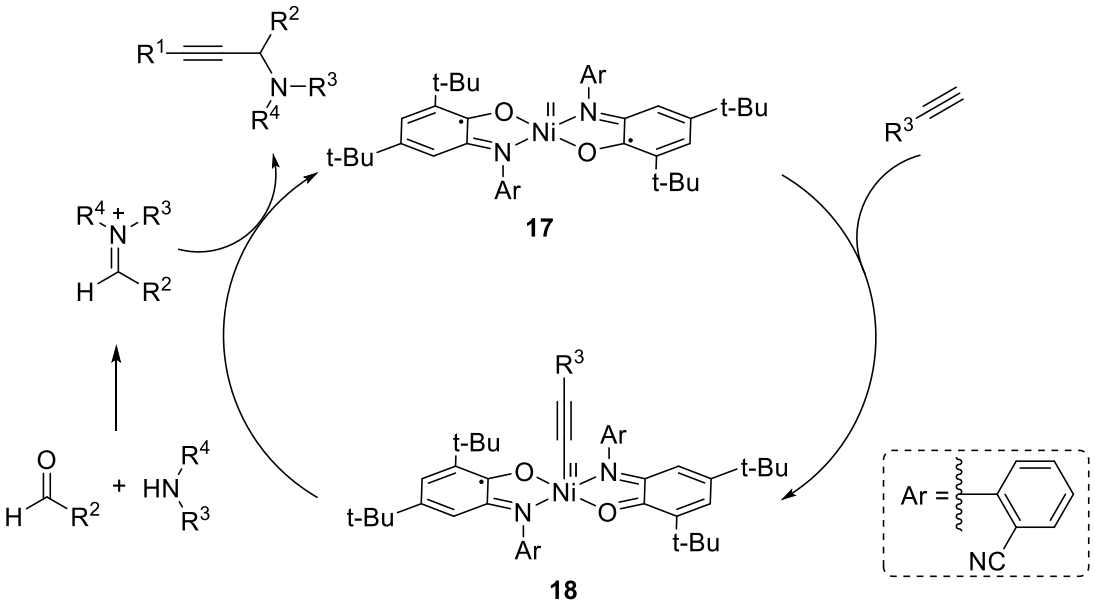

Scheme 107. Nickel(II) Complexes-catalyzed three-components coupling of aldehydes, alkynes, and amines and plausible reaction mechanism.

2.2.2 Adjustment of the Lewis acidity or basicity of a transition metal via modification of the redox state of the ligand

It is essential to note that the Lewis acid property of metal in a complex has a significant impact on the binding energy of the central metal to a non-innocent ligand or substrate in a transition metal complex. Lewis acidity can be switched on and off by altering the redox state of non-innocent ligands, which can exist in a range of oxidation states.

In 2008, the Rauchfuss group[162] reported that an iridium complex **19** bearing a non-innocent ligand amidophenolato ligand could catalytically oxidize dihydrogen through ligand-based oxidation. The non-innocent ligand undergoes single-electron oxidation, forming complex **19**, which may be combined reversibly with dihydrogen to produce complex **20**. When in the presence of a base and an oxidant reagent, complex **20** could oxidize dihydrogen to protons (**Scheme 108**). Based on the result of the kinetic isotope studies, the rate-determining step is the hydrogen bonding to metal.

[162] M. R. Ringenberg, T. B. Rauchfuss, *Eur. J. Inorg. Chem.* **2012**, *2012*, 490–495.

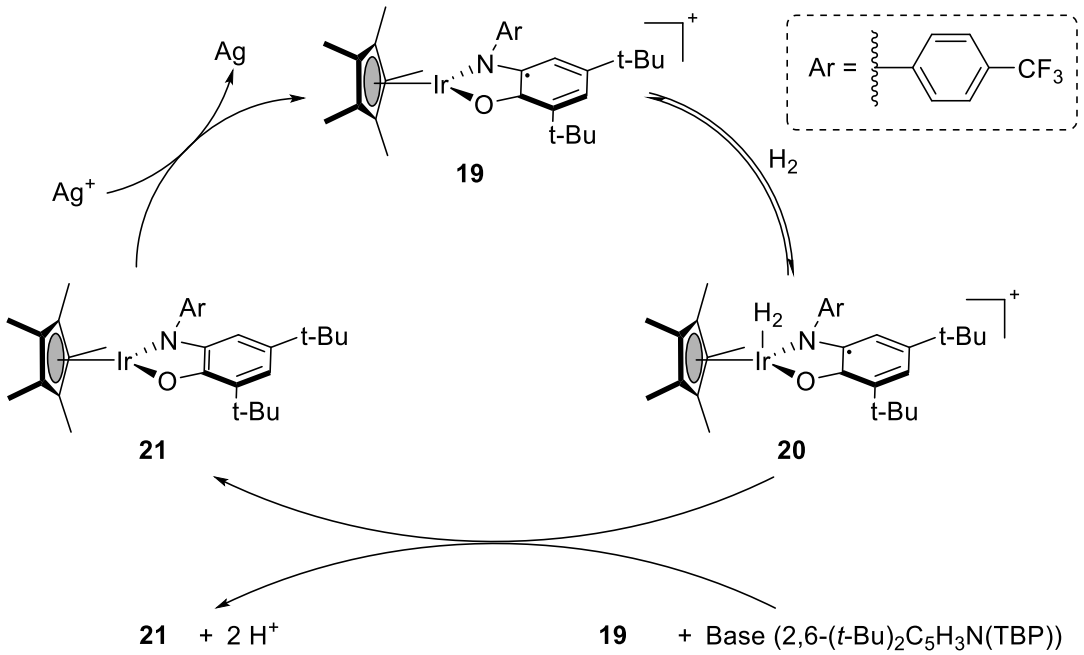

Scheme 108. Redox-switchable Lewis acid 19 catalyzed dihydrogen oxidation

Iridium complexes have been used previously by Rauchfuss, inspiring by the pioneering work, a natural progression has been made by Sarkar and co-workers[163]. The completely reduced form of the iridium complex, which was coordinated to a diaminobenzene ligand framework, was used to demonstrate dihydrogen activation.

In the beginning, two-electron oxidation of the non-innocent ligand provides an iridium complex **23** with the increased Lewis activity, which can reversibly combine with dihydrogen to form the intermediate. *p*-Benzoquinone can react with the dihydrogen complex **24** to generate the protonated species and an iridium-hydride complex **25**. Furthermore, the iridium hydride complex **25** hydride transfers the hydride to the protonated *p*-benzoquinone, giving 1,4-dihydroxybenzene and renewing the active catalyst **23**. (**Scheme 109**)

[163] S. Sobottka, M. B. van der Meer, E. Glais, U. Albold, S. Suhr, C.-Y. Su, B. Sarkar, *Dalt. Trans.* **2019**, *48*, 13931–13942.

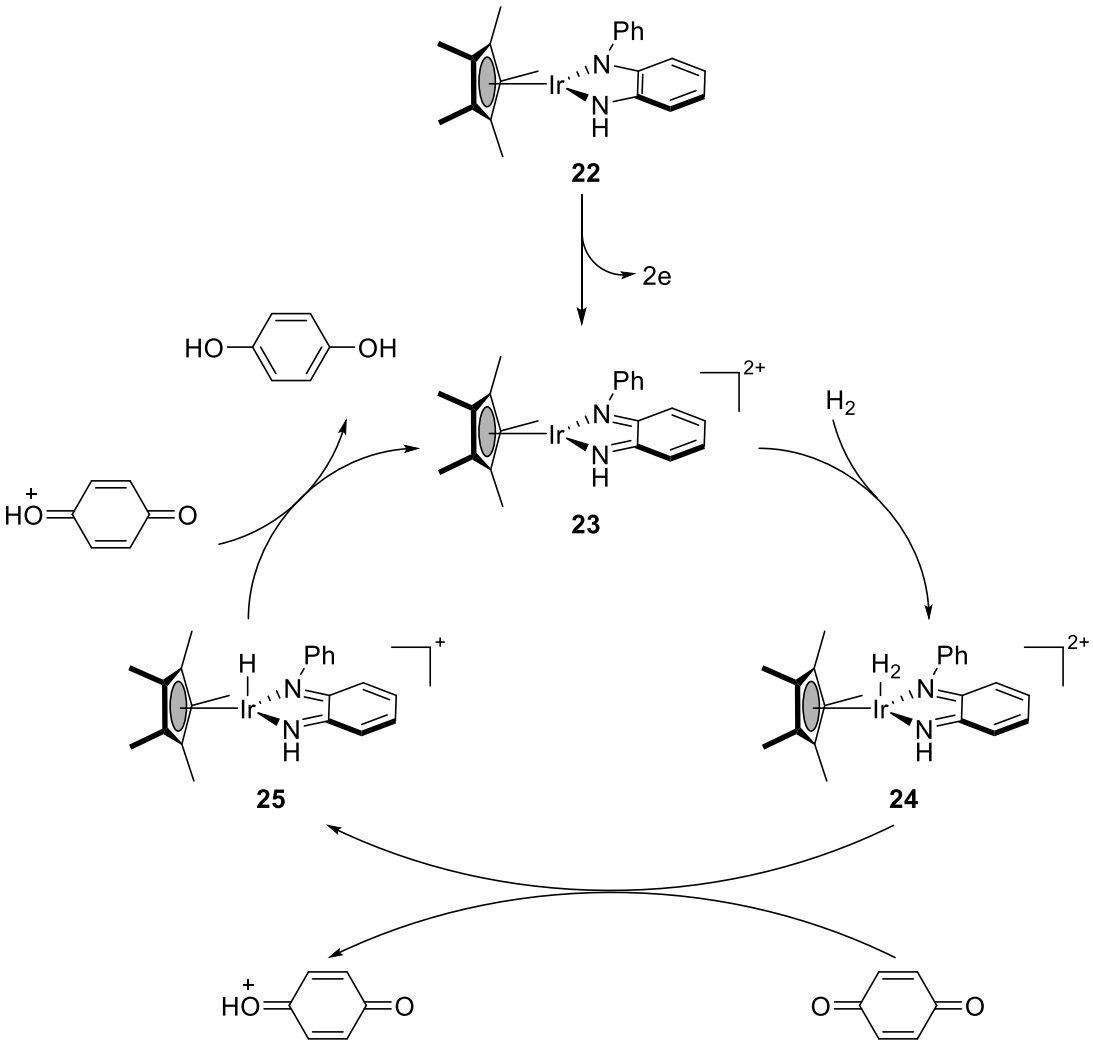

Scheme 109. Hydrogenation of quinone to 1,4-dihydroxybenzene

2.2.3 The single electron transfer process to the substrate

In 2015, the van der Vlugt group reported the potential Pd catalyst via activation of the corresponding palladium(II) precursor. The palladium(II) precursor was coordinated to a tridentate aminophenol-based NNO ligand resulting in a square plane paramagnetic Pd(II) complex **26** with a radical centered on the ligand which can be reduced to a diamagnetic complex **27** via single-electron reduction. Complex **27** may activate aliphatic azide through intramolecular non-innocent ligand-to-substrate single electron transfer to produce a nitrene radical intermediate **28**, and the matching pyrrolidine **29** was found. (**Scheme 110**)

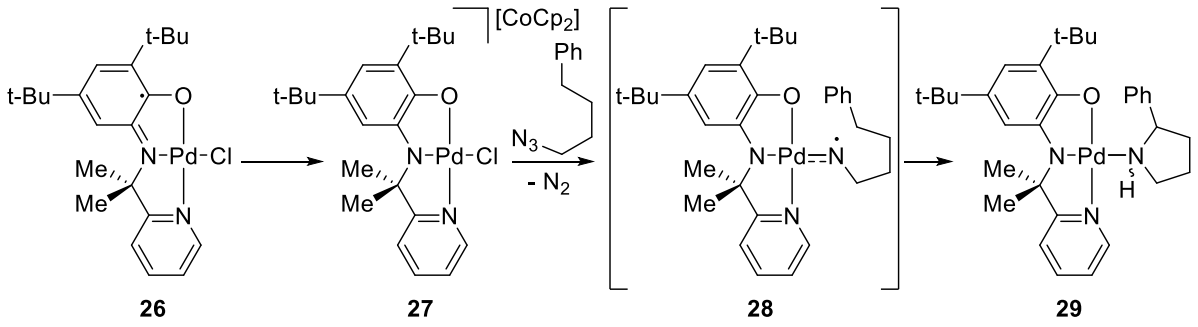

Scheme 110. Reduction of complex **26** and its ability to generate a reactive substrate-centered radical

The Pd(II) complex **30** catalyzed C(sp^3)−H amination of aliphatic azide lays the groundwork for the further utilization of the Pd(II) complex coordinated to the non-innocent pyridine–aminophenol ligand (NNO ligand). Inspired by this pioneering work, The van der Vlugt group [164] recently reported a bench-stable iron(III) complex with a non-innocent pyridine–aminophenol ligand. Moreover, the iron(III) catalyst could be utilized for direct C(sp^3)−H amination of alkyl azides to N-containing heterocyclic compounds with considerable development of turnover numbers (TONs). (**Scheme 111**)

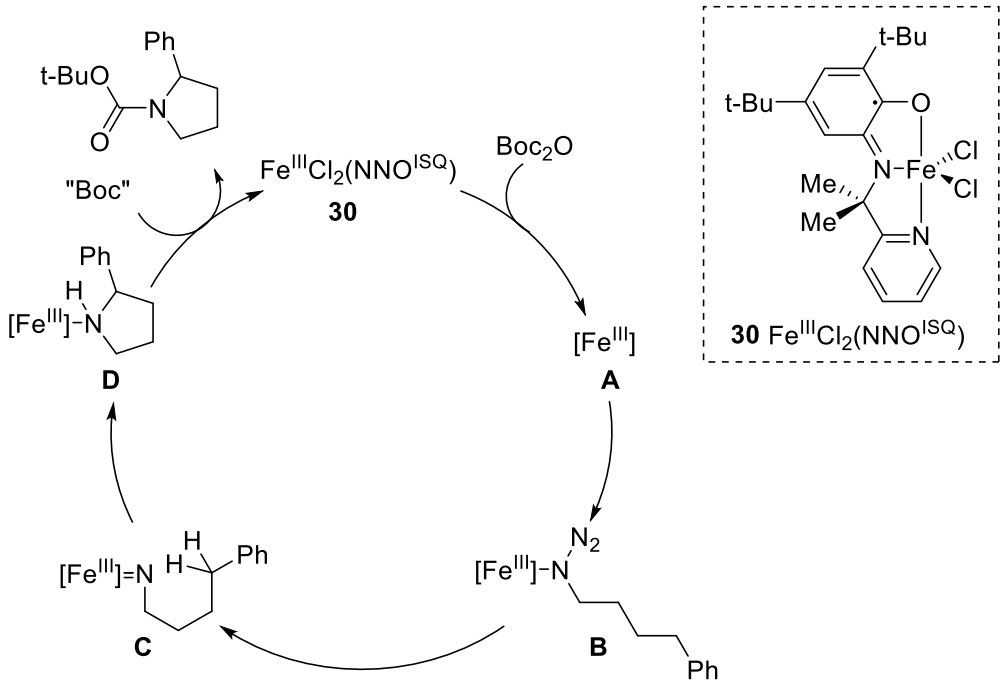

Scheme 111. Complex **30** catalyzed a reactive substrate-centered radical direct C(sp3)−H amination of aliphatic azides to N-heterocycles

[164] B. Bagh, D. L. J. Broere,V.Sinha, P. F. Kuijpers, N. P. van Leest, B. de Bruin, S. Demeshko, M. A. Siegler, J. I. van der Vlugt, *J. Am. Chem. Soc*. **2017**, *139*, 5117–5124

During the experiment, the authors noted that the generation of reaction intermediate **A** resulting from the presence of the Boc_2O. The mechanism research reveals that the rate-determining step in the overall C(sp3)-H amination process of Boc_2O, according to first-order kinetics, is a reaction with Boc_2O. Based on the observed kinetic data and the experiment facts, they suggested a plausible mechanism involving the activation of the Fe(III) catalyst. In the beginning, initial activation of complex **30** by Boc_2O at elevated temperature provides the Fe^{III} complex **A** with increased reaction activity, which can combine with azide substrate to form the intermediate **B**. Subsequent N_2 elimination of **C** could generate iron(III)-nitrenoid species **D**. The intermediate Fe(III)-(pyrrolidine) adduct **30** is generated through direct nitrene insertion or H atom abstraction. Finally, a Boc-containing species ("Boc" in **Scheme 111**) derivated from its chloride or dicarbonate can react with Fe(III)-(pyrrolidine) intermediate **30** to generate the final products and regenerated catalyst.

In 2018, the Shinobu group[165] reported that a square planar rhodium(III) complex **31** bearing amidophenolate redox-active ligands could catalyze C−H amination of xanthene with tosyl azide (TsN_3). (**Scheme 112**)

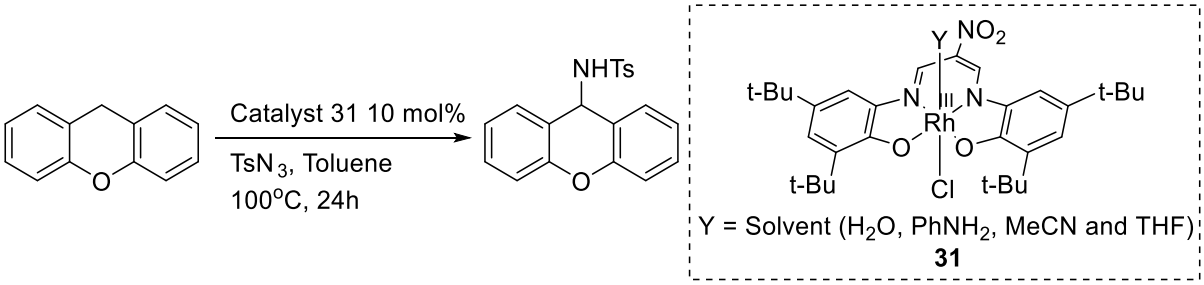

Scheme 112. Rh(II) complex-catalyzed amination of xanthene A

They proposed a mechanism that involves the complex-catalyzed amination of xanthene with distal size selectivity. The catalytic sequences include the transformation of nitrene-radical-bound to the rhodium(III) complex **31**, the amination reaction of the external substrate xanthene **A** and generation and migration of nitrene-radical intermediate •NTs. They proved that rhodium(III) intermediate **32** could be formed via a single-electron-transformation process from the non-innocent tetradentate ligand to the nitrogen atom of nitren. (**Scheme 113**)

[165] D. Fujita, H. Sugimoto, Y. Morimoto, S. Itoh, *Inorg. Chem.* **2018**, *57*, 9738–9747.

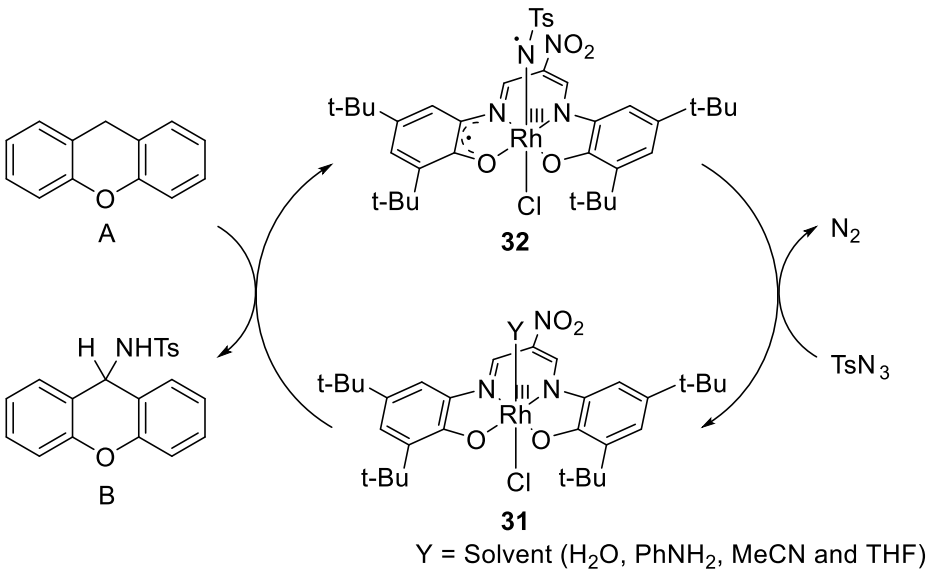

Scheme 113. Rhodium(III)-catalyzed amination of xanthene with TsN_3 and plausible reaction mechanism.

2.2.4 Cooperative reactivity assisted by the innocent ligand

The Wieghardt group demonstrated their pioneer work[166] of the non-innocent ligand tetradentate *o*-aminophenol covalently bonded to Cu(II) and Zn(II) to activate the primary hydroxyl group to provide the corresponding product. Either Cu(II) or Zn(II) complex was also regarded as an efficient catalyst for bond activation. They discovered that **33** (M-Cu, Zn) catalyst was capable of oxidizing primary alcohols rapidly to aldehydes and H_2O_2 (**Figure 112**). The catalyst **33** and a compound containing the hydroxyl group establish a quick equilibrium in the first step, in which the proton was transferred from the hydroxyl group to phenoxide of the tetradentate *o*-aminophenol ligand. The complex coordinated with the alkoxide to produce **34**. The rate-determining step, according to isotope labeling studies, was the H-atom abstraction by the oxygen of the aminophenol ligand to generate intermediate **35**. The protonated complex **35** underwent a fast intramolecular single-electron transfer, resulting in a bonded aldehyde. When the reduced complex **36** was oxidized by dioxygen, H_2O_2 was produced, as well as the active catalyst **33**. (**Scheme 114**)

[166] P. Chaudhuri, M. Hess, J. Müller, K. Hildenbrand, E. Bill, T. Weyhermüller, K. Wieghardt, *J. Am. Chem. Soc.*, **1999**, *121*, 9599–9610.

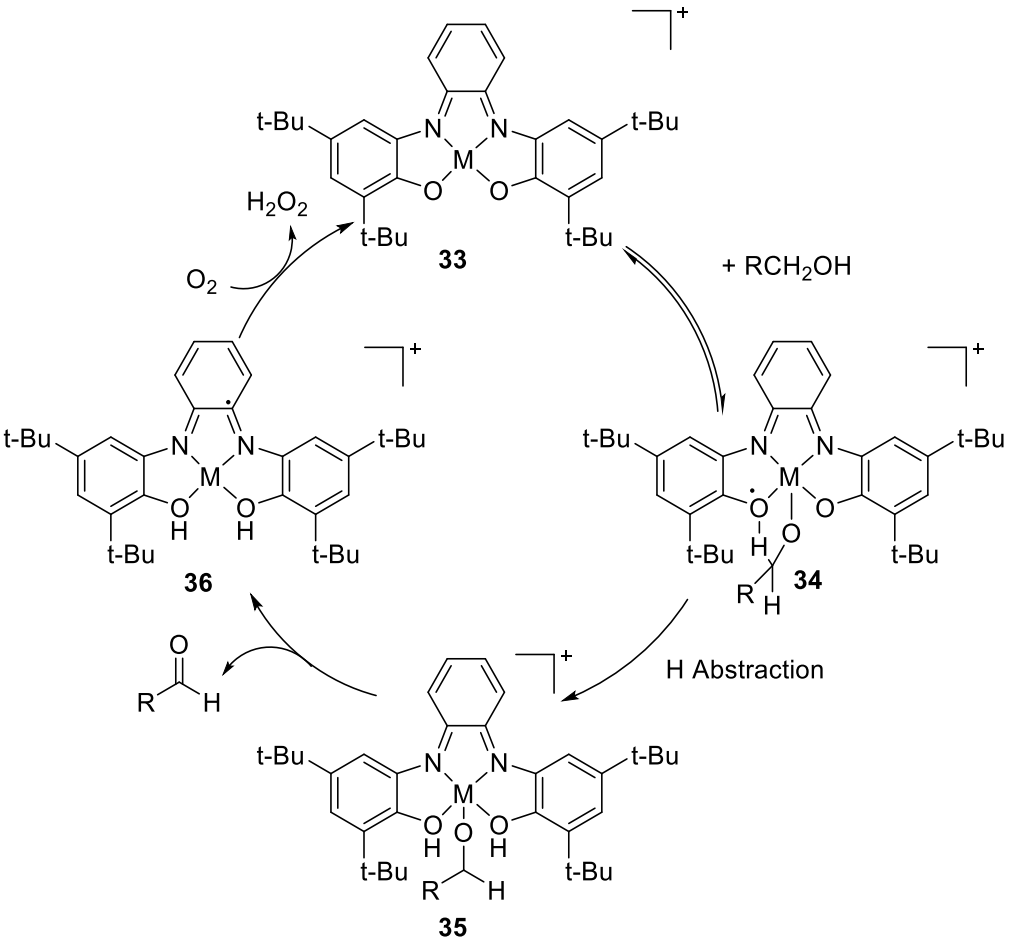

Scheme 114. Cu/Zn Complex **33** catalyzed oxidation of primary alcohols utilizing dioxygen as the oxidant.

P. Chaudhuri[167] found that the cooper complex could oxidize the main alcohol to produce the equivalent aldehyde due to the presence of a phenoxyl radical on the ligand. Copper complex **37** catalyzes the oxidation of primary alcohols in the presence of dioxygen. The mechanism suggests the first stage of coordination of copper(II) with alcohol, followed by hydrogen elimination through the phenoxyl radical, which is the reaction's kinetic determinant. Finally, the aldehyde is formed when copper(II) **39** is reduced to copper(I) **40**. Dioxygen regenerates the original species when it is reduced to hydrogen peroxide. (**Scheme 115**)

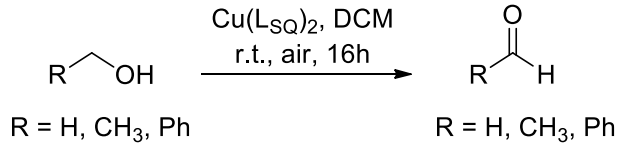

[167] C. Mukherjee, U. Pieper, E. Bothe, V. Bachler, E. Bill, T. Weyhermüller, P. Chaudhuri, *Inorg. Chem.*, **2008**, *47*, 8943–8956.

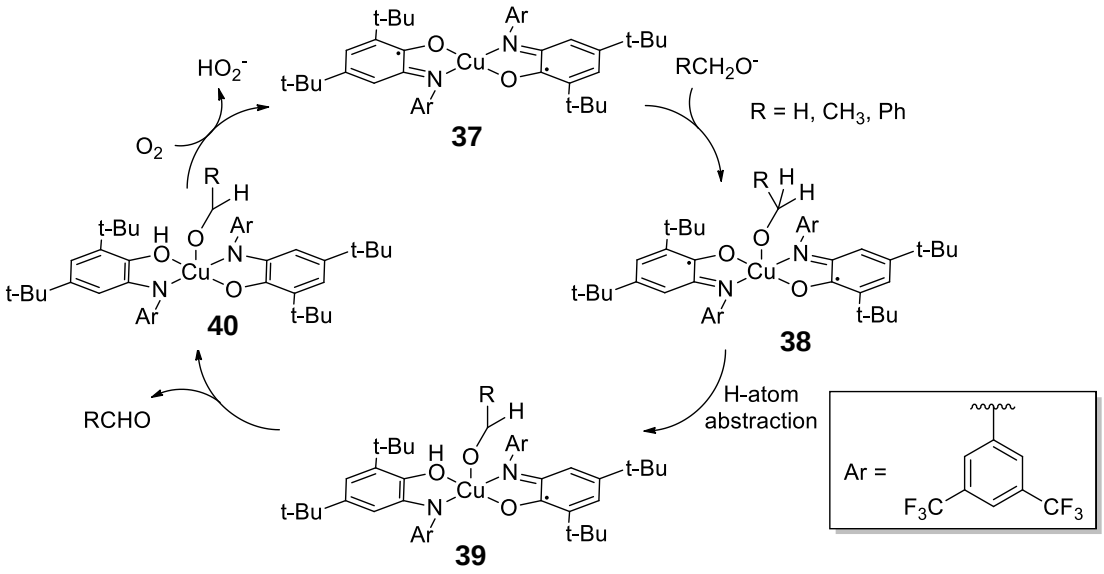

Scheme 115. Copper-catalyzed oxidation of primary alcohols and the mechanism

Chemists have used the many mechanisms of action of non-innocent ligands to perform a broad range of transformations. The non-ligand innocent has the potential to change the normal behavior of a metal in various ways, for example, by giving a noble character to a metal that is not noble or a radical reactivity to a metal that prefers bioelectronic processes. Non-innocent ligands are critical for comprehending the behavior of complexes controlled by redox ligands in relation to a particular kind of reagent (oxidant, acid, nucleophile and so on). Other systems, such as cross-coupling, may be used to essential transformations in organic synthesis, although the catalytic development conditions for many of these systems remain a problem.

As can be seen, redox-active ligands have attracted much interest because of their potential to conduct physiologically inspired changes and have been used in various synthetic applications.

2.2.5 Various applications by our group

At room temperature and in the presence of Ar, the complex $[Cu(L_{SQ})_2]$ **41** can react with one equivalent of the Umemoto reagent in CH_2Cl_2, forming the $[Cu(L_{BQ})_2CF_3]$ complex **42**. After establishing the synthesis of the $[Cu(L_{BQ})_2CF_3]$ complex, pulsed EPR studies verified the existence of the trifluoromethyl ligand. The $[Cu^{II}(L_{BQ})_2CF_3]$ complex **42** was unable to withstand spin-trapping tests with TEMPO, and therefore no CF_3-TEMPO adduct was

detected in this experiment. They hypothesized that this compound, which is derived from CF_3^+, promotes trifluoromethylation at electrophilic sites. (**Scheme 116**)

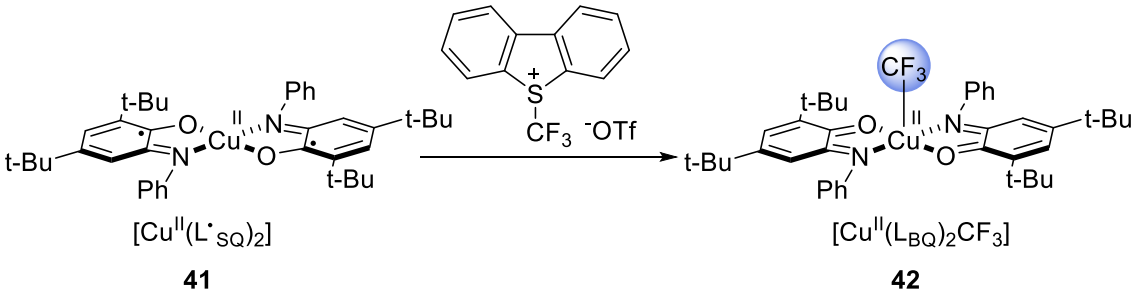

Scheme 116. Synthesis of the intermediate $[Cu(L_{BQ})_2CF_3]$ complex

It was discovered that electrophilic CF_3 sources such as the Togni II reagent could be reduced to form radicals using the copper complex $Cu(L_{SQ})_2$. Spin-trapping studies were carried out using TEMPO and stoichiometric quantities of the Togni II reagent and copper complex. The adduct CF_3-TEMPO may be produced in 69% yield from the Togni II reagent in DCM after 3 hours. (**Scheme 117**)

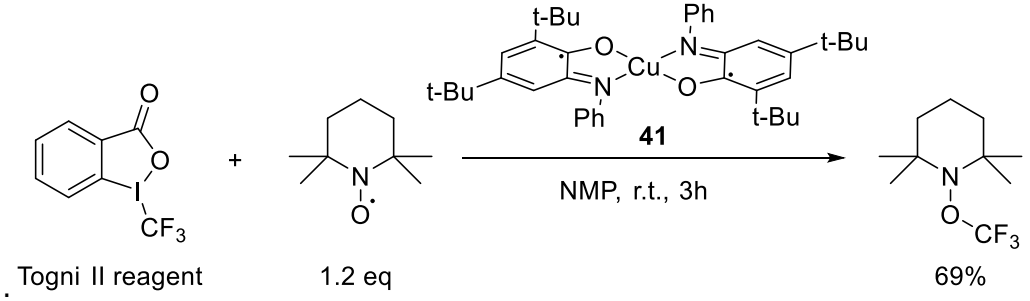

Scheme 117. Radical-trapping experiment of the trifluoromethyl group from Togni II reagent utilizing TEMPO as the scavenger

With the production of the trifluoromethyl radical in mind, radical addition studies were carried out using the copper complex $Cu(L_{SQ})_2$ in a catalytic loading. The scope of the reaction could be rapidly expanded as a result of this finding; the trifluoromethyl radical produced by reduction of the Togni II reagent may react with the alkenes or alkynes in NMP, as well as with heteroaromatic compounds such as pyrroles, indoles, or furans in DCM. (**Scheme 118**)

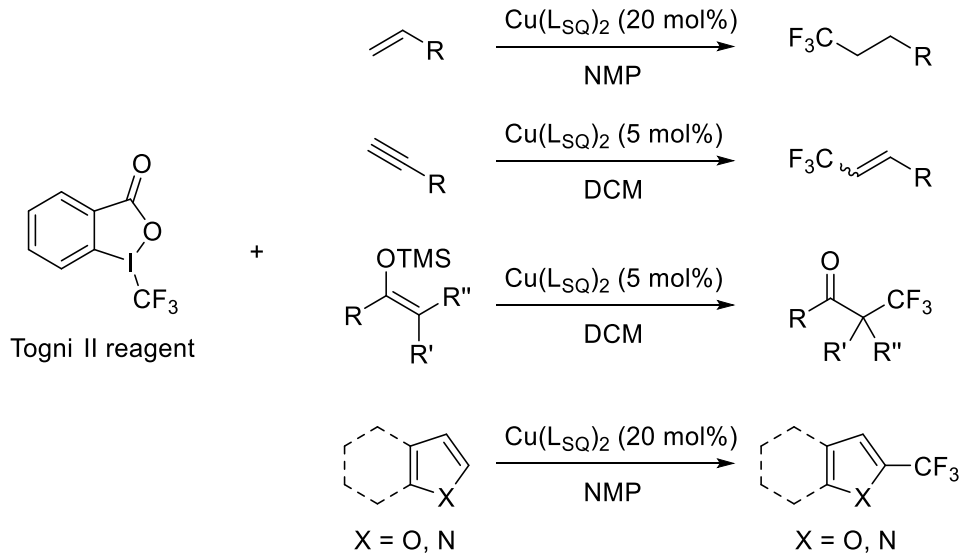

Scheme 118. The radical trifluoromethylation reactions under the catalysis of the copper complex Cu(L$_{SQ}$)$_2$

The [Cu(L$_{SQ}$)$_2$] complex's use was expanded to include the aziridination of alkenes[168]. The aziridination of substituted styrene with sulfonyl azide was reported using a copper catalyst. The compound [Cu(L$_{SQ}$)$_2$] **41** was shown to be the most effective catalyst. The NTs radical formed during the reduction of PhINTs can be added to an alkene in DCM. The reaction demonstrated a wide scope of functional group tolerance. The complex was suggested to perform the single-electron reduction of the PhINTs to create the nitrene radical, which was then trapped by the copper complex to form the intermediate mono-nitrene **A**, which was then added to the olefin for the generation of alkyl radical. The product is produced after another nitrene radical abstraction on PhINTs, and the complex **B** can then undergo a SET procedure to renew the catalyst **A**. (**Scheme 119**)

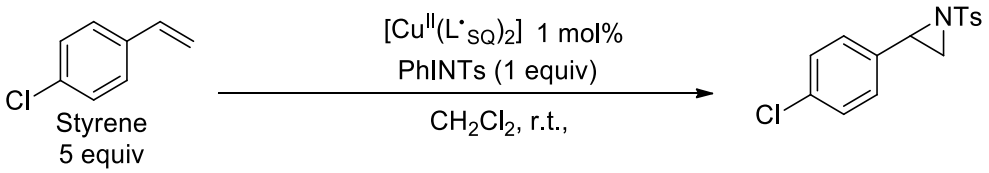

[168] Y. Ren, K. Cheaib, J. Jacquet, H. Vezin, L. Fensterbank, M. Orio, S. Blanchard, M. Desage-El Murr., *Chem. Eur. J.* **2018**, *24*, 5086 – 5090

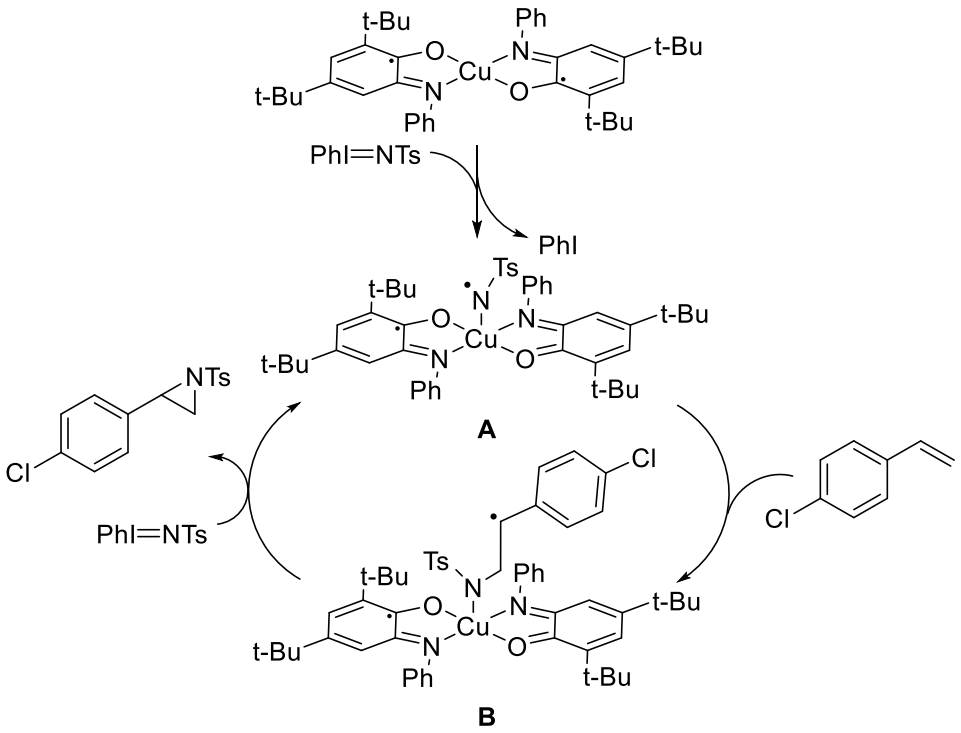

Scheme 119. The radical aziridination reaction employing [Cu(L_{SQ})$_2$] **184** as catalyst and mechanism

Based on the previous research, our group improved the reaction efficiency [169], using a more constrained non-innocent ligand that allowed copper complex **43** to transfer nitrogen- and carbon-centered groups in as little as two minutes, resulting in a significant boost in reactivity when compared to the unconstrained copper complex. (**Scheme 120**)

[169] Y. Ren, J. Forté, K. Cheaib, N. Vanthuyne, L. Fensterbank, H. Vezin, M. Orio, S. Blanchard, M. Desage-El Murr, *iScience* **2020**, *23*, 100955.

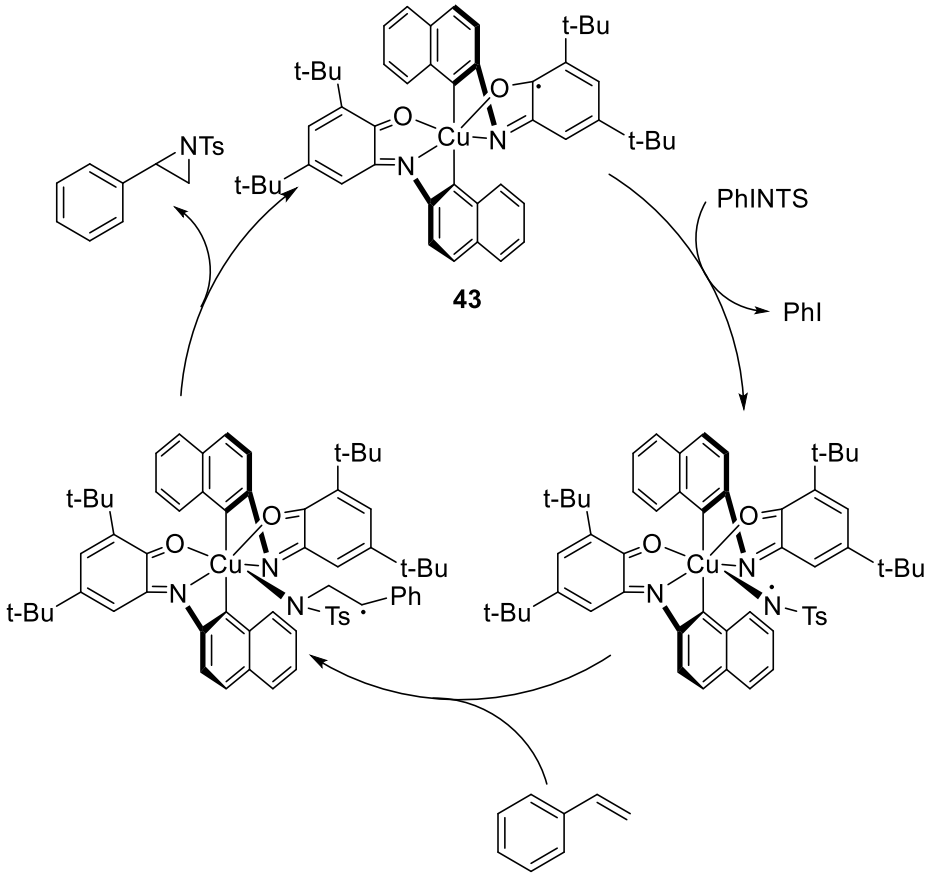

Scheme 120. The proposed mechanism of copper-catalyzed aziridination of alkene.

The scope of the [Cu(L_{SQ})$_2$] complex **43** was further extended to include the cyclopropanation of alkene. The EDA could be regarded as the resource of the carbene group.

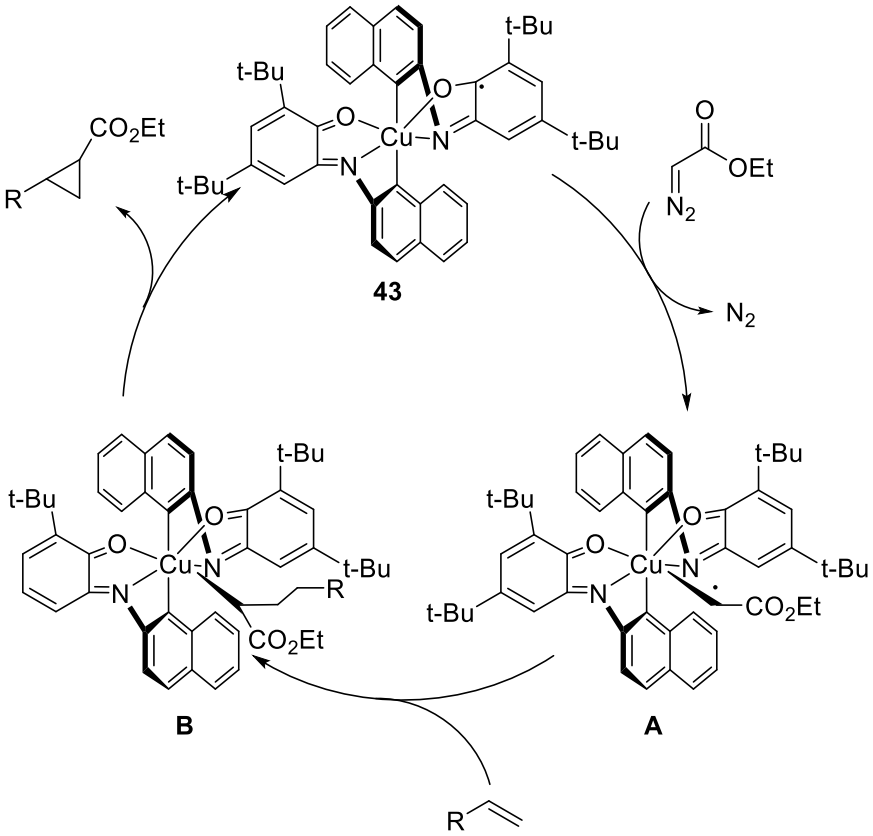

Scheme 121. The proposed mechanism of copper-catalyzed cyclopropanation of alkene.

Intermediate **A** was formed when the carbene group was inserted on initial complex **43**, and the high coordinative constrain and torsion structure of the copper complex **43** was feasible of generating the reactive group. Intermediate **A** subsequently underwent alkene insertion to yield species **B**, and released the carbon-transfer product upon ring-closure.

3. Non-innocent copper complexes-mediated oxidation of silicates

Inspired by these catalytic processes, we envisioned developing copper-mediated catalytic oxidation of alkyl bis-catecholato silicates. Copper complexes$[Cu(L_{BQ})_2(OTf)_2]$ **44** coordinated by non-innocent ligands o-benzoquinone will be prepared by oxidation from $[Cu(L_{SQ})_2]$ complexes (See **Scheme 122**). Concerning the redox properties of $Cu(L_{SQ})_2$, cyclic voltammetry will be used to determine the redox potential and the ability of these complexes to be reduced and to oxidize the silicates.

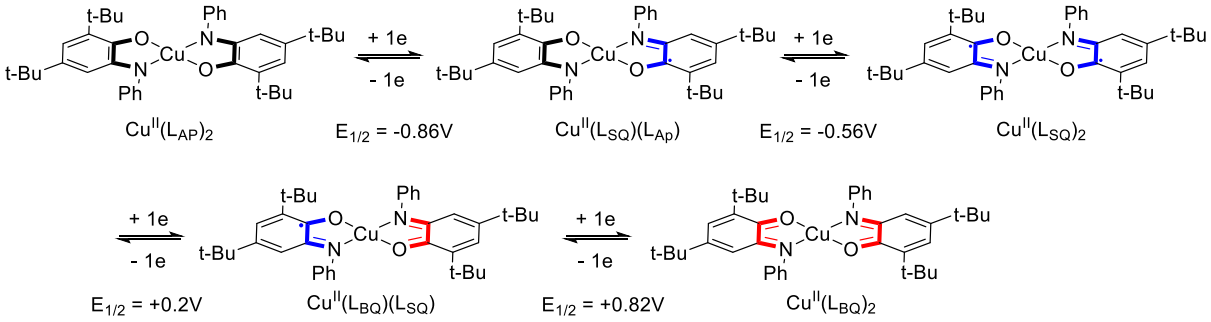

Scheme 122. Redox properties of $Cu(L_{SQ})_2$

3.1 Results and discussions

Synthesis of the complex $[Cu(L_{BQ})_2(OTf)_2]$ 44 from $[Cu(L_{SQ})_2]$ 41

The reaction of $[Cu(L_{SQ})_2]$ **41** with dibrome (Br_2) as oxidizing agent followed by the metathesis with silver trifluoromethanesulfonate (AgOTf) can lead to the formation of the corresponding $[Cu(L_{BQ})_2(OTf)_2]$ (**Scheme 123**). After filtration, $[Cu(L_{BQ})_2(OTf)_2]$ **44** can be isolated in moderate yield.

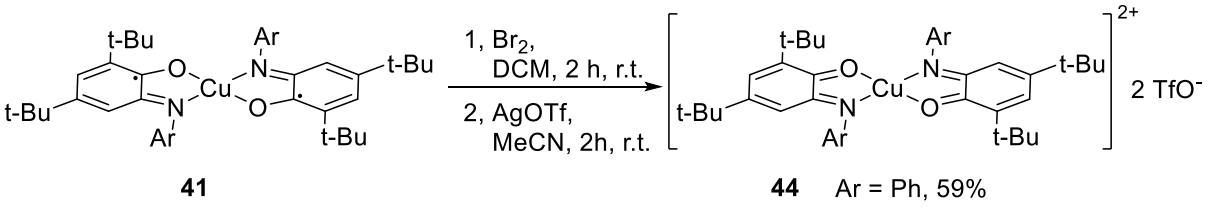

Scheme 123. Preparation of the complex $[Cu(L_{BQ})_2(OTf)_2]$ **44**

Application to the oxidation of anilinomethyl silicate and optimization of the process

Since the anilinomethyl silicate **45** has a low oxidation potential ($E_{1/2}^{ox}$ = +0.34 V *vs* SCE in DMF), the substrate is easily oxidized to produce the appropriate α-aminomethyl radical. Based on the oxidative potential of the copper complex $Cu(L_{BQ})_2(OTf)_2$ **44** ($E_{1/2}^{ox}$ = +0.82 V *vs* SCE in DCM), we anticipated that the copper complex would oxidize the silicate, thus producing the appropriate radical which can be trapped by a suitable radical acceptor

We began by studying the model allylation reaction between anilinomethyl silicate **45** and allyl sulfone **2** as a radical trap in different solvents. The use of a catalytic amount of

$Cu(L_{BQ})_2(OTf)_2$ **44** (10 % mol) in NMP as solvent provided a low yield (9%) (Table 6, entry 1). However, by changing the nature of the solvent to acetonitrile, a 15 % yield of the desired product was obtained (entry 2). The yield of **46** was improved to 18 % by running the process in THF or DCM (entry 3 or entry 4). Compared to other halide solvents, $CHCl_3$ was shown to be favorable to the reaction leading to a 19% yield (entry 5) but to only 11% in DCE (entry 6). We then selected DCM as the optimized solvent. By increasing the amount of **2** to 6 equivalents，a 25% isolated yield of **46** (entry 5). The catalyst was also subjected to a control experiment. The copper catalyst $Cu(L_{BQ})_2(OTf)_2$ **44** is necessary for the reaction to proceed, and no product can be obtained in the absence of $Cu(L_{BQ})_2(OTf)_2$ **44** (entry 8)**.** The copper catalyst in stoichiometric amount (1 equiv) was found to be detrimental no product was observed (entry 9). Excess of copper catalysts could provide the rapid generation of the corresponding radicals, and a series of radical-mediated side reactions caused this phenomenon.

Table 6. Optimization of copper-mediated oxidation of anilinomethylsilicate

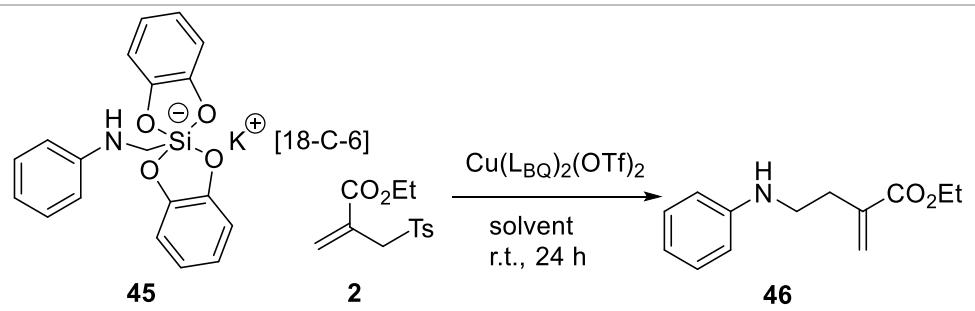

45 **2** **46**

0.2 mmol
1.0 equiv

Entry[1]	Tosylate	Solvent	Catalyst	Yield
1	4 eq	NMP	$Cu(L_{BQ})_2(OTf)_2$	9%
2	4 eq	MeCN	$Cu(L_{BQ})_2(OTf)_2$	14%
3	4 eq	DCM	$Cu(L_{BQ})_2(OTf)_2$	18%
4	4 eq	THF	$Cu(L_{BQ})_2(OTf)_2$	18%
5	4 eq	$CHCl_3$	$Cu(L_{BQ})_2(OTf)_2$	19 %
6	4 eq	DCE	$Cu(L_{BQ})_2(OTf)_2$	11%
7	6 eq	DCM	$Cu(L_{BQ})_2(OTf)_2$	25%[2]
8[3]	4 eq	DCM	$Cu(L_{BQ})_2(OTf)_2$	No product
9[4]	4 eq	DCM	$Cu(L_{BQ})_2(OTf)_2$	No product

1. Reaction conditions: **45** (0.2 mmol), **2** (0.8 mmol) and copper catalyst $Cu(L_{BQ})_2(OTf)_2$ (10 % mol) in solvent (2 mL) at room temperature under argon atmosphere stirring for 24 h. 2. Isolated yield by chromatography. 3. No Copper catalyst $Cu(L_{BQ})_2(OTf)_2$ **44** (1 equiv)was used. 4. Copper catalyst $Cu(L_{BQ})_2(OTf)_2$ **44** (1 equiv) was used.

The optimization of the copper complex

A viable approach to improve the reactivity of the system would be a synthetic modification of the catalyst to obtain a suitable redox potential. Due to the favorable electrochemical potential of copper bis-iminosemiquinonate complexes $Cu(L_{SQ})_2$ with modified *t*-butyl or CF_3 moieties ($E_{1/2}^{ox}$ [$Cu(L_{SQ})_2$ (3,5-di-*t*-Bu-substituted)] = + 0.97 V vs SCE and $E_{1/2}^{ox}$ [$Cu(L_{SQ})_2$ (4-CF_3-substituted)] = + 0.84 V vs SCE respectively)[170], we

[170] C. Mukherjee, U. Pieper, E. Bothe, V. Bachler, E. Bill, T. Weyhermüller, P. Chaudhuri, *Inorg. Chem.* **2008**, *47*, 8943–8956.

prepared different derivatives of $Cu(L_{BQ})_2(OTf)_2$ **44** via inserting electron-withdrawing or electron-donor substituents into the side phenyl group of $Cu(L_{BQ})_2(OTf)_2$ **44**.

The preparation of the derivatives of $Cu(L_{SQ})_2$ can be divided into two steps. The first step is the synthesis of the aminophenol ligand by reaction of 3,5-di-tert-butylcatechol with the substituted aniline in the presence of trimethylamine (Et_3N). After precipitation, the aminophenol ligand is isolated by filtration. The second step is the complexation reaction of copper (I) chloride with the aminophenol ligands at air atmosphere. The aminophenol ligands are oxidized to iminosemiquinonate and copper (I) to copper (II), thus leading to the $Cu(L_{SQ})_2$ complex (**Scheme 124**). According to the general procedure of preparing $Cu(L_{BQ})_2(OTf)_2$ **44** with dibrome (Br_2) (see **Scheme 123** and experiment part), we can prepare the derivatives of $Cu(L_{BQ})_2(OTf)_2$ **44a** and **44b**.

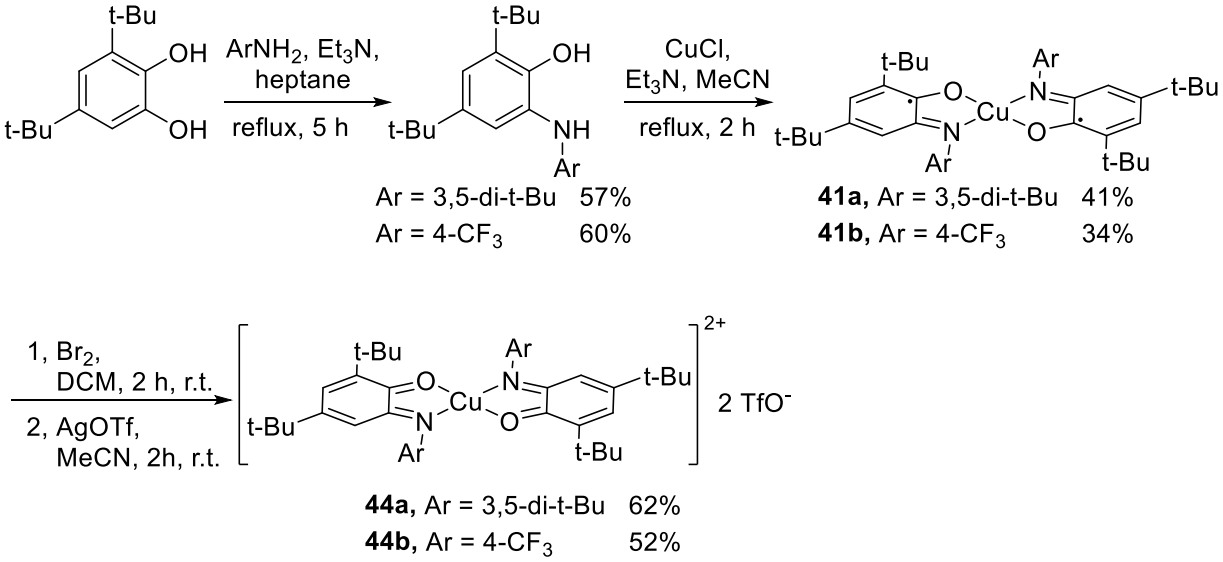

Scheme 124. The preparation of $Cu(L_{SQ})_2$ complex derivatives **44a** and **44b**

We then measured the electrochemical potentials of the 4-CF_3-substituted **44a** and 3,5-di-*t*-Bu-substituted **44b** copper(II) catalysts which are listed in Table 8. The oxidation potential of analogous complex **44a** and **44b** ($E_{1/2}^{ox}$ = +0.69 V *vs* SCE, in DCM) is slight lower than $Cu(L_{BQ})_2(OTf)_2$ **44** ($E_{1/2}^{ox}$ = +0.82 V *vs* SCE, DCM) .

Table 7. The electrochemical potentials of copper complex $Cu(L_{BQ})_2(OTf)_2$ **44** and its derivatives **44a** and **44b** in DCM.

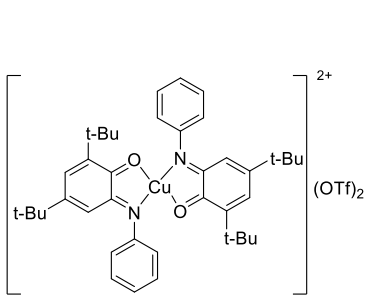

$Cu(L_{BQ})_2(OTf)_2$ **44**
(unsubstituted)

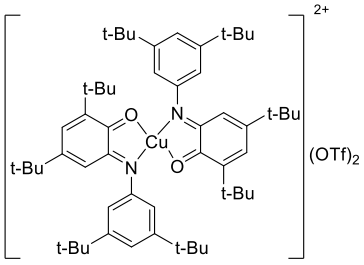

$Cu(L_{BQ})_2(OTf)_2$ **44 a**
(R = 3,5-di-t-Bu)

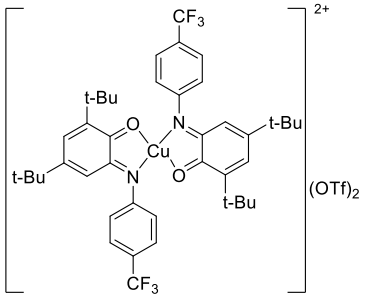

$Cu(L_{BQ})_2(OTf)_2$ **44 b**
(R = 4-CF_3)

Complex (substituent)	$E_{1/2}^{(ox2)}$	$E_{1/2}^{(ox1)}$	$E_{1/2}^{(red1)}$	$E_{1/2}^{(red2)}$
44 (unsubstituted)	+0.82	+0.17	-0.55	-0.84
44a (3,5-di-*t*-Bu)	+0.69	+0.07	-0.7	-1.02
44b (4-CF_3)	+0.69	+0.31	-0.45	-0.69

The substituted $Cu(L_{BQ})_2(OTf)_2$ catalyst **44a** with 3,5-di-t-Bu significantly decreased the yield (14 %) of the reaction (Table 9, entry 2), and the worst case was observed with the copper complex analog **44b** with a CF_3 group in position 4 (7%)(entry 3). Considering the oxidative generation of an alkyl radical employing anilinomethyl silicate **45** as a substrate, the relatively low oxidation potential of the copper (II) catalysts **44a** and **44b** ($E_{1/2}^{ox}$ = +0.69 V vs. SCE, DCM) explains why these two novel copper (II) catalysts could give poorer reaction yields even if it matched with the potential of the anilinomethyl silicate **45** ($E_{1/2}^{ox}$ = +0.34 V *vs* SCE in DMF)

Table 8. Optimization of copper catalysts $Cu(L_{BQ})_2(OTf)_2$

Entry	**Tosylate**	**Solvent**	**Catalyst**	**Yield**
1[1]	4 eq	DCM	44	18%
2	4 eq	DCM	44a	14%
2	4 eq	DCM	44b	7%

1. Reaction conditions: **45** (0.2 mmol), **2** (0.8 mmol) and copper catalyst **44** (10 % mol) in DCM (2 mL) at room temperature under argon atmosphere stirring for 24 h

According to the reaction's mechanism, the silicate ($E_{1/2}^{ox}$ = +0.34 V *vs* SCE in DMF) was oxidized by the copper catalyst $Cu(L_{BQ})_2(OTf)_2$ ($E_{1/2}^{ox}$ [$Cu(L_{BQ})_2/Cu(L_{BQ}(L_{SQ}))$] = +0.82 V *vs* SCE in DCM), yielding the anilinomethyl radical and the Cu complex ($Cu(L_{BQ})(L_{SQ})$). After that, the newly formed radical was trapped by allyl sulfone. The product was produced

by the addition and fragmentation of the C-S bond liberating a tosyl radical ($E_{1/2}^{ox}$ ($PhSO_2$•/$PhSO_2Na$) = + 0.50V). This one can oxidize the complex, thus regenerate the catalyst by forming a sulfonate anion (**Scheme 125**).

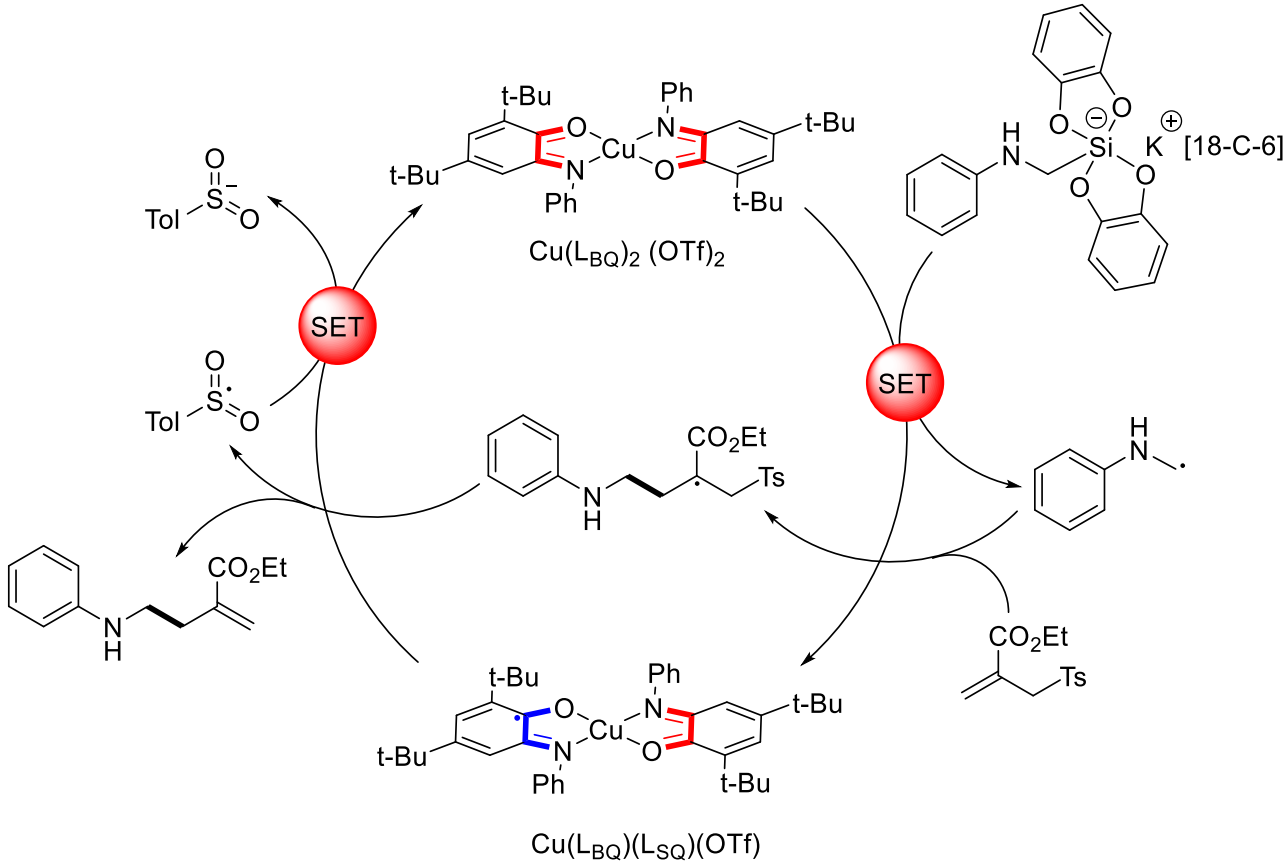

Scheme 125. Envisioned mechanism for the copper-mediated oxidation of silicates

The extension to other substrates

To generate the radical intermediate, $Cu(L_{BQ})_2(OTf)_2$ catalyst **44** may be able to oxidize the N-protected α-amino acid to produce α-amino radical after decarboxylation. By replacing the silicate substrate with sodium N-tosyl-L-prolinate, under the optimized reaction conditions, the expected allylation product was not observed. (**Scheme 126**)

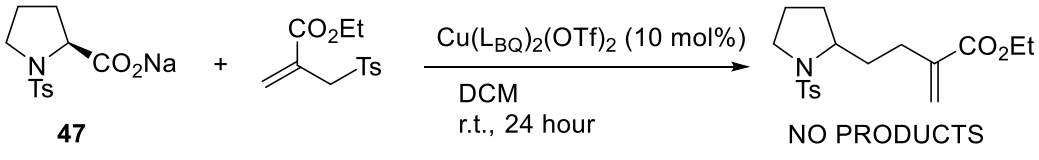

Scheme 126. The reaction of sodium tosyl-L-prolinate **47** with allylsulfone **2** catalyzed by $Cu(L_{BQ})_2(OTf)_2$ catalyst **44**

We used sodium 2-phenylacetate **48** as the substrate. However, sodium carboxylate was unable to undergo the sequential oxidation/decarboxylation reaction to react with the substrate allyl sulfone under the catalysis of $Cu(L_{BQ})_2(OTf)_2$ **44**. The expected product was not obtained. (**Scheme 127**)

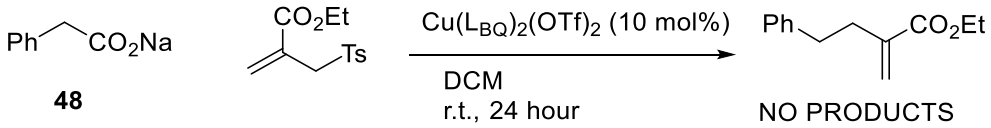

Scheme 127. The reaction of 2-phenylacetate **48** with allylsulfone **2** catalyzed by $Cu(L_{BQ})_2(OTf)_2$ catalyst **44**

As envisioned, we employed N,N-dimethylaniline as the substrate, but dimethyl aniline **49** did not react with allylsulfone substrate in the presence of the copper catalyst, even after changing the solvent from DCM to NMP. (**Scheme 128**)

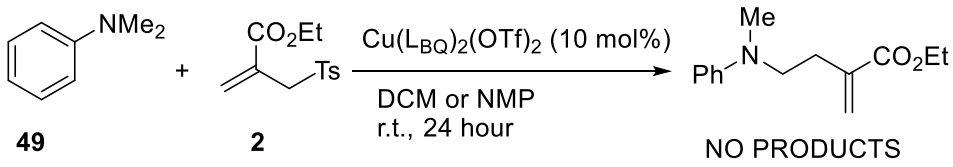

Scheme 128. The reaction of N,N-dimethylaniline **49** with allylsulfone **2** catalyzed by $Cu(L_{BQ})_2(OTf)_2$ catalyst **44**

Another option is to utilize alternative acceptors such as allyl bromides that generate a stronger oxidizing radical intermediate, a bromine radical. The allyl bromide **50** was selected as the substrate. The allyl bromide **50** did not react with the aminomethyl silicate in the presence of the oxidizing copper complex **44**. The possible reason could be attributed to the low reductive potential of **50**. It led the bromide more favorable than silicate to be reduced by the Cu catalyst and cause other side reactions. (**Scheme 129**)

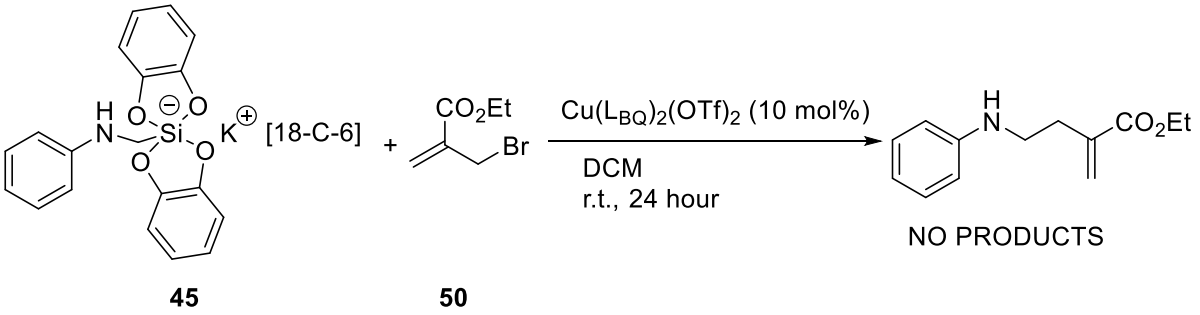

45 **50**

Scheme 129. The reaction of anilinomethyl silicate **45** with organobromide **50** catalyzed by $Cu(L_{BQ})_2(OTf)_2$ catalyst **44**

3.2. Conclusions

Last but not least, the capability of alkyl bis-catecholato silicates to be readily oxidized offers an opportunity to use these precursors in various redox catalytic systems. With single electron transfer-oxidation, organometallic complexes could contribute to the generation of radicals. A bis-iminobenzoquinone copper(II) complex has shown promise in oxidizing silicates, but further research is needed to confirm it and improve its efficiency.

3.3. Supporting informations

I. General informations

Unless otherwise noted, reactions were carried out under an argon atmosphere in oven-dried glassware. Methanol was distillated over CaH_2 and DMF was dried on molecular sieves with a *PureSolv solvent* purification system from Innovative Technology. Catechol was purchased from commercial source and purified by crystallization from chloroform. Reagents and chemicals were purchased from commercial sources and used as received. Infrared (IR) spectra were recorded on a Bruker Tensor 27 (ATR diamond) spectrophotometer. Melting points were determined on a melting point apparatus SMP3 (Stuart scientific). Electrochemical measurements were carried out an Origaflex (Origalys) electrochemical workstation. Absorption spectra of molecules were recorded at 25°C on a Cary 300 UV/Vis spectrophotometer (Agilent Technologies, Santa Clara, CA), equipped with a Peltier thermostated cell holder (t2x2 Sport/Cary300, Quantum Northwest, Liberty Lake, WA). The samples were placed in 2 mL quartz cuvettes (1 cm × 1 cm light path; Hellma Optics, Jena, Germany). Emission intensities were recorded on a Jasco FP-6200 spectrofluorometer. ^{1}H, ^{13}C and ^{19}F NMR spectra were recorded at room temperature at 400, 100 and 376 MHz respectively, on **400 MHz** Bruker AVANCE I spectrometer and at 300, 75 and 282 MHz respectively, on **300 MHz** Bruker AVANCE II spectrometer. ^{29}Si NMR spectra were recorded at room temperature at **79 MHz** on **400 MHz** Bruker AVANCE I spectrometer. Chemical shifts (δ) are reported in ppm and coupling constants (J) are given in Hertz (Hz). ^{2}H spectra were recorded at 27 °C at 600 and 92,1 MHz, respectively, on a Bruker Avance III 600 MHz spectrometer equipped with a 5 mm inverse probe head (^{1}H / ^{19}F, ^{31}P, ^{13}C). The ^{1}H NMR spectra were recorded using a pulse sequence of proton (zg30) with a spectral width of 9615 Hz, an acquisition time of 3,4 s and a number of scans of 8. The ^{2}H NMR spectra were recorded using a pulse sequence zg2h with a spectral width of 1660 Hz, an acquisition time of 4,9 s and a number of scans between 8 and 16. The spectra were analyzed with MestreNova. Abbreviations used for peak multiplicity are: s (singlet); bs (broad singlet); d (doublet); t (triplet); q (quartet); quint (quintet); sept (septet); m (multiplet) etc. Thin layer chromatographies (TLC) were performed on Merck silica gel 60 F 254 and revealed with a UV lamp (λ = 254 nm) and $KMnO_4$ staining. Flash Column Chromatographies were conducted on *Silica gel 60 M, 0.04–0.063* mm, from Macherey Nagel. High resolution mass spectrometries were performed on a microTOF (ESI). All the solvents used in flash chromatography (toluene, petroleum ether, pentane and Et_2O) were distillated.

II. Synthesis of non-inocent ligand complexes

Synthesis of aminophenol ligand (GP1)

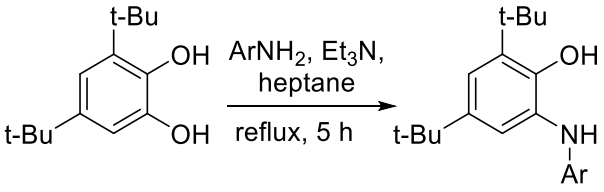

Dropwise, the appropriate aniline (12.8 mmol, 1 equiv.) and triethylamine (179 µL, 2.28 mmol, 0.1 equiv.) were added to a light brown solution of 3,5-di-tert-butylcatechol (2.86 g, 12.8 mmol, 1 equiv.) in heptane (20 mL). The dark brown slurry that resulted was refluxed for 5 hours under air. The intended product precipitated as a white powder after cooling to room temperature, which was filtered and washed with cold heptane.

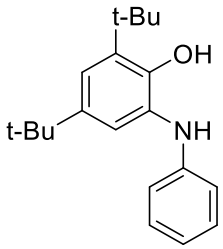

Chemical Formula: $C_{20}H_{27}NO$
Molecular Weight: 297.442

This compound Ligand L1 was synthesized according to the general procedure GP1 in 48 % yield. The characterization data were identical to those previously reported[171]

^{1}H NMR ($CDCl_3$, 400 MHz) δ 1.40 (s, 9H), 1.59 (s, 9H), 5.00 (bs, 1H, NH), 6.58 (bs, 1H), 6.76 (d, J = 8.0 Hz, 2H), 6.93 (t, J = 7.6 Hz, 1H), 7.15 (d, J = 2.0 Hz, 1H), 7.29-7.36 (m, 3H).

^{13}C NMR ($CDCl_3$, 101 MHz) δ 29.6, 31.7, 34.5, 35.1, 115.2, 119.9, 121.6, 122.0, 127.9, 129.5, 135.4, 142.3, 146.9, 149.5.

[171]C. Mukherjee, U. Pieper, E. Bothe, V. Bachler, E. Bill, T. Weyhermüller and P. Chaudhuri, *Inorg. Chem.*, 2008, **47**, 8943–8956.

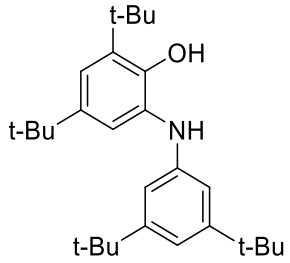

Chemical Formula: $C_{28}H_{43}NO$
Molecular Weight: 409.658

This compound Ligand L2 was synthesized according to the general procedure GP1 in 57 % yield. The characterization data were identical to those previously reported[169]

^{1}H NMR ($CDCl_3$, 400 MHz) δ 1.37 (s, 27H), 1.56 (s, 9H), 5.04 (bs, 1H), 6.34 (s, 1H), 6.63 (s, 2H), 7.03 (s, 1H) 7.15 (s, 1H) 7.29 (s, 1H).
^{13}C NMR ($CDCl_3$, 101 MHz) δ 29.6, 31.5, 31.7, 34.5, 35.0, 109.9, 114.3, 120.9, 121.4, 128.3, 135.2, 142.1, 145.6, 148.8, 152.0.

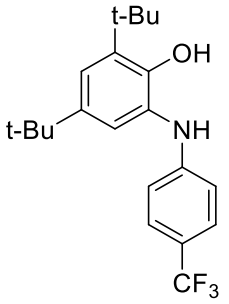

Chemical Formula: $C_{21}H_{26}F_3NO$
Molecular Weight: 365.440

This compound Ligand L3 was synthesized according to the general procedure GP1 in 60 % yield. The
characterization data were identical to those previously reported[169]

^{1}H NMR ($CDCl_3$, 400 MHz) δ 1.27 (s, 9H), 1.48 (s, 9H), 5.24 (bs, 1H), 6.15 (bs, 1H), 6.71 (d, J = 8.5 Hz, 2H), 7.05 (d, J = 2.3 Hz, 1H), 7.31 (d, J = 2.3 Hz, 1H), 7.48 (d, J = 8.0 Hz, 2H).
^{13}C NMR ($CDCl_3$, 101 MHz) δ 29.5, 31.6, 34.4, 35.2, 114.4, 121.6 (q, J = 33.3 Hz), 121.7, 122.9, 123.4 (q, J = 268.1 Hz), 126.5, 126.8 (q, J = 4.0 Hz), 135.9, 142.8, 149.4, 149.8.

Synthesis of complex Cu(L_{SQ})$_2$

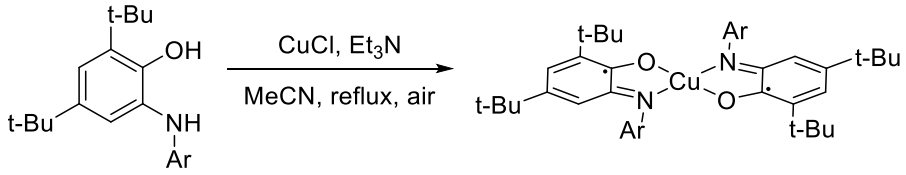

CuCl (88 mg, 0.89 mmol, 1 equiv.) and triethylamine (498 µL, 3.56 mmol, 4 equiv.) were added at 40 °C to a colorless solution of the corresponding 2-anilino-4,6-di-tert-butylphenol (1.78 mmol, 2 equiv.) in acetonitrile (20 mL). The dark green slurry that resulted was refluxed for 2 hours under air. The dark green complex produced was filtered and washed with cold acetonitrile after cooling to room temperature.

Complex **41** was synthesized according to the general procedure in 50 % yield. The characterization data were identical to those previously reported in the literature.[157]

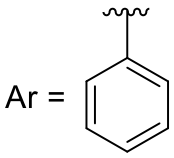

41 Chemical Formula: $C_{40}H_{50}CuN_2O_2^{2\bullet}$
Weight: 654.398

UV-vis [CH_2Cl_2; λ, nm (ε, $M^{-1}.cm^{-1}$)]: 312 (20100), 475 (4870), 811 (7365).

Complex **41a** was synthesized according to the general procedure in 41 % yield. The characterization data were identical to those previously reported in the literature.[157]

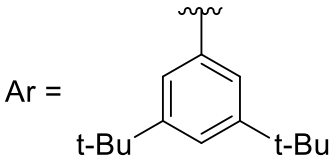

41a Chemical Formula: $C_{52}H_{73}CuN_2O_2^{2\bullet}$
Molecular Weight: 821.715

UV-vis [CH_2Cl_2; λ, nm (ε, $M^{-1}.cm^{-1}$)]: 301 (18970), 347 (8590), 455 (4680), 781 (3644).

Complex **41b** was synthesized according to the general procedure in 34 % yield. The characterization data were identical to those previously reported in the literature. [169]

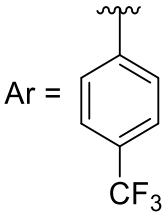

41b Chemical Formula: $C_{42}H_{48}CuF_6N_2O_2^{2\bullet}$
Molecular Weight: 790.394

UV-vis [CH_2Cl_2; λ, nm (ε, $M^{-1}.cm^{-1}$)]: 310 (22660), 777 (7690).

Synthesis of complex $Cu(L_{BQ})_2(OTf)_2$ 44

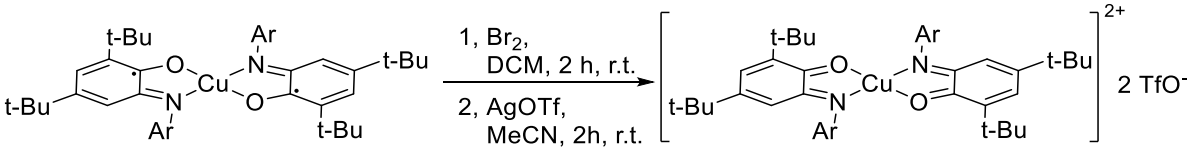

Complex **41** was added into a flame-dried Schlenk flask. Degassed DCM (9 mL) was added after the flask was backfilled three times with argon. In a Schlenk flask under an argon atmosphere, a 2.8 M bromine solution in DCM (111µl, 0.31 mmol, 1 equiv.) and silver triflate (157 mg, 0.62 mmol, 2 equiv.) were introduced. After addition 5 mL of degassed acetonitrile, the solution was stirred for 2 hours at room temperature. The filtrate was evaporated after the suspension had been filtered. DCM was used to dissolve the residue, which was then filtered. To generate the complex, the filtrate was concentrated. The UV-vis data were consistent with those reported in the literature.

Complex **44** was synthesized according to the general procedure in 59 % yield. The characterization data were identical to those previously reported in the literature.[172]

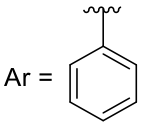

44 Chemical Formula: $C_{42}H_{50}CuF_6N_2O_8S_2$
Molecular Weight: 952.52

UV-vis [CH_2Cl_2; λ, nm (ε, $M^{-1}.cm^{-1}$)]: 290 (13990), 434 (6920), 504 (7470).

Complex **44a** was synthesized according to the general procedure in 62 % yield.

[172] J. Jacquet, P. Chaumont, G. Gontard, M. Orio, H. Vezin, S. Blanchard, M. Desage-El Murr and L. Fensterbank, *Angew. Chemie Int. Ed.*, 2016, **55**, 10712–10716.

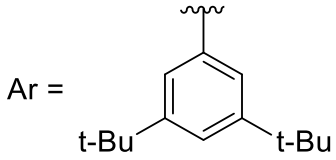

44a Chemical Formula: $C_{58}H_{82}CuF_{12}N_2O_8S_2$
Molecular Weight: 1176.94

UV-vis [CH_2Cl_2; λ, nm (ε, $M^{-1}.cm^{-1}$)]: 296 (13870), 450 (7186), 555 (8834).

Complex **44b** was synthesized according to the general procedure in 52 % yield. The characterization data were identical to those previously reported in the literature.[170]

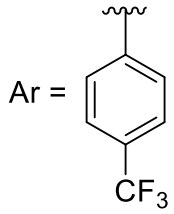

44b Chemical Formula: $C_{44}H_{48}CuF_{12}N_2O_8S_2$
Molecular Weight: 1088.51

UV-vis [CH_2Cl_2; λ, nm (ε, $M^{-1}.cm^{-1}$)]: 295 (14660), 386 (6346), 498 (5235).

III. Allylation of (biscatecholato)anilinomethyl silicate

General procedure for oxidation of (biscatecholato)anilinomethyl silicate and allylation

The copper catalyst (10 mol%), anilinomethyl silicate (0.2 mmol) and allylsulfone (0.8 mmol) were introduced in a Schlenk flask equipped with a magnetic stirring bar in which solvent (2 mL) was added. The mixture was degassed via purging with Ar. The reaction mixture then stirred at room temperature for 24 h. The reaction was quenched with saturated Na_2CO_3 aqueous solution (3 mL) and diluted with DCM (10 mL). The resulting solution was washed by saturated Na_2CO_3 aqueous solution (3×5 mL) and brine (5 mL). The combined organic layer was dried over $MgSO_4$, filtered and concentrated under pressure to give the crude product. Yield are determined by ^1H NMR using 1,3,5-trimethoxybenzene as an internal standard.

Ethyl 2-methylene-4-(phenylamino)butanoate 46

Following the general procedure with **1** (0.3 mmol, 196.2 mg). The crude product was purified by flash column chromatography (pentane/ethyl acetate, 95/5) to afford **190** as a colorless oil (11.8 mg, 18%). The spectroscopic data are in agreement with those reported in the literature[173].

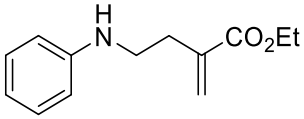

46 Chemical Formula: $C_{13}H_{17}NO_2$
Molecular Weight: 219.284

^{1}H NMR (400 MHz, $CDCl_3$): δ 7.20-7.16 (m, 2H), 6.65-6.41 (m, 3H), 6.24 (d, J = 1.4 Hz, 1H), 5.62 (d, J = 1.3 Hz, 1H), 4.24 (q, J = 7.1 Hz, 2H), 3.68 (bs, 1H), 3.30 (d, J = 6.8 Hz, 2H), 2.64 (td, J = 6.8, 1.1 Hz, 2H), 1.33 (t, J = 7.1 Hz, 3H).
^{13}C NMR (100 MHz, $CDCl_3$): δ 167.2, 148.0, 138.4, 129.3, 126.7, 117.5, 113.1, 61.0, 43.0, 32.1, 14.3.

V. Electrochemical measurements

As support electrolyte, 0.1 M Bu_4NPF_6 was used in a three-electrode cell in degassed DCM at 22°C. An AutoLab PSTAT10 electrochemical workstation was used to perform the measurements. To determine the half-wave oxidation potentials, cyclic voltammetry (CV) was used. When the scan rate was 0.1 V/s, the CV values were obtained. Wiring electrodes consisted of glassy carbon, a platinum plate and saturated calomel.

Summary of the redox potentials for the various waves of the CV of the Copper complex $Cu(L_{BQ})_2(OTf)_2$ **44** and its derivatives **44a** and **44b**.

Complex (substituent)	$E_{1/2(ox2)}$	$E_{1/2(ox1)}$	$E_{1/2(red1)}$	$E_{1/2(red2)}$
44 (unsubstituted)	+0.82	+0.17	-0.55	-0.84
44a (3,5-di-*t*-Bu)	+0.69	+0.07	-0.7	-1.02
44b (4-CF_3)	+0.69	+0.31	-0.45	-0.69

[173] C. Lévêque, L. Chenneberg, V. Corcé, C. Ollivier and L. Fensterbank, *Chem. Commun.*, 2016, **52**, 9877–9880.

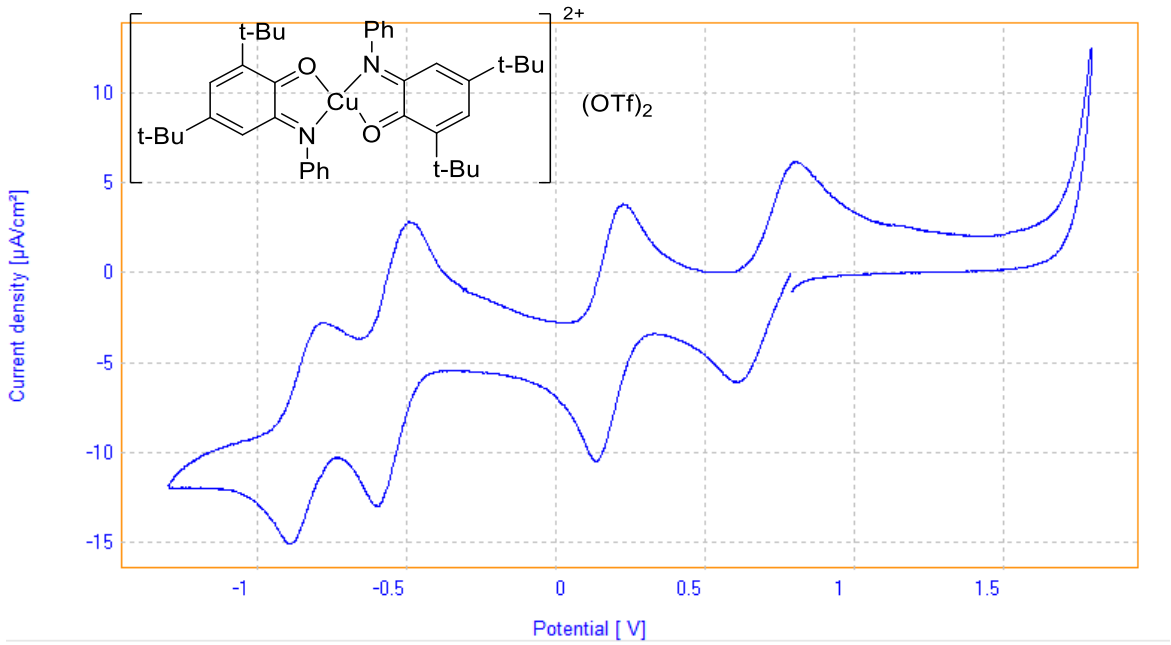

At ambient temperature, using a stable glassy carbon disk electrode (d = 3 mm) as working electrode, a SCE as reference, and Pt wire as counter-electrode (CV with 144 (2mM).), CV was conducted towards oxidative potentials and reductive potentials of DCM solution involving 0.1 M of n-Bu_4NBF_4 at a scan rate of 0.1 $V.s^{-1}$.

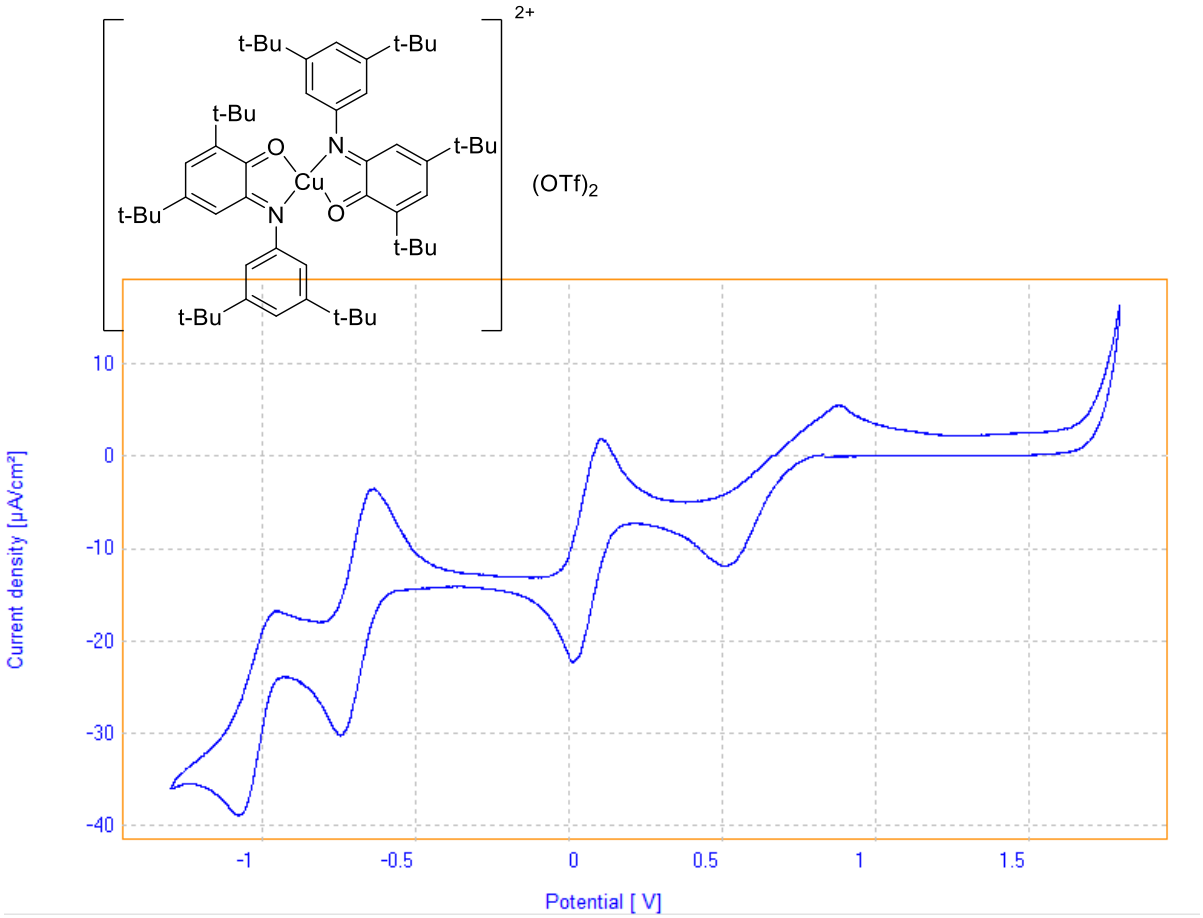

At ambient temperature, using a stable glassy carbon disk electrode (d = 3 mm) as working electrode, a SCE as reference, and Pt wire as counter-electrode (CV with 144 (2mM).), CV was conducted towards oxidative potentials and reductive potentials of DCM solution involving 0.1 M of n-Bu_4NBF_4 at a scan rate of 0.1 $V.s^{-1}$.

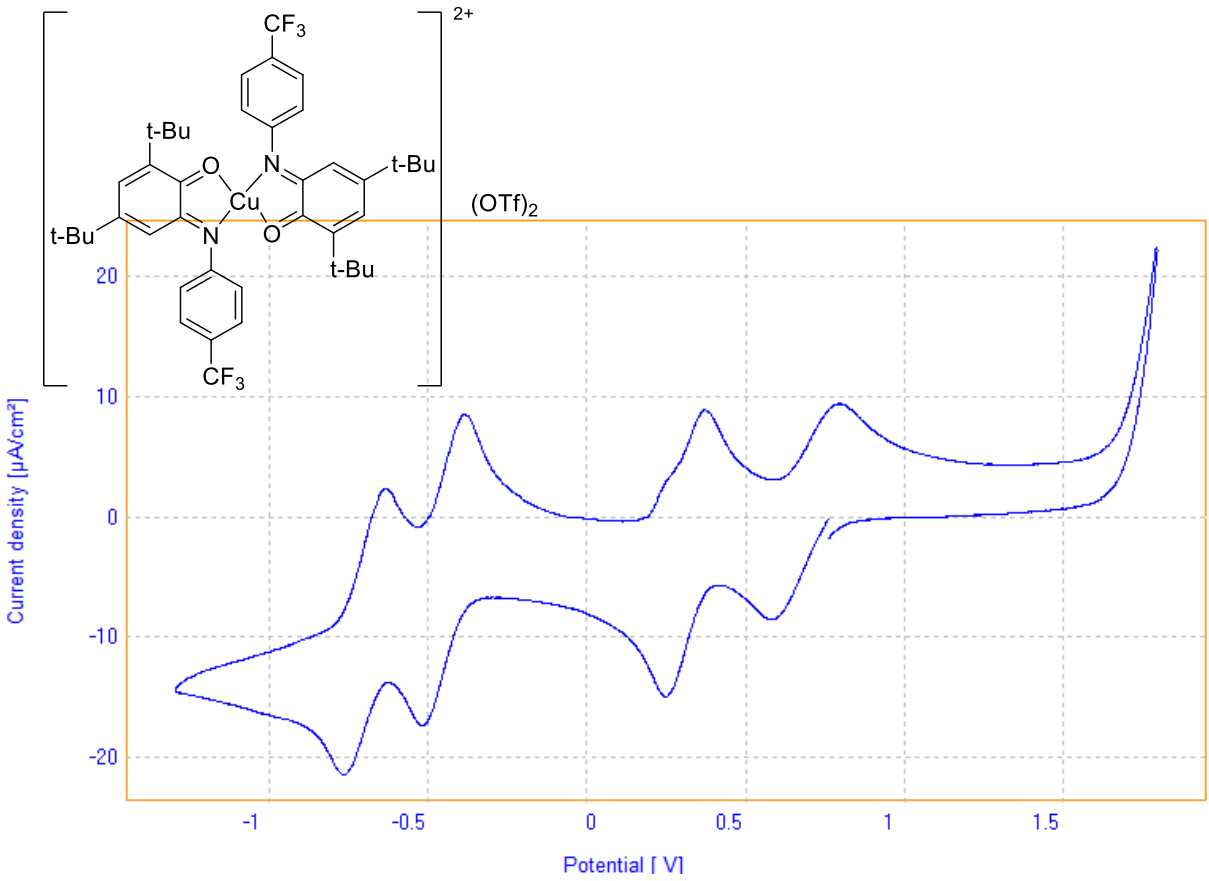

At ambient temperature, using a stable glassy carbon disk electrode (d = 3 mm) as working electrode, a SCE as reference, and Pt wire as counter-electrode (CV with 144 (2mM).), CV was conducted towards oxidative potentials and reductive potentials of DCM solution involving 0.1 M of n-Bu_4NBF_4 at a scan rate of 0.1 $V.s^{-1}$.

Chapter 3. Computational study of palmitic acid interactions with various types of cyclodextrins.

3.1 Project Aims

Due to the presence of OH and NH_2 groups that give rise to hydrogen bonding, chitosan and other similar hexasaccharides (dextran and amylopectin) have been regarded as mucoadhesive polymers. After the chemical modification of these compounds by substituting primary groups of hexasaccharides with moieties exhibiting various function groups, these compounds can be utilized in controlled drug delivery systems.[174] Pertinently, these modified hexasaccharides can form an inclusion complex with cyclodextrin. The inclusion complex has exhibited characteristics of a potential excipient for a controlled drug delivery system.[175]

In 2016, K. Bouchemal and co-workers prepared various inclusion complexes in emulsions with α-CD dissolved at atambient temperature in aqueous solutions.[176] Emulsions were prepared with numerous aliphatic acid, like hexanoic acid and octanoic acid. Inspired by the immediate result, grafted hexasaccharides including O-palmitoyl-dextran or O-palmitoyl-amylopectin and α-CD reveal platelet geometries with a diameter of less than 1μm. They have been utilized in the production of stable pickering emulsions. (see **Figure 13**)

Figure 13. TEM and Cryo-TEM observations of complexes comprises palmitic acid/α-CD.

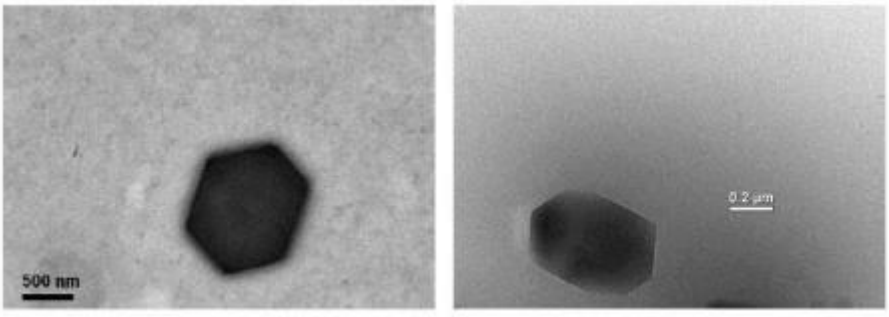

[174] J. Pushpamalar, A. K. Veeramachineni, C. Owh, X. J. Loh, *Chempluschem*, **2016**, *81*, 504–514.

[175] E. V. López, A. Luzardo Álvarez, J. Blanco Méndez, F. J. Otero Espinar, *J. Drug Deliv. Sci. Technol.*, **2017**, *42*, 273–283.

[176] R. Diaz-Salmeron, I. Chaab, F. Carn, M. Djabourov, K. Bouchemal, *J. Colloid Interface Sci*. **2016**, *482*, 48–57.

Based on their previous results, Bouchemal's group characterized the morphology and crystallinity of the particles comprised of fatty acids and α-CD inclusion complexes.[177] Hexagonal shapes of chitosan platelets observed from TEM, cryo-TEM, AFM, CLSM, and SEM images suggest the formation of crystalline structures. Different kinds of alkyl chains (oleic acid, palmitic acid, and stearic acid) grafted onto chitosan resulted in almost identical platelet shapes, strongly indicating that the interaction of fatty acids with α-CD is the driving factor for hexagonal platelet formation.

The hexasaccharide-6CDs complex contained three disaccharide repeat units. The basic units that formed the disaccharide were N-acetylglucosamine and glucuronic acid. The palmitic acid can perform esterification with the hydroxyl group of glucuronic acid. The alkyl groups of the residues of the palmitic acid were surrounded by cyclodextrin molecules.

The Ph.D. research project aims to investigate the process of removing the cyclodextrin molecular from the hexasaccharide-6CDs complex. By applying computational methodologies, we gain novel insight into the reaction mechanism underpinning this process.

The requisite extraction exhibited when removing the cyclodextrin molecule one by one from the palmitic acid-2CDs complex can be obtained via geometry optimization. After obtaining the value of the extraction energy and the insertion energy, we can potentially identify the property parameter to facilitate scanning of the hexasaccharide-6CDs complex.

At this stage, we plan to apply the extraction and insertion scanning to a set of monomer and dimer inclusion complexes of palmitic acid to provide the corresponding insertion energy and extract energy.

Finally, we aim to extend the scope of scanning into the hexasaccharide-6CDs complex.

At this stage, after comparing the value of the extraction energy of different hexasaccharide-6CDs complexes, we can select the proper type of cyclodextrin dimer in the hexasaccharide-6CDs complex. We plan to perform the scanning of the hexasaccharide-6CDs complex to remove CD one by one so as to procure the corresponding insertion energy, extract energy, and obtain the structure after scanning. Then, after comparing the value of the energy thus extracted, we can perform further scanning by utilizing the structure from the previous scanning. Through iterative scanning, we can ascertain a reasonable mechanism for the removal of cyclodextrin. (see **Figure 14)**

[177] Z. Ahmed, S. Malli, R. Diaz-Salmeron, P. L. Destruel, A. Da Costa, J. M. Guigner, F. Porcher, B. Baptiste, G. Ponchel, K. Bouchemal, *Int. J. Pharm.* **2018**, *548*, 23–33.

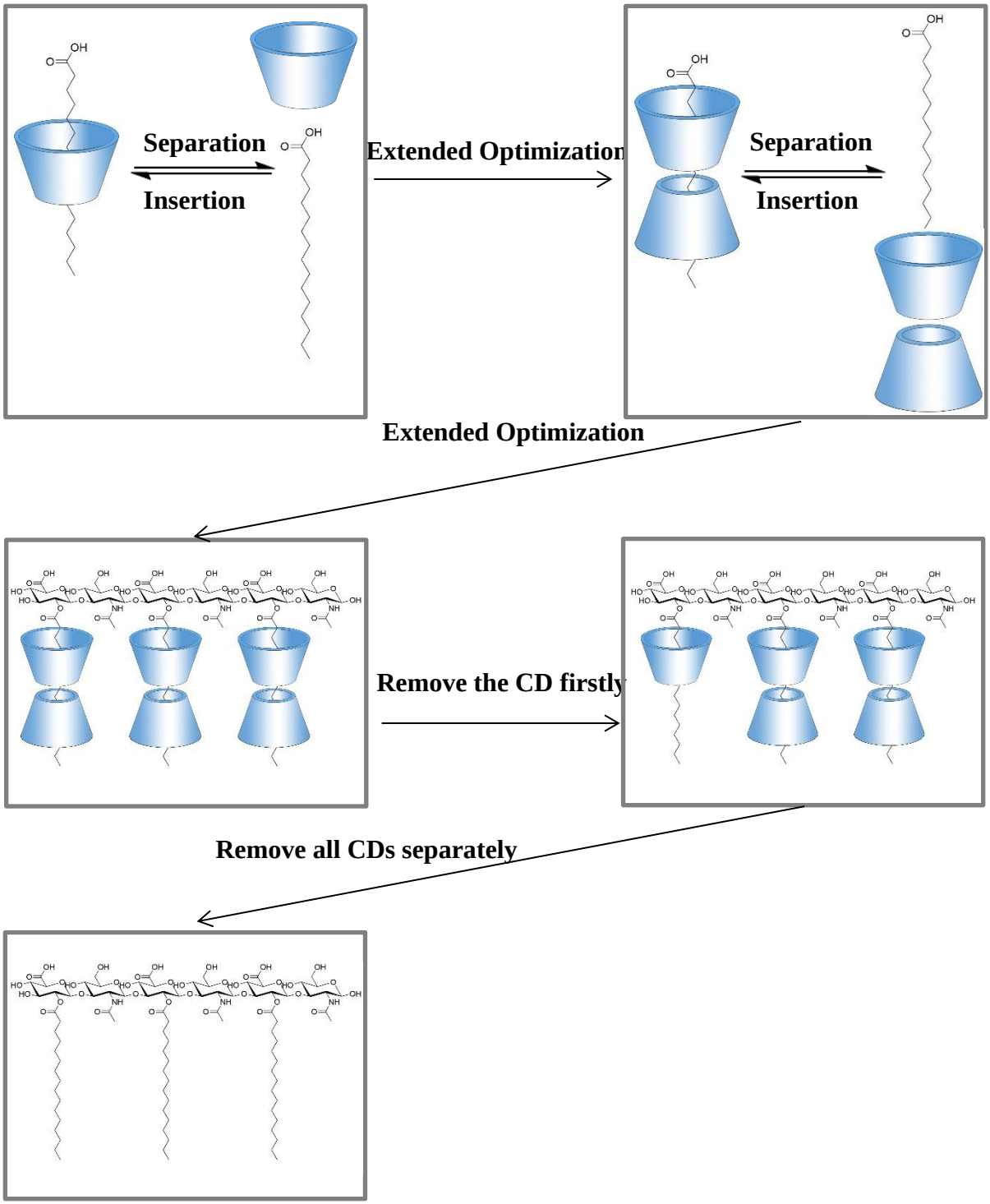

Figure 14. Steps of performing the optimization of the hexasaccharide-6CDs complex from the model of palmitic acid-cyclodextrin.

3.2 Introduction to cyclodextrin

3.2.1 Structure of cyclodextrin and correspond inclusion complexes

The α-cyclodextrin (see **Figure 15a**) comprises six glucose residues linked by α-(1, 4) glycosidic bonds. The structure of α-cyclodextrin is generally described as a shallow truncated cone (see **Figure 15b**). The glucose residue of the α-cyclodextrin has a significant impact on the hydrophile of the whole molecular structure. The outer surface of α-cyclodextrin exhibits hydrophilicity, whereas the cavity interior is covered with glycosidic oxygens and hydrogen atoms, showing its lipophilicity.

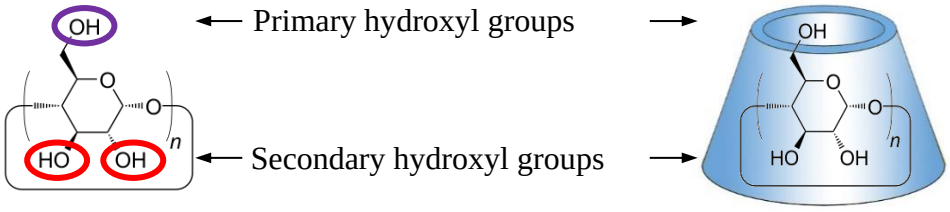

a

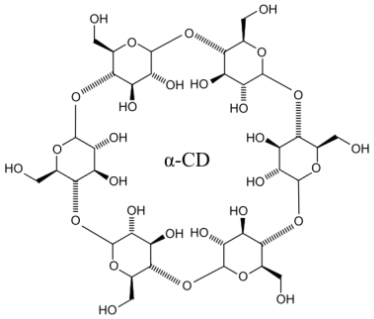

b

Figure 15. a). the different hydroxyl groups in the cyclodextrin molecular. (the different types of hydroxyl groups highlighted in Figure representation and the corresponding molecular model); b). the structure of the α-cyclodextrin

Due to the lipophilic cavity of α-cyclodextrin, the fatty acid can be regarded as the guest molecular to form host-guest type inclusion complexes with the α-cyclodextrins through non-covalent interactions. In general, various kinds of fatty acids can be selectively entrapped into cyclodextrin cavities, depending on the cavity size and geometry of the CD containers.

In 1960, H. Schlenk and D. M. Sand published a paper in which they detail the

association of α, β-cyclodextrin with organic acids.[178] In their paper, they investigated inclusion complexes of fatty acids with α-cyclodextrin with different stoichiometries and structures. Figure II-2 illustrates that there is a gradual increase in the ratio of cyclodextrin/fatty acid. Shimada later reported that lauric acid is associated with about 1.8 α-cyclodextrin molecules.[179] The evidence from published research studies[180] suggests a molecule of cyclodextrin molecule covered about six CH_2 units of a fatty acid. Thus, the

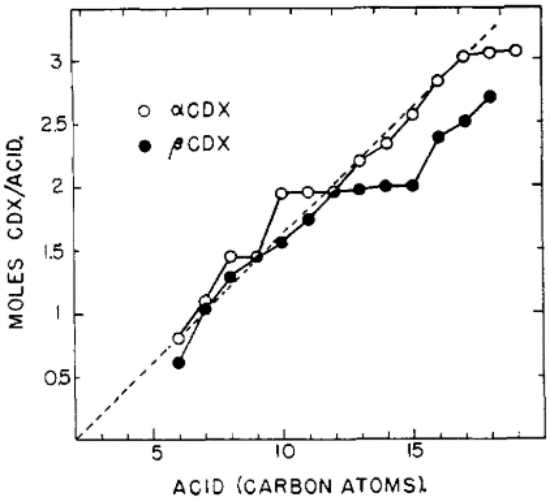

palmitic acid-cyclodextrin complex may contain two α-cyclodextrin molecules. (see **Figure 16**)

Figure 16. The relation of mole ratios of cyclodextrin/fatty acid and carbon atoms of the organic acid. The broken line has a slope of 1 cyclodextrin unit/5 CH_2.

Since there are two different hydroxyl groups (the primary hydroxyl group and the secondary hydroxyl group) in the α-cyclodextrin molecular, we can classify the palmitic acid-cyclodextrin complex into different types. In the examples involving the palmitic acid-cyclodextrin complex, the palmitic acid is thread into the cave of the α-cyclodextrin molecular. There are two different orientations between the palmitic acid and the cyclodextrin molecular.

Owing to the orientation between the hydroxyl groups in the cyclodextrin molecular and the carboxyl group of the palmitic acid, the structure of the palmitic acid-cyclodextrin

---

[178] H. Schlenk, D. M. Sand, *J. Am. Chem. Soc.*, **1961**, *83*, 2312–2320.

[179] K. A. Shimada, K. I. Kawano, J. U. Ishii, T. A. Nakamura, *J. Food Sci.*, **1992**, *57*, 655–656.

[180] a) K. Miyajima, H. Saito, M. Nakagaki, *Nippon Kagaku Kaishi*, **1987**, 306–312; b) K. Shimada, K. Fujikawa, K. Yahara, T. Nakamura, *J. Agric. Food Chem.*, **1992**, *40*, 945–948.; c) N. Jyothirmayi, C. S. Ramadoss, S. Divakar, *J. Agric. Food Chem.*, **1991**, *39*, 2123–2127.

complex can be classified into two different types (2a and 2b). These other substructures and complementary schemes are detailed in the following sections. (see **Figure 17**)

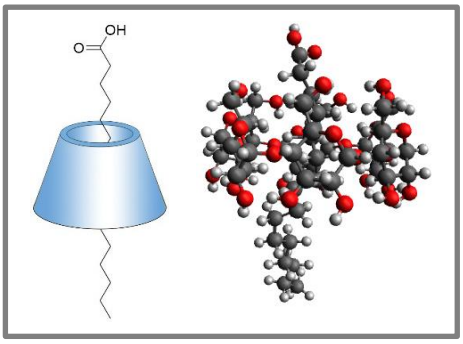

2a, Palmitic acid-cyclodextrin complex

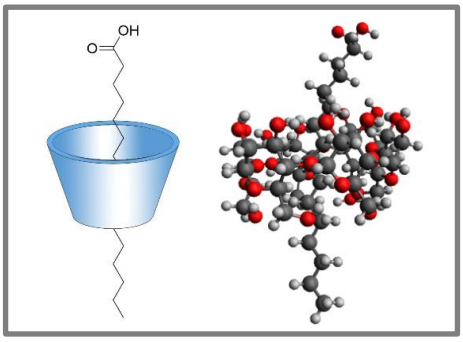

2b, Palmitic acid-cyclodextrin complex

Figure 17. The relation between cyclodextrin and palmitic acid. The scheme of the palmitic acid-cyclodextrin complex and corresponding Ball & Stick structure (cyclodextrin in blue).

Before performing an extended optimization of the palmitic acid-2cyclodextrins complex, the interaction between the two cyclodextrin molecules in one complex structure should be considered. The formation of α-cyclodextrin dimers required the association of two cyclodextrin units. Due to the different types of rims of the α-cyclodextrin are facing each other. In 2002, Carlos Jaime and his co-worker demonstrated their study about the structure and thermodynamics of α-, β-, and γ-cyclodextrin dimers[181]. They investigated the three different possible orientations between two cyclodextrin units, i.e., the primary hydroxyl groups-to-primary hydroxyl groups (3a), the secondary hydroxyl groups-to-secondary hydroxyl groups (3b), and the secondary hydroxyl groups-to-primary hydroxyl groups (3c) structures (see **Figure 18**). Intermolecular hydrogen bonding between the two cyclodextrin units has been analyzed using theoretical methods. Moreover, the calculation result in a

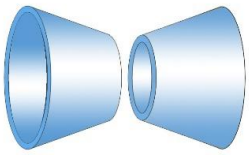

3a. α-cyclodextrin dimer (primary hydroxyl groups-to-primary hydroxyl groups)

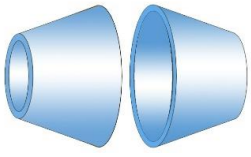

3b. α-cyclodextrin dimer (secondary hydroxyl groups-to-secondary hydroxyl groups)

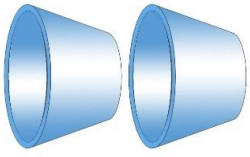

3c. α-cyclodextrin dimer (secondary hydroxyl groups-to-primary hydroxyl groups)

vacuum showed that the α-cyclodextrin dimer (3a) was the most stable dimer of the three different kinds of dimers.

[181] P. Bonnet, C. Jaime, L. Morin-Allory, *J. Org. Chem.*, **2002**, *67*, 8602–8609.

Figure 18. Three orientations for the α-cyclodextrin dimers, named 3a (primary hydroxyl groups-to-primary hydroxyl groups), 3b (secondary hydroxyl groups-to-secondary hydroxyl groups), and 3c (secondary hydroxyl groups-to-primary hydroxyl groups), respectively.

In general, there are two different orientations of α-cyclodextrin 3c (secondary hydroxyl groups-to-primary hydroxyl groups) dimers and the carboxyl group of the palmitic acid, The interactions between hydroxyl groups of the cyclodextrin can be classified into four different types: 1) primary hydroxyl groups-primary hydroxyl groups; 2) primary hydroxyl groups-secondary hydroxyl groups; 3) secondary hydroxyl groups-primary hydroxyl groups; 4) secondary hydroxyl groups-secondary hydroxyl groups. (see **Figure 19**)

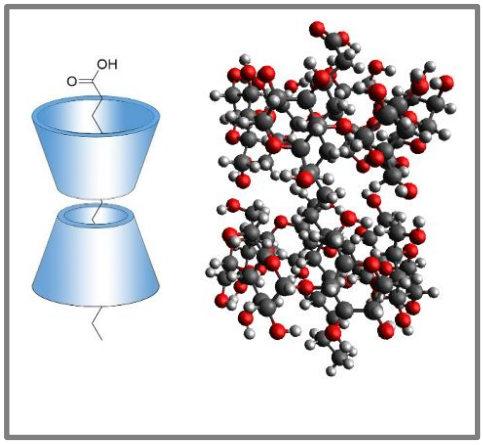

4a, palmitic acid-2CDs complex
(Primary hydroxyl-Primary hydroxyl)

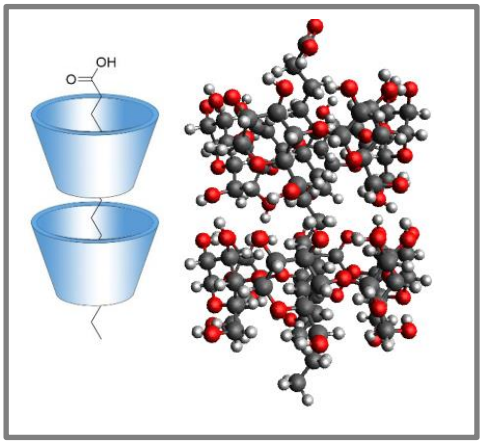

4b, palmitic acid-2CDs complex
(Primarily hydroxyl-Secondary hydroxyl)

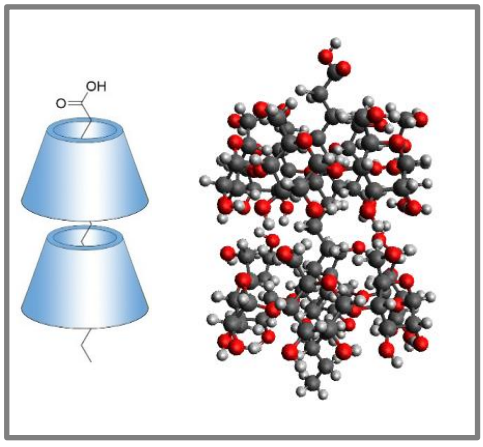

4c, palmitic acid-2CDs complex
(Secondary hydroxyl-Primary hydroxyl)

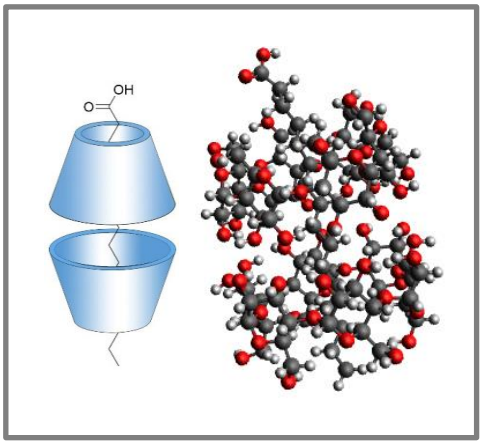

4d, palmitic acid-2CDs complex
(Secondary hydroxyl-Secondary hydroxyl)

Figure 19. the relation between the cyclodextrins and the palmitic acid. The scheme of the palmitic acid-2cyclodextrins complex and corresponding Ball & Stick structures (cyclodextrin in blue)

3.2.2 Computational Details

The initial structure of the α-cyclodextrin and the corresponding dimers were built with the help of Avogadro (Avogadro: an open-source molecular builder and visualization tool. Version 1.2.0)[182] , and the geometry of palmitic acid was extracted from a PubChem Compound Database[183] (see **Figure 20**).

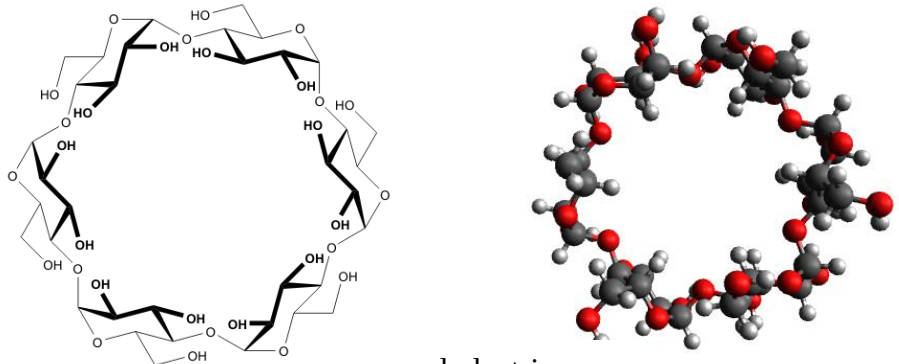

a. α-cyclodextrin

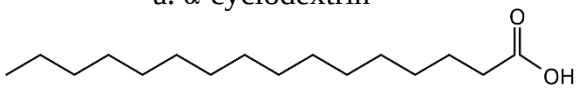

b. palmitic acid

Figure 20 Palmitic acid and α–cyclodextrin molecular structures

In the structure of the inclusion complex of α-cyclodextrin with palmitic acid, there are two possible orientations between the palmitic acid and the α-cyclodextrin. The inclusion complex that the carboxyl group is near on the primary hydroxy group side is termed 'inclusion a'. The inclusion complex that the carboxyl group is close to the secondary hydroxy group side is referred to as 'inclusion b'. (see **Figure 21**)

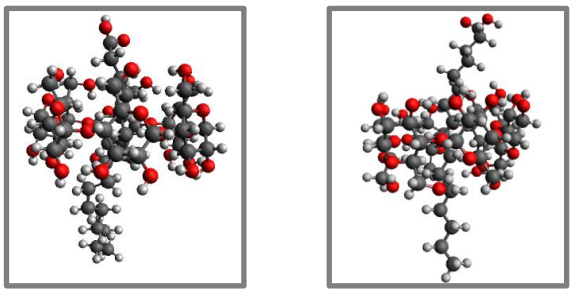

a. Inclusion a b. Inclusion b

Figure 21 The different orientation of the inclusion complex of α-cyclodextrin with palmitic acid

[182] M. D. Hanwell, D. E. Curtis, D. C. Lonie, T. Vandermeersch, E. Zurek, G. R. Hutchison, *J. Cheminform.*, **2012**, *4*, 17.

[183] E. Bolton, Y. Wang, P. Thiessen, S. Bryant, *Annu. Rep. Comput. Chem.*, **2008**, *4*, 217–241.

In creating the initial structure, it is necessary to choose an existing molecular similar to the inclusion complex of α-cyclodextrin with an aliphatic carboxylic acid as the reference. The desired structure is the crystal structure of the supramolecular complex between α-cyclodextrin and decanoic acid, obtained and described by S. Rodríquez-Llamazares and co-workers.[184] We choose the molecular (see **Figure 22**) as a referent example of complexes exhibiting 2:1 stoichiometry between the α-CD host and guest molecules with an extended hydrocarbon chain.

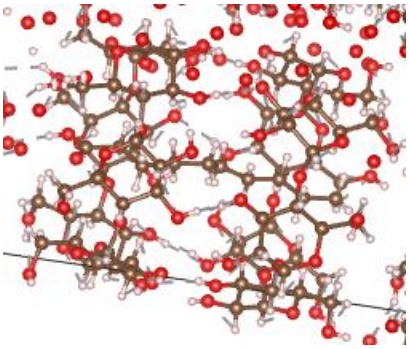

a). The X-ray structure of the supramolecular complex between α-cyclodextrin and decanoic acid

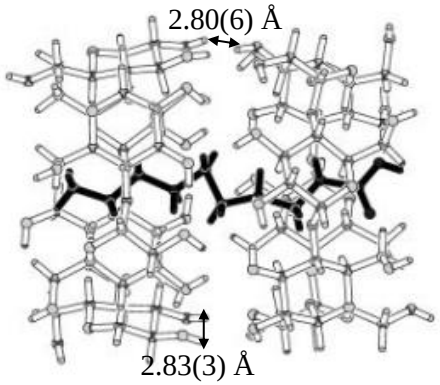

b). The decanoic acid (black) is fully enclosed in the α-CD dimer

Figure 22. The structure of the supramolecular complex between α-cyclodextrin and decanoic acid

The chosen crystal structure contains the α-cyclodextrin dimer and the guest molecules, namely the decanoic acid. The α-cyclodextrin monomers of the dimer align along its axis to form the channel. The carbon chain of the decanoic acid was threaded through the channel of the α-cyclodextrin dimer. The conformation of the α-cyclodextrin is stabilized by intramolecular H-bonds between neighboring secondary hydroxy groups of the glucose residues. Moreover, the average distance of the intramolecular H-bonds is 2.80(6) Å (range 2.69–2.95 Å).

The α-cyclodextrin monomers of the dimer formed the dimers through six H-bonds between the secondary hydroxyl groups of the glucose residues, with an average intermolecular distance of 2.83(3) Å (range 2.77–2.89 Å).

After deriving the feature of the X-ray structure of the inclusion complex with decanoic acid of α-cyclodextrin, we can then build the initial structure of the inclusion complex of α-

[184] S. Rodríquez-Llamazares, N. Yutronic, P. Jara, U. Englert, M. Noyong, U. Simon, *European J. Org. Chem.*, **2007**, 4298–4300.

cyclodextrin dimers with palmitic acid (**Figure 23**). After measuring the stretched chain conformations of the palmitic acid model, the length of the palmitic acid is 19.3(0) Å

Since the average length of the α-cyclodextrin dimer is 15.8 (8) Å, when we perform the optimization to calculate the extraction energy, we selected two fixed atoms in the palmitic acid and the α-cyclodextrin, separately, and set the distance parameter of the scan as 50 Å.

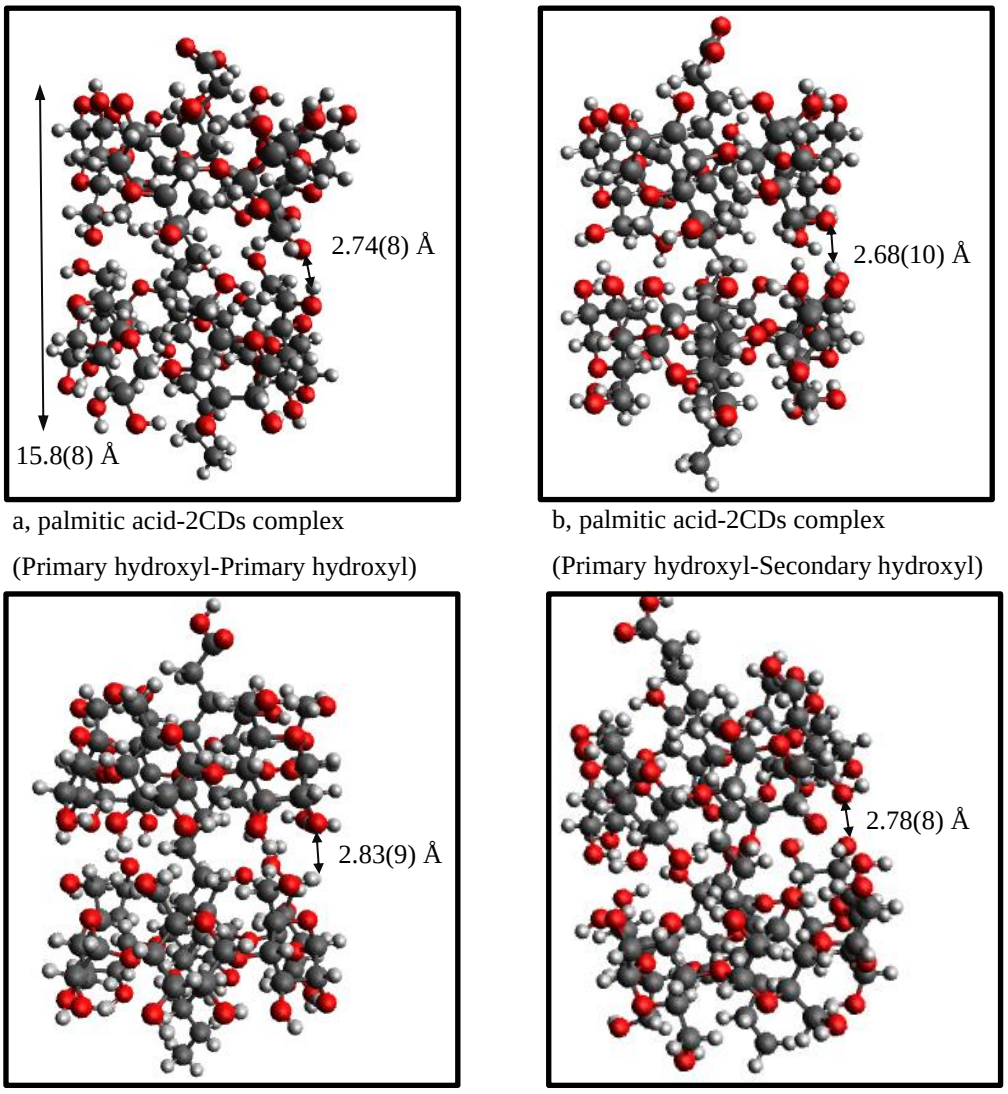

a, palmitic acid-2CDs complex (Primary hydroxyl-Primary hydroxyl)

b, palmitic acid-2CDs complex (Primary hydroxyl-Secondary hydroxyl)

c, palmitic acid-2CDs complex (Secondary hydroxyl-Primary hydroxyl)

d, palmitic acid-2CDs complex (Secondary hydroxyl-Secondary hydroxyl)

Figure 23. The structure of the inclusion complex of the α-cyclodextrin dimer with palmitic acid

The geometries of the inclusion complex of α-cyclodextrin are optimized by employing the xtb programme and applying the GFN2-xTB method. The data of the extraction energy of removing the α-cyclodextrin molecular and the corresponding insertion energy is provided by the xtb program and calculated using the GFN2-xTB method.[185]

[185] S. Grimme, C. Bannwarth, P. Shushkov, *J. Chem. Theory Comput.*, **2017**, *13*, 1989–2009.

3.3 The optimization of the inclusion complex of α-cyclodextrin

3.3.1 The optimization of the palmitic acid-cyclodextrin complex (one cyclodextrin)

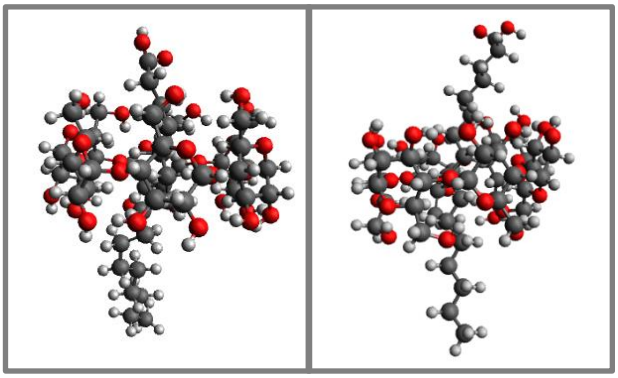

a. Inclusion complex a b. Inclusion complex b

Figure 24. The different orientation of the inclusion complex of α-cyclodextrin with palmitic acid.

We can classify the inclusion complex of α-cyclodextrin with palmitic acid into two different complexes (see **Figure 24 a** and **b**, above) due to the different directions between the cyclodextrin and the palmitic acid. The carboxyl group of inclusion complex a is close to the primary hydroxyl groups of the cyclodextrin. In contrast, the carboxyl group of inclusion b is close to the secondary hydroxyl groups of the cyclodextrin. (see **Figure 24**)

Removing the cyclodextrin molecule from the inclusion complex a

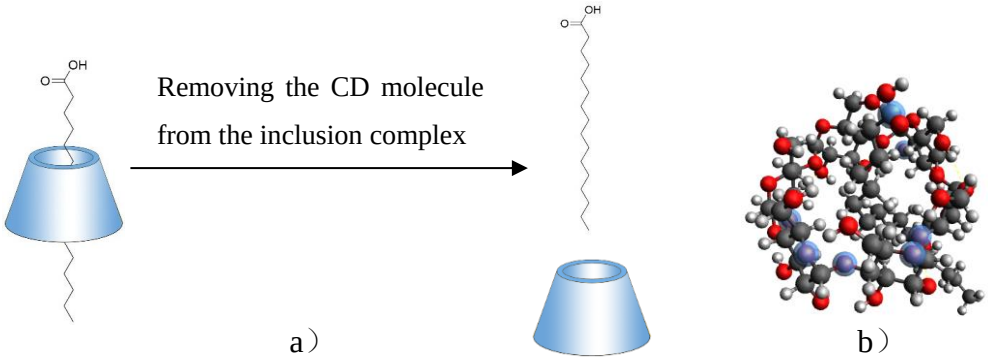

Figure 25 a) Removing the palmitic acid molecule from the inclusion complex a. b) The starting structure for geometry optimization.

The purpose of this optimization is to remove the palmitic acid from the inclusion complex a. At the beginning of the scanning, the palmitic acid is in the cave of the cyclodextrin, and the carboxy group of the palmitic acid is next to the primary hydroxyl groups of the cyclodextrin. The conformation of the inclusion complex has been described in **Figure 25**. The palmitic acid is folded in the cave of the cyclodextrin. At the end of the scanning, the palmitic acid was separated from the cyclodextrin completely. After we finish the scanning of removing the palmitic acid from the cyclodextrin, we can then plot the distance-energy curve of the scanning and obtained the corresponding extraction energy.

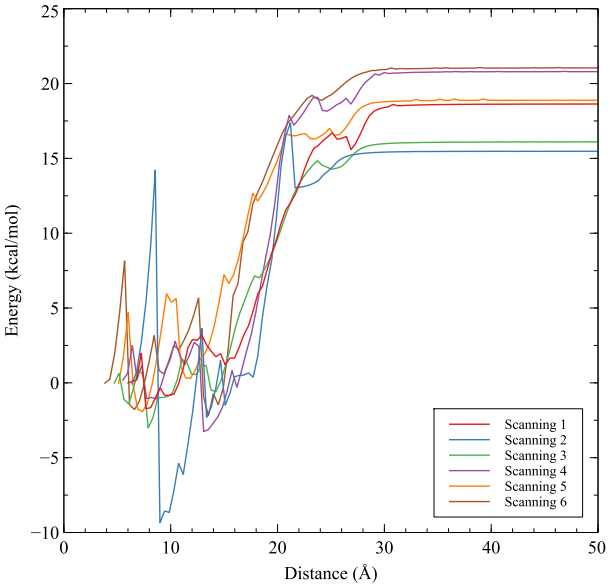

Figure 26. The energy-distance curve of inclusion complex a (Removing the palmitic acid from the inclusion complex a)

As depicted in **Figure 26**, the cyclodextrin gets close to the carboxyl group and then goes through the cave of the cyclodextrin molecules. This minimum energy was obtained by removing the cyclodextrin molecule slightly from the inclusion complex. While the distance

between cyclodextrin and palmitic acid increases, the energy of the whole system increases.

It is noteworthy that the minimum energy of scanning 2 is much lower than any other distance-energy curve. After comparing the corresponding molecule conformation of the minimum energy of scanning 2 and other distance-energy curves, we can see that the carboxyl group of the palmitic acid forms two extra hydrogen bonds with the hydroxyl groups of the cyclodextrin model (see **Figure 27**). Furthermore, the palmitic acid conformation at the minimum point of scanning 2 is more twisted than that of other scannings.

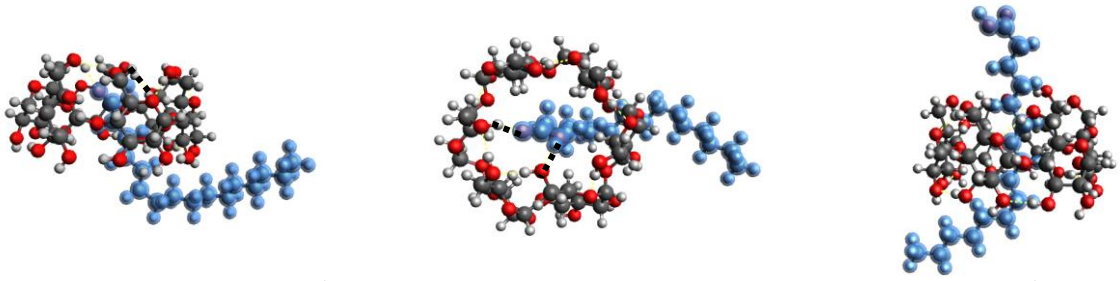

a）　　b）

Figure 27. The conformation of inclusion complex a at the minimum point of the distance energy curve. a) the conformation of inclusion complex a at the minimum point of scanning 2；b) the conformation of inclusion complex a at the minimum point of scanning 1； The palmitic acid is colored in blue for clarity. The black dash line indicates the hydrogen bond between palmitic acid and cyclodextrin molecule

The extraction energy of the monomer inclusion complex (Inclusion complex a)was summarized in **Table 9**.

Table 9. The extraction energy of the optimization (Removing the palmitic acid from the inclusion complex a)

Number of Optimization	The Energy of Start Point (kcal/mol)	The Energy of End Point (kcal/mol)	Extraction Energy (kcal/mol)	Mean value of Extraction Energy (kcal/mol)
1	0	18.63	18.63	18.48
2	-0.06	15.47	15.54	
3	0	16.10	16.10	
4	0.18	20.79	20.61	
5	-0.04	18.88	18.92	
6	-0.02	21.04	21.06	

Inserting the palmitic acid into the cyclodextrin molecule (Inclusion complex a)

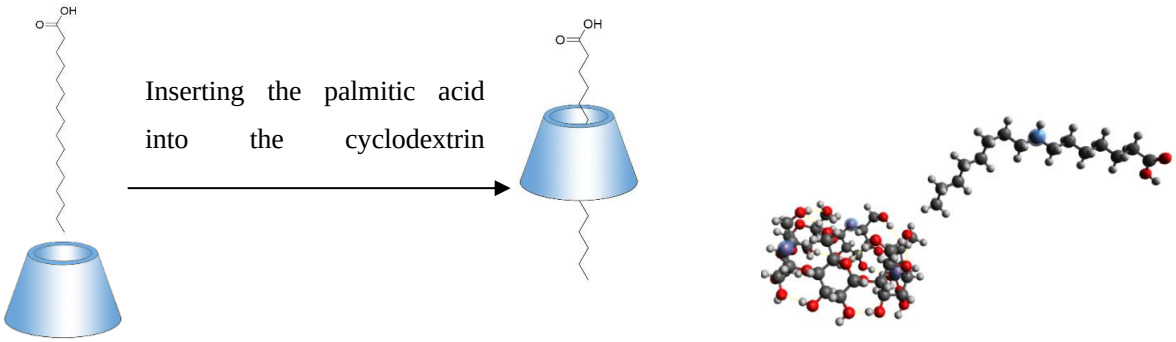

a） b）

Figure 28. a) Inserting the palmitic acid into the cyclodextrin molecule. b) The starting structure for geometry optimization.

This geometry optimization aims to insert palmitic acid into the cave of the cyclodextrin. At the start of the scanning, the palmitic acid is wholly separated from the cyclodextrin, with the end of the alkyl chain of palmitic acid adjacent to the primary hydroxyl group of cyclodextrin. The schematic figure (**Figure 28** a) illustrates the structure of the separated palmitic acid and the cyclodextrin molecule. Palmitic acid was entirely isolated from cyclodextrin at the beginning of the scannings. After completing the scanning of palmitic acid inserting into cyclodextrin, we are able to plot the distance-energy curve of geometry optimization and determine the related insertion energy.

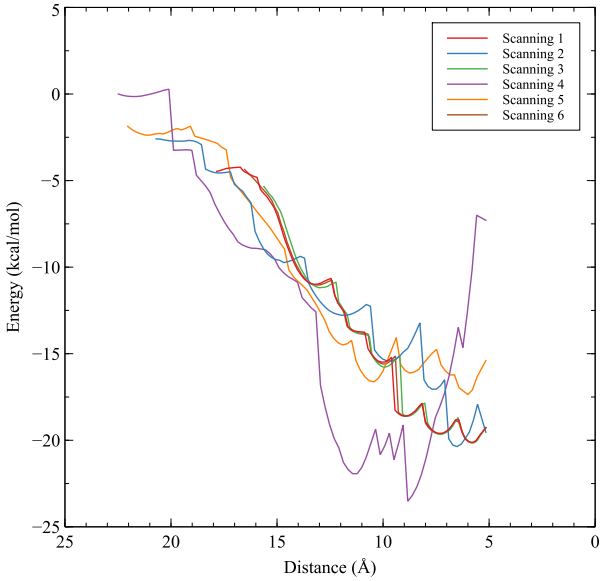

Figure 29. The energy-distance curve of inclusion complex a (Inserting the palmitic acid into the cyclodextrin molecule)

At the beginning of the scanning, the alkyl chain of the palmitic acid is near the primary

hydroxyl groups of the cyclodextrin molecular. With the movement of the palmitic acid, the end of the alkyl chain penetrates into the cave of the cyclodextrin molecular, after which point, the remaining part of the alkyl chain goes through the cave of the cyclodextrin molecular.

It is noteworthy that the minimum energy of scanning 4 is much lower than any other distance-energy curve (see **Figure 29**). The energy of the end point of scanning 4 is much higher than any other distance-energy curve. After comparing the corresponding molecule conformations of the minimum point and the end point of scanning 4, it is clear that the carboxyl group of the palmitic acid forms hydrogen bonds with the hydroxyl groups of the cyclodextrin model (see **Figure 30 a** and **b**). Comparing the molecule conformations of the minimum point and the end point of scanning 4, we can ascertain that the conformation of the palmitic acid of the end point is more folded than the minimum point. Additionally, we can see that palmitic acid of scanning 4 can form an extra hydrogen bond with the hydroxyl groups of the cyclodextrin (see **Figure 30 a** and **c**). Due to the additional hydrogen bonding, the energy of the minimum point of scanning 4 is lower than scanning 1.

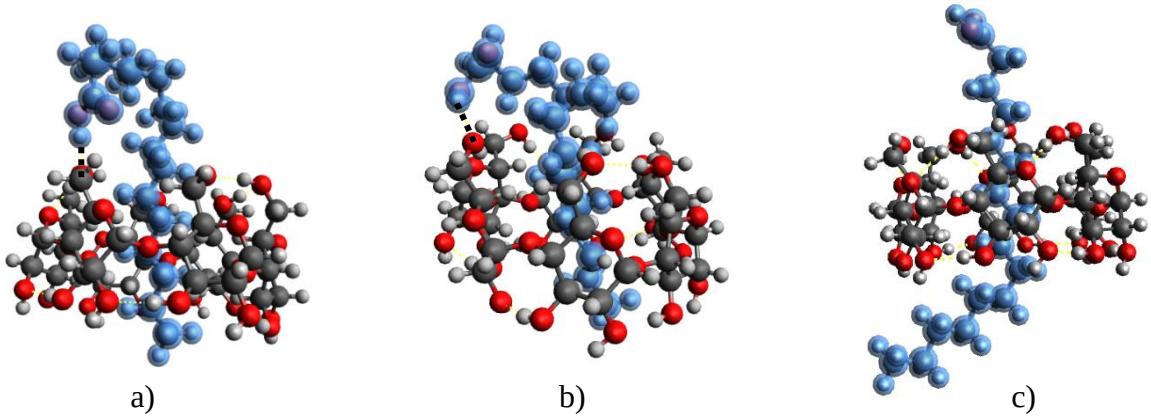

a) b) c)

Figure 30. The conformation of inclusion complex a at the minimum point of the distance energy curve.

a) the conformation of inclusion complex a at the minimum point of scanning 4; b) the conformation of inclusion complex a at the end point of scanning 4; The palmitic acid is colored in blue for clarity; c) the conformation of inclusion complex a at the minimum point of scanning 1. The black dash line indicates the hydrogen bond between palmitic acid and cyclodextrin molecule;

The insertion energy of the monomer inclusion complex (Inclusion complex a)was summarized in **Table 10**.

Table 10. The insertion energy (Insertion of palmitic acid into the cyclodextrin)

Number of scanning	The Energy of Start Point (kcal/mol)	The Energy of End Point (kcal/mol)	The Insertion Energy (kcal/mol)	Mean value of the Insertion Energy (kcal/mol)
1	-4.46	-19.27	-14.80	-16.95
2	-2.59	-19.53	-16.94	
3	-5.33	-19.28	-13.94	
4	0	-7.29	-7.29	
5	-1.86	-15.40	-13.53	
6	-4.35	-19.26	-14.91	

Removing the cyclodextrin molecule from the inclusion complex b

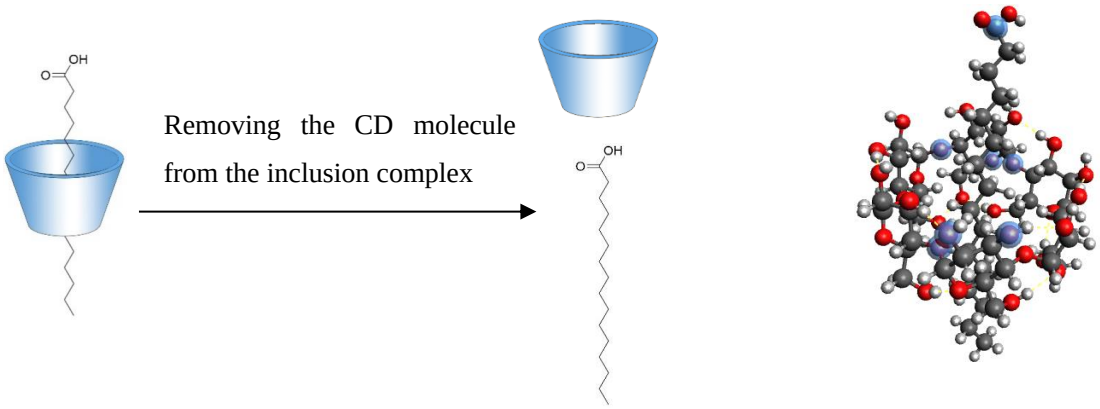

Figure 31. a) Removing the CD molecule from the inclusion complex b. b) The starting structure for geometry optimization.

The goal of the geometry optimization is to remove palmitic acid from inclusion complex b. The carboxyl group of the palmitic acid is adjacent to the secondary hydroxyl group of the cyclodextrin, and the palmitic acid is in the cave of the cyclodextrin at the beginning of the scanning. The inclusion complex conformation is detailed in **Figure 31 b**. In the cave of the cyclodextrin, the palmitic acid is folded. The palmitic acid is ultimately extracted from the cyclodextrin. With the optimization complete, we can plot the distance-energy curve that we produced and obtain the extraction energy that corresponds to the optimization.

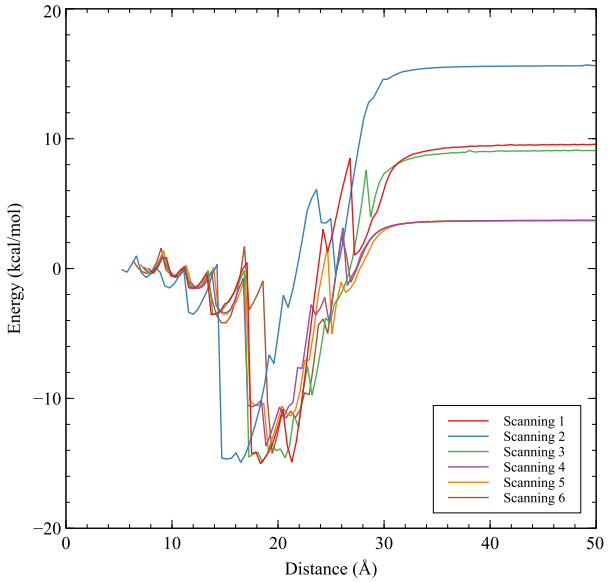

Figure 32. The energy-distance curve of inclusion complex b (Removing the palmitic acid from the inclusion complex b)

As depicted in **Figure 32**, the palmitic acid moves and then threads through the cyclodextrin molecule cave. Comparing the molecule conformations of the minimum point and the start point, we can see that the carboxyl group of the palmitic acid of the minimum point can form two extra hydrogen bonds with the hydroxyl groups of the (see **Figure 33** and **Figure 34**). The additional hydrogen bonds between palmitic acid and cyclodextrin can decrease the energy of the whole system.

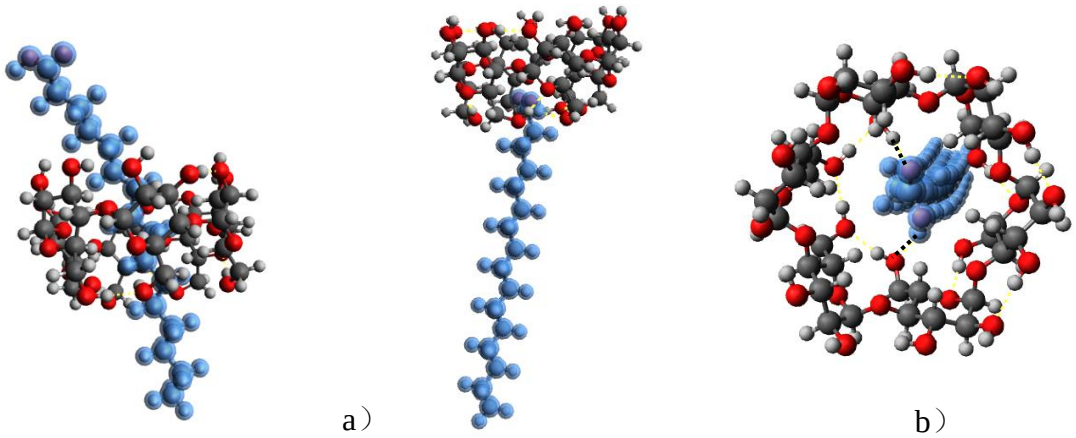

Figure 33. The conformations of inclusion complex b at the minimum point and the start point of the distance energy curve. a) the conformation of inclusion complex b at the start point of scanning 1; b) the conformation of inclusion complex b at the minimum point of scanning 1. The palmitic acid is colored in blue for clarity. The black dash line indicates the hydrogen bond between palmitic acid and cyclodextrin molecule;

With the movement of the palmitic acid, the distance between the cyclodextrin and the palmitic acid increases. The distance between the carboxyl group of the palmitic acid and the hydroxyl groups becomes so far that they can't form hydrogen bonds. So, the extraction energy between the minimum and end points is due to the additional hydrogen interaction. The mean value of the extraction energy is 20.89 kcal/mol.

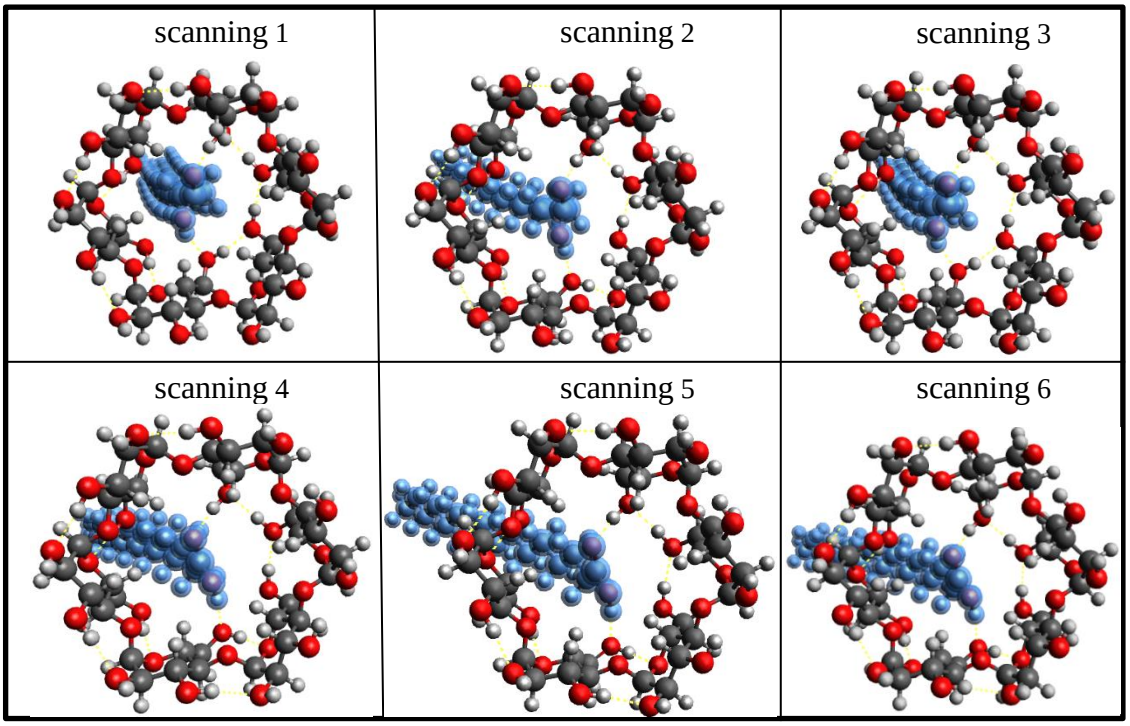

Figure 34. The conformation of inclusion complex b at the minimum point of the distance-energy curve

Based on the energy-distance curve, we can obtain the extraction energy of the scannings. The extraction energy of the extraction energy and the corresponding minimum energy are presented in **Table 11**.

Table 11. The extraction energy of the geometry optimization (Removing the palmitic acid from the inclusion complex b)

Number of scanning	The Energy of Minimum Point (kcal/mol)	The Energy of End Point (kcal/mol)	Extraction Energy (kcal/mol)	Mean value of Extraction Energy (kcal/mol)
1	-13.63	9.57	23.19	21.49
2	-14.18	15.61	29.77	
3	-14.02	9.07	23.08	
4	-13.66	3.70	17.35	
5	-13.96	3.69	17.64	
6	-14.23	3.70	17.92	

Inserting the palmitic acid into cyclodextrin molecular (Inclusion complex b)

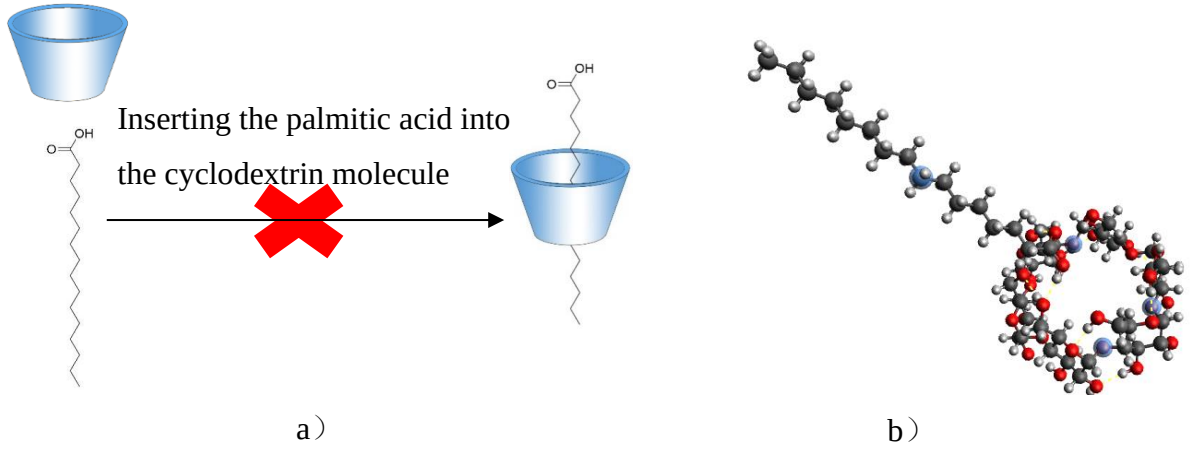

Figure 35. a) inserting the palmitic acid into the cyclodextrin molecule. b) The starting structure for geometry optimization.

This geometry optimization is aimed at inserting palmitic acid into the cave of the cyclodextrin. The palmitic acid is initially divided into its fatty acid component (the fatty acid with the alkyl chain attached to the carboxylic acid) and the cyclodextrin, with the alkyl chain of the fatty acid part of the palmitic acid connecting to the hydroxyl group of the cyclodextrin. **Figure 35** illustrates the structure of the separated palmitic acid and the cyclodextrin molecule. At the beginning of the scannings, it was only possible to insert palmitic acid into cyclodextrin. Following this, we were able to calculate the relevant insertion energy of the scanning process after completing the geometry optimization of palmitic acid inserting into cyclodextrin. (see **Figure 36**)

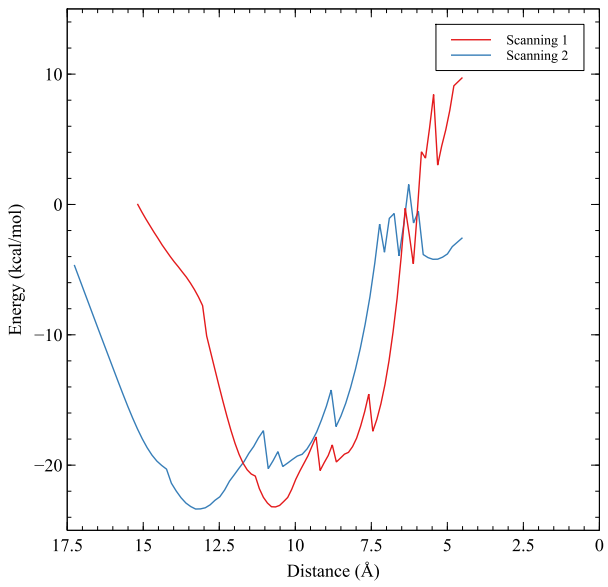

Figure 36. The energy-distance curve of inclusion complex b (Insertion of palmitic acid into the cyclodextrin)

At the beginning of the scanning, the carboxyl group is near the primary hydroxyl groups of the cyclodextrin molecular. The carboxyl group of palmitic acid gets close to the primary hydroxyl groups of the cyclodextrin. After comparing the conformation of the start point and minimum point, we can see that the carboxyl group has the potential to form additional hydrogen bonds with the hydroxyl group of cyclodextrin (see **Figure 37**). The hydrogen bonding interaction between the hydroxyl groups and the carboxyl group can be regarded as the hindrance of inserting the palmitic acid. Moreover, the narrow cave of cyclodextrin also prevented palmitic acid from inserting the cyclodextrin. Subsequently, the alkyl chain of the palmitic acid becomes folded and becomes close to the cyclodextrin molecular. Furthermore, the carboxyl group of palmitic acid still forms two hydrogen bonds with cyclodextrin (see **Figure 37**).

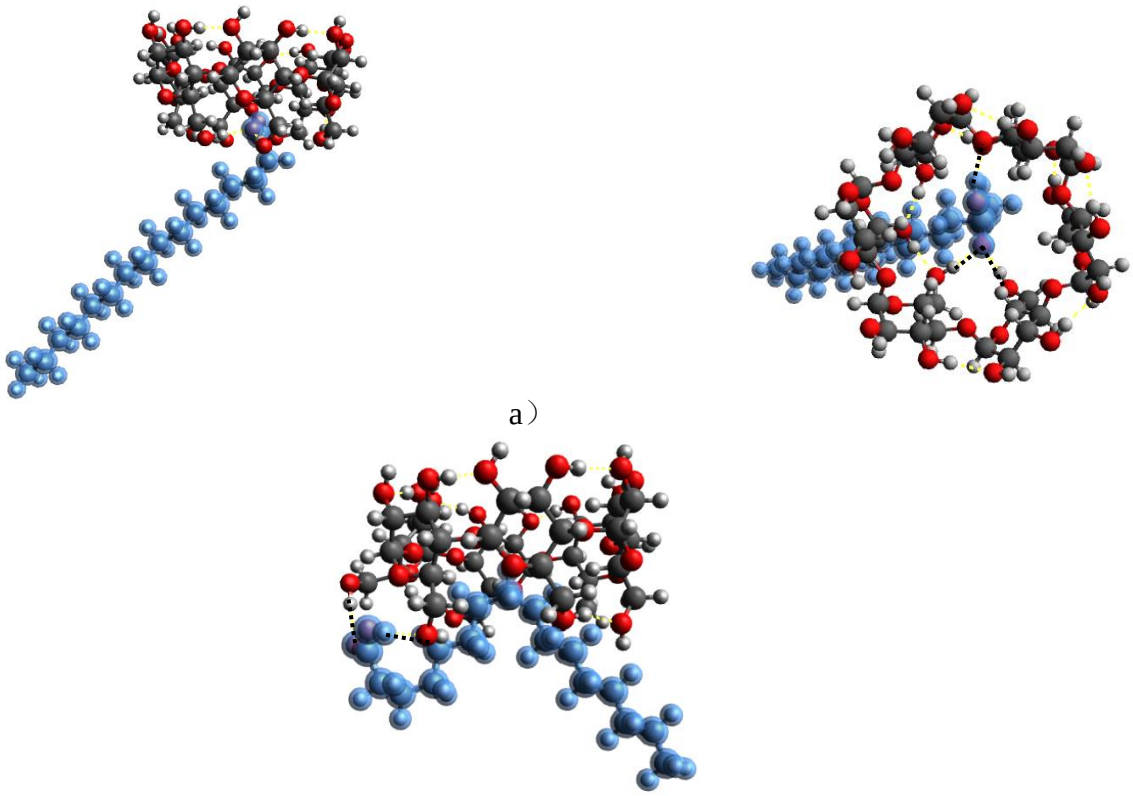

Figure 37. The conformations of inclusion complex b during scanning.

a) the conformation of inclusion complex b at the starting point of scanning 1; b) the conformation of inclusion complex b at the minimum point of scanning 1. The palmitic acid is colored in blue for clarity. The black dash line indicates the hydrogen bond between palmitic acid and cyclodextrin molecule;

Summary of the Optimization of inclusion complex a and b

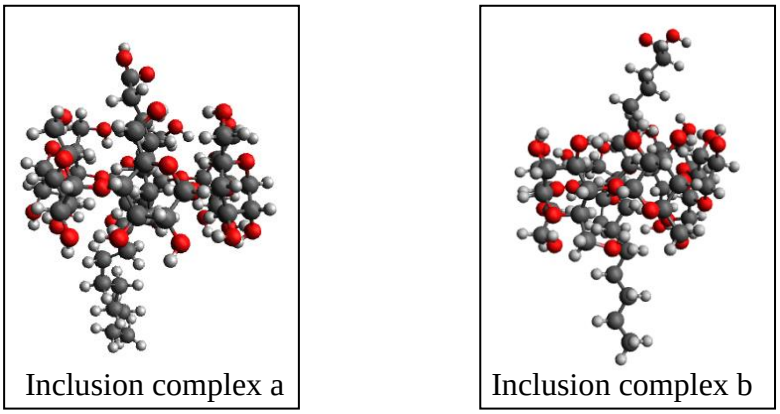

Figure 38 The different orientation of the inclusion complex of α-cyclodextrin with palmitic acid

In general, considering the relationship between the hydroxyl groups of the α-cyclodextrin and the carboxyl group of the palmitic acid, the inclusion complex can be classified into two different types: Inclusion complex a (the primary hydroxyl groups of the α-cyclodextrin is near the carboxyl group of the palmitic acid) and Inclusion complex b (the secondary hydroxyl groups of the α-cyclodextrin is near the carboxyl group of the palmitic acid). (see **Figure 38**)

The extraction energy and the insertion energy of the monomer inclusion complexes (Inclusion complex a and Inclusion complex b) were summarized in **Table 12**.

Table 12 The extraction energy and the insertion energy of complex a and b

The type of inclusion complex	Mean value of Extraction Energy (kcal/mol)	Mean value of Insertion Energy (kcal/mol)
Inclusion complex a	18.46	-16.95
Inclusion complex b	21.49	No data

At the beginning of removing cyclodextrin molecules, the palmitic acid is in the cave of the cyclodextrin molecule. With the movement of the palmitic acid, the palmitic acid and the cyclodextrin molecules become increasingly far away from each other. Concurrently, the energy of the whole system increase. Accordingly, we can calculate the extraction energy between the start point and the end point.

It is noteworthy that the formation of an additional hydrogen bond can decrease the energy of the whole system. For instance, with the movement of the palmitic acid, the palmitic acid of inclusion complex b forms additional hydrogen bonds with cyclodextrin. Thus, the extra hydrogen bond can decrease the energy of the whole system.

3.3.2 The optimization of the palmitic acid-cyclodextrins complex (two α- cyclodextrins)

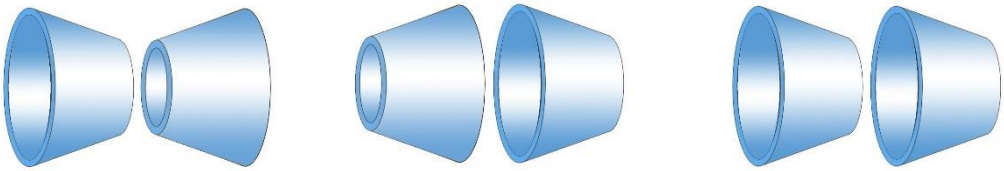

3a. α-cyclodextrin dimer (primary hydroxyl groups-to-primary hydroxyl groups)

3b. α-cyclodextrin dimer (secondary hydroxyl groups-to-secondary hydroxyl groups)

3c. α-cyclodextrin dimer (secondary hydroxyl groups-to-primary hydroxyl groups)

Figure 39. Three orientations for the α-cyclodextrin dimers, named 3a (primary hydroxyl groups-to-primary hydroxyl groups), 3b (secondary hydroxyl groups-to-secondary hydroxyl groups), and 3c (secondary hydroxyl groups-to-primary hydroxyl groups), respectively.

In general, there are three different orientations of α-cyclodextrin molecules in the dimer. We can classify them based on the different interactions of hydroxyl groups: (1) primary hydroxyl groups-primary hydroxyl groups; (2) primary hydroxyl groups-secondary hydroxyl groups; (3) secondary hydroxyl groups-secondary hydroxyl groups (see **Figure 39**). Furthermore, owing to the orientation between the hydroxyl groups of α-cyclodextrin and the carboxyl group of the palmitic acid consideration, the inclusion complexes consisting of palmitic acid and α-cyclodextrin dimer can be classified into four different types: (1) primary hydroxyl groups-primary hydroxyl groups (4a); (2) primary hydroxyl groups-secondary hydroxyl groups (4b); (3) secondary hydroxyl groups-primary hydroxyl groups (4c); (4) secondary hydroxyl groups-secondary hydroxyl groups (4d). (see **Figure 40**)

The purpose of performing the scanning to insert or extract the palmitic acid from the cyclodextrin dimer is to obtain the corresponding energy of the process. Additionally, the provided energy can support our evaluations as to the favourability of the process. Based on the scanning results, we are enabled to select which kind of inclusion complex comprises α-cyclodextrin dimer, and palmitic acid is the most appropriate structure of the hexasaccharide-6CDs complex.

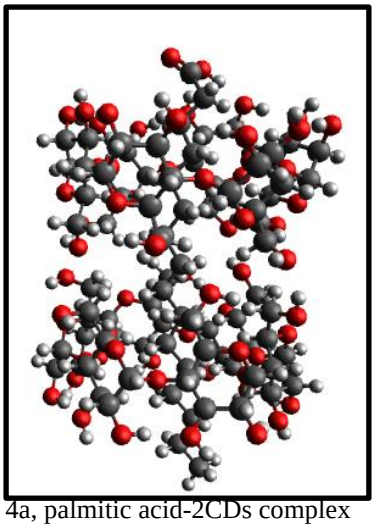

4a, palmitic acid-2CDs complex (Primary hydroxyl-Primary hydroxyl)

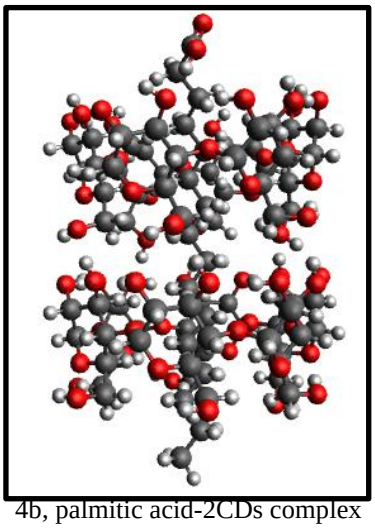

4b, palmitic acid-2CDs complex (Primary hydroxyl-Secondary hydroxyl)

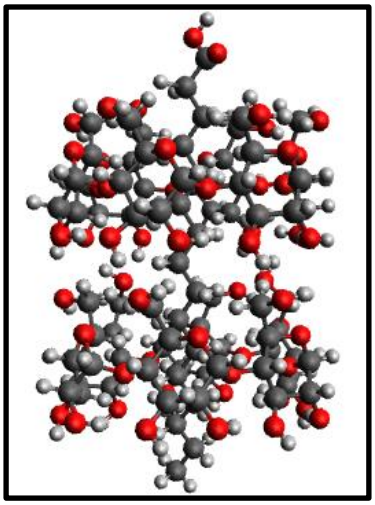

4c, palmitic acid-2CDs complex (Secondary hydroxyl-Primary hydroxyl)

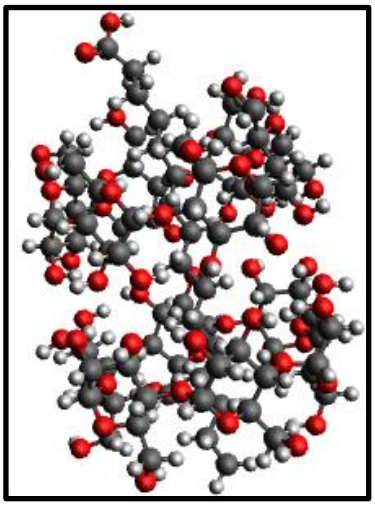

4d, palmitic acid-2CDs complex (Secondary hydroxyl-Secondary hydroxyl)

Figure 40. The structure of the inclusion complex of the α-cyclodextrin dimer with palmitic acid

Removing the cyclodextrin molecule from the inclusion complex 4a

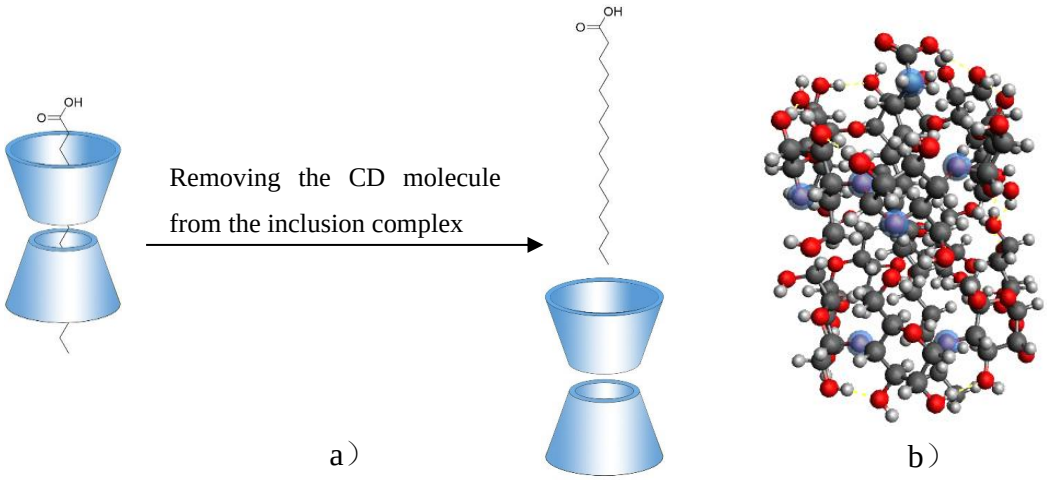

Figure 41 a) Removing the CD molecule from the inclusion complex 4a. b) The starting structure for geometry optimization.

The structure that was selected as the start structure of the scanning consists of palmitic acid and two cyclodextrins. The purpose of the scanning is to remove the palmitic acid from the dimer of the cyclodextrin altogether. Based on previous research into the interaction of two cyclodextrins, the interaction of the two cyclodextrins can be regarded as primary hydroxyl-primary hydroxyl interaction. As illustrated in **Figure 41**, the palmitic acid was twisted and lay in the cave of the cyclodextrin. The secondary hydroxyl groups of the cyclodextrin were next to the carboxyl group of the palmitic acid. At the end of the scanning, the palmitic acid was isolated from the dimer of the cyclodextrins. After the geometry optimization, We can calculate the value of the extraction energy based on the curve of the distance-energy curve.

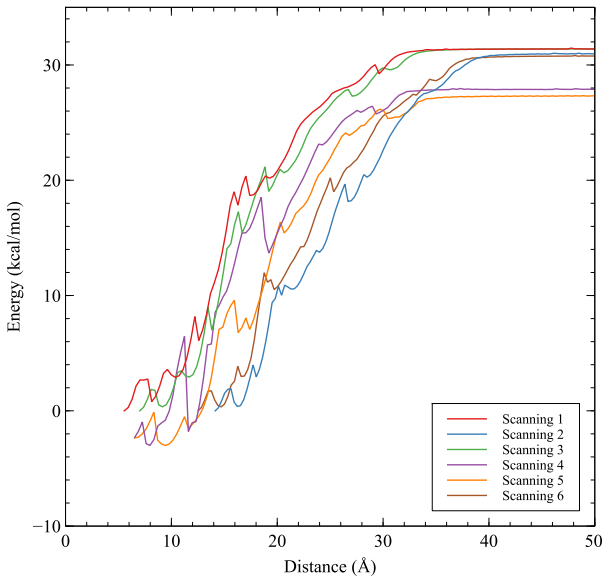

Figure 42. The energy-distance curve of palmitic acid-2CDs Complex 4a (Primary hydroxy

groups-Primary hydroxy groups) (Removing the palmitic acid from the complex 4a)

As depicted in **Figure42**, the palmitic acid was removed from the inclusion complex 4a and then went through the cave of the cyclodextrin molecules. In the reactant, the distance between the cyclodextrin and the carboxyl group of palmitic acid becomes more extensive, the energy of the whole system increases (See **Figure 42**). This mean value of the extraction energy was 30.71 kcal/mol.

The extraction energy of the geometry optimization dimer inclusion complex (Primary hydroxy groups- Primary hydroxy group) was summarized in **Table 13**.

Table 13. The extraction energy of the optimization (Primary hydroxy groups-Primary hydroxy groups)

Number of scanning	The Energy of Start Point (kcal/mol)	The Energy of End Point (kcal/mol)	Extraction Energy (kcal/mol)	Mean value of Extraction Energy (kcal/mol)
1	0	31.38	31.41	30.71
2	0	30.96	30.94	
3	0	31.39	31.37	
4	-2.31	27.88	30.17	
5	-2.35	27.32	29.65	
6	0	30.77	30.75	

Inserting the palmitic acid into cyclodextrin molecule dimer (Inclusion complex 4a)

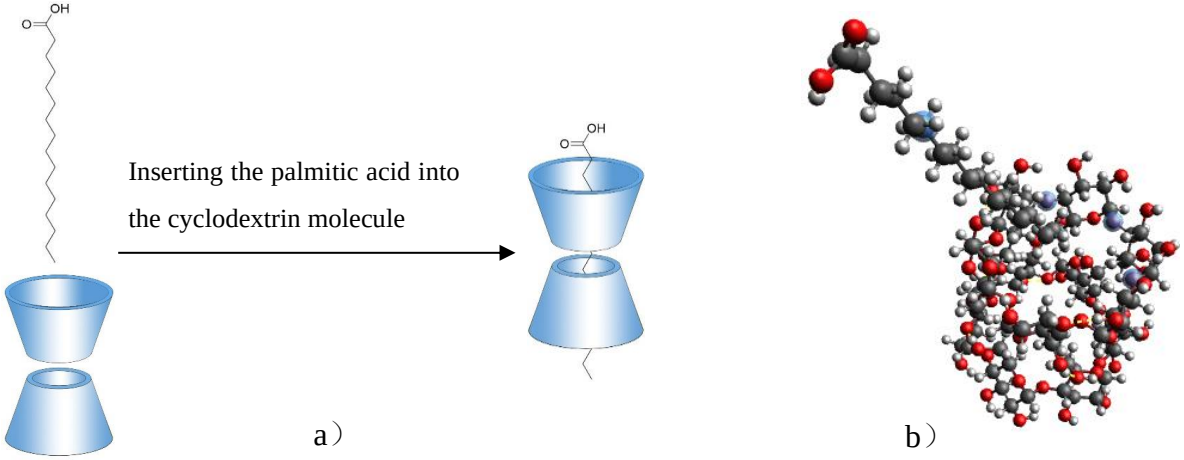

Figure 43 a) Inserting the palmitic acid into the cyclodextrin molecule (inclusion complex 4a). b) The starting structure for geometry optimization.

The goal of this is to include palmitic acid into the cave of the cyclodextrin. The starting structure for scanning is first split into two components: the palmitic acid and the cyclodextrin dimer, with the alkyl chain of the palmitic acid attaching to the hydroxyl group of the cyclodextrin. The structure of the separated palmitic acid and the cyclodextrin molecule is illustrated in **Figure 43**, and the conformation of the palmitic acid was stretched. During the process of scanning, the alkyl chain of palmitic acid comes close to the cyclodextrin dimer and is subsequently inserted into the channel of the cyclodextrin dimer. At the end of the insertion process, the palmitic acid was also stretched, and the alkyl group of the palmitic acid lays the channel of the cyclodextrin dimer. After finishing the geometry optimization of palmitic acid inserting into cyclodextrin, we can determine the insertion energy of the scanning process. (see **Figure 44**)

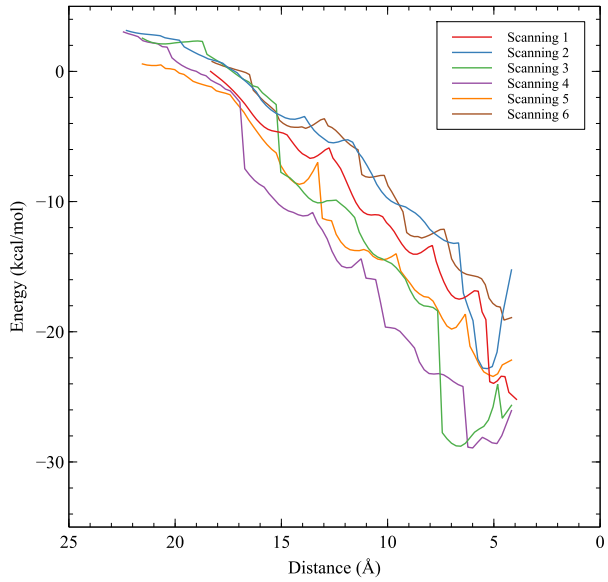

Figure 44. The energy-distance curve of inclusion palmitic acid-2CDs complex 4a (Insertion of palmitic acid into the cyclodextrin dimer)

At the beginning of the scanning, the alkyl chain of the palmitic acid approaches the secondary hydroxyl groups of the cyclodextrin molecular. When the palmitic acid begins to move towards the cave of the cyclodextrin, the end of the alkyl chain gets close to the cave of the cyclodextrin molecular. And then, the remaining part of the alkyl chain goes through the cave of the cyclodextrin molecular. The cyclodextrin and the carboxyl group of palmitic acid become closed, whereby the energy of the entire system decreases (See **Figure 44**). This mean value of the insertion energy is -25.86 kcal/mol.

The insertion energy of the geometry optimization dimer inclusion complex (Primary hydroxy groups-Secondary hydroxy group) was summarized in **Table 14**.

Table 14. The insertion energy (Primary hydroxy groups-Primary hydroxy groups)

Number of scanning	The Energy of Start Point (kcal/mol)	The Energy of End Point (kcal/mol)	The Insertion Energy (kcal/mol)	Mean value of The Insertion Energy (kcal/mol)
1	0	-25.19	-23.75	-25.86
2	3.14	-15.25	-25.79	
3	2.55	-25.65	-31.09	
4	3.02	-26.05	-31.10	
5	0.57	-22.17	-23.78	
6	0.75	-18.91	-19.65	

Removing the cyclodextrin molecule from the inclusion complex 4b

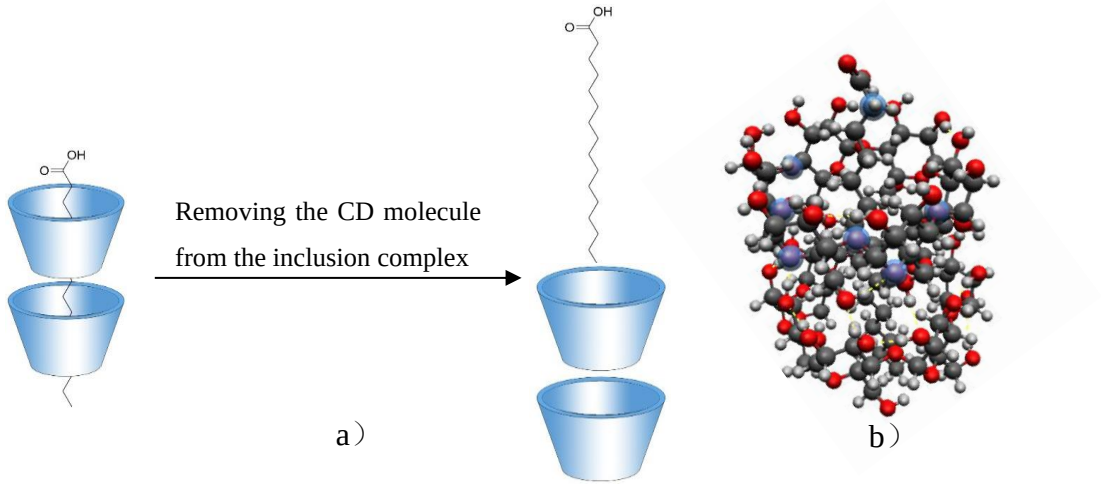

Figure 45 a) Removing the CD molecule from the inclusion complex 4b. b) The starting structure for geometry optimization.

Palmitic acid and two cyclodextrins are the pre-selected structure with which to commence scanning. The geometry optimization is aimed at removing palmitic acid entirely from the cyclodextrin dimer. The interaction of both cyclodextrins can be seen as the primary hydroxyl-secondary hydroxyl interaction based on past studies on the interaction of two cyclodextrins. The palmitic acid has been twisted and laid in the cyclodextrin cave, as shown in **Figure 45**. The cyclodextrin secondary hydroxyl groups are close to the palmitic acid carboxylic group. The palmitic acid was extracted from the dimer of cyclodextrins when the scanning was completed. Following the geometry optimization, the extraction energy value can be calculated based on the distance-energy curve. (see **Figure 45**)

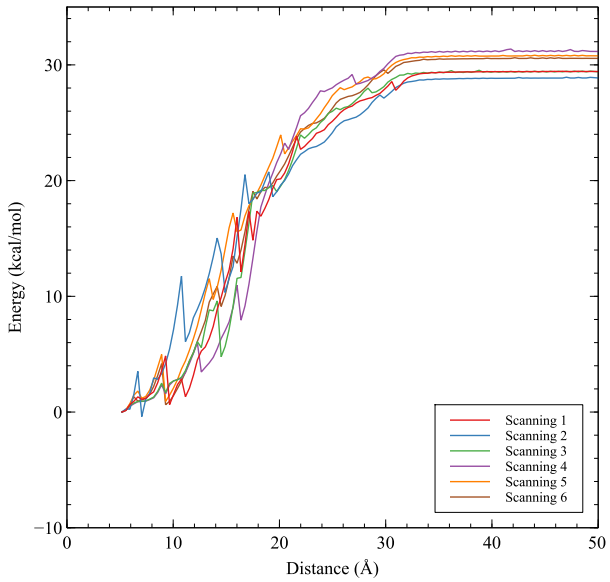

Figure 45. The energy-distance curve of palmitic acid-2CDs Complex 4b (Primary hydroxy groups-Secondary hydroxy groups) (Removing the palmitic acid from the complex 4b)

As depicted in **Figure 45**, the palmitic acid was removed from the inclusion complex 4b and then went through the cave of the cyclodextrin molecules. In the reactant, the distance between the selected atoms of cyclodextrin and the carbon atom of the carboxyl group of palmitic acid becomes more extensive, the energy of the whole system increases (see **Figure 45**). This mean value of the extraction energy is 29.81 kcal/mol.

The extraction energy of the geometry optimization dimer inclusion complex (Primary hydroxy groups-Secondary hydroxy group) was summarized in **Table 15**.

Table 15. The extraction energy of the optimization (Primary hydroxy groups-Secondary hydroxy groups)

Number of scanning	The Energy of Start Point (kcal/mol))	The Energy of End Point (kcal/mol))	Extraction Energy (kcal/mol)	Mean value of Extraction Energy (kcal/mol)
1	0	29.42	29.42	30.03
2	0	28.86	28.86	
3	0	29.39	29.39	
4	0	31.15	31.15	
5	0	30.77	30.77	
6	0	30.56	30.56	

Inserting the palmitic acid into cyclodextrin molecule dimer (Inclusion complex 4b)

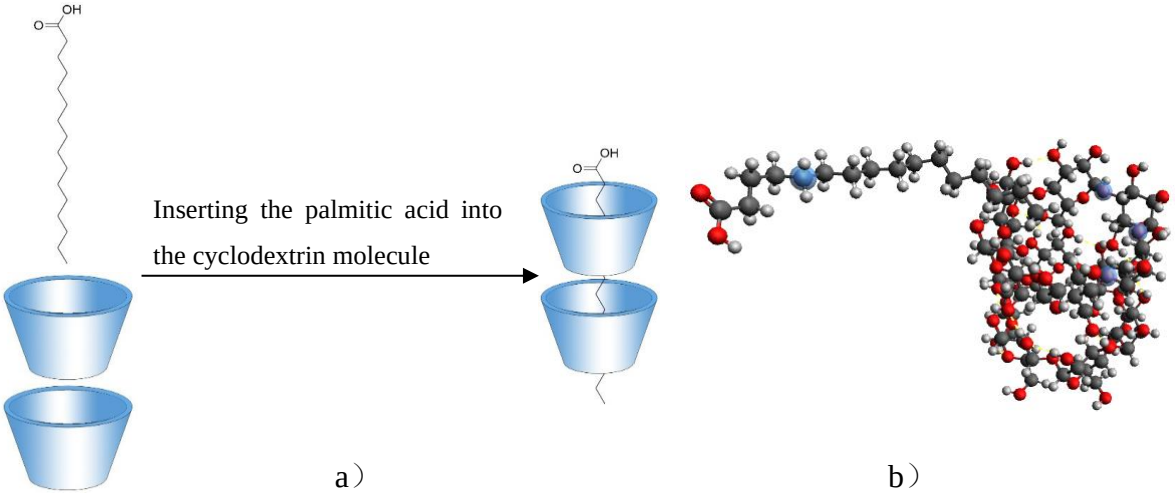

Figure 47 a) Inserting the palmitic acid into the cyclodextrin molecule (inclusion complex 4b); b) The starting structure for geometry optimization.

The purpose of this geometry optimization is to include palmitic acid into the cyclodextrin's cave. The starting structure for scanning is divided into two components: palmitic acid and cyclodextrin dimer, with the palmitic acid's alkyl chain attached to the secondary hydroxyl group of the cyclodextrin dimer. **Figure 47** illustrates the structure of the separated palmitic acid and cyclodextrin molecule, as well as the stretched conformation of the palmitic acid. During the scanning process, the alkyl chain of palmitic acid is close to the cyclodextrin dimer and then is placed into the channel of the cyclodextrin dimer. The palmitic acid was likewise stretched toward the conclusion of the insertion process, and the alkyl group of the palmitic acid formed the channel for the cyclodextrin dimer. After completing the scanning of palmitic acid inserting into cyclodextrin, we were able to obtain the relevant insertion energy of the scanning process.

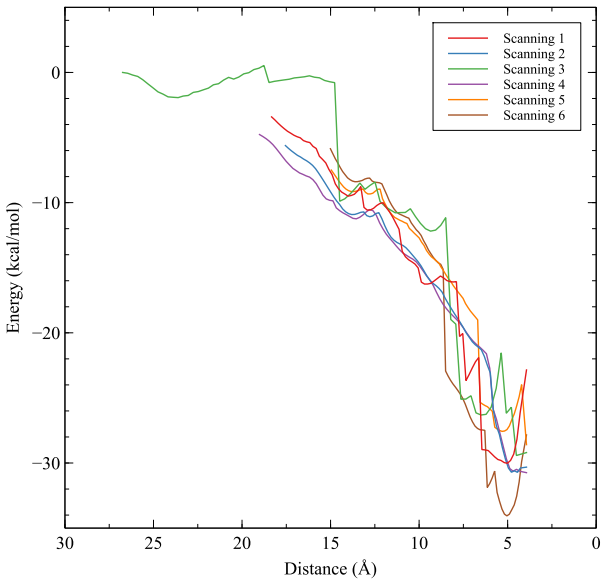

Figure 48. The energy-distance curve of inclusion palmitic acid-2CDs complex 4b (Insertion of palmitic acid into the cyclodextrin dimer)

At the beginning of the scanning, the alkyl chain of the palmitic acid approaches the secondary hydroxyl groups of the cyclodextrin molecular. With the movement of the palmitic acid, the end of the alkyl chain enters into the cave of the cyclodextrin molecular. Thereafter, the remaining part of the alkyl chain goes through the cave of the cyclodextrin molecular. The cyclodextrin and the carboxyl group of palmitic acid become close, whereby the energy of the entire system decreases (See **Figure 48**). This mean value of the insertion energy is -23.73 kcal/mol.

The insertion energy of the geometry optimization dimer inclusion complex (Primary hydroxy groups-Secondary hydroxy group) was summarized in **Table 16**.

Table 16. The insertion energy (Primary hydroxy groups-Secondary hydroxy groups)

Number of scanning	The Energy of Start Point (kcal/mol)	The Energy of End Point (kcal/mol)	The Insertion Energy (kcal/mol)	Mean value of Insertion Energy (kcal/mol)
1	-3.41	-22.85	-19.43	-23.73
2	-5.61	-30.31	-24.70	
3	0	-29.19	-29.19	
4	-4.76	-30.74	-25.97	
5	-7.49	-28.58	-21.09	
6	-5.85	-27.84	-21.98	

Removing the cyclodextrin molecule from the inclusion complex 4c

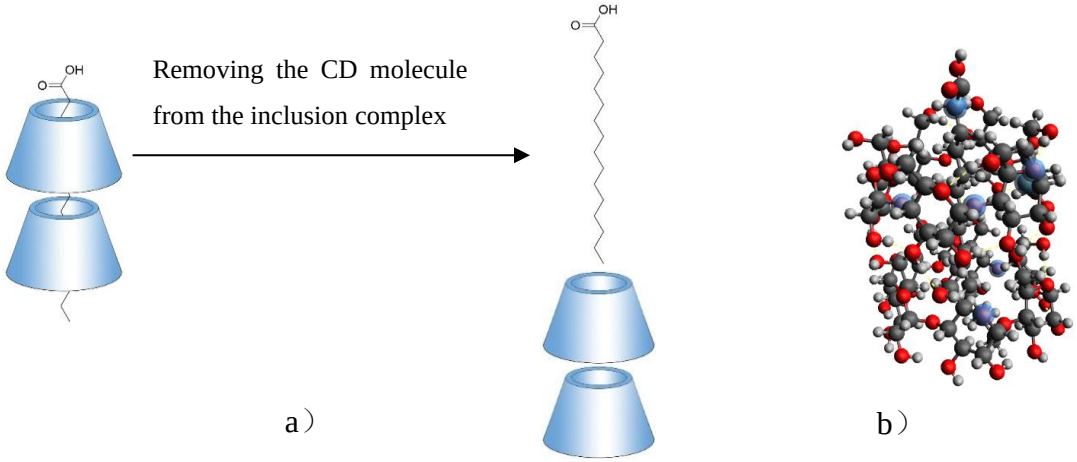

Figure 49 a) Removing the CD molecule from the inclusion complex 6c; b) The starting structure for geometry optimization.

The structure selected as the starting structure for scanning contained palmitic acid and two cyclodextrins. The geometry optimization is intended to completely remove palmitic acid from the cyclodextrin dimer. Based on previous research on the interaction of two cyclodextrins, the interaction of both cyclodextrins can be seen as a secondary hydroxyl-primary hydroxyl interaction. As illustrated in **Figure 49**, the palmitic acid is stretched and placed in the cyclodextrin cave. The secondary hydroxyl groups of cyclodextrin were near the carboxylic group of palmitic acid. When the scanning was finished, the palmitic acid was removed from the cyclodextrin dimer. Following the scanning process, the extraction energy value based on the distance-energy curve can be determined.

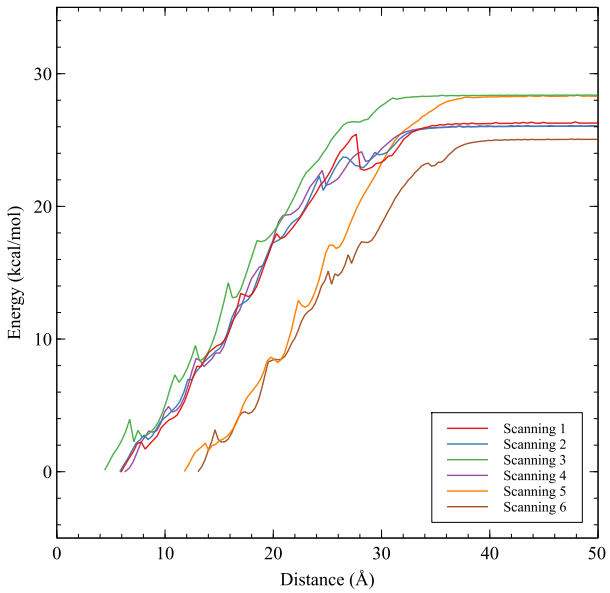

Figure 50. The energy-distance curve of palmitic acid-2CDs Complex 6c (Secondary hydroxy groups-Primary hydroxy groups) (Removing the palmitic acid from the complex 6c)

As depicted in **Figure 50,** the palmitic acid was removed from the inclusion complex 4b and then went through the cave of the cyclodextrin molecules. In the reactant, the distance between the cyclodextrin and the carboxyl group of palmitic acid became wider, whereby the energy of the whole system increases (See **Figure 50**). The mean value of the extraction energy is 26.60 kcal/mol.

The extraction energy of the geometry optimization dimer inclusion complex (Secondary hydroxy groups-Primary hydroxy group) was summarized in **Table 17**.

Table 17. The extraction energy of the optimization (Secondary hydroxy groups-Primary hydroxy groups)

Number of scanning	The Energy of Start Point (kcal/mol))	The Energy of End Point (kcal/mol))	Extraction Energy (kcal/mol)	Mean value of Extraction Energy (kcal/mol)
1	0	26.28	26.28	26.6259
2	0	26.04	25.99	
3	0.17	28.37	28.20	
4	0	26.04	26.02	
5	0	28.29	28.23	
6	0	25.05	25.01	

Inserting the palmitic acid into cyclodextrin dimer (Inclusion complex 4c)

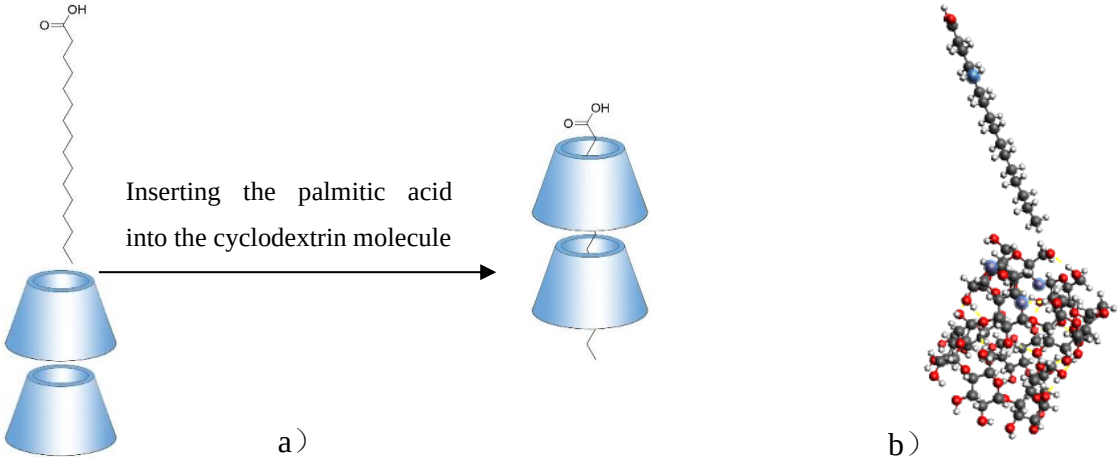

Figure 51 a) Inserting the palmitic acid into the cyclodextrin molecule (inclusion complex 6c); b) The starting structure for geometry optimization.

The goal of this optimization is to insert palmitic acid into the cave of the cyclodextrin. The initial structure for scanning comprises two parts: palmitic acid and cyclodextrin dimer, with the palmitic acid's alkyl chain linked to the cyclodextrin dimer's secondary hydroxyl group. **Figure 51** depicts the structure of the separated palmitic acid and cyclodextrin molecules, as well as the palmitic acid in its stretched conformation. During the scanning process, the palmitic acid alkyl chain is closed to the cyclodextrin dimer and then put into the cyclodextrin dimer's channel. The palmitic acid was also stretched near the end of the insertion process, and the palmitic acid's alkyl group created the channel for the cyclodextrin dimer. We were able to get the appropriate insertion energy of the scanning process following geometry optimization.

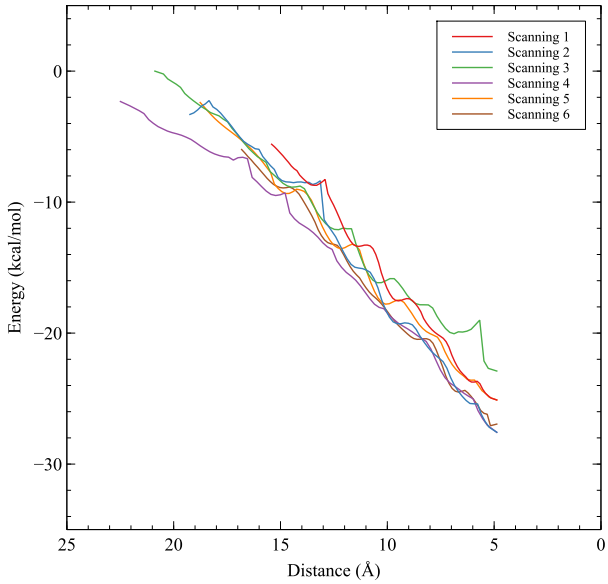

Figure 52. The energy-distance curve of inclusion palmitic acid-2CDs complex 6c (Insertion of palmitic acid into the cyclodextrin dimer)

At the beginning of the scanning, the alkyl chain of the palmitic acid approached the primary hydroxyl groups of the cyclodextrin molecular. With the movement of the palmitic acid, the end of the alkyl chain entered into the cave of the cyclodextrin molecular. Following this, the rest part of the alkyl chain went through the cave of the cyclodextrin molecular. The cyclodextrin and the carboxyl group of palmitic acid became close, whereby the energy of the entire system decreased (see **Figure 52**). This mean value of the insertion energy was -22.57 kcal/mol.

The insertion energy of the geometry optimization dimer inclusion complex (Secondary hydroxy groups-primary hydroxy group) was summarized in **Table 18**.

Table 18. The insertion energy (Secondary hydroxy groups-Primary hydroxy groups)

Number of Optimization	The Energy of Start Point (kcal/mol))	The Energy of End Point (kcal/mol))	The insertion energy (kcal/mol)	Mean value of the Insertion energy (kcal/mol)
1	-5.58	-25.10	-19.52	-22.60
2	-3.30	-27.57	-24.26	
3	0	-22.89	-22.89	
4	-2.32	-27.57	-25.25	
5	-2.39	-25.10	-22.70	
6	-5.98	-26.94	-20.96	

Removing the cyclodextrin molecule from the inclusion complex 4d

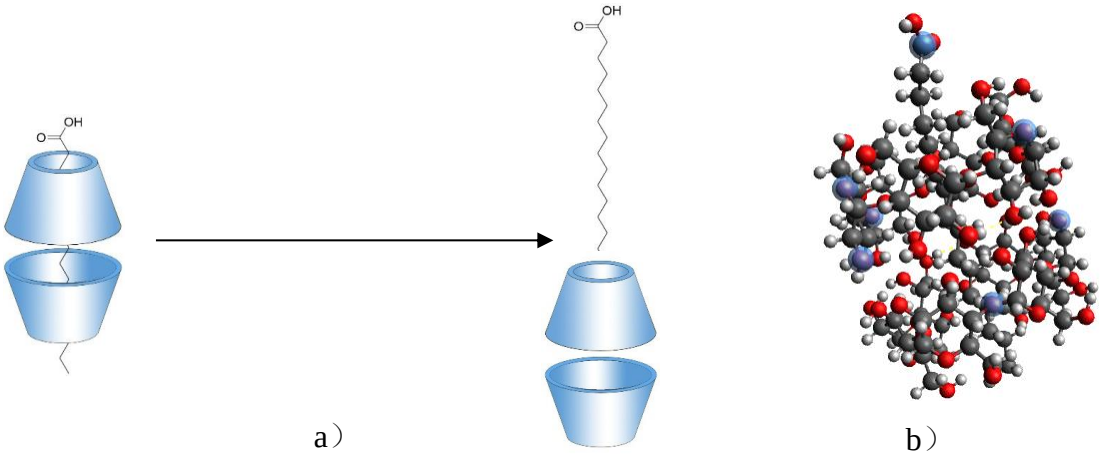

Figure 53 a) Removing the CD molecule from the inclusion complex 4d; b) The starting structure for geometry optimization.

The starting structure selected for geometry optimization included palmitic acid and two cyclodextrins. The palmitic acid is expected to be fully removed from the cyclodextrin dimer during the scanning process. A secondary hydroxyl-secondary hydroxyl interaction between the two cyclodextrins, based on a prior study on the interaction of two cyclodextrins, can be seen between the two cyclodextrins. As shown in **Figure 53**, the palmitic acid has been stretched and inserted into the cyclodextrin cave to achieve the desired result. The primary hydroxyl groups of cyclodextrin were in close proximity to the carboxylic group of palmitic acid in this structure. As soon as the scanning process had been completed, the palmitic acid was extracted from the cyclodextrin dimer. Based on the distance-energy curve, it is possible to determine the extraction energy value following geometry optimization.

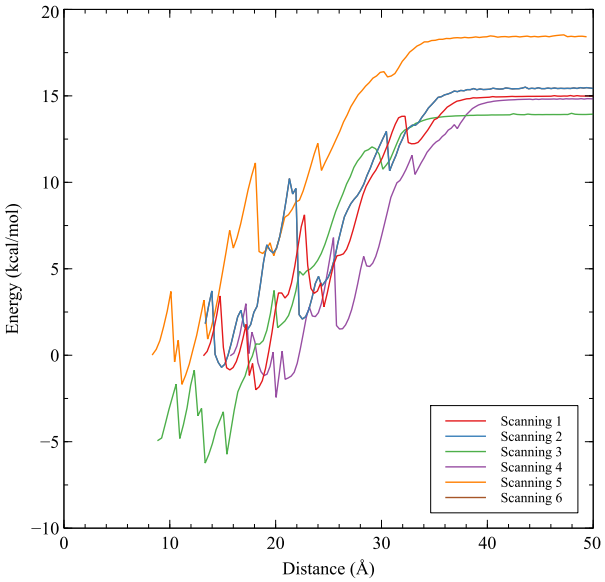

Figure 54 The energy-distance curve of palmitic acid-2CDs Complex 4d (Secondary hydroxy groups-Secondary hydroxy groups) (Removing the palmitic acid from the complex 4d)

At the beginning of the scanning, the palmitic acid model moves away from the cyclodextrin dimer. With the movement of the palmitic acid, the end of the alkyl chain thread through the channel of the second cyclodextrin molecular. And then, the rest part of the alkyl chain goes through the cave of the cyclodextrin molecular. At the end of scanning, with palmitic acid movement, the palmitic acid was obliterated from the inclusion complex, and the energy of the whole system decreased. (see **Figure 54**)

It is noteworthy that the peak of the extraction energy can be observed in the distance-energy curve. Because the channel of the cyclodextrins is not parallel, the steric hindrance of the hydroxyl group can prevent the palmitic acid molecule from threading through the cave of cyclodextrin (see **Figure 55**). When the alkyl chain of palmitic acid is between two cyclodextrin molecules, we can thus see the peak of the distance-energy curve. We can calculate the extraction energy based on the distance-energy curve. The mean value of the extraction energy is 10.12 kcal/mol (see **Table 19**).

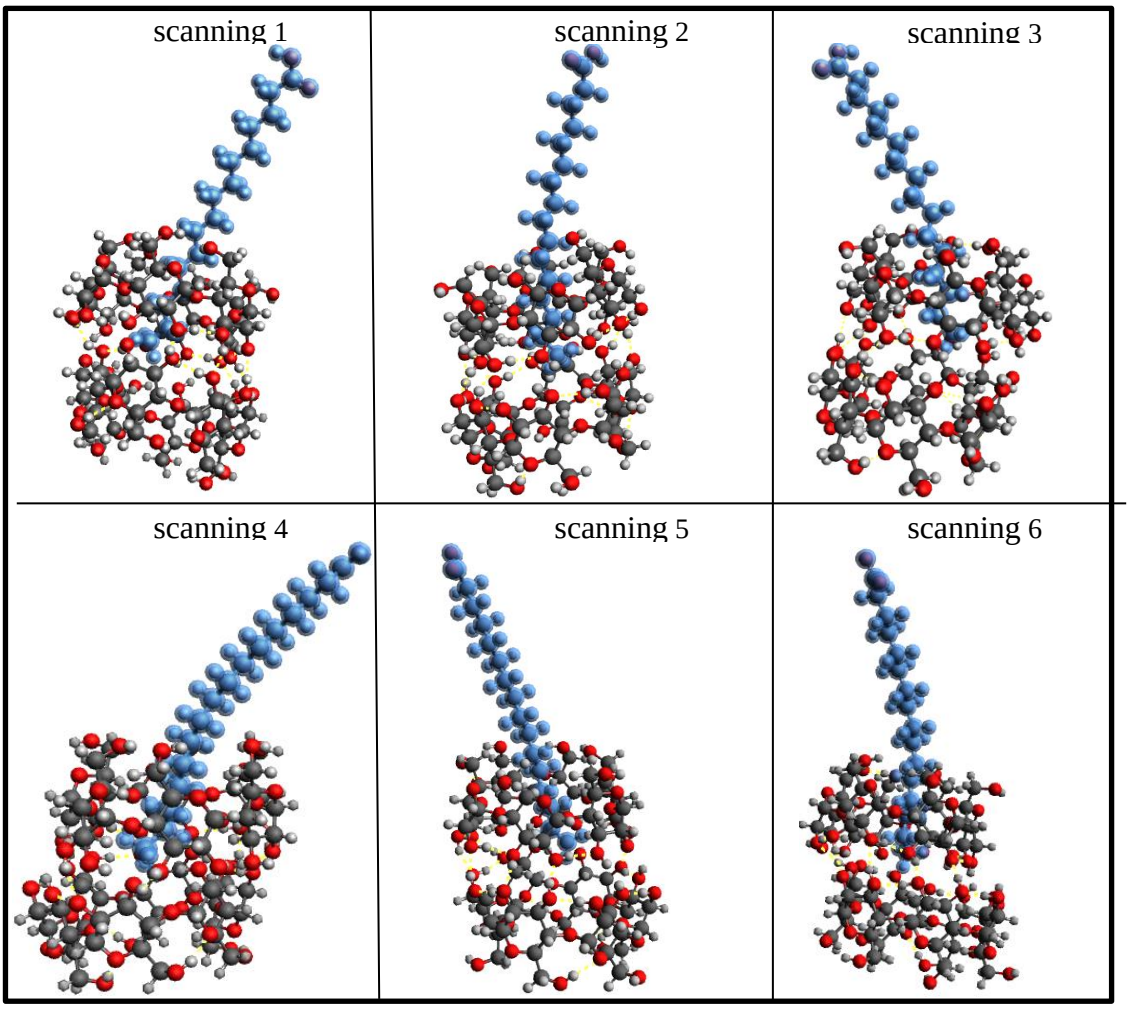

Figure 55. The conformation of inclusion complex 4d at the peak point of the distance-energy curve

The extraction energy of the geometry optimization dimer inclusion complex (Secondary hydroxy groups-Secondary hydroxy group) was summarized in **Table 19**.

Table 19. The extraction energy of the geometry optimization (Secondary hydroxy groups-Secondary hydroxy groups, The extraction energy between the lowest energy and the peak of energy curve)

Number of scanning	The Lowest Energy (kcal/mol)	The peak of the Energy curve (kcal/mol)	Extraction Energy (kcal/mol)	Mean value of Extraction Energy (kcal/mol)
1	0.82	10.93	10.11	10.13
2	-0.55	8.70	9.25	
3	-3.42	6.55	9.98	
4	0.37	9.61	9.23	
5	0	12.66	12.66	
6	0.59	10.12	9.52	

Inserting the palmitic acid into cyclodextrin dimer (Inclusion complex 4d)

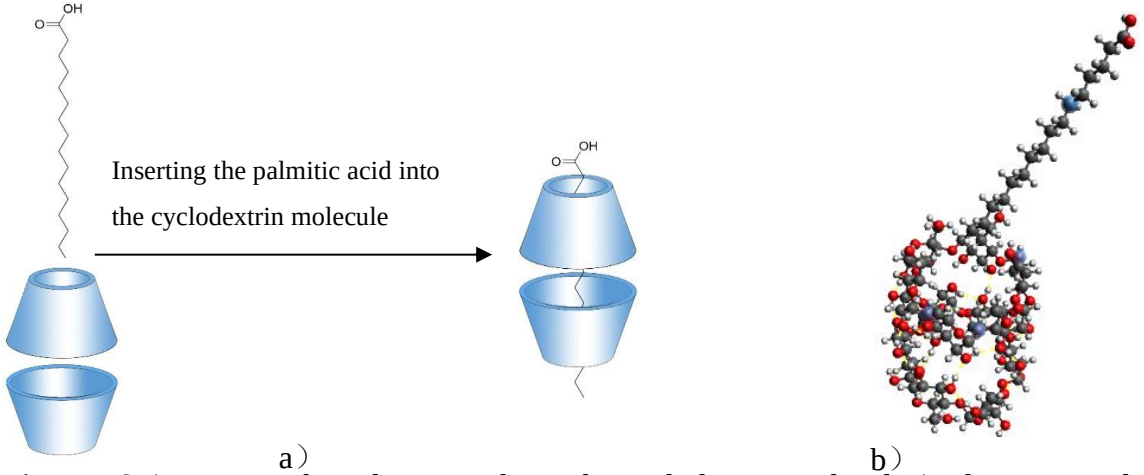

Figure 56 a) inserting the palmitic acid into the cyclodextrin molecule (inclusion complex 4d); b) The starting structure for geometry optimization.

The goal of this geometry optimization is to insert the palmitic acid into the channel of the cyclodextrin dimer. The initial structure for scanning comprises two components: palmitic acid and cyclodextrin dimer, with the alkyl chain of the palmitic acid linked to the secondary hydroxyl group of the cyclodextrin dimer. **Figure 56** illustrates the structure of the separated palmitic acid and cyclodextrin molecules, as well as the stretched conformation of the palmitic acid. During the scanning process, the alkyl chain of palmitic acid is closed off from the cyclodextrin dimer before being inserted into the channel of the cyclodextrin dimer. The palmitic acid was similarly stretched near the end of the insertion process. After finishing the geometry optimization of palmitic acid insertion into cyclodextrin, we were able to obtain the necessary extraction energy for the geometry optimization procedure. (see **Figure 57**)

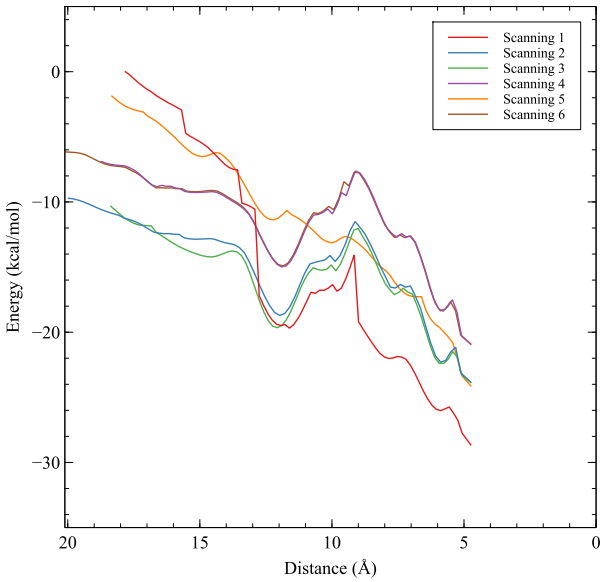

Figure 57. The energy-distance curve of inclusion palmitic acid-2CDs complex 4d (Insertion of palmitic acid into the cyclodextrin dimer)

At the beginning of the scanning, the alkyl chain of the palmitic acid is near the primary hydroxyl groups of the cyclodextrin molecular. With the movement of the palmitic acid, the end of the alkyl chain enters into the cave of the cyclodextrin molecular. Thereafter, the remaining part of the alkyl chain goes through the cave of the cyclodextrin dimer. (see **Figure 58**)

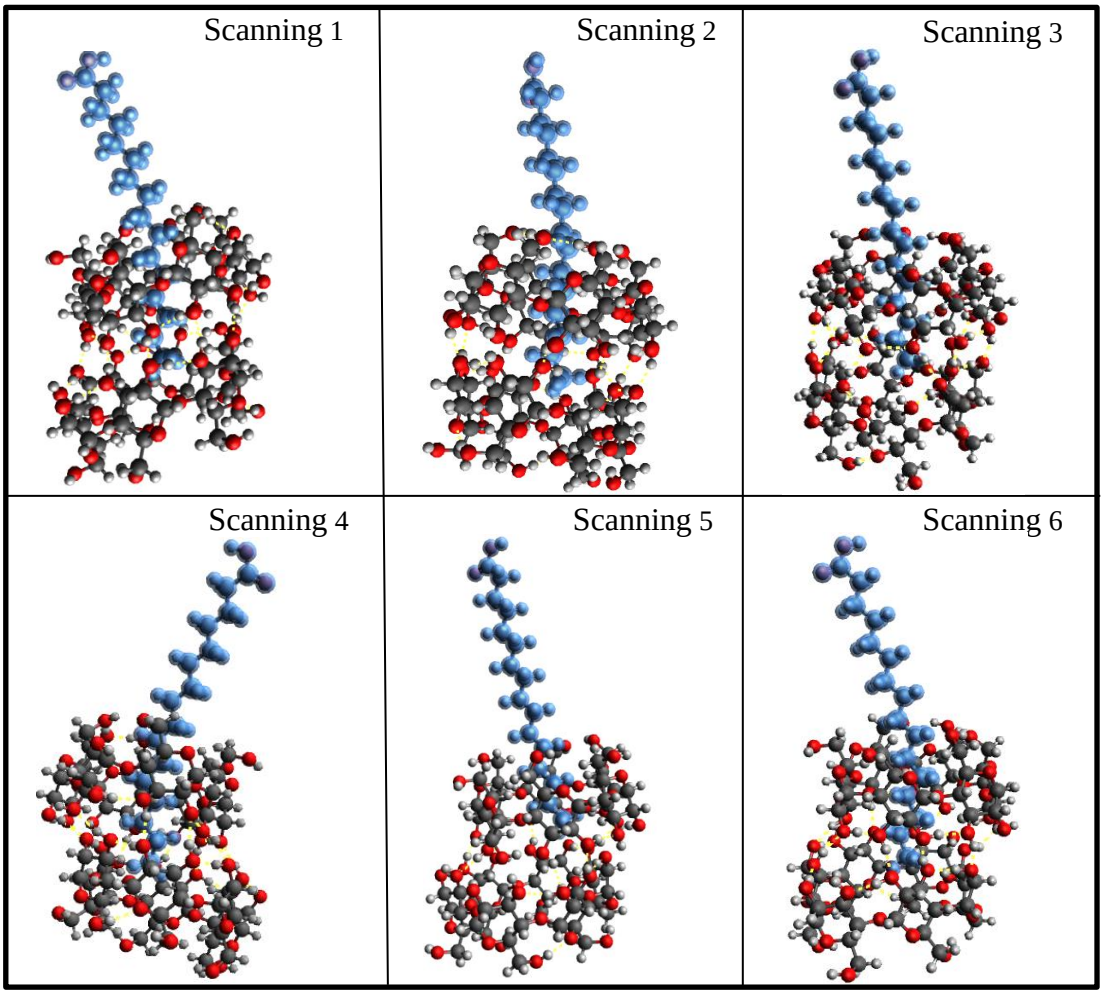

Figure 58. The conformation of inclusion complex 4d at the peak point of the distance-energy curve

It is noteworthy that the peak point of scanning can be observed in the distance-energy curve. Because the channels of the cyclodextrins are not parallel, the steric hindrance of the hydroxyl group can prevent palmitic acid from threading through the cave of cyclodextrin. We can calculate the energy barrier based on the distance-energy curve. The mean value of the energy barrier is 6.75 kcal/mol (see **Table 21**). With the movement of palmitic acid, the palmitic acid inserts into the cyclodextrin completely, and the energy of the whole system

decrease. Thus, the mean value of the insertion energy is -17.89 kcal/mol (see **Table 20**).

Table 20. The insertion energy (Secondary hydroxy groups-Secondary hydroxy groups)

Number of scanning	The Energy of Start Point (kcal/mol)	The Energy of End Point (kcal/mol)	The Insertion energy (kcal/mol)	Mean value of the Insertion energy (kcal/mol)
1	0	-28.65	-28.65	-17.89
2	-9.71	-23.83	-14.11	
3	-10.32	-23.86	-13.53	
4	-6.89	-20.91	-14.01	
5	-1.87	-24.12	-22.24	
6	-6.15	-20.92	-14.76	

As depicted in **Table 21**, we can observe the extraction energy during the insertion process and summarise the energy barrier after comparing the various scannings.

Table 21. The energy barrier of the geometry optimization

Number of scanning	The Lowest Energy (kcal/mol)	The Peak of Energy Barrier (kcal/mol)	Energy Barrier (kcal/mol)	Mean value of Energy Barrier (kcal/mol)
1	-19.40	-14.06	5.33	6.58
2	-18.56	-11.96	6.59	
3	-19.48	-12.03	7.45	
4	-14.98	-7.78	7.20	
5	-14.67	-8.36	6.31	

Summary of the geometry optimization of inclusion complex 4a,4b,4c and 4d

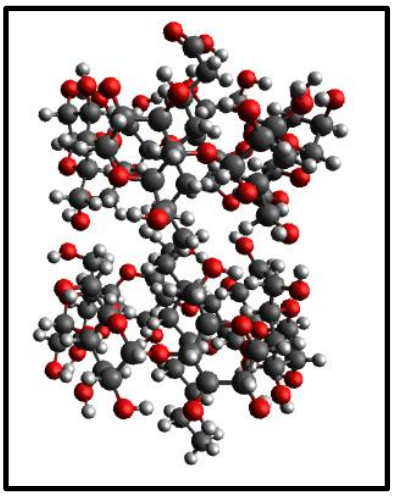

4a, palmitic acid-2CDs complex (Primary hydroxyl-Primary hydroxyl)

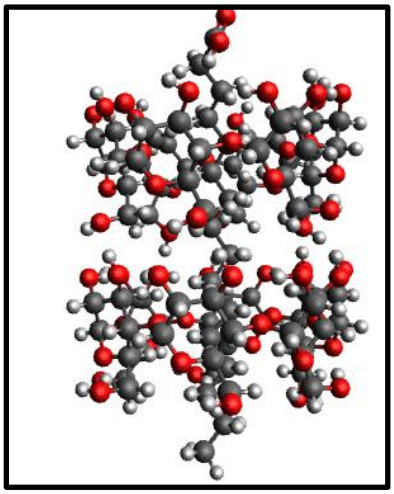

4b, palmitic acid-2CDs complex (Primary hydroxyl-Secondary hydroxyl)

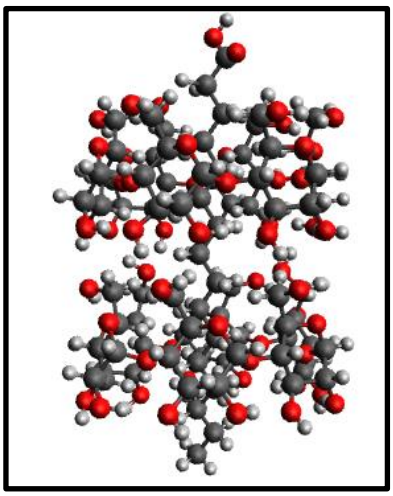

4c, palmitic acid-2CDs complex (Secondary hydroxyl-Primary hydroxyl)

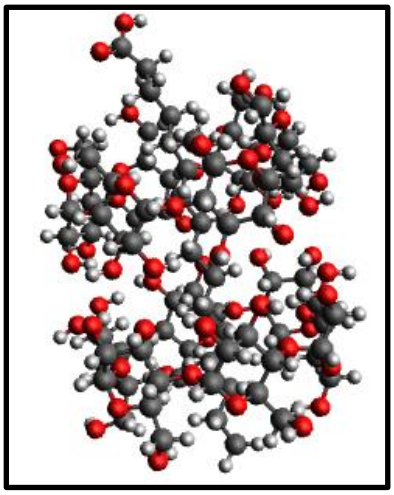

4d, palmitic acid-2CDs complex (Secondary hydroxyl-Secondary hydroxyl)

Figure 59 The structure of the inclusion complex of the α-cyclodextrin dimer with palmitic acid

Because there are three different kinds of interactions between hydroxyl groups of α-cyclodextrin, and the orientation between the hydroxyl groups of α-cyclodextrin and the carboxyl group of the palmitic acid can be classified into two different types, the inclusion complexes consisting of palmitic acid and α-cyclodextrin dimer could be classified into four different types: (1) primary hydroxyl groups-primary hydroxyl groups (4a); (2) primary hydroxyl groups-secondary hydroxyl groups (4b); (3) secondary hydroxyl groups-primary hydroxyl groups (4c); (4) secondary hydroxyl groups-secondary hydroxyl groups (4d). (see **Figure 59**)

The extraction energy and the insertion energy of the dimer inclusion complex (Inclusion complex 4a, Inclusion complex 4b, Inclusion complex 4c, and Inclusion complex 4d) were summarized in **Table 22**.

Table 22 The extraction energy and the insertion energy of complex 4a, 4b, 4c and 4d

	Mean value of extraction energy (kcal/mol)	Mean value of the insertion energy (kcal/mol)
Inclusion complex 4a	30.71	-25.86
Inclusion complex 4b	30.03	-24.58
Inclusion complex 4c	26.60	-22.57
Inclusion complex 4d	10.12	-17.89

At the beginning of removing cyclodextrin molecules, the palmitic acid is in the cave of the cyclodextrin molecules. With the movement of the cyclodextrin molecules, the palmitic acid and the cyclodextrin molecules grow further away from each other. At the same time, the energy of the whole system increases. Therefore, we can calculate the extraction energy between the start point and the end point.

At the beginning of inserting palmitic acid, the palmitic acid is near the cyclodextrin molecules. With the movement of the palmitic acid, the palmitic acid and the cyclodextrin molecules become close to each other. Furthermore, the palmitic acid was thread through the cave of cyclodextrin molecules. At the same time, the energy of the entire system decreases. So, we can calculate the insertion extraction energy between the start point and the end point.

After we obtain the extraction energy and the insertion energy of the inclusion complex, we can ascertain that the extraction energy of the inclusion complex 4a is 30.71 kcal/mol. Moreover, the corresponding insertion energy is -25.86 kcal/mol. In general, the extraction energy and the insertion energy of the inclusion complex 4a are more significant than any other inclusion complexes. (see **Table 22**) It means that it is difficult to remove the cyclodextrin molecules from complex 4a. In conclusion, the inclusion complex 4a is the most stable out of the four complexes.

The extraction energy and the inserting energy of the inclusion complex 4d are different from other inclusion complexes. The extraction energy of inclusion complex 4d is 10.12 kcal/mol. Moreover, the extraction energy of inclusion complexes 4a, 4b, and 4c are 30.71, 29.81, and 26.60 kcal/mol, respectively. The extraction energy of inclusion complex 4d is

much lower than other inclusion complexes. Similar phenomena can be observed in the scanning of insertion energy. The insertion extraction energy of inclusion complex 4a, 4b, 4c, and 4d are -25.86, -24.58, -22.57 and -17.89 kcal/mol respectively. (see **Table 22**)

It is noteworthy that the extraction energy of 4d could be obtained as the difference between the peak and the start point of the energy-distance curve, while the extraction energy of other complexes could be obtained as the difference between the endpoint and the start point of the energy-distance curve. Moreover, similar extraction energy can be observed via reverse scanning.

In inclusion complex 4d, the channels of the cyclodextrins are not parallel. The steric hindrance of the hydroxyl group could prevent the palmitic acid molecule from threading through the cave of cyclodextrin. When the alkyl chain of palmitic acid is between two cyclodextrin molecules, we could ascertain the peak of the distance-energy curve during the scanning. (see **Figure 60**)

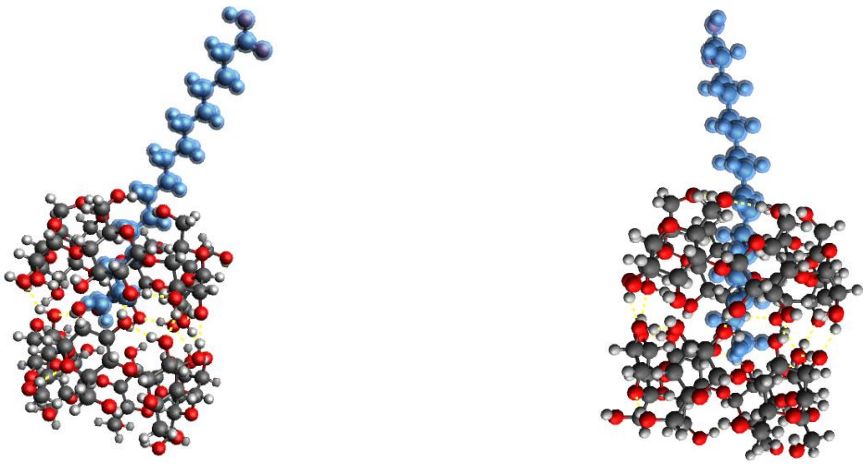

a）　　b）

Figure 60. a) The conformation of inclusion complex 4d at the peak point of the distance-energy curve (removing the cyclodextrin molecule from the inclusion complex 4d). b) The conformation of inclusion complex 4d at the peak point of the distance-energy curve (Inserting the palmitic acid into cyclodextrin molecular 4d).

3.3.3 The scanning of the hexasaccharide cyclodextrin complex

Based on the result of removing the cyclodextrin from the cyclodextrin-palmitic acid complex, we selected the cyclodextrins whose interaction is primary hydroxyl group-primary hydroxyl group as the start structure.

The aim of the first scanning is to explore the minimum extraction energy after removing the first cyclodextrin. In this case, three unique scanning paths can give three different precise energies of the identical hexasaccharide cyclodextrin can be obtained via three different scanning pathways. After comparing the extract energy value, we can select the most reasonable pathway to get the target molecule for the next scanning. (see **Figure 61**)

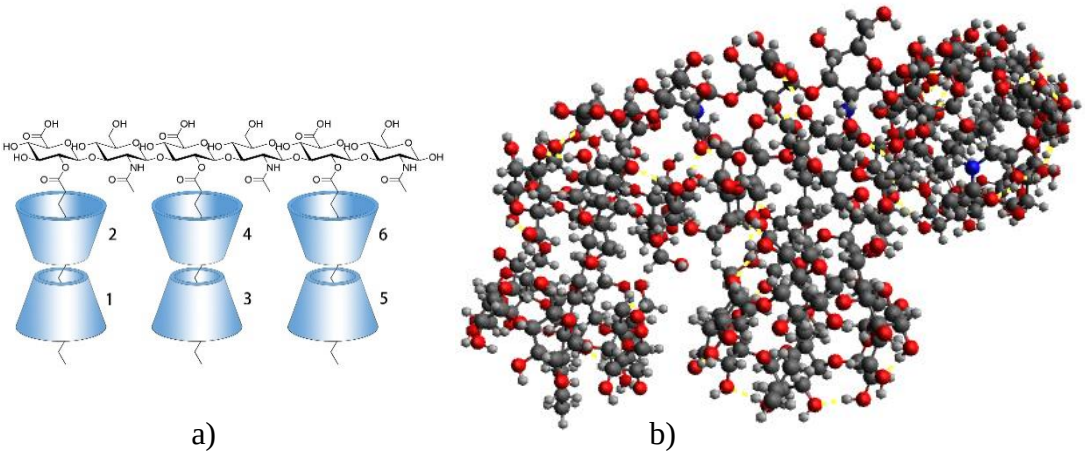

a) b)

Figure 61. a) The schematic diagram of the hexasaccharide cyclodextrin complex; b) The structure of the hexasaccharide cyclodextrin complex

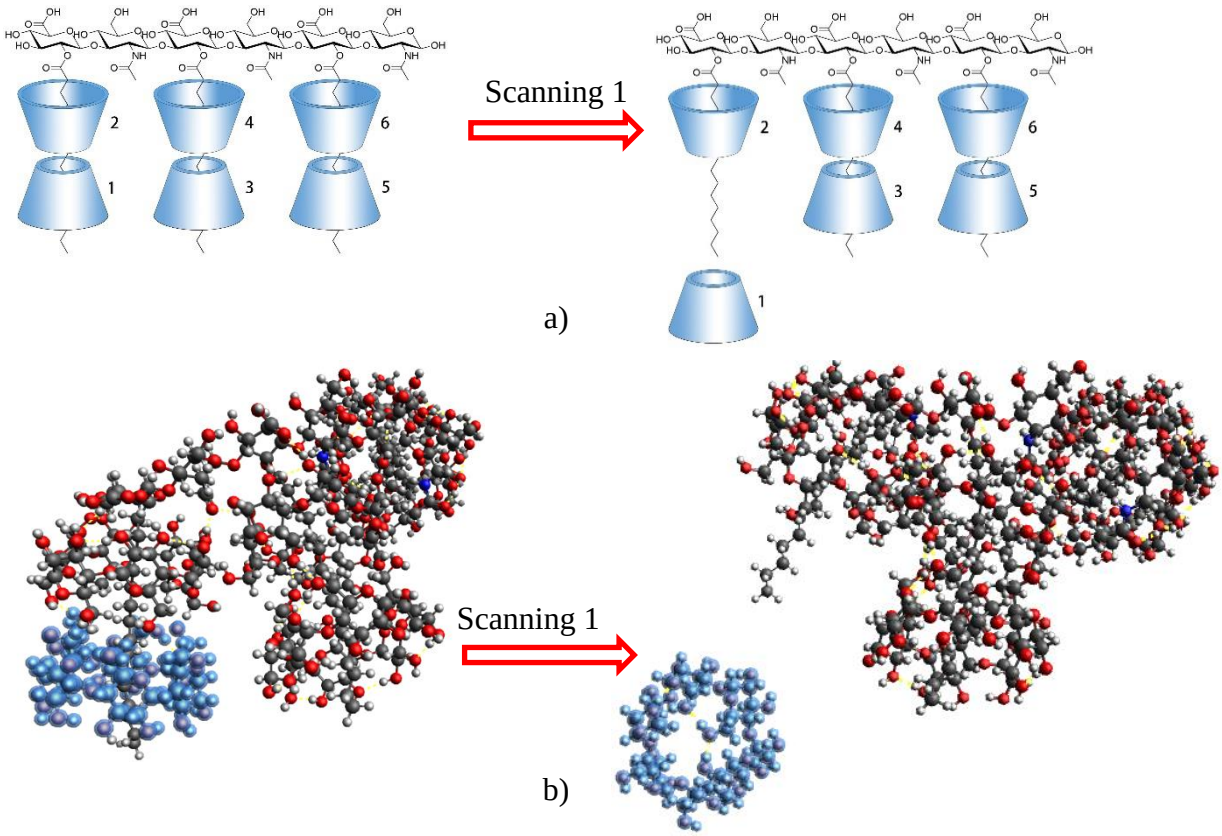

Figure 62. a) The schematic diagram of removing the CD#1 from the hexasaccharide cyclodextrin complex; b) The process of removing CD#1 the hexasaccharide cyclodextrin complex (The removed cyclodextrin is colored in blue for clarity.)

CD#1 was removed from the complex. During the process, CD#1 went away from the complex. Due to the interaction between CD#1 and CD#2, CD#2 moves slightly but still remains around the lipid chain.

The goal of this scanning is to remove the cyclodextrin molecule from the inclusion complex. The initial structure of the inclusion complex for scanning consists of two components: a hexasaccharide molecule and six cyclodextrin molecules. In the conclusion complex, the alkyl chain of the hexasaccharide is laid in the channel of the corresponding cyclodextrin dimer. The schematic diagram (**Figure 62**) illustrates the stretched conformation of the alkyl chain of the hexasaccharide, and the alkyl chains were thread through the channel formed by the adjacent cyclodextrin molecules. During the scanning process, the cyclodextrin molecule of hexasaccharide was separated from the alkyl chain. At the end of the scanning process, the removed cyclodextrin was isolated from the remainder of the hexasaccharide-5CDs complex, whereby the hexasaccharide-5CDs complex's conformation changed slightly. The conformation of the alkyl chain from which the cyclodextrin was removed remained stretched by the end of the insertion process. We were able to obtain the necessary extraction

energy for the scanning procedure after completing the scanning of palmitic acid insertion into cyclodextrin.

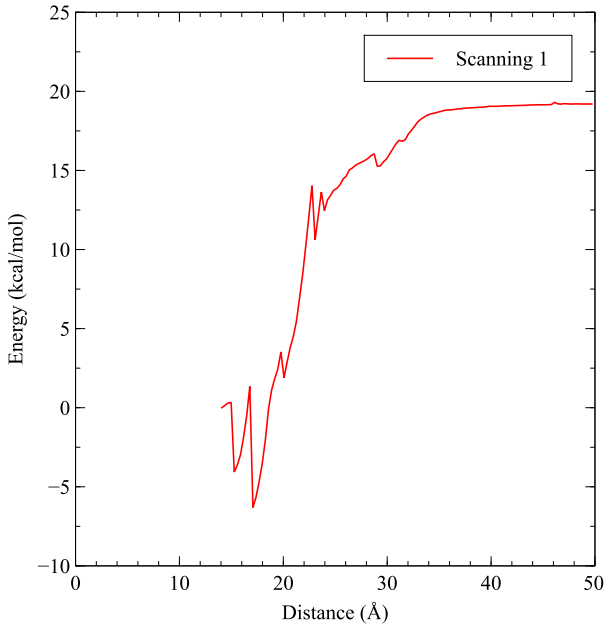

Figure 63 The energy-distance curve of the hexasaccharide cyclodextrin complex (Removing the cyclodextrin CD#1 from hexasaccharide cyclodextrin complex)

The extraction energy of removing CD#1 is 19.21 kcal/mol. (see **Figure 63**)

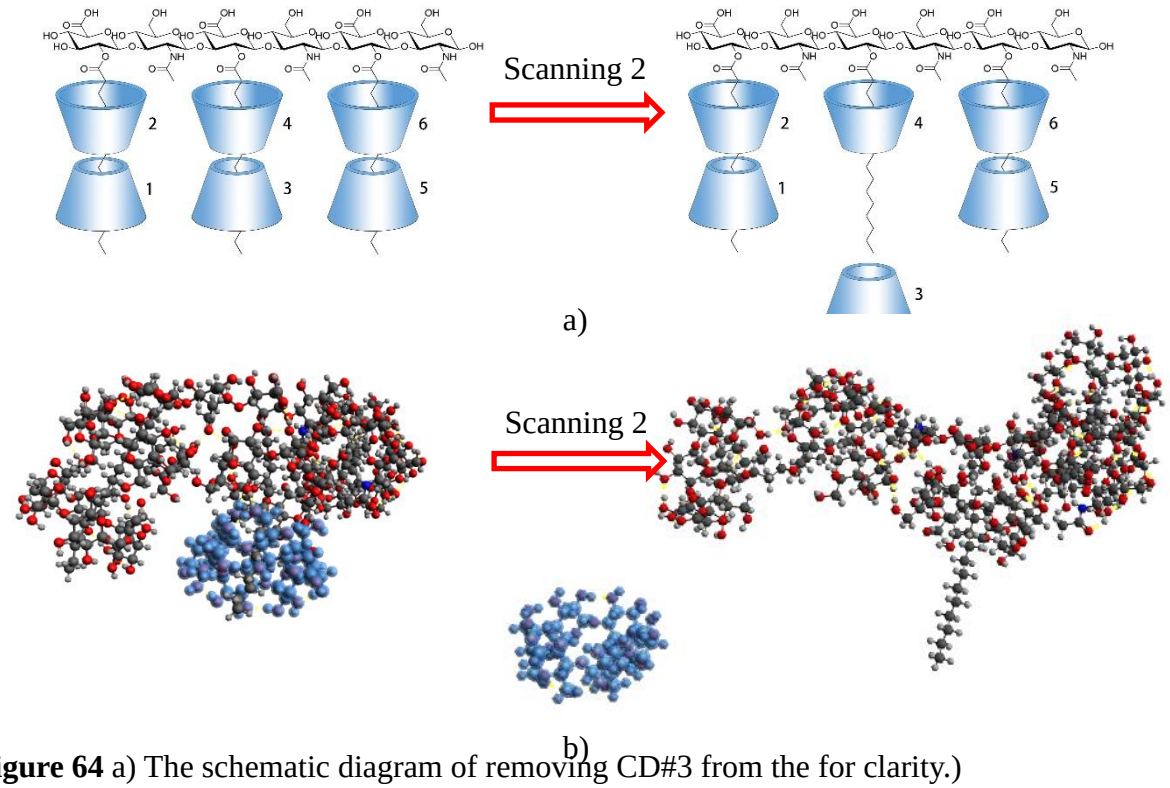

Figure 64 a) The schematic diagram of removing CD#3 from the for clarity.)

This scanning procedure aims to remove the cyclodextrin molecule from the inclusion complex. The inclusion complex for scanning initially comprises two components: a hexasaccharide molecule and six cyclodextrin molecules. The alkyl chain of hexasaccharide is inserted into the channel of the matching cyclodextrin dimer in the conclusion complex. The schematic diagram (see **Figure 64**) depicted the hexasaccharide's alkyl chain in a stretched conformation, with the alkyl chains threaded through a channel formed by neighboring cyclodextrin molecules. The hexasaccharide cyclodextrin molecule was isolated from the alkyl chain during the scanning process. Following the scanning procedure, the removed cyclodextrin was separated from the remaining hexasaccharide-5CDs complex, and the conformation of the hexasaccharide-5CDs complex was slightly altered. At the end of the insertion procedure, the conformation of the alkyl chain from which cyclodextrin was removed remained extended. After successfully scanning of extracting the cyclodextrin from the hexasaccharide-6CDs complex, we were able to acquire the extraction energy for the scanning process.

The whole process of scanning can be depicted in **Figure 64**, and CD #3 was removed from the complex. CD#3 went away from the complex during the process and moved close to CD#1. Due to the interaction between CD#3 and CD#1, CD#1 moved following CD#3. At the end of the process, CD#1 was still around the lipid chain.

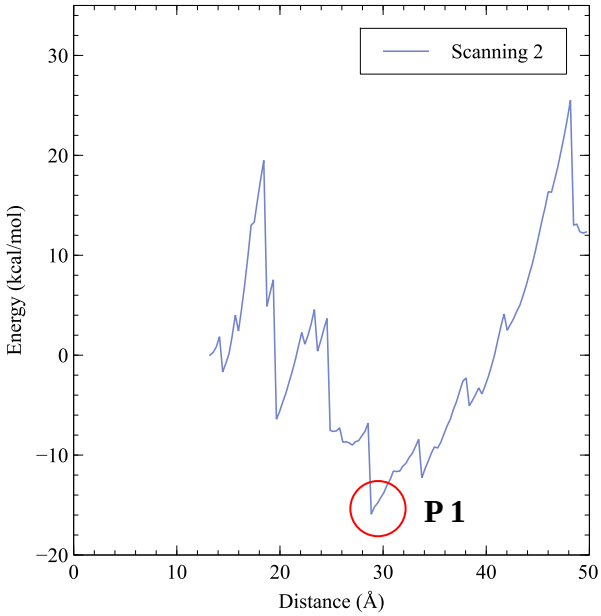

Figure 65. The energy-distance curve of the hexasaccharide cyclodextrin complex (Removing the cyclodextrin CD#3 from hexasaccharide cyclodextrin complex)

The extraction energy of removing CD#3 is 12.31 kcal/mol. (see **Figure 65**)

We can identify the differences between these structures by comparing the starting structure of scanning 2 to the structures of the minimum point **P1**. At the minimal point **P1**, the secondary hydroxyl groups of CD#3 can form hydrogen bonds with CD#5. CD#5 and CD#4 are still around the lipid chain in **P1**. With an increase in the distance between the cyclodextrin CD#3 and the palmitic acid residue, CD#3 became totally detached from the lipid chain. Additionally, the lipid chain containing cyclodextrin CD#4 was in a stretched conformation. CD#4 was still close to the carboxyl group of the fatty-acyl group. (see **Figure 66**) The extraction energy for this step is 12.31 kcal/mol.

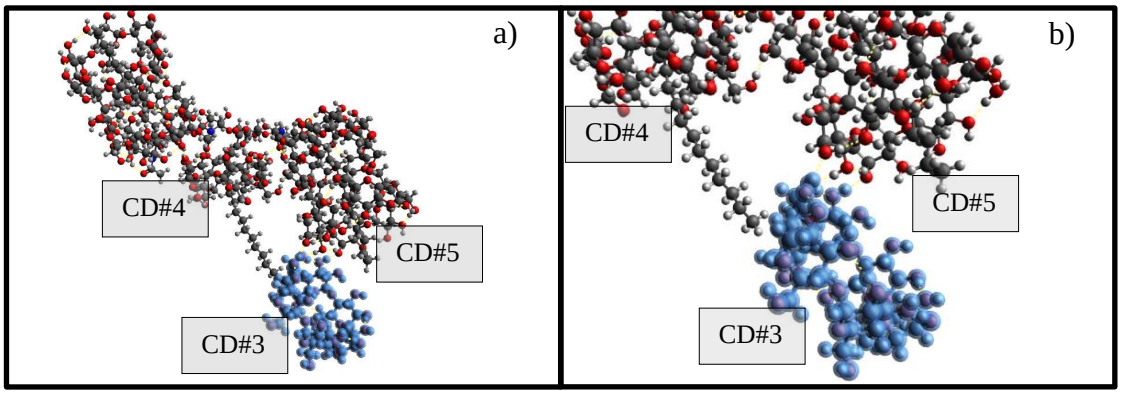

Figure 66 a) The structure of the minimum point **P1** hexasaccharide cyclodextrin complex. b) The position of CD#5 and CD#4 relative to the removed CD#3. (The removed cyclodextrin CD#3 is colored in blue for clarity, and the black dash line indicates the hydrogen bond between CD#3 and CD#5)

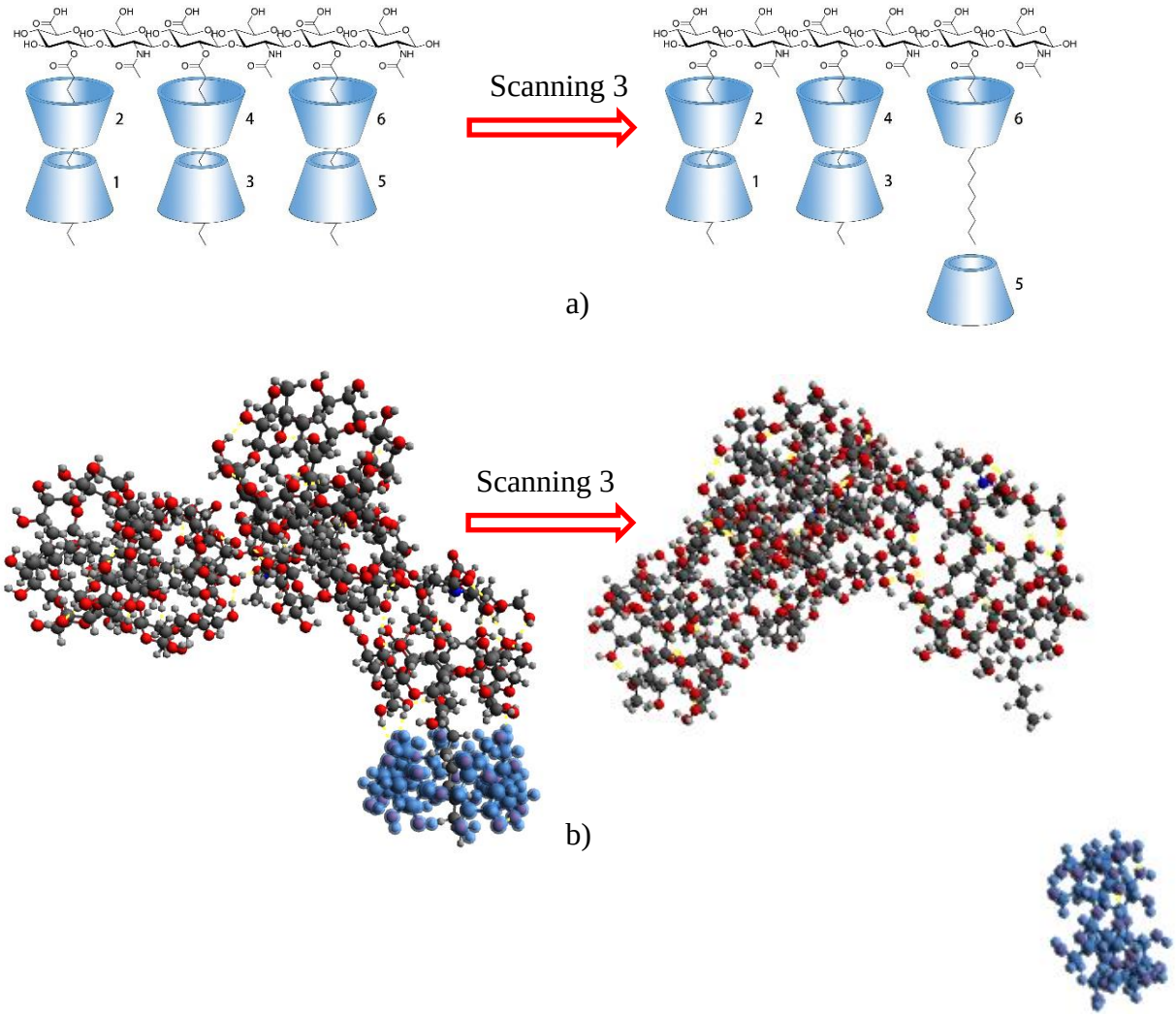

Figure 67. a) The schematic diagram of removing the CD#5 from the hexasaccharide cyclodextrin complex; b) The process of removing the CD#5 the hexasaccharide cyclodextrin complex (The removed cyclodextrin is colored in blue for clarity.)

This scanning aims at removing the cyclodextrin molecule from the inclusion complex. A hexasaccharide molecule was combined with six cyclodextrin molecules to form the starting structure of the inclusion complex, ready for scanning. The alkyl chain of the hexasaccharide is present in the channel of the cyclodextrin dimer. As seen in **Figure 67**, as scanning commenced, the hexasaccharide molecules were wrapped around an extended alkyl chain, which was then threaded through the channel produced by the cyclodextrin molecules. The hexasaccharide molecule, which was combined with the alkyl chain, was separated from the blue-colored cyclodextrin during the scanning process. After the cyclodextrin was removed, the hexasaccharide-5CDs complex was left behind, but the structure of the hexasaccharide-5CDs complex changed. At the end of the extraction process, the conformation of the alkyl chain was still stretched.

The schematic **Figure 67** was used to depict the process of removing CD#5 from the

complex. During the process, CD#5 went away from the complex. Following the movement of CD#5, CD#6 moved close to CD#5 because of the interaction between the two CDs. At the end of the process, CD#1 was at the end of the lipid chain.

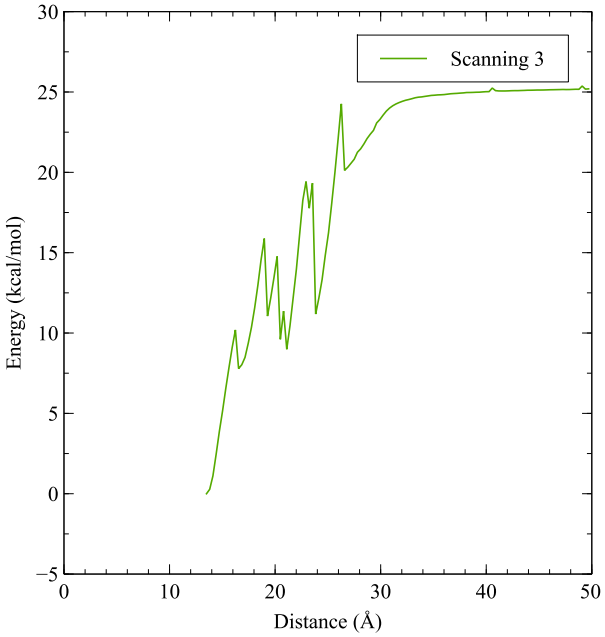

Figure 68. The energy-distance curve of the hexasaccharide cyclodextrin complex (Removing the cyclodextrin CD#5 from hexasaccharide cyclodextrin complex)

After performing the scanning, based on the distance-energy curve, we can get the extraction energy of removing CD#5 is 25.17 kcal/mol. (see **Figure 68**)

After performing a set of scannings, we summarized the data of the extraction energy of the cyclodextrin-hexasaccharide complex in **Table 23**.

Table 23. The extraction energy of the scanning

Description	The Energy of Start Point (kcal/mol)	The Energy of End Point (kcal/mol)	Extraction Energy (kcal/mol)
Remove Cyclodextrin 1	0	19.20	19.20
Remove Cyclodextrin 3	0	12.32	12.32
Remove Cyclodextrin 5	0	25.19	25.19

A structure was chosen which included the deleted cyclodextrin CD#3 based on the outcome of removing the first cyclodextrin molecular from the hexasaccharide cyclodextrin complex. CD#3 has been removed from the inclusion complex, and it draws near to CD#1, owing to the interaction between the two-CD molecules.

The goal was to investigate the extraction energy of the whole system while deleting the second cyclodextrin. We can also obtain the extraction energy of removing the second cyclodextrin from the system that includes the removed cyclodextrin CD#3. We can compare the different extraction energies once we obtain different extraction energy by performing the scannings of the starting structure that does not include the removed cyclodextrin CD#3. Another goal of this scanning was to discover a more reasonable pathway to remove the cyclodextrin molecule from the entire system. (see **Figure 69**)

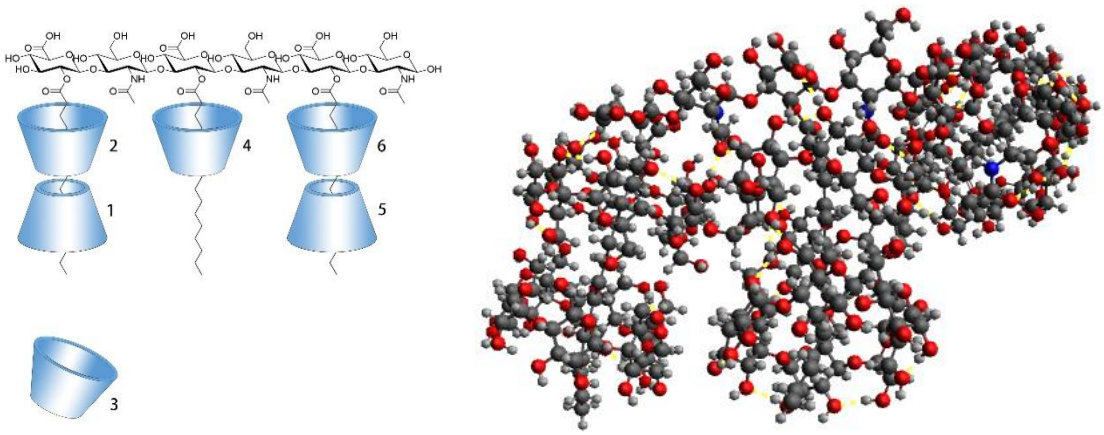

a) b)

Figure 69. a) The schematic diagram of the hexasaccharide cyclodextrin complex; b) The structure of the hexasaccharide cyclodextrin complex

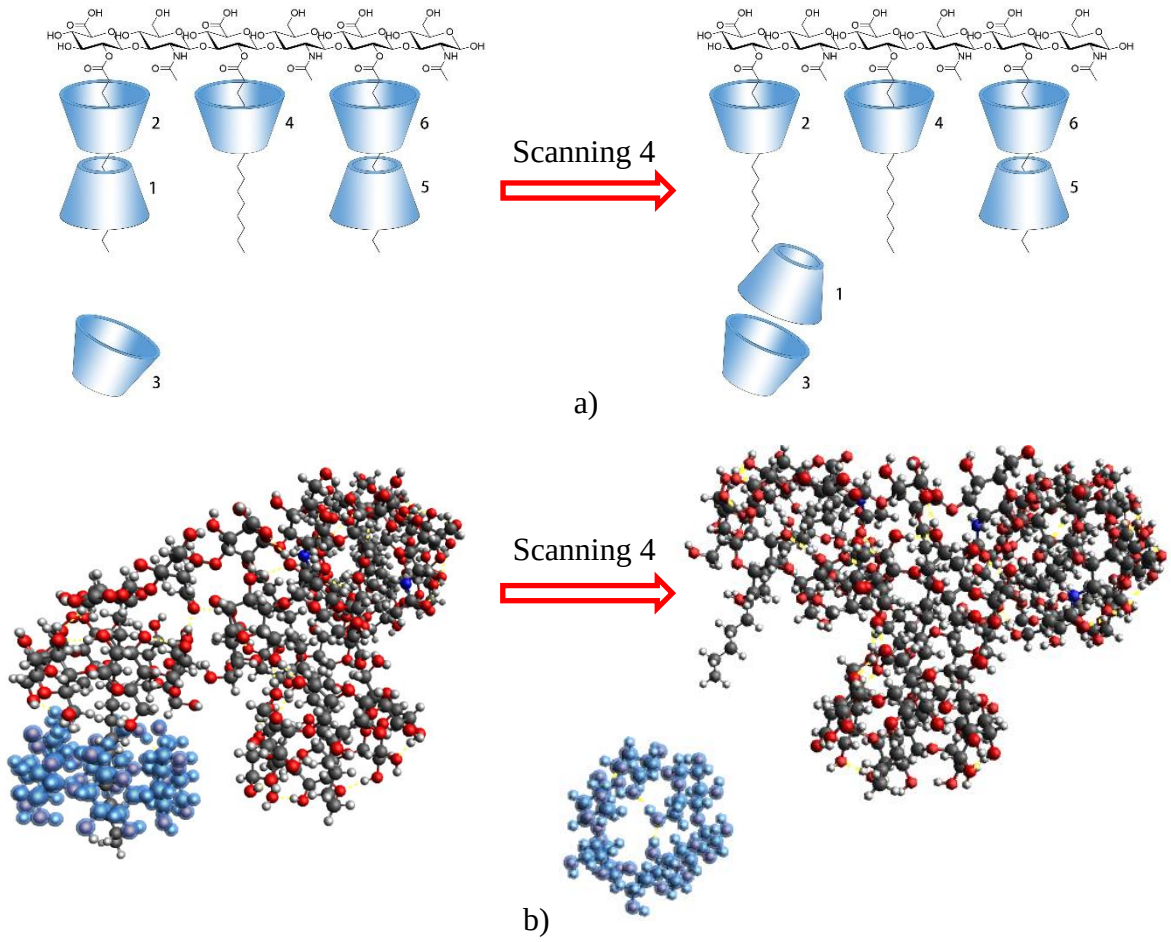

Figure 70. a) The schematic diagram of removing the CD#1 from the hexasaccharide cyclodextrin complex; b) The process of removing CD#1 the hexasaccharide cyclodextrin complex (The removed cyclodextrin is colored in blue for clarity.)

Removing the cyclodextrin molecule (CD#1) from the inclusion complex is the goal of this scanning. The inclusion complex was formed from hexasaccharide molecules coupled with five cyclodextrin molecules to produce the starting structure, and the removed cyclodextrin molecule (CD#3) also was regarded as a component of the starting structure. The alkyl chain of the hexasaccharides was laid in the channels of the corresponding cyclodextrin dimer. In **Figure 70b**, when the extended alkyl chain hexasaccharide molecules were first wrapped around, this alkyl chain of the inclusion compound was threaded through the channel generated by the cyclodextrin molecules. During the scanning procedure, the blue-colored cyclodextrin molecule moved away from the hexasaccharide-5CD complex to facilitate the new inclusion complex. After the cyclodextrin was removed, the other parts of the new formed the hexasaccharide-4CDs complex, still retaining the same position. Despite the alkyl

chain being substantially extended, the conformation was nevertheless substantially changed. When the scanning process ended, based on the distance-energy curve, we were able to ascertain the appropriate extraction energy for the removal of the cyclodextrin molecule (CD#1).

The process of removing CD#1 is depicted in **Figure 70b**. CD#1 was removed from the complex and moved during the process. CD #1 went toward CD#3. Due to the interaction between CD#1 and CD#3, CD#3 and CD#1 combined together and went away from the complex by the end of the process. Furthermore, the energy of the entire system decreased (the value of energy that characterized CD's removal from the system came to -17.75 kcal/mol).

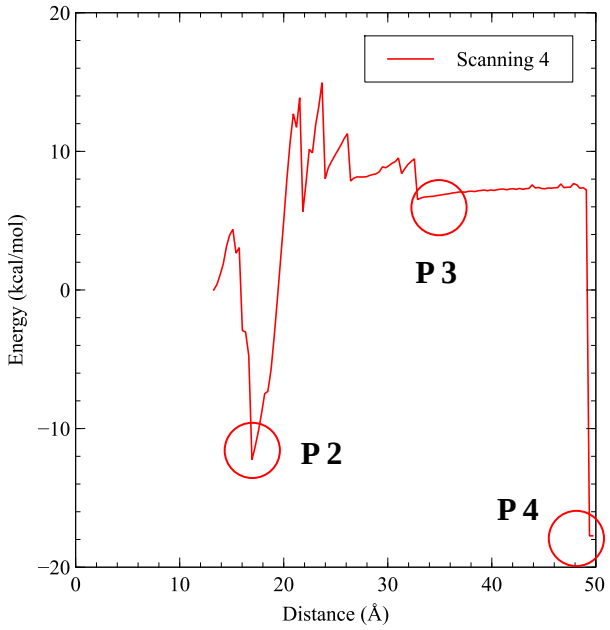

Figure 71 The energy-distance curve of the hexasaccharide cyclodextrin complex (Removing the cyclodextrin CD#1 from hexasaccharide cyclodextrin complex)

As the energy-distance curve of Scanning 4 (see **Figure 71**) is mentioned in this section, some representative points may be noticed throughout the scanning process. We were able to identify the differences between these structures by comparing the start structure of scanning 4 to the structures of the minimum points (**P2** and **P4**) and the reference point **P3** that the system energy became stable at this point.

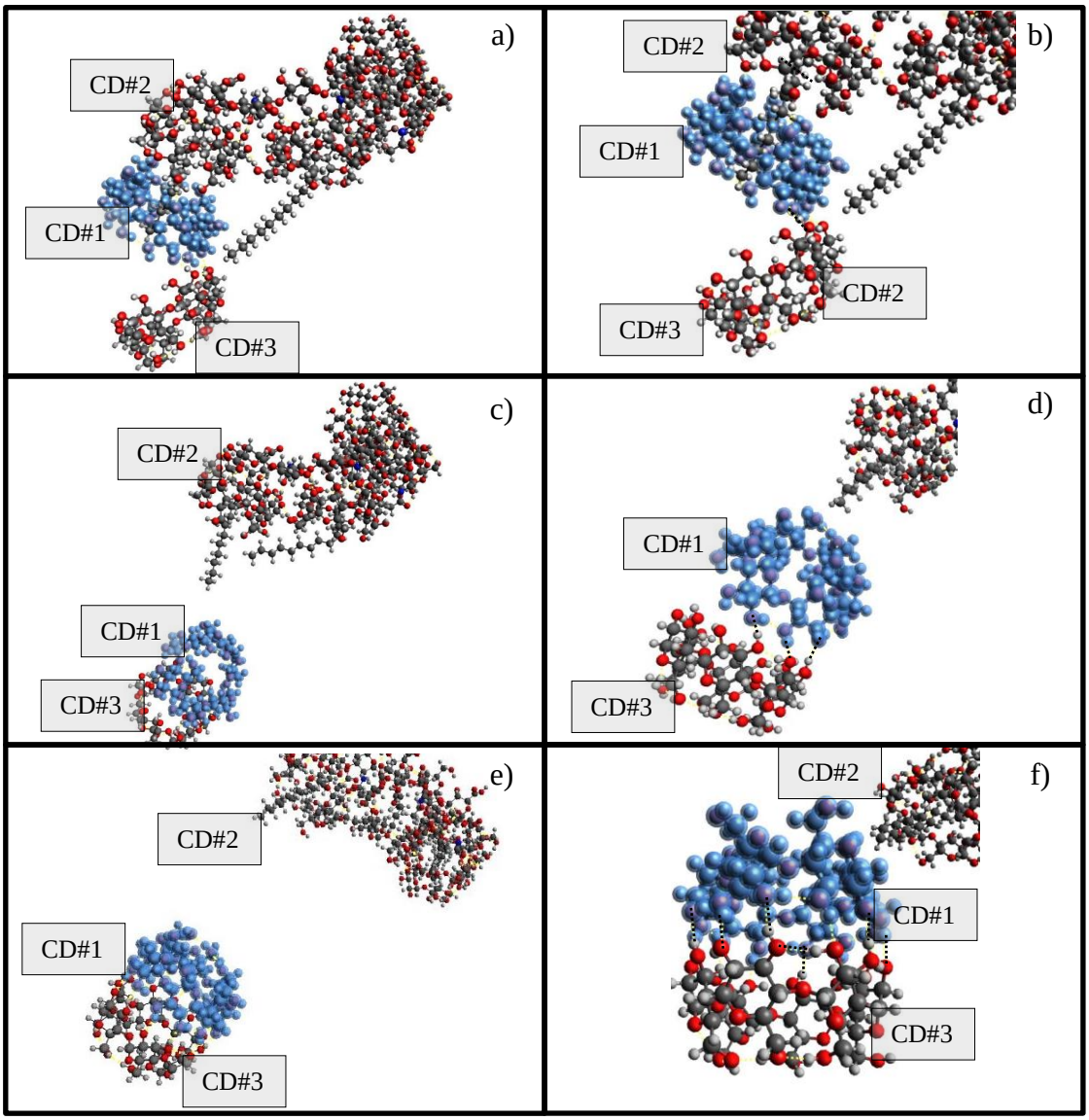

Figure 72. a) The structure of the minimum point **P2** hexasaccharide cyclodextrin complex. b) The position of CD#3 relative to the removed CD#1. c) The structure of the minimum point **P3** hexasaccharide cyclodextrin complex. d) The position of CD#3 relative to the removed CD#1. e) The structure of the minimum point **P4** hexasaccharide cyclodextrin complex. f) The position of CD#4 relative to the removed CD#2 (The removed cyclodextrin CD#1 is colored in blue for clarity, and the black dash line indicates the hydrogen bond between CD#3 and CD#1)

CD#1 moved away from the alkyl group and closer to CD#3 at the minimum point **P2**. Between the hydroxyl groups of CD#1 and CD#3, a hydrogen bond of the cyclodextrin CD#3 can form. In the structure of **P2**, CD#1 is still towards the end of the lipid chain, while CD#3 is fully detached from the inclusion complex. The energy barrier between **P2** and **P3** is 12.25 kcal/mol.

CD#1 was fully detached from the lipid chain when the distance between the

cyclodextrin CD#1 and the palmitic acid residue increased. Furthermore, the alkyl chain folded. The hydroxyl groups of CD#1 can establish several hydrogen bonds with CD#3 at reference point **P3**. Furthermore, CD#2 was still close to the carboxyl group of the fatty-acyl group. The extraction energy of this step is 8.38 kcal/mol.

After comparing the structures at the selected point at **P3** and **P4**, we can find that at the end point **P4**, the extra hydrogen bonds formed between the hydroxyl group between CD#3 and CD#1 lead to the dimerization of the cyclodextrin molecules. The dimerization of two cyclodextrins can cause the decrease of energy dramatically. Owing to this fact, we set **P3** as the end point as the selected point and tried to recalculate the extraction energy of removing CD#1. The energy difference between the minimum point **P4** and the reference point **P3** is -18.69 kcal/mol. (see **Figure 72**)

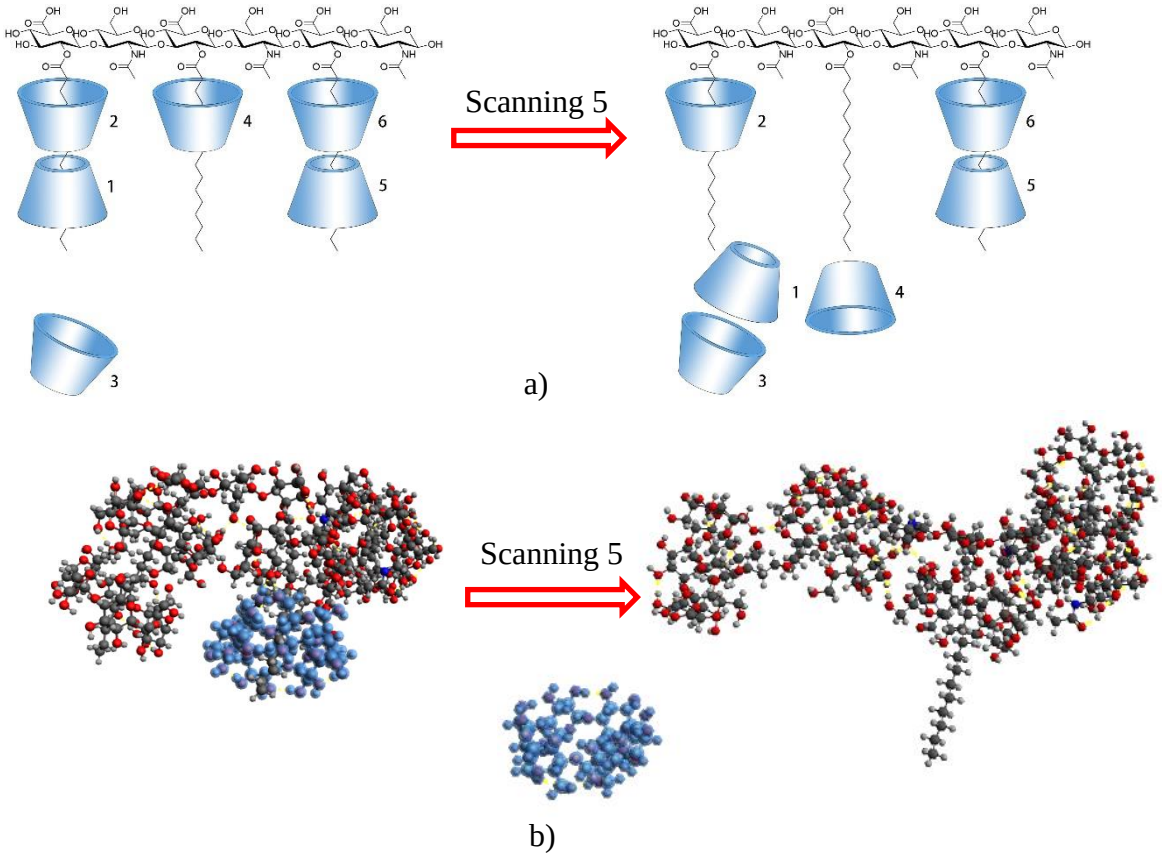

Figure 73 a) The schematic diagram of removing the CD#4 from the hexasaccharide cyclodextrin complex; b) The process of removing the CD#4 the hexasaccharide cyclodextrin complex (The removed cyclodextrin is colored in blue for clarity.)

This scanning is aimed at removing the cyclodextrin molecule (CD#4) from inclusion complexes. Hexasaccharide molecules and five cyclodextrin molecules were attached to the corresponding alkyl chain of the residue of palmitic acid to form the inclusion complex. This complex was constructed using a hexasaccharide molecule and five cyclodextrin molecules. Additionally, CD#3, which has been removed, was regarded as an ingredient of the starting structure. In **Figure 73**, the extended alkyl chains of hexasaccharides that were wrapped around cyclodextrin molecules were threaded in the channels of cyclodextrin. After this, the alkyl chain of the inclusion compound was threaded through the channel formed. Blue-colored cyclodextrin molecules left the hexasaccharide-5CD complex during the scanning procedure to give rise to a new inclusion complex. Other elements of the hexasaccharide-4CDs complex retain their positions after the cyclodextrin was removed. The structure of the alkyl chain was drastically altered despite the extension of the alkyl chain. When the scanning procedure was concluded, we found the optimal extraction energy to remove the cyclodextrin

molecule based on the distance-energy curve.

Figure 73 depicted the process of extracting CD#4. CD#4 was removed from the complex and moved during the process. CD #3 was connected with CD#1 and moved together. After CD#4 went away from the complex, the corresponding lipid chain became folded.

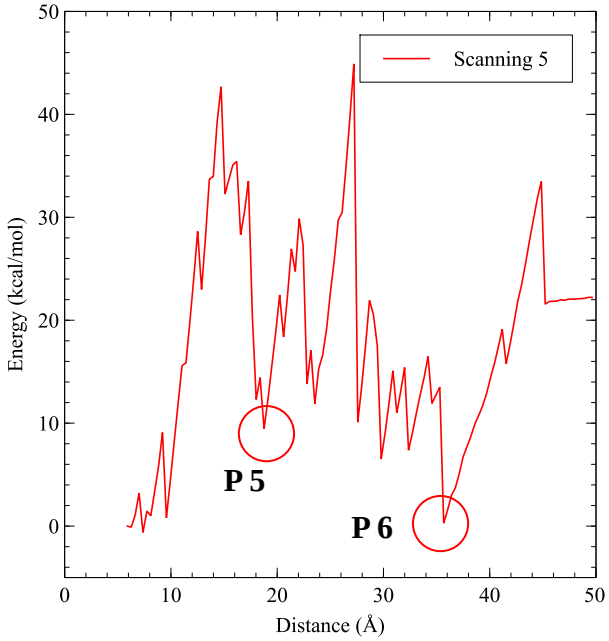

Figure 74. The energy-distance curve of the hexasaccharide cyclodextrin complex (Removing the cyclodextrin CD#4 from hexasaccharide cyclodextrin complex)

The extraction energy of removing CD#4 is 22.20 kcal/mol (see **Figure 74**)

As shown in the energy-distance curve of scanning 5 (**Figure 74**), several minimum points may be detected throughout the scanning process. We can determine the differences between these structures by comparing the start structure of scanning 5to the structures of the minimum points **P5** and **P6**.

At the minimum point **P5**, the hydroxyl group of CD#5 may form hydrogen bonds with CD#2 and CD#6 respectively. CD#4 moved slightly and was still around the end of the alkyl chain. Between the minimum positions **P5** and starting point, the energy barrier is 39.31 kcal/mol. (see **Figure 74**)

CD#4 can establish hydrogen bonds with the corresponding hydroxyl groups of CD#5 and CD#6 independently at the minimum point **P6**. When CD#4 was removed, the alkyl chain became folded. In the structure of **P6**, CD#1 has been dissociated from the inclusion complex and joined to CD#3 to form a dimer, while CD#2 remained towards the end of the lipid chain. (see **Figure 75**)

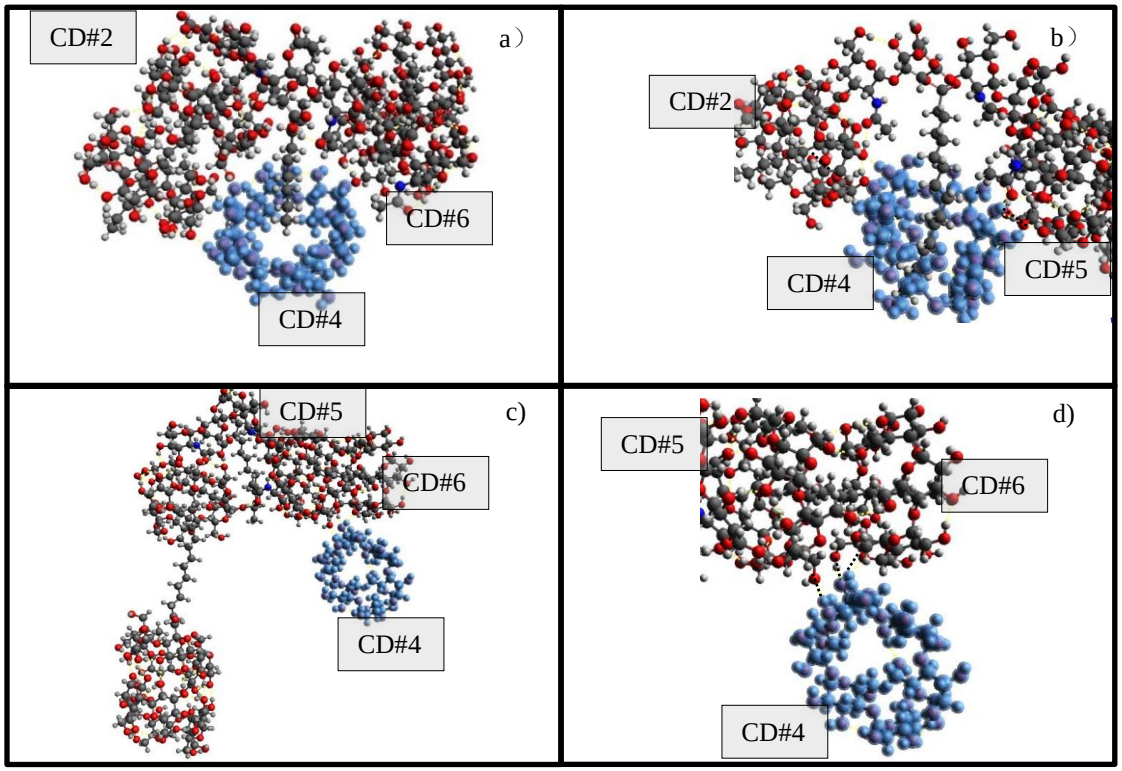

Figure 75. a) The structure of the minimum point **P5** hexasaccharide cyclodextrin complex. b) The position of chitosan residue relative to the removed CD#4. c) The structure of the minimum point **P6** hexasaccharide cyclodextrin complex. d) The position of chitosan residue relative to the removed CD#4. (The removed cyclodextrin CD#4 is colored in blue for clarity, and the black dash line indicates the hydrogen bond between CD#4, CD#5 and CD#6)

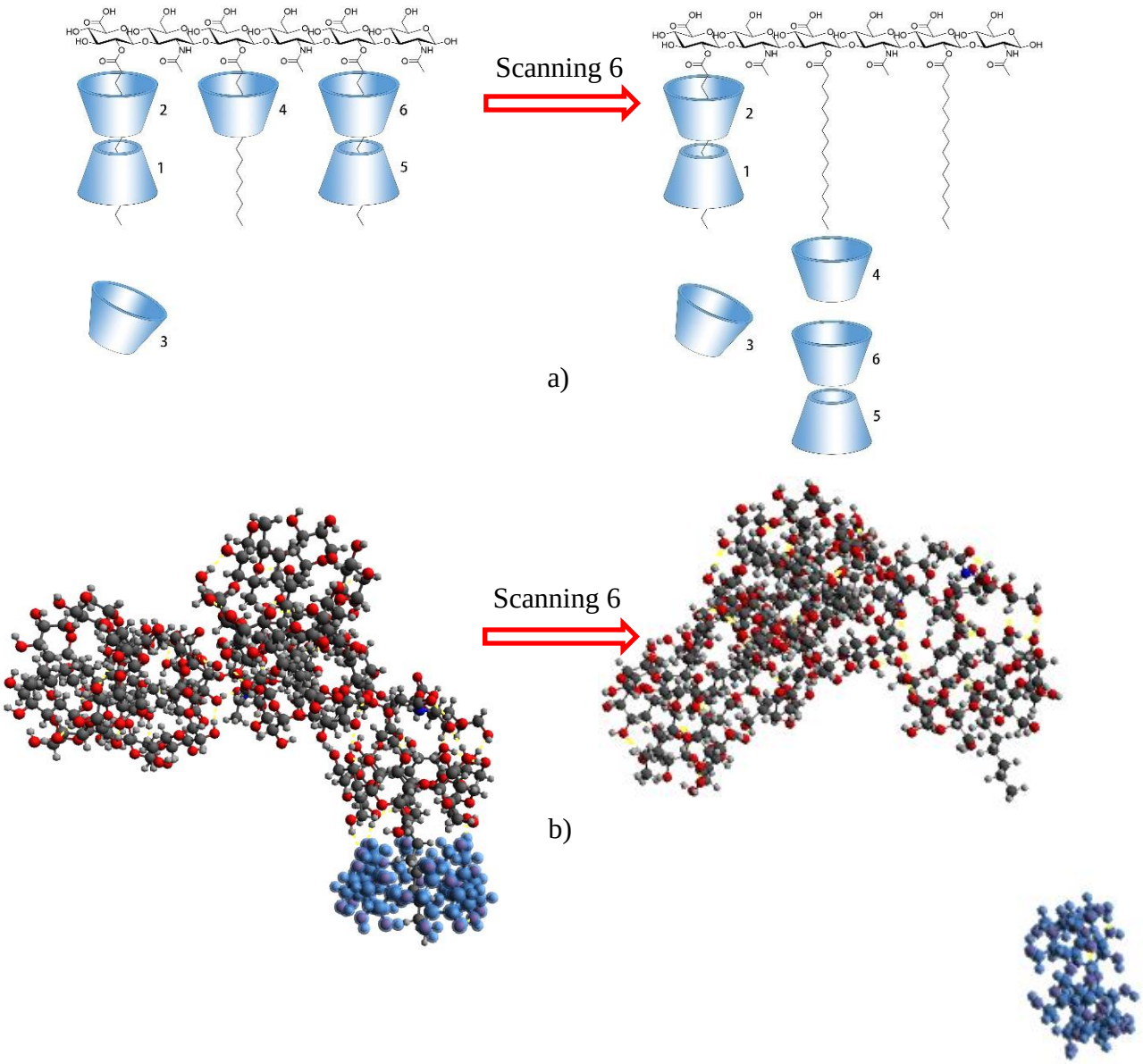

Figure 76. a) The schematic diagram of removing the CD#5 from the hexasaccharide cyclodextrin complex; b) The process of removing the CD#5 the hexasaccharide cyclodextrin complex (The removed cyclodextrin is colored in blue for clarity.)

This scanning is intended to remove the cyclodextrin molecule (CD#5) from the inclusion complexes. Five cyclodextrin molecules were linked to the hexasaccharide molecule bearing the appropriate alkyl chain of the palmitic acid residue. Additionally, CD#3, which was isolated from the hexasaccharide-5CD complex, was considered a component of the start structure. Hexasaccharide alkyl chains were stacked in their corresponding cyclodextrin dimer channels. The extended alkyl chain of the inclusion complex was wrapped around the cyclodextrin molecules. After this, the inclusion compound's alkyl chain was threaded through the channel. During the whole scanning, the blue-colored cyclodextrin molecules (see **Figure 76**b) separated from the hexasaccharide-5CD complex, forming a new inclusion complex.

Other components of the hexasaccharide-4CDs complex retain their locations following the removal of the cyclodextrin. Despite the alkyl chain's expansion, the structure of the alkyl chain was significantly altered. At the end of the scanning procedure, we determined the ideal extraction energy for removing the cyclodextrin molecule by utilizing the distance-energy curve.

The procedure of removing CD#5 is illustrated in **Figure 76b**. When CD#5 was removed from the complex. The lipid chain that CD#5 and CD#6 was around moved away from the CD molecules. During the process, CD#5 and CD#6 moved together, and the hydroxyl group of CD#5 was associated with CD#4. So, the position of CD#4 is fixed due to the interaction of hydroxyl groups, and the corresponding lipid chain moved away from CD#4. CD#3 went away from the complex, and its interaction with CD#1 led to the movement of CD#1. At the end of the process, CD#4, #5, and #6 were connected together, and CD#3 is far away from the complex.

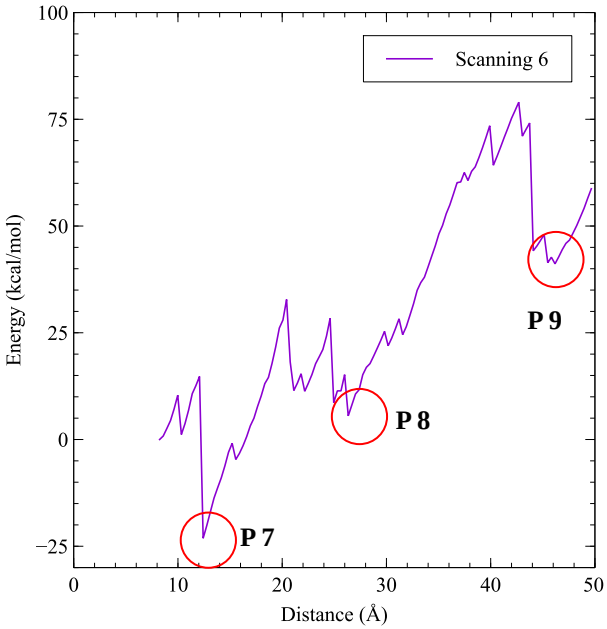

Figure 77. The energy-distance curve of the hexasaccharide cyclodextrin complex (Removing the cyclodextrin CD#5 from hexasaccharide cyclodextrin complex)

The extraction energy of removing CD#5 is 58.67 kcal/mol (see **Figure 77**)

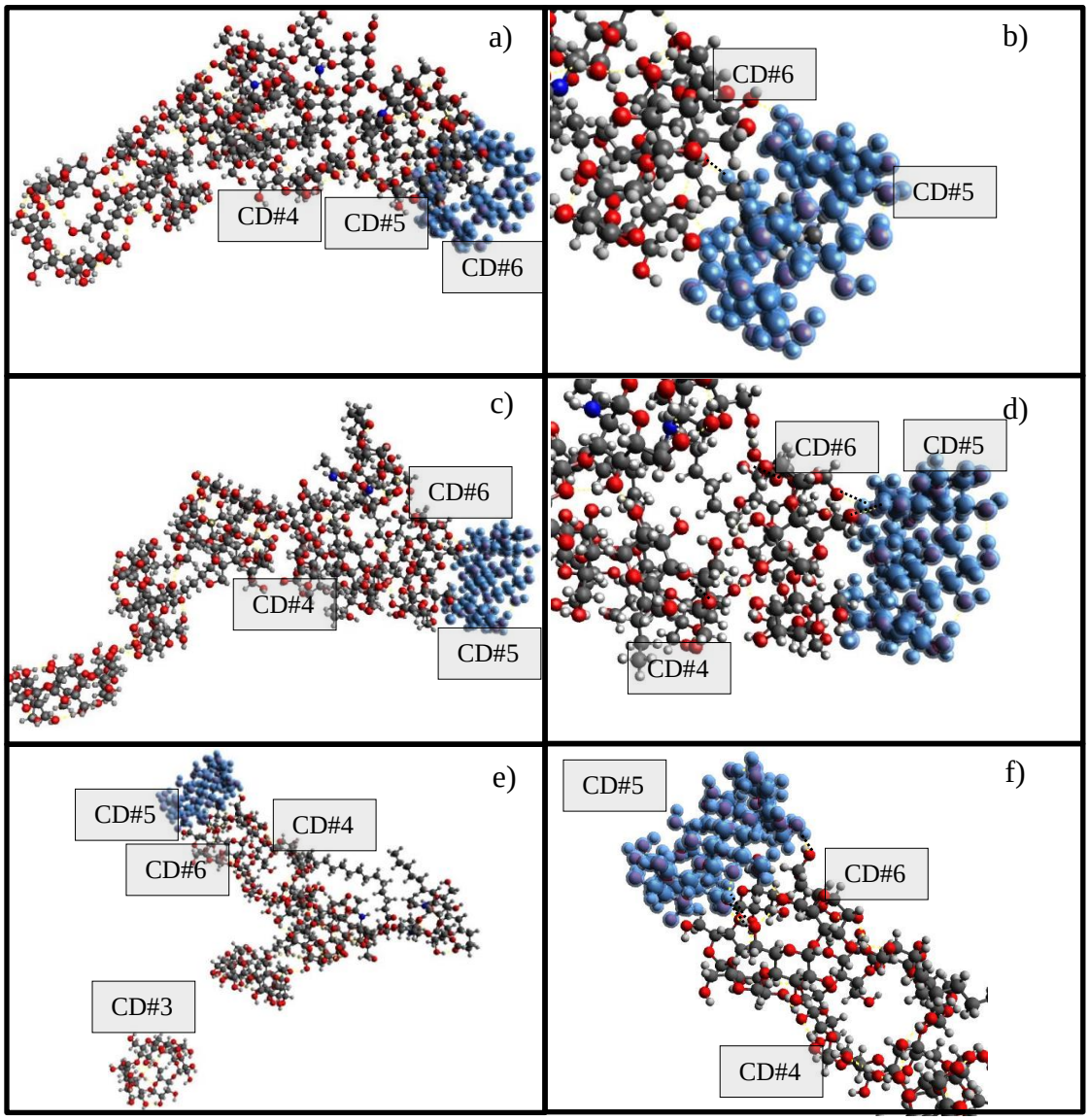

Figure 78. a) The structure of the minimum point **P7** hexasaccharide cyclodextrin complex. b) The position of CD#6 and chitosan residue relative to the removed CD#5. c) The structure of the minimum point **P8** hexasaccharide cyclodextrin complex. d) The position of CD#6 relative to the removed CD#5. e) The structure of the minimum point **P9** hexasaccharide cyclodextrin complex. f) The position of CD#6 relative to the removed CD#5 (The removed cyclodextrin CD#5 is colored in blue for clarity, and the black dash line indicates the hydrogen bond between CD#4 and CD#2)

As shown in the energy-distance curve of scanning 6 (**Figure 78**), several minimum points may be detected throughout the scanning process. We can determine the differences between these structures by comparing the start structure of scanning 6 to the structures of the minimum points **P7**, **P8**, and **P9**. CD#3's hydroxyl group may establish hydrogen bonds with

CD#1 at the minimum position P6. As a result of the hydrogen connection formed between CD#3 and CD#1, CD#1 shifted away from the alkyl chain to some degree. CD#5 remained in close proximity to the alkyl chain and established a hydrogen connection with CD#6. Between the minimum positions **P7** and starting point, the energy difference is -23.10 kcal/mol. (see **Figure 78**)

With an increase in the distance between the cyclodextrin CD#5 and the palmitic acid residue, CD#5 and CD#6 were entirely detached from the lipid chain. Additionally, the lipid chain folds. CD#5 maintained the hydrogen connection with CD#6 at the minimum point **P8**. Additionally, as a result of the hydrogen connection formed between CD#4 and CD#6, CD#4 tends to drift somewhat away from the alkyl chain. The extraction energy for this phase is 28.64 kcal/mol. (see **Figure 78**)

CD#6 was successfully isolated from the hexasaccharide cyclodextrin complex, and CD#4 was then removed from the lipid chain. However, throughout the whole process, the hydroxyl groups of CD#5, CD#6, and CD#4 may create hydrogen bonds. CD#1 and CD#2 are still wrapped around the alkyl group at the minimum point **P9**, but the other two alkyl groups have folded. The extraction energy for this step is 35.85 kcal/mol. (see **Figure 78**)

After performing various scannings, we summarise the data of the extraction energy of the cyclodextrin-hexasaccharide complex in **Table 24.**

Table 24. The extraction energy of the Scanning (second time)

Description	The Energy of Start Point (kcal/mol)	The Energy of End Point (kcal/mol)	Extraction Energy (kcal/mol)
Remove Cyclodextrin 1	0	7.67	7.68
Remove Cyclodextrin 4	0	22.22	22.22
Remove Cyclodextrin 5	0	58.72	58.72

Owing to the result of removing the first cyclodextrin molecular from the hexasaccharide cyclodextrin complex, we selected the structure that including the removed cyclodextrin CD#3. And in the scanning of removing the second cyclodextrin, because of the interaction between CD#1 and CD#3, the movement of CD#3 lead to the movement of CD#1. The existence of CD#3, which has been removed from the inclusion complex, in the whole system can cause dimerization with other removing cyclodextrin—CD #3. So, we selected the structure of the hexasaccharide cyclodextrin complex containing five cyclodextrin molecules.

The purpose was to explore the extraction energy of the whole system while removing the second cyclodextrin. First of all, we have already got the extraction energy of removing the second cyclodextrin from the system, which was consisted of six cyclodextrin molecules. Then, we perform the scanning of removing the cyclodextrin from the system containing five cyclodextrin molecules. After getting the extraction energy of removing the second cyclodextrin separately, we can compare the different values of the extraction energy. Then, we can find a more reasonable method of removing the cyclodextrin molecule from the whole system. (see **Figure 79**)

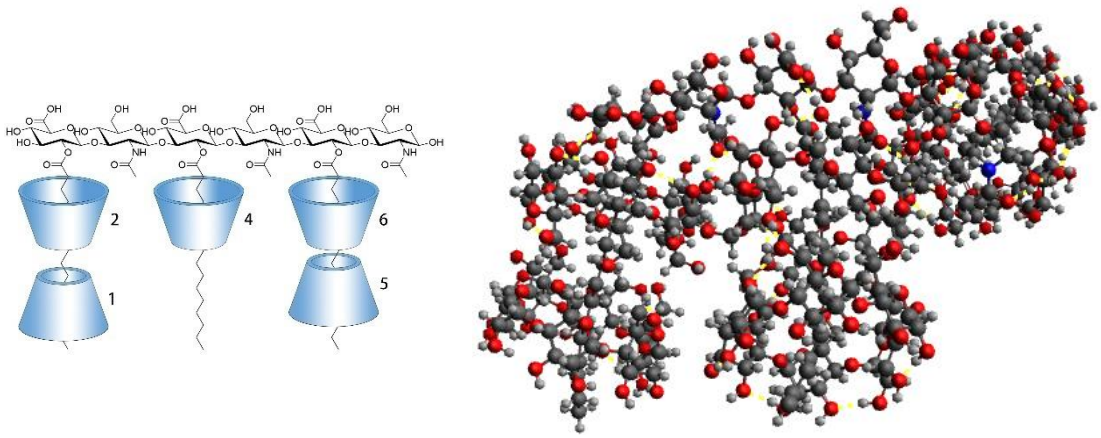

a) b)

Figure 79. a) The schematic diagram of the hexasaccharide cyclodextrin complex; b) The structure of the hexasaccharide cyclodextrin complex

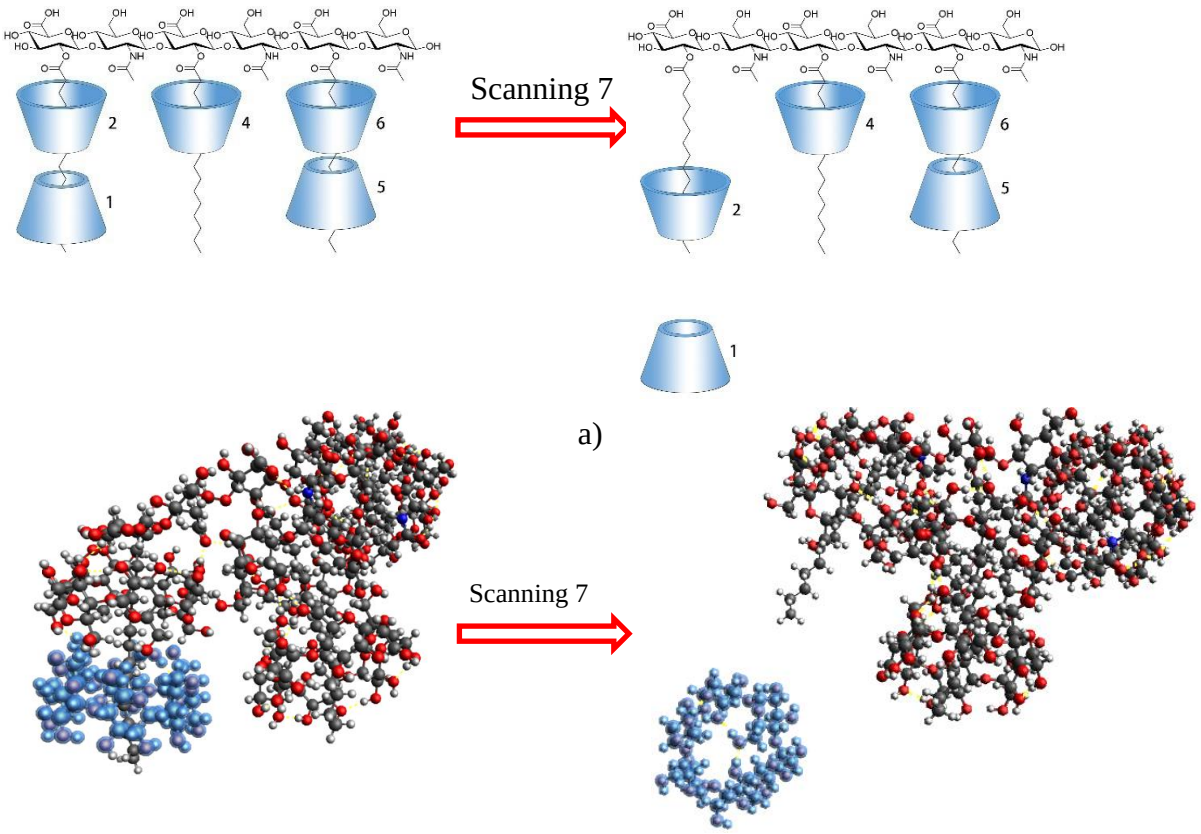

Figure 80. a) The schematic diagram of removing the CD#1 from the hexasaccharide cyclodextrin complex; b) The process of removing CD#1 the hexasaccharide cyclodextrin complex (The removed cyclodextrin is colored in blue for clarity.)

The aim of scanning is to remove cyclodextrin (CD#1) from inclusion complexes. The inclusion complex was formed by a hexasaccharide and five cyclodextrin molecules connected to the alkyl chain of the palmitic acid residue. A hexasaccharide -5CDs complex was obtained as the result of the previous scanning. Also, Hexasaccharide alkyl chains were stacked in cyclodextrin dimer channels. The extended alkyl chain hexasaccharide molecules were wrapped around the cyclodextrin molecules to form a channel (**Figure 80**). The alkyl chain of the inclusion compound was then threaded through the channel. During scanning, the blue cyclodextrin molecule departed the hexasaccharide-5CD complex, forming a new inclusion complex. Other components of the hexasaccharide-4CDs complex remain in place when the blue-colored cyclodextrin is removed from the hexasaccharide-5CD complex. Despite the alkyl chain extension, the structure was dramatically altered. Using the distance-energy curve, we discovered the extraction energy of removing the cyclodextrin molecule.

Figure 80b shows the extraction of CD#1. CD#1 was removed from the hexasaccharide-cyclodextrin complex. Further, the interaction of the hydroxyl groups between CD#1 and CD#2 lead to the movement of CD#2. During the process that CD#1 was removed from the lipid chain, the lipid chain became folded, and the distance between the lipid and CD#1 increased. At the end of the Scanning, CD#2 was still around the lipid chain.

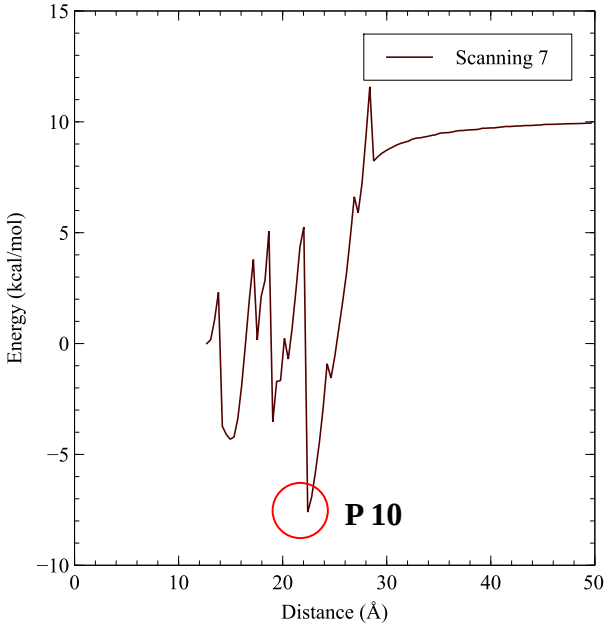

Figure 81 The energy-distance curve of the hexasaccharide cyclodextrin complex (Removing the cyclodextrin CD#1 from hexasaccharide cyclodextrin complex)

The extraction energy of removing CD#1 is 9.94 kcal/mol (see **Figure 81**)

By comparing the start structure of scanning 7 to the structures of the minimum points **P10**, we may discover the differences between these structures. At **P10**, the secondary hydroxyl groups of CD#2 and CD#1 can establish hydrogen bonds. Due to the hydrogen bonding effect, the movement of CD#1 causes CD#2 to move significantly, but CD#2 remains at the end of the alkyl chain. CD#1 got entirely separated from the lipid chain as the distance between it and the palmitic acid residue increased. (see **Figure 82**)

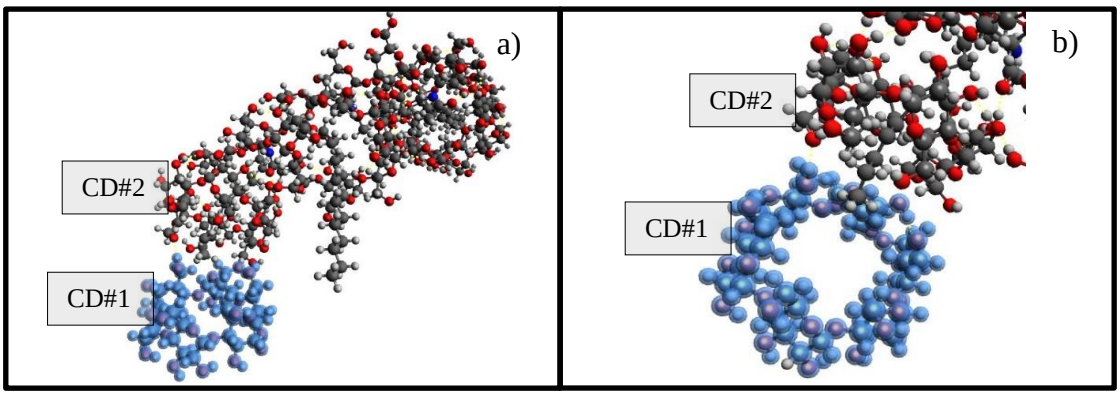

Figure 82. a) The structure of the minimum point **P10** hexasaccharide cyclodextrin complex.

b) The position of chitosan residue relative to the removed CD#1. (The removed cyclodextrin CD#1 is coloured in blue for clarity, and the black dash line indicates the hydrogen bond between CD#1 and CD#2)

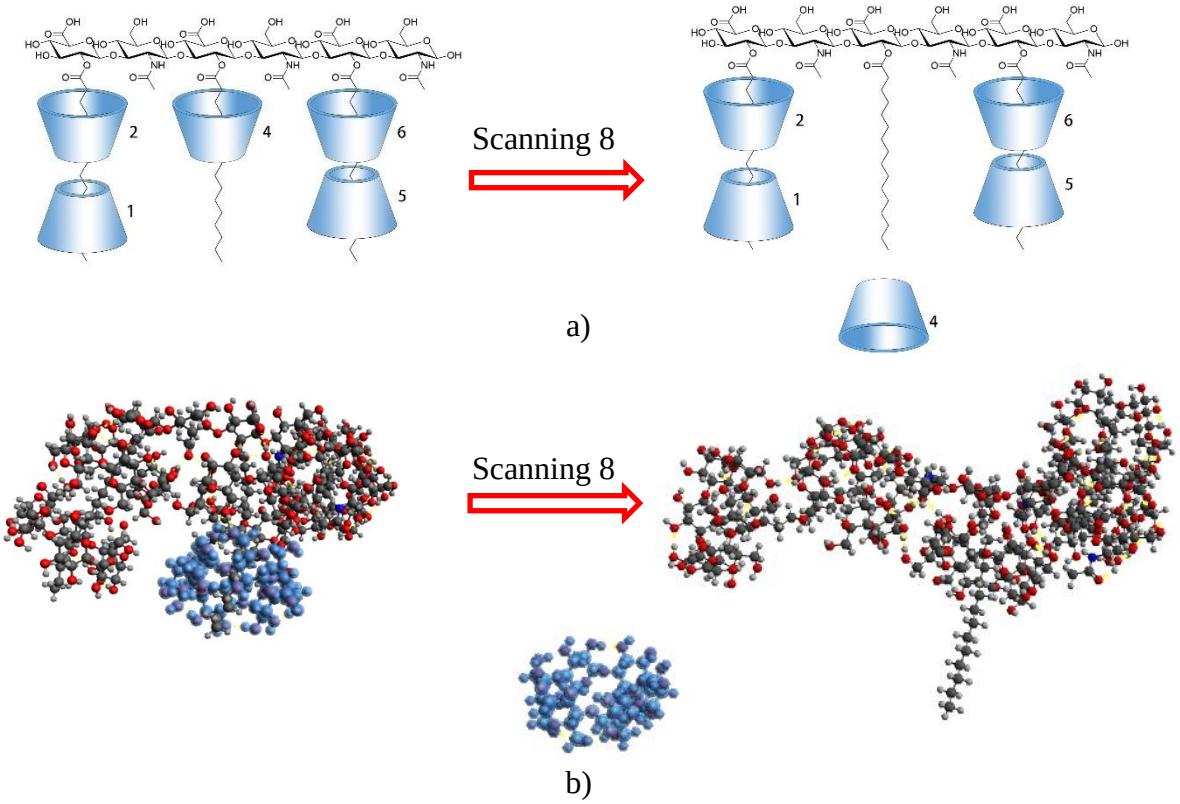

Figure 83 a) The schematic diagram of removing CD#4 from the for clarity.)

This scanning is targeted at removing the cyclodextrin molecule (CD#4) from the inclusion complex. A hexasaccharide molecule is combined with five cyclodextrin molecules to form the starting structure of the inclusion complex for scanning. The alkyl chain of the hexasaccharide is present in the channel of the cyclodextrin dimer. As seen in **Figure 83 b**, the hexasaccharide molecule was wrapped around three extended alkyl chains, which were then threaded through the channels produced by the cyclodextrin molecules. The cyclodextrin was separated from the hexasaccharide molecule, which was combined with the alkyl chain during the scanning process. After the cyclodextrin was removed, the hexasaccharide-4CDs complex was left behind, but the structure of the hexasaccharide-5CDs complex changed. After completing the scanning of extraction of cyclodextrin from the hexasaccharide-5CDs complex, we were able to acquire the requisite extraction energy for the scanning.

Figure 83 shows the removal process of CD#4. When CD#4 was removed from the hexasaccharide-cyclodextrin complex, the hydroxyl group of CD#1 was affected by the corresponding hydroxyl group of CD#4, so the leaving of CD#4 led to the movement of CD#1. At the end of the Scanning, CD#1 was still around the lipid chain. At the same time, due to the leaving of CD#4, the distance of CD#2 and CD#6 decreased, and CD#2 became

close to CD#6. The hydroxyl groups of CD#2 can be affected by CD#6 in the final structure. After CD#4 was extracted from the lipid chain, the corresponding lipid chain became folded.

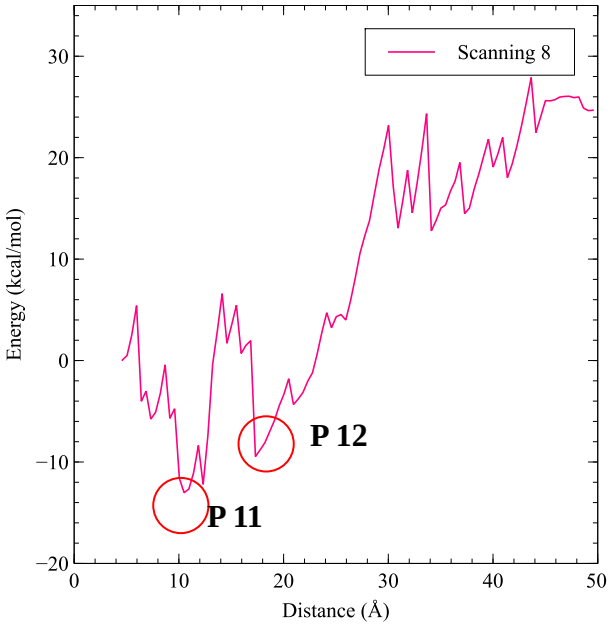

Figure 84. The energy-distance curve of the hexasaccharide cyclodextrin complex (Removing the cyclodextrin CD#4 from hexasaccharide cyclodextrin complex)

The extraction energy of removing CD#4 is 24.64 kcal/mol

As shown in **Figure 84**, the energy-distance curve of scanning 8 presented in this chapter, two minimum points may be detected throughout the scanning process. We can find similarities between these structures by comparing the start structure of scanning 8 to the structures of the minimum points **P11** and **P12**. At the minimum point **P11,** a hydrogen bond between the hydroxyl groups of CD#2, CD#5, and the chitosan residue can be established. CD#2 is still towards the end of the lipid chain in the structure of **P11**. Between **P11** and the start point, there is -13.06 kcal/mol energy difference.

With an increase in the distance between the cyclodextrin CD#4 and the palmitic acid residue, CD#4 became entirely detached from the lipid chain. CD#4 may form a hydrogen bond with CD#2 at the minimum point **P12**. Additionally, the lipid chain gets twisted, and the lipid chain's carboxyl group may establish a hydrogen bond with CD#5. Additionally, an energy barrier (19.61 kcal/mol) exists between **P11** and **P12**. (see **Figure 85**)

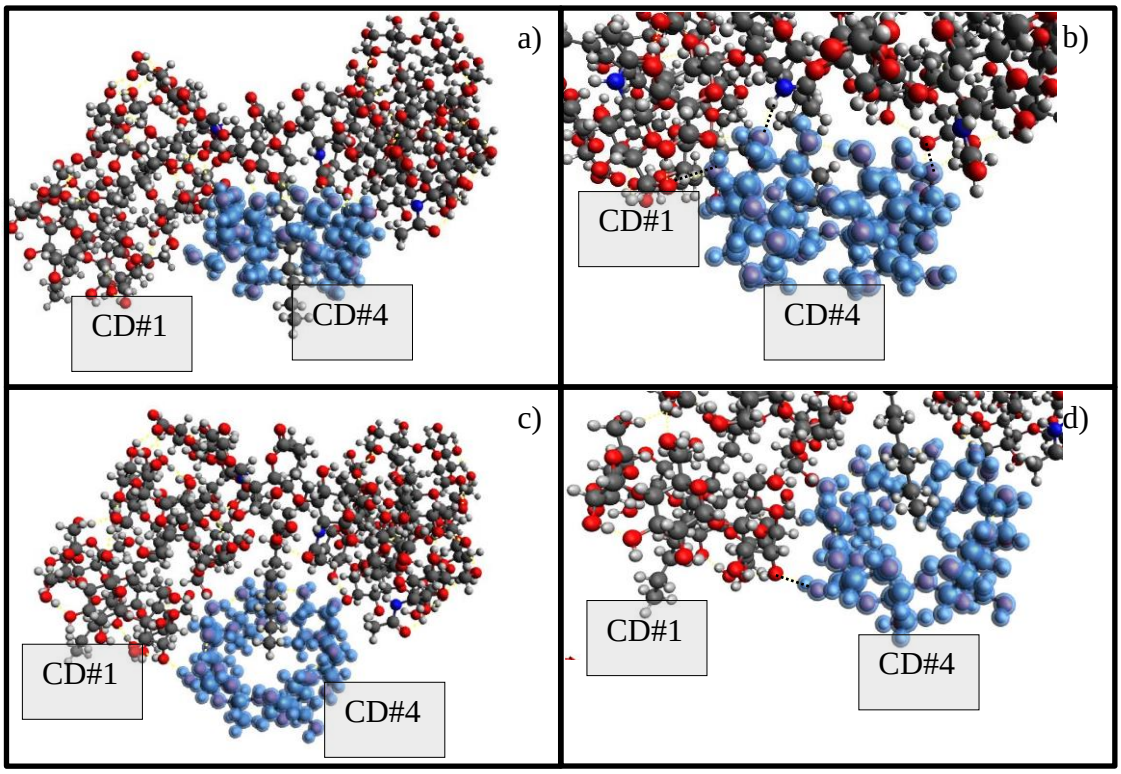

Figure 85 a) The structure of the minimum point **P11** hexasaccharide cyclodextrin complex. b) The position of CD#1 and CD#5 relative to the removed CD#4. c) The structure of the minimum point **P12** hexasaccharide cyclodextrin complex. d) The position of CD#1 relative to the removed CD#4. (The removed cyclodextrin CD#5 is colored in blue for clarity, and the black dash line indicates the hydrogen bond between CD#4 and CD#2)

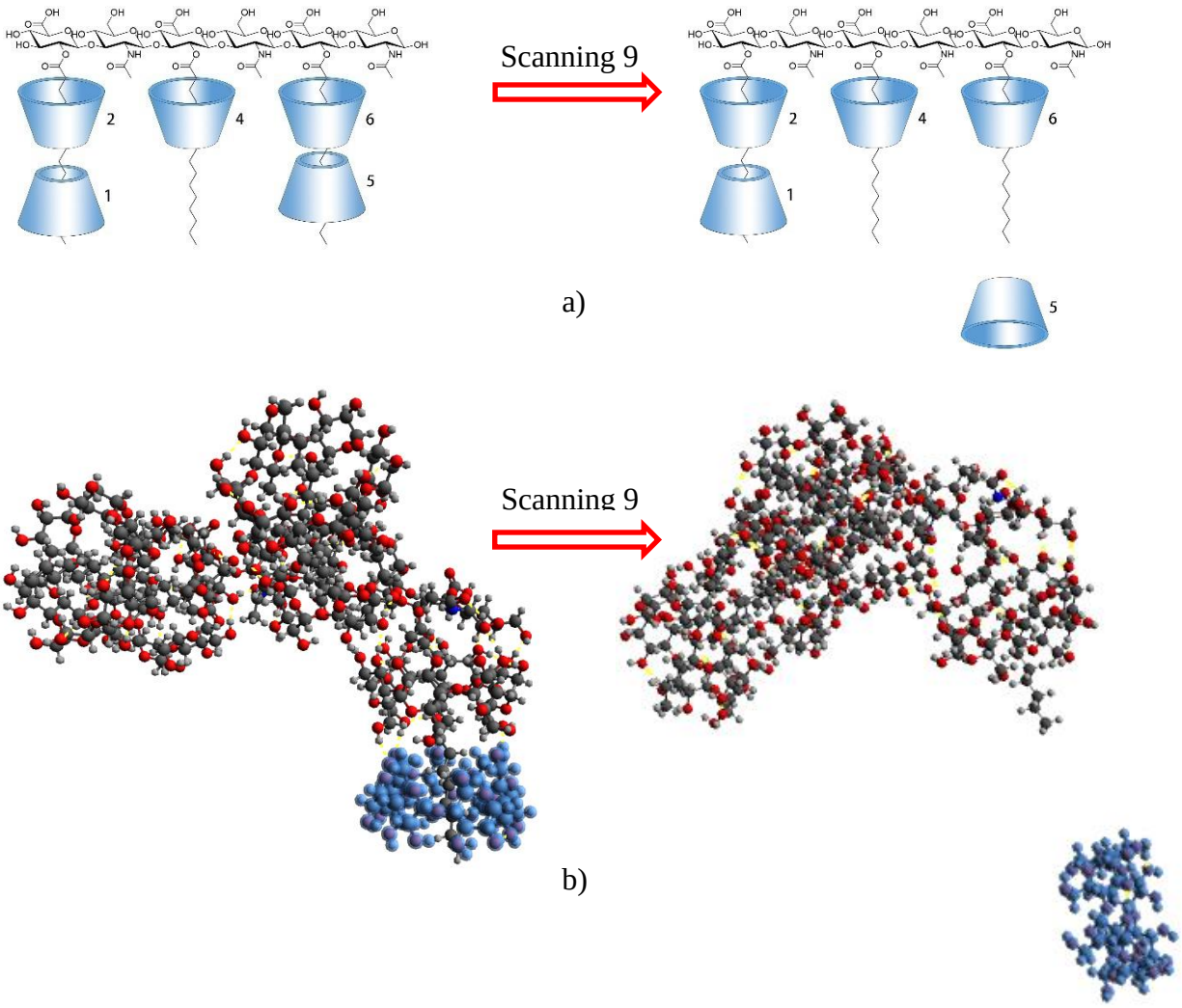

Figure 86 a) The schematic diagram of removing the CD#5 from the hexasaccharide cyclodextrin complex; b) The process of removing the CD#5 the hexasaccharide cyclodextrin complex (The removed cyclodextrin is colored in blue for clarity.)

The scanning is used to remove cyclodextrin (CD#5) from the inclusion complex. After removing CD#3, a hexasaccharide and five cyclodextrin molecules were employed to produce this scanning structure. Also, cyclodextrin dimer channels stacked the alkyl chains of the hexasaccharide. The extended alkyl chain hexasaccharide molecules formed a conduit around the cyclodextrin molecules (**Figure 86**). The alkyl chain of the inclusion compound was then threaded through the channel. This new inclusion complex was formed when the blue-colored cyclodextrin molecule left the hexasaccharide-5CDs complex. When cyclodextrin is separated, other hexasaccharide-4CDs complex members remain. The distance-energy curve revealed the appropriate extraction energy for removing cyclodextrin.

As depicted in **Figure 86**, after comparing the conformation of the inclusion complex at the beginning of the scanning, when CD#5 was removed from the hexasaccharide-

cyclodextrin complex, considering the influence of the hydroxyl groups between CD#5 and CD#6, CD#6 moved slightly and was still around the lipid chain.

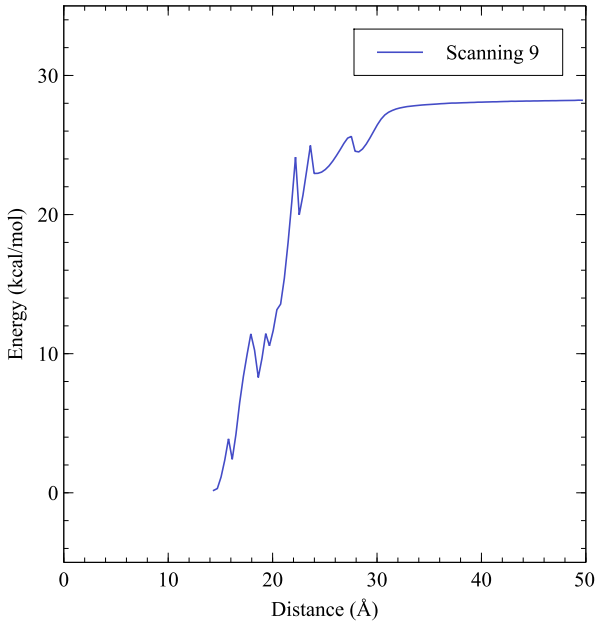

Figure 87 The energy-distance curve of the hexasaccharide cyclodextrin complex (Removing the cyclodextrin CD#5 from hexasaccharide cyclodextrin complex)

The extraction energy of removing CD#5 is 25.86 kcal/mol (see **Figure 87**)

After performing various scannings, we summarise the data of the extraction energy of the cyclodextrin-hexasaccharide complex in **Table 25.**

Table 25. The extraction energy of the scanning

Description	The Energy of Start Point (kcal/mol)	The Energy of End Point (kcal/mol)	Extraction Energy (kcal/mol)
Remove Cyclodextrin 1	0	9.94	17.54
Remove Cyclodextrin 4	0	24.67	24.64
Remove Cyclodextrin 5	0.17	28.21	28.05

After removing the second cyclodextrin molecular from the hexasaccharide cyclodextrin complex, we selected the structure that did not contain the removed cyclodextrins CD#3 and CD#1. We thus selected the structure of the hexasaccharide cyclodextrin complex containing four cyclodextrin molecules.

The purpose was to explore the extraction energy of the whole system while removing the third cyclodextrin. After removing two cyclodextrin molecules from the hexasaccharide cyclodextrin complex, we obtain the structure containing four cyclodextrin molecules. Then, we attempt to perform the scanning to remove the cyclodextrin CD#2, CD#4, and CD#5, separately. After ascertaining the extraction energy of removing the second cyclodextrin separately, we are able to compare the different values of the extraction energy. Then, we can find a more reasonable method of removing the cyclodextrin molecule from the whole system. (see **Figure 88**)

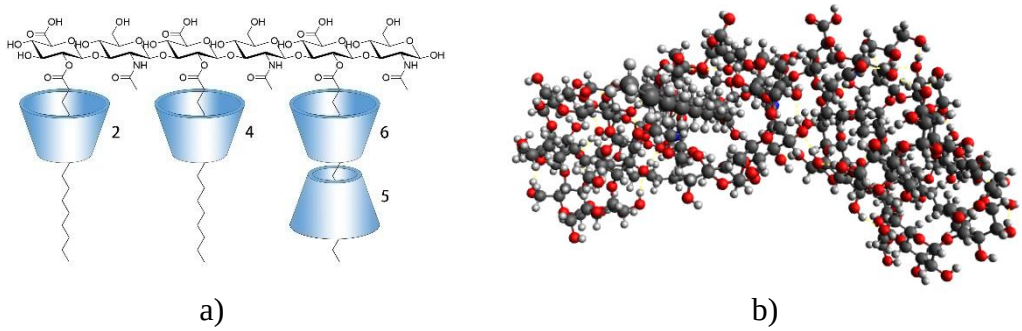

a) b)

Figure 88. a) The schematic diagram of the hexasaccharide cyclodextrin complex; b) The structure of the hexasaccharide cyclodextrin complex

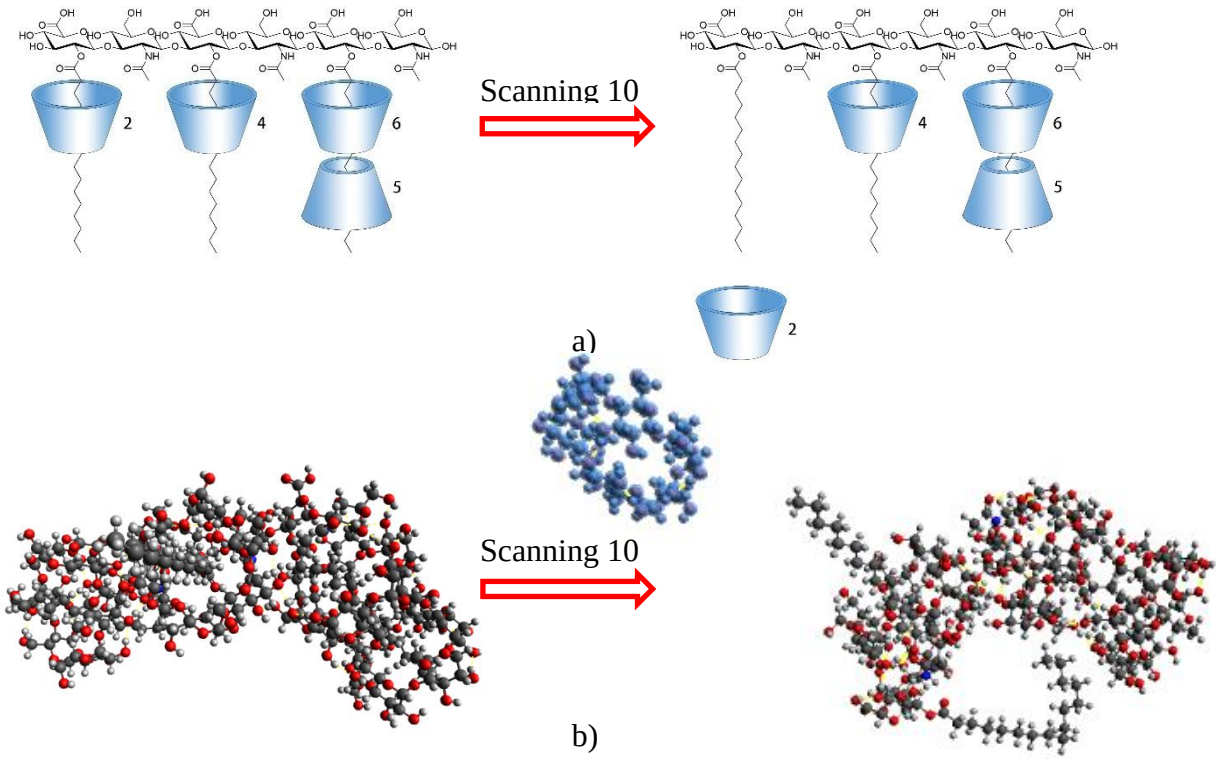

Figure 89. a) The schematic diagram of removing the CD#2 from the hexasaccharide cyclodextrin complex; b) The process of removing CD#2 the hexasaccharide cyclodextrin complex (The removed cyclodextrin is colored in blue for clarity.)

The scanning procedure is used to extract cyclodextrin (CD#2) from the inclusion complex containing four cyclodextrin molecules. After removing CD#1 and CD#3, this scanning structure was created using a hexasaccharide and four cyclodextrin molecules. Additionally, at the beginning of the scanning, the extended alkyl chains of hexasaccharides were laid in the cave of the cyclodextrin or its corresponding dimer (**Figure 89**). Then, the blue-colored cyclodextrin molecule was removed away from the hexasaccharide-4CDs complex. By the end of the scanning, this new inclusion complex formed. When cyclodextrin was removed, the other components of the hexasaccharide-3CDs complex remained. After performing the scanning, we obtained the structure of the hexasaccharide-3CDs complex. The distance-energy curve can be used to calculate the extraction energy of removing cyclodextrin(CD#2). As seen in **Figure 89**, CD#2 was removed from the hexasaccharide-cyclodextrin complex. And the interaction of the hydroxyl groups between CD#4 and CD#2 prevents CD#2 from leaving the system. During the process that CD#2 was removed from the lipid chain, the lipid chain became folded, and the distance between the lipid and CD#2 increased. At the end of the scanning, CD#2 was separated from the lipid chain.

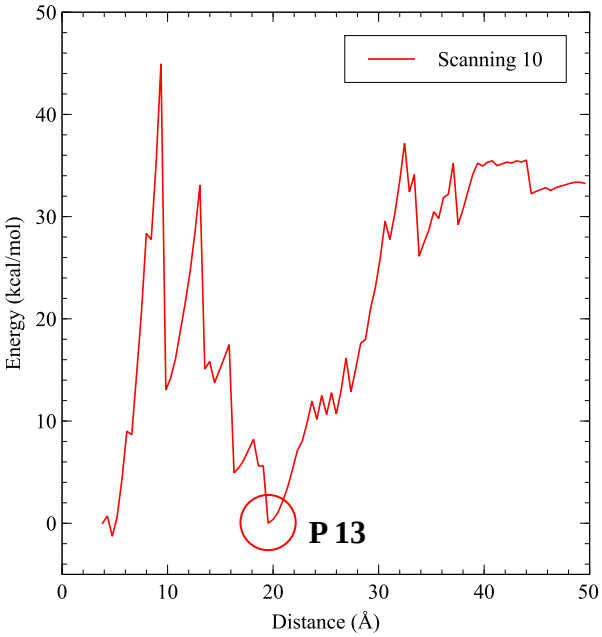

Figure 90. The energy-distance curve of the hexasaccharide cyclodextrin complex (Removing the cyclodextrin CD#2 from hexasaccharide cyclodextrin complex)

The extraction energy of removing CD#2 is 33.25 kcal/mol (see **Figure 90**)

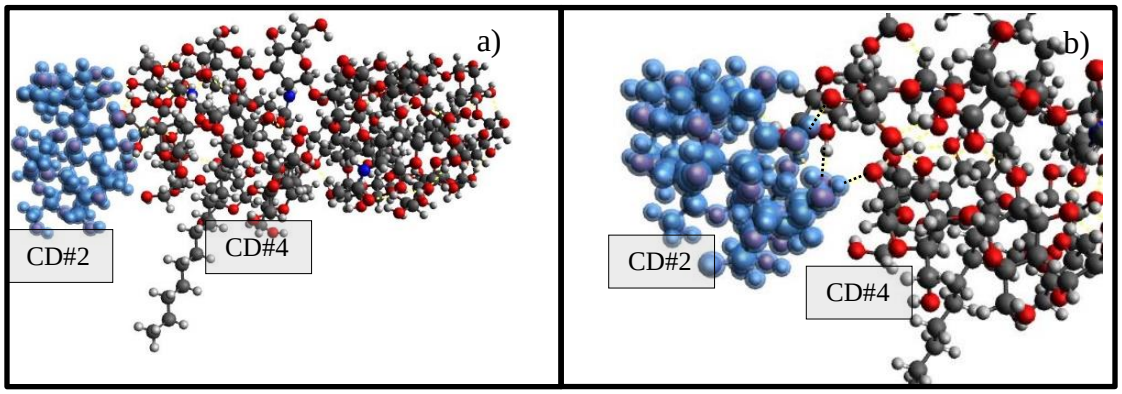

Figure 91 a) The structure of the minimum point **P13** hexasaccharide cyclodextrin complex b) The position of chitosan residue relative to the removed CD#2 (The removed cyclodextrin CD#2 is colored in blue for clarity, and the black dash line indicates the hydrogen bond between CD#2 and chitosan residue)

Throughout the scanning process, the lowest point can be identified, as shown in this chapter's energy-distance curve of Scanning 10 (see **Figure 91**). By comparing the two structures, we find a discrepancy between the starting structure of scanning 10 and the structure of minimum point **P13**. At **P13**, the hydroxyl groups of the cyclodextrin CD#2 can form hydrogen bonds with the hydroxyl groups of the cyclodextrin CD#4 and the chitosan residue. Additionally, the **P13** lipid chain became more twisted than its original state. There is an energy barrier of 44.95 kcal/mol between the starting point and **P13**. Finally, at the end of the scanning, CD#2 was separated from the hexasaccharide cyclodextrin.

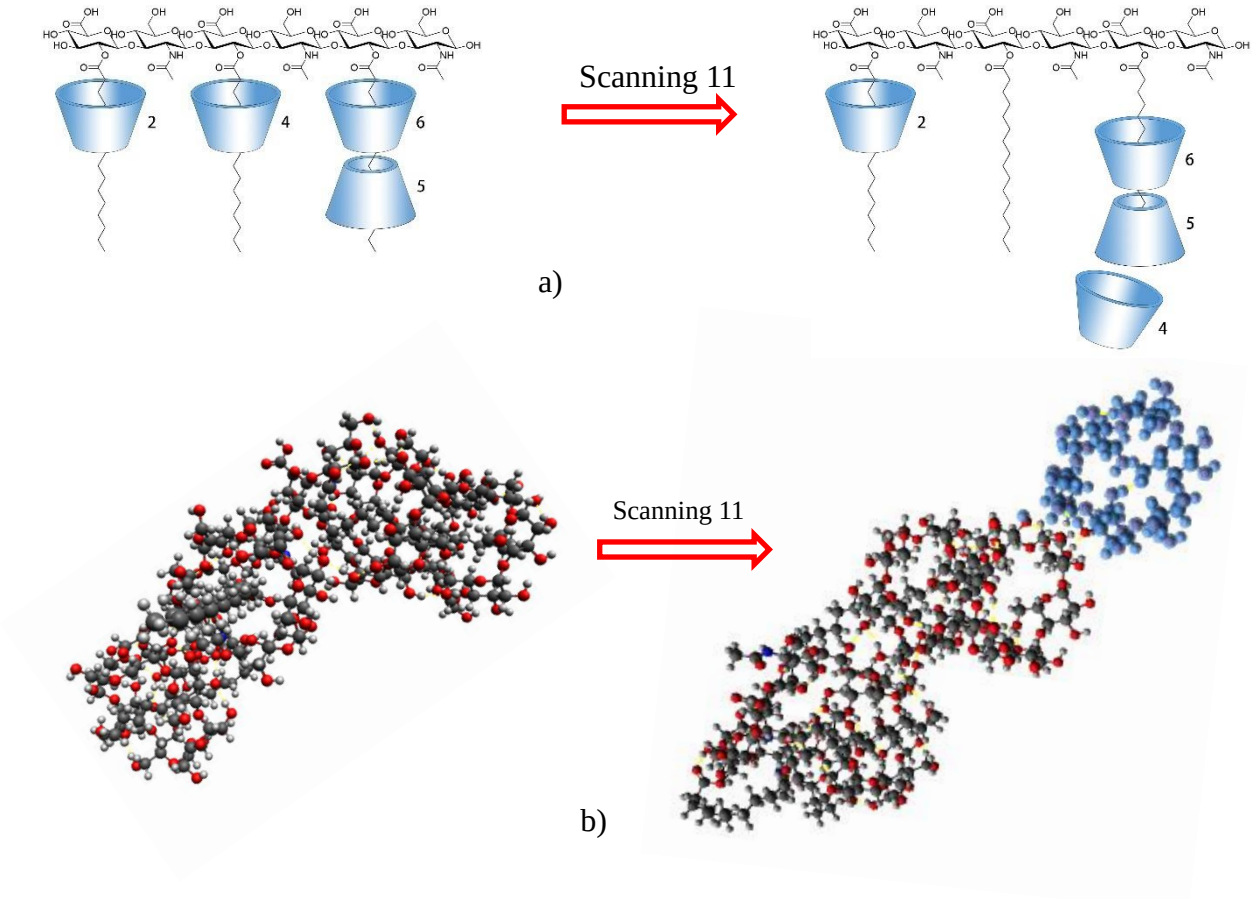

Figure 92. a) The schematic diagram of removing CD#4 from the hexasaccharide cyclodextrin complex; b) The process of removing CD#4 the hexasaccharide cyclodextrin complex (The removed cyclodextrin is colored in blue for clarity.)

This scanning is used to extract cyclodextrin (CD#4) from an inclusion complex containing four cyclodextrin molecules. After removing CD#1 and CD#3, the structure for scanning was produced, which contained four cyclodextrin molecules and a hexasaccharide. Additionally, at the start structure of the scanning, the hexasaccharide's extended alkyl chains were deposited in the cave of cyclodextrin or its dimer (**Figure 92**). The blue cyclodextrin molecule was then extracted from the hexasaccharide-4CDs inclusion complex. This new inclusion complex was generated as a result of the scanning. When the cyclodextrin component of the hexasaccharide-4CDs complex is removed, the remaining components of the new hexasaccharide-3CDs complex remain. The structure of the hexasaccharide-3CDs complex was altered slightly. The distance-energy curve can be used to calculate the extraction energy associated with the removal of the cyclodextrin (CD#4).

When CD#4 was removed from the hexasaccharide-cyclodextrin complex, considering the CD#2 is near CD#4, the hydroxyl group of CD#4 was affected by the hydroxyl group of

CD#2, so the leaving of CD#4 lead to the movement of CD#2. At the end of the Scanning, CD#2 was still around the lipid chain. At the same time, due to the left of CD#4, the distance between CD#4 and CD#6 decreased, and CD#4 became close to CD#6. The hydroxyl groups of CD#4 can be affected by CD#6 in the final structure. After CD#4 left from the lipid chain, the corresponding lipid chain became folded.

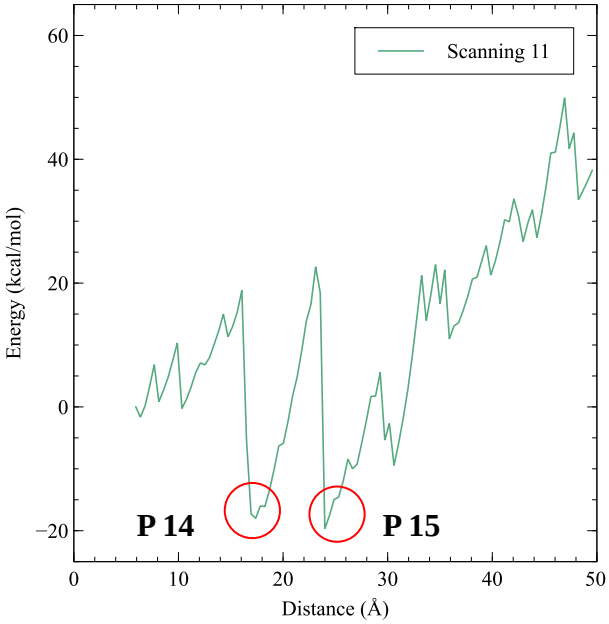

Figure 93. The energy-distance curve of the hexasaccharide cyclodextrin complex (Removing the cyclodextrin CD#4 from hexasaccharide cyclodextrin complex)

After performing scanning 11, we can calculate the extraction energy based on the energy-distance curve. The extraction energy of scanning 11 is 38.21 kcal/mol. (see **Figure 93**)

As shown in **Figure 93**, two minimum points may be observed during the scanning process. We were able to identify similarities between these structures by comparing the start structure of scanning 11 to the structures of the minimum points **P14** and **P15**. At the lowest position **P14**, the hydrogen bonds can form between the hydroxyl groups of CD#2, CD#5, and CD#4. CD#2 remains at the end of the lipid chain in the structure of **P14**. Between **P14** and the starting position, there is a -18.00 kcal/mol energy difference.

When the distance between cyclodextrin CD#4 and the palmitic acid residue increased, CD#4 became entirely separated from the lipid chain. Additionally, after the removal of CD#4, the corresponding lipid chain became more folded, and the lipid chain's carboxyl group formed a hydrogen bond with CD#5. There was also an energy barrier between **P14** and **P15** (40.63 kcal/mol). During the whole process, however, the hydroxyl groups of CD#2 and CD#5 still could establish hydrogen bonds with CD#4. CD#4 was isolated from the lipid chain at the minimum point **P15**. (see **Figure 94**)

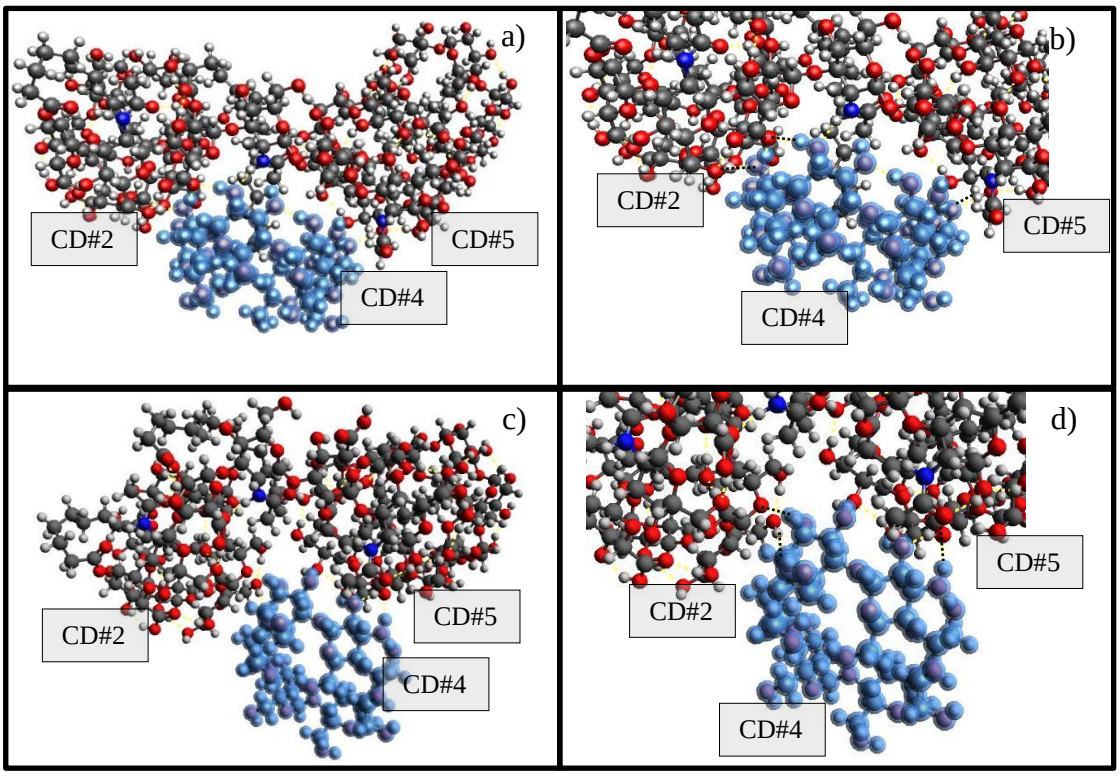

Figure 94. a) The structure of the minimum point **P14** hexasaccharide cyclodextrin complex. b) The position of CD#2 and chitosan residue relative to the removed CD#4. c) The structure of the minimum point **P15** hexasaccharide cyclodextrin complex. d) The position of CD#2 relative to the removed CD#4. (The removed cyclodextrin CD#4 is coloured in blue for clarity, and the black dash line indicates the hydrogen bond between CD#2, CD#5 and CD#2)

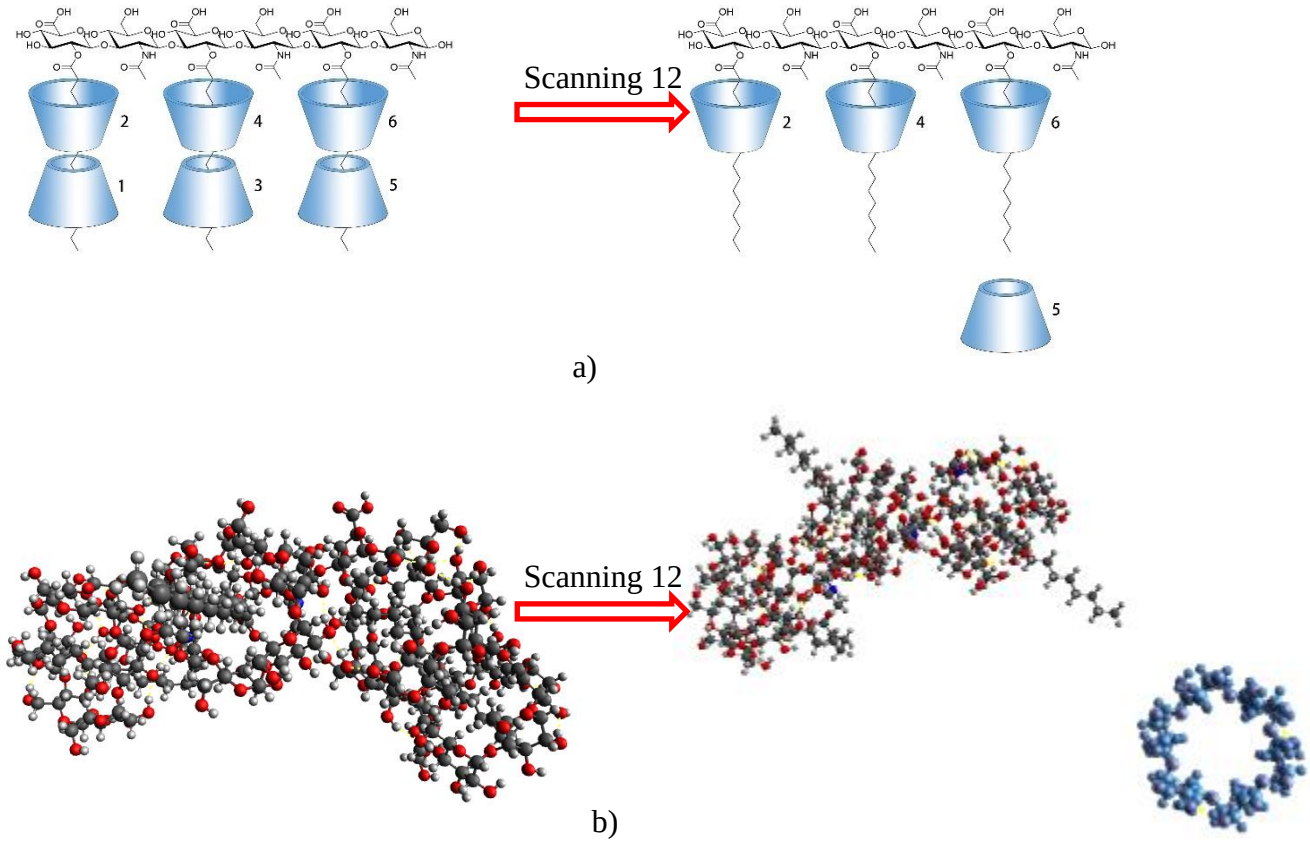

Figure 95. a) The schematic diagram of removing the CD#5 from the hexasaccharide cyclodextrin complex; b) The process of removing the CD#5 the hexasaccharide cyclodextrin complex (The removed cyclodextrin is colored in blue for clarity.)

This scanning is used to remove cyclodextrin (CD#5) from an inclusion complex containing four cyclodextrin molecules. After CD#1 and CD#3 were removed, the scanning structure was constructed by using a hexasaccharide and four cyclodextrin molecules. Furthermore, as the hexasaccharide structure of the scanning was starting, alkyl chains that had been extended into the cyclodextrin or dimer molecule were deposited into the cave (**Figure 95**). Following the extraction of the hexasaccharide-4CDs inclusion complex, the blue cyclodextrin molecule was isolated. As a result of the scanning, a novel inclusion complex was created. Furthermore, the structure of the novel inclusion complex, the hexasaccharide-3CDs complex, was very minimally changed. Based on the distance-energy curve, the extraction energy of removing CD#5 can be calculated.

When CD#5 was removed from the hexasaccharide-cyclodextrin complex, considering the influence of the hydroxyl groups between CD#5 and CD#6, CD#6 moved slightly and was still around the lipid chain. Finally, CD#5 was removed from the system completely.

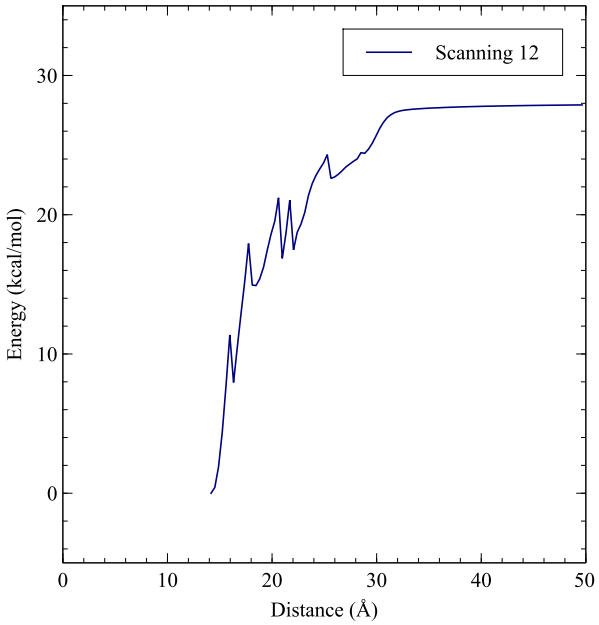

Figure 96. The energy-distance curve of the hexasaccharide cyclodextrin complex (Removing the cyclodextrin CD#5 from hexasaccharide cyclodextrin complex)

After performing the scanning, we can get the value of the extraction energy based on the distance-energy curve. The extraction energy of removing CD#5 is 27.88 kcal/mol. (see **Figure 96**)

After performing various scannings, we summarise the data of the extraction energy of the cyclodextrin-hexasaccharide complex in **Table 26**.

Table 26. The extraction energy of the scanning

Description	The Energy of Start Point (kcal/mol)	The Energy of End Point (kcal/mol)	Extraction Energy (kcal/mol)
Remove Cyclodextrin 2	0	33.25	33.25
Remove Cyclodextrin 4	0	38.21	38.21
Remove Cyclodextrin 5	0	27.88	27.88

We selected a structure that did not contain the deleted cyclodextrins CD#5, CD#3, and CD#1 after removing the fourth cyclodextrin molecule from the. The hexasaccharide complex structure, including three cyclodextrin molecules, has been selected.

The goal was to investigate the entire system's extraction energy while deleting the fourth cyclodextrin. As the result of the scannings, we have already obtained the structure of the hexasaccharide cyclodextrin complex with three cyclodextrin molecules. Then we try to scan each cyclodextrin CD#2, CD#4, and CD#6 independently to gain the corresponding extraction energy value. We can compare the different values of the extraction energy after obtaining the extraction energy of removing the second cyclodextrin separately. Then we would like to establish a more appropriate method by which to get rid of the cyclodextrin molecule from the system as a whole. (see **Figure 97**)

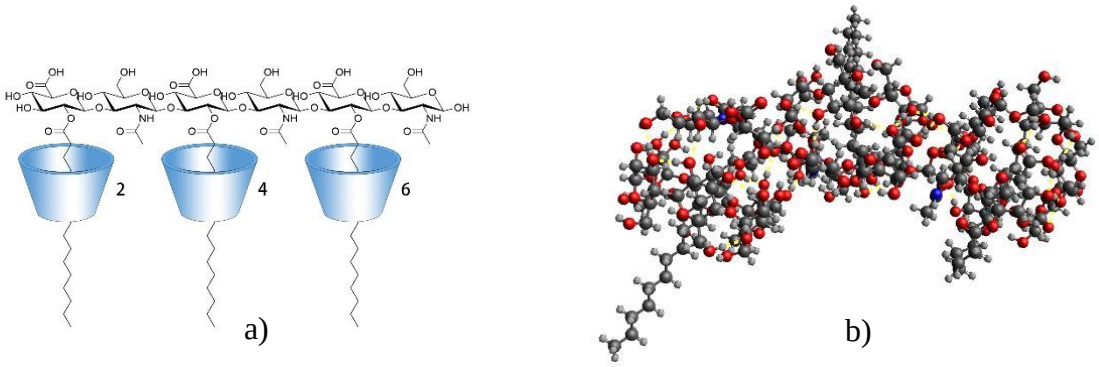

Figure 97. a) The schematic diagram of the hexasaccharide cyclodextrin complex; b) The structure of the hexasaccharide cyclodextrin complex

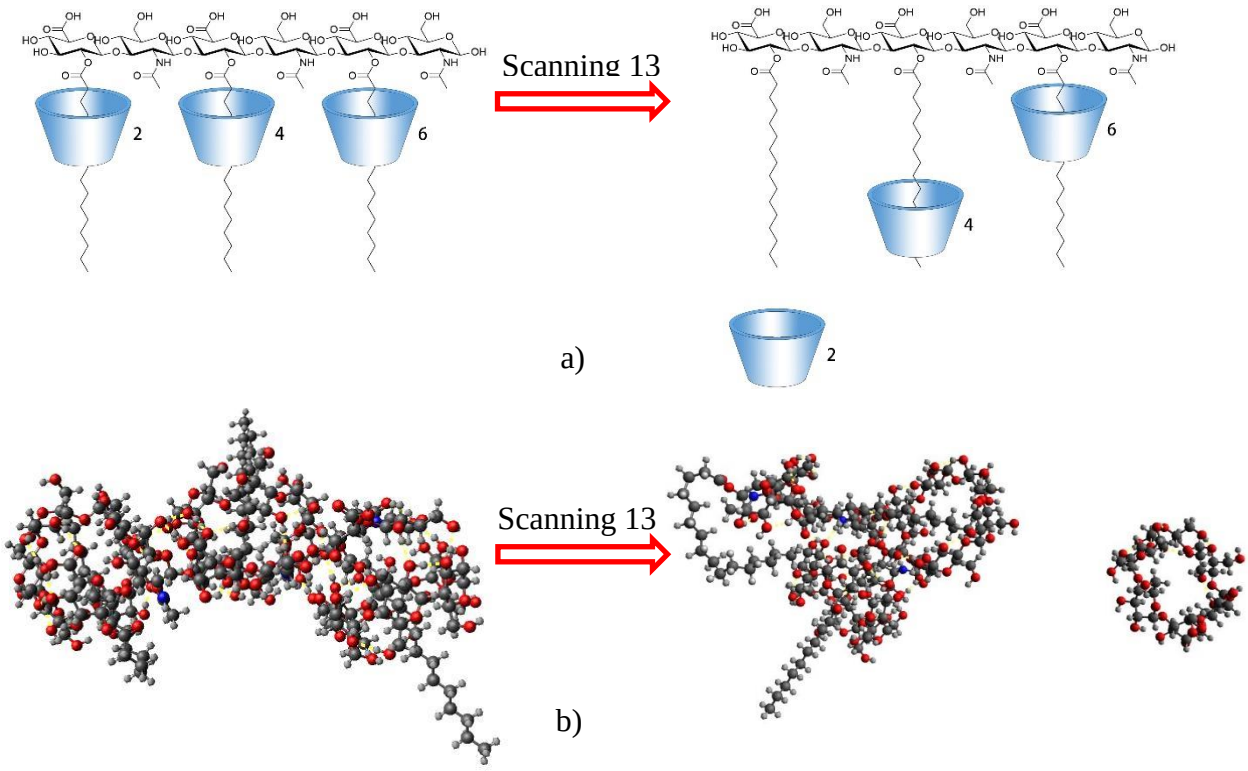

Figure 98. a) The schematic diagram of removing the CD#2 from the hexasaccharide cyclodextrin complex; b) The process of removing CD#2 the hexasaccharide cyclodextrin complex (The removed cyclodextrin is colored in blue for clarity.)

The purpose of this scanning is to dissociate the cyclodextrin molecule (CD#2) from the inclusion complex. Inclusion complexes are formed from a hexasaccharide molecule coupled with three cyclodextrin molecules. **Figure. 98** illustrated a three-fold extended alkyl chain wrapped around three cyclodextrin molecules. During the scanning process, the blue-colored cyclodextrin was separated from the hexasaccharide-3CDs complex molecule. Once the cyclodextrin was removed, the novel inclusion complex, the alky group of the hexasaccharide-2CDs complex became twisted. We were finally able to scan in the cyclodextrin in the form of palmitic acid due to having acquired the necessary extraction energy.

The hexasaccharide-cyclodextrin complex was removed from CD#2. Furthermore, the hydroxyl groups of CD#4 and CD#2 engage, preventing CD#2 from exiting the system. CD#4 similarly tended to shift away from the lipid chain upon CD#2 leaving the system. The lipid chain became folded, and the distance between the lipid and CD#2 grew during the removal of CD#2 from the lipid chain. CD#2 was isolated from the lipid chain at the end of the scanning. (see **Figure 98**)

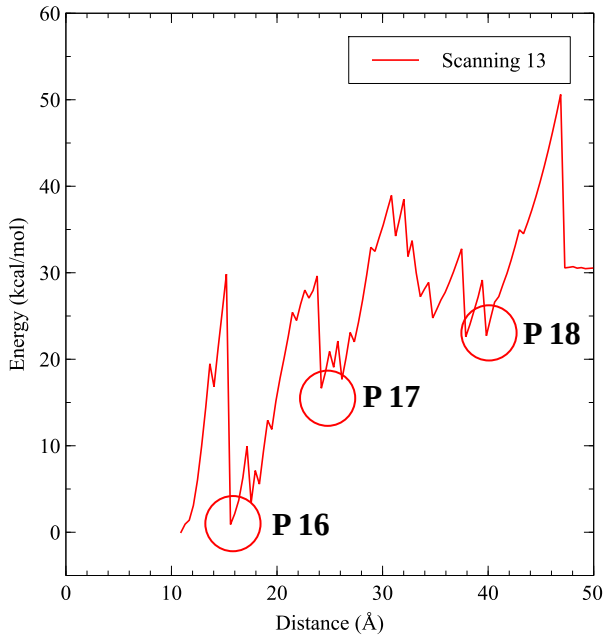

Figure 99. The energy-distance curve of the hexasaccharide cyclodextrin complex (Removing the cyclodextrin CD#2 from hexasaccharide cyclodextrin complex)

The extraction energy of removing CD#2 is 30.47 kcal/mol(see **Figure 99**)

As the energy-distance curve of scanning 13 (**Figure 99**) described in this chapter, the process of scanning, several minimum points can be observed. After Comparing the start structure of scanning 13 and the structures of minimum points **P16**, **P17,** and **P18,** we can find the differences between these structures. In the minimum point **P16**, the hydrogen bond of the cyclodextrin CD#2 can form between the hydroxyl group of CD#2, CD#4, and chitosan residue respectively. In the structure of **P16**, CD#2 is still around the end of the lipid chain. This step has an energy barrier of 29.84 kcal/mol. (see **Figure 99**)

With the distance between the cyclodextrin CD#2 and the palmitic acid residue increase, CD#2 was completely separated from the lipid chain. Moreover, the lipid chain becomes folded. In the minimum point **P17**, CD#2 can form the hydrogen bond with CD#4. Furthermore, CD#4 is still near the carboxyl group of the lipid chain. This step has an energy barrier of 27.03 kcal/mol. (see **Figure 100**)

When CD#2 was removed from the hexasaccharide cyclodextrin complex, CD#4 subsequently moved to the end of the lipid chain. However, the hydroxyl groups of CD#2 and CD#4 can form hydrogen bonds during the whole process. In the minimum point **P18**, CD#4 is at the end of the lipid chain, and CD#2 was removed entirely from the system. This step has an energy barrier of 21.25 kcal/mol. (see **Figure 100**)

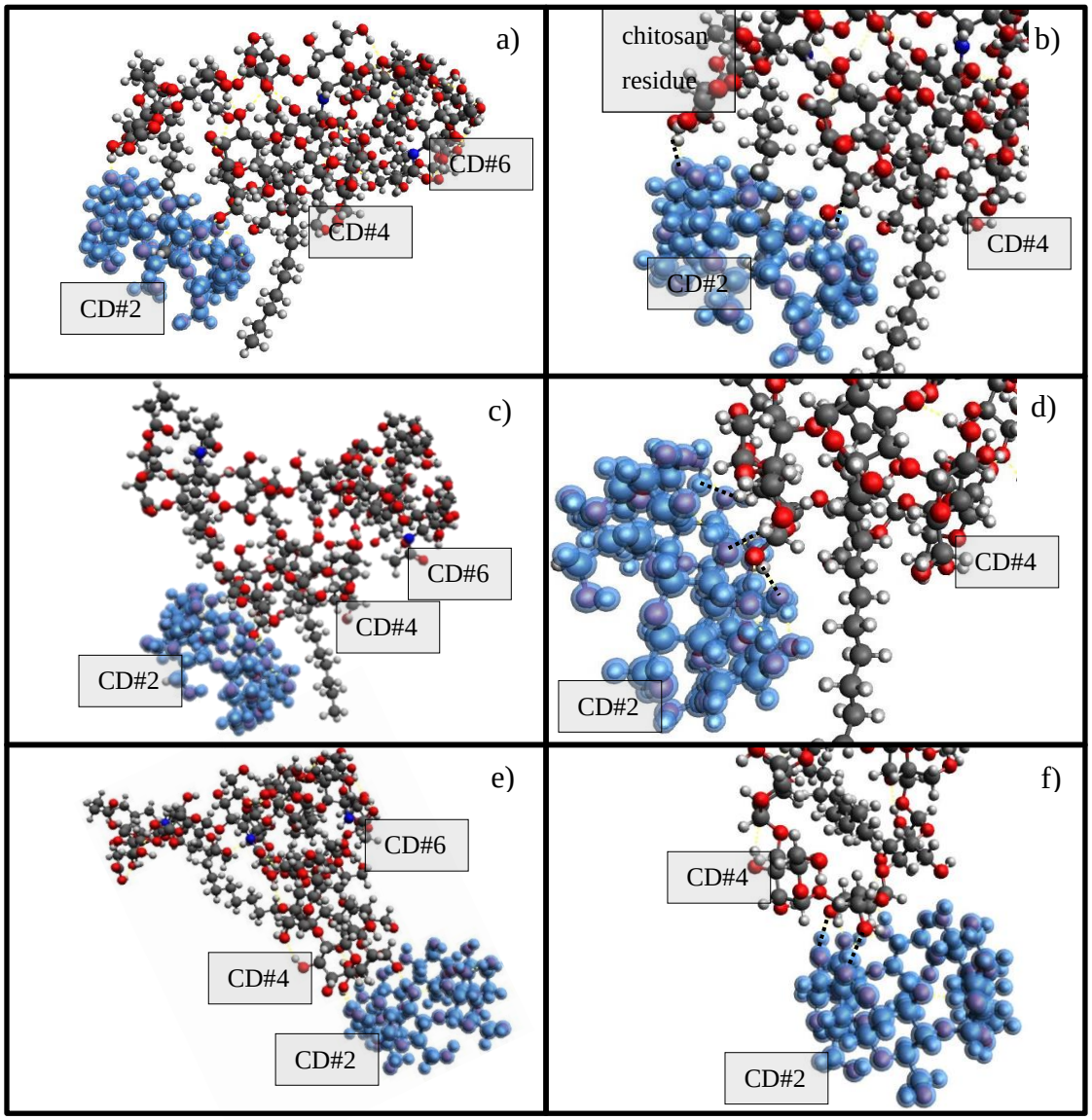

Figure 100. a) The structure of the minimum point **P16** hexasaccharide cyclodextrin complex. b) The position of CD#4 and chitosan residue relative to the removed CD#2. c) The structure of the minimum point **P17** hexasaccharide cyclodextrin complex. d) The position of CD#4 relative to the removed CD#2. e) The structure of the minimum point **P18** hexasaccharide cyclodextrin complex. f) The position of CD#4 relative to the removed CD#2 (The removed cyclodextrin CD#2 is coloured in blue for clarity, and the black dash line indicates the hydrogen bond between CD#4 and CD#2)

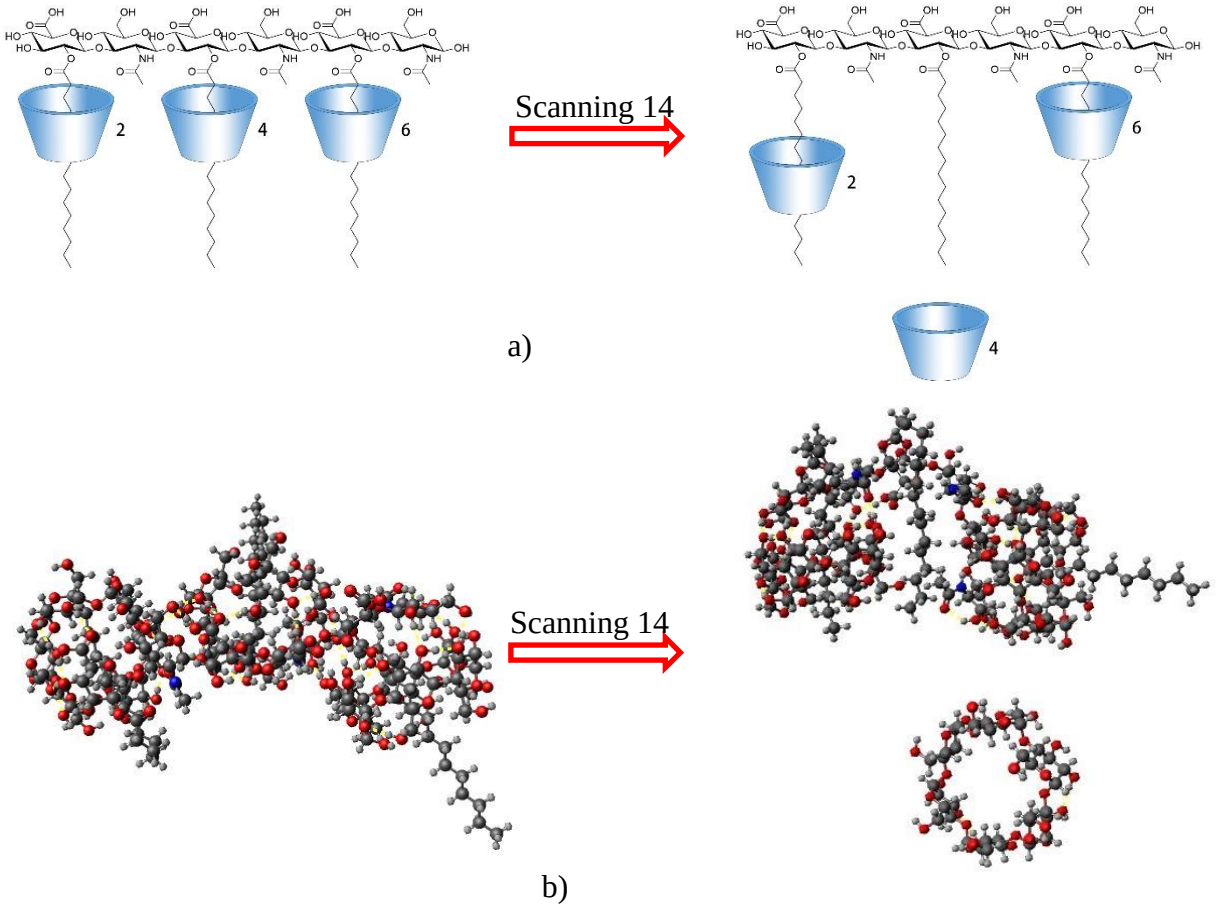

Figure 101. a) The schematic diagram of removing the CD#4 from the hexasaccharide cyclodextrin complex; b) The process of removing the CD#2 the hexasaccharide cyclodextrin complex

This scanning is intended to separate the cyclodextrin molecule (CD#4) from the inclusion complex. A hexasaccharide molecule was linked to three cyclodextrin molecules to create inclusion complexes for scanning. Three-fold extended alkyl chains wrapped around three cyclodextrin molecules were depicted in **Figure 101**. In the start structure, CD#1, #3, and #5 have been removed from the system. The blue-colored cyclodextrin was extracted from the hexasaccharide-3CDs complex. During the scanning process, when the cyclodextrin was removed, the alkyl group of new inclusion complexes that were not surrounded by the cyclodextrin molecules became twisted. Due to the acquisition of the requisite extraction energy, we were ultimately able to plot the distance-energy curve after scanning.

At the end of the scanning, as CD#2 is close to CD#4, the hydroxyl group of CD#4 was affected by the hydroxyl group of CD#2, causing CD#2 to migrate when CD#4 was removed from the hexasaccharide-cyclodextrin complex. CD#2 was remained surrounding the lipid chain at the end of the scanning. After CD#4 departs the lipid chain following the scanning procedure, the matching lipid chain folds. (see **Figure 102**)

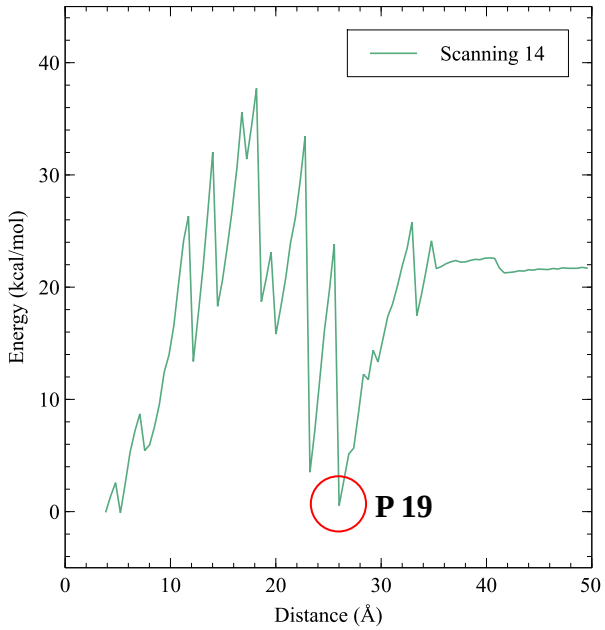

Figure 102. The energy-distance curve of the hexasaccharide cyclodextrin complex (Removing the cyclodextrin CD#4 from hexasaccharide cyclodextrin complex)

The extraction energy of removing CD#4 is 21.76 kcal/mol (see **Figure 102**).

As the energy-distance curve of scanning 14 is described in this chapter, the minimum point can be observed during the process of scanning. After Comparing the start structure of scanning 14 and the structure of minimum point **P19**, we can find a difference between these two structures. In the minimum point **P19**, the hydrogen bond of the cyclodextrin CD#4 can form between the hydroxyl group of CD#4 and CD#6. However, the distance of the hydroxyl group of CD#2 and CD#4 is so long that they cannot form any hydrogen bond. In the hexasaccharide cyclodextrin complex structure at minimum point **P19**, the cyclodextrin CD#4 was separated from the residue of the lipid chain completely. (see **Figure 103**)

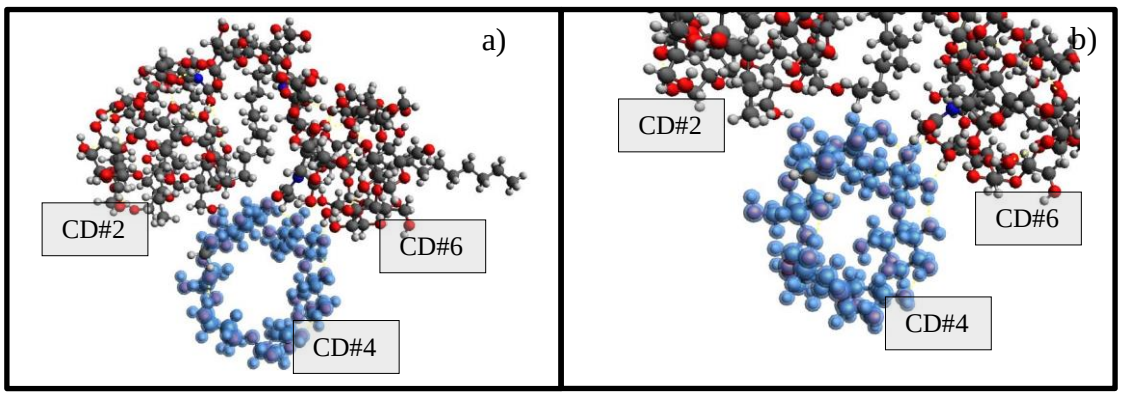

Figure 103 a) The structure of the minimum point **P19** hexasaccharide cyclodextrin complex (The removed cyclodextrin CD#4 is colored in blue for clarity.) b) The position of CD#2 and CD#6 relative to the removed CD#4 (The removed cyclodextrin CD#4 is colored in blue for clarity and the black dash line indicates the hydrogen bond between CD#4 and CD#6)

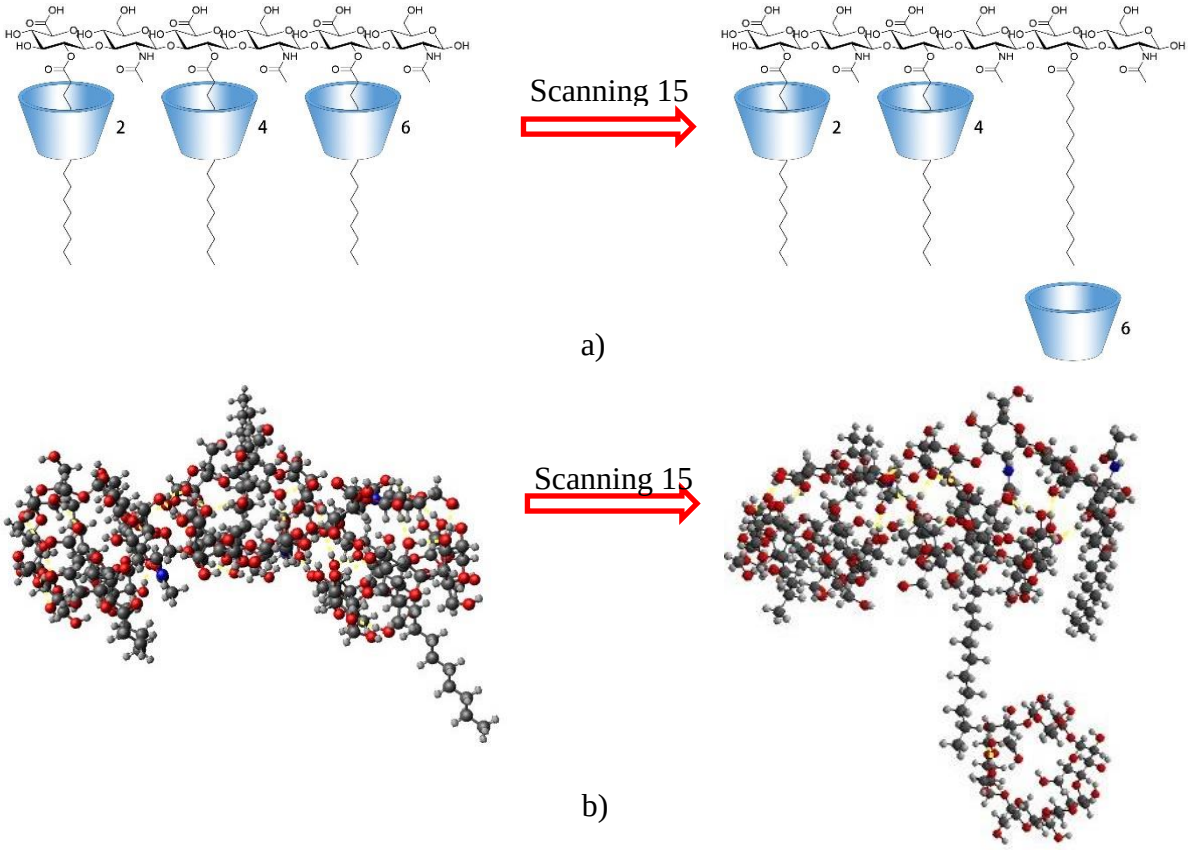

Figure 104. a) The schematic diagram of removing CD#6 from the hexasaccharide cyclodextrin complex; b) The process of removing CD#6 the hexasaccharide cyclodextrin complex

The purpose of this scanning is to detach the cyclodextrin molecule (CD#5) from the inclusion complex. A hexasaccharide molecule that was bonded to three cyclodextrin molecules was regarded as the inclusion complexes for scanning. **Figure 104** illustrates three extended alkyl chains wrapped around three cyclodextrin molecules. CD#1, #3, and #5 have been removed from the system's initial structure. Blue-colored cyclodextrin was isolated from the hexasaccharide-3CDs complex. When the cyclodextrin was removed during the scanning process, the alkyl group of the new inclusion complex became distorted since it was not surrounded by cyclodextrin molecules. After acquiring the required extraction energy, we were able to plot the distance-energy curve.

The purpose of this scanning is to remove CD#6 from the hexasaccharide cyclodextrin complex. At the beginning of the scanning, three cyclodextrins molecules were contained in the hexasaccharide cyclodextrin complex. During the whole process of scanning, CD#2 and CD#4 were at the initial position, and we removed CD#6 separately.

As depicted in **Figure 104**, at the beginning of the scanning process, when CD#6 was

removed from the hexasaccharide-cyclodextrin complex, considering the influence of the hydroxyl groups between CD#4 and CD#6, CD#6 moved slightly and was still around the lipid chain. Finally, CD#6 was entirely removed from the system. As depicted in **Figure 104 b**, at the beginning of the scanning process, When CD#6 was removed from the hexasaccharide-cyclodextrin complex, considering the influence of the hydroxyl groups between CD#4 and CD#6, CD#6 moved slightly and was still around the lipid chain. Finally, CD#6 was removed from the system completely.

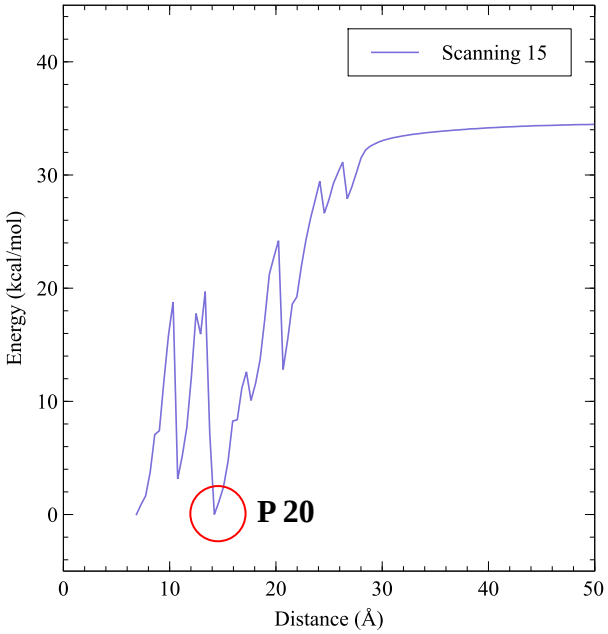

Figure 105. The energy-distance curve of the hexasaccharide cyclodextrin complex (Removing the cyclodextrin CD#6 from hexasaccharide cyclodextrin complex)

Based on the energy-distance curve of removing the cyclodextrin CD#6, the extraction energy of removing CD#6 is 34.45 kcal/mol. (see **Figure 105**)

The minimum point can be observed during the scanning process, as shown in the energy-distance curve of Scanning 15 (**Figure 105**) detailed in this chapter. After comparing the start structure of scanning 14 and the structure of minimum point **P20**, we can find a difference between these two structures. At the minimum point **P20**, the hydroxyl groups of the cyclodextrin CD#6 might form the hydrogen bonds with the hydroxyl groups of CD#4, the chitosan residue, and CD#6 separately. Moreover, the lipid chain becomes more folded than the start structure. This step has an energy barrier of 19.69 kcal/mol. Then, with the increase of the distance between CD#6 and the corresponding lipid chain, the hydroxyl groups cannot form hydrogen bonds anymore. At the end of the scanning, CD#6 was removed from the hexasaccharide cyclodextrin finally. (see **Figure 106**)

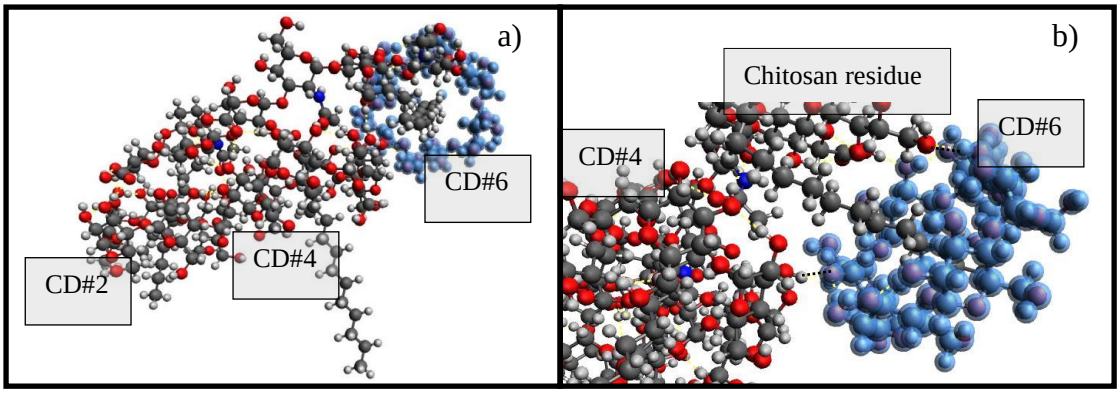

Figure 106 a) The structure of the minimum point **P20** hexasaccharide cyclodextrin complex (The removed cyclodextrin CD#6 is colored in blue for clarity.) b) The position of CD#4 relative to the removed CD#6 (The removed cyclodextrin CD#6 is colored in blue for clarity and the black dash line indicates the hydrogen bond between CD#4, chitosan residue and CD#6)

After performing various scannings, we summarize the extraction energy of the cyclodextrin-hexasaccharide complex in **Table 27**.

Table 27. The extraction energy of the scanning

Description	The Energy of Start Point (kcal/mol)	The Energy of End Point (kcal/mol)	Extraction Energy (kcal/mol)
Remove Cyclodextrin 2	0	30.54	30.54
Remove Cyclodextrin 4	0	21.69	21.69
Remove Cyclodextrin 6	0	34.47	34.47

After extracting the fourth cyclodextrin molecule from the hexasaccharide-3cyclodextrin complex, we chose a structure that did not include the removed cyclodextrins CD#1, CD#3, CD#4, and CD#5. The structure of the hexasaccharide complex, which contains two cyclodextrin molecules, has been chosen. (see **Figure 107**)

The aim is to look into the extraction energy of the whole system while removing the fourth cyclodextrin. We have previously acquired the structure of the hexasaccharide-cyclodextrin complex with two cyclodextrin molecules as a result of these scannings of the hexasaccharide-3CDs complex. After that, we attempt to scan each cyclodextrin CD#2 and CD#6 separately to get the extraction energy value. After scanning the hexasaccharide-2CDs complex, we were able to compare the different extraction energy values. Then we'd have to devise a more appropriate method of extracting the cyclodextrin molecule from the whole system. (see **Figure 107**)

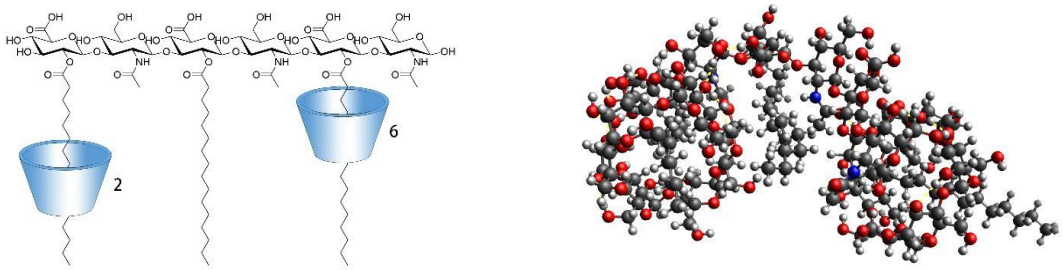

a) b)

Figure 107 a) The schematic diagram of the hexasaccharide cyclodextrin complex; b) The structure of the hexasaccharide cyclodextrin complex

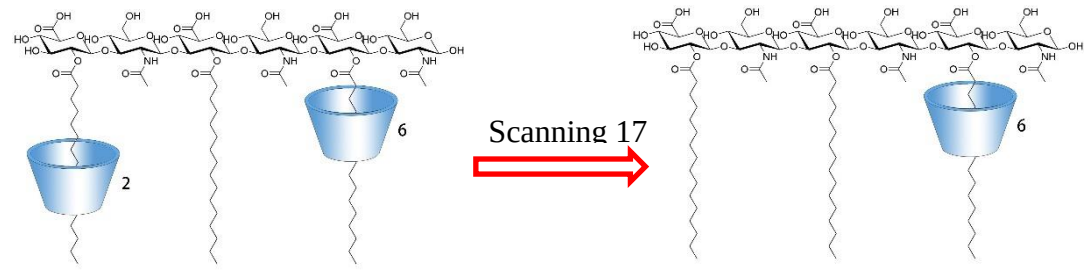

a)

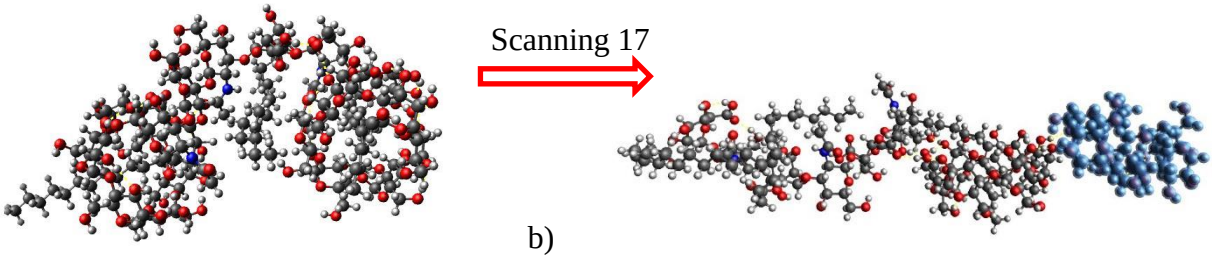

b)

Figure 108 a) The schematic diagram of removing CD#2 from the hexasaccharide cyclodextrin complex; b) The process of removing CD#2 the hexasaccharide cyclodextrin complex (The removed cyclodextrin is colored in blue for clarity.)

The purpose of this scanning is to dissociate the cyclodextrin molecule (CD#2) from the inclusion complex. Inclusion complexes are formed from a hexasaccharide molecule coupled with three cyclodextrin molecules. **Figure 108** illustrates a three-fold extended alkyl chain wrapped around three cyclodextrin molecules. During the scanning process, the blue-colored cyclodextrin was removed from the hexasaccharide-2CDs complex molecule. Once the cyclodextrin was removed, the alky group of the novel hexasaccharide-CD complex became twisted. We were finally able to scan in the cyclodextrin in the form of palmitic acid due to having acquired the necessary extraction energy.

The hexasaccharide-cyclodextrin complex was removed from CD#2. Furthermore, the hydroxyl groups of CD#6 were engaged in the process, preventing CD#2 from exiting the system. CD# 6 similarly tended to shift away from the lipid chain when CD#2 left the system. The lipid that didn't contain the cyclodextrin molecule got folded, and the distance between the lipid and CD#2 grew during removing CD#2 from the lipid chain. CD#2 was isolated from the lipid chain at the end of the scanning.

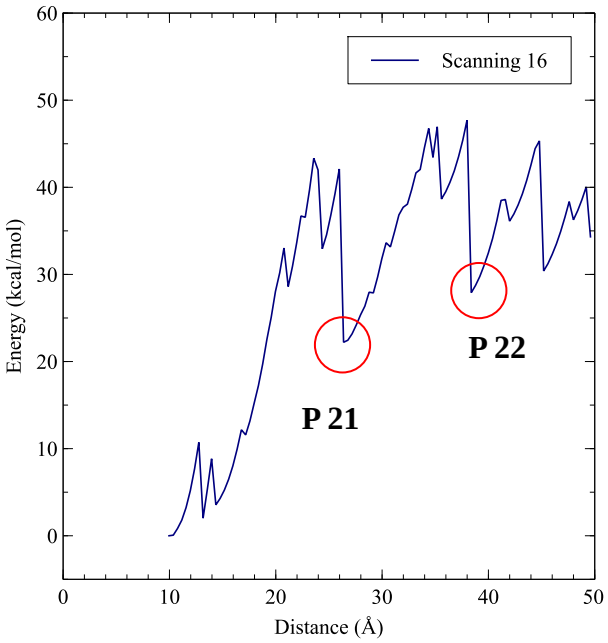

Figure 109. The energy-distance curve of the hexasaccharide cyclodextrin complex (Removing the cyclodextrin CD#2 from hexasaccharide cyclodextrin complex)

The extraction energy of removing CD#2 is 34.31 kcal/mol. (see **Figure 109**)

As the Energy-distance curve of scanning 16 (**Figure 109**) described in this chapter, the process of scanning, several minimum points can be observed. After comparing the start structure of scanning 16 and the structures of minimum points **P21** and **P22,** we can find the differences between these structures. In the minimum point **P21**, The cyclodextrin CD#2 was separated from the lipid chain completely and moved closed to CD#6 and the chitosan residue. The hydroxyl groups of CD#2 can form hydrogen bonds with CD#6 and chitosan residue separately. At this time, CD#6 is still near the carboxyl group of the lipid chain. The conformation of the fatty acyl chains with no cyclodextrin became folded.

After we compared the conformations of **P21** and **P22**, we can find that CD#2 can form the hydrogen bond with CD#6 during the whole process, and CD#2 can't form the hydrogen bond with the chitosan residue in the minimum point **P21**. The increasing distance between CD#2 and the chitosan residue can be the cause. The movement of CD#2 caused the movement of CD#6, and CD#6 was still at the end of the lipid chain. (see **Figure 110**)

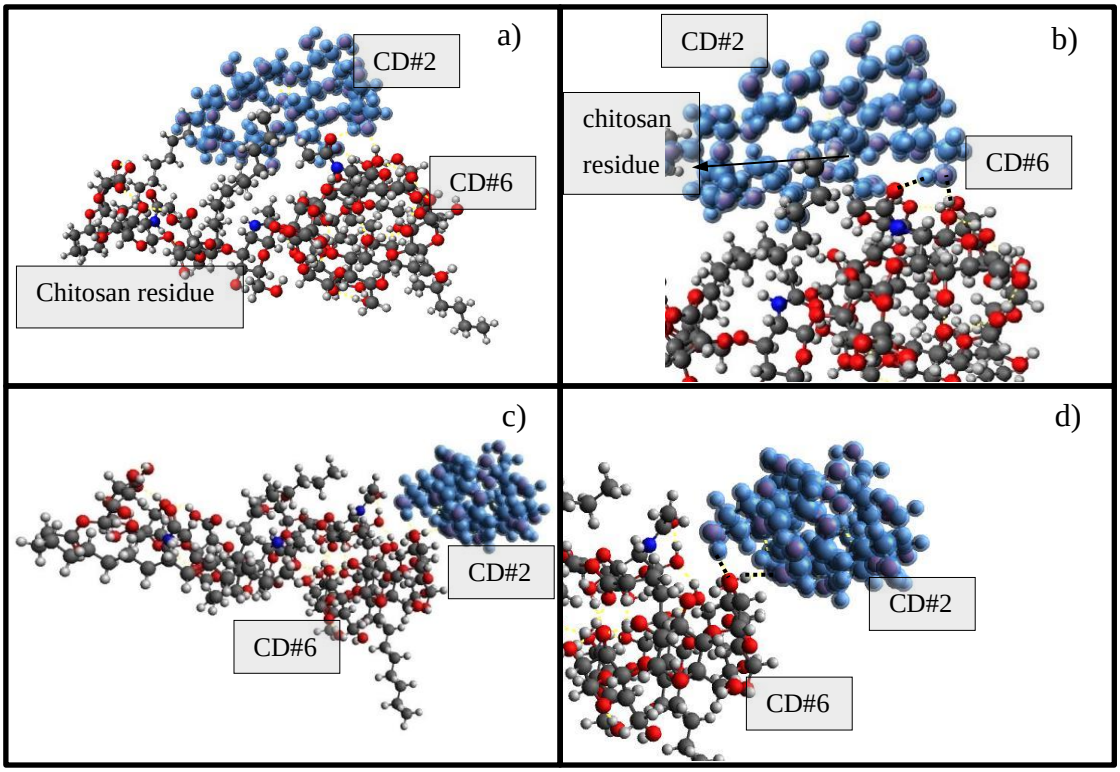

Figure 110. a) The structure of the minimum point **P21** hexasaccharide cyclodextrin complex. b) The position of CD#4 and chitosan residue relative to the removed CD#2. c) The structure of the minimum point **P22** hexasaccharide cyclodextrin complex. d) The position of CD#4 relative to the removed CD#2. (The removed cyclodextrin CD#2 is colored in blue for clarity, and the black dash line indicates the hydrogen bond between CD#4 and CD#2

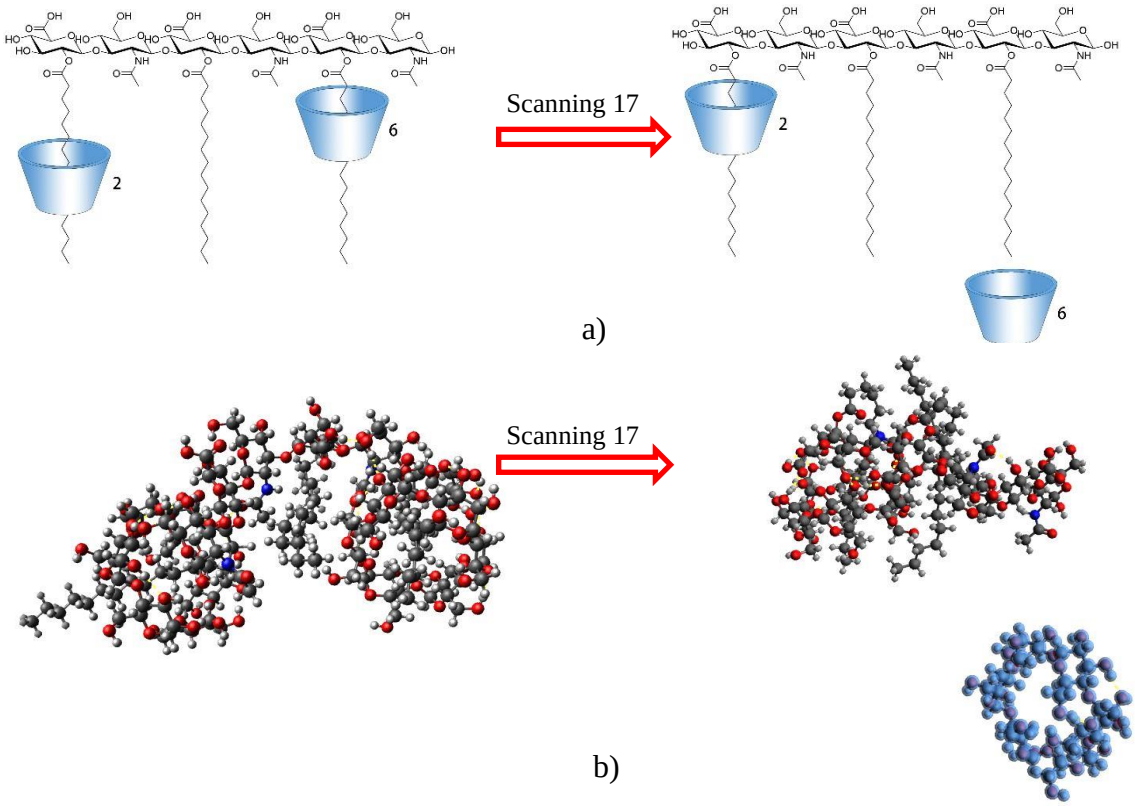

Figure 111. a) The schematic diagram of removing CD#6 from the hexasaccharide cyclodextrin complex; b) The process of removing CD#6 the hexasaccharide cyclodextrin complex

This scanning is performed in order to separate the cyclodextrin molecule (CD#6) from the inclusion complex. The inclusion complex for scanning was considered to be a hexasaccharide molecule attached to two cyclodextrin molecules. Three extended alkyl chains are wrapped around two cyclodextrin molecules in **Figure 111**. CDs #1, #3, #4, and #5 have been removed from the starting structure. Cyclodextrin with a blue color was extracted from the hexasaccharide-2CDs complex. When the cyclodextrin was removed during the scanning process, the new inclusion complex's alkyl group became distorted.

The purpose of this scanning is to remove CD#6 from the hexasaccharide cyclodextrin complex. At the beginning of the scanning, two cyclodextrins molecules were contained in the hexasaccharide cyclodextrin complex. During the whole process of scanning, CD#2 was at the initial position, and we removed CD#6 separately.

As depicted in **Figure 111**, at the beginning of the scanning process, When CD#6 was removed from the hexasaccharide-cyclodextrin complex, considering the interaction of the hydroxyl groups between CD#6 and chitosan residue, CD#6 began to move slightly. Finally,

CD#6 was removed from the system completely.

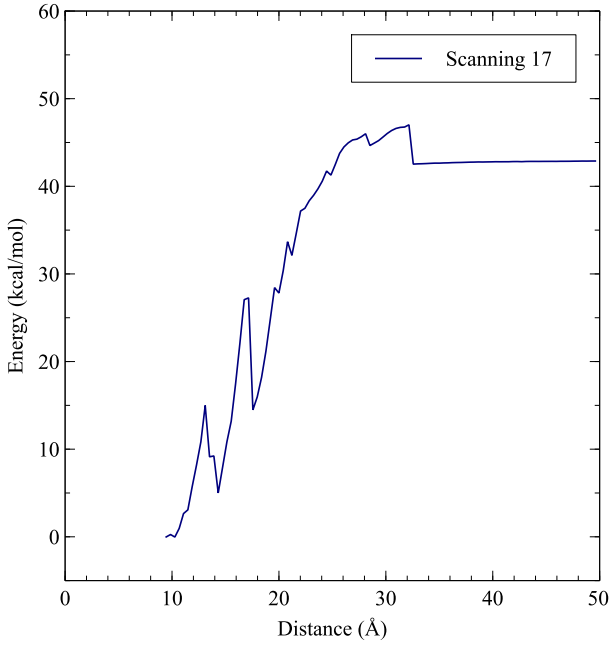

Figure 112. The energy-distance curve of the hexasaccharide-cyclodextrin complex (Removing the cyclodextrin CD#6 from hexasaccharide-cyclodextrin complex)

Based on the energy-distance curve of removing the cyclodextrin CD#6, the extraction energy of removing CD#6 is 42.90 kcal/mol. (see **Figure 112**)

After performing various scannings, we summarize the extraction energy of the hexasaccharide-cyclodextrin complex in **Table 28**.

When removing CD#2 from the hexasaccharide-2CDs complex, the corresponding extraction energy is lower than the extraction energy of removing CD#6 from the hexasaccharide-2CDs complex. So, we selected the hexasaccharide-cyclodextrin complex that included the cyclodextrin CD# 6 as the starting structure of the next scanning.

Table 28. The extraction energy of the scanning

Description	The Energy of Start Point (kcal/mol)	The Energy of End Point (kcal/mol)	Extraction Energy (kcal/mol)
Remove Cyclodextrin 2	0	34.31	34.31
Remove Cyclodextrin 6	-0.01	42.89	42.90

After extracting the fifth cyclodextrin molecule from the hexasaccharide-2cyclodextrin complex, we got a structure that included the cyclodextrin CD# 6. The structure of the hexasaccharide-cyclodextrin complex, which contains one cyclodextrin molecule, has been chosen. (see **Figure 113**)

The goal was to investigate the entire system's extraction energy while deleting the fourth cyclodextrin. As the result of these scannings of hexasaccharide-2cyclodextrin complex, we have already obtained the structure of the hexasaccharide-cyclodextrin complex with one cyclodextrin molecule. Then we try to scan cyclodextrin CD#6 to gain the corresponding extraction energy value. We could get the final structure after we performed the scanning of the hexasaccharide-cyclodextrin complex. Then we would have to figure out a better way to extract the cyclodextrin molecule from the system as a whole.

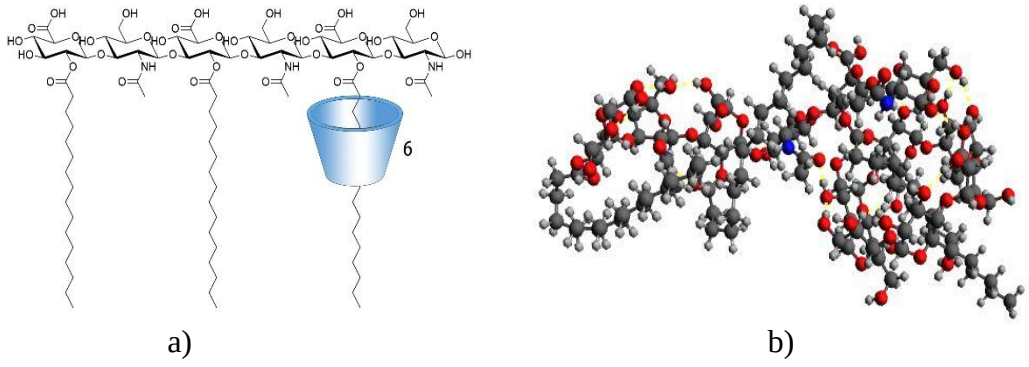

a) b)

Figure 113 a) The schematic diagram of the hexasaccharide cyclodextrin complex; b) The structure of the hexasaccharide cyclodextrin complex

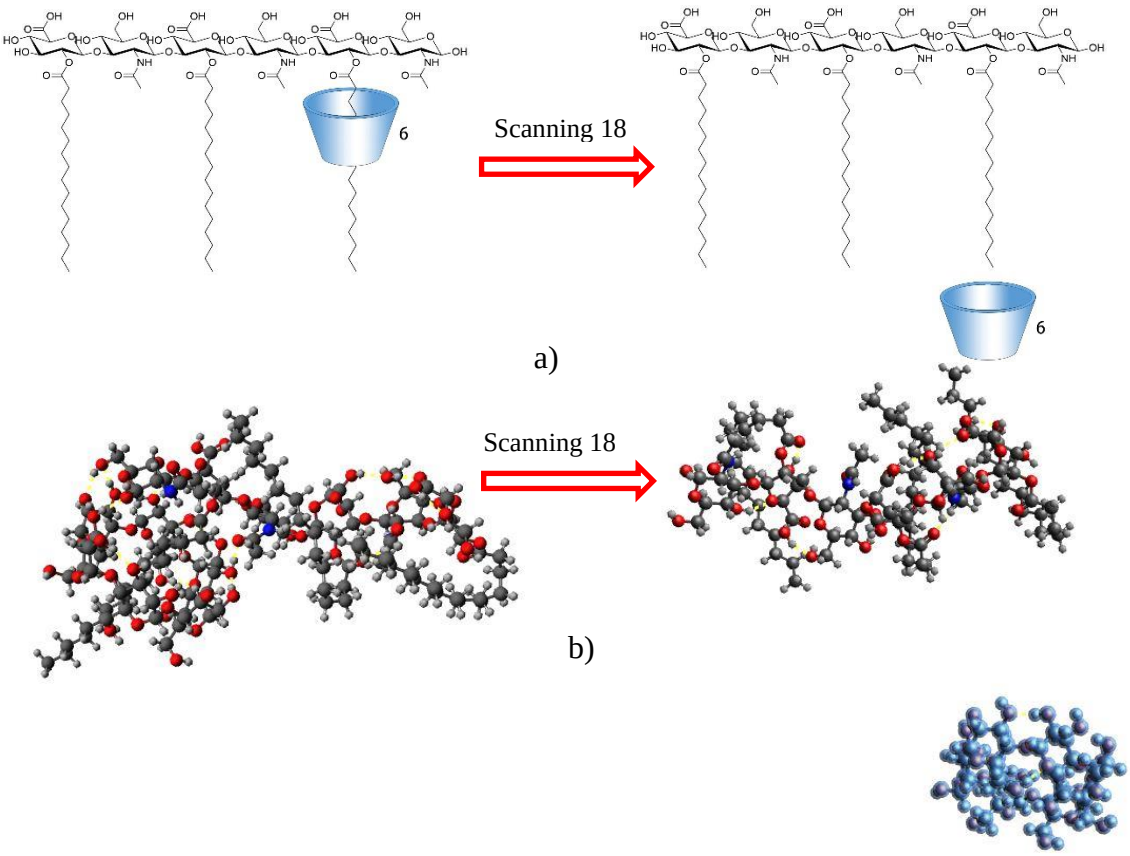

Figure 114 a) The schematic diagram of removing the CD#6 from the hexasaccharide cyclodextrin complex; b) The process of removing the CD#6 the hexasaccharide cyclodextrin complex (The removed cyclodextrin is colored in blue for clarity.)

The purpose of this scanning is to dissociate the cyclodextrin molecule (CD#6) from the inclusion complex. Inclusion complexes are formed from a hexasaccharide molecule coupled with three cyclodextrin molecules. **Figure 114** illustrates an extended alkyl chain wrapped around one cyclodextrin molecule. During the scanning process, the blue-colored cyclodextrin was removed from the hexasaccharide-CDs complex molecule. When CD#6 was removed from the hexasaccharide-cyclodextrin complex, the lipid that didn't contain the cyclodextrin molecule got folded. We were finally able to perform a scan of the hexasaccharide-cyclodextrin complex and get the final structure of the hexasaccharide with no cyclodextrin.

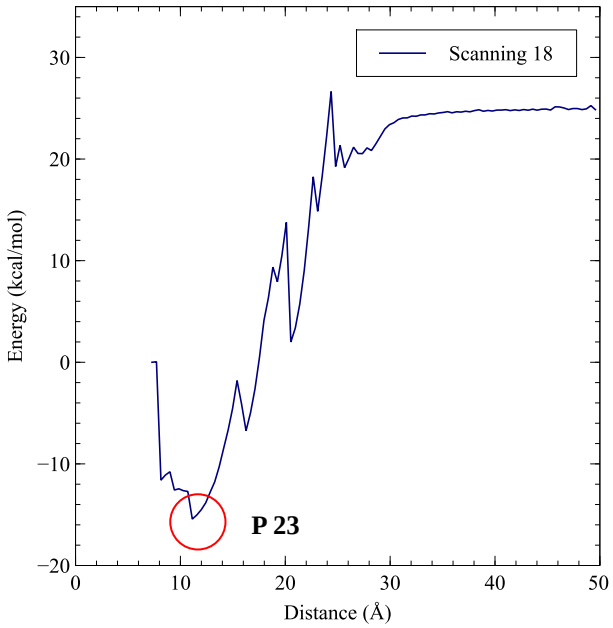

Figure 115 The energy-distance curve of the hexasaccharide-cyclodextrin complex (Removing the cyclodextrin CD#6 from hexasaccharide-cyclodextrin complex)

The extraction energy of removing CD#6 is 24.85 kcal/mol (see **Figure 115**)

As the energy-distance curve of scanning 18 (**Figure 116**) described in this chapter, in the minimum point **P23**, several hydrogen bonds can form between the hydroxyl groups of CD#6 and the chitosan residue. CD#6 was still around the alkyl chain at this time. The cyclodextrin CD#6 was entirely isolated from the lipid chain when the distance between it and the palmitic acid residue increased. (see **Figure 116**)

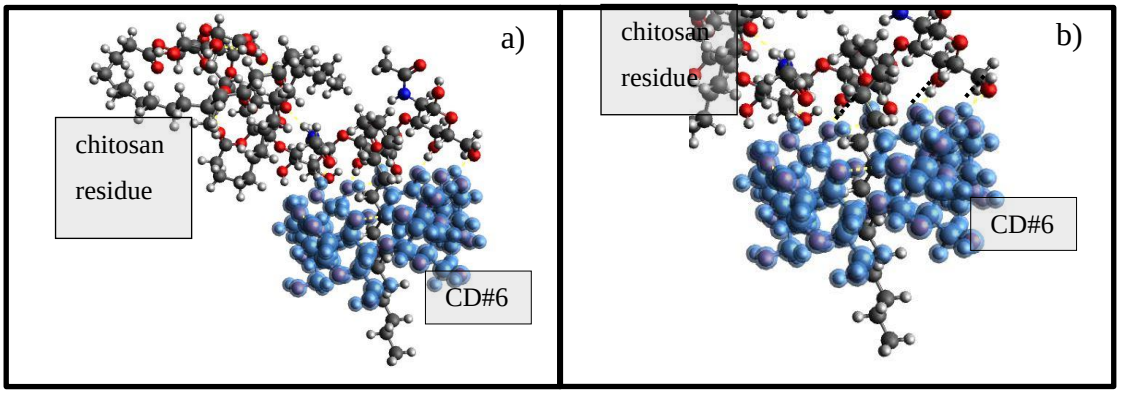

Figure 116. a) The structure of the minimum point **P23** hexasaccharide cyclodextrin complex. b) The position of chitosan residue relative to the removed CD#6. (The removed cyclodextrin CD#6 is colored in blue for clarity, and the black dash line indicates the hydrogen bond between CD#6 and chitosan residue.)

After performing the scanning of the hexasaccharide-cyclodextrin complex, we summarize the extraction energy of the hexasaccharide-cyclodextrin complex in **Table 29**.

Table 29. The extraction energy of the Scanning

Description	The Energy of Start Point (kcal/mol)	The Energy of End Point (kcal/mol)	Extraction Energy (kcal/mol)
Remove Cyclodextrin 6	0	24.85	24.85

Discussion

The energies obtained from the scanning will be discussed in this section for scanning of the hexasaccharide cyclodextrin complex.

At first, we would like to find the relationship between the monomer and dimer inclusion complex of palmitic acid. The structure of α-cyclodextrin is generally described as a tapered cylinder in **Figure 117**. The primary hydroxyl groups are on the narrow side, and the secondary hydroxyl groups are on the wide side.

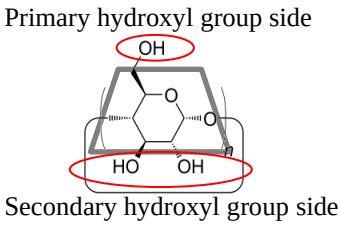

Figure 117. The structure of α-cyclodextrin

The monomer inclusion complex of palmitic acid can be classified into two different types of monomer inclusion (inclusion a and inclusion b).In inclusion a, the carboxyl group of the palmitic acid is next to the primary hydroxyl group side of the cyclodextrin. In inclusion b, the carboxyl group of the palmitic acid is next to the secondary hydroxyl group side of the cyclodextrin. (Figure 117.)

Based on the interaction between the hydroxyl group sides of the cyclodextrins of the dimer, the dimer inclusion complexes can be classified into four different types: 1, the interaction is between the primary hydroxyl group side of cyclodextrin and the primary hydroxyl group side of the other cyclodextrin of the same dimer inclusion, and the carboxyl group of the palmitic acid is next to the secondary hydroxyl group side of the cyclodextrin (pri-pri); 2, the interaction is between the primary hydroxyl group side of cyclodextrin and the secondary hydroxyl group side of the other cyclodextrin of the same dimer inclusion, and the carboxyl group of the palmitic acid is next to the secondary hydroxyl group side of the cyclodextrin (pri-sec); 3, the interaction between the secondary hydroxyl group side of cyclodextrin and the primary hydroxyl group side of the other cyclodextrin of the same dimer inclusion, and the carboxyl group of the palmitic acid is next to the primary hydroxyl group side of the cyclodextrin (sec-pri); 4, the interaction is between the secondary hydroxyl group side of cyclodextrin and the secondary hydroxyl group side of the other cyclodextrin of the same dimer inclusion, and the carboxyl group of the palmitic acid is next to the primary hydroxyl group side of the cyclodextrin (sec-sec). (see **Figure 118.**)

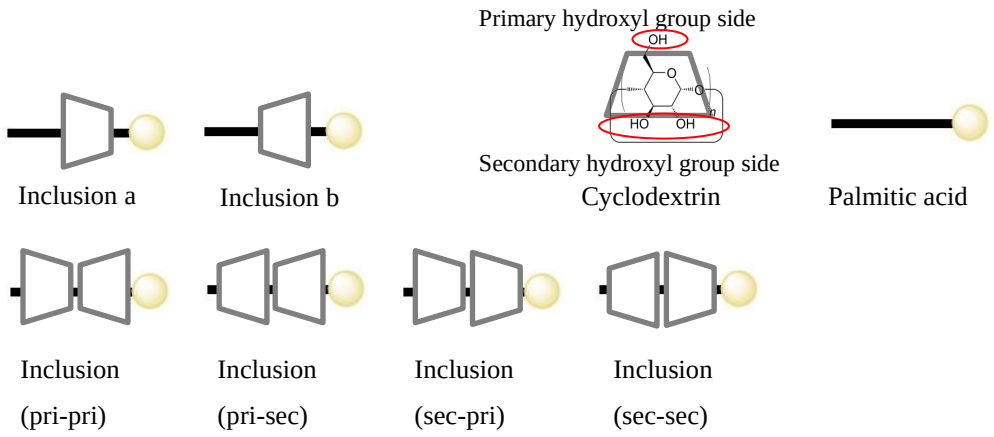

Figure 118. The classification of monomer and dimer inclusion complex of palmitic acid

In order to compare the different phenomenons between removing the cyclodextrin from the monomer and dimer inclusion complex of palmitic acid, the average distance-energy curves of the corresponding monomer and dimer inclusion complex were put together (**Figure 119**). And the corresponding conformation of the configuration states marked in **Figure 119** was also listed in **Figure 120**.

A is the conformation of starting structure of inclusion a, B is the conformation of starting structure of inclusion b, C is the conformation of starting structure of inclusion pri-pri, D is the conformation of starting structure of inclusion pri-sec, E is the conformation of starting structure of inclusion sec-pri, and F is the conformation of starting structure of inclusion sec-sec. When the system energy became stable, G is the configuration state of inclusion a with palmitic acid not interacting with cyclodextrin, H is the configuration state of inclusion b with palmitic acid not interacting with cyclodextrin, I is the configuration state of inclusion pri-pri with palmitic acid not interacting with cyclodextrin dimer, J is the configuration state of inclusion pri-sec with palmitic acid not interacting with cyclodextrin dimer, K is the configuration state of inclusion sec-pri with palmitic acid not interacting with cyclodextrin dimer, and L is the configuration state of inclusion sec-sec with palmitic acid not interacting with cyclodextrin dimer. M is the minimum point of the energy-distance curve of inclusion b. At the end of the scanning, the corresponding cyclodextrin molecule was removed completely.

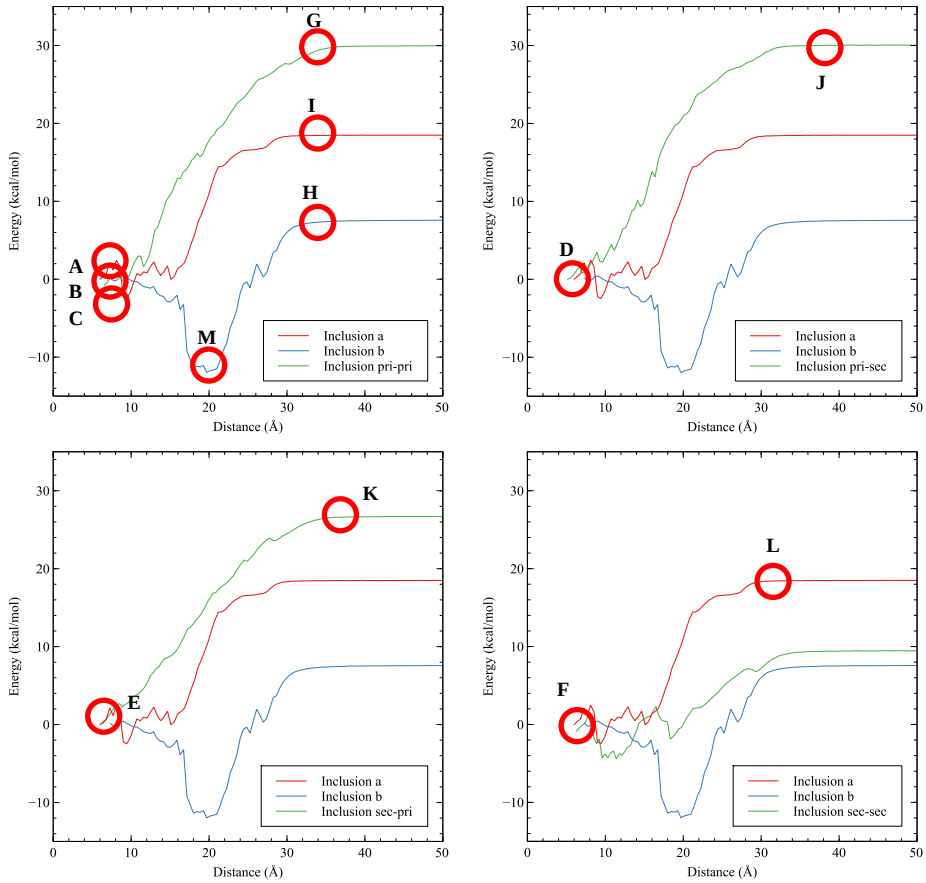

Figure 119. The average energy-distance curve of monomer and dimer inclusion.

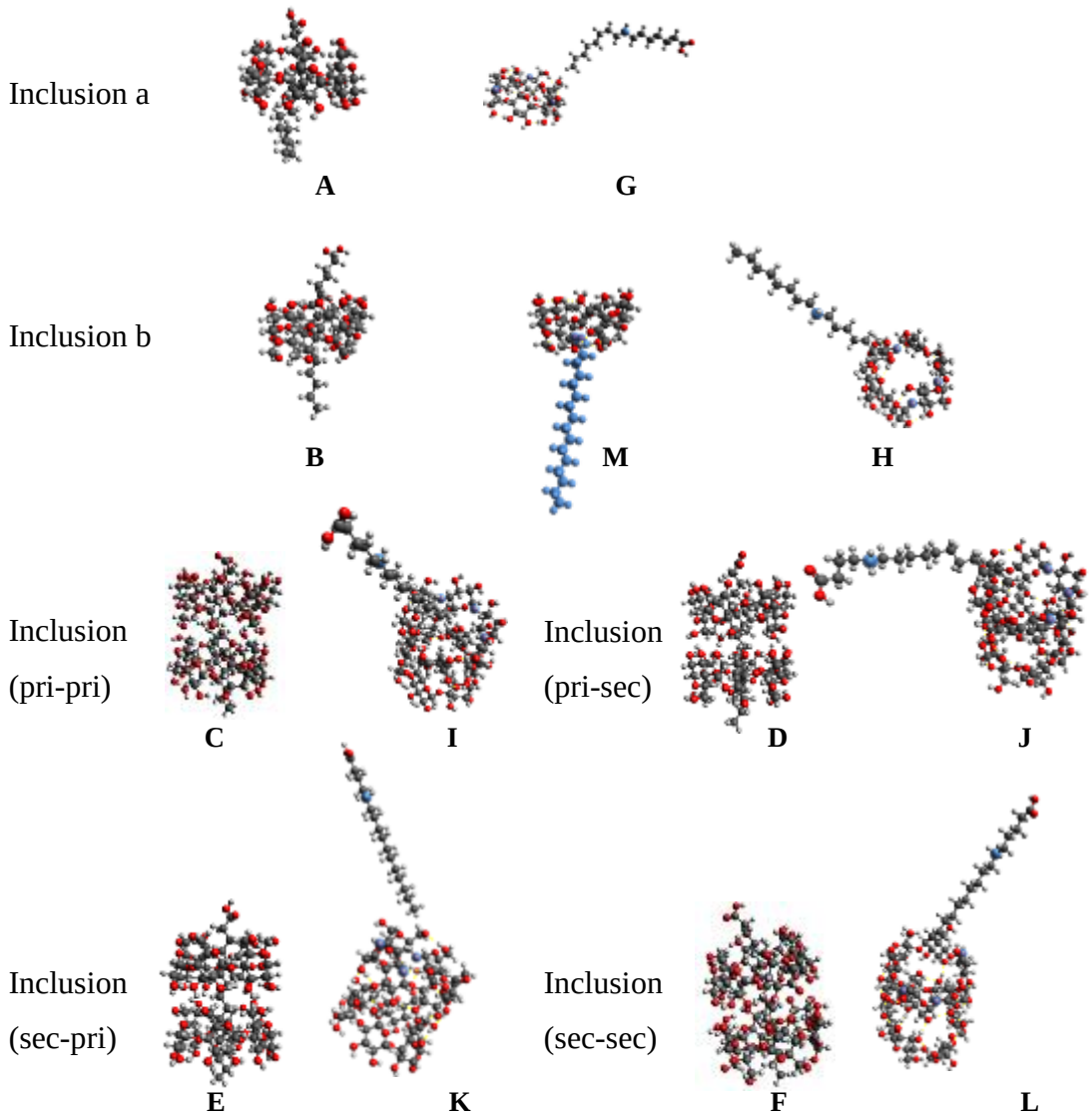

Figure 120. The conformation of the marked configuration states (The point A-M depicted in **Figure 119**)

At the conformation of start structure A and B, the palmitic acid (in either inclusion a or inclusion b) was completely laid in the cave of cyclodextrin; At the conformation of starting structure C, D, E, and F, the palmitic acid in every start structure conformation was laid entirely in the cave of the dimer of cyclodextrins. The palmitic acid didn't interact with the cyclodextrin molecule at the configuration states G, H, I, J, K, and L. At the configuration states M, the carboxyl group of palmitic acid interacts with the hydroxyl group of cyclodextrin molecule.

There are a set of differences between the extraction energies that can be obtained from the monomer and dimer inclusion complex. By comparing the extraction energy of monomer and dimer inclusion complex of palmitic acid, for the monomer inclusion complex of palmitic

acid, the extraction energy of inclusion a is 18.46 kcal/mol, and the extraction energy of inclusion b is 20.49 kcal/mol separately. In contrast, for the dimer inclusion complex of palmitic acid, the extraction energy of inclusion pri-pri is 30.71 kcal/mol, the extraction energy of inclusion pri-sec is 30.03 kcal/mol, the extraction energy of inclusion sec-pri is 26.60 kcal/mol, and the extraction energy of inclusion sec-sec is 10.12 kcal/mol. In most situations (like inclusion pri-pri, inclusion pri-sec and inclusion sec-pri), the extraction energy of the dimer inclusion complex of palmitic acid is higher than the monomer inclusion

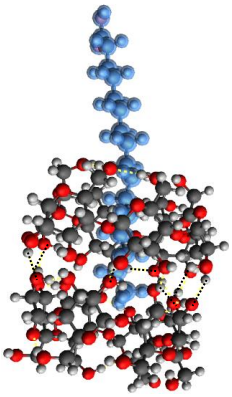

complex of palmitic acid. In contrast, the extraction energy of inclusion sec-sec is lower than other inclusion complexes.

Figure 121. The hydrogen bonds between the two cyclodextrins of inclusion sec-sec (black dash line indicated the hydrogen bond)

In inclusion sec-sec, the extra hydrogen bonds between the cyclodextrins of the dimer can form a more stable dimer, and the extra stability of the dimer can decrease the system energy. So the extraction energy of inclusion sec-sec is lower than other inclusions (10.12 kcal/mol). (see **Figure 121**)

During the process of the scanning as the envisioned plan, we can remove the cyclodextrin molecule one by one from the hexasaccharide-cyclodextrin complex. Because three palmitic acid branches were attached to the hexasaccharide molecule, when we performed scannings of the same starting structure, there are three possible cyclodextrin molecules that can be removed in the incoming scannings. Three different extraction energies of the same hexasaccharide cyclodextrin molecule can be obtained via three distinct pathways of scannings. After comparing the obtained value of the extraction energy, we can choose the most reasonable pathway to obtain the target structure utilized in the subsequent scanning. By repeating this process, we can find a suitable mechanism pathway for removing the cyclodextrin molecule that followed the minimum energy principle. Additionally, we can remove all the cyclodextrins by employing this method.

We can perform the scanning and get the corresponding extraction energy can be obtained via every scanning process. Based on the given value of the extraction energy, the order of removing cyclodextrin molecules from the cyclodextrin-hexasaccharide complex was as depicted in **Figure 122**. The pathway of scannings and these extraction energies have systematically been listed in **Figures 122** (under the corresponding removing CD molecule via scanning).

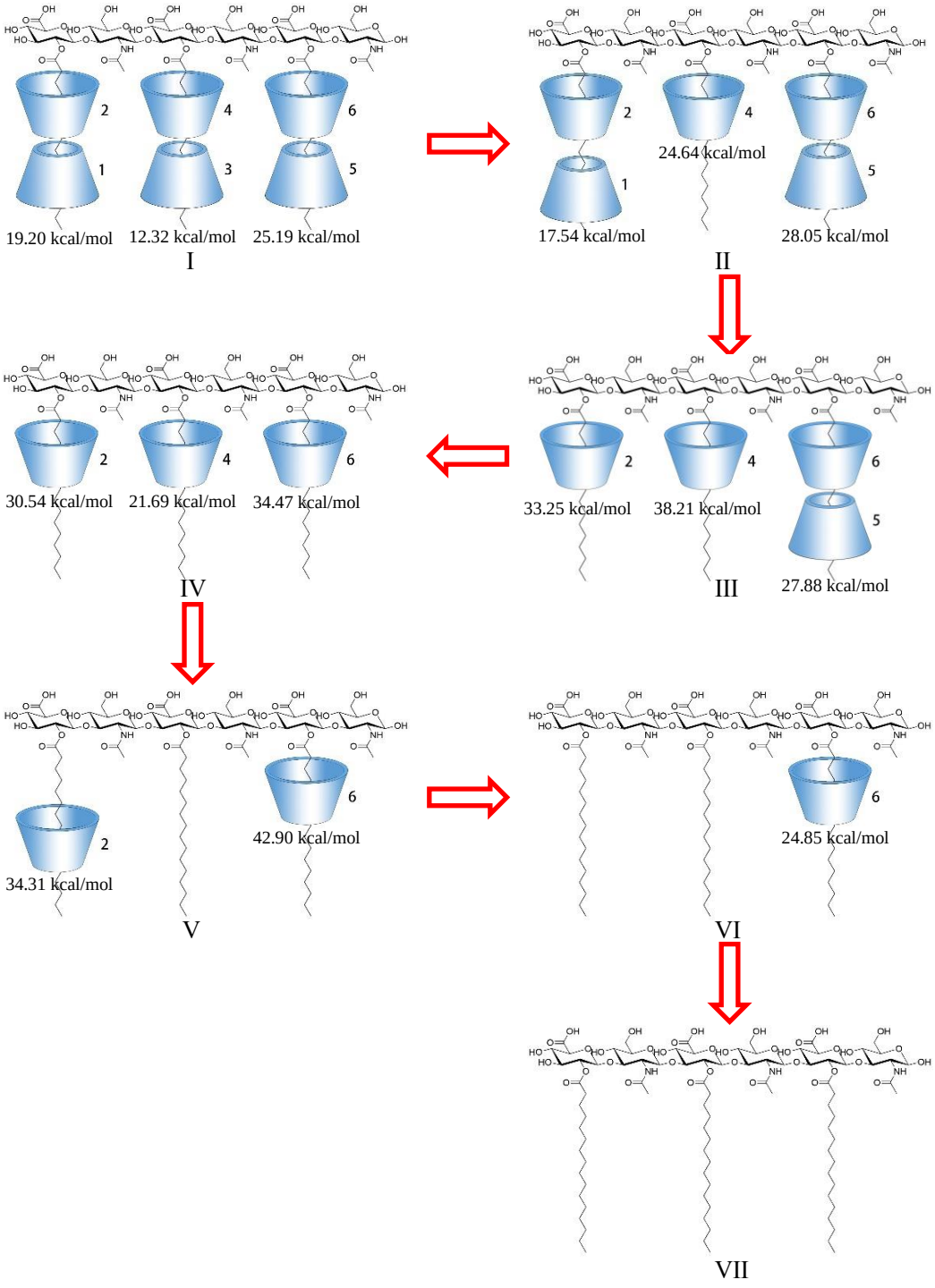

Figure 122. A proposed reasonable pathway of removing the cyclodextrin molecules

After performing the scanning of the hexasaccharide-cyclodextrin complex I, when we removed cyclodextrin #3, we can get the lowest energy structure of scannings of hexasaccharide-cyclodextrin complex I. The minimum value of the extraction energy is 12.32 kcal/mol.

At the minimum point of the scannings of starting structure I (see **Figure 123**), the secondary hydroxyl groups of cyclodextrin #5 and cyclodextrin #3 can form hydrogen bonds. Cyclodextrin #5 and cyclodextrin #4 were still at the end of the lipid chain. Cyclodextrin #3 was completely separated from the lipid chain. Additionally, the carboxyl group of the palmitic acid was still near cyclodextrin #4.

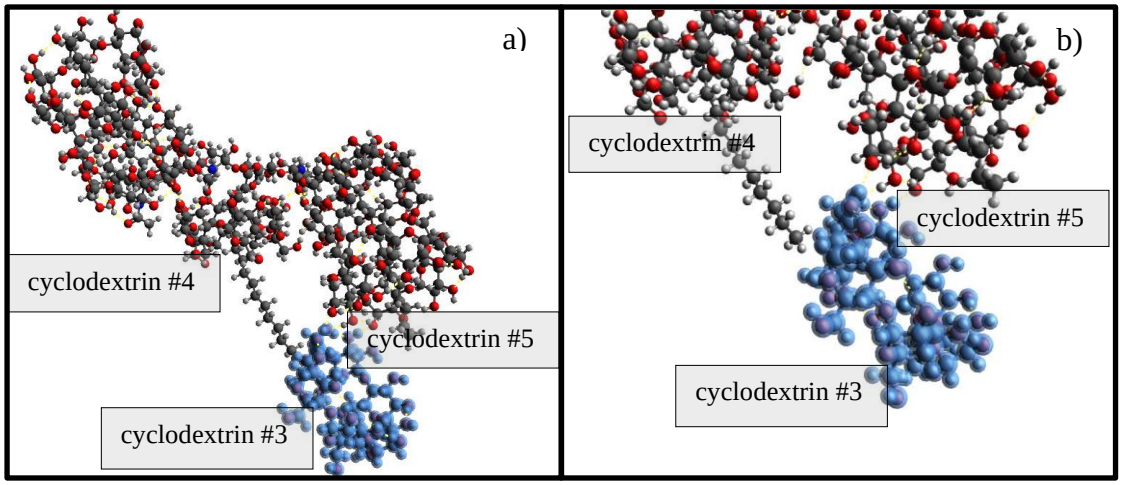

Figure 123. a) The structure of the minimum point of hexasaccharide cyclodextrin complex I. b) The position of cyclodextrin #5 and cyclodextrin #4 relative to the removed cyclodextrin #3. (The removed cyclodextrin #3 is colored in blue for clarity, and the black dash line indicates the hydrogen bond between cyclodextrin #3 and cyclodextrin #5)

The suitable result of these scannings of starting structure I was the hexasaccharide-cyclodextrin complex II. It can be employed as the starting structure of the next scannings. The corresponding minimum value of the extraction energy is 17.54 kcal/mol (when we removed cyclodextrin # 1 from starting structure II).

At minimum points of the scannings of structure II (see **Figure 124**), the secondary hydroxyl groups of cyclodextrin #2 and cyclodextrin #1 can form hydrogen bonds. Considering the interaction between cyclodextrin #2 and cyclodextrin #1, the movement of cyclodextrin #1 made cyclodextrin #2 move significantly, but cyclodextrin #2 was still around

the alkyl chain. Finally, cyclodextrin #1 was removed completely from the lipid chain as the distance between cyclodextrin # 1 and the palmitic acid residue increased.

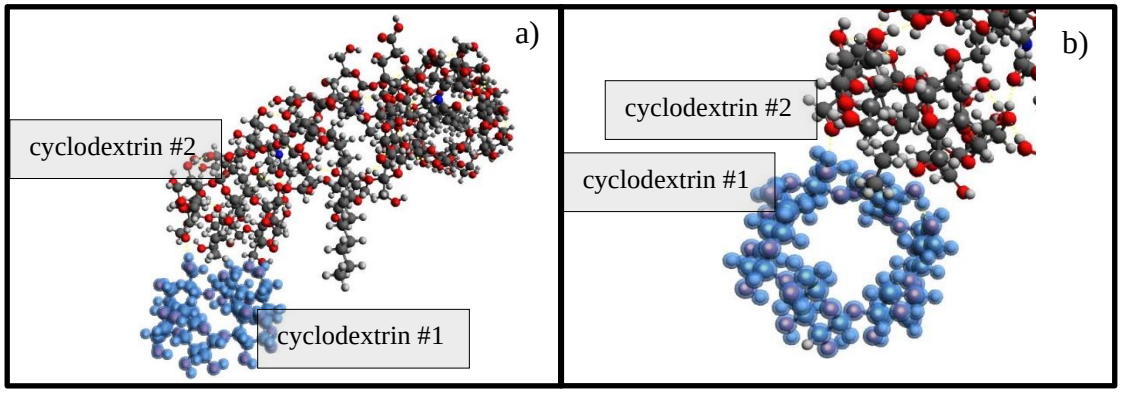

Figure 124. a) The structure of the minimum points of hexasaccharide cyclodextrin complex II. b) The position of chitosan residue relative to the removed cyclodextrin #1. (The removed cyclodextrin #1 is colored in blue for clarity, and the black dash line indicates the hydrogen bond between cyclodextrin #1 and cyclodextrin #2)

After performing the scannings of the hexasaccharide-cyclodextrin complex, when we removed cyclodextrin #5, we can get the lowest energy structure of scannings of hexasaccharide-cyclodextrin complex IV. The minimum value of the extraction energy is 27.88 kcal/mol.

At the minimum point of the scannings of structure III (**Figure 125**), when cyclodextrin #5 was removed from the hexasaccharide-cyclodextrin complex III, because of the interaction between the hydroxyl groups of cyclodextrin #5 and cyclodextrin #6, cyclodextrin #6 moved slightly and was still around the lipid chain. Finally, cyclodextrin #5 was removed from the system completely.

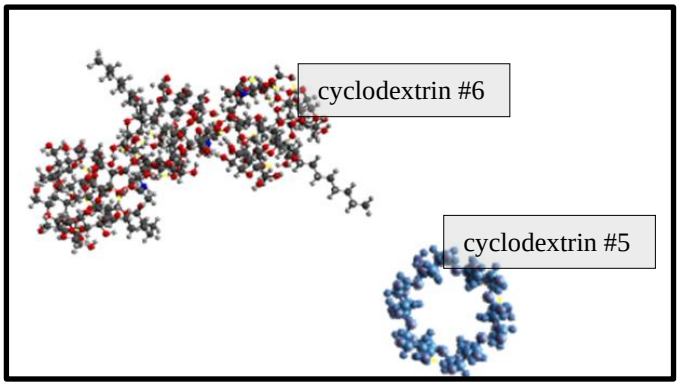

Figure 125. The structure of the minimum points of hexasaccharide cyclodextrin complex III.

The following scannings of hexasaccharide-cyclodextrin complex IV can get the

hexasaccharide-cyclodextrin complex V as the lowest energy structure of scannings of hexasaccharide-cyclodextrin complex IV. When we remove cyclodextrin # 4 from starting structure IV, the corresponding minimum value of the extraction energy is 21.69 kcal/mol.

At the minimum point of the scannings of structure IV (see **Figure 126**), the hydroxyl groups of cyclodextrin #4 and cyclodextrin #6 can form hydrogen bonds. However, the distance of the hydroxyl group of cyclodextrin #2 and cyclodextrin #4 is so long that they can not form the hydrogen bond. At the minimum point, cyclodextrin #4 was removed from the end of the lipid chain completely.

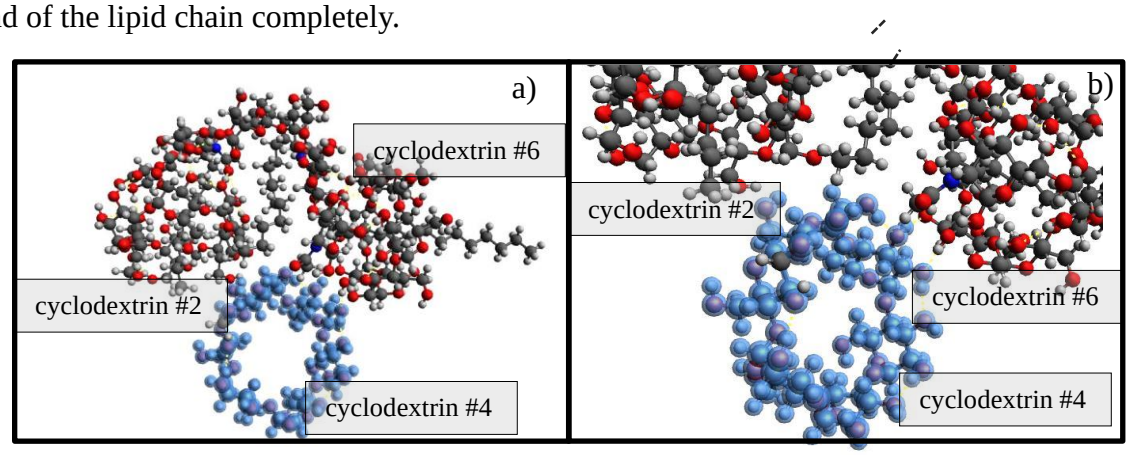

Figure 126. a) The structure of the minimum point of hexasaccharide cyclodextrin complex (The removed cyclodextrin #4 is colored in blue for clarity.) b) The position of cyclodextrin #2 and cyclodextrin #6 relative to the removed cyclodextrin #4 (The removed cyclodextrin #4 is colored in blue for clarity and the black dash line indicates the hydrogen bond between cyclodextrin #4 and cyclodextrin #6)

The following scannings of hexasaccharide-cyclodextrin complex V can get the hexasaccharide-cyclodextrin complex VI as the lowest energy structure of scannings of hexasaccharide-cyclodextrin complex V. When we removed cyclodextrin # 2 from starting structure V, the corresponding minimum value of the extraction energy is 34.31 kcal/mol.

In the minimum point of the scannings of starting structure V, cyclodextrin #2 is separated from the lipid chain completely and moves closed to cyclodextrin #6 and the chitosan residue. The hydroxyl groups of cyclodextrin #2 can form hydrogen bonds with cyclodextrin #6 and chitosan residue separately. At this time, the movement of cyclodextrin #2 causes the movement of cyclodextrin #6, and cyclodextrin #6 is still near the carboxyl group of the lipid chain. The conformation of the alkyl chains with no cyclodextrin becomes folded. (**Figure 127**)

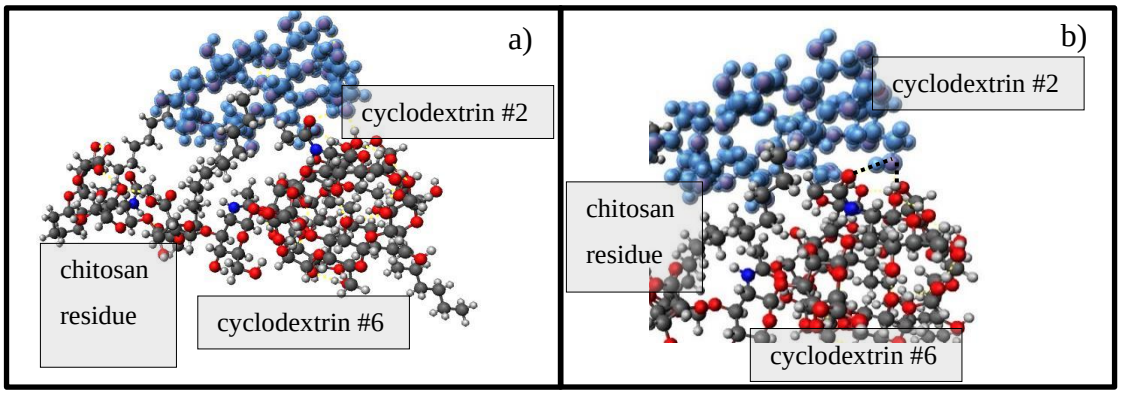

Figure 127. a) The structure of the minimum point of the hexasaccharide-cyclodextrin complex. b) The position of CD#4 and chitosan residue relative to the removed CD#2. (The removed cyclodextrin CD#2 is colored in blue for clarity, and the black dash line indicates the hydrogen bond between CD#4 and CD#2

The following scannings of hexasaccharide-cyclodextrin complex VI can get the hexasaccharide compound VII as the final structure of scannings of hexasaccharide-cyclodextrin complex VI. When we remove cyclodextrin # 2 from starting structure V, the corresponding minimum value of the extraction energy is 24.85 kcal/mol.

In the minimum point of the scannings of starting structure VI, the hydroxyl groups of cyclodextrin #6 can form several hydrogen bonds with the chitosan residue through its hydroxyl group. Cyclodextrin #6 is still towards the end of the lipid chain at this point. With an increase in the distance between cyclodextrin #6 and the palmitic acid residue, cyclodextrin #6 becomes entirely isolated from the lipid chain. (see **Figure 128.**)

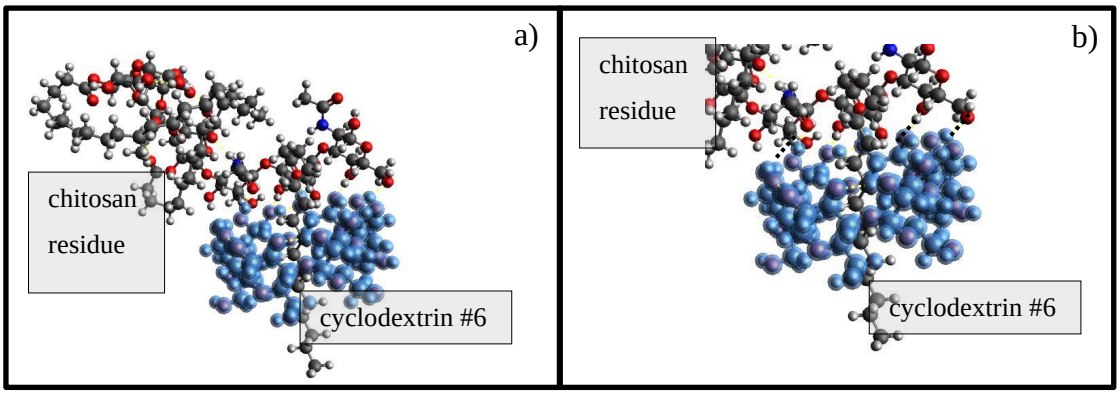

Figure 128. a) The structure of the minimum point of hexasaccharide cyclodextrin complex. b) The position of chitosan residue relative to the removed cyclodextrin #6. (The removed cyclodextrin #6 is colored in blue for clarity, and the black dash line indicates the hydrogen bond between cyclodextrin #6 and chitosan residue.)

The appropriate pathway of removing all the cyclodextrin molecules from the hexasaccharide-cyclodextrin complex can be found via this method of scanning.

Conclusion:

Based on the obtained extraction energy, there is a plausible mechanism that allows us to remove cyclodextrin molecules one by one to get the branched saccharide without cyclodextrin molecules. It helps us have a better understanding of the reaction mechanism of the formation of the hexasaccharide-cyclodextrin complex.

On the other hand, the cooperativity of hydrogen bonds is not only able to have an effect on the extraction energies of the hexasaccharide-cyclodextrin complex but is also able to explain the stability of these conformations of intermediates. We hope that such cooperativity of hydrogen bond would be useful for providing insights into the mechanism of the extraction of cyclodextrin from hexasaccharide-cyclodextrin complex and inclusion complex. For instance, a partial reason for the transformation of the conformation of the hexasaccharide-cyclodextrin complex, which was caused by the cooperative movement of two cyclodextrin molecules (see **Figure 127**), can lie in the interaction of the intermolecular hydrogen bonds between cyclodextrin molecules. We think that the findings of this study will be helpful for such detailed research in future studies.

General Conclusion

Visible-light photoredox catalysis has proven to be an effective redox process for the production of radical species. This catalytic method, which employs visible light, has a number of advantages in terms of a mild, selective, and environmentally friendly process. Alkyl bis-catecholato silicates have proven to be a promising precursor of radical, which can participate in the C-C bond formation. The transformation has a wide range, and it seems that the process is tolerant to the presence of different functional groups

In the first part, we have completed an extensive investigation of phenyl silicates with substituted catecholate ligands. The reactivity of the newly synthesized phenyl silicates was studied. It was found that the phenyl radical was produced and trapped when the catecholate moiety was substituted, particularly with the 4-cyanocatecholato ligand. These findings were supported by computational investigations. According to the second section, the ability of alkyl bis-catecholate silicates to be easily oxidized gives the opportunity to use them in different redox systems. Through single electron transfer, organometallic complexes containing non-innocent ligands can contribute to radical production. Oxidation of silicates by a bis-iminobenzoquinone copper(II) complex has shown encouraging initial results, but further research is needed.

In the third part, we suggest a feasible mechanism based on the calculated extraction energy that enables us to remove cyclodextrin molecules one by one to get the branched saccharide without cyclodextrin molecules. It contributes to a better understanding of the reaction process of extracting cyclodextrin molecules from the hexasaccharide-cyclodextrin complex. The cooperativity of hydrogen bonds is considered during the whole process. It not only affects the extraction energies of the hexasaccharide-cyclodextrin complex but also explains the stability of these intermediate conformations.

Single electron transfer oxidation of bis-catecholato silicates for the formation of alkyl and aryl radicals. Computational study of palmitic acid interactions with various types of cyclodextrins.

Abstract: The radical-mediated reactions provide a powerful and efficient tool to synthesize challenging organic molecules relying on novel radical precursors. The application of radical-medicated reactions using bis-catecholato silicates as substrate in photoredox catalysis gains sustained attention from chemists because of their high synthetic potential ane their environment-friendliness. We designed and prepared phenyl silicates with substituted catecholate ligand, which could undergo photooxidation to generate phenyl radical. The application of bis-catecholato silicates can be extended to a redox non-innocent system like bis-iminobenzoquinone copper(II) complex. The third part of this thesis has focused explore the interaction between palmitic acid and various types of cyclodextrins. We suggest a feasible mechanism based on the calculated extraction energy

Keywords: bis-catecholato silicates, photoredox catalysis, non-innocent ligand, cyclodextrin

Oxydation par transfert monoélectronique de bis-catécholato silicates pour la formation de radicaux alkyle et aryle. Étude computationnelle des interactions de l'acide palmitique avec différents types de cyclodextrine.

Résumé : Les réactions radicalaires constituent un outil puissant et efficace pour synthétiser des molécules organiques complexes à partir de nouveaux précurseurs radicalaires. Dans ce cadre, les chimistes se sont interessés à l’utilisation des bis-catécholato silicates comme substrats en catalyse photoredox en raison de leur fort potentiel synthétique et pour un meilleur respect de l'environnement. Nous avons alors conçu et préparé des silicates de phényle avec un ligand catécholate diversement substitué, pouvant subir une photooxydation pour générer un radical phényle. Les bis-catécholato silicates d’alkyles peuvent être oxydés par un système redox non-innocent comme les complexes bis-iminobenzoquinone cuivre(II). La troisième partie de cette thèse s'est attachée à explorer l'interaction entre l'acide palmitique et différents types de cyclodextrines. Nous suggérons un mécanisme basé sur l'énergie d'extraction calculée.

Mots clés : bis-catécholato silicates, catalyse photoredox, ligand non-innocent, cyclodextrine